Tectonic-Erosion Interactions: Insights from the paleo-drainage of the Brahmaputra River

Thesis submitted in accordance with the requirements of Lancaster University for the degree of Doctor of Philosophy

Gwladys B. C. Govin

Supervision: **Yani Najman**, Lancaster Environment Centre

Co-supervision: **Peter van der Beek**, ISTerre (Grenoble, France)

Pascale Huyghe, ISTerre (Grenoble, France)

May 2017

ABSTRACT

This thesis investigates the interactions between tectonics and erosion in the eastern Himalaya through the study of paleo-Brahmaputra deposits in the foreland basin. Sediment depositional dating of two sedimentary sections is performed using magnetostratigraphy, apatite fission-track and luminescence dating. Provenance analysis using zircon and apatite U-Pb dating allows the reconstruction of the Miocene-Quaternary paleo-drainage of the Brahmaputra River and the documentation of the tectonic evolution of two poorly understood Himalayan features: the Shillong Plateau and the Namche Barwa Syntaxis.

The Shillong Plateau is the only elevated topography in the Himalayan foreland and the timing of its surface uplift is debated. Decoupling between of the time of rock exhumation and surface uplift has been explained by differences in rock erodibilities of the plateau between the Shillong Precambrian basement and the overlying Cenozoic sedimentary rock. New detrital zircon U-Pb data and lithospheric stress field modelling presented here date the rise of the Plateau between 5.2 Ma and 4.4 Ma leading to the redirection of the Brahmaputra River at that time, and the role of tectonics in the rise of the plateau is invoked.

The Namche Barwa syntaxis is located at the eastern Himalayan termination and its development is widely debated. It has been subjected to anomalously young (<10 Ma) peak metamorphism, and unusually high exhumation rates (up to 10 mm/yr), in comparison with the Himalayan main arc of the orogen. However, the timing of the onset of rapid exhumation of the Namche Barwa syntaxis is poorly constrained (between 10 and 3 Ma). Focusing on the proximal detrital record of material eroded from the syntaxis, new rutile U-Pb, white-mica $^{40}Ar/^{39}Ar$ and zircon fission-track data, together with published data are incorporated in a thermokinematic model which suggests an older onset (>10 Ma) of rapid exhumation, and at high but not extreme rates (<5 mm/yr).

THESIS STRUCTURE

This manuscript is a thesis by papers divided into six sections. These is an introduction followed by four scientific papers published, submitted or in preparation for submission, with a discussion incorporating these four chapters in an overall conclusion. The supplementary material provided presents detailed methodology and data tables for each paper. Constructed from two field areas each with their respective research questions, this thesis contains two sub-projects which are linked together in the introduction and the discussion sections. Chapters 1 and 2 focus on the Shillong Plateau region and chapters 3 and 4 on the eastern syntaxis. This paragraph provides information on the structure, a brief summary of the content and the contribution of the author for each chapter.

Introduction – This chapter provides a broad overview of the nature and the geological history of the Himalayan orogeny including an explanation of the significance of this study in the perspective of developing our understanding of the processes involved in the Himalayan orogenic evolution. The objectives of the present thesis are described and followed by a description of the study areas and a summary of the approach and methods used as part of this study. Parts of this chapter are inspired or issued from Robert (2008), Henderson (2010), Chirouze (2011), Abrahami (2015) and (Mascle et al., 2010).

Chapter 1 – Late Miocene-Pleistocene evolution of India-Eurasia convergence partitioning between the Bhutan Himalaya and the Shillong Plateau: New evidences from foreland basin deposits along the Dungsam Chu section, eastern Bhutan. Paper by Coutand, I.; Barrier, L.; Govin, G.; et al. published in 2016 in *Tectonics* (DOI: 10.1002/2016TC004258). Focusing on a foreland basin Siwalik sediment section exposed to the north of the Shillong plateau in south-eastern Bhutan, this chapter uses a combination of detailed sedimentology, palynology, apatite fission-track, vitrinite reflectance and magnetostratigraphy analyses to reconstruct the environment of deposition of these sedimentary rocks through time. The outcomes of this study are related to the rise of the Shillong Plateau and its potential climatic consequences. It constitutes a relevant introduction to, and provides the depositional dating of the sedimentary rocks also investigated in chapter 2. The author of the thesis (third author of the publication) collected and analysed the magnetostratigraphic samples of the upper part of the studied sedimentary section (samples SA1 to SA140). The same author has interpreted the magnetostratigraphic results from the entire section, including the lower part of the section which was sampled and analysed prior to the start of the Ph.D. The magnetostratigraphic correlations and the writing of the magnetostratigraphic section have also

been done by G. Govin. G. Govin also helped in the use of Qupydon software to decipher the best correlation and contributed to the writing of the entire paper manuscript. The preferred correlation of this publication is the Qupydon best correlation; however the third author prefers to rely on correlation C, which is the best manual correlation, the closest from the Qupydon best correlation. The reason for this preference is the more realistic correlation of Chrons in the upper part of the section using the manual correlation (see Appendix V). The later correlation is therefore selected for the subsequent study of chapter 2.

Chapter 2 - **Timing and mechanism of the rise of the Shillong Plateau in the Himalayan foreland.** Paper by Govin, G.; Najman, Y.; Copley, A.; et al. submitted twice to *Geology*, each time rejected with invited resubmission. The last rejection dates from April 2017 and the reviewer's main comments mostly relate to a request to rewrite the introduction to help a broader readership understand the wider significance of the work. Resubmission is planned post thesis submission. This manuscript investigates the time and mechanism of Shillong plateau topographic uplift. It provides the first precise dating of the Shillong topographic growth and a novel explanation for the transition from rock exhumation matched by erosion to surface uplift. The dating of the latter transition has been performed using an original approach of provenance analysis using zircon U-Pb dating in the Dungsam Chu sedimentary section (dated by magnetostratigraphy in chapter 1). The results provide evidence of a drainage reorganisation due to the rise of the Plateau such that the Brahmaputra River has been redirected due to the Shillong Plateau uplift. The cause of the transition from exhumation to surface uplift of the Shillong Plateau has previously only been explained by a difference in erodibility of the sedimentary rocks overlying the plateau and the hard Shillong Precambrian bedrock. This study proposes another explanation and highlights the role of another factor in the mechanism of this transition by modelling lithospheric stresses in the Shillong region. The first author has collected and analysed the samples, interpreted the results, conceived the model of the evolution of the Brahmaputra River incorporating data from this study and published data. The same author has written the manuscript, with the exception of the lithospheric stresses modelling part developed by A. Copley.

Chapter 3 - **Paleo-drainage evolution and rapid exhumation of the Namche Barwa Syntaxis recorded in the Siwaliks of the easternmost Himalaya (Arunachal Pradesh, India).** This manuscript has been submitted in April 2017 to *American Journal of Science* by Govin, G., Najman, Y., Dupont-Nivet, G. et al. This chapter investigates the Late Neogene-Quaternary drainage evolution in the syntaxis region. Using apatite fission-track, magnetostratigraphy and luminescence dating, this study

constrains the depositional age frame and presents detailed sedimentology of the Siwalik sedimentary rocks the most proximal to the eastern syntaxis. The provenance analysis of these deposits has been performed using apatite and zircon U-Pb. The first author has collected the samples and realised the sedimentological descriptions and interpretations. G. Govin also collected the magnetostratigraphic and zircon U-Pb data and interpreted the entire data-set (including the Luminescence and apatite double data provided by the co-authors P. O'Sullivan and C. Mark) and written the manuscript. This chapter constitutes the basis of the study for the chapter 4, as it describes and dates the Sibo-Remi-Siang sedimentary section and constrains the provenance of these deposits.

Chapter 4 – Onset of rapid exhumation in the Namche Barwa syntaxis. This study has been conducted by Govin, G., Najman, Y., van der Beek, P et al., and will be submitted to a broad audience journal in the near future. It has been presented in a talk format by the first author at the EGU general assembly 2017 (April 2017). This manuscript investigates the debated onset of the rapid exhumation of the Namche Barwa syntaxis using thermochronological and geochronological detrital dating of the Sibo-Remi-Siang section sedimentary rocks. Detrital zircon fission-track, white-mica ^{40}Ar-^{39}Ar and rutile U-Pb data have been acquired and interpreted by the first author who has also collected and prepared the samples. The results, along with published data from bedrock and detrital data from the eastern syntaxis region have been incorporated in a 1D version of the thermokinematic model *Pecube*, to reconstruct the syntaxis evolution from Miocene to present day. The modelling part of the chapter has been performed by P. van der Beek, and the manuscript, including the model interpretations, written by the first author.

Discussion - This final chapter collectively summarises, discusses and concludes the major results and discoveries of the preceding papers. It also suggests the nature of potential further work relevant to solve the new research questions that arise from this thesis.

TABLE OF CONTENT

TABLE OF FIGURES

TABLE OF TABLES

INTRODUCTION

1. THE HIMALAYA

1.1. Major challenges in studying the Himalaya

1.1.1. Geography of the Himalaya

The Himalayan arc is the largest and highest modern-day mountain belt on Earth. With a width of 160 to 320 km, the Himalayan belt extends in an E-W arc shape with a length of ~2400 km (Fig. 1). The Himalaya hosts India, Tibet, Nepal, Bhutan, Pakistan and Afghanistan. At least the 100 highest summits on the planet are Himalayan with Mount Everest as the highest (8848 m) in Nepal (and Tibet), K2 (8610 m) in Pakistan occupying second position and Kangchenjunga (8586 m) on the Nepal-Indian boundary with the third highest position. Adjacent to the belt in the north lies the Tibetan plateau at an elevation averaging more than 4500 m and stretching over ~1000 km north-south and 2500 km east-west. The Himalayan belt is drained by two major river systems, both sourced in Mount Kailash in Tibet, north of Nepal. To the west of this summit, the Indus flows westward along the India-Asia suture zone, north of the Himalayan belt before crossing the range southward at the western Himalayan termination, to reach the foreland basin and the Indus Fan in the Arabian Sea. To the east of Mount Kailash, the Yarlung-Tsangpo flows eastward along the suture zone, along the southern edge of the Tibetan Plateau, before crossing the Himalayan range at its eastern tip, then drains the eastern Himalayan foreland basin as the Brahmaputra River before reaching the Bengal Fan in the Indian Ocean.

Fig. 1: *Geography and drainage map of the Himalayan range. Figure from* https://goo.gl/images/QCaSuL

1.1.2. Challenges for Himalayan inhabitants

The Himalayan inhabitants face challenges of various natures at the present day and in the future. The vast remoteness of many Himalayan villages makes living conditions particularly arduous, especially in the modern world globalisation context. The diversity of Himalayan societies is strongly influenced by religions and cultural traditions. Although Buddhism, Hinduism, and Islam are the most popular influences, the lifestyle of many Himalayan communities has developed in symbiosis with their environment. The culture and faith of most Himalayan people involve the surroundings, with many legends and holy places (Fig. 2). For example, Mount Kailash, located in the southern Tibetan Plateau is the centre of the Buddhist universe. The Tantric Buddhists regard Mount Kailash as home of the supreme blissed Buddha Demchok. For the Hindus, Mount Kailash is where “Lord Shiva”, the destroyer of evil, is in perpetual meditation with his Shakti Parvati, translated as “daughter of mountains”. Additionally, the mountain is at the heart of six mountain ranges symbolizing a lotus, and represents the pillar of the world with four faces legendary known as made of crystal, ruby, gold, and lapis lazuli. The Bön, a Tibetan religion, regard the mystical Mount Kailash as the seat of all spiritual power. Every year, thousands of people make a pilgrimage to Kailash, following a tradition thousands of years old. Climbing on the Mount Kailash is a dire sin for all religions that worship the mountain which is believed to lead to heaven. The Chinese authorized a Spanish team to climb Mont Kailash in 2001, but it provoked international disapproval which led to the prohibition of any attempt to climb the peak. Reinhold Messner said: "If we conquer this mountain, then we conquer something in people's souls”. This illustrates how threatened are the thousands year old traditions in Himalayan regions due to the fast and recent expansion of tourism. As well as the introduction of western technologies, mass tourism has deep influence on local communities and their environment, in some instance causing unfortunate detrimental effects. Pollution is one on them, as for the Everest region, heavily visited and polluted by the vast increase of visiting tourists and mountaineers but also at a larger scale involving waste management difficulties in the Himalayan countries. Water is particularly sensitive to these problems, and very efficient in spreading pollution. The Asian monsoons dominate the economies of half of the global population; they are a capital factor for agriculture, transport, infrastructures and more generally for humans; they feed the rivers providing people fresh water. They are controlled by the worldwide warming climate, and their climatic impact is highly important. The devastating floods in Pakistan in 2010 attest to this global environmental sensitivity. The Himalayan civilisations and the entire Asian population are threatened by natural catastrophes and their consequences. The geo-hazards characterised by low probability and high consequence events, threaten catastrophic events. They are often focused in limited areas but their consequences can be global as growing densely

populated areas, and at a larger scale of the entire Himalayan region and its sphere of influence. For instance events such as landslides, glacial damming breakups are often limited to small scale impact. However, localised earthquakes lead to a high probability of damages at a large distance from the epicentre. The earthquake of April 2015 in Nepal and its aftershocks have impacted a large area including regions in India, China and Bangladesh, although at various intensities. The damages caused by this earthquake were also of various subsequent natures such as avalanches, landslides, and glacial dams bursting.

For these reasons, studying the Himalayan belt is of primary importance in the general perspective of understanding the processes causing increased risk. The interaction between climatic forces and topographic evolution in active mountain belts are an important sub-set of these processes. The study of geology in the Himalaya is necessary to understand the complex links and feedbacks between climate, topography and erosion.

Fig. 2: *Photograph of Mount Kailash from https://goo.gl/images/q1asxa*

1.1.3. Himalayan exploration history

The Himalayan belt provides a great opportunity, not only to understand ancient orogenesis and orogenic formation and development, but also to study the timing and sequence of the Himalayan collision and convergence events and how they interact with other aspects of the Earth system. Like the mountaineering expeditions, the scientific expeditions began in the 20th century in the

Himalayas. A famous Swiss geologist, Augusto Gansser (1919-2012) started to explore the Himalayas in 1936. The report of his detailed studies was published in 1939, entitled “Central Himalaya – Geological observations of the Swiss Expedition 1936”. From these various discoveries such as the Indus suture zone concept and the first geological map of the Himalayas (Fig. 3), including numerous publications, Augusto Gansser received the title of “Baba-ye Himalaya” (father of the Himalaya) from Peshawar University in Pakistan. Augusto Gansser opened the route to nearly a century of Himalayan geological research, of which knowledge is still to be learned from these fascinating mountains.

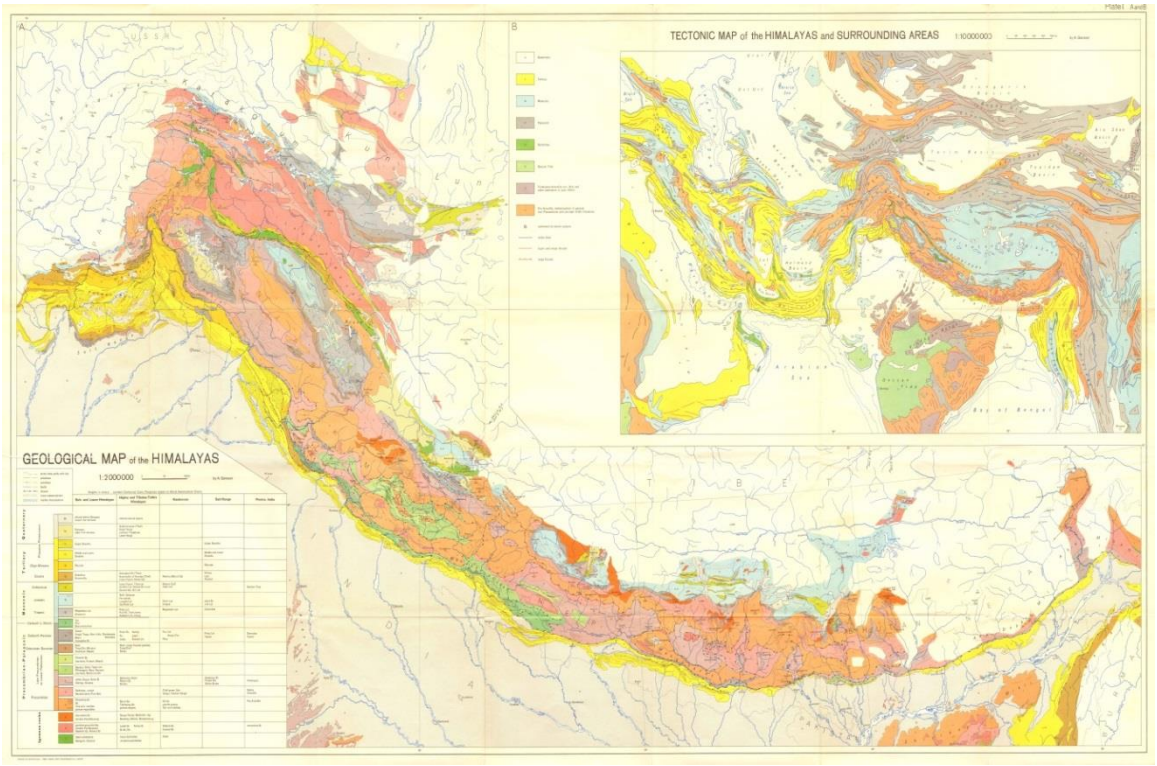

Fig. 3: *Geological map of the Himalaya, from Augusto Gansser (1964) - https://goo.gl/images/mFYijJ*

1.2. The Himalayan belt as a natural laboratory

1.2.1. Tectonics, climate and erosion processes

The Himalayan orogen is a natural laboratory to understand mountain building and evolution, and the processes involved, through various and complementary scientific disciplines. The mountain belt’s topography results from the interaction between « internal » and « external processes » within the range. Internal processes are defined by the tectonics and the resulting continental deformation. Tectonics initiates and develops positive relief, i.e. massifs, and negative relief, i.e. basins, along major tectonic features. This relief influences the repartition of precipitation (Bookhagen and Burbank, 2006; Grujic et al., 2006; Roe, 2005) and facilitates erosion through slope

steepening. External processes are related to climate, which influence the topographic evolution with erosion and sedimentation processes, through precipitation, large scale temperature changes and the impact of climate on drainage network and vegetation (e.g. Bonnet and Crave, 2003; Bookhagen et al., 2005a; Dadson et al., 2003; Reiners et al., 2003). Feedbacks between tectonic and climate via erosion have been documented by the scientific community over the past two decades (Fig. 4). Erosion and transport of material from high elevations towards low elevations, i.e. foreland or distal basins, lead to mass redistribution at the surface Earth. The mass equilibration is associated with a isostatic rebound, which is the uplift of the continental lithosphere in the source region (Whipple, 2009).

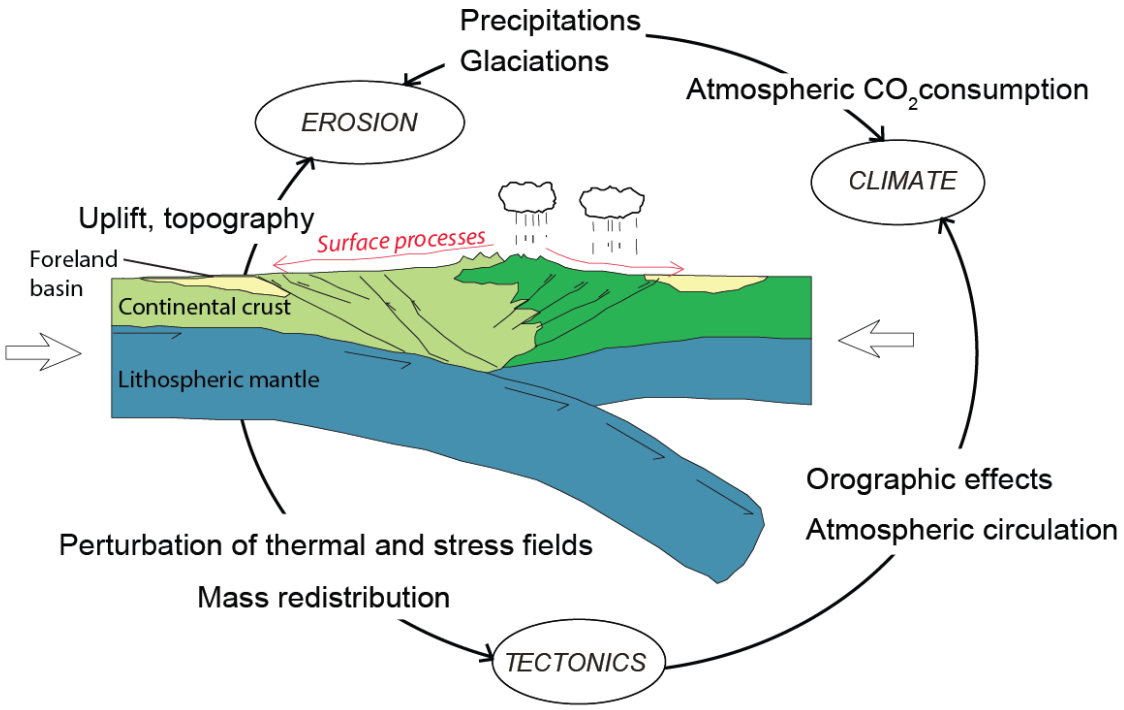

Fig. 4: *Relations between tectonics, climate and erosion, modified after Beaumont et al. (2000).*

Additionally, rock erosion and weathering influence atmospheric CO_2 concentration through two major reactions: silicates hydrolyse and carbonate dissolution. The dissolution and precipitation of carbonate rocks have a null balance at the geological scale in terms of atmospheric CO_2 consumption. However, the mean residence time of a limestone at the Earth's surface being around 500 Ma, carbonate formation is regarded as atmospheric carbonate storage at a long time scale. By contrast, silicate rocks hydrolysis is a very efficient reaction for consumption of atmospheric CO_2. This gas is one of the important greenhouse gases regulating the temperature of the atmosphere. Therefore, an increase in silicate weathering would lead to climate cooling (Raymo and Ruddiman, 1992). Through these mechanisms and chemical reactions, the erosion and alteration processes

impact on the climate. These two examples of coupling highlight the complexity of the exchanges and interactions between the different terrestrial, atmospheric and marine environments and reservoirs; and therefore the complexity of the main controlling factors: tectonics and climate via erosion (Molnar, 2009; Whipple, 2014).

Studying surface processes and their quantification is necessary to understand the evolution of the topography and the main factors involved. The Himalayan range is influenced by very active tectonic and climatic processes. Indeed, the climate in the Himalayan region is dominated by the Asian monsoon, a seasonal phenomenon which corresponds to large changes of wind directions, leading to variability in the intensity and the spread of rainfalls throughout a year. Additionally, the Himalayan range is defined in an active tectonic context, with a relatively constant convergence rate since ~12 Ma (15-20 mm.yr-1; Avouac, 2003; Mugnier et al., 2004) and a high seismic hazard with earthquakes of magnitude higher than Mw=8. The sedimentary record, material eroded from the mountain belt transported by rivers and deposited in the low relief areas such as the Himalayan foreland basin and as distal as the Indus and the Bengal Fans, represent fundamental archives of the history of their source area and their depositional environment. The study of these sediments is critical to constrain the global evolution of surface processes at the basin scale, from the source areas to the depositional areas of these sedimentary rocks; and allows us to unravel the climatic, tectonic and erosion history of the mountain range. Numerous tools have been developed to analyse in detail these sediments and to track the temporal variation of the sedimentary accumulation, flux and erosion from the source area. Petrographic, isotopic and geochronological studies allow the acquisition of quantitative information of the relative contribution relative of the different source areas (e.g. Garzanti et al., 2004; Najman, 2006). Thermochronology, geochronology and provenance studies in the sedimentary record also allow the reconstruction of the tectonic history of the mountain belt (e.g. Lang et al., 2016). The comparison of the chronology of the sedimentary records with the climatic indicators such as palynology analysis allows determination of the influence of the climatic variabilities on the studied area (Kudrass et al., 2001). The Himalayan belt represents an ideal study area to understand the interplays between tectonics, erosion and climate.

1.2.2. Topographic aspect

The Himalayan belt has a first order homogeneous topography along strike which could be divided into four main units (Bookhagen and Burbank, 2006; Duncan et al., 2003; Yin et al., 2006) (Fig. 5). The Ganga and Brahmaputra plains with very flat topographies, present elevations ranging between 100 and 200 m, with the exception of the 1800 m high Shillong Plateau, the only elevated

topography in the Himalayan foreland basin. The Himalayan foothills are located in the frontal zone of the range, they are about one hundred kilometres wide and culminate at a mean elevation of 2000 m (Bookhagen and Burbank, 2006). North of the Himalayan foothills, the altitude sharply increases, over a band wide of ~50 km. This is the high part of the belt, which comprises the highest summits and an important relief with steep slopes, its elevation averages 5000 m. The Tibetan Plateau to the north, presents a low relief of high altitude (4500-5000 m), and extends over more than 1000 km to the north. These topographic units are less well defined in the eastern and western regions of the range, where the transition between the front of the range and the high relief zone is not as well defined (Yin et al., 2006), especially in Bhutan and further to the east where the transversal slopes are smoother (Bookhagen and Burbank, 2006; Duncan et al., 2003).

1.2.3. Climatic aspect

The climate in the Himalayan region is dominated by two major atmospheric systems, the Indian Summer Monsoon (ISM) and the Westerlies (Kotlia et al., 2015). In the northern hemisphere summer, air masses enriched in moisture are transported from the Bay of Bengal towards the Himalayan range (e.g. Molnar et al., 2010). In winter, the moisture is mostly carried from the Mediterranean, Black and Caspian seas by the Westerlies (Benn and Owen, 1998; Cannon et al., 2015). The Westerlies have a stronger influence on the western Himalaya (Cannon et al., 2015; Caves et al., 2015; Kotlia et al., 2015), whereas the eastern Himalaya, more proximal to the Bay of Bengal, is characterised by high humidity (Bookhagen and Burbank, 2010). On the Indian continent, the Westerlies are called the dry season or the winter monsoon whereas the ISM is called the wet season and constitutes 60 to 90% of the annual precipitations in the range (Bookhagen and Burbank, 2010) and in the plain (Rao, 1973). The initiation of the ISM has been suggested to occur at the Paleogene-Neogene transition or in Late Eocene times and its temporal variations are thought to influence the erosion rates in the Himalaya (Bookhagen et al., 2005a; 2005b; Clift et al., 2008a; Clift et al., 2008b; Licht et al., 2014; Thiede et al., 2005; Thiede et al., 2004; Vance et al., 2003; Wobus et al., 2003).

1.2.4. Interplays between tectonics, climate and erosion

The Himalayan range acts as an orographic barrier and therefore has a major influence on global and local climate (Boos and Kuang, 2010; Molnar et al., 2010). Bookhagen and Burbank (2006; 2010) have studied the spatial distribution of the precipitations along the Himalayan range using satellite records over a 10 years period (1998-2007) (Fig. 5). They observed a spatial correlation between the topography of the orogen and the distribution of the precipitation (Bookhagen and Burbank, 2006;

2010). Indeed, the parts of the range presenting well defined transitions between the foothills and the high range are affected by two bands of precipitation whereas precipitation is more diffuse and better spread over the different topographic units at the eastern and western Himalayan terminations. Additionally, the results show that the southern slope of the Shillong Plateau is characterised by high precipitation.

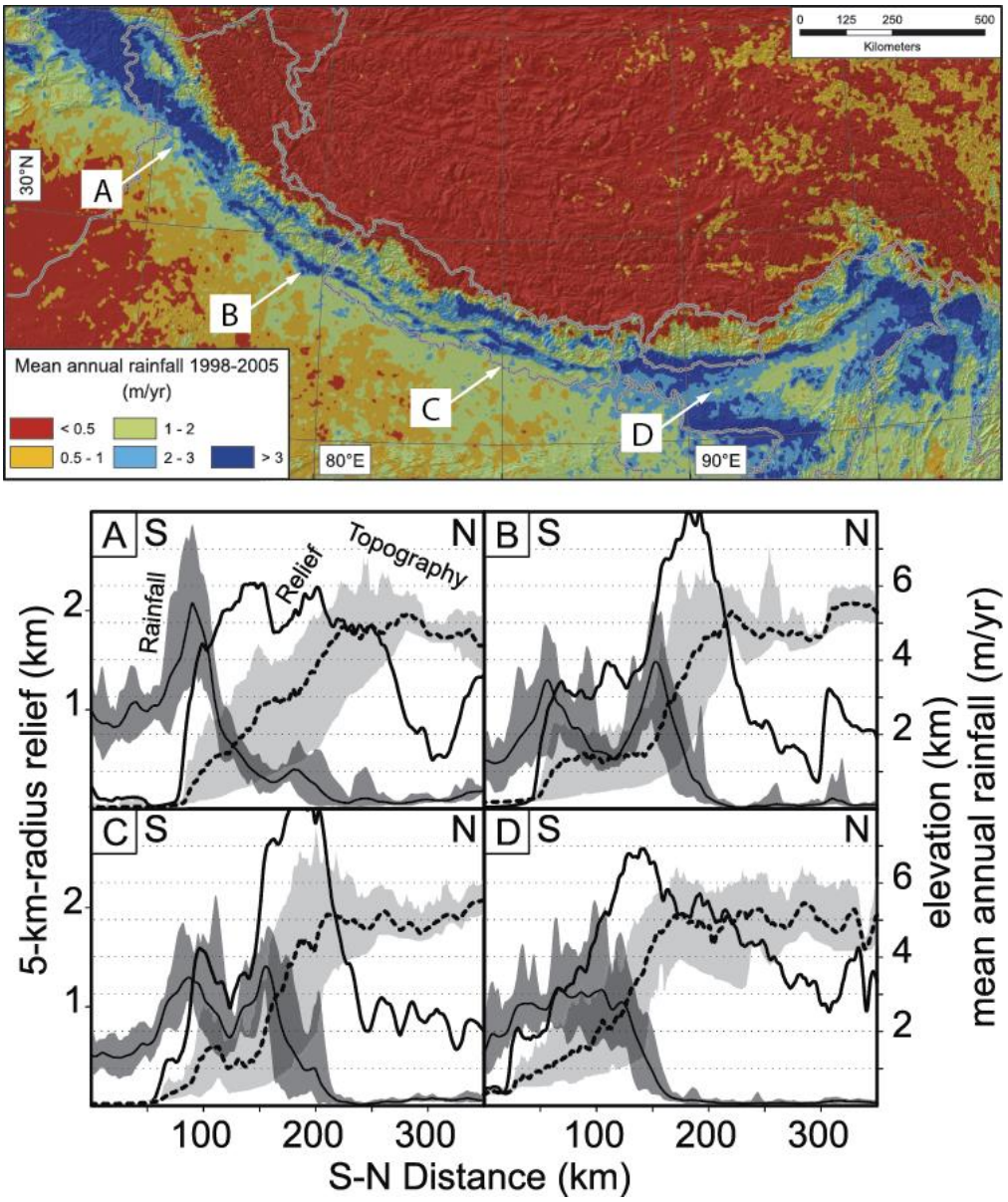

Fig. 5: *Top figure - Calibrated TRMM-based monsoon rainfall amounts averaged from January 1998 to December 2005. The data comprises instantaneous rainfall measurement with a spatial resolution of ~5 x 5 km. Bottom figure - Swath profiles running from south (S) to north (N) from the a) north-western, b) and c) central, and d) eastern Himalaya as indicated on the top figure. Shaded areas denote ±2σ ranges. Light grey shading denotes topographic and dark grey shading rainfall profiles. Heavy, black line indicates relief. (Bookhagen and Burbank, 2006)*

The extensive Himalayan river drainage network is considered to be controlling 25% of the global sediment budget (Raymo and Ruddiman, 1992). The Asian monsoon strengthening led to a higher amount of rainfall in the southern edge of the Himalaya, increasing the net discharge of the southern Himalaya. During the summer monsoon, the amount of precipitations and the river discharge are reduced in the drier region of the northern and central regions of the Himalaya. This creates semi-arid environments where much of the summer river discharge is derived from the melting of snow cover. River courses can be strongly influenced by tectonic uplift (Friend et al., 1999). The structural features and the bedrock lithologies can control river paths, the latter are likely modified by tectonic uplift during orogenic development (Stokes et al., 2008). Transverse rivers bisect large scale geological features (Oberlander, 1985), whereas rivers flowing parallel to the strikes of such structures are known as longitudinal or axial. The drainage pattern in the Himalaya is unusual: the central part of the range is drained by the Ganga and its tributaries, and the eastern and western terminations are exclusively drained by the Brahmaputra and the Indus rivers, respectively. The latter rivers take their source in Mount Kailash and have near symmetrical courses, each of them flowing along the range in opposite directions as axial rivers. They become transversal when crossing the eastern and western terminations before flowing in the foreland basin to eventually reach the Bengal and the Indus Fans, respectively. Another characteristic of the Himalayan drainage network is that the high range does not constitute a major drainage barrier despite its high elevation. As the Indus and the Brahmaputra, numerous rivers flowing in the Himalayan foreland basin have their source to the north of the high range. The gaps allowing these rivers to reach the south of the range are characterized by high exhumation rates (Burbank et al., 1996; Jessup et al., 2008; Thiede et al., 2006; Zeitler et al., 2001). It is widely considered that the mountain landscapes and their geomorphology are mainly shaped through erosion. Sediments are removed and redistributed in the lithosphere, and the resulting mass re-equilibration can lead to lithospheric uplift and rock exhumation through isostatic rebound. Rock exhumation is the result of erosion and uplift. In other words, the creation of high topography lead to isostatic rebound and fresh rock exposure erosion, and therefore exhumation processes.

Numerous studies suggest that a strong coupled feedback mechanism exists between erosion and tectonic forcing where surface erosion can encourage metamorphic exposure and lithospheric deformation (e.g. Avouac and Burov, 1996; Beaumont et al., 1992; Willett, 1999; Zeitler et al., 2014; Zeitler et al., 2001). Zeitler et al. (2001) proposed that the rapid exhumation and young peak metamorphism of the Himalayan syntaxes has been enhanced by intense river incision. In this model, the tectonic aneurysm model, the removal of upper crustal layers by erosion and incision

weakens the lithospheric crust and allows warmer material from mid crustal depths to flow towards the surface in an attempt to fill the topographic gap created by erosion. In this hypothesis, if the erosion persists, exhumation and upward flow of crustal material will occur, sustaining high relief and elevation. In this context of ductile material exhumation, decompression melting and low pressure/high temperature metamorphism of this lower crustal material may occur (see summary in Bracciali et al., 2015). Similarly, the Channel Flow model (Beaumont et al., 2001) suggests that focused erosion on the southern front of the Tibetan Plateau has encouraged the ductile extrusion of the Greater Himalayan units. However, these models are challenged (e.g. Bracciali et al., 2015; Hubbard, 1989; Robert, 2008; Wang et al., 2014b; Yin, 2006) and the debate remains as to whether erosion is a triggering factor for tectonics, or if it is the contrary, the exhumation and uplift as the trigger of intense erosion.

Overall, tectonics and climate are inter-dependent; the tectonics of orogens is moderated by climate through erosion. Rock exposure by tectonics or erosion is critical to the feedback governing changes in climate, whilst topography influences rainfall. In order to better constrain the interplay between tectonic-climate-erosion processes in the Himalaya, it is necessary to acquire a good understanding of the nature and timing of Himalayan events involving these factors.

1.3. Geology of the Himalaya

The Himalaya and the Tibetan Plateau result from continental collision between Indian and Asian lithospheric plates (Powell and Conaghan, 1973). The Indian plate separated from Gondwana between 120 and 130 Ma (Metcalfe, 1996) and progressed northward, the Indian plate eventually subducting below the Asian margin (Dercourt et al., 1993). The subsequent closure of the Tethyan sea portion which existed between the Indian and Asian plates has been dated at 50-55 Ma (DeCelles et al., 2004; Najman et al., 2012; Rowley, 1996). In the western part of the Himalaya, the closure of the Tethys was accommodated by two north dipping subduction zones active in the latest Cretaceous-Paleogene times ; one subduction zone was under the south Asian active margin, at the modern Shyok suture zone and the other subduction was intra-oceanic, localised further south and corresponding to the modern Indus suture zone (Corfield et al., 1999; Mahéo et al., 2000; Reuber et al., 1987; Robertson, 2000). Two volcanic arcs formed as a consequence, the Transhimalayan Andean-style batholith which crops out along the southern Asian margin (e.g. Honegger et al., 1982) and an intra-oceanic arc (e.g. Dietrich et al., 1983). This process has functioned until the India-Asia continent-continent collision in early Eocene times (Dupont-Nivet et al., 2010; Najman et al., 2010; Najman et al., 2017; Zhuang et al., 2015), with a sharp decrease of convergence rates between the

two plates from ~15 cm.yr^{-1} to 4-5 cm.yr^{-1} (Guillot et al., 2003; Molnar and Tapponnier, 1975; Patriat and Achache, 1984). The resulting crustal thickening and shortening has led to the formation of the Tibetan Plateau and the Himalayan belt (Hodges, 2000; Yin and Harrison, 2000). The collision and the continuous convergence have then deformed both lithospheric plates and to the progressive formation of an orogenic prism constituted of a successive stacking of Indian plate crust sheets. This deformation has affected a large part of the Asian continent, from the Hindu Kush to the China Sea and from the southern edge of the Himalayan belt to Siberia, and led to the south-eastward lateral extrusion of the Eurasian continent (Molnar and Tapponnier, 1975; Replumaz and Tapponnier, 2003; Tapponnier et al., 1982; Tapponnier et al., 2001). The deformation remains active at the present day and the resulting earthquakes affect the entire Himalayan system (Kumar et al., 2006).

The total shortening accommodated by the Himalayan range is estimated from reconstruction of the relative movement of the tectonic plates. Over a total post-collision convergence of 2600±900 km between India and Asia, 1700±610 km are associated with the Asian block deformation (Achache et al., 1984; Besse and Courtillot, 1988; 1991; Patriat and Achache, 1984). The remaining 900 km are regarded as accommodated by Himalayan shortening (Le Pichon et al., 1992).

The Himalayan mountain belt strikes in a general NW-SE direction and delimitates the Tibetan Plateau to the north from the Indian sub-continent to the south. The range's eastern and western extremities are the Himalayan syntaxes, respectively the Namche Barwa and the Nanga Parbat syntaxes. The main geological terranes which comprise the Himalaya are described as follows, from north to south (Figs. 6 and 7).

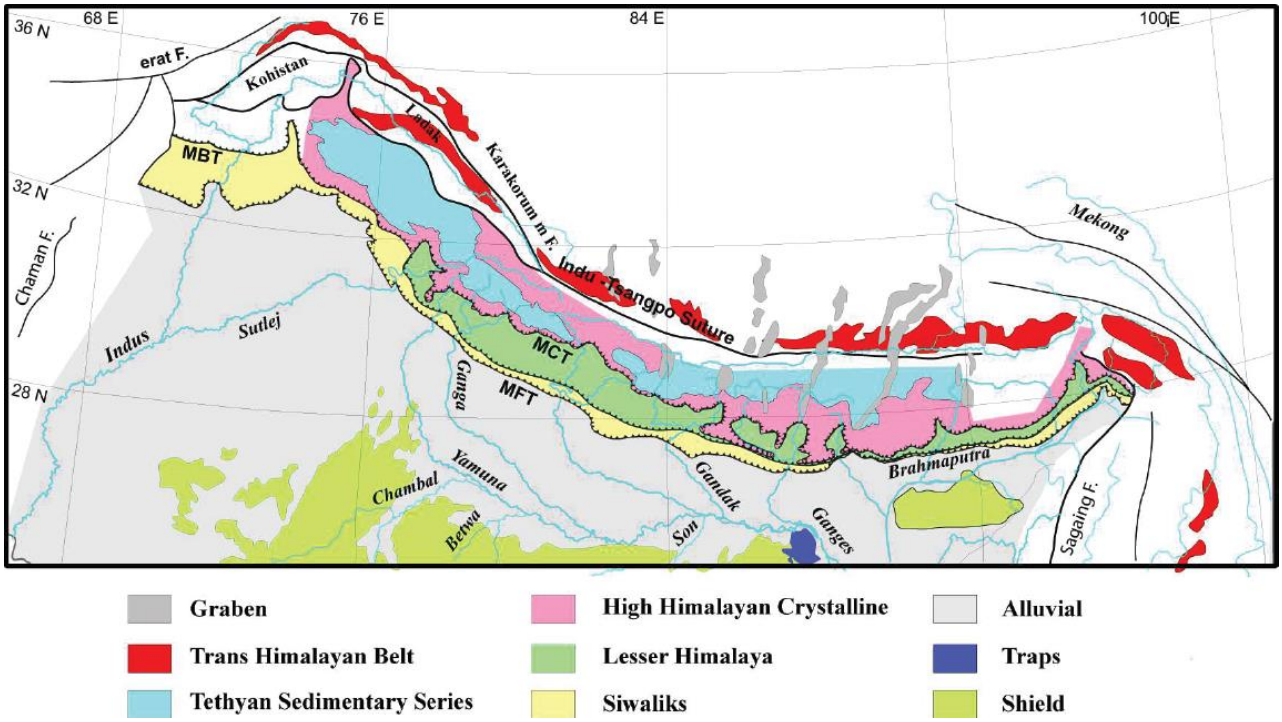

Fig. 6: *General and simplified geology of the Himalayan range (Galy and France-Lanord, 1999; Robert, 2008).*

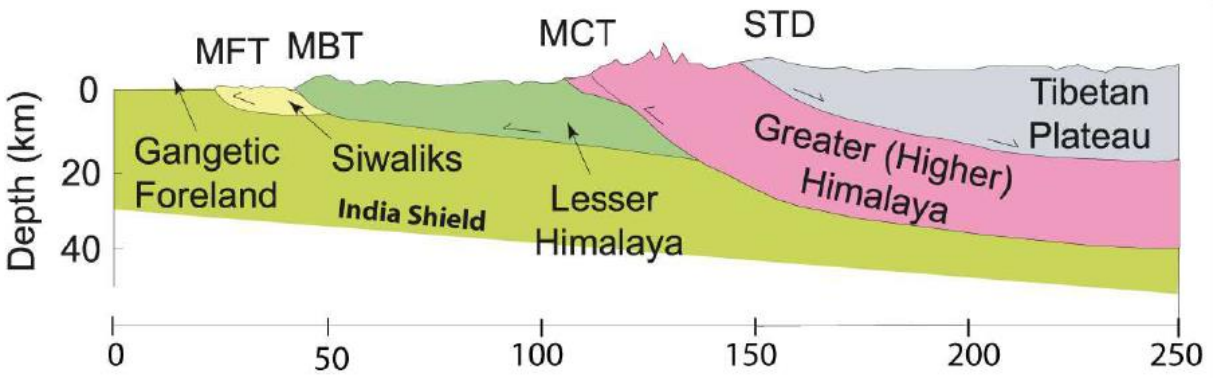

Fig. 7: *Simplified N-S geologic cross-section of the central Himalayan range showing the main Himalayan faults and tectonostratigraphic units. Abbreviations are: MFT- Main Frontal Thrust; MBT – Main Boundary Thrust; MCT – Main Central Thrust; STD – South Tibetan Detachment. (Bookhagen and Burbank, 2006; Robert, 2008)*

The Lhasa and Karakoram Blocks, to the far north of the Himalayan are both considered of similar affinity and to represent the original Eurasian continental plate (e.g. Gaetani, 1997; Gaetani et al., 1990; Le Fort et al., 1994; Rolland et al., 2002a), now separated by the Karakoram Fault (Searle et al., 1988). The Lhasa-Karakoram Block is composed of metamorphic basement of Mid Proterozoic –

Early Cambrian age, overlain by Palaeozoic to Mesozoic low grade meta-sediments (Yin and Harrison, 2000).

The Kohistan Ladakh Island Arc formed as a result of intra oceanic subduction within the Tethys Ocean and lies at the southern margin of the Lhasa-Karakoram Block. The Kohistan Ladakh Island Arc migrated further north due to the oceanic crust subduction under the Eurasian margin. The subsequent arc-continent collision eventually occurred at Mid-Cretaceous to Early-Paleogene times (e.g. Clift et al., 2000; Maheo et al., 2006; Najman et al., 2017; Robertson and Degnan, 1994; Rolland et al., 2000; Rolland et al., 2002b; Schärer et al., 1984; Searle et al., 1988; Sutre, 1990; Treloar et al., 1996; 1989), creating the Shyok Suture Zone (SSZ; Robertson and Collins, 2002). Northward subduction of oceanic lithosphere beneath the Eurasian southern margin continued after arc-continent collision (e.g. Allegre et al., 1984; Garzanti et al., 1987; Honegger et al., 1982) leading to Andean style plutonism and volcanism forming the granodioritic continental arc of the Transhimalayan Batholith.

The Transhimalayan batholiths are extensively distributed over ~2500 km across the Lhasa terrane of southern Tibet. This elongated and continuous magmatic belt of Cretaceous-Paleogene age is characterized by geochemical variations throughout its length. Numerous Transhimalayan batholiths have been sub-categorised and classified according to their location and geochemistry (e.g. Lin et al., 2013), see Fig. 8. The main Transhimalayan suite is the Gangdese Batholith that consists dominantly of Cretaceous to Eocene metaluminous granitoids with I-type geochemical affinity (Debon et al., 1986; Ji et al., 2009a; b; Wen et al., 2008; Wu et al., 2010). The Bomi-Chayu Batholith is another Transhimalayan suite, located in the eastern Himalaya (Chiu et al., 2009; Lin et al., 2013), see Fig. 8. The Gangdese Batholith or the entire Transhimalayan magmatic belt in general, has long been regarded as the main continental arc component produced by northward subduction of the Neo-Tethyan oceanic slab beneath the Lhasa terrane.

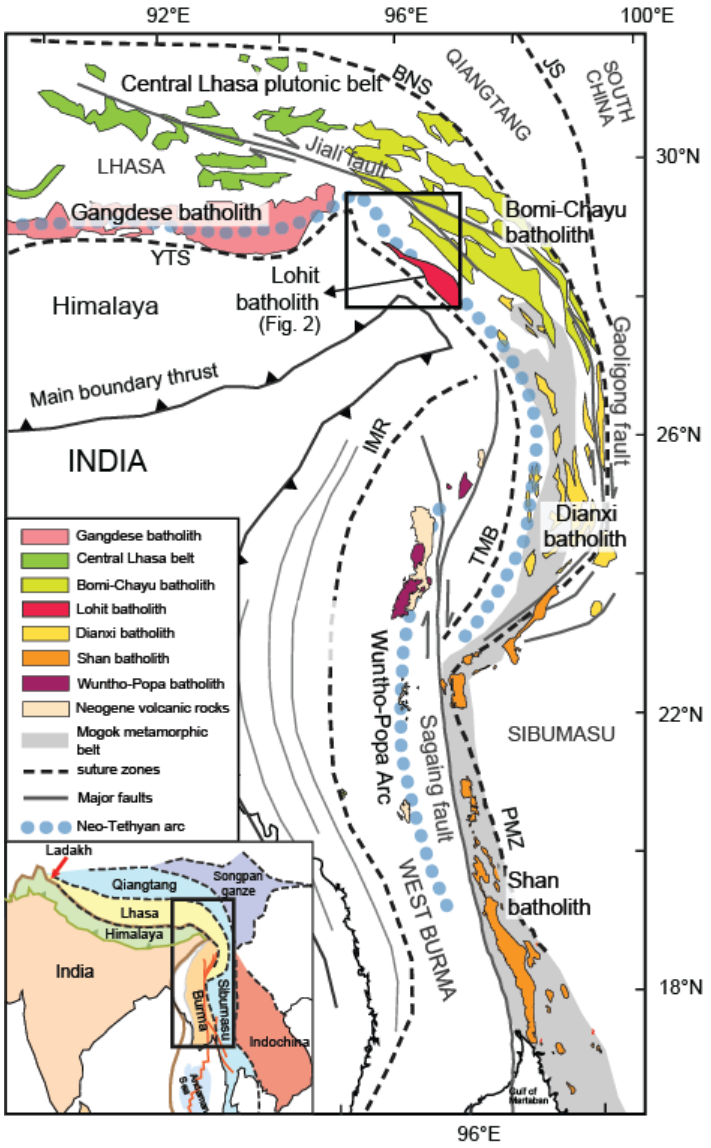

Fig. 8: *Sketch geological map showing the distribution of major batholiths from southern Tibet to west Burma. JS, Jinshajiang suture; BNS, Bangong-Nujiang suture; YTS, Yarlung-Tsangpo suture; PMZ, Paung Lauang-Mawchi zone; IMR, Indo-Myanmar ranges; TMB, Tagaung-Myitkyina belt. (Lin et al., 2013 and references therein)*

The collision is recorded by the Indus-Yarlung suture zone (IYSZ), which juxtaposes the remnants of the pre-collision Indian passive margin sequence onto the Transhimalayan Asian batholiths and the Neo-Tethyan ophiolites (Hébert et al., 2012 and references therein).The Indus-Yarlung Suture Zone represents the line of collision between the Eurasian and Indian plates (Gansser, 1964). The suture zone is mainly composed of the Cenozoic Indus Basin sedimentary rocks (Clift et al., 2001; Searle et al., 1990; Wu et al., 2007) deposited in a basin setting evolving from forearc to intermontane during the initial phases of India-Eurasia collision. Therefore, the Cenozoic Indus Basin sediments record the pre-collisional marine to post-collisional continental history (Henderson et al., 2010; 2011; Searle et

al., 1990; van Haver, 1984). Basaltic pillow lavas of the Dras Arc units corresponding to Tethyan Cretaceous intra-oceanic volcanism and associated volcanoclastic turbidite sediments deposited in the forearc of the Nidam Formation are also present in the Suture Zone along with the Aptian platform carbonates of the Khalsi Limestone (Clift et al., 2000; Reuber, 1989; Robertson and Degnan, 1994; Sutre, 1990). The Indus Basin sediments either are thrust bound or overlie unconformably the Transhimalaya rocks to the north (Gansser, 1977).

South of the Indus-Yarlung Suture Zone are the main Himalayan litho-tectonic units extending throughout the entire Himalayan arc and separated by north dipping crustal faults (Le Fort, 1975; Yin and Harrison, 2000). These units present variations restricted to certain part of the orogen (e.g. windows, klippens, gneiss domes or out-of-sequence thrusts) (Hodges, 2000).

The Tethyan Himalayan Series lie directly to the south of the Indus-Yarlung Suture Zone, and are composed of marine carbonate and siliciclastic sedimentary rocks. They were deposited during Late Proterozoic to Eocene times on the Indian continental passive margin and are intercalated with Paleozoic and Mesozoic volcanic rocks (Gaetani and Garzanti, 1991; Garzanti et al., 1986; Yin et al., 2006). Lying in the southern part of the Tibetan Plateau, the Tethyan Himalayan Series lithology and stratigraphy varies along the orogen and is also present in more meridional location within the belt as tectonic klippens. The Tethyan Himalaya is delimited to the north by the normal fault system of the South Tibetan Detachment which was active until Early Miocene time (Burchfiel et al., 1992; Kellett et al., 2013).

The crystalline Greater Himalayan Series crop out to the south of the Tethyan Himalayan Series and comprise part of the highest Himalayan summits. They consist of Neoproterozoic – early Palaeozoic metasedimentary rocks and associated Cambro-Ordovician intrusive rocks of Indian plate origin (schist, gneisses, and migmatites deformed and metamorphosed) (DeCelles et al., 2000; Gansser, 1983; Gehrels et al., 2003; Myrow et al., 2003; Parrish and Hodges, 1996; Richards et al., 2005). High grade metamorphism and intrusive crystalline complexes generally compose the Greater Himalayan Series. The Himalayan orogenesis affected the Greater Himalayan Series with a polyphase metamorphic event in the Cenozoic. Barrovian-to-Buchan style prograde metamorphism occurred between 37-25 Ma (Searle et al., 1992; Simpson et al., 2000; Vance and Harris, 1999; Vannay and Hodges, 1996; Walker et al., 1999) with subsequent leucogranites intrusion between 25-12 Ma as a result of decompression melting of the Indian Plate during the advanced stages of collision (Gansser, 1964; Guillot et al., 1993; Hodges et al., 1996; Le Fort, 1975; Le Fort, 1996; Le Fort et al., 1987;

Parrish and Hodges, 1996; Prince et al., 1999; Searle et al., 1997; Simpson et al., 2000; Vance and Harris, 1999). In the western Himalayan extremity region, the Greater Himalayan Series can be difficult to differentiate from the Tethyan Himalayan Series and is present as a sedimentary series of low-grade metamorphism (Yin et al., 2006). The Greater Himalayan Series are bounded to the south by the Main Central Thrust (MCT). The MCT is defined as a ductile shear zone wide of between few tens of meters to few kilometres (Le Fort, 1975) which initiated at least between 23-20 Ma (Hodges et al., 1996; Hubbard, 1989).

Adjacent to the Greater Himalayan Series to the south are the Lesser Himalayan Series, predominantly composed of low-grade (greenschist facies) to unmetamorphosed Proterozoic to Early Miocene sedimentary rocks from the Indian shelf (DeCelles et al., 1998b; Frank et al., 1995b; Oliver et al., 1995; Tewari, 1993; Valdiya, 1980; Valdiya and Bhatia, 1980; Yin et al., 2006). Meta-volcanic rocks and intrusive gneisses are also present in this unit (e.g. DeCelles et al., 1998a; Frank et al., 1995a; Upreti, 1999), as well as Palaeocene-Eocene limestone formations in rarer abundance. Fossil assemblages lacking within the Lesser Himalaya led to difficulties in attempting stratigraphic reconstruction. However the Lesser Himalaya is divided into two groups (e.g. Myrow et al., 2003), separated by a discordance (Upreti, 1999) in some regions: 1) the Paleo-Proterozoic to Meso-Proterozoic volcano-clastic sedimentary rocks and orthogneisses of the Inner Lesser Himalaya and 2) the dominantly Neoproterozoic-Cambrian phyllites and marbles of the Outer Lesser Himalaya (Richards et al., 2005), the marbles being associated with quartz-arenite of Mesozoic series of the Gondwana (Gansser, 1964) and Cenozoic series. The Lesser Himalayan series are delimited to the south by the Main Boundary Thrust (MBT) and are also present in tectonic windows. The initiation of the MBT is estimated at 12 to 10 Ma (Delcaillau, 1997; Meigs et al., 1995) or latter, at ~8 Ma (Huyghe et al., 2005).

South of the MBT lies the Sub-Himalayan unit, which comprises Himalayan foreland basin sediments of Eocene to Pleistocene age. Among these sediments constituting the erosion products of the Himalayan range, the Miocene to Pleistocene Siwalik Series form an apron in the southern edge of the front belt (Yin et al., 2006). These are detrital fluvial deposits sub-divided in three units, the Upper, Middle and Lower Siwaliks (Gautam and Appel, 1994; Gautam and Fujiwara, 2000; Ojha et al., 2009). The oldest Lower Siwaliks consist of clayey sandstones deposited by meandering rivers (Nakayama and Ulak, 1999). The typical sandstones of the Middle Siwaliks were deposited by sandy braided rivers and the Upper Siwalik by conglomeratic braided rivers. The Siwalik sedimentary rocks are exposed along the range over a width varying between 40 km in Nepal and few kilometres only

in north-eastern India. The Main Frontal Thrust (MFT) system emplaces the Siwalik sedimentary rocks over the modern day foreland basin sediments of the Indo-Gangetic plains (Gansser, 1983; Hodges, 2000; Molnar, 1984). The MFT is the most recent thrust and the most external to the range. It defines the front of the range and progresses southward. It has initiated at about 2 Ma in the Central Himalaya (Mugnier et al., 2004; van der Beek et al., 2006) and is seismically active (Lavé et al., 2005; Mugnier et al., 2013).

Structural and geophysical studies have suggested that the major thrusts of the fold and thrust Himalayan belt are linked in depth as a main crustal décollement, the Main Himalayan Thrust (MHT), along which the Indian plate is underplated under Tibet (Avouac, 2003; Nábělek et al., 2009; Schulte-Pelkum et al., 2005; Zhao et al., 1993). Additionally, various investigations have provided evidence of lateral variations of the structure of the MHT along the range (Berger et al., 2004; Coutand et al., 2014; Robert et al., 2011). The MHT appears to have a ramp-flat-ramp geometry with lateral variations in the localisation, the depth and the dip of the ramps (Avouac, 2003; Jouanne et al., 2004; Schulte-Pelkum et al., 2005).

The Himalayan syntaxes are distinct from the main central part of the range. The development of the Himalayan syntaxes remains highly debated; they have been subjected to anomalously young (<10 Ma) high grade metamorphism, melting and high rates of exhumation (>5 to 10 km/Myr) (Booth et al., 2009; Booth et al., 2004; King et al., 2016; Lang et al., 2016; Seward and Burg, 2008; Zeitler et al., 2014), compared to the central Himalaya where Early Miocene metamorphism and modern exhumation rates of ~2mm/yr are common (e.g. Thiede and Ehlers, 2013). They are constituted of Greater Himalayan gneiss domes which form important massifs of high elevation. These massifs are the Nanga Parbat to the west and the Namche Barwa to the east. These syntaxes present numerous similarities and an important symmetry. Sharp changes in orientation of the main structures which turn at 90°, forming tectonic windows cutting the overlying terrane are observed in the syntaxial regions. The Nanga Parbat exhumes across the Kohistan Ladakh arc terrane whereas the Namche Barwa exhumes through the Transhimalayan batholiths. Additionally, these two massifs are highly incised by the Indus and Yarlung-Brahmaputra rivers, respectively.

2. STUDY AREAS AND OBJECTIVES OF THE Ph.D.

In this section, the study areas of the thesis are presented as well as the questions investigated further in this manuscript. The eastern Himalayas constitute the focus of this Ph.D. and are characterised by the eastern syntaxis and the neighbouring Shillong plateau.

2.1. The Shillong Plateau

A unique feature in the Himalayas, the Shillong plateau is the only elevated topography in the Himalayan foreland basin. Located south of the orogen deformation front, it forms a 1600 m high, 40000 km^2 Indian plate Precambrian basement tilted northward by 2-4 ° and overlain by a few patches of Cenozoic sedimentary rocks (Biswas et al., 2007; Clark and Bilham, 2008; Yin et al., 2010). Being the wettest place on Earth on its southern flank (Bookhagen and Burbank, 2010), it has also been described as a barrier preventing winds transporting moisture from the Bay of Bengal towards the Himalayan front (Bookhagen et al., 2005a; Grujic et al., 2006). The Shillong plateau has been proposed to have had a major influence on eastern Himalayan tectonics in terms of strain partitioning as well as on regional climate leading to reduced erosion rates in the orogen in its lee. To understand these tectonic-erosion-climate couplings in the eastern Himalayas, constraining the timing of the Shillong Plateau surface uplift is critical.

The Shillong plateau, along with the Mikir hills, is located between the Indo-Burman Range to the east and south and the Himalayan range to the north and is surrounded by the Brahmaputra River to the north and west. It is a crystalline Protero-Paleozoic basement (Chatterjee et al., 2007; Ghosh et al., 1994; Mitra and Mitra, 2001) bounded by two steep reverse and seismically active faults which are possibly of crustal scale (Mitra et al., 2005). The northern WNW-ESE trending fault is named Oldham Fault and was the site of the largest recorded intraplate earthquake (Bilham and England, 2001; Oldham, 1899; Rajendran et al., 2004). The southern E-W trending Dauki Fault juxtaposes the Shillong Precambrian metamorphic and intrusive rock basement against the 18 km thick Cenozoic sedimentary rocks from the southern adjacent Surma basin (Alam et al., 2003; Johnson and Alam, 1991). The Shillong Plateau has been proposed to be uplifted either 1) as a popup structure along the Oldham and Dauki Faults (Bilham and England, 2001; Islam et al., 2011); 2) through the Dauki Fault being a north dipping thrust implying the Oldham Fault to be a back thrust (Yin et al., 2010); or 3) as a fault propagation fold where the Oldham structure would be a back thrust and the Dauki structure the surface expression of a blind fault dipping northward (Clark and Bilham, 2008). The plateau is separated from the Mikir hills by the NW-SE trending Kopili shear zone (Kayal et al., 2010) which accommodates the differential clockwise rotation between the Shillong and the eastern

Assam blocks by a 3 mm.yr^{-1} dextral displacement (Vernant et al., 2014). The plateau is located where the forebulge of the Himalayan foreland basin should be in NE India (Rath et al., 1997; Singh et al., 1998) and it has been suggested that the Himalayan forebulge and foredeep have been replaced by a shallow basin floor north of the Shillong plateau (Clark and Bilham, 2008; Dasgupta et al., 1987). Continental sedimentary rocks aged Late Cretaceous lie unconformably on the Shillong basement in its southern, eastern and western part, indicating that the basement surface itself has been exposed to erosion at this time (Biswas et al., 2007). Then the plateau has been submerged and buried under a Cenozoic shallow marine and deltaic sedimentary cover reaching at least 3 km in thickness (Chakraborty, 1972). This sedimentary cover contains the erosion production of the Himalaya deposited by the palaeo-Brahmaputra in its flood plain from Early Miocene times (Bracciali et al., 2015) until the uplift of the Shillong Plateau in Pliocene times (Johnson and Alam, 1991; Najman, 2006; Najman et al., 2016; Uddin and Lundberg, 1999).

Climatic models have been proposed such as the Shillong plateau acting as a shield located in the Indian Summer Monsoon trajectory, perturbing the regional precipitation pattern (Grujic et al., 2006). Apatite fission-track data from an EW transect along Bhutan indicate slower erosion rates in the lee of the Shillong plateau rain shadow, than in western Bhutan. Additionally, a deceleration in erosion rates in eastern Bhutan, i.e. in the region protected from the summer monsoon, has been observed after 5.9 Ma. This timing has been interpreted as the maximum age of the onset of Shillong plateau uplift (Grujic et al., 2006). This hypothesis has been questioned by Adlakha et al. (2013), Adams et al. (2015) and Coutand et al. (2014) who prefer these variations in erosion rates to be explained by variable strain partitioning controlling the exhumation of the plateau. Presenting a unique geometry in comparison with the Himalayan arc (Bendick and Bilham, 2001), the Shillong absorbs up to 1/3 of India-Asia convergence in the eastern Himalayas, protecting Bhutan from seismic risk at the expense of Bangladesh (Bilham and England, 2001). Considering the Indian-Sunda plates convergence, the Shillong plateau uplift might also have played an important role in facilitating the recent and fast westward propagation of Indo-Burman Ranges outer wedge (Maurin and Rangin, 2009). These combined processes might have been responsible for major changes in the paleo-drainage of the Brahmaputra River. Also, Clark and Bilham (2008) propose that the potential coeval kinematic changes (e.g. initiation of EW extension in Central Tibet, eastward expansion of high topography in Tibet, onset of rotation of crustal fragments in SE Tibet and reestablishment of eastward subduction beneath the IBR) could have been originated by the onset of Shillong plateau exhumation. Better constraint to the Shillong plateau evolution is essential to understand associated climate-tectonism-erosion couplings in the eastern Himalayas.

The timing of Shillong plateau uplift has been debated since the last two decades. Exhumation rate studies of the Shillong Precambrian bed rock differ from modern GPS velocity measurements (Vernant et al., 2014). A decoupling between rock exhumation and surface uplift has thus been suggested. Paleo-erosion surfaces in the denudated northern part of the plateau and Cretaceous apatite (U-Th)/He and fission-track ages suggest the absence of significant burial after this time (Biswas et al., 2007). However, Cenozoic burial heating from a thick sedimentary cover followed by the plateau exhumation initiated at least 15-9 Ma ago have been determined from bedrock thermochronology in the southern part of the plateau (Biswas et al., 2007; Clark and Bilham, 2008). Different sediment cover and basement erodibilities has been proposed to explain the chronological decoupling between exhumation and surface uplift, the latter remaining poorly constrained at some time after 3-4 Ma (e.g. Biswas et al., 2007). In the Surma basin, a shift in sediment thickening direction from south to north has been studied and interpreted as the change from a passive margin to a flexural basin resulting from loading by the uplifting Shillong Plateau. Johnson and Alam (1991) and Uddin and Lundberg (2004) suggested this major subsidence associated with the Shillong plateau uplift to be occurring in Pliocene times. However, using seismic data and sedimentary record in the Surma basin, along with flexural modelling, Najman et al. (2016) propose the Shillong Plateau topographic growth to be aged 3.5 to 2 Ma.

The aim of the chapters 2 and 3 is to precisely constrain the timing of the rise of the Shillong Plateau, and to better understand the causes of its surface uplift.

2.2. The Namche Barwa syntaxis

Located at the eastern termination of the Himalaya, the Namche Barwa syntaxis corresponds to the NE Indian plate indentor and presents outstanding characteristics arousing a wide interest in the earth scientists' community. The Namche Barwa region is dominated by extreme relief and deep, steep gorges (up to 5.6 km of local relief ; Korup et al., 2010)). In the core of the syntaxis, the Namche Barwa and the Gyala Peri massifs reach elevations of >7 km. The Tsangpo gorge, a <200-m wide, 200-km long fluvial knick-zone descending >2 km between the Namche Barwa and the Gyala Peri peaks is one of the deepest on Earth (e.g., Lang et al., 2013; Zeitler et al., 2001). With highest recorded erosional exhumation rates recorded on the planet (>5 mm/yr)(Larsen and Montgomery, 2012; Stewart et al., 2008), the eastern syntaxis (only 2 % of the Yarlung-Tsangpo drainage area) contributes up to 50-70% of the Brahmaputra sediments (Enkelmann et al., 2011; Garzanti et al., 2004; Lang et al., 2013; Singh and France-Lanord, 2002; Stewart et al., 2008).

The Namche Barwa syntaxis is composed of medium to high grade metamorphic crystalline rocks (schist, gneisses, and migmatites deformed and metamorphosed) of the Greater Himalaya intruded by Miocene Leucogranites. The structural trend bends around the eastern syntaxis, changing from E-W to N-S striking. The Indian plate rocks are thought to have deformed into a sharp NE terminating complex antiformal uplift, that has folded the YTSZ (Burg et al., 1997). The resulting elongated NE plunging antiform (Burg et al., 1997) characterizing the Namche Barwa massif, has been suggested to expand both vertically and laterally and migrated northward since its initiation (Seward and Burg, 2008). The MCT segments bounding the syntaxis have strike-slip components that are left-lateral and right-lateral to the west and to the east of the syntaxis, respectively (e.g. Burg et al., 1998). The northern tip of the syntaxis, cored by the Namche Barwa and the Gyala Peri massifs, is bounded by the IYSZ with the dextral Jiali–Parlung Fault zone to the NE (timing of the main stage motion between 18 and 12 Ma (Lee et al., 2003)) and the north dipping Nam-La thrust to the south of the Namche Barwa (e.g. Zeitler et al., 2014). The latter has been proposed to acts as a southern boundary of a pop-up structure with the Namche Barwa massif at its core (Ding et al., 2001).

Very young bedrock thermochronological ages within the syntaxis record late Neogene (<10 Ma) high grade metamorphism and rapid syntaxial exhumation (e.g., Booth et al., 2009; Burg et al., 1998; Ding et al., 2001; Finnegan et al., 2008; Seward and Burg, 2008; Stewart et al., 2008; Zeitler et al., 2014). In comparison, peak metamorphism in the main arc of the range occurred in the Early Miocene, and lower exhumation rates of ~2 km/Myr are typical (e.g., Thiede and Ehlers, 2013 and references therein). The youngest phase of metamorphism restricted to the ~40 by 40 km area in the NE tip of the syntaxis, within the Namche Barwa and Gyala Peri massifs has been recorded by 3–10 Ma with bedrock U–Pb zircon dating (Booth et al., 2004; Zeitler et al., 2014). The exceptionally young geo- and thermo-chronologic ages of this domal pop-up (rutile U-Pb <3 Ma) imply very high exhumation rates (>4 km/Myr) (Bracciali et al., 2016 and references therein). By contrast, the SW part of the syntaxis, south of the domal pop up, show generally older ages (Palin et al., 2014), with rutile U-Pb >9 Ma (Bracciali et al., 2016) and the entire syntaxial anticline shows evidence of Miocene (ca 24 to 16 Ma) metamorphic events within GHS rocks similar to the main part of the Himalaya (Burg et al., 1998; Palin et al., 2014). The decompression related to exhumation has been controversially suggested to have occurred after 4 Ma (Burg et al., 1998; Seward and Burg, 2008) and around 10 Ma (Booth et al., 2009; Zeitler et al., 2014; Zeitler et al., 2001) from bedrock studies. Published Neogene detrital thermochronological data from the eastern Himalayan foreland basin have inferred the syntaxial exhumation 1) to have increased by a 5 to 10-fold increase between 5 and 6 Ma (Lang et al., 2016); 2) did not accelerate significantly before 4 Ma (Chirouze et al., 2013); 3)

had not significantly initiated prior to late-Pliocene time, and exhumed a at rates >4 km/Myr in the last 3 Myr (Bracciali et al., 2016).

Several models have been proposed to explain the syntaxial rapid exhumation, and remain questioned. Bendick and Ehlers (2014) have modelled the 3-D thermomechanical evolution of plate collision with non-planar geometries, and explain the localized deformation and exhumation of the eastern syntaxis by the subduction geometry implying collision and deformation of geometrically-stiffened syntaxial indentor in subducting slab. Structural buckling due to contraction in the orogenic indenter corner has also been suggested as an explanation for the rapid exhumation of the Namche Barwa syntaxis (Burg et al., 1997). Additionally, the peculiar drainage in the syntaxis area, for instance with its “big bend” (Zeitler et al., 2014), has been suggested to have evolved as a direct consequence of the syntaxial development, through river distortion and capture events (e.g. Clark et al., 2004; King et al., 2016). Alternatively, thermomechanical feedback has been suggested to explain the rapid exhumation, in which focused and intense incision of the Yarlung River after capture by the Siang-Brahmaputra led to rapid exhumation of the Namche Barwa massif, weakened the lower crust and set up tectonic inflow of material into what has been termed a “tectonic aneurism” (Koons et al., 2013; Zeitler et al., 2014; Zeitler et al., 2001). The latter model is challenged by the work of Wang et al. (2014b) suggesting that fluvial incision in the Namche Barwa region is the result of an increase in rock uplift after ~4 Ma; an uplift at this time being consistent with bedrock geochronological and thermochronological ages from Burg et al. (1998), Finnegan et al. (2008) and Seward and Burg (2008). Additionally, detrital studies have suggested that the timing of capture is of Early-Middle Miocene times (Bracciali et al., 2015; Lang and Huntington, 2014). Bracciali et al. (2016) invoke the ductile extrusion of weak lower crust from beneath Tibet possibly by “channel flow” decompression (Beaumont et al., 2001), initiating modestly in Miocene times followed by a Pleistocene acceleration of the syntaxis exhumation.

In order to better document the models proposed to explain the outstanding syntaxial exhumation, the main objectives of chapter 2 and 3 are to constrain the timing of the onset of the rapid exhumation of the Namche Barwa syntaxis, and the exhumation rates prior to and after the onset.

3. APPROACH

The Brahmaputra River flows to the north and the west of the Shillong Plateau and carries erosion products of the Namche Barwa syntaxis. Its deposits in the Himalayan foreland basin are the key elements of this thesis and are described in this section as their study constitutes the approach of this research work.

3.1. The Brahmaputra River

The Brahmaputra takes its source at Mount Kailash, where it is called the Yarlung-Tsangpo River, and flows for more than 1000 km to the east along the suture zone, before crossing the range to the south. Its course describes a 180 degrees turn when incising between the Gyala Peri and the Namche Barwa massifs, within the Himalayan eastern syntaxis. Downstream of Namche Barwa, the Yarlung-Tsangpo River becomes the Siang River until it reaches the foreland basin in Arunachal Pradesh where it takes its most famous name, the Brahmaputra River. In the Brahmaputra flood plain, the river flows westward and turns southward, flowing around the Shillong Plateau, before reaching the Bay of Bengal.

Since the Brahmaputra drains the Namche Barwa syntaxis, and its course has likely been perturbed by the uplift of the Shillong Plateau, the study of the Brahmaputra deposits allows us to answer the main research questions of this thesis.

In the foreland basin, the Shillong Plateau rise is thought to have shifted the Brahmaputra north and west from its previously relatively straight SSW direction, in Miocene times (e.g. Chirouze et al., 2013; Najman et al., 2016; Uddin and Lundberg, 1999). Upstream of the foreland basin, hypotheses on the palaeo-drainage of the Yarlung-Tsangpo River and its continuation as the Brahmaputra are numerous and remain debated. Harrison et al. (1992) argue that the modern drainage had been installed before the Himalayan orogenesis, while Bracciali et al. (2015) and Robinson et al. (2014) suggest that it has been installed since the early Miocene; and others propose that the modern drainage has been installed at least since 10 Ma (Brookfield, 1998; Chirouze et al., 2013; Lang and Huntington, 2014; Royden et al., 2000; Seeber and Gornitz, 1983). These various studies that propose river capture rather than antecedence suggest that the palaeo-Yarlung-Tsangpo had flowed further to the east into the Red and/or Irrawaddy rivers, east of the Namche Barwa (Bracciali et al., 2015; Brookfield, 1998; Clark et al., 2004; Lang and Huntington, 2014; Seeber and Gornitz, 1983). Then the Siang River likely captured the Yarlung-Tsangpo by 1) headward erosion (Clark et al., 2004), 2) lateral propagation of the massif (Seward and Burg, 2008) or 3) glacial dams mechanisms (Cina et

al., 2009). This capture could partly explain the impressive Tsangpo gorge knick point and the coincidence of fluvial incision and rapid rock exhumation (Zeitler et al., 2001). However, isotopic geochemistry data from the Bengal Fan supports the idea of a Yarlung-Tsangpo-Brahmaputra system depositing into the Bengal fan since the Mid-Miocene (Galy et al., 2010). Rapid erosion in the eastern Syntaxis explains the dominant input from the Namche Barwa area in the isotopic signature of modern Brahmaputra sediments in Assam, with minor contribution from Himalayan tributaries (Singh and France-Lanord, 2002).

This work investigates the Neogene-Quaternary evolution of the paleo-Brahmaputra River to inform the tectonic history of the Shillong Plateau and the eastern syntaxis through provenance analysis in the foreland basin sediments.

3.2. The Himalayan foreland basin Siwalik sediments

A foreland basin is defined as a region of potential sediment accommodation formed in response to the growth of an orogenic belt (DeCelles and Giles, 1996) and filled with its erosion products. The Himalayan foreland basin contains the Paleogene-Quaternary erosion products of the range: the Siwalik sedimentary rocks which are deformed as the fold and thrust belt propagates southward. These sediments form an apron along the southern flank of the Himalayan belt (Yin et al., 2006); they are located between the MFT and the MBT. The Siwalik Group is divided into three distinct units based on sedimentary facies: the Lower, Middle and Upper Siwaliks (DeCelles et al., 1998b; Yin et al., 2006). Up-section coarsening in the Siwaliks is interpreted as due to the progressive transition from deposition by low-gradient sinuous channels in a fluvio-deltaic setting to deposition by steep braided rivers in alluvial fans along the Himalayan front, as the Main Frontal Thrust propagated southward (Chirouze et al., 2012; Coutand et al., 2016). The Lower Siwaliks are mainly composed of alternating fine-grained sandstones and siltstones with common leaf-impressions and paleosols, interpreted in this area as deposited in a fluvio-deltaic plain environment (Chirouze et al., 2012; Coutand et al., 2016). The Middle Siwaliks, interpreted as a braided fluvial facies, consist of massive medium- to coarse-grained sandstone layers, with frequent cross-bedding, soft sedimentary deformation and increasing occurrence of conglomerates up-section. The Upper Siwaliks are mainly composed of conglomerates interbedded with sandstones and some siltstones, interpreted as pebbly braided-river deposits (e.g., Chirouze et al., 2012; Cina et al., 2009; Coutand et al., 2016; Lang and Huntington, 2014).

The Siwalik sedimentary rocks provide important information for the understanding of orogenesis as they record evidence of the tectonic (e.g., Coutand et al., 2016; DeCelles et al., 1998b; Lang et al., 2016; Szulc et al., 2006), erosional (e.g., Bernet et al., 2006; Chirouze et al., 2013; Harrison et al., 1993; van der Beek et al., 2006) and climatic (e.g., Quade et al., 1995a; Vögeli et al., in press) evolution of the hinterland.

3.3. Provenance analysis in the Siwaliks

Provenance studies help to unravel 1) the unroofing history of the source and 2) the potential control of foreland basin tectonics on the palaeo-drainage networks (DeCelles and Giles, 1996). The Brahmaputra River presents a characteristic Asian margin provenance signature as it drains rocks from the Mesozoic-Paleogene Transhimalayan batholiths in the southern Tibetan plateau before reaching the foreland. These rocks have a distinct composition and age characteristics useful to unravel erosion and sediment transport history (e.g. Cina et al., 2009). The distinction between Jurassic to Early Cenozoic Transhimalayan batholith of the Lhasa terrane and the mainly Proterozoic Himalayan rocks largely composed of variably metamorphosed Proterozoic-Eocene rocks with a few Miocene leucogranites (Chu et al., 2006; Mo et al., 2007) constitute relevant signals for provenance analysis. This method has been applied in the eastern Himalayan foreland basin to better constrain the palaeo-drainage system in this region using εHf, bulk εNd data and zircon U-Pb dating (e.g. Bracciali et al., 2015; Chirouze et al., 2013; Cina et al., 2009; Lang and Huntington, 2014). In the Surma remnant ocean basin, Bracciali et al. (2015) observed palaeo-Brahmaputra detritus from c.a. 18 Ma to 2.5 Ma interpreted as the result of an early Miocene Yarlung-Tsangpo-Siang capture. Numerous provenance studies have been performed on the Siwaliks in the eastern part of the Himalayan foreland (Fig. 9) and it has been inferred that the palaeo-Brahmaputra did not reach the Tista river NW of the Shillong plateau in Siwalik times (Cina et al., 2009) but it had flowed, from east to west, through the Siang section (Lang and Huntington, 2014), the Likabali section (Lang and Huntington, 2014), possibly in the Subansiri section (modern river sample shows Brahmaputra signature interpreted to be eroded from Neogene Siwalik deposits) (Cina et al., 2009), Kimin section, Itanagar section (Lang and Huntington, 2014) as Brahmaputra signature have been observed in all present Siwalik units. The Kameng section contains Gangdese batholith detritus from 7 to 3 Ma (Chirouze et al., 2013; Cina et al., 2009), see Fig. 9.

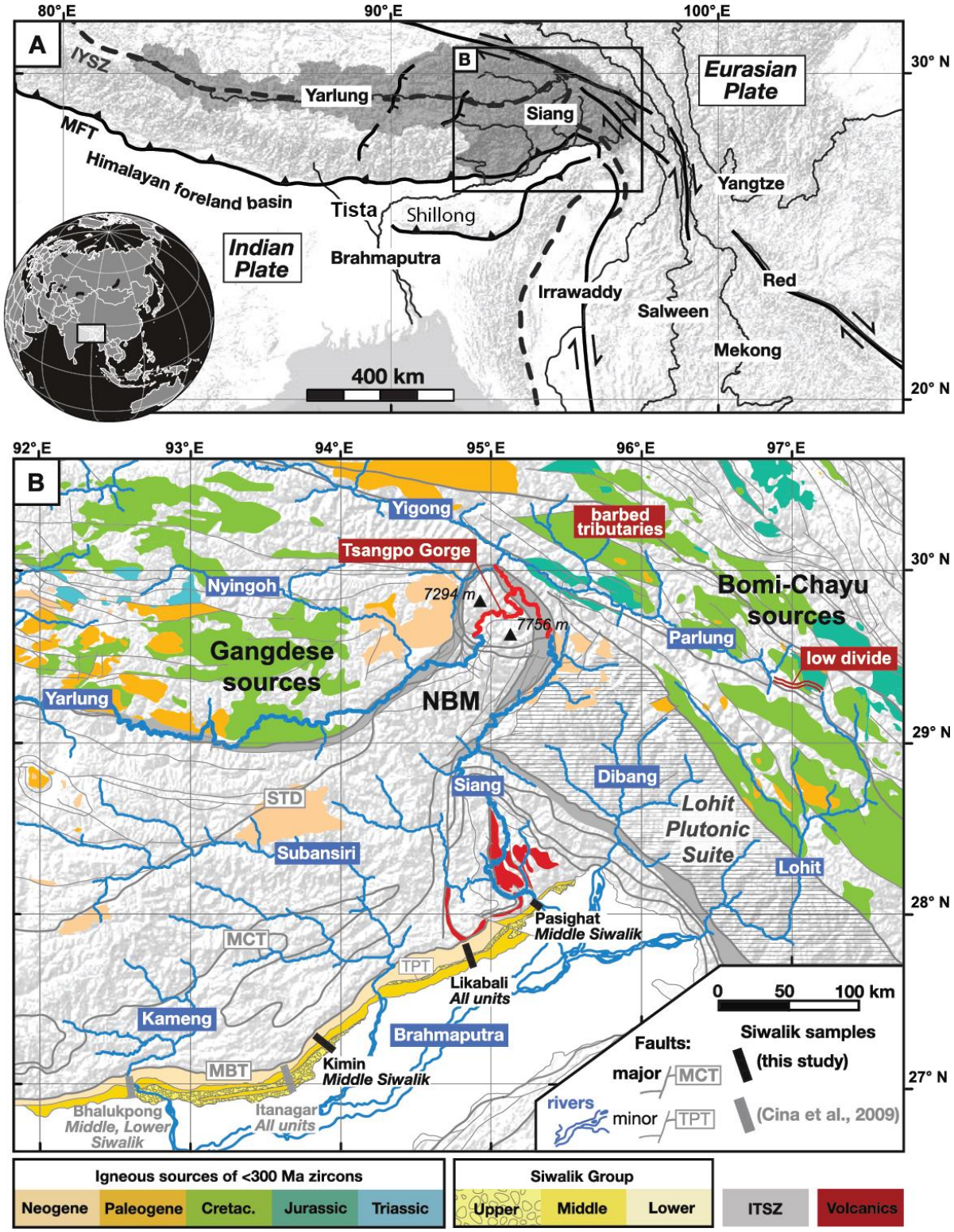

Fig. 9: *Map of the eastern Himalayan syntaxis region (Lang and Huntington, 2014 and references therein). (a)The Yarlung River follows the Indus–Yarlung Suture Zone (IYSZ, dashed) along the southern margin of Tibet before sharply turning southward to flow through the eastern Himalayan syntaxis, becoming the Siang River prior to joining the Brahmaputra River in the eastern Himalayan foreland basin (drainage area shaded). (b) Regional geological map illustrating potential source*

areas for <300 Ma zircons in igneous rocks north of the IYSZ and within the eastern Himalaya. Major tectonic features are labelled for reference: the Tipi Thrust (TPT), Main Boundary Thrust (MBT), Main Central thrust (MCT), and South Tibetan Detachment (STD).

Additionally, 1) the very young (10 to <1 Ma) mineral growth and cooling ages of the Namche Barwa syntaxis (Booth et al., 2004; 2009; Bracciali et al., 2016; Burg et al., 1998; Ding et al., 2001; Finnegan et al., 2008; Zeitler et al., 2014) and 2) geochronological and thermochronological ages distinctive of the syntaxis in particular zircon rim U-Pb ages <10 Ma Bracciali et al. (2016), constitute a clear syntaxial signature. These diagnostic ages for specific thermochronological and geochronological systems have been used in the eastern Himalayan Siwaliks to track the eastern syntaxial detritus (Bracciali et al., 2016; Lang et al., 2016). Lang et al. (2016) applied zircon fission-track and white mica ^{40}Ar-^{39}Ar dating on sedimentary rocks from the Siji section; they suggest an acceleration of the eastern syntaxis exhumation rates between 6 Ma and 5 Ma.

The approach of this thesis is to track paleo-Brahmaputra and syntaxial deposits in two Siwalik sections. The first one, the Dungsam Chu section is located in the north of the Shillong Plateau. The depositional dating and sedimentary analysis of the Dungsam Chu is presented in chapter 1. The provenance analysis through zircon U-Pb geochronological system is described in chapter 2. Together, chapter 1 and 2 date the onset of the rise of the Shillong Plateau as deduced from shifting of the Brahmaputra River, and investigate its causes and consequences.

The second section, the Sibo-Remi-Siang section is the easternmost Siwalik section and the most proximal to the syntaxis. The depositional dating, sedimentology analysis and U-Pb geochronological analysis for provenance is detailed in chapter 3. The syntaxial provenance analysis and constraint to exhumation of the syntaxis from data from the Sibo-Remi-Siang section has been carried out using thermochronology and rutile U-Pb geochronology and is summarized in chapter 4. Both chapter 3 and 4 document the Neogene-Quaternary evolution of the Namche Barwa syntaxis.

4. METHODS

This section describes the methods used in this thesis work. Analyses performed by the author are developed here whilst data provided by collaborators are only briefly mentioned. Complementary information for each analytical method used in this manuscript is provided in the appropriate chapters and the corresponding appendices.

4.1. Depositional age determination

The main sedimentary depositional age determination of this work has been realised through magnetostratigraphy, for both Dungsam Chu and Sibo-Remi-Siang section (chapters 1 and 3). Therefore, general notions of magnetism and its application to the magnetostratigraphic dating of sedimentary rocks are presented here, followed by a brief description of complementary dating methods used in this thesis. The main descriptions of magnetism principles of this section are issued from Butler (1992).

4.1.1. Magnetic field

The magnetic field H (Note that the variables formatted in bold are vectors throughout the section) is characterized by intensity and direction has a fundamental unit of A/m (SI). The magnetic moment is noted M of fundamental unit A.m^2 and tends to align the axis of a dipole parallel to the magnetic field such as:

$$\mathrm{E} = -\mathrm{M}.\mathrm{H} = -\mathrm{M}.\mathrm{H}.\cos(\theta)$$

where E is the potential energy and θ the angle between M and H.

The magnetic intensity, J, or magnetization of a material is the sum of the magnetic moments per unit of volume enclosing those magnetic moments:

$$\mathrm{J} = \left(\sum\nolimits_{\mathrm{i}} \mathrm{M_i}\right)/\mathrm{volume}$$

where $\mathrm{M_i}$ is the constituent magnetic moment.

In paleomagnetism, the direction of a vector such as the surface geomagnetic field is usually defined by the angles shown in Fig. 10a. The vertical component, $\mathrm{H_v}$, of the surface geomagnetic field, H, is defined as positive downwards and is given by:

$$\mathrm{H_v} = \mathrm{H}.\sin(\mathrm{I})$$

where H is the magnitude of H and I is the inclination of H from horizontal, ranging from –90° to +90° and defined as positive downward.

The horizontal component, H_h, is given by:

$$H_h = H.\cos(I)$$

and the geographic north and east components are respectively:

$$H_n = H.\cos(I).\cos(D)$$

$$H_e = H.\cos(I).\sin(D)$$

where D is the declination, i.e. the angle from geographic north to horizontal component, ranging from 0° to 360°, positive clockwise. The determination of I and D completely describes the direction of the geomagnetic field.

A concept that is central to many principles of paleomagnetism is that of the geocentric axial dipole (GAD), shown in Fig. 10b. In this model, the magnetic field produced by a single magnetic dipole at the centre of the Earth and aligned with the rotation axis is considered. In this model, the inclination of the field can be determined by:

$$\tan(I) = 2.\tan(\lambda)$$

where λ is the geographic latitude, ranging from –90° at the south geographic pole to +90° at the north geographic pole. This relationship between I and λ is often referred to as "the dipole equation" and is essential to understanding most of paleogeographic and tectonic applications of paleomagnetism.

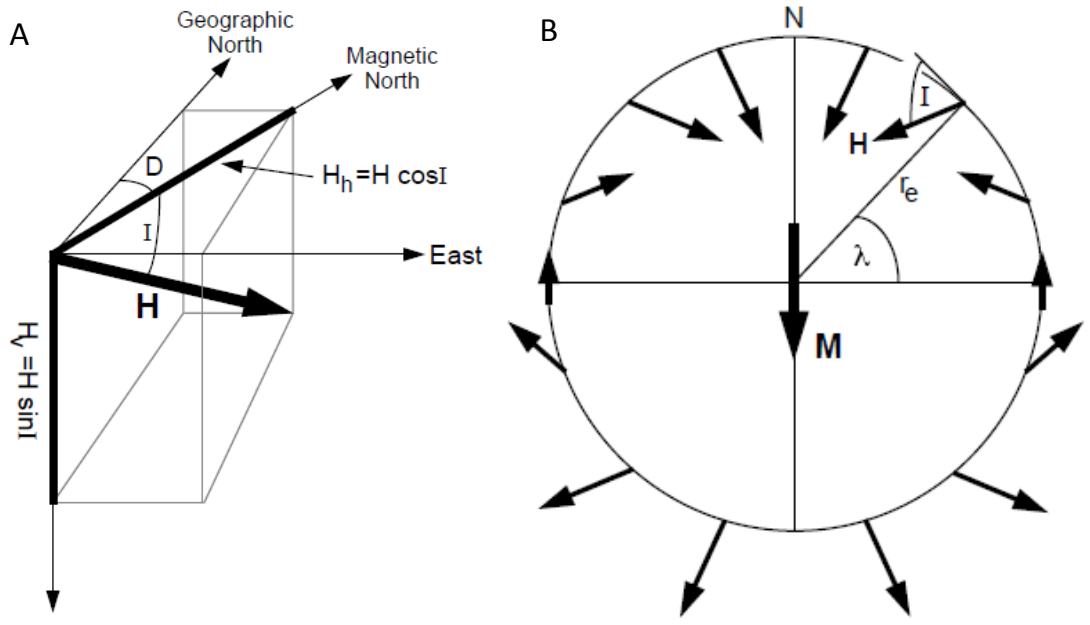

Fig. 10: *(a) Principal components of the Earth magnetic field* ***H****. (b) Geocentric Axial Dipole model (after Butler, 1992 and references therein).*

4.1.2. Natural Remanent Magnetism (NRM)

In situ magnetization of rocks is the vector sum of two components:

$$J = J_i + J_r$$

where J_i is the induced magnetization and J_r is the natural remanent magnetism. The magnetic susceptibility, χ, can be regarded as the magnetizability of a substance. Presence of the local geomagnetic field, H, produces the induced magnetization:

$$J_i = \chi . H$$

Where the bulk susceptibility, χ, is the susceptibility resulting from contributions of all minerals. This induced magnetization J_i usually parallels the local geomagnetic field and can be the dominant component for many rock types. However, acquisition of induced magnetization is a reversible process without memory of past magnetic fields. It is the remanent magnetization that is of concern in paleomagnetism.

The Natural Remanent Magnetization (NRM) is the remanent magnetization present in a rock sample prior to laboratory treatment. NRM depends on the geomagnetic field and geological processes during rock formation and during the history of the rock. NRM is typically composed of more than one component. The NRM component acquired during rock formation is referred to as primary NRM and is the component sought in most paleomagnetic investigations. However, secondary NRM components can be acquired subsequent to rock formation and can alter or obscure primary NRM. The secondary components of NRM add vectorially to the primary component to produce the total NRM:

$$\text{NRM} = \text{primary NRM} + \text{secondary NRM}$$

4.1.3. Detrital Remanent Magnetism

Detrital remanent magnetism (DRM) is acquired during deposition and lithification of sedimentary rocks. When a detrital rock is deposited, magnetic particles contained in the sedimentary material from the suspended load are subjected to water friction forces, gravity and a magnetic field. Suspended load will orientate parallel to the magnetic field. During deposition, the major part of the particles will conserve this orientation which is the orientation of the natural Remanent magnetisation of deposition. This orientation classically presents an error in inclination towards the horizontal plane. However, in an environment where hydrodynamic forces are important, this orientation is not perceptible. On the contrary, when the sediment is recent, the cohesion between particles is low and magnetic particles can re-orientate in the magnetic field at the time, especially if grainsize is low. It is an early post-detrital magnetisation which generally does not present bias on the inclination. This implies a time difference between the deposition and the acquirement of this

magnetisation. However, in the Himalayan foreland basin, the high accumulation rates lead to no significant time difference in the dating. The sediment is then buried and compacted mechanically. During diagenesis, post-deposition physical and chemical processes such as dissolution, precipitation, cementation or bioturbation can affect the magnetization and the material is susceptible to acquiring a secondary magnetisation and therefore effect on the paleomagnetic record.

4.1.4. Magnetic field inversion and GPTS

Numerous inversions of the Earth's magnetic field occurred over geologic time. These inversions allowed the establishment of a magnetic polarity stratigraphic scale, with periods of normal or reverse polarities. These inversions are worldwide documented and reported in geomagnetic polarity time scales (GPTS) where the time of the inversions has been constrained using independent dating methods. For instance, in Neogene times, geochronology on lavas and bio-stratigraphy in sedimentary rocks are the main independent dating techniques to constrain inversion times. For older periods, inversions observed in oceanic floor in both sides of oceanic ridges are used, assuming a constant extensional rate. Several GPTS have been elaborated, in this thesis the GPTS of Gradstein et al. (2012) is used.

4.1.5. Magnetostratigraphy

The principle of paleomagnetic dating is to correlate the GPTS with a succession of measured inversions in a sedimentary sequence for which the dating is unknown, unlike the stratigraphic positions of the periods. The inversion periods of the GPTS are called chrons and are of variable duration as the magnetic inversions are of aleatory occurrence. This length variability is used for the correlations; it allows the dating of sedimentary sections and to deduce accumulation rates. This approach is based on fundamental hypotheses regarding the sedimentation processes: 1) the sedimentation must be continuous in time, without significant sedimentary gaps or erosion unconformity over a period sufficiently long to identify enough inversions; 2) the sedimentation rate must be relatively constant on short time scales, as the thicknesses of the detected inversions will be correlated with the length of the GPTS inversions.

Magnetostratigraphy dating allows the dating in a "pseudo-absolute" way of sedimentary sequences, poorly or not constrained with classical absolute dating such as biostratigraphy or isotopic methods. In fluvial continental series without magmatic rocks, the isotopic dating of sedimentary deposition is very difficult.

4.1.6. Analytical procedure

Samples are collected and orientated at regular stratigraphic intervals in a sedimentary section. Then the samples are thermally demagnetised in an amagnetic oven. The thermal demagnetisation is based on the Curie temperature principle. Above this temperature, any magnetic body loses its magnetisation. The thermal demagnetisation of the samples is performed through temperature steps. At each temperature step, magnetic grains exposed to temperature higher than their respective demagnetisation temperature lose their magnetization orientation and re-orientate in the current local magnetic field. As the samples are cooled in a null field magnetic chamber, they present a remanent magnetisation carried exclusively by particles of higher Curie temperature than the temperature at which they have been exposed. In this way, increasing stepwise the temperature of the samples allows identification of the different components of the Remanent magnetisation and the minerals which carry them, and eventually the polarity of the period they are contained in. From the results of all samples from a sedimentary succession, a polarity column can be realised and correlated to the GPTS.

4.1.7. Maximum depositional age constraint

Since magnetostratigraphy is a "pseudo-absolute" dating method, a correlation can only be successful if independent time constrains are provided. Indeed, correlating without a required minimum knowledge on the approximate time of deposition is very difficult considering the high number of reversals in geological history. A relevant method for sedimentary sections without ash layers or biostratigraphy is detrital thermochronology. In this thesis, the apatite fission-track thermochronological system has been used to define maximum depositional ages. Unless reset, an apatite grain cannot be deposited prior to its fission-track age. Consequently, the apatite fission-track age is regarded as a maximum age for the deposition of the sediments deposited above the apatite sample in the stratigraphic section. This method is briefly described in the thermochronology section, and detailed further in chapter 1 and 3 as it has been respectively performed by I. Coutand and P. O'Sullivan.

4.1.8. Age uncertainties

The uncertainties on magnetostratigraphic ages are of several natures. They can be related to the chosen correlation. Indeed, several correlations are possible for a sedimentary sequence (see chapter 1 and 3), and arguments to discriminate between correlations are not necessary possible. The preferred correlation is the main factor of bias. The quality of a correlation is dependent on the quality of the column (sampling density, magnetic properties, lithology and continuous exposure of

outcrop). Additionally, the hypothesis that the accumulation rate is relatively constant is also a source of uncertainty in the correlation and therefore the dating.

4.1.9. Other applications

Magnetostratigraphy offers other applications, for instance in chapter 3, it helped in the choice of a relevant "absolute" dating technique. Sedimentary rocks from the Sibo outcrop of the combined Sibo-Remi-Siang section (chapter 3) were not of sufficient exposure to allow magnetostratigraphic dating. These sedimentary rocks have been estimated to be of Late Quaternary age based on field observations. Towards the objective of dating more precisely these sedimentary rocks, paleomagnetic analysis has been carried out and the results indicate deposition during a normal polarity period. An age between 0 and 0.8 Ma has been inferred from this results, as the last and current period is normal since 0.8 Ma. Consequently, luminescence dating for this time scale has been performed. This method will not be developed in this section, as it has been carried out by S. Lowick in Bern University, but described in chapter 3 and the corresponding appendix.

4.2. Provenance analysis

The provenance analysis of this thesis involves isotopic dating of different minerals, using different isotopic systems. These can be grouped in two main categories, U-Pb geochronology and thermochronology. Although both categories imply temperature, in this section, U-Pb geochronology refers to temperature of crystallisation whereas thermochronology dating it based on lower temperatures. However, in chapter 3, rutile U-Pb dating is regarded and used as a thermochronological system contrarily to zircon U-Pb which is only used as a geochronological system throughout the manuscript. For this reason rutile U-Pb dating will be mentioned in both categories.

4.2.1. Mineral separation

The samples collected in the field areas were prepared in order to extract the minerals of interest for the provenance analysis. A series of laboratory stages allowing the separation are described here. Sample preparation was conducted at Lancaster University for the crushing, sieving and part of the picking stages and at NIGL, BGS (Keyworth) for the density and magnetic separations.

The first step is to dry the rock samples at a temperature low enough to avoid any crystal resetting, for instance <35 °C has been adopted by the author. A small fraction of each sample has been stored at this step, for storage and archive. The remaining fractions were crushed using a jaw crusher at

Lancaster University to reduce the rocks to sand samples. The resulting material was sieved using a 500 µm sieve at Lancaster University. The >500 µm fraction was packed for storage. The fine fractions were washed with tap water at NIGL, and processed through a Haultain superpanner for wet gravimetric separation. The separates have been dried at <35 °C. Then white micas for ^{40}Ar-^{39}Ar dating were handpicked from the light fraction at Lancaster University. The remaining light fractions were stored. A hand magnet was used to remove the major part of magnetic minerals, in any, from the dry heavy fraction. The resulting low magnetic sample separate was poured into a dropping funnel containing di-iodomethane. This heavy liquid has a density of which has a density of ~3.3 which allows minerals of higher ρ to be separated, for instance zircon and rutile grains. Heavy minerals sink to the bottom of the dropping funnel, whereas light ones float. Apatites are of a lower density, and the light fractions from the heavy liquid separation were sent to ISTerre (Grenoble, France) for separation through lower density heavy liquid (density of ~3.1). The remaining fractions were collected on separate filter papers and rinsed with acetone, then dried under a heat lamp. The resulting heavy fractions were stepwise passed through Franz isodynamic barrier laboratory separator. This magnetic separation was kept to a minimum to avoid biasing mineral populations. The resulting separates were of different magnetic strength, and the low-magnetic fractions were used for rutile and zircon handpicking. Zircon and rutile grains were handpicked at NIGL or Lancaster University, taking special care to select all grain types with respect to morphology, colour and grain size. More than 100 zircons and rutile grains were separately mounted in epoxy, polished and photographed to help identify the grains of U-Pb dating. The zircon mounts were also imaged by cathodo-luminescence using an FEI Scanning Electron Microscope at NIGL to ensure suitable core or rims areas were targeted during analysis. During core analysis, all grains were targeted, with no selection relative to morphology or size of grains. For zircon fission-track analysis, more than 300 zircon grains were mounted in Teflon at ISTerre by the author for some samples. Throughout the entire sample preparation process, large efforts were made to prevent sample contamination.

4.2.2. U-Pb Geochronology

The U-Pb dating method is used for dating minerals that crystallised during the cooling of igneous melts. The method is based on the uranium radioactive decay scheme. The measurement of parent and daughter isotopes in the mineral allows us to determine its U-Pb age. The parent isotope ^{238}U decays to daughter isotope ^{206}Pb with a constant λ of 1.55125 x 10^{-10} yr^{-1}, and the decay of ^{235}U to ^{207}Pb has a radioactive constant λ of 9.8485 x 10^{-10} yr^{-1} (Jaffey et al., 1971). These decay processes are described in the following equations:

$$\left[\frac{^{206}Pb}{^{204}Pb}\right]_P = \left[\frac{^{206}Pb}{^{204}Pb}\right]_I + \frac{^{238}U}{^{204}Pb}\left(e^{\lambda_{238}t} - 1\right)$$

$$\left[\frac{^{207}Pb}{^{204}Pb}\right]_P = \left[\frac{^{207}Pb}{^{204}Pb}\right]_I + \frac{^{235}U}{^{204}Pb}\left(e^{\lambda_{235}t}-1\right)$$

where P is the current abundance of nuclide, I is the initial abundance of nuclide and t is the age of the system. The isotope ^{204}Pb is non-radiogenic and thus used as a stable reference isotope in the above equations.

Because the half-life of ^{235}U is considerably shorter than that of ^{238}U, ^{235}U has been consumed more rapidly by radioactive decay, leading to a present-day ^{238}U/^{235}U ratio of 137.818 (Hiess et al., 2012). As a result, the ^{235}U/^{207}Pb ratio is more difficult to measure precisely in younger samples than the ^{238U}/^{206}Pb ratio. For this reason, ^{238}U/^{206}Pb ages are generally preferred for younger grains (<1200 Ma in this study), whereas ^{207}Pb/^{206}Pb ages are preferred for older grains. (Gehrels et al., 2006).U and Pb elements in silicates can be mobile during weathering and metamorphism (Davis and Krogh, 2001; Neymark and Amelin, 2008; Roberts and Finger, 1997). As a result, the mineral dated may not necessarily remain as a closed U-Pb system, and this directly impacts on the accuracy of the U-Pb age determinations. The unique property of the U-Pb system involving two separate decay schemes with common parent and daughter nuclides is that it allows us to assess whether a mineral has suffered system disturbance.

When a system has remained closed throughout its lifetime, i.e. no parent or daughter isotopes have escaped, correction has been made for initial common Pb (see below), then the measured age of the system is concordant. In this closed system context, the mineral undergoing U-Pb decay will plot on the concordia curve (the locus of all points where the ^{207}Pb/^{235}U and ^{206}Pb/^{238}U ages are equal; Fig. 11). This case is ideal, but in some cases the system opens and the mineral experiences lead loss. Consequently, the ratios will be discordant and the measured ^{206}Pb*/^{238}U (* refers to radiogenic) value will be lower than the concordant value. The discordant ages are plotted along a linear array between the point on the concordia at which the open system developed and a lower intercept, called a discordia. The lower intercept between the discordia and concordia lines commonly corresponds to the time at which the system opened, and the upper intercept to the age of the crystallisation of the mineral. If the lead loss is only partial the age can be obtained, however, the dating is impossible if the system has suffered total Pb* loss as the point will return to the origin (t = 0) on the concordia diagram.

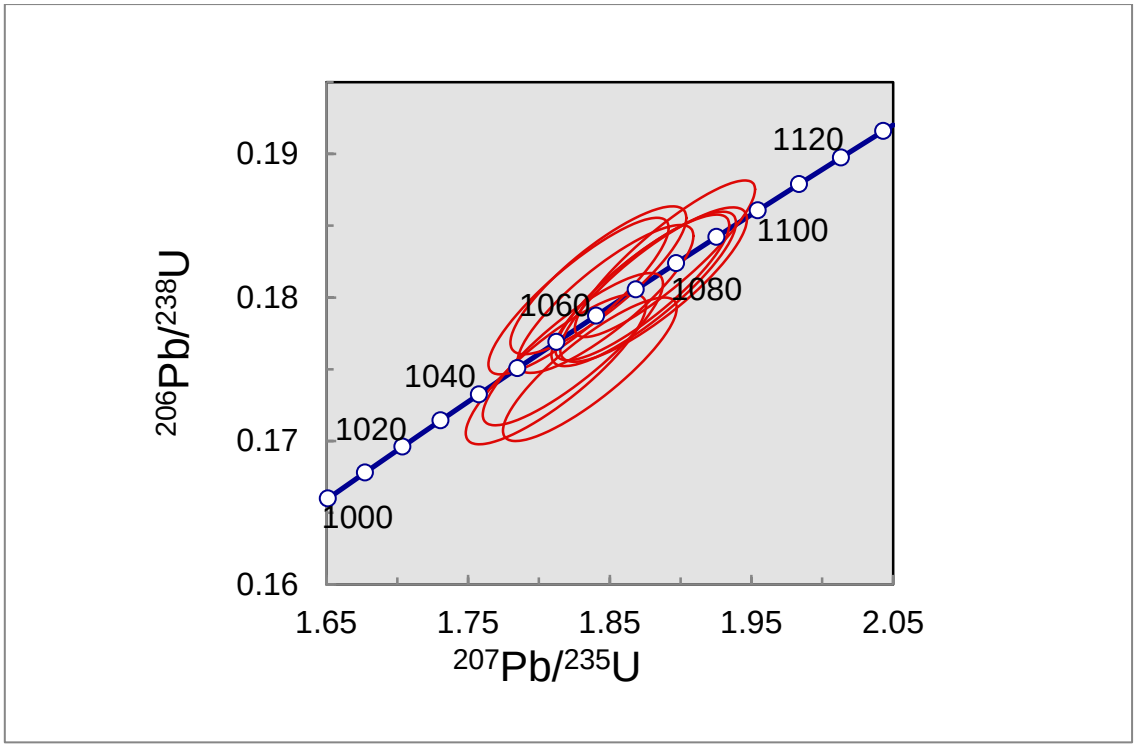

Fig. 11: *Zircon U-Pb concordia diagram of standard 91500 (Wiedenbeck et al., 2004) used for U-Pb dating in this study. Analyses are plotted as Wetherill concordia diagram, using the Isoplot v. 4.14 add-in for Microsoft Excel (Ludwig, 2003). The dotted dark blue line is the concordia curve where ages are indicated in Ma. Data point ellipses are at the 2σ level.*

The effects of Pb-loss can be minimized by using minerals which strongly bind uranium in their crystal lattice, and which have low Pb-diffusion rates. Zircon ($ZrSiO_4$), rutile (TiO_2) and apatite ($Ca_5(PO_4)_3(F,Cl,OH)$) are suitable minerals for U-Pb dating. They occur as accessory minerals in igneous rocks, have a high temperature sensitivity for Pb diffusion at >900 °C for zircon; 575±75 °C for rutile and 375-550 °C for apatite (Bracciali et al., 2016; Cherniak et al., 1991; Cherniak, 2010; Cherniak and Watson, 2001; Cochrane et al., 2014; Mezger et al., 1989; Schmitz and Bowring, 2003; Smye and Stockli, 2014) and are ultra-stable (zircon and rutile) and stable (apatite) heavy minerals (Morton and Hallsworth, 1999 and references therein). These properties make these minerals relatively resistant to weathering and post-crystallisation events (e.g. metamorphism) that might reset their respective system.

Zircon has traditionally been the most commonly used mineral for U-Pb dating. Zircon strongly incorporates uranium during crystallisation, while, common lead is largely excluded. The levels of common Pb present in zircon are generally low enough that no correction for common Pb is required. By contrast, rutile and apatite commonly incorporate relatively high levels of common Pb

during crystallisation, and as a result may give discordant ages. For rutile and apatite, it is commonly necessary to apply a common Pb correction. In this study, rutile model ages were derived following the approach of Bracciali et al. (2013), by regressing data points through a fixed terrestrial common Pb composition (0.844±0.008) on Tera-Wasserburg plots. Apatite U-Pb data processing was performed using an iterative approach to obtain a $^{207}Pb/^{206}Pb$ intercept value based on a starting estimate generated from the terrestrial Pb evolution model of Stacey and Kramers (1975) as described in Chew et al. (2011). This was used to calculate apatite ^{207}Pb-corrected $^{206}Pb/^{238}U$ ages.

With detrital mineral data, it is difficult to constrain whether discordance is entirely due to the presence of common Pb, or whether there is a component of Pb-loss. For this reason, in attempting to determine the youngest age component in a sample, it is important to identify populations of young grains with consistent 206Pb/238U ages, rather than relying on single grain ages. It may also be appropriate to perform multiple spot analyses on young grains in order to test for Pb-loss.

Zircon, rutile and apatite U-Pb dating provides the ages of source rocks, which could be derived from both igneous and high grade metamorphic terranes, or may be recycled from second cycle sedimentary sources. Apatite is more brittle than zircon and rutile, and is less likely to survive multiple recycling. The U-Pb zircon dating method has been widely applied in the Himalaya, both in detrital and source characterisation studies (e.g. Bracciali et al., 2015; DeCelles et al., 2004; Gehrels et al., 2008). However, apatite U-Pb dating in Himalaya has not been investigated as far the author is aware. Consequently, this thesis provides the first Himalayan apatite U-Pb dataset. Detrital zircon and apatite U-Pb dating are used for provenance analysis sensu-stricto, i.e. to investigate the paleodrainage of the Brahmaputra River, in chapter 2 and 3 of this thesis whereas rutile U-Pb is used as thermochronometer documenting the Namche Barwa syntaxis evolution in chapter 4.

The author has dated, regressed and interpreted zircons and rutiles with I. Millar using a laser ablation inductively coupled plasma mass spectrometer (LA-ICPMS) at the NERC Isotope Geoscience Laboratory, Keyworth (UK), and an ion probe at GRPG Nancy (France) (for part of the samples in chapter 2). The apatite U-Pb data was provided as part of apatite double-dating (fission-track and U-Pb) performed by P. O'Sullivan, regressed by C. Mark and interpreted by the author. Full details on the analytical methods are provided in appropriate chapters and appendices.

4.2.3. Thermochronology

Thermochronological dating allows the reconstruction of the temperature evolution in rock formations and to deduce exhumation rates. The thermochronological methods date the moment when a mineral is exposed to a temperature at which the isotopic-mineral system is sensitive. This temperature corresponds to the maximum temperature under which the products of radioactive decay of radiogenic isotopes are conserved within the mineral in the case of white-mica ^{40}Ar-^{39}Ar or rutile U-Pb systems for example; or the retention of latent tracks of spontaneous fission of ^{238}U in the case of apatite or zircon fission-track systems for example. This temperature, commonly called closure temperature, is specific to the thermochronological system considered and depends on the cooling rates of the mineral (Dodson, 1973) (Fig. 12).

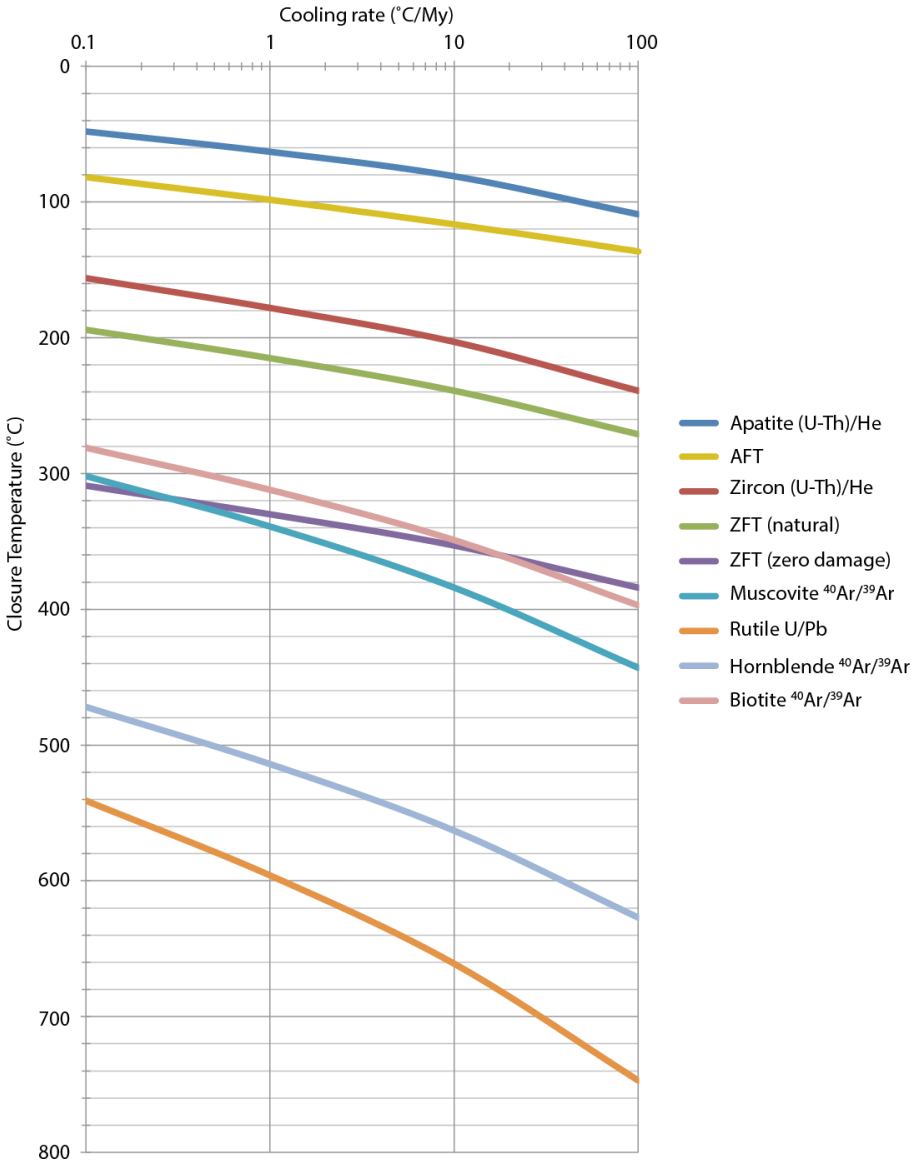

Fig. 12: *Effective closure temperature (Tc) as a function of cooling rate for common He, Fission-track (FT), Ar-Ar and U-Pb thermochronometers (modified after Reiners and Brandon, 2006).*

The reconstruction of the temperature history allowed by this type of dating has a wide application field in geosciences: the estimation of denudation or exhumation rates in orogenic or stable continental zones (e.g. Fitzgerald et al., 1995; Gallagher et al., 1998), the burial history in sedimentary basins (e.g. Armstrong, 2005; Najman et al., 2001; Najman et al., 1997), the dating of fault activity (e.g. Tagami, 2005) and also the tracking of detrital sediments (Carter and Moss, 1999; Hurford and Carter, 1991; Najman, 2006; White et al., 2002).

In this section, the author presents the thermochronological techniques of apatite and zircon fission-track, and white-mica ^{40}Ar-^{39}Ar systems and how the results are used in this study. Note that the apatite fission-track dating presented in this thesis has been performed by the traditional external detector method (e.g. Gallagher et al., 1998) and interpreted by I. Coutand in chapter 1 and by ICP-MS method (Donelick et al., 2005) by P. O'Sullivan. Both zircon fission-track dating, carried out using the external detector method, and white-mica ^{40}Ar-^{39}Ar dating have been acquired by the author under the guidance of M. Bernet at ISTerre (France) and J. Wijbrans and L. Gemignani at the VU University (The Netherlands), respectively.

4.2.3.1. FISSION-TRACK DATING

This section describes the general principles of zircon (and apatite) fission-track dating and the analytical technique of zircon fission-track dating using the external detector method carried out by the author.

4.2.3.1.a. Fission-tracks formation

Zircon (and apatite) fission-track, ZFT (and AFT), method is based on the accumulation of damages (the fission-track) within zircon (and apatite) crystals. These tracks are formed by spontaneous fission of heavy atomic nuclei such as ^{235}U, ^{238}U and ^{232}Th. The amount of spontaneous tracks formed by other isotopes other than ^{238}U is neglected since their half-life decay constant is very long and their proportion is low in zircon and apatite minerals. The ^{238}U isotope decays through emission of α particle or by spontaneous fission. There are about 2 x 10^6 disintegrations through α emission per spontaneous fission; it thus represents a minor decay mode. The fission of a Uranium atom leads to the release of two daughter ions ejected in opposite directions with a total kinetic energy in the order of 200 MeV creating a track in the crystal, linked to the ionisation of the atoms encountered (Fig. 13). Above the closure temperature, the resulting tracks in the crystal anneal and the mineral fission-track age is reset, whereas below the closure temperature, tracks are retained in the mineral. The closure temperature range, called the annealing zone (PAZ) for the zircon fission-track system, is

ranges between ~200 and 450 °C (Bernet, 2009; Tagami et al., 1998), and ~100±20 for the apatite fission-track system (Wagner and Van den haute, 1992), Fig. 12. Minerals that have suffered re-heating to PAZ temperatures can be affected by partial track annealing, and therefore partial age resetting, in which case the fission-track age determined will be younger. The tracks can only be observed using a transmission electron microscope. It is only after chemical etching that the tracks are revealed and observable with an optical microscope (x 1000).

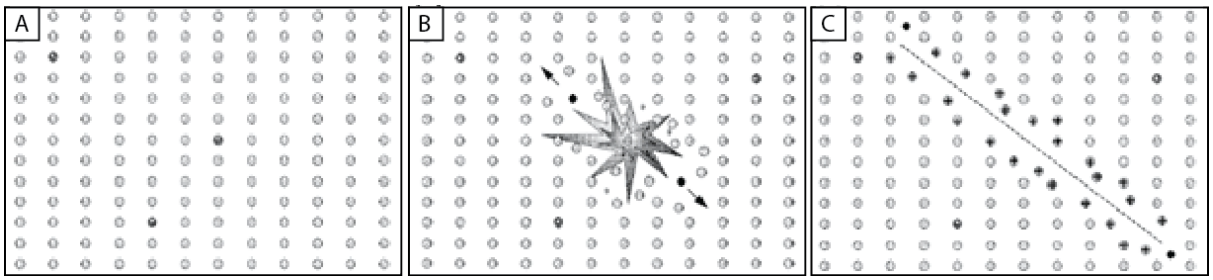

Fig. 13: *Cartoon representation of the ion spike explosion model and the formation of fission tracks in a mineral. (a) Trace amounts of radioactive ^{238}U are present in the crustal lattice (dark circles). (b) Spontaneous fission of ^{238}U. (c) Resulting fission track. (Gallagher et al., 1998)*

4.2.3.1.b. Dating of the system closure

The conventional fission-track method and the most widely used is the external detector method (Fig. 14), which the author has adopted for zircons. Another method using ICP-MS has been performed on apatites by P. O'Sullivan at *Geosep* (USA) as described in chapter 3 and the corresponding appendix.

The external detector method consists of counting the spontaneous tracks in the zircon (or apatite) crystals and the induced tracks in an external detector (micas with low Uranium content) in contact with the crystal during irradiation with thermal neutrons in a nuclear reactor (Gallagher et al., 1998).

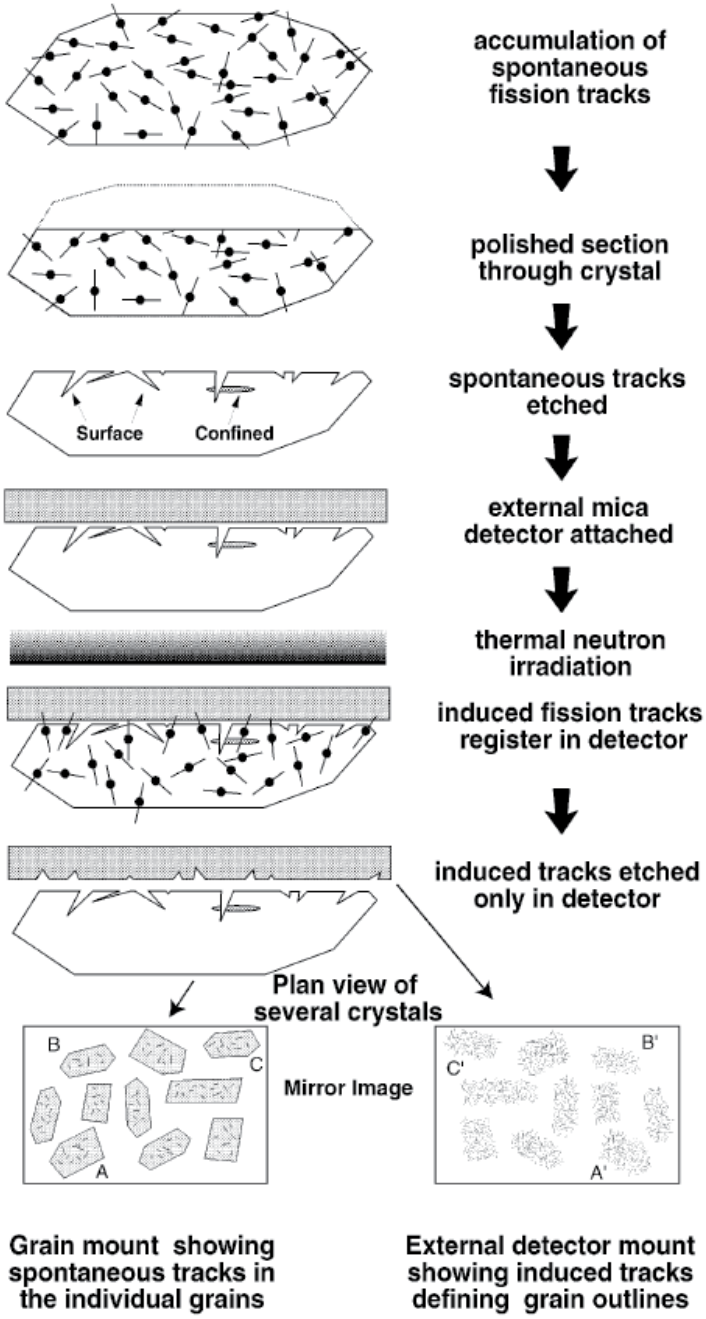

Fig. 14: *The external detector method (Gallagher et al., 1998 and references therein).*

For an effective age determination, knowledge of the relative abundance of the parent and daughter elements is necessary. Considering that each spontaneous track corresponds to the fission of an atom ^{238}U, the track density is a function of the initial ^{238}U content and the time at which the closure isotherm has been crossed. Spontaneous track density per surface unit ρ_s is estimated by counting using an optical microscope after etching of the polished crystal. The determination of the initial ^{238}U content in the crystal can be deciphered from the measurement of the ^{235}U content, since the

$^{238}U/^{235}U$ ratio is constant and equal to 137,88. The sample irradiation by thermic neutrons provokes ^{235}U fission only which creates a new set of tracks, the induced tracks. Damages formed by these induced tracks are recorded in the external detector. Similarly to the spontaneous tracks, the induced track density ρ_i is determined by counting after etching of the mica sheet. ρ_i is function of the initial ^{235}U content in the crystal and of the irradiation intensity, i.e. the fluence ϕ (neutrons.cm^{-2}). Fission-track dating is described with the following fundamental equation:

$$t = \frac{1}{\lambda_d} \ln\left(1 + \frac{\rho_s g \lambda_\alpha \phi \sigma I}{\rho_i \lambda_f}\right)$$

where t is the age; ρ_s and $\rho_i$are the spontaneous and induced track density, respectively; λ_d is the total radioactive decay constant; λ_α is the radioactive decay constant of ^{238}U per α emission (1,55125 x 10^{-10}.yr^{-1}); λ_f is the radioactive decay constant of ^{238}U through spontaneous fission-track (8,216 x 10^{-17}.yr^{-1}); g is the geometric factor of the mineral, dependant on the system considered; ϕ is the neutron fluence; σ is the efficient section of ^{235}U by thermal neutron capture (570,8 x 10^{-22}.cm^{-2}); and I is the $^{235}U/^{238}U$ ratio (7,2527 x 10^{-3}).

The fluence ϕ parameter is estimated through track counting on two standard glasses of known ^{235}U content, mounted with external detectors (dosimeter) attached to the samples during irradiation. The track density of the dosimeter (ρ_d) allow determining the fluence ϕ since the uranium content is known, using the following equation:

$$\phi = B\rho_d$$

where B is a dosimeter constant.

In these equations, parameters such as λ_f or B are difficult to evaluate accurately. The problem can be tackled using a calibration constant ζ (Hurford and Green, 1983). This constant allows the estimation of these parameters using standard material of known age. For instance, Fish Canyon Tuff standard, aged of 27,98±0.15 Ma (Dazé et al., 2003) has been used in chapter 3. The calibration parameter is defined by the following equation:

$$\zeta = \frac{B\sigma I}{\lambda_f}$$

The injection of the later equation in the first equation gives:

$$t = \frac{1}{1 + \lambda_d} \ln\left(\lambda_d + \frac{\rho_s}{\rho_i} \rho_d \zeta g\right)$$

The determination of ρ_s and ρ_i in the standard samples of known age (t_{st}) allows the determination of ζ as following:

$$\zeta = \frac{e^{\lambda_\alpha t_{st}} - 1}{\frac{\rho_{s\,(st)}}{\rho_{i(st)}} \rho_d \lambda_\alpha g}$$

Note that the ζ factor depends on the track counter, and can vary throughout the life of the operator.

A detailed methodology of the fission-track analysis of this project is provided in each chapter involving fission-track dating (chapter 1, 3 and 4).

4.2.3.2. WHITE-MICA ^{40}Ar-^{39}Ar

This section describes the general principles of white-mica ^{40}Ar-^{39}Ar dating carried out by the author, and further details are provided in chapter 4 and the corresponding appendices.

The white-mica ^{40}Ar-^{39}Ar dating method is based on the decay of ^{40}K to the isotope radiogenic ^{40}Ar with a decay constant of 5.81 x 10^{-11} yr^{-1} and described by the following equation:

$$^{40}\mathrm{Ar}* = \frac{\lambda_e}{\lambda} {}^{40}\mathrm{K}(e^{\lambda t} - 1)$$

Where $^{40}\mathrm{Ar}*$ is the argon radiogenic isotope, λ_e is the decay constant for $^{40}\mathrm{K}$ through electron capture, and λ is the total decay constant of $^{40}\mathrm{K}$.

Before the development of the ^{40}Ar-^{39}Ar method, the K-Ar method was initially used. In the former K-Ar analysis, K and Ar were analysed separately, involving sample splitting and accuracy problems. The new ^{40}Ar-^{39}Ar method allows simultaneous measurement of both ^{40}Ar and ^{39}Ar and this presents the advantages of improvement on precision, accuracy and error reduction, in comparison with the older approach.

Prior to analysis, the white-mica samples along with the reference materials are irradiated in a nuclear reactor. The irradiation induces the decay reaction: ^{39}K + n → ^{39}Ar + p through a fast neutrons bombardment which converts part of the ^{39}K into ^{39}Ar. The resulting ^{39}Ar content is used as a proxy for the determination of the initial ^{39}K content in the sample. Prior to irradiation the reference material, a standard of known age, is analysed in order to calculate the ^{39}K content transformed into ^{39}Ar during the irradiation. The relatively long half-life of the ^{39}Ar (269 years) allows approximating this isotope as stable over the time length between the irradiation and the measurement. The age equation modified for ^{40}Ar-^{39}Ar dating is consequently as following:

$$\mathrm{t} = \frac{1}{\lambda} \ln\left(\frac{^{40}\mathrm{Ar}*}{^{39}\mathrm{Ar}} \mathrm{J} + 1\right)$$

where t is the ^{40}Ar-^{39}Ar age; λ is the radioactive decay constant of ^{40}K (~5,5 x 10^{-10} $year^{-1}$, corresponding to a half-life of ~1.25 billion years); and J is the irradiation factor, i.e. the fluence of

the neutron bombardment during irradiation; the denser the flow of neutron particles is, the more atoms of ^{40}K will convert to ^{40}Ar. The easiest way to quantify J is to assume that $J_{sample} = J_{standard}$ since the age of the standard is known.

After irradiation, the radioactive samples must be safely cooled down before the analysis can be performed. The samples are then degassed through heating which causes the mineral crystal structure to degrade, allowing trapped gas to release. The ^{40}Ar-^{36}Ar and ^{39}Ar-^{36}Ar ratios are simultaneously measured with a noble gas mass spectrometer. These ratios are plotted on a straight isochron line of a slope proportional to the ^{40}Ar-^{39}Ar age of the sample (Fig. 15). In this way the ^{40}Ar-^{39}Ar age can be determined, and then corrected. Because neutron activation is non-selective, interference of argon isotopes derived from other nuclides is frequent during the irradiation, i.e. ^{40}Ca and ^{42}Ca, ^{40}K, ^{35}Cl and ^{37}Cl ($^{40}K + n \rightarrow {}^{40}Ar + p$; $^{40}Ca + n \rightarrow {}^{36}Ar + n\,\alpha$; $^{40}Ca + n \rightarrow {}^{37}Ar + \alpha \rightarrow {}^{37}Cl$; $^{42}Ca + n \rightarrow {}^{39}Ar + \alpha \rightarrow {}^{39}K$; $^{35}Cl + n \rightarrow {}^{36}Cl \rightarrow {}^{36}Ar$; $^{37}Cl + n \rightarrow {}^{38}Cl \rightarrow {}^{38}Ar$), and the resulting argon excess is corrected using appropriate correction factors. Additionally, contamination with atmospheric argon (representing 1% of the atmospheric composition of the Earth) is avoided by use of a sealed vacuum within the mass spectrometer created prior to analysis. Despite this precaution, atmospheric contamination can still occur either within the mass spectrometer or prior to analysis and an atmospheric argon correction is necessary. This correction is based on the known atmospheric $^{40}Ar/^{36}Ar$ ratio, equal to 296, and consists on subtracting 296 times the measured ^{36}Ar from the measured ^{40}Ar, such that the remaining ^{40}Ar content represents the radiogenic ^{40}Ar.

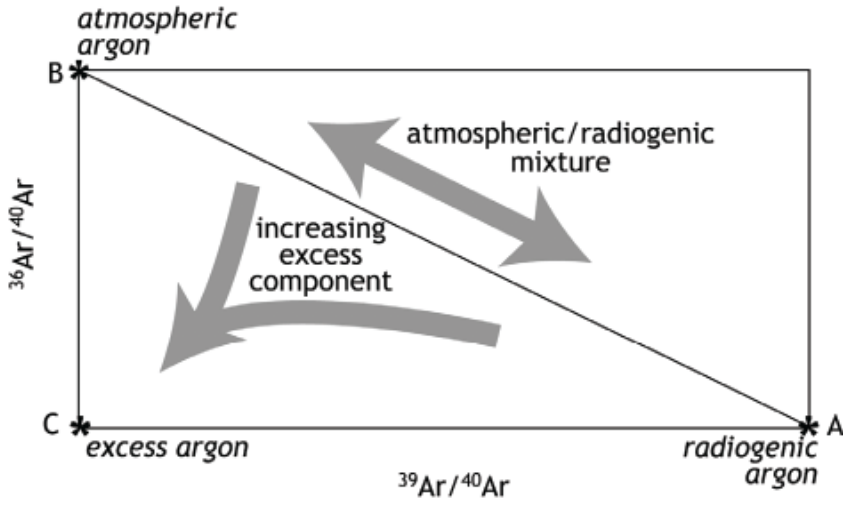

Fig. 15: *Argon isotope correlation diagram, showing a correlation between atmospheric and radiogenic argon components forming an isochron. Any pure ^{40}Ar component would lie at the origin and thus any excess argon component tends to pull the point B towards the origin. (Kelley, 2002)*

Muscovite ($KAl_2(AlSi_3O_{10})(F,OH)_2$) is composed of ~9.7 % of potassium, rendering this mineral suitable for ^{40}Ar-^{39}Ar dating method. The closure temperature of white-mica ^{40}Ar-^{39}Ar varies between 300 and 450 °C (Jäger, 1967; McDougall and Harrison, 1999). Above this temperature range, the system opens and argon gas is released from the crystal and the white-mica ^{40}Ar-^{39}Ar age is therefore reset. Under this temperature, the system is closed and its age is recorded within the crystal.

White-mica ^{40}Ar-^{39}Ar dating of this project was performed on a ThermoFisher Helix MC+ multi-collector noble gas mass spectrometer, as detailed in the supplementary material of chapter 4.

4.2.3.3. DETRITAL THERMOCHRONOLOGY

Detrital rocks are composed of grains which arise from different areas of the orogen and which have recorded different cooling histories. This record is then buried in sedimentary basins along the range. A detrital rock can therefore record the exhumation of different source areas within the orogen and a burial history within the basin. Deciphering the message archived in the sediment thus represents a major challenge in this approach.

In this thesis, thermochronology is used for two main aims: 1) determining the maximum depositional age of the sedimentary rock and 2) reconstructing the cooling and exhumation history of the source massif. If thermochronological ages are not reset, they can inform both questions. For both aims, the minimum age peak population for each thermochronological system is of primary importance. The way to define the youngest age populations within a sample is described in the methodology of each relevant chapter (chapter 1, 3 and 4) and involves statistical analysis. For both aims, it is necessary to date a sufficient amount of grains so that the populations are well defined (note that this is also important for the provenance analysis of this thesis involving apatite and zircon U-Pb, in chapter 2 and 3). The required number of dated grains to determine efficiently the populations in a detrital sample remains poorly constrained (Vermeesch, 2004). In this study, the number of dated grains has been targeted to more than a hundred. However, because of limitations such as the low abundance of grains of a specific mineral, their quality for dating, and the costs of analyses, this value has only rarely been reached.

As mentioned previously, apatite fission-track is used for maximum depositional age determination (chapters 1 and 3), since it has a lower closure temperature compared to the other thermochronological systems used in this study. Indeed, the lower closure temperature of the

apatite fission-track dating implies a higher sensitivity of the system to resetting. Therefore, apatite fission-track ages are more likely to be younger than ages from other higher closure temperature system within the same sample (see discussion in chapter 4). Consequently, if apatites are not reset after their deposition, the maximum depositional age determined with apatite fission-track will be closer to the true depositional age than if determined with a higher closure temperature system. Post-depositional resetting by burial heating can be assessed in several ways. For instance additional vitrinite reflectance analysis has been performed in chapter 1, to determine the maximum temperature at which a stratigraphic layer has been exposed. Comparison of this maximum temperature with the closure temperature of apatite fission-track indicates if the system is likely to have suffered total or partial annealing. In chapter 3, analysis of the evolution of the minimum age peak throughout the sedimentary section has been performed, as well as a comparative study of the nearby Siwalik sections. In this study, apatite fission-track dating is strictly used to determine the minimum depositional age and to constrain the magnetostratigraphic correlations; whereas higher closure temperature thermochronological systems are only used for tectonic reconstruction of the source area. These distinct uses of the thermochronological systems are a strategical choice to avoid circular reasoning in the lag times study (see below).

Zircon fission-track, white-mica ^{40}Ar-^{39}Ar and rutile U-Pb dating have been used for exhumation reconstruction of the source area in chapter 4. Once the minimum age peak has been determined for the thermochronological system considered, and the dating of sediment deposition is constrained, for instance through magnetostratigraphy, lag-times can be deduced (Fig. 16). The lag time can be defined as the time difference between the thermochronological age (for instance, the minimum age peak) and the depositional age of the sample (Garver and Brandon, 1994; Garver et al., 1999). It is, in other words, the time difference between the age of the closure of the thermochronological age in the source area and the age of deposition of the eroded material.

Rocks from the source area are exhumed from deeper warm crustal zones to the surface, such that they cross the closure isotherm and the lag time begins. Lag times can be transformed to exhumation rates, assuming simplifying hypotheses. The first hypothesis is that the time of transport of the sediment from the moment when the rock reaches the surface and the moment when it is deposited is insignificant compared to the time from the closure of the system to the moment when the rock reaches the surface, i.e. the exhumation time. In an active mountain belt, this hypothesis is likely (Bernet et al., 2004b). Another necessary hypothesis is the estimations of the geothermal gradients and, in the case of rapid exhumation zones (>1 km/Ma), the induced isotherms

perturbation must be taken into account. These estimations are integrated in a model developed by P. van der Beek (UJF Grenoble); and are described in chapter 4 and the corresponding appendices.

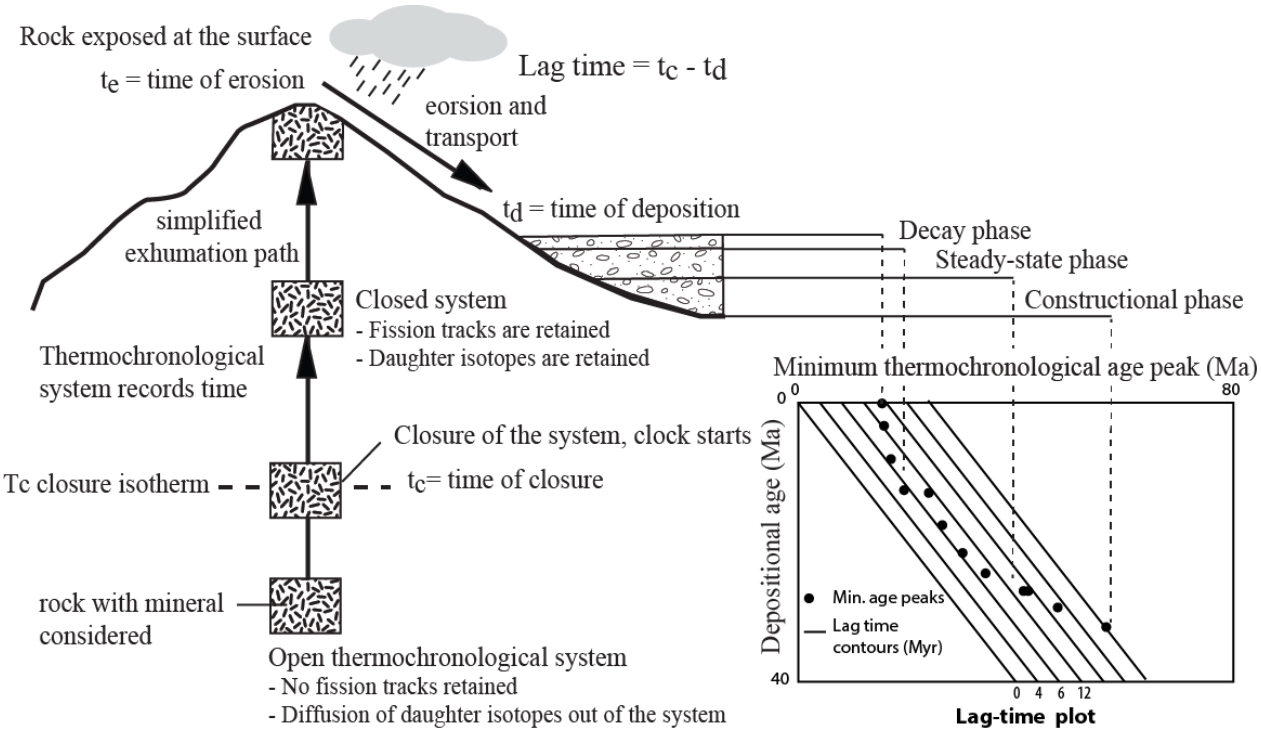

Fig. 16: *The lag-time of a sample is the time required for the sample to cool, get exhumed to the surface, and then get deposited in a nearby basin. As a rock is exhumed to the surface, the rock cools below the closure temperatures of the different thermochronometers: when this happens, various isotopic clocks start. Eventually the rock reaches the surface where it is subject to erosion. Apatite, zircon, mica and rutile grains are released into sediment and transported by glaciers and rivers into the adjacent basins, where they are deposited. The time for erosion and sediment transport is generally regarded as geologically instantaneous (e.g. Bernet et al., 2004a), but this is not always the case. The lag time integrates the time between closure and the time of deposition, and mainly represents the time needed to exhume the rock to the surface. The lag-time plot represents the calculated lag times for the youngest components in the samples where different evolution phase in the source region are identified. (modified after Bernet and Garver, 2005)*

CHAPTER 1

Late Miocene-Pleistocene evolution of India-Eurasia convergence partitioning between the Bhutan Himalaya and the Shillong Plateau: New evidences from foreland basin deposits along the Dungsam Chu section, eastern Bhutan

Isabelle Coutand[1], Laurie Barrier[2], **Gwladys Govin[3]**, Djordje Grujic[1], Carina Hoorn[4], Guillaume Dupont-Nivet[5], and Yani Najman[3]

1-Department of Earth Sciences, Dalhousie University, Halifax, Nova Scotia, Canada

2-Institut de Physique du Globe de Paris, Sorbonne Paris Cité, Université Paris Diderot, UMR 7154 CNRS, Paris, France

3-Lancaster Environment Centre, University of Lancaster, Lancaster, UK

4-Institute for Biodiversity and Ecosystem Dynamics, University of Amsterdam, Amsterdam, Netherlands

5-Géosciences Rennes UMR-CNRS 6118, Rennes, France

Tectonics, 2016, 35. DOI : 10.1002/2016TC004258

ABSTRACT

The Shillong Plateau is a unique basement-cored uplift in the foreland of the eastern Himalaya that accommodates part of the India-Eurasia convergence since the late Miocene. It was uplifted in the late Pliocene to 1600 m, potentially inducing regional climatic perturbations by orographically condensing part of the Indian Summer Monsoon (ISM) precipitations along its southern flank. As such, the eastern Himalaya-Shillong Plateau ISM is suited to investigate effects of tectonics, climate, and erosion in a mountain range-broken foreland system. This study focuses on a 2200m thick sedimentary section of the Siwalik Group strategically located in the lee of the Shillong Plateau along the Dungsam Chu at the front of the eastern Bhutan Himalaya. We have performed magnetostratigraphy constrained by vitrinite reflectance and detrital apatite fission-track dating, combined with sedimentological and palynological analyses. We show that (1) the section was deposited between ~7 and 1Ma in a marginal marine deltaic transitioning into continental environment after 5 Ma, (2) depositional environments and paleoclimate were humid with no major change during the depositional period indicating that the orographic effect of the Shillong Plateau had an unexpected limited impact on the paleoclimate of the Bhutanese foothills, and (3) the diminution of the flexural subsidence in the basin and/or of the detrital input from the range is

attributable to a slowdown of the displacement rates along the Main Boundary Thrust in eastern Bhutan during the latest Miocene-Pleistocene, in response to increasing partitioning of the India-Eurasia convergence into the active faults bounding the Shillong Plateau.

1. INTRODUCTION

Sedimentary archives of the Neogene-Quaternary Siwalik Group preserved in the Himalayan foreland basin have been extensively documented along the Himalayan arc from Pakistan to Nepal, providing valuable information on mountain building in space and time, past organization of drainage networks, and paleoclimate (e.g. Najman, 2006, and references therein). Recent studies have also focused on sections of the Siwalik Group in eastern India, in the states of West Bengal (More et al., 2016) and Arunachal Pradesh (Chirouze et al., 2012; Chirouze et al., 2013; Lang et al., 2016); however, there is still a lack of information in the frontal Bhutan Himalaya, leaving about 400 km along the strike of the orogen of undocumented foreland basin deposits regarding ages, thicknesses, sedimentary facies, and depositional paleoenvironments. Bhutan is located directly north of the Shillong Plateau, the only raised topography in the foreland of the Himalayas (Fig. 17), which corresponds to a 1600m high ancient erosion surface tilted northward by 2–4° (Biswas et al., 2007; Clark and Bilham, 2008). This plateau is made of Proterozoic-Paleozoic basement (Chatterjee et al., 2007; Ghosh et al., 1994; Mitra and Mitra, 2001; Selvam et al., 1995; Yin et al., 2010), uplifted along steep and seismically active crustal-scale reverse faults: the E-W trending Dauki Fault in the south and the inferred WNW-ESE trending Oldham Fault in the north (Bilham and England, 2001; Biswas and Grasemann, 2005; Mitra et al., 2005; Rajendran et al., 2004); (Fig. 17). The Shillong Plateau is bounded to the east by a NW-SE trending shear zone, the Kopili fracture zone (Kayal et al., 2010), accommodating right-lateral displacement at a rate of 3 mm/yr through the differential clockwise rotation between the Assam and Shillong blocks (Vernant et al., 2014); to the west it is marked by the NW-SE trending Goalpara right-lateral shear zone (Diehl et al., 2016). At the longitude of central and eastern Bhutan, the Himalayan foreland corresponds to a “broken foreland basin” (e.g. Jordan, 1995; Strecker et al., 2011), with a foredeep that may be <1 km thick, in contrast to areas west and east of Bhutan where the Brahmaputra/Ganges foredeep reaches depths >4 km (Dasgupta, 2000; Verma and Mukhopadhyay, 1977; Vernant et al., 2014, Figure 1b). On the Dauki Fault at the southern front of the Shillong, horizontal displacement averaged over the last 9–15 Ma was estimated at 0.65–2.3 mm/yr (Biswas et al., 2007) or 1–2.9 mm/yr (Clark and Bilham, 2008), while GPS data indicate much faster modern rates increasing eastward from 3 to 7 mm/yr (Vernant et al., 2014), suggesting that the amount of India-Eurasia convergence accommodated on the Dauki Fault is up to 3 times faster than the average rate in the past 10 Ma (Vernant et al., 2014). The

surface uplift of the Shillong Plateau has occurred in the Pliocene between 3–4Ma (Biswas et al., 2007) and 3.5–2Ma (Najman et al., 2016), thereby disturbing Indian Summer Monsoon (ISM) precipitations migrating northward from the Bay of Bengal by orographically condensing portion of these moisture-bearing winds along its southern flank (Bookhagen and Burbank, 2010). Over the last 8 to 6 Ma, spatial and temporal variations in exhumation and erosion rates were documented in the Bhutan Himalaya (Coutand et al., 2014; Grujic et al., 2006; McQuarrie and Ehlers, 2015). Grujic et al. (2006) proposed that these variations were the result of climatic changes in the lee of the Shillong Plateau, a hypothesis later modulated by Adams et al. (2015), Biswas et al. (2007), and Coutand et al. (2014) who proposed instead that most of the variations reflected increased contractional strain partitioning into the Shillong Plateau. As of now, it remains debatable as to whether tectonic or climatic processes related to the formation of the Shillong Plateau have had the most measurable impact on the upper crustal exhumation of the Bhutan Himalaya.

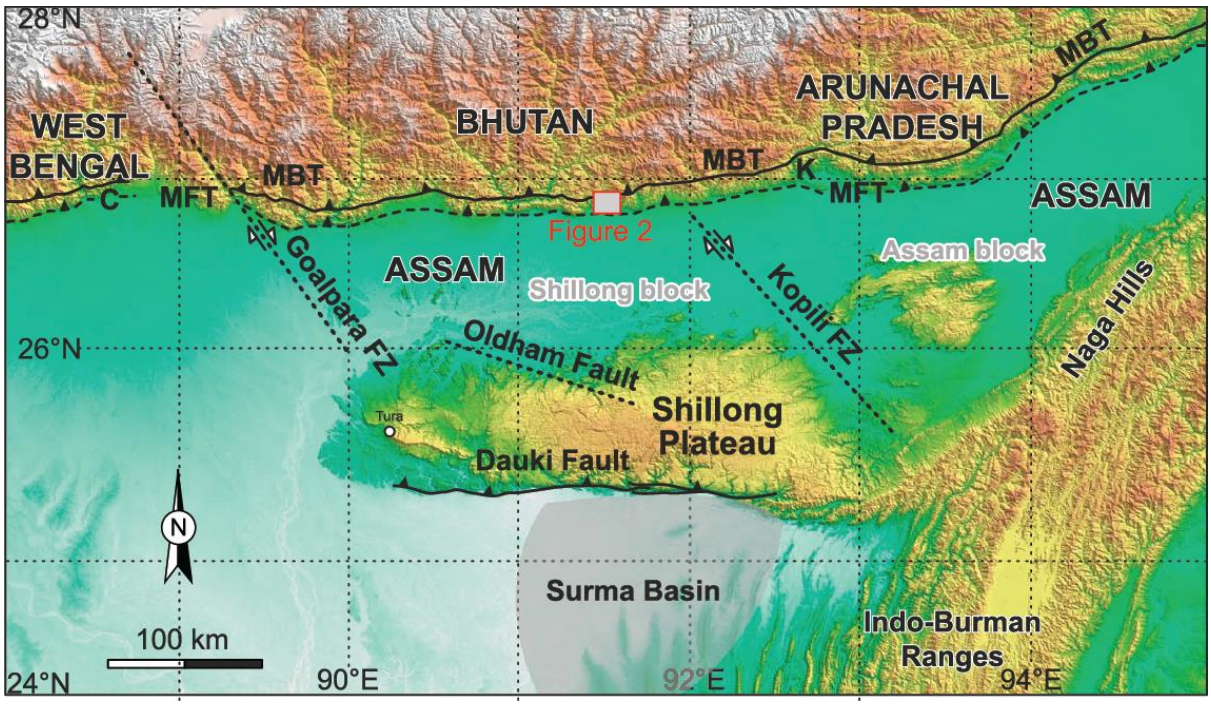

Fig. 17: *Digital topography and major structural features of southern Bhutan and Shillong Plateau area. Elevation data are from Shuttle Radar Topography Mission 3 data (U.S. Geological Survey). Structural data are from Gansser (1983), Biswas and Grasemann (2005), and Hirschmiller et al. (2014). The light shaded area south of the Shillong Plateau represents the location of the Surma Basin after Najman et al. (2016). Abbreviations are MBT: Main Boundary Thrust, MFT: Main Frontal Thrust, C: Churanthi river section (More et al., 2016), and K: Kameng section (Chirouze et al., 2012; Chirouze et al., 2013).*

To address this question, this study takes advantage of a strategically located foreland basin sedimentary section exposed along the Dungsam Chu near the town of Samdrup Jongkhar at the front of the eastern Bhutan Himalaya (26.8°N, 91.5°E) (Figs. 17 and 18). To decipher the sedimentary record through time, we have performed geochronological (magnetostratigraphy constrained by vitrinite reflectance data and detrital apatite fission-track dating), sedimentological, and palynological analyses on this 2200m thick continuous stratigraphic section of the Siwalik Group deposits. We provide new evidences supporting an increasing strain partitioning of the India-Eurasia convergence into the Shillong Plateau since the latest Miocene.

2. GEOLOGICAL SETTING

The Dungsam Chu section located in the foothills of the Himalaya in eastern Bhutan (Figs. 17 and 18) is composed of synorogenic Neogene-Quaternary foreland sediments of the Siwalik Group forming a 2216m thick section with a continuous exposure on freshly eroded stream banks. The section belongs to the modern Himalayan foreland fold-and-thrust belt as defined by Hirschmiller et al. (2014) and is bounded to the north by the Main Boundary Thrust (MBT), along which the Lesser Himalayan Sequence (LHS) has been thrust over the Siwalik Group since the late Miocene (10–12 Ma) (Coutand et al., 2014), and to the south by the Main Frontal Thrust (MFT), which juxtaposes the Siwalik Group strata against the modern Ganges-Brahmaputra plain alluvial sediments (Figs. 17 and 18) (e.g. Burgess et al., 2012, and references therein). Based on detrital thermochronology and/or the presence of growth strata, ongoing displacement on the MFT is suggested to have started ~2 Ma ago in central and western Nepal (Mugnier et al., 2004; van der Beek et al., 2006) and ~1 Ma ago in Arunachal Pradesh (Chirouze et al., 2013), while the timing remains undetermined in Bhutan.

The three lithostratigraphic subgroups of the lower, middle, and upper Siwaliks crop out along the Dungsam Chu section. All along the Himalayan range, the recognition of these subgroups is based on textural differences, specifically on the proportion of different grain sizes (for a definition, see Auden (1935), Gautam and Rösler (1999), and Quade et al. (1995a). Typically, the coarsest sediments of the lower, middle, and upper Siwalik subgroups correspond to thin-bedded fine- to medium-grained sandstones, thick-bedded medium to coarse-grained sandstones, and thin- to thick-bedded conglomerates, respectively. Accordingly, along the Dungsam Chu section, the boundary between the lower and middle Siwalik subgroups occurs at the first occurrence of few meters thick coarse-grained sandstone packages upsection, while the transition between the middle and upper Siwalik subgroups is where conglomeratic layers first appear (Bhargava, 1995; Gansser, 1983) (Fig. 18).

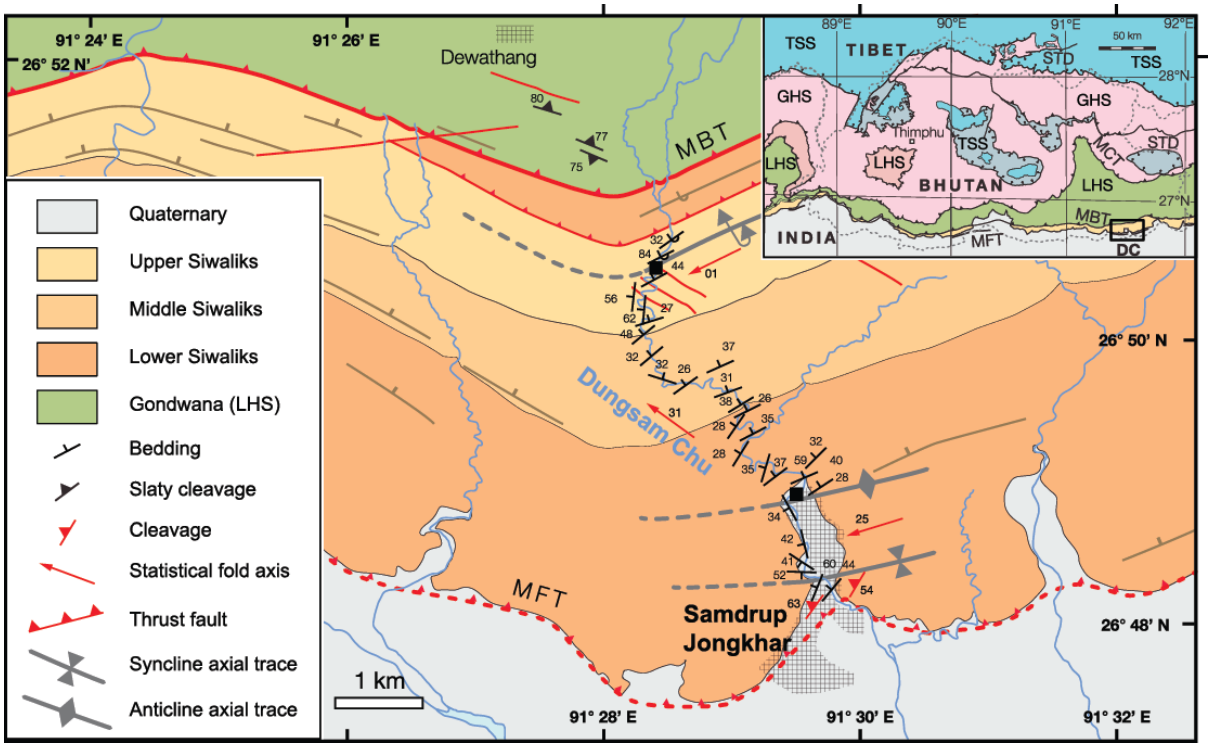

Fig. 18: *Geological map of the Siwalik Group around the Dungsam Chu (for location, see black frame labelled DC on the geological map of Bhutan in inset and red frame in Fig. 17). Abbreviations are TSS: Tethyan Sedimentary Sequence, STD: South Tibetan Detachment, GHS: Greater Himalayan Sequence, LHS: Lesser Himalayan Sequence, MBT: Main Boundary Thrust, and MFT: Main Frontal Thrust. The Dungsam Chu section presented in this study stretches from the anticline axial plane trace to the south (26.807567°N, 91.502100°E) to the overturned syncline axial plane trace to the north (26.834967°N, 91.483617°E) (black squares).*

3. DATING OF THE DUNGSAM CHU SEDIMENTARY SECTION

To constrain the age of the Siwalik Group deposits in eastern Bhutan, we have dated the Dungsam Chu section using magnetostratigraphy constrained by vitrinite reflectance data combined with detrital apatite fission-track (DAFT) dating (Fig. 19).

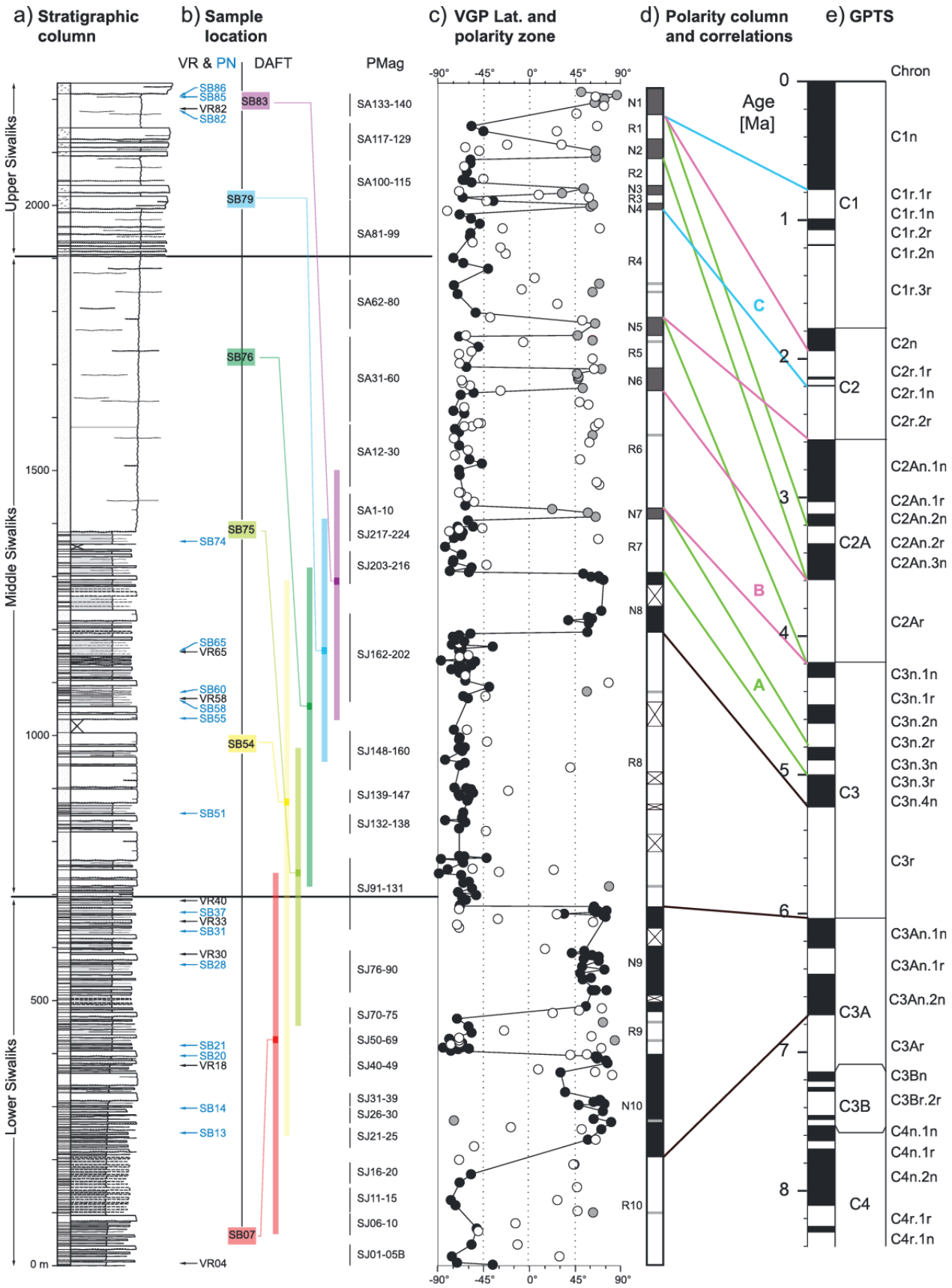

Fig. 19: *Sample location and magnetostratigraphy results of the Dungsam Chu section. (a) Simplified stratigraphic column (for details, see Fig. 26). The horizontal scale labels C, s, S, p, c, and B are*

abbreviations for clay, silt, sand, pebbles, cobbles, and boulders. (b) Locations of vitrinite reflectance (VR), palynology (PN), detrital apatite fission-track (DAFT), and magnetostratigraphy (PMag) samples. Maximum depositional ages deduced from DAFT are indicated by the DAFT P1 age (solid color square) and the associated 1σ errors (light coloured bars). (c) Virtual geomagnetic poles (VGP latitude) are indicated by black dots for reliable Q1 and Q2 ChRM directions, open circles depict unreliable Q3 and Q4 directions, and grey dots indicate unreliable isolated polarity directions in the lower part (below 1400m level) and normal polarity directions in the upper part (above 1400m level) that are unreliable due to potential normal overprints (see text). (d) Polarity column defined from our magnetostratigraphic measurements where black and white intervals indicate normal (N) and reverse (R) polarity zones, respectively. Grey intervals represent poorly constrained polarities defined either by only one or by potentially biased normal overprints in the upper part (above 1400m level). Intervals with a cross indicate gaps in the sampling. (e) Proposed correlations of the polarity column to the geomagnetic polarity timescale (GPTS) of Gradstein et al. (2012). Black solid lines indicate the robust correlation of the lower part based on the combination of DAFT and reliable paleomagnetic data. Green, purple, and light blue solid lines indicate uncertain correlations A, B, and C, respectively, for the upper part of the record based on DAFT and paleomagnetic data potentially biased by normal overprints. GPTS created using TSCreator v. 6.4 software from https://engineering.purdue.edu/Stratigraphy/tscreator/index/index.php based on timescale of Gradstein et al. (2012).

3.1. Peak temperatures from vitrinite reflectance

Vitrinite reflectance analysis is used to quantify the heating of the sediments during burial and, in this study, helped to select the thermochronometer most appropriate to constrain the depositional ages of the sedimentary series. Sampling strategy and analytical procedure are provided in Text S1 in the supporting information (ASTM, 2010; Barker and Pawlewicz, 1994). The samples collected for the vitrinite reflectance analysis are composed of large coaly or banded coal particles with almost no mineral matter. They are entirely made of vitrinite, mostly derived from woody tissues, with almost no other macerals such as organic constituents derived from other non-woody tissue like spores, pollen, resin, or other oxidized constituents (i.e., fusinites) (ICCP, 2001). All the samples yielded values below 0.5% Rm, in the upper to lower range of lignite (Fig. 20a and Figure A of Appendix I). The peak temperatures of the stratigraphically lower seven samples range between 59.5±3.5 and 75.8±6.1°C, without a distinguishable trend upsection, yielding a mean burial temperature of 67.1±5.5°C for the lower part of the section (Fig. 20a).

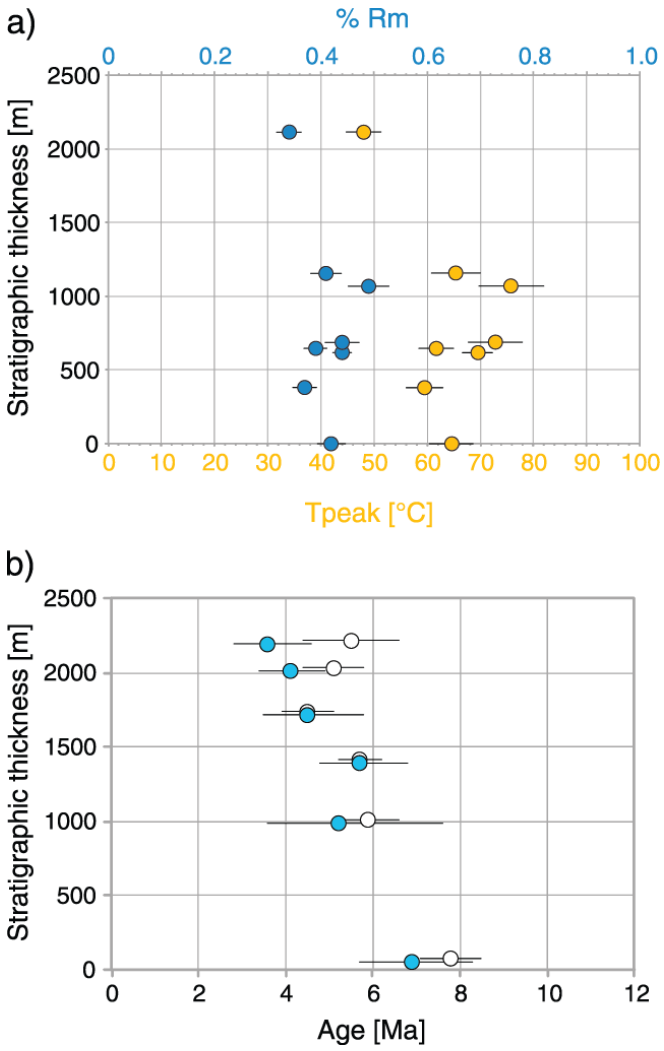

Fig. 20: *(a) Vitrinite reflectance data plotted against stratigraphic depth. In blue are the Rm % and in orange are the peak temperatures calculated according to the calibration of the Rm by Barker and Pawlewicz (1994). (b) Detrital apatite fission-track mean central ages (white circles) and P1 ages (blue circles) plotted as a function of stratigraphic thickness from the bottom (0 m) to the top (2,216 m) of the section.*

This lack of temperature gradient with increasing depth may be attributed to different factors:

1. The samples were collected along a northward tilted section; hence, upsection, the samples migrate along the depositional profile toward thicker portions of the Siwalik sedimentary wedge. Equivalent spatial trend of burial temperatures was observed in the North Alpine Foreland basin (Mazurek et al., 2006).

2. Basin modelling there (e.g. Mazurek et al., 2006) indicates that geothermal gradients can substantially deviate from linearity due to the lower thermal conductivity of weakly consolidated sediments at the surface as compared with the underlying basement rocks.

3. Rapid cycles of burial and exhumation of Siwalik sediments have likely prevented thermal equilibration at the scale of the basin (see example of the intramontane Angastaco Basin in NW Argentina (Coutand et al., 2006)). In this type of young (<15 Ma) dynamic orogenic sedimentary basins, thermal states are transient and rapidly vary along and across strike implying that our observations are hardly comparable with similar data collected >100 km east in Arunachal Pradesh by Chirouze et al. (2013) and several hundreds of kilometres west in central Nepal by (Mugnier et al., 1995).

Thus, the maximum burial Tpeak at the base of the section is significantly lower than the closure temperature of ~120±20°C apatite fission-track thermochronometry, excluding full thermal resetting of this radiometric system. Furthermore, the mean burial temperature of the basal sediments (67.1±5.5°C) is in the range of the lowermost thermal levels of the apatite fission-track partial annealing zone (for details, see Text S2 in the supporting information), suggesting that minimal to no partial resetting of the thermochronometric system occurred after deposition of the base of the section and hence mostly preserved the thermochronometric signal from the source area.

3.2. Detrital Apatite Fission-Track (DAFT) Thermochronometry

Vitrinite reflectance results yielded maximum burial temperatures that suggest that DAFT thermochronometry is likely to yield unreset cooling ages representing a maximum depositional age of the strata from which the detrital sample is derived. For details on DAFT method and sampling, see Appendix I (Brandon, 1992; Brandon, 1996; Brandon, 2002; Coutand et al., 2014; Donelick et al., 2005; Galbraith and Green, 1990; Reiners and Brandon, 2006; Vermeesch, 2012).

The central age of the basal samples is the oldest at 7.8±0.7 Ma (sample SB07) (Table 1 and Fig. 20b; raw data are available in Table S1 of Appendix I). From sample SB54 up to sample SB83 at the top of the section, the central ages are younger and vary from 4.5±0.6 Ma to 5.9±0.7 Ma but remain identical within error (Fig. 20b). Three out of the seven samples fail the χ^2 test (Galbraith, 2005) with $P(\chi^2)$<5% (Table 1), indicating that dispersion in the fission-track grain-age distributions may be significant. Apatite fission-track samples collected from bedrock samples across the modern landscape in eastern Bhutan vary significantly in a north-south direction (Coutand et al., 2014). Therefore, the age dispersion observed in the detrital data along the Dungsam Chu section may be attributed to different provenance areas characterized by different exhumation rates in the upstream catchments.

Altogether, vitrinite reflectance and DAFT data clearly indicate that no partial resetting occurred along the section. In fact, the bottommost sample yields maximum burial temperatures of 65±4°C and the temperature of the uppermost levels of the apatite fission-track partial annealing zone is comprised between 75 and 60°C for holding time of 1 to 10 Ma, respectively (e.g. Reiners and Brandon, 2006). Moreover, central DAFT ages decrease upsection (Figs. 19 and 20b and Table 1), while the opposite would be expected if the samples had been reset in the sedimentary basin and subsequently re-exhumed. To better constrain the stratigraphic age of the section, we have extracted the youngest component of the detrital age signal by decomposing the fission-track grain-age distribution into peaks using the Binomfit software (Brandon, 1992; Brandon, 1996; Brandon, 2002) (Table 1). The three samples failing the χ^2 test (samples SB54, 79, and 83) and the basal sample SB07 yield two peaks. The older peak (P2) represents a minor component of about 10% of the total detrital fraction for most of the samples and up to 30% for sample SB83 at the top of the section (Table 1). The younger peak (P1) represents the mode of AFT age derived from the fastest-eroding parts of the source catchment. The fact that P1 gets younger upsection (Fig. 20b), and that there is a marked dispersion of single-grain ages, supports vitrinite reflectance results suggesting that burial heating has little or not reset AFT single-grain ages after deposition. Therefore, we use P1 as a proxy for the maximum depositional age of the Siwalik Group along the Dungsam Chu sedimentary section. This implies that the sediments cannot be older than 6.9–1.2/+1.4 Ma at the bottom of the section (sample SB07) and 3.6–0.8/+1.0 Ma at the top (sample SB83) (Table 1 and Fig. 20b). Our results are supported by unpublished detrital zircon (U-Th)/He data collected from a sample located a few meters underneath our basal sample, yielding discordant single-grain ages with a younger cluster at 7Ma (N. McQuarrie, personal communication, 2016).

Table 1: *Detrital apatite fission-track results*[a]

Sample	Number of Grains	Cumulative Stratigraphic Thickness (m)	Spontaneous Track Density ($\rho_s \times 10^6$ cm^{-2}) (N_s)	Induced Track Density ($\rho_i \times 10^6$ cm^{-2}) (N_i)	Dosimeter Track Density ($\rho_d \times 10^6$ cm^{-2}) (N_d)	$P(\chi^2)$ (%)	Central Age ± 1σ (Ma)	U (ppm)	P_1 (Ma)	P_1 95%CI (%)	P_2 (Ma)	P_2 95%CI (%)
SB07	23	50	0.1383 (194)	4.6433 (6,513)	1.4585 (5,090)	38.8	7.8 ± 0.7	42	6.9–1.2/+1.4	88.8	12.2–3.3/+4.5	11.2
SB54	26	985	0.0978 (183)	4.7313 (8,850)	1.4889 (5,090)	1.7	5.9 ± 0.7	42	5.2–1.6/+2.4	86.2	10.0–8.0/+39.5	13.8
SB75	21	1390	0.0830 (126)	4.0221 (6,104)	1.4865 (5,291)	18.8	5.7 ± 0.5	36	5.7–0.9/+1.1	100	x	x
SB76	14	1715	0.0635 (59)	3.8566 (3,581)	1.4882 (5,291)	51.5	4.5 ± 0.6	44	4.5–1.0/+1.3	100	x	x
SB79	24	2010	0.1098 (195)	5.6400 (10,018)	1.4899 (5,291)	0.0	5.1 ± 0.7	50	4.1–0.7/+0.8	90.4	12.7–2.9/+3.8	9.6
SB83	17	2193	0.1227 (137)	6.2963 (7,028)	1.4916 (5,291)	0.0	5.5 ± 1.1	62	3.6–0.8/+1.0	69.5	15.2–4.5/+6.3	30.5

[a]Abbreviations are N, number of individual grains dated per sample; ρ_s, spontaneous track density; ρ_i, induced track density; N_s, number of spontaneous tracks counted; N_i, number of induced tracks counted; ρ_d, induced track density in external detector adjacent to dosimetry glass; N_d, number of tracks counted in determining ρ_d; $P(\chi^2)$, χ^2 probability. Apatite aliquots were mounted in araldite epoxy on glass slides, ground and polished to expose internal grain surfaces, then etched for 20 s in 5.5 M HNO_3 at 21°C to reveal spontaneous fission tracks. All mounts were prepared using the external detector method [*Hurford and Green*, 1983]. Samples and CN5 glass standards were irradiated with thermal neutrons in the Oregon State University reactor. After the irradiation, the low-*U* muscovite detectors that covered apatite grain mounts and glass dosimeter were etched in 40% HF for 45 min at 21°C to reveal induced fission tracks. Samples were then analyzed using a Kinetek computer-controlled stage driven by the FTStage software [*Dumitru*, 1993] attached to a Zeiss Axioplan microscope. Dry counting was done at a magnification of ×1000, and fission track ages were calculated using a weighted mean Zeta calibration factor based on International Union of Geological Sciences ages standards [*Hurford*, 1990; *Miller et al.*, 1985]. Based on 23 analyses, the Zeta the ζ for the operator (I. Coutand) is 370.6 ± 5.0.

3.3. Paleomagnetic Analysis

To date the sedimentary section, we undertook a magnetostratigraphic study constrained by vitrinite reflectance and DAFT data. For details on sampling and analytical procedure, see Text S3 in the supporting information.

3.3.1. Magnetization Characteristics

Initial Natural Remanent Magnetization (NRM) intensities vary between 10^5 and 10^1 A/m and generally increase upsection, suggesting an increasing concentration of strongly magnetic iron oxides such a magnetite. Throughout the section, we observed various thermal demagnetization behaviours from which Characteristic Remanent Magnetization (ChRM) components were defined and plotted on vector end point diagrams and stereographic projections (Fig. 21). Two different thermal demagnetisation behaviours related to lithological changes characterize the lower (below 1400 m) and the upper (above 1400 m) parts of the sedimentary section.

In the lower part composed of the lower and middle Siwalik subgroups where the samples are fine grained, (paleomagnetic samples SJ1- SJ224; for sample location, see Fig. 19), demagnetizations were mostly complete below 400°C (Figs. 21a and 21c). A viscous low temperature component was often removed below 150°C, while a low-temperature component (LTC) of normal polarity generally demagnetized between 130 and 300°C and was interpreted as an overprint. A medium temperature component (MTC) was also typically demagnetized between 130 and 400°C and often overlapped with the LTC along great circle paths on stereographic projections (Fig. 21d). This MTC displays either normal or reversed polarity directions and was interpreted as representing the ChRM in the lower and middle Siwalik subgroups. Above 300°C, an increase in both remanence intensity and susceptibility is characteristic of the transformation of iron sulphides into magnetite upon heating. This suggests that iron sulphides, such as greigite, may be carrying the ChRM in the rocks of the Siwalik Group as it was observed elsewhere in the eastern Himalaya (Chirouze et al., 2012).

The upper part of the section, composed of the middle and upper Siwalik subgroups, is characterized by an abrupt increase of the sample grain size from fine- to dominantly medium-grained sandstones (paleomagnetic samples SA1-SA140; for sample location, see Fig. 19). These samples yielded generally higher initial NRM intensities but more erratic unstable thermal demagnetization paths such that many samples did not yield interpretable directions (Figs. 21e and 21f). This is attributed to the larger grain size yielding multidomain magnetic grains (Butler, 1992). The samples that did yield interpretable demagnetization paths had much higher unblocking temperatures ranging from 300 to

600°C and sometimes extending up to 680°C. This behaviour is typical of a remanence dominated by magnetite-like minerals and the occasional occurrence of hematite.

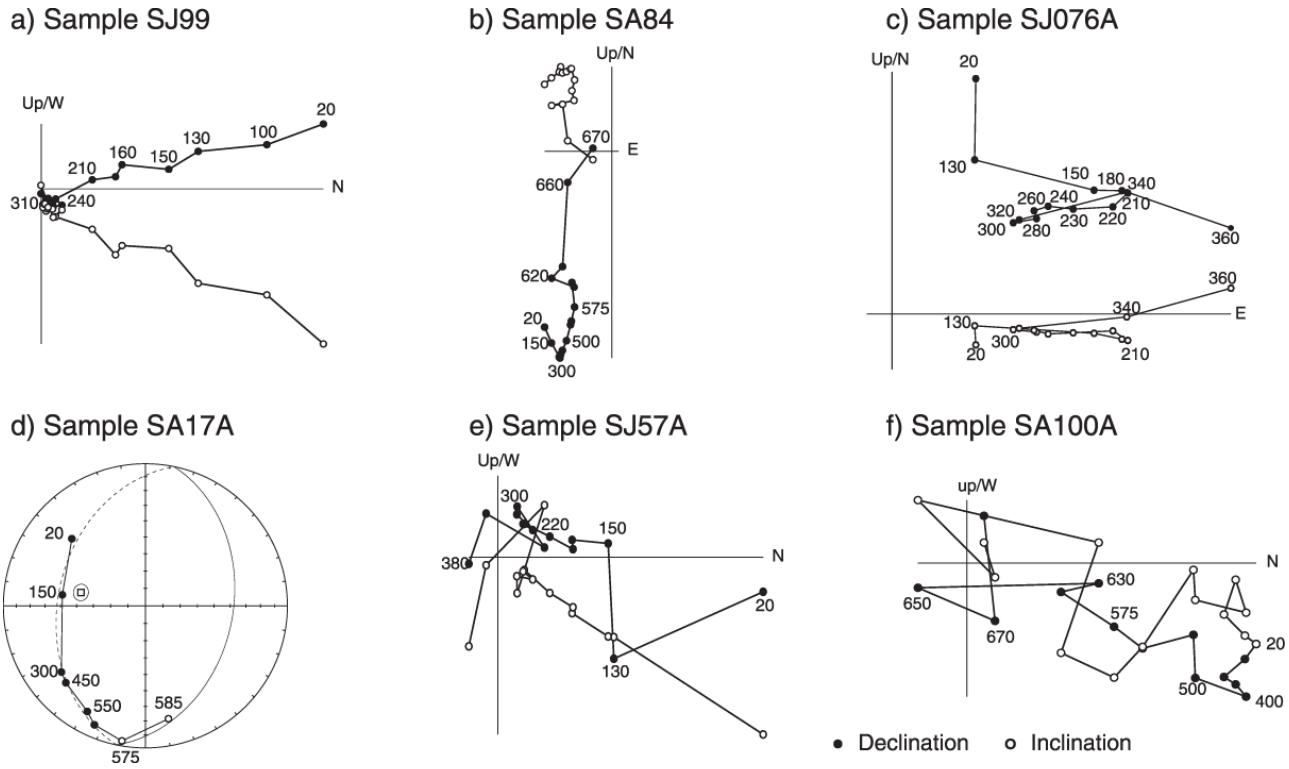

Fig. 21: *Representative thermal demagnetization diagrams. Full and open symbols are projections on the horizontal and vertical planes, respectively. The numbers next to the symbols indicate the temperature of demagnetization step in °C. (a and b) Reliable direction and polarity from group Q1. (c and d) Reliable polarity but unreliable direction from group Q2. Fig. 21d is a typical demagnetization path on which great circle analysis was performed on stereographic projection (McFadden and McElhinny, 1988). (e and f) Unreliable direction and polarity from group Q3. Samples SJ are from the lower part of the section, while samples SA are from the upper part of the section.*

3.3.2. ChRM Direction Analyses

ChRM directions were calculated using a minimum of four consecutive heating steps usually decreasing toward the origin such that line fits were generally not anchored to the origin. Some demagnetization paths showing a steady direction but no significant decrease in intensity upon demagnetization were forced through the origin (Fig. 21; data are provided in Table S2 of Appendix I). Line fits with a Maximum Angular Deviation (MAD) above 30° were systematically rejected. Because of the common occurrence of secondary overprints with normal polarities, sometimes persisting at relatively high demagnetization temperatures, a careful selection of ChRM directions was performed by ordering them into four quality groups (Table S2 of Appendix I). In the Quality 1

(Q1) group are the ChRM directions of normal or reversed polarity from which a well-defined direction was determined from stable and linear demagnetization paths, yielding MAD typically below 15° (Figs. 21a and 21b). In the Quality 2 (Q2) group, normal or reversed polarities are clearly defined but the directions are less reliable because of directional scatter and/or overlapping secondary overprint (Figs. 21c and 21d). The polarity determination of Quality 3 (Q3) remains ambiguous due to the weakness of the signal and/or strong overlapping with the normal secondary polarity (Figs. 21e and 21f). This group also includes poorly indurated samples that were destroyed before we could process enough measurements to extract reliable ChRM directions.
The Quality 4 (Q4) group includes data displaying outlying directions that were rejected following an iterative cutoff protocol described in the paragraph below.

The reversed polarity directions were more reliably identified than normal ones because the latter may have resulted from a full overprint of an originally reversed direction. The distinction between a primary component and a normal secondary overprint was also aided by the fact that the primary directions have been affected by significant counter-clockwise rotations about vertical axes (Fig. 22). Great circle analysis (McFadden and McElhinny, 1988) was applied to some Q2 and Q3 samples, when the contribution of the direction of the secondary normal polarity overlapped a reversed polarity direction carried by only a few points.

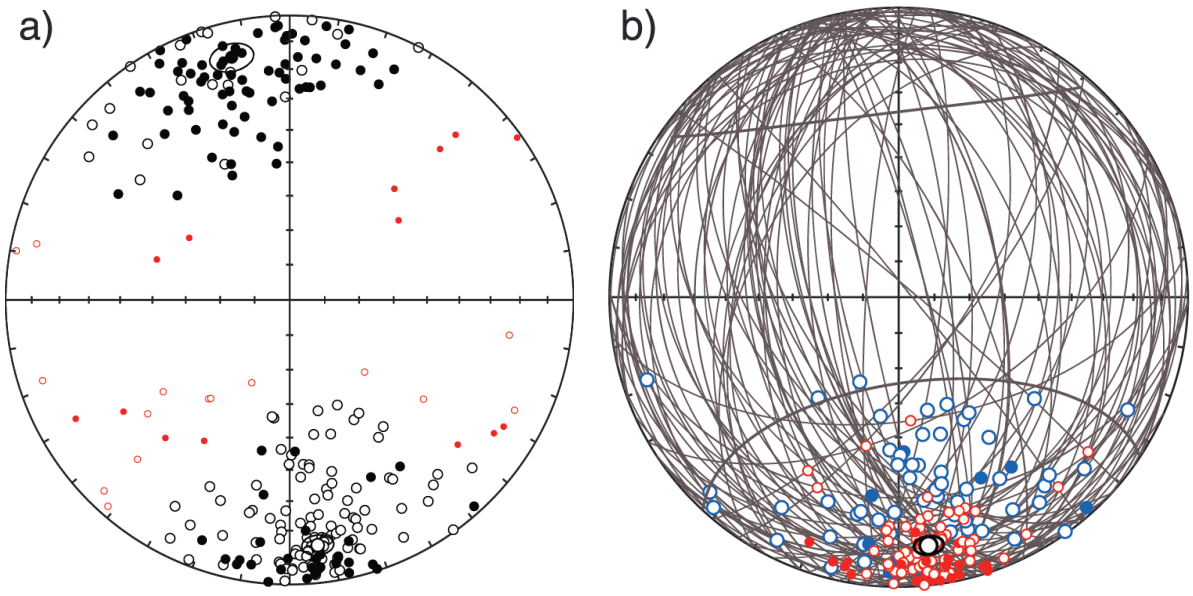

Fig. 22: *(a) Stereographic projections of Q1 and Q2 ChRM directions projected on the lower (filled symbols) and upper (open symbols) hemispheres. Directions reported in red have VGP over 45° from the mean VGP and were iteratively cut off. (b) Great circle analysis. The set point (black dot) is*

defined by the mean of Q1 directions (blue dots). Obtained reversed directions (red points) are defined by the point on each great circle that is nearest to the set point. Filled (open) symbols are projections on the lower (upper) hemisphere.

For this procedure the mean of the Q1 reverse polarity directions was used as set point, and the procedure described by (McFadden and McElhinny, 1988) was used to extract the primary direction from the great circle analysis (Fig. 22). To remove greatly outlying and transitional directions, an iterative cutoff was applied to the virtual geomagnetic poles (VGPs) derived from the obtained ChRM Q1 and Q2 directions. VGP directions lying more than 45° from the mean VGP were iteratively cut off and rejected in the Q4 quality group. This procedure was performed on normal and reversed polarity data sets separately. The remaining Q1 and Q2 ChRM directions cluster in antipodal fashion after tilt correction, suggesting a primary origin of normal and reversed polarities (Fig. 23).

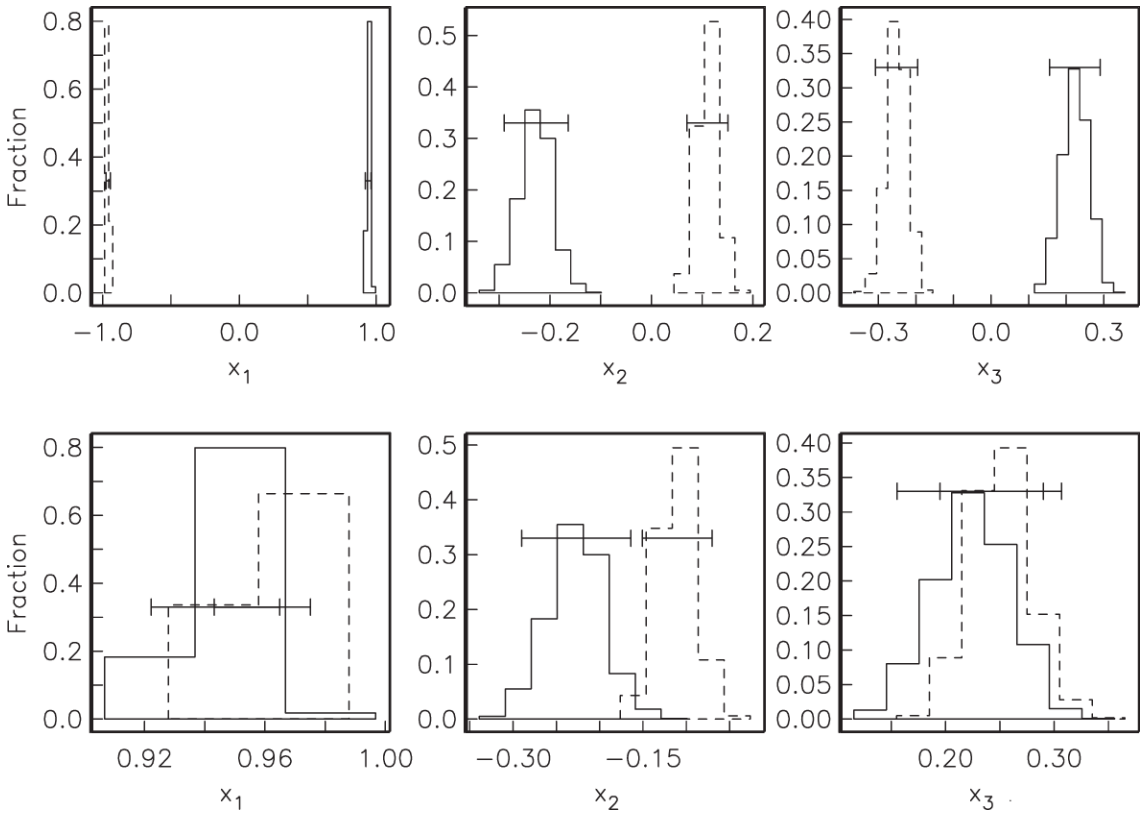

Fig. 23: *The reversals test (Tauxe, 1998) applied to Q1 and Q2 ChRM directions is negative as shown in this figure. In this test normal and reversed directions are compared in X, Y, Z coordinates (top row) before and (bottom row) after flipping reversed directions into normal coordinates. The test is positive if these directions are indistinguishable at 95% level of confidence such that their 95% confidence interval overlaps on bottom diagrams. In XYZ coordinates, 95% confidence intervals of average normal and reverse directions are statistically different as shown in the figure.*

The section being monoclinally tilted, a fold test was not applicable. The reversals test (Tauxe, 1998), applied to Q1 and Q2 ChRM directions, was negative after flipping reversed directions to antipodal normal orientations. The negative reversals test is expected with data including partially overprinted directions obtained from great circle analysis, but it does not affect the validity of the reversed polarity determinations. The resulting set of 220 Q1 and Q2 ChRM directions provides paleomagnetic polarity determination at an average interval of 10m throughout the stratigraphic section with several larger gaps due to a lack of outcrop or the inadequacy of rock type (usually weathered coarse-grained sandstones) that yielded non-interpretable demagnetization paths (Fig. 19). Reversed polarity directions were unequivocally recognized, but normal polarity directions have been determined more cautiously with regard to possible secondary normal overprints.

In the lower part of the section, normal polarities are well expressed in linear demagnetization paths and systematically observed in consecutive intervals yielding credit to these normal polarity zones. In addition, normal overprints observed in reversed polarity samples of the lower part usually do not persist above 300°C such that higher-temperature normal directions can be confidently identified. In the upper part of the section, however, normal polarity directions are often unstable, not systematically consecutive, and normal overprints of reversed direction are found in high-temperature ranges suggesting that some samples have been fully remagnetized.

3.3.3. Magnetostratigraphy: C Correlation to the Geomagnetic Paleomagnetic Polarity Timescale

Because the dating from biostratigraphy or volcanic ash layers is not possible, our magnetostratigaphic study relies on detrital apatite fission-track analysis to provide independent constraints for the correlation of our paleomagnetic results with the geomagnetic polarity timescale (GPTS) of Gradstein et al. (2012). Several layers in the section are thus assigned a maximum depositional age based on unreset DAFT ages from the sedimentary series (Figs. 19b and 19d and Table 1). Polarity zones are defined by at least two consecutive paleomagnetic sites bearing the same polarity such that isolated points were discarded from the definition of polarity zones. Twenty polarity zones including 10 normal (N1 to N10) and 10 reversed (R1 to R10) were identified in the section (Fig. 19). Because normal overprinting commonly occurs in the coarser-grained top part of the section, the normal zones (N2, N3, N4, and N5) are considered less reliable and have been given less weight in the following correlations.

3.3.3.1. Correlation of the Lower Part of the Section

DAFT data suggest that the stratigraphic age at the bottom of the section is younger than 6.9–1.2/+1.4 Ma (Table 1). As a starting point for our correlations, we used the longest observed reversed polarity interval R8 yielding the most reliable result below the 1400m level within fine-grained facies in the lower to middle Siwalik subgroups. In the age range allowed by DAFT data, there are three possible correlations of the long reversed interval R8: (a) a combination of C3Br.2r to C3A (starting at 7.454 and ending at 6.733 Ma, respectively), (b) C3r (6.033–5.235 Ma), or (c) C2Ar (4.187–3.596 Ma) (Figs. 19d and 19e). Correlating R8 with C2Ar is easily rejected because the short N8, N7, and N6 overlying R8 likely do not represent the relatively long dominantly normal interval C2A. Correlating R8 to C3Br.2r and C3Ar implies that the two normal chrons within C3B have been missed, while below R8, the dominantly normal polarity zones N9 to N10 provide a good counterpart to C4n chrons. However, above R8, the relatively short N8 and N7 do not provide a good fit to the relatively long normal chrons of C3A without involving substantial variations in sediment accumulation rate. Finally, correlating R8 with C3r provides the best fit without chron omission and significant accumulation rate variations. Below R8, N9 and N10 can be easily linked to C3An.1n and C3An.2n, respectively, while above, N8 fits well with Cn3.4n. This correlation places the base of our stratigraphic section at <7Ma and the lower to middle Siwalik subgroups boundary at ~6 Ma. This is our preferred correlation for the basal part of the Dungsam Chu section.

3.3.3.2. Correlation of the Upper Part of the Section

The upper part of the section comprises coarser-grained lithologies and is more challenging to interpret. It is bracketed at the bottom by R8 that we preferentially correlate with C3r and constrained by a maximum depositional age of 3.6–0.8/+1.0 Ma by DAFT data at the top. Under these conditions, we hereafter investigate the possibilities of correlating the most reliable long reversed zones R6 and R4 to the longest reversed chrons C2Ar, C2r, or C1r.3r (Fig. 19).

3.3.3.2.1. Correlation A

Correlation A relies on correlating R4 with C2Ar (start at 4.187 Ma) and R6 to C3n.2r (start at 4.799 Ma). In this case, each normal polarity zone between R4 and R8 has a matching chron within the GPTS without omission. R5, R6, and R7 correlate with C3n.1r, C3n.2r, and C3n.3r (starting at 4.493, 4.799 and 4.997 Ma), respectively. The normal zones N5, N6, N7, and N8 are consequently correlated with C3n.1n to C3n.4n (starting between 4.300 and 5.235 Ma). This correlation places the middle to upper Siwalik subgroups boundary at ~4 Ma and implies that the top of the section is about 3Ma in age.

3.3.3.2.2. Correlations B and C

In correlation B, we link R6 to C2Ar (4.187–3.596 Ma), N7 to C3n.1n, and hence assume that C3n.2n and C3n.3n have been missed. Normal zones N5 and N6 fit relatively well with C2An.1n and C2An.3n chrons with a potentially missed normal zone between N5 and N6 corresponding to C2An.2n that could coincide with the isolated normal polarity point located within the R5 zone. Above N5, two correlations can be proposed. Either (B) the zones R1, R2, R3, and R4 correspond to the dominantly reversed interval C2r (ranging between 1.945 and 2.581 Ma) assuming that N2, N3, or N4 are normal overprints or (C) the zones R1, R2, R3, and R4 correspond to the reverse chrons from C1r.1r to C2r.2r (ranging between 0.781 and 2.581 Ma) assuming that N2, N3, or N4 are normal polarity zones within the corresponding chrons range. Correlations B and C place the middle to upper Siwalik subgroups boundary at 2–2.5 Ma and 1.5 Ma, respectively.

It remains difficult to discriminate between correlation A, which a priori yields a better pattern fit to the GPTS, and correlations B or C, which cannot be rejected because of the potential secondary overprints in the upper part of the section.

3.3.4. Magnetostratigraphic Correlations Using Qupydon Software

To quantify the ambiguities in the manual (i.e., deterministic) magnetostratigraphic correlations, we have performed stochastic modelling of the polarity column using the software Qupydon (Lallier et al., 2013) implementing the Dynamic Time Warping algorithm. Input data are the geomagnetic polarity timescale (GPTS) of (Gradstein et al., 2012) and the thicknesses of polarity zones measured in the Dungsam Chu sedimentary section. By constraining the length of the GPTS, we have explored the above discussed correlation schemes by performing two sets of correlations (Table 2).

As a reference polarity section, we first selected the segment of the GTPS that covers all the known depositional ages of Siwaliks (e.g. Ojha et al., 2009), which range from chron C1n to C5ADr (0–14.775 Ma). Our polarity column contains 19 polarity zones, and the reference section of the GTPS contains 80 chrons. Accordingly, we have calculated 20,000 correlations and analysed the 5000 best correlations determined via the best fit (or “minimum cost” (Lallier et al., 2013)) correlation. The numerical algorithm includes three calculation parameters: a maximum substitution, a gap factor, and a substitution distance. The maximum substitution is the maximum number of reference chrons that may be correlated to one chron of our polarity column. A gap factor equal to 0 yields a correlation with higher sedimentation rate, while a high gap factor (e.g. 10) stretches the correlation within the imposed reference timescale. A substitution distance equal to 1 allows short-term

variation in sedimentation rate, while for a substitution distance >1, the software is forced to find correlations that minimize local variations of the sedimentation rates inducting gaps in the correlation (Lallier et al., 2013).We set the values of those three parameters by trial and error. We set the gap factor between 10 and 0, the maximum substitution to 10, and in all our analyses, substitution distances of 1 or 2 yielded significantly lower cost correlations than a substitution distance of 10.

Table 2: *List of magnetostratigraphic correlations, the modelling parameters, and the costs of the best correlations*[a]

Reference Ages (Ma)	Reference Chrons	Nbr Res	Maximum Path	Gap Factor	Maximum Substitution	Substitution Distance	Cost	Run Name
0–14.8	C1n-C5ADr	5,000	20,000	0	10	1	6.09	Q1
0–14.8	C1n-C5ADr	5,000	20,000	0	5	1	6.09	Q2
0–14.8	C1n-C5ADr	5,000	20,000	0	10	10	30.86	Q3
0–14.8	C1n-C5ADr	5,000	20,000	10	10	1	12,353.00	Q4
9.740–14.8	C5n.1n-C5ADr	1,000	10,000	0	10	1	6.30	Q5
9.740–14.8	C5n.1n-C5ADr	1,000	10,000	0	5	2	10.88	Q6
9.740–14.8	C5n.1n-C5ADr	1,000	10,000	0	10	10	31.91	Q7
9.740–14.8	C5n.1n-C5ADr	1,000	10,000	10	10	1	35897.30	Q8
0–8.664	C1n-C4r.2r.1n	1,000	10,000	0	10	1	5.92	Q9
0–8.664	C1n-C4r.2r.1n	1,000	10,000	0	5	2	9.76	Q10
0–8.664	C1n-C4r.2r.1n	1,000	10,000	1	10	1	14.16	Q11
0–8.664	C1n-C4r.2r.1n	1,000	10,000	0	10	10	51.17	Q12

[a]Three groups of stochastic analyses with different reference age constraints were performed. For each age group we ran four experiments with different modeling parameters (gap factor, maximum substitution, and substitution distance). For the definition of the parameters for stochastic magnetostratigraphic correlation, refer to *Lallier et al*. [2013]. The best runs are Q1, Q2, Q5, and Q9. Q5 is incompatible with DAFT data and hence was discarded; Q1, Q2, and Q9 yielded nearly identical correlations with Q9 having the lower cost. Shadings define three different groups of models covering different time periods (reported in the first column of the table labeled "age reference").

When setting the age of the base of the Siwalik Group at ~14 Ma as is suggested elsewhere along the strike of the range (e.g. Ojha et al., 2009), statistical distribution of the 5000 best correlations yielded a large range of correlations (Table 2). However, along the Dungsam Chu section, because the DAFT analysis indicates that the base cannot be older than ~7 Ma, we have performed a second correlation using a reference scale covering chrons C1n-C4r.2r (0–8.771 Ma) (Table 2 and Fig. 25). In all the analyses, we observed that the cost of correlation starts to decrease for the best 100 correlations (see related discussion by Lallier et al. (2013)), while the approximately 20 best correlations yield the least scatter. The best runs are Q1, Q2, Q5, and Q9 (Table 2). Q5 is incompatible with DAFT data and hence was discarded; Q1, Q2, and Q9 yielded nearly identical correlations with Q9 having the lower cost and representing the best model. For this model, we therefore further analysed the 13 best correlations in which the 14 older polarity zones yield the same goodness of fit to the reference scale, while the top 5 zones display some scatter (Fig. 24). The top of this correlation is similar to slightly younger than the manual correlation C, the top polarity zone correlating with C1r.3r (1.185–1.778 Ma) or C2r.2r (2.148–2.581 Ma), with the former having

higher probability (Fig. 25c). The bottom of the section correlates well with chron C3Ar (6.733–7.140 Ma).

We conclude that the stochastic correlation Q9 close to manual correlation C is the best option for the Dungsam Chu section, with an age at the base of ~7 Ma and at the top of ~1 Ma (Fig. 25c).

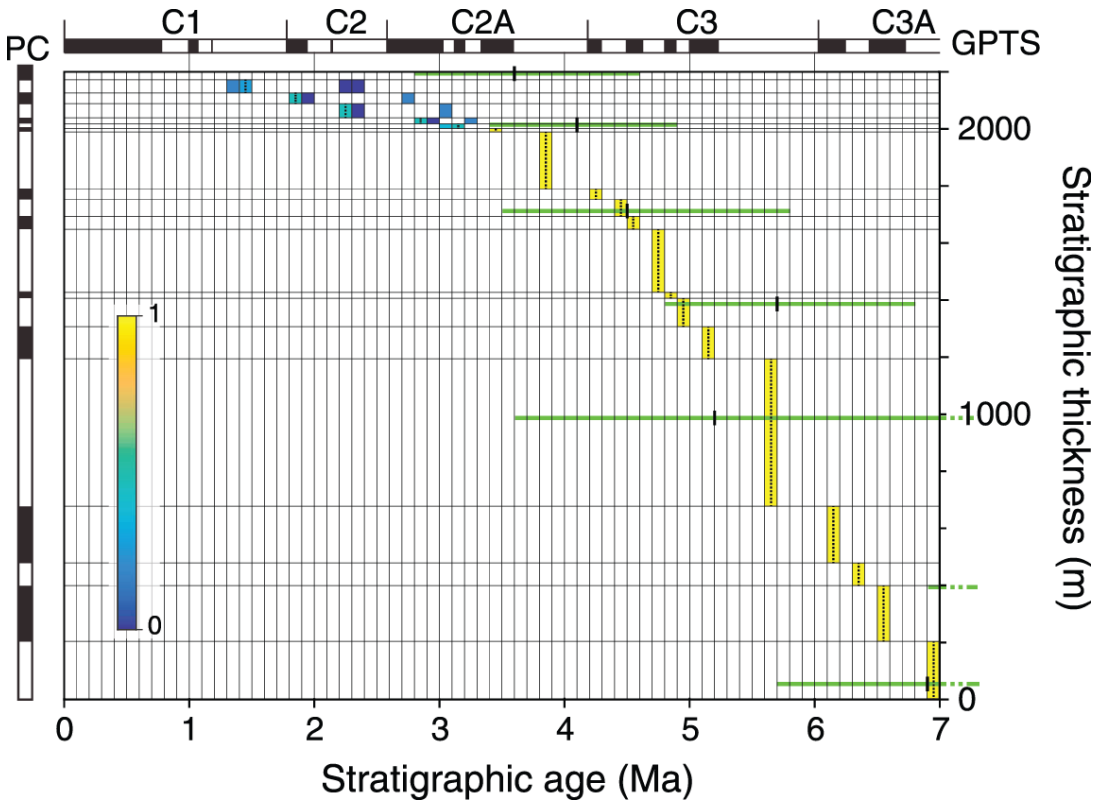

Fig. 24: *Weighted density age versus depth plot of the 13 best correlations for the Dungsam Chu section for the best run Q9. On the top is the GTPS chart, and on the left side is our polarity column (PC). Results with reference scale C1n-C4r.2 r (from GPTS of Gradstein et al. (2012)). Number of results = 1000, maximum paths = 10,000, gap factor = 0, maximum substitutions = 10, and substitution distance = 1. Dashed vertical lines indicate the "best solution" (cost = 5.9), also indicated in Fig. 25. Horizontal green lines are the detrital apatite fission-track ages. The color column to the right is the weighted density of points indicative of the goodness of fit.*

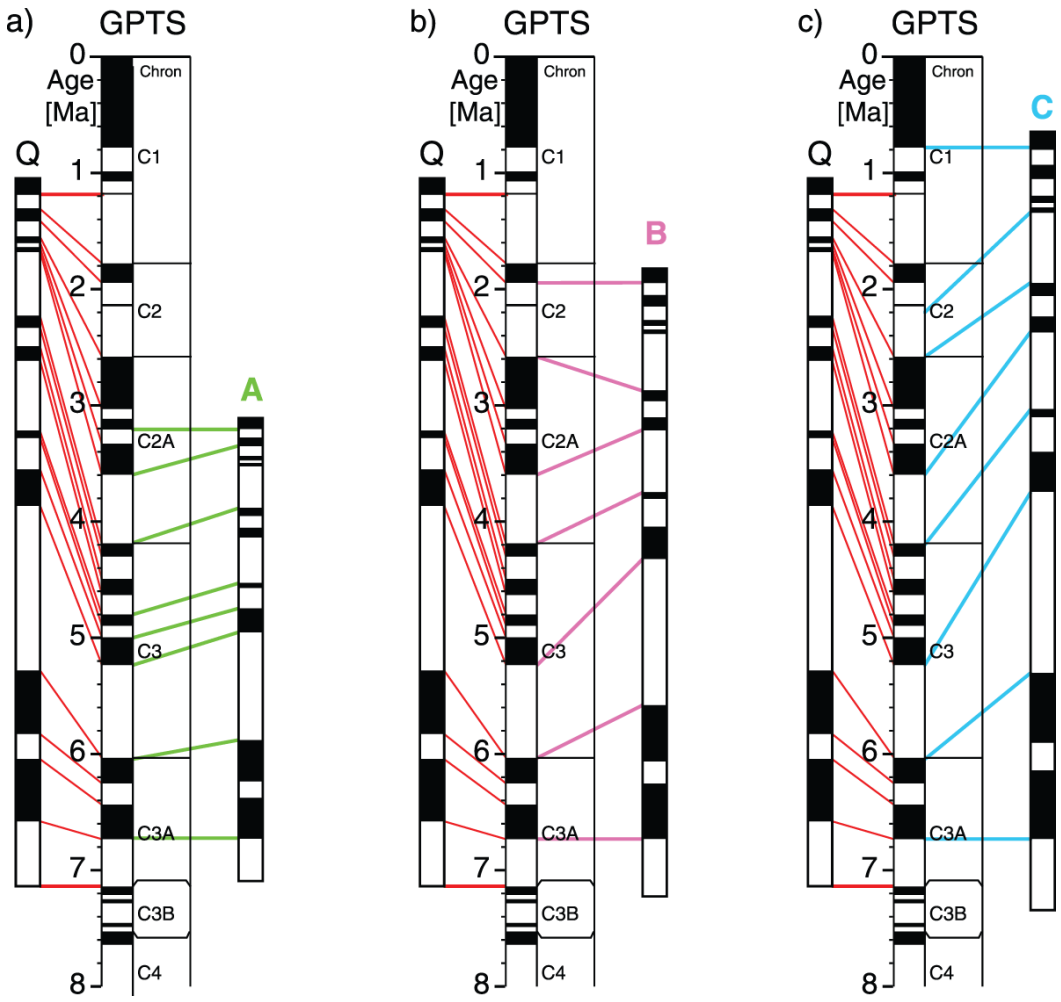

Fig. 25: *(a–c) Comparison of the best stochastic correlation with deterministic correlations A, B, and C. In the middle is the GTPS of Gradstein et al. (2012). To the left is the best correlation obtained by the Qupydon software using the younger part of the reference scale (Q9). To the right are the manual correlations A, B, and C.*

4. SEDIMENTOLOGY

In addition to geochronological analyses, we have performed a sedimentological study of the Siwalik deposits to establish the nature and changes of their sedimentary environments in eastern Bhutan.

4.1. Facies Analysis

We carried out a sedimentological analysis using a standard method of facies analysis. Twelve facies were identified on the basis of their lithology, sedimentary structures, and trace fossils before being interpreted in terms of depositional processes (Table 3). Along the Dungsam Chu section, these facies co-occur in four assemblages, which were interpreted in terms of depositional environments (Table 4). Indeed, facies assemblages are more representative of depositional environments than

individual facies alone, the latter rather depending on the sediment nature or on elementary hydrodynamic, bioturbation, and pedogenic processes.

The facies assemblages were recognized in specific locations throughout the sedimentary section and used to divide it into four units bearing different environmental characteristics. The distribution of these units was documented by a stratigraphic column constructed from outcrop observations along the Dungsam Chu transect (Figs. 18 and 26). Along this transect, horizontal distances were measured using both a GPS and a decametre scale before being converted into sediment thicknesses using strike and dip measurements.

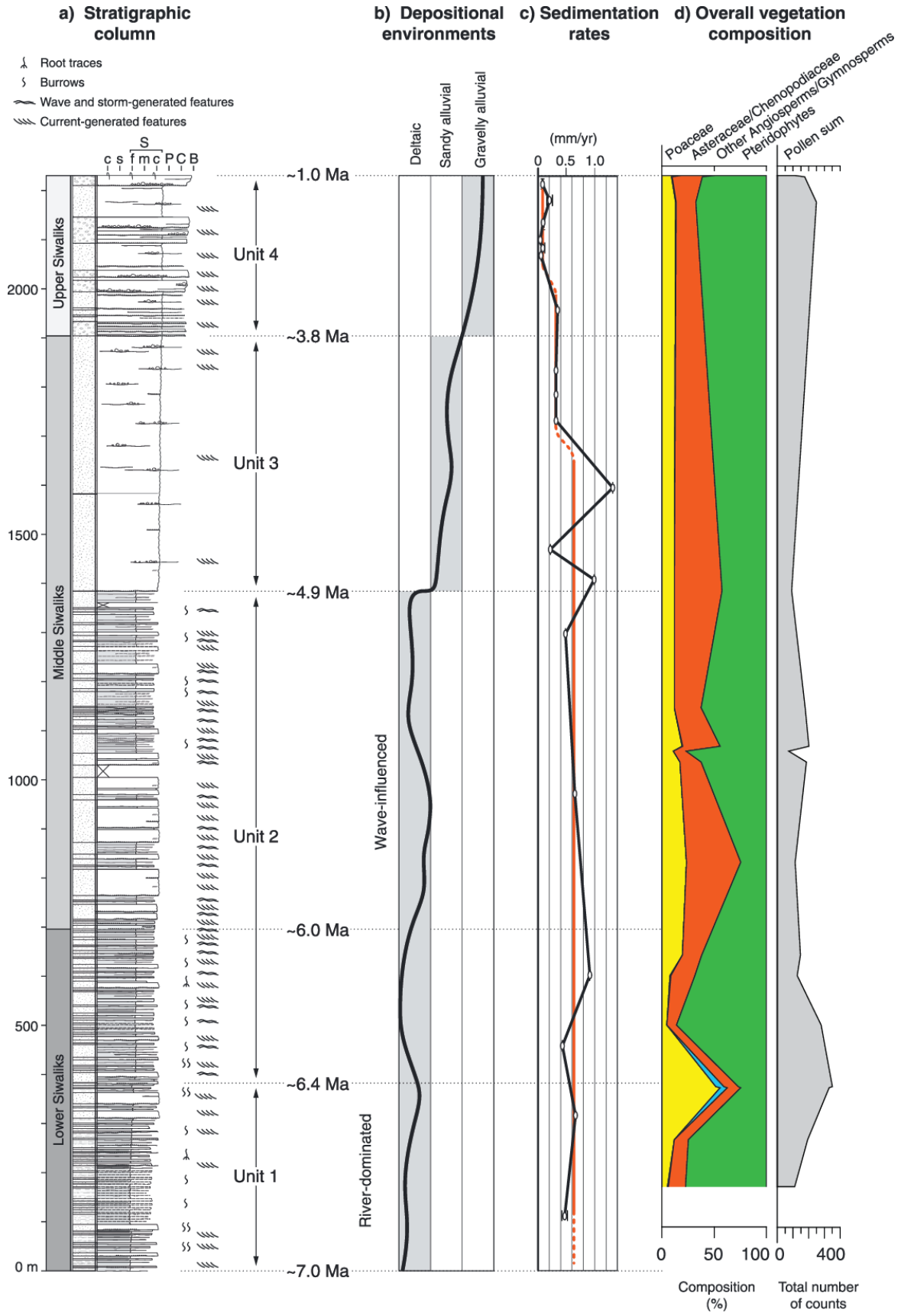

Fig. 26: *Measured sedimentary section of the Siwalik Group deposits exposed along the Dungsam Chu near Samdrup Jongkhar (see Fig. 17 for location). (a) Stratigraphic column. The horizontal scale*

labels C, s, S, P, C, and B are abbreviations for clay, silt, sand, pebbles, cobbles, and boulders. Current-generated features include current-ripple laminations, tabular cross beddings, through cross beddings, and flat beddings. Wave-generated features comprise undulating and wave-ripple laminations. (b) Depositional environment evolution. (c) Sedimentation rate evolution obtained for the best correlation from Qupydon.

Descriptions and interpretations of the four identified units in terms of depositional processes and environments are presented below, from the bottom (unit 1) to the top (unit 4) of the section. Unit 1 comprises eight facies: one pedogenic (F1), two clayey (F2 and F3), one heterolithic (F4), and four sandy facies (F5, F8, F9, and F10) (for a detailed description, see Tables 3 and 4 and Fig. 27). Among these facies, the presence of thick-bedded (centimetres to meters thick) dark grey to black claystone layers indicates subaqueous sediment fallout from suspension; massive or normally graded to flat- and cross-laminated sandstones and occasional soft-sediment deformation point to subaqueous gravity flow; flat- to cross-bedded sandstones combined with climbing and wave ripples, as well as bioturbation (among which burrows of Planolites and Diplocraterion), suggest the deposition of a sandy bed load transported by subaerial to subaqueous either confined or unconfined flow (the difference is not discernible in the field). Altogether, these deposits are interpreted as representing different parts of a river-dominated deltaic system (e.g. Collinson, 1969; Hyne et al., 1979; Marshall, 2000; Tye and Coleman, 1989). This system may have developed in either a lacustrine or a marine environment because inferred depositional processes can occur in both settings (e.g. Collinson, 1969; Hyne et al., 1979; Marshall, 2000). Moreover, the sedimentary series does not contain any macrofossil or microfossil (e.g. shells or foraminifera) that can help to discriminate the nature of the water body. At first glance, a lack of obvious marine evidence thus suggests a lacustrine delta. However, the occurrence of trace fossils of marine affinity like Diplocraterion and glauconite in clay composition (Grujic, personal communication, 2016), together with some mangrove to freshwater swamp pollen taxa (Nypa and Neocouperipollis; for details, see section 5), suggests an environment influenced by brackish water and indicates that a marine interpretation is viable. At its top, unit 1 grades quickly (within a few meters) into unit 2 where new facies (F6 and F7) appear, their first occurrence being dated at ~6.4 Ma. Unit 2 comprises 10 facies: one pedogenic (F1), two clayey (F2 and F3), two heterolithic (F4 and F6), and four sandy facies (F5, F7, F8, F9, and F10) (Tables 3 and 4 and Fig. 27). Facies characteristics are similar to unit 1 but additionally include massive or wavy- to flaser-bedded sandstones with undulating, hummocky, and swaley laminations of wave ripples indicating deposition or reworking by waves. These deposits represent a wave-influenced deltaic depositional system (e.g. Chan and Dott Jr, 1986; Helland-Hansen, 2010; McCormick and Grotzinger,

1993; Myrow et al., 2008). As for unit 1 and without clear sedimentary features, trace fossils, or fossils supporting one hypothesis or the other, this deltaic environment may have developed in either a lacustrine or a marine setting. However, the occurrences of trace fossils of marine affinity like Diplocraterion, of glauconite (D. Grujic, personal communication, 2016) and of some mangrove to freshwater swamp pollen taxa (Nypa and Neocouperipollis, together with Pelliciera and Brownlowia; for details, see section 5), associated with the wave-influenced facies, rather indicate that the deltaic system of unit 2 was subjected to intermittent marine influences. At the top, unit 2 sharply gives way to unit 3 at ~4.9 Ma. Unit 3 comprises two sandy facies (F10 and F11) (Tables 3 and 4 and Fig. 27). In this unit, the presence of massive or bedded sandstones with erosional basal surfaces, meter-scale compound cross beds, and scattered pebbles indicates the deposition of a sandy and pebbly bed load transported by subaerial either stream or sheet flows. These deposits are interpreted as representing a sandy alluvial environment (e.g. Jo et al., 1997; Marshall, 2000; McCormick and Grotzinger, 1993; Miall, 1977; Miall, 1985; Wizevich, 1992). At its top, unit 3 shifts to unit 4 over a sharp transition dated at ~3.8 Ma. Unit 4 comprises three facies: two sandy facies (F10 and F11) and one conglomeratic facies (F12) (Tables 3 and 4 and Fig. 27). Facies characteristics are similar to unit 3 but additionally include massive or bedded conglomerates with erosional basal surfaces suggesting the deposition of a gravelly bed load transported by subaerial either stream or sheet flows. These deposits represent a gravelly alluvial environment (e.g. Jo et al., 1997; McCormick and Grotzinger, 1993; Miall, 1977; Miall, 1985). The limited lateral extent of the studied section and its rock exposure (a few tens of meters) precludes clear determination of the channel pattern (braided or meandering) and organization (radial or not) of this alluvial system. Yet the analogy of our observations with the modern fluvial fans in the Himalayan foreland basin suggests that units 3 and 4 likely represent the distal and more proximal parts, respectively, of a braided-streamflow fan environment (Jain and Sinha, 2003; Kumar et al., 2004; Shukla et al., 2001). In unit 4, a few pollens of mangrove to freshwater swamp taxa (Neocouperipollis and Nypa; for details, see section 5) are also found. However, in the absence of other marine criteria (sedimentary figures, trace fossils, or clays) and provided that these taxa may also occur in tidally influenced rivers and freshwater swamps relatively far inland (Giesen et al., 2007; Morley, 1991; Tomlinson and Tomlinson, 1994), this is not necessarily inconsistent with an alluvial interpretation for the associated deposits.

Table 3: *Summary of the facies characteristics observed in the Dungsam Chu Section and their interpretations in terms of depositional processes*

Facies Code	Facies Description	Inferred Depositional Processes	Environmental Interpretation	References
F1 (Figure 11a)	Root traces	Pedogenic processes	Paleosols	*Retallack* [1988]
F2 (Figure 11b)	Centimeters to decimeters thick, dark grey to black, silty carbonaceous shales, massive to flat laminated, with gradational to sharp basal surfaces, and frequent plant fragments	Organic-rich subaqueous suspension fallout	Interfluve or interdistributary-bay deposits	*Helland-Hansen* [2010], *Hyne et al.* [1979], and *Tye and Coleman* [1989]
F3 (Figure 11c)	A decimeter to meters thick, dark grey, silty shales to sandy siltstones, massive to flat laminated, with gradational to sharp basal surfaces, and occasional plant fragments	Subaqueous suspension fallout	Interdistributary-bay or prodelta to offshore deposits	*Helland-Hansen* [2010], *Hyne et al.* [1979], and *McCormick and Grotzinger* [1993]
F4 (Figure 11d)	Decimeters to meters thick, thin-bedded heterolithics, with gradational to sharp basal surfaces, occasional soft-sediment deformation structures, and plant fragmentsHeterolithic packages are composed of (1) millimeters to a decimeter thick, dark to light grey, clayey siltstones to fine-grained sandstones, massive or flat to undulating laminated, and (2) millimeters to a decimeter thick, light grey to yellow, fine- to coarse-grained sandstones, massive or normally graded to flat and cross laminated, with flat to irregular basal surfaces, rip-up clasts, and occasional burrows	Deposition from subaqueous gravity flows alternating with suspension fallout	Distal delta front to prodelta deposits	*Tye and Coleman* [1989], *Gani and Bhattacharya* [2007], *Helland-Hansen* [2010], and *Plink-Björklund and Steel* [2006]
F5 (Figure 11e)	Decimeters to a meter thick, light grey, medium- to coarse-grained sandstones, massive or with centimeters to a decameter thick sequences of normally gradings and flat laminations, as well as sharp to erosional basal surfaces, frequent lignite grains, and occasional burrows	Deposition from subaqueous gravity flows	Distal delta front deposits	*Gani and Bhattacharya* [2007], *Myrow et al.* [2008], and *Plink-Björklund and Steel* [2006]
F6 (Figure 11f)	Decimeters to meters thick, thick-bedded heterolithics, poorly to moderately bioturbated, with gradational to sharp basal surfaces, occasional soft-sediment deformation structures, and lignite grains Heterolithic packages are composed of (1) a centimeter to centimeters thick, dark to light grey, clayey siltstones to fine-grained sandstones, massive or flat-laminated, and (2) centimeters to decimeters thick, light grey to yellow, fine- to coarse-grained sandstones,	Deposition from combined subaqueous oscillatory and unidirectional flows alternating with suspension fallout	Distal delta front deposits	*Buatois* [2012], *Chan and Dott* [1986], *Helland-Hansen* [2010], and *McCormick and Grotzinger* [1993]

Table 3 (*continued*)

Facies Code	Facies Description	Inferred Depositional Processes	Environmental Interpretation	References
	massive or wavy to flaser bedded, with sharp to erosional basal surfaces, and dark to light grey laminae of clayey siltstones to medium-grained silty sandstones, as well as frequent undulating, hummocky, and swaley laminations of wave ripples, intrabed gutter casts, and lignite grains, and numerous burrows (among which *Planolites* and *Diplocraterion*)			
F7 (Figures 11g–11k)	Decimeters to meters thick, light grey to yellow, fine- to coarse-grained sandstones, undulating laminated or wavy to flaser bedded, poorly to thoroughly bioturbated, with sharp to erosional basal surfaces, dark to light grey laminae of fine- to medium-grained silty sandstones, as well as hummocky and swaley lamination of wave ripples, intrabed gutter casts, soft-sediment deformation structures, lignite grains, and numerous burrows (among which *Planolites* and *Diplocraterion*)	Deposition from combined subaqueous oscillatory and unidirectional flows	Proximal delta front deposits	*Buatois* [2012], *Chan and Dott* [1986], *Gani and Bhattacharya* [2007], *Helland-Hansen* [2010], and *McCormick and Grotzinger* [1993]
F8 (Figure 11l)	A decimeter to decimeters thick, light grey, medium- to coarse-grained sandstones, flat laminated to cross laminated, with sharp to erosional basal surfaces, frequent climbing ripples, lignite grains, and lignite laminations, as well as occasional wave ripples and burrows	Deposition of a sandy bed load transported by subaerial to subaqueous unconfined flows	Mouth bar to proximal delta front deposits	*Buatois* [2012], *Marshall* [2000], *Plink-Björklund and Steel* [2006], and *Tye and Coleman* [1989]
F9 (Figure 11m)	Decimeters to meters thick, light grey to yellow, coarse-grained sandstones, massive or flat bedded to tabular and trough cross bedded (<1 m), with sharp to erosional basal surfaces, frequent lignite grains, lignite laminations, and soft-sediment deformation structures, as well as occasional climbing and wave ripples, rip-up clasts, and burrows	Deposition of a sandy bed load transported by subaerial to subaqueous confined or unconfined flows	Terminal distributary channel to mouth bar deposits	*Buatois* [2012], *McCormick and Grotzinger* [1993], *Olariu and Bhattacharya* [2006], *Plink-Björklund and Steel* [2006], and *Tye and Coleman* [1989]
F10 (Figure 11n)	Decimeters to tens of meters thick, light grey to yellow, coarse-grained sandstones, massive or flat bedded to tabular and trough cross bedded (<1 m), with erosional basal surfaces and meter-scale compound cross beds,	Deposition of a sandy bed load transported by subaerial stream or sheet flows	Sand bed channel or sheetflood deposits	*Buatois* [2012], *Jo et al.* [1997], *Marshall* [2000], *Miall* [1977, 1985], and *Wizevich* [1992]

Table 3 *(continued)*

Facies Code	Facies Description	Inferred Depositional Processes	Environmental Interpretation	References
	frequent reactivation surfaces, and lignite grains, occasional climbing ripples (units 1 and 2) or extrasize clasts (units 3 and 4), and rare soft-sediment deformation structures			
F11 (Figure 11o)	A decimeter to a meter thick, light grey to yellow, coarse-grained pebbly sandstones, massive or flat bedded to tabular and trough cross bedded (<1 m), with sharp to erosional basal surfaces, and occasional lignite clasts	Deposition of a sandy and pebbly bed load transported by subaerial stream or sheet flows	Pebbly sand bed channel or sheetflood deposits	*Jo et al.* [1997], *Miall* [1977, 1985] and *Wizevich* [1992]
F12 (Figure 11p)	A decimeter to tens of meters thick, pebble to cobble conglomerates, clast supported but sandy matrix rich, massive or tabular cross bedded, with erosional basal surfaces, and frequent winnowed gravels at the top	Deposition of a gravelly bed load transported by subaerial stream or sheet flows	Gravel bed channel or sheetflood deposits	*Jo et al.* [1997], *Miall* [1977, 1985], and *Ramos and Sopeña* [1983]

Table 4: *Summary of the characteristics of the facies assemblages, corresponding units observed in the Dungsam Chu section, and their interpretations in terms of depositional environments*

Occurrence	Facies Assemblage	Facies Environmental Interpretation (See Table 3)	Inferred Depositional Environment	References
Unit 1	Facies F1, F2, F3, F4, F5, F8, F9, and F10, with glauconite and mangrove to freshwater swamp pollen taxa	Assemblage of offshore, prodelta, delta front, mouth bar, sand bed distributary channel or sheetflood, and interfluve or interdistributary bay deposits with minor paleosols	River-dominated deltaic environment with marine influences	*Hyne et al.* [1979], *Marshall* [2000], and *Tye and Coleman* [1989]
Unit 2	Facies F1, F2, F3, F4, F5, F6, F7, F8, F9, and F10, with frequent occurrences of oscillatory flows, *Diplocraterion*, glauconite, and mangrove to freshwater swamp pollen taxa	Assemblage of offshore, prodelta, delta front, mouth bar, sand bed distributary channel or sheetflood, and interfluve or interdistributary bay deposits with minor paleosols	Wave-influenced deltaic environment with marine influences	*Chan and Dott* [1986], *Helland-Hansen* [2010], *McCormick and Grotzinger* [1993], and *Myrow et al.* [2008]
Unit 3	Facies F10 and F11	Assemblage of sand bed channel or sheetflood deposits	Sandy alluvial environment, probably a distal braided-streamflow fan system	*Jo et al.* [1997], *Marshall* [2000], *McCormick and Grotzinger* [1993], *Miall* [1977, 1985], and *Wizevich* [1992]
Unit 4	Facies F10, F11, and F12, with mangrove to freshwater swamp pollen taxa	Assemblage of sand bed and gravel bed channel or sheetflood deposits	Gravelly alluvial environment, probably a proximal braided-streamflow fan system	*Jo et al.* [1997], *McCormick and Grotzinger* [1993], and *Miall* [1977, 1985]


A
B
C
D
E
F
G
H

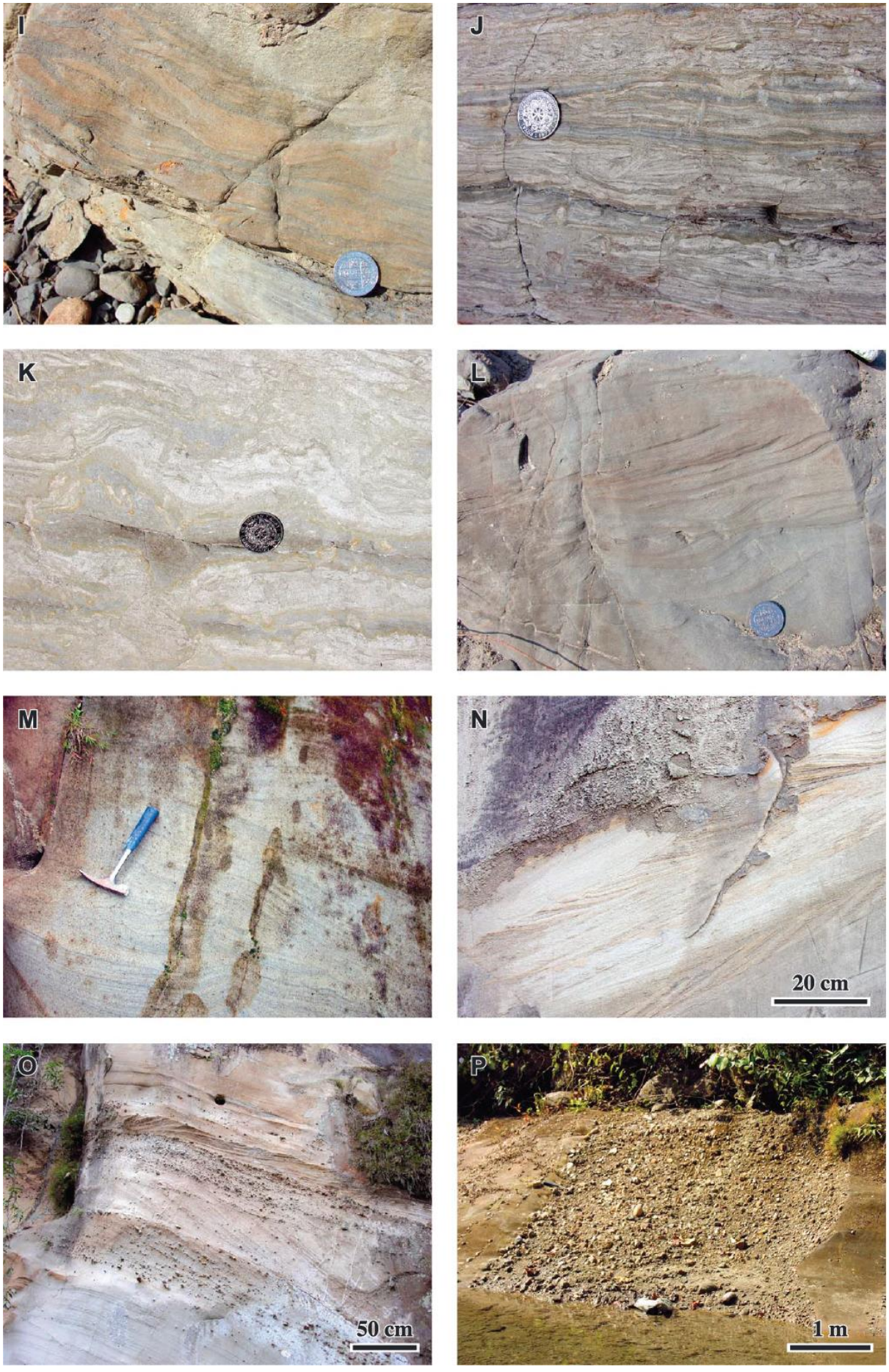
I
J
K
L
M
N
20 cm
O
50 cm
P
1 m

Fig. 27: *Photographs of outcrops depicting the most typical facies observed in the Dungsam Chu sedimentary section. (a) Facies F1 (units 1 and 2): example of a root trace. (b) Facies F2 (units 1 and 2): carbonaceous shale. (c) Facies F3 (units 1 and 2): noncarbonaceous shale. (d) Facies F4 (units 1 and 2): heterolithics with flat and undulating laminations, some rip-up clasts, and irregular surfaces of the base of the sandstone layers. (e) Facies F5 (units 1 and 2): centimetres to a decimetre thick sequences of normal gradings and flat laminations. (f) Facies 6 (unit 2): a sandstone layer of this heterolithic facies showing flaser beddings, undulating and swaley laminations, and intrabed gutter casts. Among other burrows, note the decimetre-scale Diplocraterion and the frequent millimetre-scale Planolites. (g and h) Facies 7 (unit 2): sandstone with disturbed laminations, wavy to flaser beddings, soft-sediment deformation structures, and millimetre- to centimetre-scale burrows. (i) Facies 7 (unit 2): sandstone with wavy to flaser beddings and wave ripples. (j) Facies 7 (unit 2): sandstone with flaser beddings, undulating, hummocky, and swaley laminations of wave ripples, and millimetre- to centimetre-scale burrows. (k) Facies 7 (unit 2): sandstone with disturbed laminations, soft-sediment deformation structures, and pervasive bioturbation. (l) Facies 8 (units 1 and 2): sandstone with cross laminations and climbing ripples. (m) Facies 9 (units 1 and 2): sandstone with flat and cross beds, lignite laminations, and soft-sediment deformation structures. (n) Facies 10 (units 1–4): sandstone with climbing-ripple cross-laminations, flat and cross beds, and reactivation surfaces. (o) Facies 11 (units 3 and 4): sandstone with flat and cross beds underlined by scattered pebbles. (p) Facies 12 (unit 4): conglomerate with an erosional basal surface and winnowed gravels at the top.*

4.2. Sedimentation Rates

Using our preferred magnetostratigraphic correlation, we have constructed two sedimentary accumulation curves for the Dungsam Chu section. First, we have used the median value for the calculated sediment accumulation rates from Qupydon and the median age for each polarity zone (Fig. 26c) and second, we have plotted the measured sedimentary thickness against the ages of corresponding GPTS 2012 chrons (Figs. 26c and 28). The first curve provides instantaneous sedimentation rates for each chron, while the second one smooths the signal over several chrons and yields a longer-term trend in accumulation rates. In units 1 and 2, sedimentation rates range between 0.4 and 0.6 mm/yr with a peak at 0.9 mm/yr at the base of unit 2. Unit 3 displays scattered rates at the base with two peaks at 1.0 and 1.3 mm/yr and stable values of 0.3 mm/yr in the upper half portion continuing into the lower part of unit 4, decreasing to values <0.1 mm/yr at the top of the section. The slopes of the best fit lines for the three groups of datapoints in Fig. 28 indicate a clear tendency for a slowdown of the sediment accumulation rates from ~0.63 mm/yr in units 1, 2,

and base of unit 3 to ~0.3 mm/yr at the top of unit 3 and the base of unit 4 and ~0.07 mm/yr at the top of the section (see also the red curve in Fig. 26c).

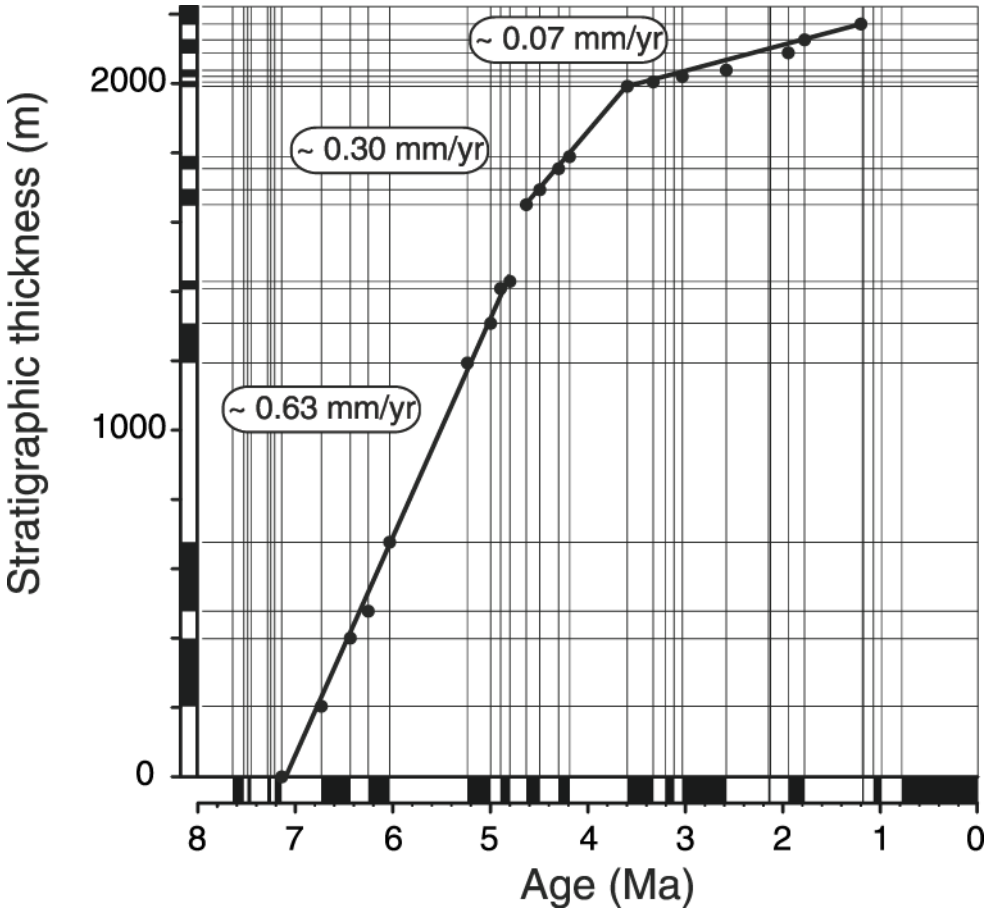

Fig. 28: *Age versus depth plot of the Dungsam Chu section using the correlation from Fig. 25c.*

5. PALYNOLOGY

To constrain the local paleoclimate and complement our understanding of the paleodepositional environment, we have looked for the palynological content of the sediments at Dungsam Chu. Sampling strategy and analytical procedure are described in Text S4 in the supporting information (Hoorn et al., 2000; Traverse, 1988).

In this exploratory palynological study of the Siwaliks sediments in Bhutan we have listed the sporomorphs by their botanical affinity, or with a form generic name, or morphological indication and type number (see caption Fig. 29). The taxa were further grouped into four main categories (Poaceae, other herbs, angiosperms/gymnosperms, and pteridophytes; see Table 5), in order to compare the Dungsam section with the Surai Khola section in Nepal (Hoorn et al., 2000) (Figure B of Appendix I). Overall, the pollen diversity is high with over 100 form genera (Table S3 of Appendix I)

observed in 16 samples (for sample location, see Fig. 19b). Pre-Cenozoic sporomorphs were uncommon and listed under “corroded/indeterminate sporomorphs” in Table S3 of Appendix I. This was not expected, given the deltaic (i.e., river-influenced) nature of the depositional environment and the common occurrence of these forms in Siwalik deposits documented elsewhere (e.g. in West Bengal, More et al., 2016)). This suggests that sediment reworking has had no marked influence on the pollen composition of the Dungsam Chu section. Ferns and fern allies (Pteridophytes) are very abundant and range mostly from 50 to 75% throughout the section (Table S3 of Appendix I, Table 5 and Fig. 26d). They are indicative of humid, wet local conditions and are often found in the presence of a mountain forest. Bhattarai et al. (2004) have demonstrated that in Nepal, the maximum fern richness along the topographic gradient is found at around 2000m and that at these elevations, ferns are strongly dependent on moisture and do not tolerate frost. The presence of Ceratopteris and Selaginella (Table S3 of Appendix I) is also typical for open freshwater conditions. Poaceae are frequent (5–25%), with peak occurrences (~50%) in the lower part of environmental unit 2 (Table S3 of Appendix I, Table 5 and Fig. 26d). Peaks of Asteraceae occurrence (5%) coincide with the Poaceae record. In contrast with findings in Pakistan (De Franceschi et al., 2008), the Bhutanese record presents low abundance to absence of Chenopodiaceae-Amaranthaceae in the Dungsam Chu samples, which is a group of wide ecological range, but particularly common in arid environments. Taxa of broadleaved, deciduous forest, such as Alnus, Betula, Corylus, Myrica, and Fagaceae (Table S3 of Appendix I), occur throughout the section but in relatively low abundances which, combined with the presence of taxa from high elevations (Ericaceae), suggest the presence of a broadleaved, deciduous forest over a pronounced topographic gradient. The presence of tropical lowland taxa such as Sapotaceae, Anacardiaceae, Bombacoideae, and Rubiaceae is representative of the pollen influx from a lowland, evergreen rain forest. In contrast, the tree pollen referred to as “other Angiosperms/Gymnosperms” in Fig. 26c, from unit 2, suggests less open vegetation until the top of the section. Finally, there are punctuated single occurrences of mangrove to back-mangrove taxa indicative a coastal setting such as Brownlowia in the bottom half of unit 2. Brownlowia may also occur in tidally influenced freshwater swamps along the coastal plain (Morley, 1991; Tomlinson and Tomlinson, 1994). In addition, several single occurrences of palm tree-type pollens such as Nypa and the extinct Neocouperipollis representing palms from the coastal environment, and extending toward tidally influenced rivers and freshwaters swamps further inland (Giesen et al., 2007; Monga et al., 2015), are observed along the entire section (Table S3 of Appendix I).

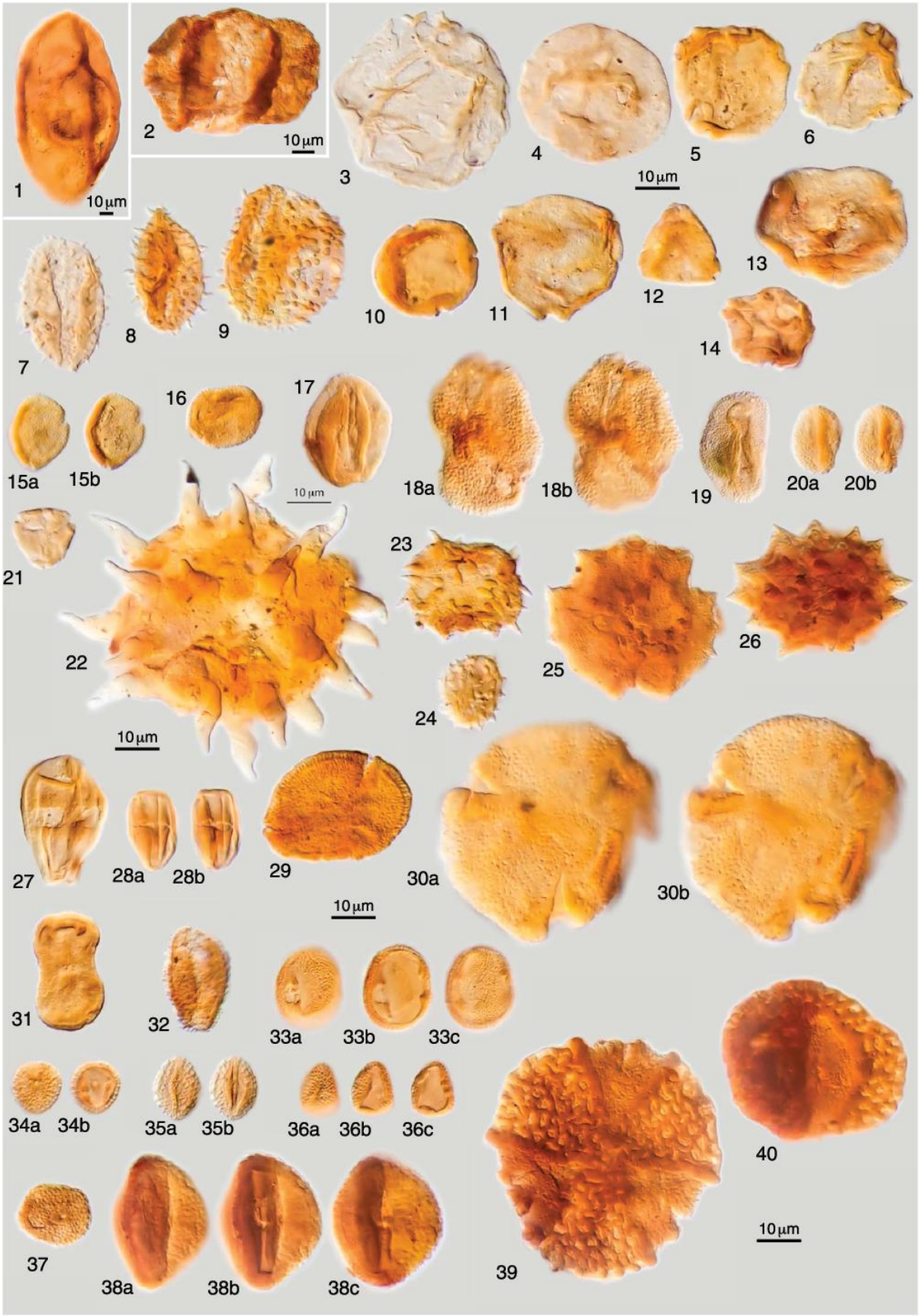
1
10 µm
2
10 µm
3
4
5
6
10 µm
7
8
9
10
11
12
13
14
15a
15b
16
17
10 µm
18a
18b
19
20a
20b
21
22
10 µm
23
24
25
26
27
28a
28b
29
10 µm
30a
30b
31
32
33a
33b
33c
34a
34b
35a
35b
36a
36b
36c
37
38a
38b
38c
39
40
10 µm

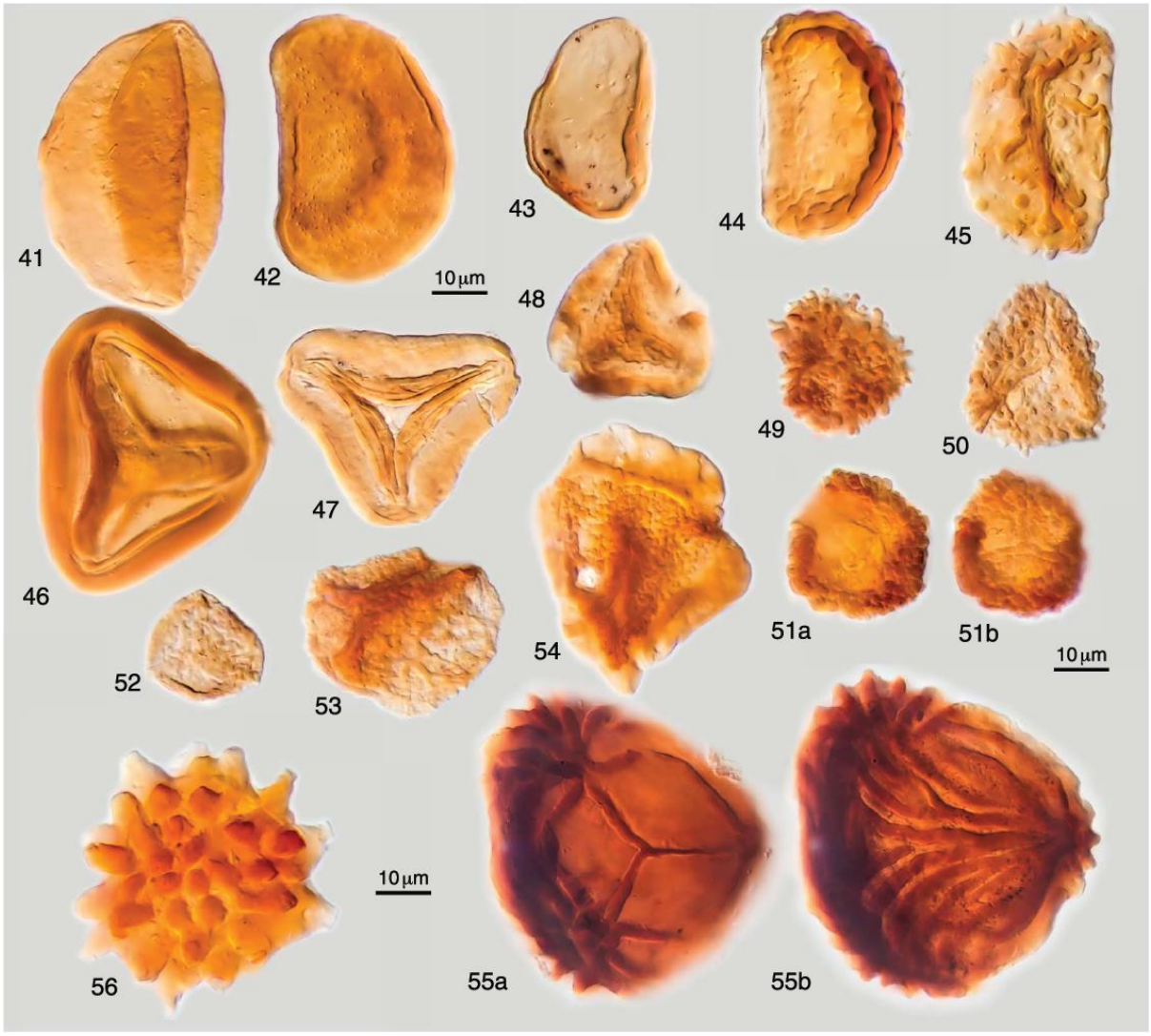

Fig. 29: *Optical micrographs of representative sporomorph taxa of the Neogene-Pleistocene Dungsam Chu section, Bhutan. The sample number and England Finder reference are given for each specimen. (1) Magnolia type; slide PN28-4; EF: E18-F18. (2) Reworked bisaccate; slide PN51-4; EF: U24-25/4-3. (3) Poaceae; slide PN85-4; EF: S30. (4) Platanus? (Type 39); slide PN85-4; EF: D22-4. (5) Myricoid-Betuloid type; slide PN21A-4; EF: Q33-3. (6) Myricoid-Betuloid type; slide PN21A-4; EF: T16-2. (7) Nypa (Type 38); slide PN21-4; EF: S13-3. (8) Nypa (Type 38); slide PN37-4; EF: R26-3. (9) Neocouperipollis (Type 36); slide PN37-4; EF: P12-2. (10) Meliaceae (Type 9); slide PN20A-4; EF: O34-3 (see also PN28-4; R31). (11) Corylus (Types 48 and 55); slide PN14B-4; EF: K-L23. (12) Juglandaceae/Pandaceae? (Type 19); slide PN28-4; EF: Q13-14/4-3. (13) Carpinus? (Type 63); slide PN85-4: U20-3. (14) Alnus; slide PN13A-4; EF: M22-23. (15a-b). Rubiaceae (Types 7 and 25); slide PN28-4; EF: T-U18. (16) Rubiaceae? (Type 6); slide PN20A; EF: E-F18/3-1. (17) Quercus; slide PN85-4; EF: H31. (18a-b) Alangium (Type 10); slide PN20A; EF: Q35-2. (19) Reticulate, tricolporate (Type 66); slide PN85-4; M20/1-2. (20a-b) Reticulate, tricolporate (Type 66); slide PN85-4; EF: W-V27-28. (21) Myrtaceae; slide PN13A-4: EF: M26. (22) Malvaceae? (Type 52); slide PN14B; EF: O20-4. (23) Nypa*

(Type 50); slide PN14B; EF: L-M/23-24. (24) Asteraceae; slide PN20A; EF: K34-1. (25) Asteraceae, Centaurea type; slide PN21-4; EF Q-R/31/3-1. (26) Asteraceae? slide PN20A; EF: J18. (27) Sapotaceae? (Type 65); slide PN85-4; EF: V25/1-2. (28a-b) Sapotaceae (Type 87-91); slide PN60-4; EF: S31-1. (29) Brownlowia (Type 18); slide PN28-4; EF: Q25-26/2-1. (30a-b) Alangium (Type 42); slide PN37-4; EF: X23-3. (31) Acanthaceae, Justicia type (Type 75); slide PN51A-4; EF: L19-1. (32) Oncosperma (Types 21 and 47); slide PN28-4; EF: R25/1-3. (33a-c) Anacardiaceae? (Type 32); slide PN37; EF: L28. (34a-b) Mitragyna, Rubiaceae; slide PN60-4; EF: N31-32. (35a-b) Reticulate, tricolpate indet.; slide PN60-4; EF: L32-3. (36a-c) Rubiaceae, reticulate, triporate (Types 74 and 86); slide PN60-4; EF: M28. (37) Rubiaceae, reticulate, and triporate (Types 74 and 86); slide PN55-4; EF: K-L/33-34. (38a-c) Verrucate and tricolporate (Type 61); slide PN85-4; EF: P27-3. (39) Caesalpiniaceae? (Type 73); slide PN51A-4; EF: M27-2. (40) Caesalpiniaceae? (Type 73); slide PN51A-4; EF: H-J28/4-2. (41) Indeterminate sporomorph; Slide PN28-4; E: O15-3? (42) Monolete spore; slide PN20A; EF: E24-3. (43) Polypodiaceae; slide PN85-4; J23 and J28-29. (44) Nephrolepis, Davalliaceae; slide PN20A; EF: N15. (45) Stenochlaena palustris, Blechnaceae; slide PN85-4; EF: U29/1-2. (46) Pteris type, Pteridaceae (Type 60); slide PN85-4; EF: N15-2. (47) Pteris type, Pteridaceae (Type 11); slide PN20A; EF: Q16-3. (48) Pteris type, Pteridaceae (Type 30); slide PN21A-4: EF: Q25-2. (49) Selaginella? (Type 77); slide PN31A-4; EF: N24-4. (50) Selaginella (Type 62); slide PN85-4; EF: R26-27/4-3. (51a-b) Verrucate/gemmate, trilet (Microlepia?) (Type 37); slide PN37-4; EF: Q-R16/4-2. (52) Lycopodium cernuum type (Type 34); slide PN37-4; EF: P21/2-4. (53) Praedapollis sp. (Type 35); slide PN37-4; EF: P19-1 and S30-2. (54) Pteris type, Pteridaceae (Type 33); slide PN37-4; EF: O20-1. (55a-b) Ceratopteris, Pteridaceae; slide PN21A-4; EF: Q32-2. (56) Bryophyte/Hepatic spore? (Type 51); slide PN14B; EF: O21-3.

Table 5: *Summary of the palynological group counts*[a]

	PN13	PN14	PN20	PN21	PN28	PN31	PN37	PN51	PN55	PN58	PN60	PN65	PN74	PN82	PN85	PN86
Stratigraphic thickness (m)	252	297	398	416	568	630	666	854	1032	1067	1081	1158	1366	2180	2205	2209
Poaceae	6	23	185	182	13	10	29	27	32	8	39	21	11	33	16	21
Asteraceae	1		22	27		1					1			1	1	
Other Angiosperms/ Gymnosperms	18	26	43	48	26	29	27	59	38	9	72	46	42	47	51	38
Pteridophytes	86	144	81	95	240	87	91	28	116	56	89	111	39	169	107	58
SUM	**111**	**193**	**331**	**352**	**279**	**127**	**147**	**114**	**186**	**73**	**201**	**178**	**92**	**250**	**175**	**117**
Pteridophytes indeterminate	2	26	10	18	7	7	3	9	8	2	6	6	4	37	24	5
All corroded/indeterminate	20	43	34	37	23	18	28	100	47	18	34	35	15	81	53	10

[a]Boldface highlights the sum for each column.

6. DISCUSSION

6.1. Age of the Siwalik Group

Magnetostratigraphic results suggest that along the Dungsam Chu, the age of the base of the section is at ~7 Ma (Fig. 25c), the boundaries between the classic lithological subgroups of the Siwalik Group being determined at ~6 Ma for the lower to middle Siwalik subgroups and at ~3.8 Ma for the middle to upper Siwalik subgroups, while the top of the section is ~1 Ma (Figs. 25c and 26). Previous magnetostratigraphic correlations in the Neogene-Quaternary Himalayan foreland basin from Pakistan to Arunachal Pradesh document ages ranging from 8 to 12Ma for the lower to middle Siwalik transition (e.g. Chirouze et al., 2012; Gautam and Fujiwara, 2000; Ojha et al., 2009; Ojha et al., 2000; Tokuoka et al., 1986) and from 2 to 3.5 Ma for the middle to upper Siwalik transition (e.g. Behrensmeyer et al., 2007; Ojha et al., 2009; Sanyal et al., 2004) (Fig. 30a). Therefore, in the Dungsam Chu section, the boundary between the lower and middle Siwalik subgroups is 2 to 6 Ma younger than documented elsewhere along the Himalayan arc. Furthermore, the duration of deposition of the middle Siwalik subgroup varies from 3 to 6 Ma in central and western Nepal (Surai and Muksar Khola sections) (Ojha et al., 2009) to about 2–3Ma in Bhutan (Dungsam Chu section) to as long as 8Ma in Arunachal Pradesh (Kameng section, Fig. 30a) (Chirouze et al., 2012).

Apparently, the Kameng section differs significantly from the Nepalese and Bhutanese sections (Fig. 30a) although these differences are not straightforward to explain. Indeed, it has been clearly demonstrated that vertical transitions between lithostratigraphic formations and their lateral diachroneity cannot be interpreted simply in terms of tectonic and climatic forcing, especially in foreland basins (e.g. Barberà et al., 2001; Burbank et al., 1986; Charreau et al., 2009; Heermance et al., 2007). These changes reflect the 4-D space-time evolution of depositional profiles documented by one-dimensional vertical sections located at different positions, more proximal or more distal, with respect to the mountain range and its foreland. Consequently, extensive and careful spatiotemporal constraints, both parallel and perpendicular to the orogenic system, are necessary to properly discuss what controls the vertical and lateral transitions between the lithostratigraphic formations in a foreland basin. Additionally, a sedimentological and stratigraphical reading of such variations in terms of paleoenvironmental, paleogeographical, and sequential evolution is often more pertinent than a strictly lithostratigraphic approach.

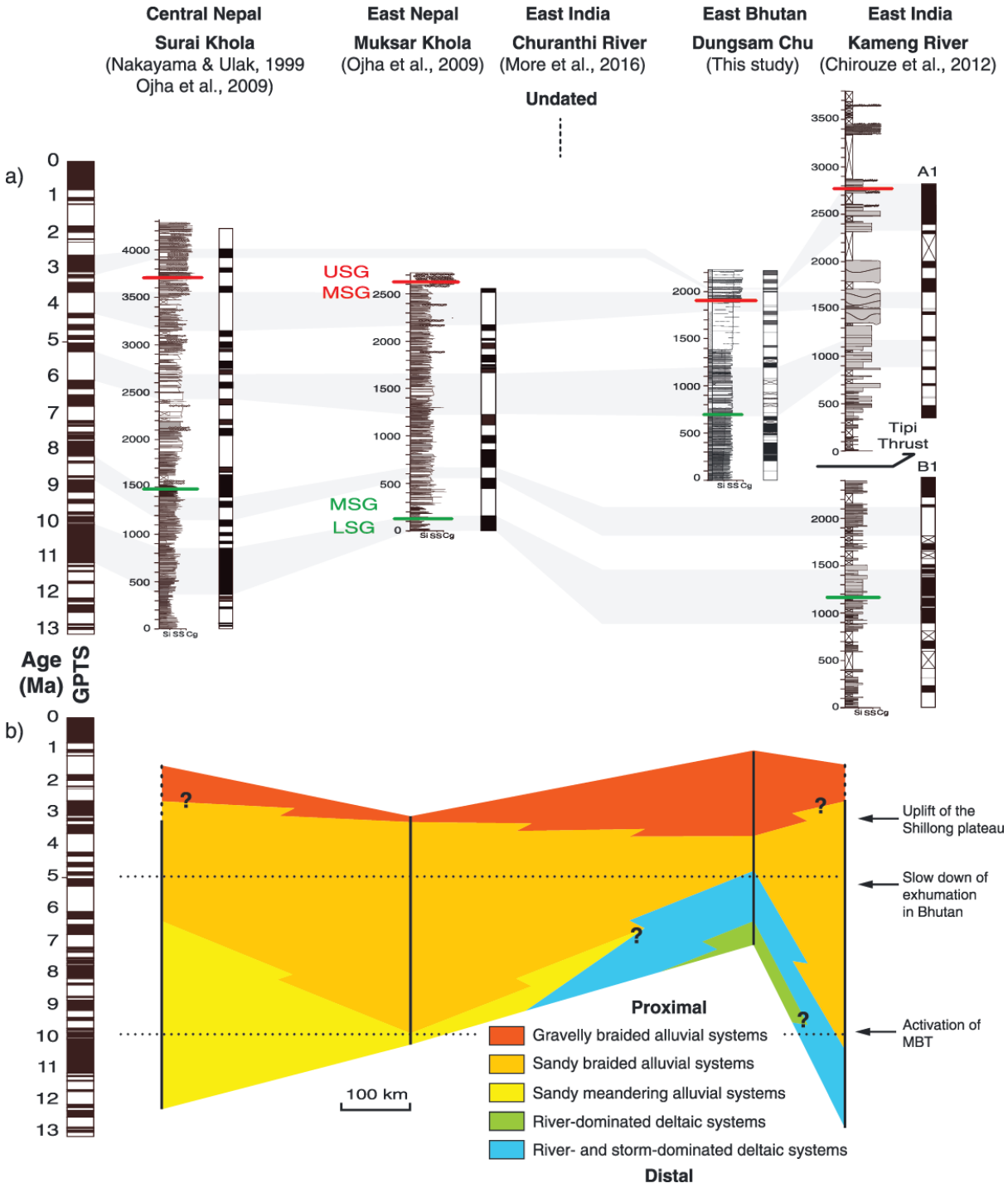

Fig. 30: *(a) Summary of magnetostratigraphic correlations to the GPTS of stratigraphic sections of Siwalik deposits along the eastern Himalayan arc (modified after Hirschmiller et al. (2014)). USG: upper Siwalik subgroup, MSG: middle Siwalik subgroup, LSG: lower Siwalik subgroup. Si, SS, and Cg are abbreviations for siltstone, sandstone, and conglomerate. (b) Lateral variations of depositional environments. Stratigraphic sections are from Nakayama and Ulak (1999) and Ojha et al. (2009) (Surai and Muksar Khola), this study (Dungsam Chu), and Chirouze et al. (2012) (Kameng River).*

6.2. Depositional Environments and Paleogeography

The Siwalik Group in Bhutan shows an overall distal to proximal trend as observed everywhere else in the Himalayan foreland basin (e.g. Chirouze et al., 2012; DeCelles et al., 1998b; Kumar et al., 2003; Nakayama and Ulak, 1999). This long-term progradational trend, which is typical of the filling sequence of foreland basins at their active margin (e.g. Jordan, 1995; Puigdefàbregas et al., 1986; Schlunegger et al., 1997; Sinclair and Allen, 1992; Stockmal et al., 1992) is controlled by the propagation of the deformation front, generally together with an increasing erosion and sediment flux, related to the horizontal and vertical growth of the adjacent mountain range.

To the west of the system, the sedimentary paleoenvironments are thus interpreted as meandering and braided fluvial depositional systems (lower and middle Siwalik subgroups) grading into alluvial fan systems (upper Siwalik subgroup) (Fig. 30b). This kind of environmental evolution is uniformly observed from Pakistan (Abbasi and Friend, 2000; Willis, 1993; Zaleha, 1997) to western India (Brozovic and Burbank, 2000; Johnson et al., 1983; Kumar et al., 2003; 2004; Suresh et al., 2004) and Nepal (DeCelles et al., 1998b; Huyghe et al., 2005; Nakayama and Ulak, 1999; Ojha et al., 2009). In some places, floodplains with intermittent lacustrine conditions attributed to seasonal flooding are also recorded (DeCelles et al., 1998b; Hoorn et al., 2000) but always in a continental environment. A paleoenvironmental change occurs east of Nepal where thick deltaic deposits appear in the lower and middle Siwalik subgroups (Fig. 30b). Along the Churanthi River in West Bengal (Fig. 17), brackish water to shallow marine conditions are documented by palynological data and trace fossils in the undated middle Siwalik subgroup (More et al., 2016). Farther east, our observations indicate that along the Dungsam Chu, the basal environmental units 1 and 2 correspond to deposits of a river-dominated deltaic system and a wave-influenced deltaic environment, respectively, associated with marine trace fossils, glauconite, and some coastal pollen taxa, suggesting a marine setting before ~5 Ma (Fig. 30b). After that, the deposits grade to units 3 and 4, which represent a sandy and a gravelly alluvial system, respectively. Along the Kameng section in Arunachal Pradesh (Fig. 17), Chirouze et al. (2012) also describe a lacustrine to marine deltaic environment in the lower Siwalik subgroup (Dafla Formation) before ~10.5 Ma (Fig. 30b). Moreover, the overlying braided river sediments of the middle Siwalik subgroup (Subansiri Formation) and alluvial fan deposits of the upper Siwalik subgroup are reported to both bear paleobotanical evidences of brackish water or near coastal environments (e.g. Chirouze et al., 2012; Mehrotra et al., 1999; Singh and Tripathi, 1989). We speculate that these brackish water to shallow marine paleoenvironments are linked to those observed to the northeast of the Shillong Plateau in the foreland of the Naga Hills of Assam (e.g.

Bhandari et al., 1973; Reimann and Hiller, 1993) and to the south in the well-dated Surma Basin of northern Bangladesh (e.g. Alam et al., 2003; Najman et al., 2012; Worm et al., 1998) (Fig. 17).

In the foreland of the Naga Hills in Assam, paleoenvironmental data indicate marine influence during the Neogene, although the chronological constraints on sediment deposition remain poorly constrained (Bhandari et al., 1973; Evans, 1932; Mallet, 1876; Reimann and Hiller, 1993). The Miocene Surma Group displays fossil assemblages pointing toward shallow marine to brackish water environments, whereas the overlying Mio-Pliocene Tipam Group is characterized by lithologic characteristics and floral assemblages symptomatic of a fluvial environment in a subtropical to temperate climate (e.g. Bhandari et al., 1973; Reimann and Hiller, 1993).

The Surma Basin in Bangladesh also records nearshore to marine conditions in strata contemporaneous with the marine facies recorded in Bhutan (e.g. Johnson and Alam, 1991). The latest Miocene-Pliocene Surma Group consists of the Bhuban and Bokabil Formations. The Bhuban Formation displays a proximal marine deltaic system associated with mangrove taxa and is interlayered with shallow marine incursions. The overlying Bokabil Formation is characterized by the presence of foraminiferal tests associated with mangrove taxa. The top of the Surma Group is characterized by the Upper Marine Shale, which represents the final marine incursion to this area, dated at 2.5–3.9 Ma. Above this, the overlying Tipam and Dupi Tila Formations were then deposited in a fluvial environment (e.g. Gani and Alam, 2004; Johnson and Alam, 1991; Najman et al., 2012; Worm et al., 1998).

There are extensive lateral variations in lithologies and thicknesses of the different sediment sequences described in those different areas, some of them located quite far (a few hundred kilometres) from the Dungsam Chu section. However, we speculate that the observations collectively suggest that the marine incursions emanating from the Bay of Bengal to the south and recorded both in the Naga Hills and the Surma Basin until the deposition of fluvial facies from ~3.9 Ma may have had a peripheral impact on the facies observed at the front of the Himalayan range in eastern India (Chirouze et al., 2012; More et al., 2016) and in Bhutan until at least ~5 Ma. Our hypothesis supports a post-Miocene full continentalisation of the eastern Himalayan foreland basin, much later in time than previously suggested in this area (e.g. Alam et al., 2003; Johnson and Alam, 1991) and than farther west. In Nepal the peripheral foreland basin shows clear evidence for an extensive unconformity separating marine facies below and fluvial facies above (DeCelles et al., 1998a). The youngest marine facies are generally considered to be Mid-Eocene in age although this

matter remains debated (e.g. Bhatia and Bhargava, 2006; Najman, 2007), while the fluvial facies commenced, at the latest, by 20 Ma (Ojha et al., 2009; White et al., 2002), which is at least 15 Ma earlier than observed in Bhutan.

The post-Miocene continentalisation of the Dungsam Chu region and the eastern Himalayan foreland basin likely result from a combination of two main factors including (1) the long-term progradation of the foreland depositional landscape related to the growth of the Himalayan orogenic wedge, which has probably produced a southward migration of the shoreline of the Bay of Bengal, and (2) the long-term sea level fall initiated since the late Miocene (Hansen et al., 2013; Miller et al., 2005). Superimposed on this second-order eustatic trend, a relative sea level high occurred before 4.9 Ma (Hansen et al., 2013; Miller et al., 2005) which potentially has promoted a marine influence in our study area until the wave-influenced deltaic environment changed for a river-dominated environment. Finally, the deformation and surface uplift of the Shillong block must have decreased the subsidence of the eastern Himalayan foreland before creating a topographic barrier into the basin after 4–3 Ma (Biswas et al., 2007; Najman et al., 2016).

6.3. Palynology and Paleoclimate

The predominance of grass and fern sporomorphs and a highly diverse assemblage of angiosperms and pteridophytes, which collectively are typical for tropical lowland vegetation, characterize the composition of the palynological assemblage in the Dungsam Chu section. In essence, this assemblage is comparable to the palynological results obtained in central Nepal along the Surai Khola (Hoorn et al., 2000) (Figure B of Appendix I), but the larger variety of lowland taxa in eastern Bhutan suggests a more diverse tropical lowland vegetation upstream of the sedimentary basin.

In terms of temporal evolution, the composition of the palynological assemblage does not significantly change through the 7–1 Ma interval documented by the Dungsam Chu section. In contrast, the Surai Khola section shows a shift at around 6.5 Ma, when ferns drop and grasses predominate from then onward (Hoorn et al., 2000). The Bhutanese record thus resembles the pre-6.5 Ma Nepalese record, rather than its post-6.5 Ma temporal equivalent (Figure B of Appendix I). This suggests that the environment and probably the paleoclimate in Bhutan, in the lowland and floodplain, were consistently more humid than the coeval environments and paleoclimate in Nepal, as is the case nowadays (Bookhagen and Burbank, 2006; 2010). The palynological record thus indicates that the orographic perturbation of ISM precipitations exerted by the surface uplift of the

Shillong Plateau 4–3 (Biswas et al., 2007) to 3.5–2 Ma ago (Najman et al., 2016) did not measurably modify the wet local climate observed in the Bhutanese foothills since 7 Ma.

6.4. Accumulation Rates and Deformation

In foreland basins, the rates of sediment preservation are conditioned by the spatiotemporal evolution of the subsidence, which primarily generate accommodation space for deposits, and by sediment supply derived from the erosion of the adjacent mountain range (DeCelles and Giles, 1996). Consistent with the forelandward migration of the basin flexure associated with the lateral and vertical growth of the orogenic system, the foredeep depozones of foreland basins are generally characterized by an overall acceleration of subsidence through time recorded by increasing accumulation rates and convex up subsidence curves (e.g. Charreau et al., 2009; Ojha et al., 2009; Xie and Heller, 2009). For the Himalayan foreland basin, such increasing or constant accumulation rates calculated from the non-decompacted sedimentary thicknesses of the Siwalik deposits have been mostly interpreted in terms of flexure associated with the slip history of the Main Boundary Thrust (MBT) (e.g. Burbank et al., 1996; Meigs et al., 1995; Ojha et al., 2009). Contrary to other foreland sedimentary sections from Pakistan to Arunachal Pradesh (See Chirouze et al., 2012, Figure 10; Ojha et al., 2009, Figure 13), the Dungsam Chu section has a unique characteristic which is that the accumulation rate decreases steadily from ~0.63 mm/yr between ~7 and ~4.5 Ma to ~0.3 mm/yr between ~4.5 and ~3.5 Ma and ~0.07 mm/yr between ~3.5 and ~1 Ma (Figs. 26c and 28). Different mechanisms including climatically or tectonically driven decrease in subsidence and/or in sediment supply to the foreland basin may potentially account for this deceleration of accumulation rate in eastern Bhutan. First, the detrital influx entering the basin may have decreased due to a climatically driven slowdown of erosion in the hinterland of the orogen. Second, a tectonically driven decrease in subsidence could have resulted from the forelandward propagation of the fold-and-thrust belt and the integration of the study area into the thrust-wedge depozone of the basin. Third, the subsidence and/or the sediment supply may have diminished due to a tectonically driven decrease of shortening rates along the frontal Himalayan structures generating decay of crustal thickening and erosion in the hinterland and decay of the lithospheric flexure in the foreland. First, in Bhutan, a decrease in detrital influx may have resulted from a climatically driven slowdown of erosion in the range during the Pliocene (Grujic et al., 2006), in response to the surface uplift and orographic effect of the Shillong Plateau (Biswas et al., 2007). Yet the lack of paleoclimatic changes in our palynological data and the steady stable isotopic record from authigenic clay minerals across the stratigraphic section (D. Grujic, personal communication of unpublished data, 2016) refute this hypothesis. Second, a tectonically driven decrease in subsidence in relation with the propagation of

the deformation front toward the foreland could also be plausible. Indeed, the Dungsam Chu section has migrated from the foredeep to the wedge-top depozone of the basin (e.g. DeCelles and Giles, 1996), since it is currently located in the hanging wall of the Main Frontal Thrust (MFT) (Fig. 18). Therefore, the time at which this thrust was activated becomes of critical importance. Based on detrital thermochronology and/or the presence of growth strata, ongoing displacement on the MFT is suggested to have started ~2 Ma ago in western and central Nepal (Mugnier et al., 2004; van der Beek et al., 2006) and ~1 Ma ago in eastern India in Arunachal Pradesh (Chirouze et al., 2013) and possibly at an unspecified younger time (Burgess et al., 2012), while the timing remains undetermined in Bhutan. However, the accumulation rates at Dungsam Chu have decayed since at least 4.5 Ma. Given the post ~2–1 Ma MFT activation documented along the eastern Himalayan arc, it hence seems reasonable to assume that during most of its deposition, the Dungsam Chu section remained located in the foredeep depozone and has not experienced a reduced creation of accommodation space due to the forelandward propagation of the Himalayan deformation front (MFT) before the Pleistocene. Third, the last option available to explain the deceleration of accumulation rates observed in eastern Bhutan is a tectonically driven decrease in subsidence and/or detrital influx due to a change in the deformation of the range and its foreland. What makes the Dunsgam Chu section special along the Himalayan arc is its location north of the Shillong Plateau, a unique basement-cored uplift in the Himalayan foreland (Fig. 17). At the longitude of central and eastern Bhutan, the Himalayan foreland corresponds to a broken foreland basin (e.g. Jordan, 1995; Strecker et al., 2011), rather than a classical foreland system (e.g. DeCelles and Giles, 1996). In this area, the foredeep is very shallow (maybe <1 km), in contrast to areas west and east of Bhutan (depths >4 km) (Dasgupta, 2000; Verma and Mukhopadhyay, 1977; Vernant et al., 2014, Figure 1b). The exhumation/cooling of the Shillong Plateau's basement initiated 9–15 Ma ago (Biswas et al., 2007; Clark and Bilham, 2008) and its surface uplift 3–4 Ma (Biswas et al., 2007) to 3.5–2 Ma ago (Najman et al., 2016). Both likely have had a significant influence in a reorganization of the regional paleogeography and the partitioning of India-Eurasia convergence along the Bhutanese range front. Based on thermokinematic modelling of thermochronometric data tied to a sequential balanced cross section, McQuarrie and Ehlers (2015) suggested that in the LHS of eastern Bhutan, shortening rates decreased between 8 and 0 Ma. Inverting a thermochronometric data set using 3-D thermokinematic modelling, Coutand et al. (2014) inferred a 50% decrease in long-term exhumation rates at~6 Main eastern Bhutan. At the time, Coutand et al. (2014) were not able to differentiate whether this drop in erosion rate should be attributed to climatic- or tectonic-related processes. Because in the Dungsam Chu section there is a lack of change of both the palynological record (Fig. 26d and Table S3 of Appendix I) and stable isotope climatic proxies (Grujic, personal communication

of unpublished data, 2016) after 6.5 Ma (for most of the section deposition), we contend that tectonics had a prominent influence on the nature and magnitude of the foreland basin filling in eastern Bhutan. The onset of the Shillong block's deformation and the slowdown of the displacement rates along the MBT in eastern Bhutan during the latest Miocene-Pleistocene would have had a direct impact on the accommodation space created in the basin, as well as on the detrital influx derived from the Himalayan orogenic wedge, decreasing them both. In the northeastern corner of India, plate reconstruction suggests that the convergence between India and Eurasia has been 44 mm/yr over the past ~11 Ma (Molnar and Stock, 2009), out of which GPS measurements indicate that a contraction of 14–17 mm/yr (Vernant et al., 2014) is currently accommodated in Bhutan. The discrepancy observed between long-term (0.65–2.9 mm/yr over the last 10 Ma (Biswas et al., 2007; Clark and Bilham, 2008)) and short-term (3–7 mm/yr (Vernant et al., 2014)) contraction rates accommodated on the Dauki Fault suggests that the amount of horizontal shortening accommodated by the Shillong Plateau has increased during the last 10 Ma, while it has concomitantly decreased by 3–8 mm/yr in the Bhutan Himalaya (Vernant et al., 2014). We hence attribute the late Miocene-Pleistocene decrease in sedimentary accumulation rates observed in eastern Bhutan to a tectonically driven change in subsidence and/or detrital influx in the basin, in response to an increasing partitioning of the India-Eurasia total convergence into the Shillong Plateau.

7. CONCLUSIONS

This multidisciplinary study of the exposed Siwalik Group along the Dungsam Chu in eastern Bhutan leads to the following conclusions:

(1) Magnetostratigraphy constrained by vitrinite reflectance and detrital AFT data indicate that the Siwalik Group was deposited during the latest Miocene and the Pleistocene, between ~7 Ma and ~1 Ma.

(2) Depositional environments include river-dominated and wave-influenced deltaic systems at the base which, associated with marine trace fossils, glauconite, and some coastal pollen taxa, suggest a marine setting potentially linked to marine incursions from the Bay of Bengal. At around 5 Ma, a transition to a sandy and then gravelly alluvial environment occurs. Together with the sedimentological observations in eastern India (West Bengal, Arunachal Pradesh, and Assam) and northern Bangladesh, this paleoenvironmental evolution is consistent with a post-Miocene complete

continentalisation of the eastern Himalayan foreland basin at least 15 Ma later than is observed in the western Himalayan foreland basin.

(3) The sporomorphs represent taxa from different vegetation types in the proximal Himalayan orogenic system and point to diverse tropical lowlands and rain forest vegetation throughout the ~7–1 Ma time period. The palynological record also indicates that depositional environments and paleoclimate were consistently more humid in Bhutan than the coeval in Nepal. This is similar to modern precipitation patterns along the strike of the Himalaya, which are characterized by an east-to-west decrease in ISM precipitation intensity. Furthermore, no major change in moisture or temperature is documented in Bhutan between 7 and 1 Ma, indicating that the orographic blockage of ISM precipitations exerted by the surface uplift of the Shillong Plateau 3.5–2 Ma ago did not measurably modify the wet local climate documented in the Bhutanese foothills since 7 Ma.

(4) During the last 7 Ma, the sustained decrease in accumulation rates of the Siwalik Group sediments in the Dungsam Chu section results from a progressive diminution of the flexural subsidence in the basin and/or of the detrital input from the range, which we attribute to the onset of the Shillong block's deformation and a slowdown of the displacement rates along the MBT in eastern Bhutan during the latest Miocene-Pleistocene, in response to an increasing partitioning of the India-Eurasia convergence into the Shillong Plateau.

ACKNOWLEDGMENTS

Fieldwork was supported by the France-Stanford Foundation (I.C.) and the Natural Sciences and Engineering Research Council of Canada (discovery grant RGPIN 371671 to I.C. and RGPIN 04297 do D.G.). I.C. thanks ETH Zürich for financial support (visiting professorship grant) during the writing of the manuscript. G.G. and Y.N. acknowledge financial support from a Marie Curie Initial Training Network iTECC funded by the EU REA under the FP7 implementation of the Marie Curie Action, under grant agreement 316966. C. Hoorn thanks the Hugo de Vries-Fonds (http://www.hugodevriesfonds.nl/) for financial support and R. Morley, K. Richards, and K. Paudayal for assisting her with the identification of selected pollen and spores. We thank A. Philip for the palynological processing and J. van Arkel for microphotography. The work of L. Barrier for this publication is the IPGP contribution 3665.

SUPPLEMENTARY MATERIAL

The supplementary material of this chapter is presented in Appendix I as listed here.

Methods:

- Vitrinite reflectance: sampling strategy and analytical procedure
- Detrital apatite fission-track (DAFT) thermochronometry method and sampling
- Paleomagnetic analysis: sampling and analytical procedure
- Sedimentological analysis: method
- Palynological analysis: sampling and analytical procedure

Data tables:

- Table S1: Vitrinite reflectance data
- Table S2: Magnetostratigraphy data
- Table S3: Palynological data

CHAPTER 2

Timing and mechanism of the rise of the Shillong Plateau in the Himalayan foreland

Gwladys Govin [1], Yani Najman [1], Alex Copley [2], Ian Millar [3], Peter van der Beek [4], Pascale Huyghe [4], Djordje Grujic [5], and Jesse Davenport [6]

[1] ***LEC, Lancaster University, Library Avenue, Lancaster LA1 4YQ, UK***

[2] *Department of Earth Sciences, Cambridge University, Downing St, Cambridge CB2 3EQ, UK*

[3] *Geochronology and Tracers Facility, NIGL, British Geological Survey, Keyworth, UK*

[4] *ISTerre, Université Grenoble Alpes, CS 40700, 38058 Grenoble Cedex 9, France*

[5] *Department of Earth Sciences, Dalhousie University, Halifax B3H 4R2, Canada*

[6] *CRPG, 15 Rue Notre Dame des Pauvres, 54500 Vandœuvre-Lès-Nancy, France*

Manuscript submitted twice to Geology, each time rejected with invited resubmission. It will be formatted and re-submitted in the same journal, post Ph.D. thesis submission.

ABSTRACT

The Shillong Plateau is the only elevated topography in the Himalayan foreland. Knowledge of its surface-uplift history is important for understanding couplings between erosion, climate and tectonics, as well as strain partitioning within the Himalaya. Exhumation of the plateau was initiated by 9–15 Ma. Surface uplift only began in the Pliocene but its timing of initiation is not well constrained. We use the sedimentary record of the Himalayan foreland basin north of the Shillong Plateau to show that the paleo-Brahmaputra river was redirected north and west by the rising plateau between 5.2-4.4 Ma. The onset of surface uplift has previously been explained by the erosion level reaching resistant Precambrian basement. We suggest that this onset is instead a result of convergence of the Shillong and the Tibetan plateaus, leading to increased fault-slip rates in response to stresses caused by the Indian lithosphere bending beneath the Himalaya.

1. INTRODUCTION

The interplay of tectonics, lithospheric structure, erosion and climate in the evolution of collisional belts is highly complex (e.g. Garcia-Castellanos and Jiménez-Munt, 2015). It has been suggested that the 1600 m high Shillong Plateau formed in response to an along-strike change in strain partitioning in the orogen (Clark and Bilham, 2008). Additionally, lower exhumation rates in the Himalaya north of the Shillong Plateau, compared to elsewhere along the range, have been attributed to changes in strain partitioning due to Shillong Plateau development (e.g. Coutand et al., 2014), or the plateau acting as an orographic barrier to precipitation caused by the Indian Summer Monsoon (Grujic et al., 2006).

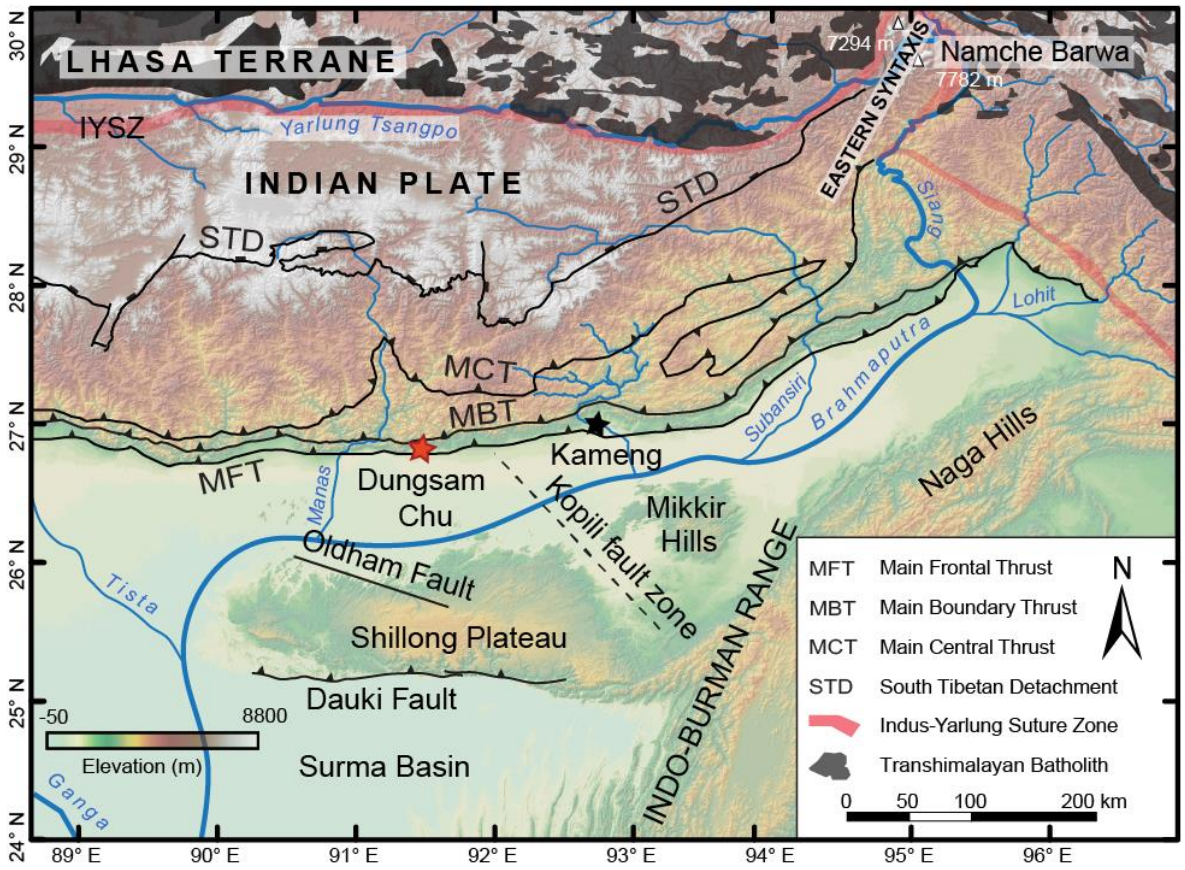

Fig. 31: *Topography and main geologic features of the eastern Himalaya (modified from Lang and Huntington, 2014; Long et al., 2011). Red and black stars represent the Dungsam Chu and Kameng sections, respectively.*

The timing and cause of the plateau's surface uplift remain poorly understood. Thermochronological data indicate that basement rock exhumation was initiated between 9-15 Ma (Biswas et al., 2007; Clark and Bilham, 2008). Surface uplift of sufficient magnitude to create remarkable flexural loading of the Indian plate is recorded much later, at 3.5 Ma in the Surma Basin south of the plateau

(Najman et al., 2016). However, the timing of initiation and early stages of surface uplift remain unknown. Additional evidences for the conversion of rock uplift into surface uplift sometime in the Pliocene include: 1) a slowdown of basement cooling rates from 4-6 Ma; 2) the removal of >6000 m of Cenozoic sediments overlying a well-preserved Cretaceous paleo-surface with very little incision of the top of the basement; and 3) the presence of marine/proximal delta sediments <9 Ma on the plateau. Surface uplift therefore appears to be decoupled from exhumation, and occurred after a period when rock uplift was compensated by surface erosion (± isostatic adjustment) (Biswas et al., 2007). However, when and why the transition occurred remains uncertain.

It has been suggested that surface uplift of the Shillong Plateau, along with the westward propagation of the Indo-Burman ranges (Chirouze et al., 2013; Najman et al., 2016), diverted the Brahmaputra River from a relatively straight SSW direction into its present course between the Himalaya and the Shillong Plateau (e.g. Johnson and Alam, 1991; Uddin and Lundberg, 1999). Therefore, documenting the first occurrence of paleo-Brahmaputra deposits in the foreland basin directly north of the plateau constrains the minimum age of initiation of its surface uplift. Here we report new provenance analysis of Himalayan foreland-basin sediments (Siwalik Group) from Bhutan. We use these, together with published data, to propose a model of the Brahmaputra drainage evolution from Late Miocene to present, and determine when the river was deflected due to the initiation of uplift of the Shillong Plateau. Furthermore, we model the evolution of the lithospheric stress field in the Shillong region as it approached the Himalayan orogen, in order to assess the role of tectonics in the transition from exhumation to surface uplift.

2. GEOLOGICAL CONTEXT

The Indus-Yarlung suture zone in southeastern Tibet (Fig. 31) is the boundary between Mesozoic-Paleogene Transhimalayan batholiths in the Lhasa terrane to the north, and Indian plate rocks to the south (Le Fort, 1975). Along the southern Himalayan edge, the Sub-Himalaya is a southward-propagating foreland fold-and-thrust belt bounded by the Main Boundary Thrust and the Main Frontal Thrust (Hirschmiller et al., 2014).

The Yarlung River flows eastward along the suture zone, before crossing the Himalayan range at the eastern syntaxis as the Siang River (Fig. 31). Downstream, the Siang reaches the foreland basin and becomes the Brahmaputra River. The Yarlung-Brahmaputra connection exists since the Early Miocene (e.g. Bracciali et al., 2015 and references therein). The Brahmaputra currently flows north

and west of the Shillong to the Bay of Bengal. Before the rise of the plateau, it took a more direct SSW course to its mouth (Uddin and Lundberg, 1999).

The Shillong Plateau is located within the region affected by flexure of the Indian Plate beneath the Himalaya (Hammer et al., 2013). The Shillong and adjacent Mikir hills are mainly formed of Proterozoic-Paleozoic basement rocks overlain by outliers of Cenozoic sedimentary rocks (Mitra and Mitra, 2001). The plateau is bounded by two steep, active, crustal-scale reverse faults (Mitra et al., 2005): the northern WNW-ESE trending Oldham Fault and the southern E-W trending Dauki Fault. The latter juxtaposes Precambrian basement against the Cenozoic sediments of the Surma Basin to the south, with a vertical offset of ~10 km (Biswas et al., 2007). The Shillong Plateau has been uplifted either as a pop-up structure (Bilham and England, 2001), along the Dauki Fault as a north dipping thrust (Seeber and Armbruster, 1981), as a fault-propagation fold (Clark and Bilham, 2008), or as an asymmetric basement-cored uplift (Biswas et al., 2007) implying lithospheric bending in the forebulge (e.g. Hilley et al., 2005).

3. PROVENANCE ANALYSIS

Here we report detrital zircon U-Pb data from the Dungsam Chu section of the Siwaliks located directly north of the Shillong Plateau (Figs. 31 and 32). Unlike other Siwalik sections in the eastern Himalaya (e.g. the Kameng section of Chirouze et al., 2013), encroachment of the Brahmaputra in this region could only have occurred through northward deflection of its course due to the uplift of the plateau.

Transhimalayan zircons are typically of Cretaceous-Paleogene age and constitute a distinct component of the detritus in the Brahmaputra River (e.g. Gehrels et al., 2011). In contrast, zircons derived from Himalayan drainages are dominated by Proterozoic, Cambro-Ordovician and Miocene zircons from the Indian plate (e.g. Cina et al., 2009; Gehrels et al., 2011; Lang and Huntington, 2014) (Fig. 32). The presence of Transhimalayan detritus in Siwalik sediments east of the Dungsam Chu section indicates that a longitudinal river system, the Brahmaputra River, draining the southern Lhasa block and flowing through the Siang River, or further to the east, was established by 7 Ma (Chirouze et al., 2013; Cina et al., 2009; Govin et al., in review; Lang and Huntington, 2014) (Fig. 33).

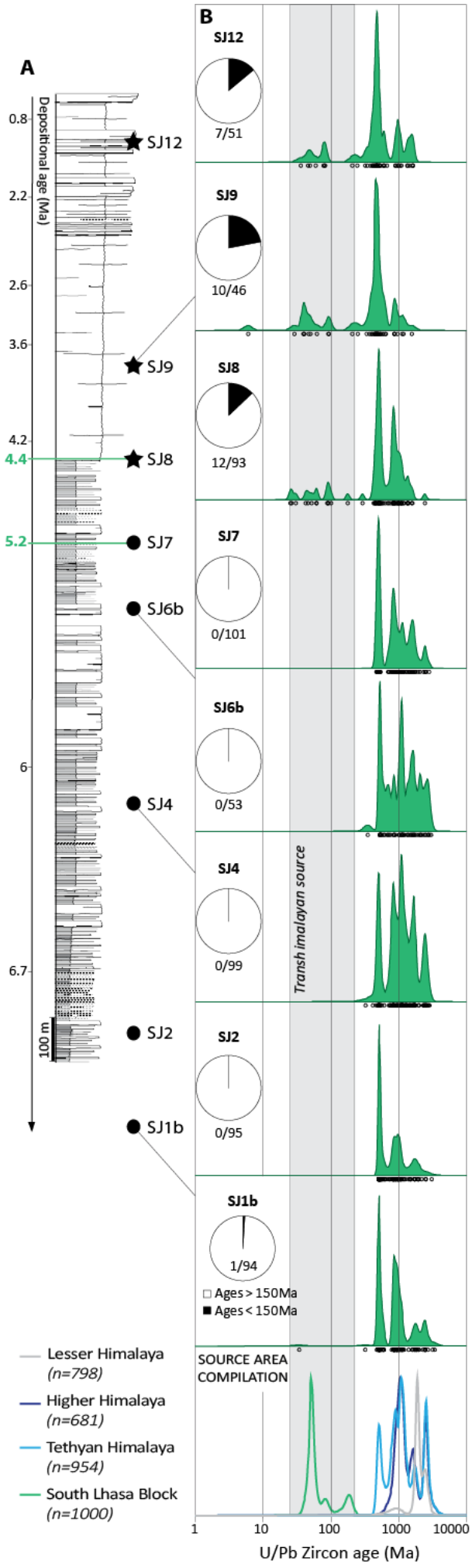
A
B
Depositional age (Ma)
0.8
2.2
2.6
3.6
4.2
4.4
5.2
6
6.7
100 m
SJ12
SJ9
SJ8
SJ7
SJ6b
SJ4
SJ2
SJ1b
7/51
10/46
12/93
0/101
0/53
0/99
0/95
1/94
Transh imalayan source
□ Ages > 150Ma
■ Ages < 150Ma
Lesser Himalaya (n=798)
Higher Himalaya (n=681)
Tethyan Himalaya (n=954)
South Lhasa Block (n=1000)
SOURCE AREA COMPILATION
1
10
100
1000
10000
U/Pb Zircon age (Ma)

Fig. 32: *(a) Sedimentary log of the Dungsam Chu section and depositional ages determined with magnetostratigraphy (Coutand et al., 2016), see Appendix IV; (b) detrital zircon U-Pb ages. Stars and dots represent samples with and without paleo-Brahmaputra signature, respectively. Data are plotted as kernel density plots (Vermeesch, 2012). Pie charts show the fraction of zircon U-Pb ages <150 Ma, x/xx = number of <150 Ma grain analyses remaining after data screening / total number of grain analyses. Ages from Dungsam Chu samples are compared to characteristic ages of zircons from different Himalayan source units from Hu et al. (2012) and references therein, presented in the source-area compilation. Ages characteristic of Transhimalayan sources are highlighted by the grey band.*

Zircons from eight sandstones from the Dungsam Chu section were dated using the CAMECA IMS 1270 ion-microprobe at CRPG (France) and the Nu Instruments AttoM single-collector inductively coupled plasma mass spectrometer (SC-ICP-MS) at NIGL (UK). Sample locations, methods and data are presented in Appendix II. The sampled sandstones were deposited between 7 and 1 Ma (Coutand et al., 2016). Samples SJ1b-SJ7 (≥4.4 Ma) contain only one zircon of Cretaceous-Paleogene age among 450 dated zircons (Fig. 32). We argue that this is negligible and could be due to minor sample contamination either in-situ or during sample preparation. In contrast, samples SJ8-SJ12 (≤5.2 Ma) show a minimum of 13% of Cretaceous-Paleogene grains, which we interpret as being derived from the Transhimalaya. The zircon U-Pb data therefore show a shift to Brahmaputra-type values between 5.2-4.4 Ma.

4. DISCUSSION

4.1. Brahmaputra paleo-drainage

Foreland basin sediments have previously been studied for provenance northeast and south of the Shillong Plateau. We combine these with our new results into an evolutionary model of Brahmaputra drainage (Fig. 33). Since Transhimalayan deposits are documented in the paleo-Brahmaputra catchment upstream of the Dungsam Chu area, as far north as the Siang location from the late Miocene, a hypothetical transverse Yarlung-Brahmaputra connection west of the Siang is unlikely (e.g. Cina et al., 2009; Lang and Huntington, 2014; Fig. 33). Furthermore, detrital rutile U-Pb ages characteristics of the syntaxis (<9 Ma, Bracciali et al., 2016) are found in sample SJ8 (see Appendix VII), implying that these deposits are sourced from the Siang River. Therefore, the arrival of Transhimalayan detritus at Dungsam Chu between 5.2-4.4 Ma reflects diversion of the paleo-Brahmaputra River to this location. Prior to this time, Dungsam Chu Siwalik sediments were deposited exclusively by transverse rivers draining the southern slopes of the Himalaya.

Prior to 7 Ma, the Brahmaputra flowed directly SSW to the Bengal Fan (Fig. 33a; Uddin and Lundberg, 1999). By 7 Ma, the paleo-Brahmaputra reached the paleo-location of the Kameng section (Chirouze et al., 2013; Fig. 33). Unlike Dungsam Chu, the Kameng site is not within the sphere of influence of the plateau uplift on the drainage pattern. Therefore, the presence of paleo-Brahmaputra deposits in the Kameng section at that time might be due to an earlier rise of the Mikir Hills, deflecting the river northward. Although the timing of uplift of the Mikir Hills is unknown, their location north-east of the Shillong suggests that they may have been uplifted before the plateau, if the uplift history is affected by proximity to the Himalaya (see below).

Between 5.2-4.4 Ma, the paleo-Brahmaputra reached Dungsam Chu due to the uplift of the Shillong Plateau deflecting the river north- and westward. Coeval paleo-Brahmaputra deposits, arguably not recycled from older units, are also found in the Surma Basin (Bracciali et al., 2015). This could be explained by an unequal distribution in time and space of displacements on the Oldham and Dauki Faults (Biswas et al., 2007), resulting in an irregular uplift pattern and frequent switching of the Brahmaputra to courses east and west of the rising plateau.

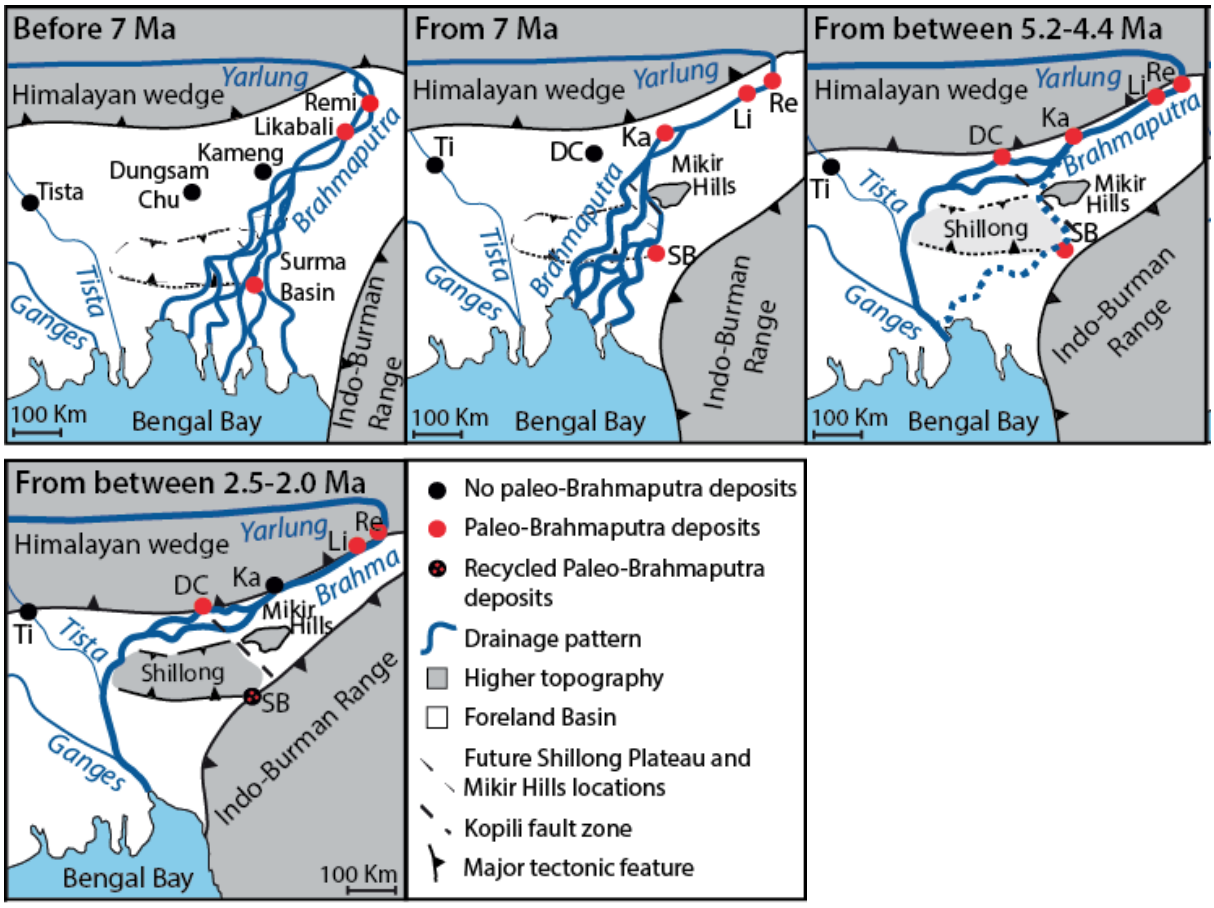

Fig. 33: *Late-Miocene to present evolutionary model of the Brahmaputra drainage system (modified from Chirouze et al., 2013), constructed using provenance studies from various sedimentary sections: Dungsam Chu (this study); Likabali (Lang and Huntington, 2014); Remi (Govin et al., in review); Tista (Cina et al., 2009); Kameng (Chirouze et al., 2013) and Surma Basin (Bracciali et al., 2015).*

After 2.5-2.0 Ma, the paleo-Brahmaputra course east of the plateau closed due to the combination of westward propagation of the Indo-Burman Ranges and the plateau rise (Najman et al., 2016). Since then, the river has flowed exclusively to the north and west of the plateau.

4.2. Causes of the transition from rock uplift to surface uplift

Decoupling between exhumation and surface uplift has been proposed to result from differences in erodibility between basement rocks of the plateau and the overlying Cenozoic sedimentary cover (Biswas et al., 2007). At present, basement rocks are the dominant source of sediment south of the plateau (Najman et al., 2012). However, Himalayan-derived Cenozoic sedimentary cover rocks previously overlying the plateau were the primary material eroded and deposited in the bounding basin until as recently as 1.5 Ma; the difference in sediment source being clearly recorded by contrasting white-mica ^{39}Ar-^{40}Ar and zircon fission-track ages of the basement and cover rocks (Bracciali et al., 2016). Thus, there appears to be a 3-4 Myr hiatus between the surface uplift (5.2-4.4 Ma) and the time of transition from predominantly cover to basement erosion (after 1.5 Ma). This suggests that the transition from sediment to basement erosion is not the dominant factor responsible for the change from exhumation to surface uplift of the Shillong Plateau.

A possible tectonic driver for that change could involve an increase in slip rates of the faults bounding the plateau, such that surface denudation could no longer keep pace with rock uplift, causing topography growth. Because the Shillong lies in the foreland basin of the southward advancing Himalaya, the stresses acting on the faults bounding the plateau would have changed through time. Copley et al. (2011) calculated the stress state in the Indian plate, considering the far-field plate driving forces, the buoyancy force exerted on India by the Tibetan Plateau, and the stresses induced by bending of the Indian lithosphere beneath the Himalaya, using a model in which Indian crust is broken by faults within the foreland. The methodology is therefore distinct from purely elastic flexural models, and the important input into the model is the seismogenic thickness (Mitra et al., 2005), not the elastic thickness calculated assuming an unbroken elastic plate (Craig and Copley, 2014) (see Appendix II). The calculations of Copley et al. (2011) show that the maximum differential stress on the faults, and in the upper part of the underlying ductile mantle, increases by a

factor of ~1.5 as the Indian lithosphere bends beneath the Himalaya over a wavelength of hundreds of kilometres.

Fault-slip rates are thought to be non-linearly related to the stress state at the base of the seismogenic layer, either through non-linearity in the rate-state friction equations that describe the loading of faults by aseismic creep on their down-dip extensions (Marone, 1998), or by stress accumulation due to pervasive dislocation creep immediately beneath the seismogenic layer (Zoback and Townend, 2001). Regardless of which of these mechanisms is responsible for fault loading, the non-linear relationship between applied stress and fault-loading rate for both mechanisms means that an increase in differential stress near the brittle-ductile transition by a factor of ~1.5 could result in a slip-rate increase by a factor of 2, and possibly higher (see Appendix II). Such an increase in slip rate is a plausible cause for the transition from only exhumation to exhumation and surface uplift in the Shillong region. The apparent ~3-fold increase in slip rate on the faults bounding the Shillong Plateau since the Miocene, inferred from comparing GPS and geological estimates (Biswas et al., 2007; Clark and Bilham, 2008), is consistent with our suggestions.

The timescale for such a change depends upon how long it takes the plateau to be transported through the region affected by bending stresses as India underthrusts the Himalaya. The width of the negative gravity anomaly associated with the foreland basin further west indicates the width of the region subject to significant bending stresses (see Appendix II). The complex geometry of faults and basins makes this distance difficult to pinpoint in the Shillong region itself. However, we assume that the bending stresses occur over a similar distance from the Himalayan front in the region of the Shillong Plateau as further west. The depth distribution of earthquakes is the same in these two regions (Craig et al., 2012), suggesting that the material properties of the Indian lithosphere change minimally along-strike and that this assumption is justified. This logic implies that the Shillong has been transported ~150 km into the region affected by stresses relating to the bending of the Indian lithosphere beneath southern Tibet. At a convergence rate of ~15 mm/yr between Shillong and southern Tibet (Vernant et al., 2014), it would take ~10 Myr for the region that is now the Shillong Plateau to have been transported this distance into the foreland basin, and be increasingly affected by the bending stresses. Such a timescale is consistent with the lag-time between the onset of exhumation (9-15 Ma) and surface uplift (~5.2-4.4 Ma) of the Shillong region.

5. CONCLUSIONS

We date the initiation of topographic growth of the Shillong Plateau and ensuing modification of the paleo-drainage of the Brahmaputra River between 5.2-4.4 Ma. Rock uplift in the plateau was balanced by surface erosion between 9-15 Ma and 5.2-4.4 Ma, such that no topography was created, a situation potentially enhanced by the high erodibility of the Cenozoic sedimentary cover of the plateau (Biswas et al., 2007). We link plateau-surface uplift to accelerated displacement along the Dauki Fault caused by bending stresses resulting from the northward underthrusting of the Indian plate beneath Tibet.

ACKNOWLEDGEMENTS

We acknowledge financial support from Marie Curie Initial Training Network iTECC funded by the EU REA under the FP7 implementation of the Marie Curie Action, under grant agreement 316966. DG thanks the Herbette Foundation for financial support during the writing of the manuscript at the University of Lausanne.

SUPPLEMENTARY MATERIAL

The supplementary material of this chapter is presented in Appendix II as listed here.

Analytical and numerical methods:

- Zircon U-Pb dating
- Stress calculation

Data tables:

- Table S1: Sample location
- Table S2: Zircon U-Pb data from source-areas compilation
- Table S3A: Zircon U-Pb Ion Probe data
- Table S3B: Zircon standard U-Pb Ion Probe
- Table S4A: Zircon U-Pb laser ablation data
- Table S4B: Zircon standard U-Pb laser ablation

CHAPTER 3

Paleo-drainage evolution and rapid exhumation of the Namche Barwa Syntaxis recorded in the Siwaliks of the easternmost Himalaya (Arunachal Pradesh, India)

Gwladys Govin [1], Yani Najman [1], Guillaume Dupont-Nivet [2, 3, 4] Ian Millar [5], Peter van der Beek [6], Pascale Huyghe [6], Paul O'Sullivan [7], Chris Mark [8] and Natalie Vögeli [6]

1- Lancaster Environment Centre, Lancaster University, UK

2- Géosciences Rennes UMR-6118, CNRS - Université de Rennes 1, France

3-Department of Earth and Environmental Sciences, Potsdam University, Germany

4- Key Laboratory of Orogenic Belts and Crustal Evolution, Ministry of Education, Beijing, China

5- Geochronology and Tracers Facility, NIGL, British Geological Survey, Keyworth, UK

6- ISTerre, Université Grenoble Alpes, Grenoble, France

7- GeoSep Services, Moscow, Idaho 83843, USA

8-Department of Geology, Trinity College Dublin, Dublin, Ireland

Manuscript submitted to American Journal of Science in April 2017

ABSTRACT

The Siwalik sedimentary rocks of the Himalayan foreland basin preserve a record of Himalayan orogenesis, paleo-drainage evolution, and erosion. This study focuses on the still poorly studied easternmost Himalaya Siwalik record located directly downstream of the Namche Barwa syntaxis. We use luminescence, magnetostratigraphy, and apatite fission-track dating to constrain the depositional ages of three Siwalik sequences: the Sibo outcrop (Upper Siwaliks at ~190 ka), the Remi section (Middle and Upper Siwaliks at ~0.8-6.5 Ma), and the Siang section (Middle Siwaliks at ~7-11 Ma). Cretaceous-Paleogene detrital zircon and apatite U-Pb ages, characteristic of the Transhimalayan Gangdese Batholiths that crop out north-west of the syntaxis, are present throughout the Sibo-Remi-Siang succession. They indicate a continuous Transhimalayan provenance and confirm the existence of a Yarlung-Brahmaputra connection since at least the Late Miocene. Early Cretaceous zircon and apatite U-Pb ages are rare in the Sibo-Remi-Siang succession, but abundant in modern Siang River sediments. These ages are characteristic of the Transhimalayan Bomi-Chayu batholiths, which crop out east of the syntaxis and are eroded by the Parlung River, a

modern tributary of the Siang River. The difference in relative abundance of Early Cretaceous U-Pb ages between the modern and ancient sediments indicates capture of the Parlung by the Siang within the last ~190 kyr. Additionally, apatite and zircon U-Pb dating suggest input from the young metamorphic syntaxis in the Sibo-Remi-Siang section since at least ~6 Ma, and therefore the onset of rapid exhumation of the syntaxis by that time. Approximately concomitant increase in zircons aged 500 Ma may reflect greater exhumation of the Tethyan Himalayan associated with syntaxial evolution, or change in the palaeo-drainage routing from Yarlung-Lohit-Brahmaputra to Yarlung-Siang-Brahmaputra.

1. INTRODUCTION

The study of Himalayan foreland basin sediments provides important complementary information to bedrock analysis for the understanding of orogenesis. It is particularly valuable where bedrock regions are inaccessible, or where the early record of metamorphism and exhumation has been lost in the bedrock record due to overprinting by later metamorphism or removal by erosion. In the Himalaya, Neogene-Quaternary sedimentary rocks of the Siwalik Group form an apron along the southern flank of the range (Yin et al., 2006). The sedimentary record of material eroded from the orogen and preserved in the Siwalik Group record evidence of the tectonic (e.g. Coutand et al., 2016; DeCelles et al., 1998b; Lang et al., 2016; Szulc et al., 2006), erosional (e.g. Bernet et al., 2006; Chirouze et al., 2013; Harrison et al., 1993; van der Beek et al., 2006) and climatic (e.g. Quade et al., 1995a; Vögeli et al., in press) evolution of the hinterland.

The eastern and western Himalayan syntaxes are the loci of young (<10 Ma) high-grade metamorphism, melting and extreme rates of exhumation of up to 5-10 km/Myr (Booth et al., 2004; 2009; Lang et al., 2016; Seward and Burg, 2008; Zeitler et al., 2014). In comparison, peak metamorphism in the main arc of the range occurred in the Early Miocene, and lower exhumation rates of ~2 km/Myr are typical (e.g. Thiede and Ehlers, 2013 and references therein). Models proposed to explain the development of the Himalayan syntaxes (e.g. Bendick and Ehlers, 2014; Burg et al., 1997; Zeitler et al., 2001; 2014) predict different onset timing and rates of exhumation. However, the exhumation history of the syntaxes remains insufficiently constrained to test the models. We focus here on the eastern Namche Barwa syntaxis. A wealth of existing bedrock exhumation ages and readily accessible - yet until recently poorly explored - sedimentary records make this area ideally suited to investigate the controversy. Bedrock studies of the Namche Barwa syntaxis have been interpreted to imply extremely rapid exhumation since either 3-4 Ma (Seward and Burg, 2008) or 8-10 Ma (Zeitler et al., 2014). In contrast, detrital studies have inferred ages of 7

Ma to <3 Ma (Bracciali et al., 2016; Chirouze et al., 2013; Lang et al., 2016) for the onset of rapid exhumation in the eastern syntaxis.

Bendick and Ehlers (2014) modelled the 3-D thermomechanical evolution of plate collision with non-planar geometries, and explained the localized deformation and exhumation of the eastern syntaxis by the subduction geometry. Structural buckling due to contraction in the orogenic indenter corner has also been suggested as an explanation for the rapid exhumation of the Namche Barwa syntaxis (Burg et al., 1997). Alternatively, thermomechanical feedback has been suggested to explain the rapid exhumation, in which focused rapid incision of the Yarlung River after capture by the Siang-Brahmaputra led to rapid exhumation of the Namche Barwa massif, weakened the lower crust and set up tectonic inflow of material into what has been termed a "tectonic aneurism" (Koons et al., 2013; Zeitler et al., 2001). However, detrital studies have suggested that the timing of capture is early-middle Miocene (Bracciali et al., 2015; Lang and Huntington, 2014), while the onset of rapid incision may not have taken place until the early Quaternary (P. Wang and others, 2014), suggesting a major time difference between the two and casting doubt on a direct link. Despite this disconnect, a self-sustaining feedback between erosion, deformation and rock uplift could still be operating. Indeed, metamorphism, partial melting and focused deformation has been proposed to begin when the southeastern Tibetan Plateau was uplifted at ca.10 Ma (Zeitler et al., 2014) and likely remained active since due to feedback between these processes and erosion (Bracciali et al., 2016; Zeitler et al., 2014). In order to better document this hypothesis, it is necessary to investigate the poorly constrained Neogene-Quaternary drainage evolution and the associated timing of river capture and exhumation (e.g. Bracciali et al., 2016; King et al., 2016; Lang et al., 2016).

This study focuses on sedimentary sections located directly downstream of, and most proximal to, the eastern Himalayan syntaxis, which record the evolution of this anomalously exhuming region. We constrain the depositional age frame of the sedimentary record using infrared-stimulated luminescence (IRSL), magnetostratigraphy and apatite fission-track (AFT) analyses and assess the provenance of these deposits using U-Pb dating of apatite, and zircon cores and rims.

2. BACKGROUND

2.1. Main geologic features of the Himalaya

The collision between the Indian and Asian plates in early Eocene times (Dupont-Nivet et al., 2010; Najman et al., 2010; Yin and Harrison, 2000; Zhuang et al., 2015) and the associated crustal thickening and shortening has led to the formation of the Tibetan Plateau and the Himalayan belt

(Hodges, 2000; Yin and Harrison, 2000) (Fig. 34). North-dipping crustal faults extending throughout the entire E-W Himalayan arc separate the main Himalayan units (Le Fort, 1975; Yin and Harrison, 2000). Collision took place along the Indus-Yarlung suture zone (IYSZ), which juxtaposes the remnants of the pre-collision Indian passive margin sequence to the south and the Transhimalayan Asian batholiths and Neo-Tethyan ophiolites to the north (Hébert et al., 2012 and references therein). The Mesozoic-Paleogene Transhimalayan Andean-type batholiths adjacent to the Indus-Yarlung suture zone (Chu et al., 2006) provide evidence for an Andean-style margin prior to collision. The Transhimalayan rocks in the eastern Himalaya include the Cretaceous-Paleogene Gangdese and Bomi-Chayu batholiths (e.g. Chiu and others, 2009; J.G. Wang and others, 2014).

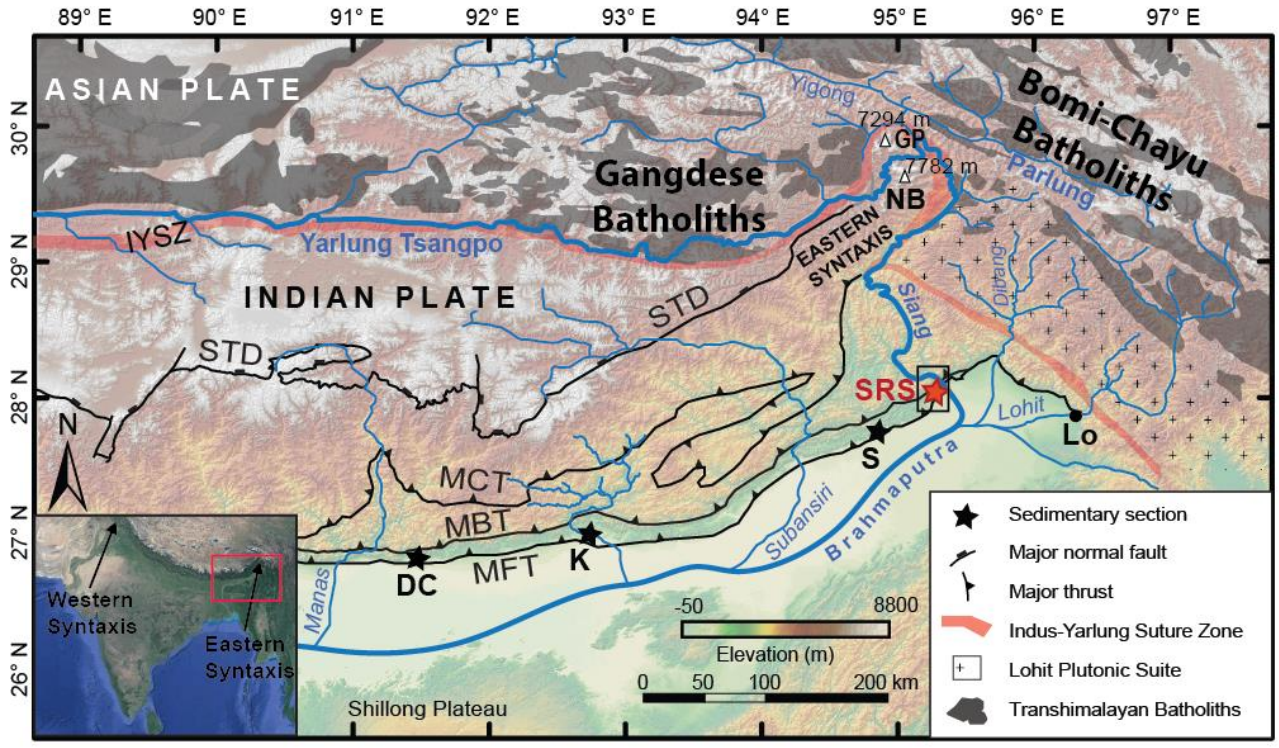

Fig. 34: *Digital elevation model and main geologic features of the eastern Himalaya (modified from Lang and Huntington, 2014; Govin and others, in review and references therein). The red star labelled SRS represents the Sibo-Remi-Siang section; the black stars show other dated Siwalik sections in the eastern Himalaya: S – Siji, K - Kameng and DC – Dungsam Chu. Lo indicates the Lohit modern riverbed sample from Cina et al. (2009). Black box indicates location of Fig. 35. Abbreviations are: NB - Namche Barwa, GP – Gyala Peri, MFT - Main Frontal Thrust, MCT - Main Central Thrust, MBT - Main Boundary Thrust, STD - South Tibetan Detachment and IYSZ - Indus-Yarlung Suture Zone.*

South of the Indus-Yarlung suture zone, the Tethyan Himalayan Series are composed of Upper-Proterozoic to Eocene sedimentary to low-grade meta-sedimentary rocks deposited on the northern Indian pre-collision passive margin. According to the map of Zeitler et al. (2014), the Tethyan Himalaya wraps around the eastern syntaxis, where it terminates, with no further outcrop further east. The medium- to high-grade metamorphic rocks (schists, gneisses, and migmatites) of the Greater Himalayan Series crop out south of the Tethyan Himalayan Series and are separated from them by the extensional South Tibetan Detachment. The Greater Himalayan Series are intruded by Miocene leucogranites and bounded by the Main Central Thrust in the south. South of the Main Central Thrust, the Lesser Himalayan Series are composed of low-grade Proterozoic meta-sediments along with late Paleozoic, Mesozoic and Paleogene sedimentary rocks. Both the Greater and Lesser Himalayan Series originate from the Indian plate. South of the Lesser Himalayan Series, the Sub-Himalayan sedimentary fold-and-thrust belt is bounded by the Main Boundary Thrust to the north and the Main Frontal Thrust to the south. The Sub-Himalayan Series contain the Neogene to Quaternary detrital sediments of the Siwalik Group. Undeformed Recent deposits of the Himalayan foreland basin occur south of the Main Frontal Thrust (Gansser, 1983; Hodges, 2000).

2.2. Structure of the eastern Himalaya

At the eastern termination of the Himalaya, the structural trend bends around the eastern syntaxis, changing from E-W to N-S striking. In the core of the syntaxis, the Namche Barwa and the Gyala Peri massifs reach elevations of >7 km (Fig. 34). This region is dominated by extreme relief and deep, steep gorges. The Tsangpo gorge, a <200-m wide, 200-km long fluvial knick-zone descending >2 km between the Namche Barwa and the Gyala Peri peaks, is one of the deepest on Earth (e.g. Lang et al., 2013; Zeitler et al., 2001). The syntaxis constitutes an antiformal structure, exposing high-grade metamorphic rocks of Indian origin (Burg et al., 1997). The north-plunging antiform characterizing the Namche Barwa massif has been suggested to have expanded both vertically and laterally through time, and is thought to have migrated northward since its initiation (Bracciali et al., 2016; King et al., 2016; Seward and Burg, 2008). Very young bedrock thermochronological ages within the syntaxis record late Neogene (<10 Ma) metamorphism and rapid syntaxial exhumation (e.g. Booth et al., 2009; Burg et al., 1998; Ding et al., 2001; Finnegan et al., 2008; Seward and Burg, 2008; Stewart et al., 2008; Zeitler et al., 2014). Due to these extreme erosion rates, the Namche Barwa may contribute up to 50-70% of the Brahmaputra sediments (Enkelmann et al., 2011; Garzanti et al., 2004; Lang et al., 2013; Singh and France-Lanord, 2002; Stewart et al., 2008).

2.3. Drainage of the eastern Himalaya

The Brahmaputra River is sourced at Mount Kailash in southern Tibet and flows more than 1000 km eastwards along the suture zone as the Yarlung Tsangpo. It crosses the range to the south and turns 180 degrees after incising a deep gorge between the Gyala Peri and the Namche Barwa massifs. At this turn the river connects with the tributary Parlung River to the north, which is itself connected to the Yigong River a few tens of kilometres upstream (Fig. 34). The Yigong River flows toward the southeast whereas the Parlung River upstream of its confluence with the Yigong River flows toward the NW and erodes the Bomi-Chayu batholiths ENE of the eastern syntaxis (Fig. 34). Downstream of the Namche Barwa massif, the Yarlung Tsangpo becomes the Siang River until it reaches the foreland basin in Arunachal Pradesh, where it becomes the Brahmaputra River. In the foreland, the tributary Lohit River, flowing SW and also draining the Bomi-Chayu batholith, connects with the Brahmaputra River along with other eastern tributaries such as the Dibang River, which erodes the Lohit plutonic suite (Fig. 34).

The evolution of the complex drainage pattern in the eastern Himalayan region remains incompletely understood. This river network is suggested to result from drainage reorganization as a consequence of river-capture and -reversal events (Clark et al., 2004; Clift et al., 2006). The Brahmaputra River probably captured the Yarlung Tsangpo in Early-Miocene times (Bracciali et al., 2015; Lang and Huntington, 2014; Robinson et al., 2014). The Sr–Nd–Os isotopic composition of sediments from the Bengal Fan supports the idea of drainage stability of the southeastern Tibetan Plateau and the captured Yarlung-Brahmaputra system feeding the Bengal Fan since the Mid-Miocene (Galy et al., 2010). It has been proposed that, prior to capture, the paleo-Yarlung-Tsangpo flowed further to the east into the Red and/or Irrawaddy rivers (Brookfield, 1998; Clark et al., 2004; Robinson et al., 2014), although this scenario has recently been questioned (Licht and others, 2013; J.G. Wang and others, 2014). The drainage evolution since Miocene times involves various hypotheses such as the Yarlung flowing through the Parlung River to the Irrawaddy River, prior to its capture by the Siang through headward erosion, leading to Parlung River reversal (Clark et al., 2004). Alternatively, recent studies have argued that the Parlung-Yarlung connection postdates the establishment of the Yarlung-Siang connection and occurred during the Quaternary (King et al., 2016; Lang and Huntington, 2014), possibly related to lateral propagation of the Namche Barwa massif (Seward and Burg, 2008). Lang and Huntington (2014) proposed that prior to this capture event, a paleo-Parlung-Lohit connection existed upstream of the Brahmaputra-Lohit confluence.

2.4. Provenance analyses in the eastern Himalaya

The Yarlung-Siang-Brahmaputra River drains the Transhimalayan Gangdese batholith in the southern Tibetan plateau. These Gangdese rocks have distinct compositional and age characteristics (as recorded by whole-rock Sr and Nd isotope ratios as well as Hf isotopes and U-Pb ages in zircons), different from rocks of the Indian plate Himalayan units south of the Indus-Yarlung Suture Zone. The Himalayan units are largely composed of Proterozoic-Eocene rocks variably metamorphosed during the Cenozoic, with Miocene leucogranites (DeCelles et al., 2004; Gehrels et al., 2011). The Tethyan Himalaya differs from the Greater Himalaya in its distinctive population of zircons aged 500 Ma. These ages from the Indian plate contrast with the typically Cretaceous-Early Paleogene zircons of the Gangdese batholiths (Chu et al., 2006; Mo et al., 2007). Early Cretaceous ages are poorly represented in the Transhimalayan Gangdese batholith zircon U-Pb signal, but are abundant in the Bomi-Chayu igneous sources east of the Namche Barwa syntaxis (Booth et al., 2004; Chiu et al., 2009; Haproff et al., 2013; Lang and Huntington, 2014; Liang et al., 2008; Xu et al., 2012; Zhang et al., 2012). Additionally, the Lohit Plutonic Suite (Fig. 34) has been suggested to be a source of Early- and Late-Cretaceous zircons (Cina et al., 2009; Haproff et al., 2013). This characterization of zircon U-Pb ages has allowed partial reconstruction of the paleo-drainage system in the eastern Himalayan region (e.g. Bracciali and others, 2015; Cina and others, 2009; Lang and Huntington, 2014). Whereas zircon U-Pb dating is widely used in the eastern Himalaya, no apatite U-Pb dating has yet been performed in this area. Therefore, apatite U-Pb age characterization of both the eastern syntaxis and the Transhimalayan batholith source remains unconstrained.

The Namche Barwa massif of the eastern syntaxis is characterized by very young (10 to <1 Ma) mineral growth and cooling ages (Booth et al., 2004; 2009; Bracciali et al., 2016; Burg et al., 1998; Ding et al., 2001; Finnegan et al., 2008; Zeitler et al., 2014). Geochronological and thermochronological ages distinctive of the syntaxis have been described by Bracciali et al. (2016); in particular zircon rim U-Pb ages <10 Ma constitute a clear syntaxial signature. These diagnostic ages for specific thermochronological and geochronological systems have been used in the eastern Himalayan foreland basin to track the eastern syntaxis detritus (Bracciali et al., 2016; Lang et al., 2016).

2.5. Sedimentary record of the eastern Himalaya

The Siwalik Group in the Himalayan foreland is divided into three distinct units based on sedimentary facies: the Lower, Middle and Upper Siwaliks (DeCelles et al., 1998b; Yin et al., 2006). Up-section coarsening in the Siwaliks of the eastern Himalaya is interpreted as the progressive transition from deposition by low-gradient sinuous channels in a fluvio-deltaic setting to deposition by steep braided rivers in alluvial fans along the Himalayan front, as the Main Frontal Thrust propagated southward (Chirouze et al., 2012; Coutand et al., 2016). The Lower Siwaliks are mainly composed of alternating fine-grained sandstones and siltstones with common leaf-impressions and paleosols, interpreted in this area as deposited in a fluvio-deltaic plain environment (Chirouze et al., 2012; Coutand et al., 2016). The Middle Siwaliks, interpreted as a braided fluvial facies, consist of massive medium- to coarse-grained sandstone layers, with frequent cross-bedding, soft sedimentary deformation and increasing occurrence of conglomerates up-section. The Upper Siwaliks are mainly composed of conglomerates interbedded with sandstones and some siltstones, interpreted as pebbly braided-river deposits (e.g. Chirouze et al., 2012; Cina et al., 2009; Coutand et al., 2016; Lang and Huntington, 2014).

Only three Siwalik sections have hitherto been dated by magnetostratigraphy in the eastern foreland basin (Fig. 34): the Dungsam Chu section in Bhutan (Coutand et al., 2016), the Kameng section in western Arunachal Pradesh (Chirouze et al., 2012), and the Siji section in eastern Arunachal Pradesh (Lang et al., 2016). In these sections, the oldest Lower Siwalik sedimentary rocks have been dated at ~13 Ma, with a Lower-Middle Siwalik transition estimated at ~10.5 Ma in the Kameng (Chirouze et al., 2012), and as young as 6 Ma in Dungsam Chu (Coutand et al., 2016).

3. THE SIBO-REMI-SIANG SUCCESSION

We have studied Siwalik sedimentary rocks at three different locations (Remi, Sibo and Siang) within a 20 km-long segment along the eastern Himalayan front (Fig. 35).

Middle and Upper Siwalik rocks are exposed at these locations, as defined by correlation with the typical Middle and Upper Siwalik lithologies throughout the basin described above. These are the most easterly dated sections of the Siwaliks, with the Siang section located where the modern Siang River reaches the foreland basin. The main sedimentary characteristics in these locations are similar to the Upper and Middle Siwalik sedimentary rocks of the eastern Himalaya described previously; more detailed sedimentological descriptions are presented in Table 6. Clast counts in each section have been performed in the field (Figs. 36, 37 and 38), to supplement isotopic provenance data. One

hundred pebbles per location were counted and determined with regard to their lithology. Clasts were randomly selected by counting the first hundred encountered in a sample bag for outcrops, and along an arbitrary line in the riverbed for modern river sediments.

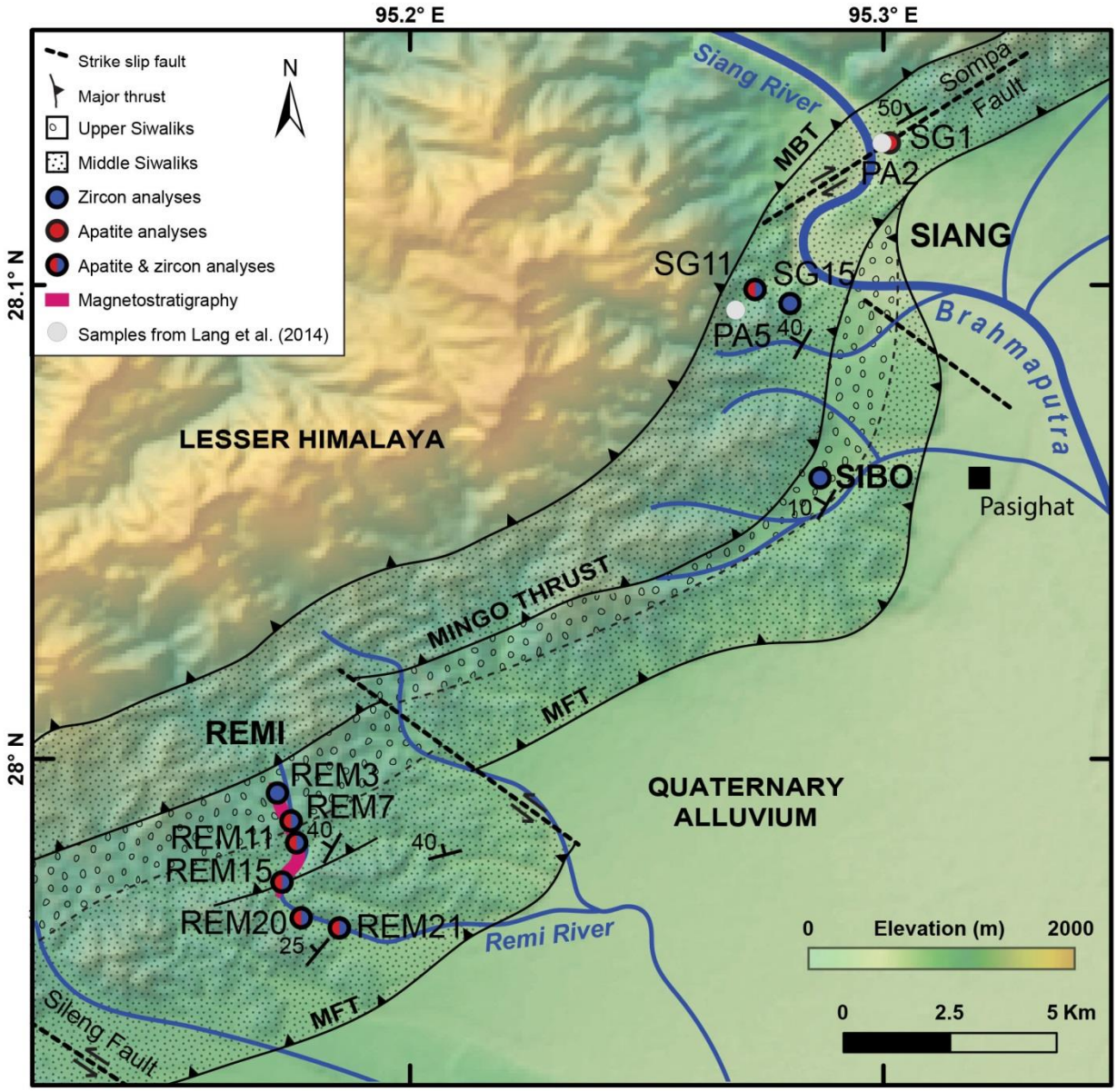

Fig. 35: *Digital elevation model and main geologic features of the study area (modified after Luirei and Bhakuni, 2008 and Srivastava and others, 2009). Samples are indicated according to the method applied (mineral analysed); samples in white are from Lang and Huntington (2014), samples in blue and red are from this study.*

***Table 6**: Sedimentological descriptions of Siwalik sedimentary rocks from the Sibo, Remi and Siang locations, eastern Arunachal Pradesh.*

LOCATION	UNIT	LITHOLOGY	SEDIMENTARY FEATURES	CLASTS
SIBO	Upper Siwaliks	Medium to coarse-grained sandstones, coarsening up-section, alternating with conglomerates, the proportion of which increases up-section	Very few lenses of clays	Sub-angular to well rounded; 10-170 mm long axis; 5-90 mm short axis
REMI	Upper Siwaliks	Interlayered medium-grained sandstones and conglomerates. Thickness of conglomerate bands increases up-section to reach several meters; matrix grain size also coarsens up-section	Occasional finer-grained layers from claystones to fine-grained sandstones; frequent coal fragments	Sub-angular to rounded; 5-95 mm short axis; 10-130 mm long axis
	Middle Siwaliks	Cliffs up to 20 m high of "salt and pepper" medium-grained to pebbly sandstones. Sandstone beds are up to tens of meters thick. Coarsening up-section with an increasing occurrence of pebbly material	Occasional pebbly layers at the base of sandstone beds; intercalated silt or mud lenses. Common large-scale cross-bedding, fossil wood and coal fragments; medium-grained sandstones occasionally bioturbated	Angular to rounded; 5-65 mm short axis; 5-100 mm long axis
SIANG	Middle Siwaliks **East bank**	Cliffs up to 20 m high of medium to coarse-grained "salt and pepper" and orange-weathered coloured sandstone. Mica rich sandstones overlained by Quaternary conglomeratic terraces. Occurrence of pebbles, the proportion of which increases up-section	Common carbonised fossil wood of millimetre- to meter size (up to 3.80 m); frequent cross bedding and centimetre-scale diagenetic nodules; occasional roots and bioturbation, ripple marks and channels; common wood clasts	Centimetre-scale siltstone pebbles (2-30 cm long axis); millimetre- to centimetre-scale quartz-arenite pebbles at the base of the sand beds; presence of a meter thick quarzitic conglomerate bed (clast sizes of 5-10 cm).
	Middle Siwaliks **West bank**	Greenish to light grey salt and pepper fine to coarse-grained sandstone; containing muscovite, biotite, garnet, amphiboles, hornblende and perhaps chlorite and/or epidote	Less indurated, compared with the east bank, indistinct bedding, finer-grained and more weathered	Presence of coal

3.1. Sibo outcrop

The Sibo outcrop exposes ~20 stratigraphic meters of Upper Siwalik sedimentary rocks tilted 10° towards the NW (Fig. 36). A large-scale channel fill is clearly observed in the upper part of the outcrop. In the lowermost part of the outcrop, the sandstones contain a significant amount of muscovite; in contrast, no muscovite has been observed in the sandy matrix of the nearby conglomerates. The dominant clast material in the Sibo section is quartz-arenite as illustrated in the clast count results (Fig. 36). The modern Sibo riverbed comprises numerous quartz-arenite pebbles with subordinate basalt and sandstone clasts.

Fig. 36: *Photograph of the Sibo Upper Siwalik outcrop. The main paleo-channel is highlighted by the dashed line, the SIBO sample is represented with a black square. The pie chart shows the clast-count results of the conglomerate (location is indicated by the black dot).*

3.2. Remi section

The Remi section is composed of ~700 m of Upper Siwaliks and 1200 m of Middle Siwaliks, homoclinally tilted ~40° towards the NW (Fig. 37). The section is bounded to the north by the north-dipping Mingo Thrust and to the south by the Main Frontal Thrust (Fig. 35).

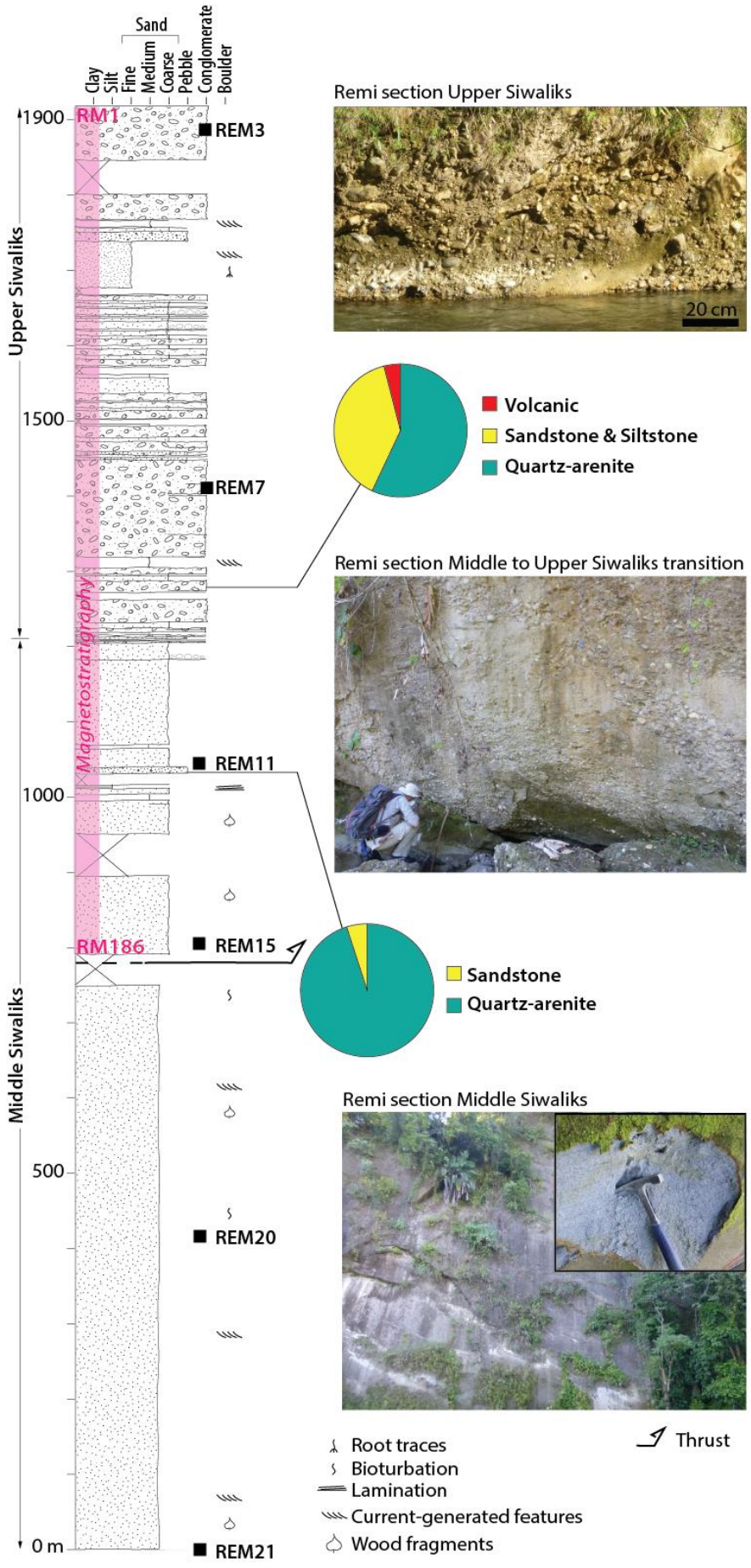
Clay
Silt
Sand
Fine
Medium
Coarse
Pebble
Conglomerate
Boulder
1900
1500
1000
500
0 m
Upper Siwaliks
Middle Siwaliks
Magnetostratigraphy
RM1
RM186
REM3
REM7
REM11
REM15
REM20
REM21
Remi section Upper Siwaliks
20 cm
Volcanic
Sandstone & Siltstone
Quartz-arenite
Remi section Middle to Upper Siwaliks transition
Sandstone
Quartz-arenite
Remi section Middle Siwaliks
Thrust
Root traces
Bioturbation
Lamination
Current-generated features
Wood fragments

Fig. 37: *Stratigraphic profile of the Remi section and photographs of Upper Siwalik, Middle to Upper Siwalik transition and Middle Siwalik outcrops. Current-generated features include tabular cross-bedding, trough cross-bedding, and flat bedding. Results of clast counts are shown in pie charts. The part of the section sampled for magnetostratigraphy is highlighted in pink, the upper- and lowermost magnetostratigraphic samples are indicated. Geochronological samples are shown with black squares.*

A minor north-dipping thrust in the upper part of the Middle Siwaliks has also been observed (below and south of sample REM15 in Figs. 35 and 37, respectively). The Siwalik rocks in the Remi section coarsen up-section, from medium sandstones to conglomerates. The sandstones are often weathered and poorly indurated. Apart from cross-bedding, features indicating paleo-current directions are rare. It was not possible to precisely measure paleo-current directions in the section. The clasts from the Remi section are mainly composed of quartz-arenite and sandstone (Fig. 37), whereas the modern Remi riverbed material is mainly composed of gneiss and quartz-arenite pebbles.

3.3. Siang section

The Siang section is crossed by the Siang River, and is therefore composed of two separate outcrops located on the east and west banks of the river, respectively (Figs. 35 and 38). On both banks, Middle Siwalik sandstones crop out, dipping 35 to 55° to the NW, in tectonic contact with the Lesser Himalayan Series to the north along the Main Boundary Thrust. The west-bank outcrop appears more weathered and finer-grained than the east-bank outcrop. Additionally, the bedding orientation with respect to the location of both outcrops leads us to suggest an older age for the west-bank outcrop in comparison with the east-bank outcrop. The modern Siang riverbed is mainly composed of quartz-arenite, volcanic, metasedimentary, carbonate and plutonic pebbles, with subordinate gneisses, meta-breccias and sandstones (Fig. 38).

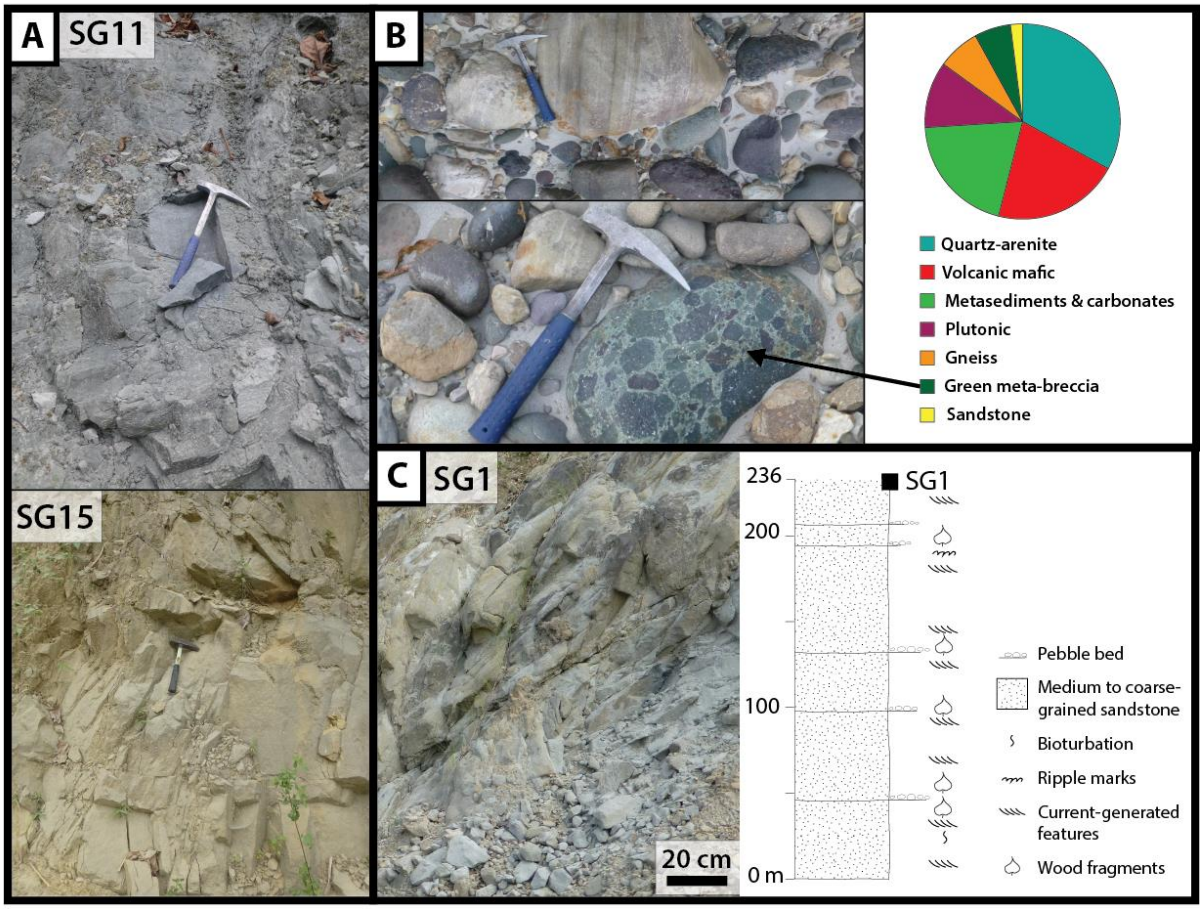

Fig. 38: *(a) Photograph of Middle Siwalik outcrop from the west bank of the Siang section at the locations of samples SG11 and SG15. (b) Photographs of the modern Siang River bed; pie chart shows results of the clast count at this location. The bottom photograph shows a green meta-breccia clast. (c) Stratigraphic log of the east-bank Siang section and photograph of the SG1 sample location.*

4. METHODS

4.1. Depositional dating

In order to date the deposition of the sedimentary rocks from the compiled Sibo-Remi-Siang succession, we used luminescence dating for the Sibo outcrop, apatite fission-track dating to determine maximum depositional ages for the Remi and Siang sections, and magnetostratigraphy to date the upper part of the Remi section.

4.1.1. Luminescence dating

The Upper Siwalik conglomerates at Sibo are only slightly tilted (10° to the NW), suggesting a young depositional age. Two core samples have been analysed using the magnetostratigraphic method described below. They showed normal directions, implying a Middle Pleistocene or younger age, as the Earth's magnetic-field polarity is normal since 0.8 Ma. Luminescence dating was carried out at

the Luminescence Laboratory of the University of Bern (Switzerland) to refine the age of these sedimentary rocks. Sampling was performed using a paleomagnetic drill to extract the SIB core sample (2.5 cm in diameter), taking care to avoid exposure to light. This sample was prepared and analysed along with samples from Abrahami et al. (in review), with the same methodology and in the same conditions (see Appendix III). Since preliminary Optically Stimulated Luminescence (OSL) analysis of quartz led to dim signals that rendered further measurements impractical, we applied Infrared-Stimulated Luminescence (IRSL) of feldspar instead, using the $IRSL_{50}$ protocol (e.g. Lowick et al., 2012). Dose recovery tests were performed to confirm the efficiency of the protocol and the dose-rate response calculation was used to determine the equivalent dose (D_e). Central-age and minimum-age models (Galbraith et al., 1999) were applied to determine the age and the dispersion of the D_e distribution, and to identify the population of D_e values representing well-bleached grains prior to burial. Fading tests were conducted on six aliquots in order to correct the burial age and avoid age underestimation.

4.1.2. Apatite fission-track dating

Apatite fission-track (AFT) analysis has been carried out to constrain the maximum depositional ages for sedimentary rocks from the Remi and Siang sections. Six medium- to coarse-grained sandstones from the Remi section and two from the Siang section were sampled at regular stratigraphic intervals (Fig. 35). The youngest sample from the Remi section (REM3) did not contain sufficient apatite to allow robust dating. Apatite separation was performed at ISTerre, Université Grenoble Alpes (France) using standard techniques; fission-track analysis was performed by GeoSep Services (USA) using the LA–ICP–MS method (Donelick et al., 2005). Full details of sample preparation and analytical procedures are provided together with data tables in Appendix III.

The youngest age peak for each sample was identified using the minimum age-peak method implemented in the Density Plotter software (Vermeesch, 2012). Minimum age peaks were generated using the dataset of ages between 0 and 20 Ma, in order to reduce the error on the minimum age peak. We use the resulting minimum ages obtained with this method to constrain the maximum depositional age for each sample. As the AFT system is partially annealed at temperature between ~60-120°C (Gallagher and others, 1998; Reiners and Brandon, 2006), it is possible that the more deeply buried samples do not retain their pre-depositional age signal. We assess the possibility of post-depositional AFT annealing in our samples using the observed age-depth pattern (van der Beek et al., 2006; see section 6.1).

4.1.3. Magnetostratigraphy

Only the upper part of the Remi section has sufficient continuous exposure to allow meaningful magnetostratigraphic sampling and analysis. A total of 186 paleomagnetic sites were sampled at stratigraphic intervals of 5-6 meters on average, with some larger gaps due to the lack of outcrop or unsuitable lithologies (weathered gravelly sandstone). Remanent magnetizations of samples were analysed on a 2G Enterprises DC SQUID cryogenic magnetometer inside a magnetically shielded room, at the Geosciences Rennes paleomagnetic laboratory (France). Details of the sampling strategy and analysis are provided in Appendix III.

4.2. Provenance analysis

4.2.1. Zircon U-Pb geochronology

U-Pb dating was carried out on detrital zircon cores from Sibo, Remi and Siang samples, in order to decipher the provenance of the deposits from these sections. In addition, U-Pb dating of thin zircon rims from Remi samples was also performed to compare with the analyses of Bracciali et al. (2015), who found zircon rim ages <10 Ma, interpreted as young metamorphic overgrowths characteristic of the syntaxis, in paleo-Brahmaputra deposits south of the Shillong Plateau.

Nine medium- to coarse-grained samples were selected at regular stratigraphic intervals throughout the compiled section. One sample is from the Sibo outcrop, six are from the Remi section and two from the Siang section (Fig. 35). Remi samples have been analysed for both zircon rims and cores, detected using cathodoluminescence imaging prior to analysis. For the Siang samples, we compare our data with that of Lang and Huntington (2014), who previously dated zircons from the Siang section using the U-Pb method (Fig. 35). Zircon grains were separated and imaged at Lancaster University and at the NERC Isotope Geosciences Laboratory (NIGL, UK), as detailed in Appendix III. Zircon U-Pb dating was performed at NIGL (UK) using a Nu Instruments AttoM single-collector inductively coupled plasma mass spectrometer (SC-ICP-MS).

Several rim-dating methods were tried, using different laser-spot diameters, to increase the chances of measuring the <20-µm rims in the most robust way. Because a thin laser spot leads to increased fractionation of U and Pb, it can be challenging to obtain clear and precise ages for such small surfaces. We tried raster and single-spot techniques on normal grain mounts and on the external surfaces of grains with thin rims that had been extracted from the mounts. We carried out several measurements of the same rim when preliminary ages were young. The young (<100 Ma) grains are commonly discordant due to their low U content and relatively high common Pb. For this reason,

and because of the fractionation bias related to the small laser-spot diameter, we use a different screening procedure for rims and cores, being less selective for the rim than for the core ages. We also regressed data points for the likely youngest rims measured through a fixed common Pb composition. The analytical data and details of standard calibration and isotopic corrections are presented in Appendix III.

4.2.2. Apatite U-Pb geochronology

The use of the LA-ICP-MS technique for AFT analyses has the advantage that it permits apatite U-Pb ages to be determined on the same grains in the same analytical session (see Appendix III for detailed description of the analytical procedure, age correction, and data processing). Apatite U-Pb age treatment followed the approach of Chew et al. (2011), using an iterative approach to obtain a $^{207}Pb/^{206}Pb$ intercept value based on a starting estimate generated from the terrestrial Pb evolution model of Stacey and Kramers (1975). This was used to calculate a ^{207}Pb-corrected $^{238}U/^{206}Pb$ age. Since the ^{207}Pb-based correction assumes U-Pb* (radiogenic Pb) concordance, which may not be the case for detrital grains, knowledge of likely source area ages is required to discriminate partially reset ages in the same manner as for detrital AFT analysis. As none of the apatite U-Pb ages were concordant, data screening was performed with a similar approach to that described by Zattin et al. (2012) and Mark et al. (2016). Apatite U-Pb results are discussed in the U-Pb geochronology section where they are compared with zircon U-Pb data.

5. RESULTS

5.1 Luminescence dating

IRSL results are presented in Table 7. The dose-response curve shows a saturation plateau reached at ~1.2 kGy (Fig. 39a) and all D_e values range between 300 and 800 Gy (Fig. 39b). This resulted in a mean burial dose of 430±21 Gy, and an uncorrected age of 115±11 ka. The D_e distribution shows measurements for the 28 aliquots describing 25% over-dispersion, similar to the samples from Abrahami et al. (in review), suggesting partial bleaching is not a problem in these samples. Fading tests were relatively uniform and result in a mean g-value used for D_e correction of 4.73±0.83 % per decade. As the signal is too high on the dose-response curve to make a reliable correction for fading, the resulting corrected age of 190±18 ka must be regarded as a minimum age.

***Table 7**: Infrared Stimulated Luminescence results. Abbreviations are: $n_{tot:}$ number total of aliquots analysed; n: number of aliquots showing good signal; OD: over-dispersion of De; g-value: measured fading rate; De: estimated Dose. Age is the minimum age without fading correction and Age c. is the minimum age corrected for fading.*

Sample	Depth (m)	Grain size (µm)	Radionuclide concentration (ppm)			Dose rate (Gy ka^{-1})	n_{tot} n	OD (%)	g-value %/decade	D_e (Gy)	Age (ka)	Age c. (ka)
			K (%)	Th	U							
SIB	0.2	150-200	1.9±0.1	11.0±0.6	2.4 ±0.1	1.8±0.1	28 27	25	4.7±0.8	430.7±21.0	115.9±11.0	**190.2±18.2**

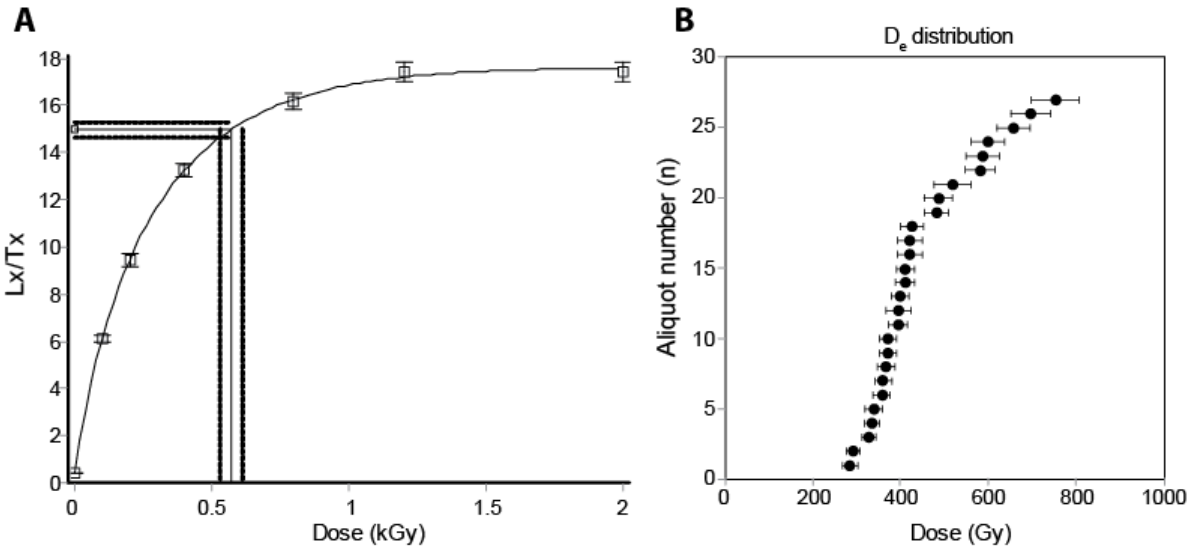

***Fig. 39:** Infrared Stimulated Luminescence dating (IRSL) analysis. (a) Dose-response curve. (b) D_e values of SIB aliquots.*

5.2. Apatite fission-track dating

Single-grain apatite fission-track ages range between ~2 and 500 Ma. The minimum age populations generated from our results are generally and within error younging from the stratigraphically lowest sample in the Siang section (SG15), with a minimum age population of 10.3±1.4 Ma, to the uppermost sample in the Remi section (REM7), with a minimum age population of 4.4±1.1 Ma (Fig. 40).

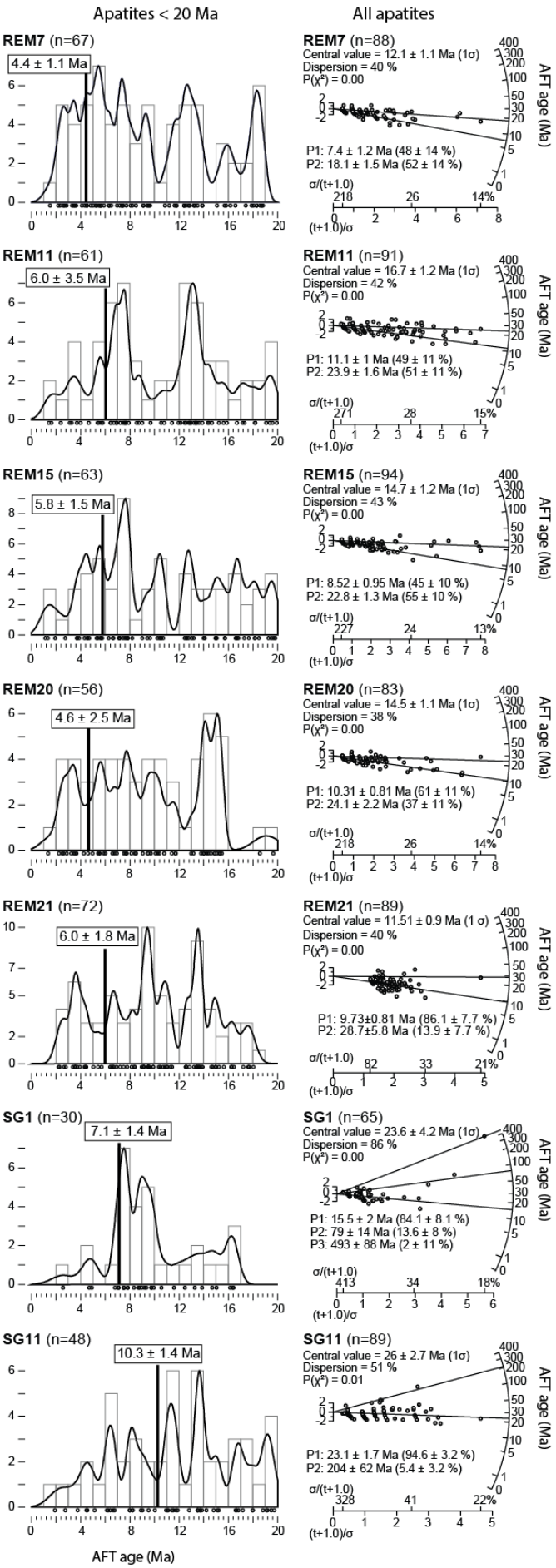
Apatites < 20 Ma
All apatites
REM7 (n=67)
4.4 ± 1.1 Ma
REM7 (n=88)
Central value = 12.1 ± 1.1 Ma (1σ)
Dispersion = 40 %
P(χ²) = 0.00
P1: 7.4 ± 1.2 Ma (48 ± 14 %)
P2: 18.1 ± 1.5 Ma (52 ± 14 %)
REM11 (n=61)
6.0 ± 3.5 Ma
REM11 (n=91)
Central value = 16.7 ± 1.2 Ma (1σ)
Dispersion = 42 %
P(χ²) = 0.00
P1: 11.1 ± 1 Ma (49 ± 11 %)
P2: 23.9 ± 1.6 Ma (51 ± 11 %)
REM15 (n=63)
5.8 ± 1.5 Ma
REM15 (n=94)
Central value = 14.7 ± 1.2 Ma (1σ)
Dispersion = 43 %
P(χ²) = 0.00
P1: 8.52 ± 0.95 Ma (45 ± 10 %)
P2: 22.8 ± 1.3 Ma (55 ± 10 %)
REM20 (n=56)
4.6 ± 2.5 Ma
REM20 (n=83)
Central value = 14.5 ± 1.1 Ma (1σ)
Dispersion = 38 %
P(χ²) = 0.00
P1: 10.31 ± 0.81 Ma (61 ± 11 %)
P2: 24.1 ± 2.2 Ma (37 ± 11 %)
REM21 (n=72)
6.0 ± 1.8 Ma
REM21 (n=89)
Central value = 11.51 ± 0.9 Ma (1 σ)
Dispersion = 40 %
P(χ²) = 0.00
P1: 9.73±0.81 Ma (86.1 ± 7.7 %)
P2: 28.7±5.8 Ma (13.9 ± 7.7 %)
SG1 (n=30)
7.1 ± 1.4 Ma
SG1 (n=65)
Central value = 23.6 ± 4.2 Ma (1σ)
Dispersion = 86 %
P(χ²) = 0.00
P1: 15.5 ± 2 Ma (84.1 ± 8.1 %)
P2: 79 ± 14 Ma (13.6 ± 8 %)
P3: 493 ± 88 Ma (2 ± 11 %)
SG11 (n=48)
10.3 ± 1.4 Ma
SG11 (n=89)
Central value = 26 ± 2.7 Ma (1σ)
Dispersion = 51 %
P(χ²) = 0.01
P1: 23.1 ± 1.7 Ma (94.6 ± 3.2 %)
P2: 204 ± 62 Ma (5.4 ± 3.2 %)
AFT age (Ma)
σ/(t+1.0)
(t+1.0)/σ

Fig. 40: *Apatite fission-track data for samples from the Remi and Siang sections. The left column shows ages <20 Ma for each sample, plotted as adaptive Kernel density plots (Vermeesch, 2012) with overlying histograms; n=number of grains <20 Ma. Framed number shows the minimum age peak generated with Density Plotter program (Vermeesch, 2012). The right column shows AFT data reported in radial plots and considering the total number of dated grains in each sample, indicated next to sample name (n=X). The central age, dispersion, χ^2 probability and main peak ages (± 1σ, with percentages referring to the relative importance of each peak) are indicated.*

5.3. Magnetostratigraphy

5.3.1. Magnetization characteristics

The initial Natural Remanent Magnetization (NRM) intensities range from 10^{-5} to 10^{-1} A/m and generally increase up-section. This increase, also observed in the bulk susceptibility, likely reflects a higher concentration of strongly magnetic iron oxides, such as magnetite, in the upper levels of the section. Two clearly different thermal demagnetization behaviours, separated by the stratigraphic level 1200 m, represent a change in both lithology and demagnetization behaviour. We used these behaviours to define Characteristic Remanent Magnetization (ChRM) components, plotted on vector end-point diagrams and stereographic projections (Fig. 41).

Demagnetizations from the lower part (below the 1200 m-level) were mainly complete below 550 °C (Fig. 41c) and a viscous low-temperature component (VLTC) often removed below 200 °C. A low-temperature component (LTC) of normal polarity mostly demagnetized between 150 and 300 °C was interpreted as an overprint. A medium-temperature component (MTC), generally demagnetized between 150 and 400 °C, often overlapped with the LTC along great circle paths on stereographic projections (Fig. 41). This MTC, of normal or reversed polarity directions, was interpreted as representing the ChRM. The increase in remanence intensity and susceptibility upon heating above ~300 °C is characteristic of iron sulphide transformation to magnetite. As also observed in other sections from the eastern Himalayan Siwaliks (Chirouze et al., 2012; Coutand et al., 2016), this suggests that iron sulphides, such as greigite, might be carrying the ChRM.

The upper part of the section (above the 1200 m-level) is characterized by a dramatic increase in grain size (Fig. 37). Generally, samples yielded higher initial NRM intensities than in the lower part of the section. However, the thermal demagnetization paths were more erratic and unstable, and many samples did not yield interpretable directions (e.g. Figs. 41e and 41f). This is explained by the larger grain size, which yields multi-domain magnetic grains (Butler, 1992). Samples presenting

interpretable demagnetization paths have generally much higher unblocking temperatures, between 300 and 670 °C, suggesting magnetite-like minerals and the occasional occurrence of hematite.

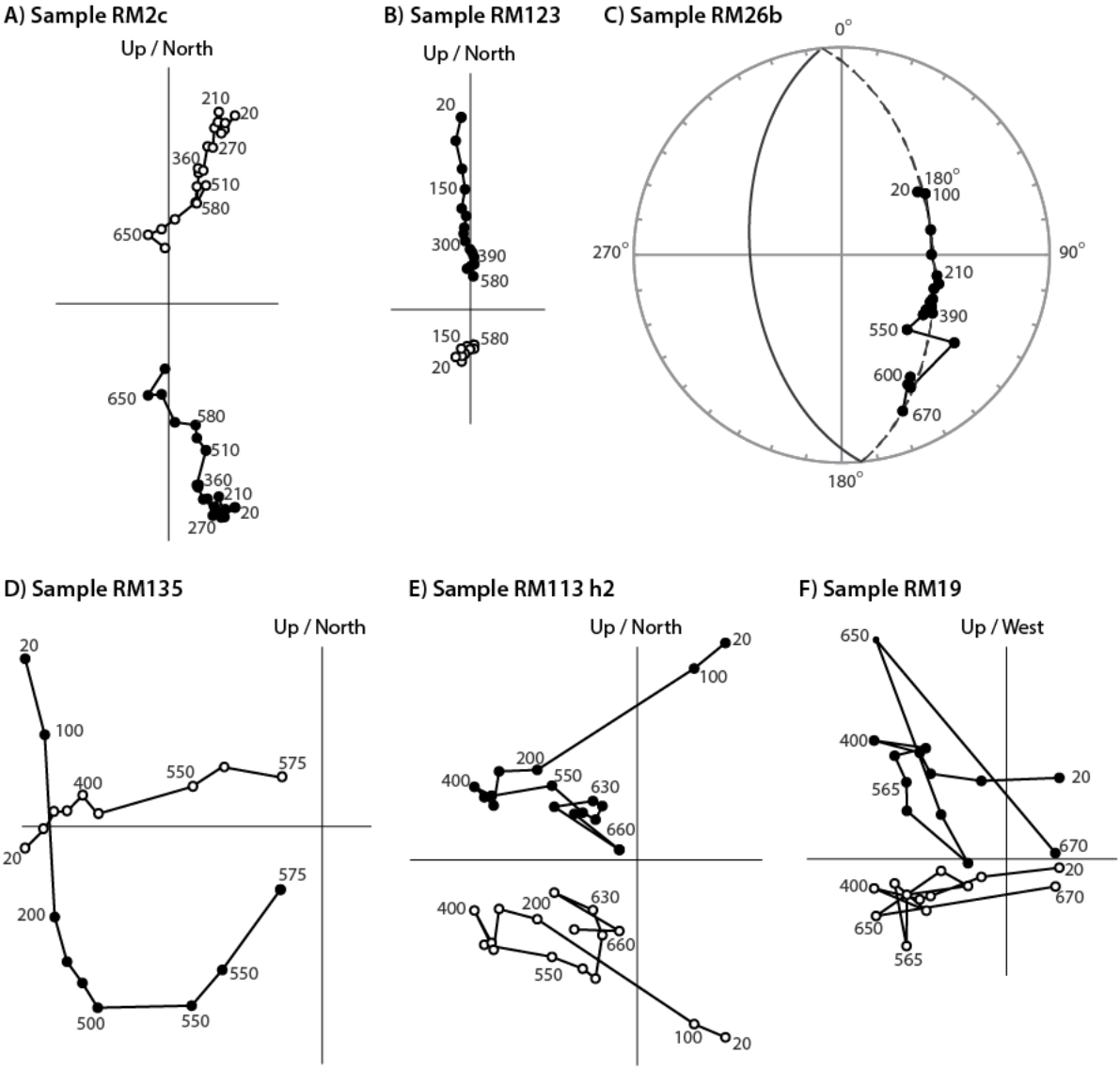

Fig. 41: *Representative thermal demagnetization paths presented on vector-end point diagrams and stereographic projection (c). Full and open symbols are projections on the horizontal and vertical plane, respectively. The numbers next to the symbols indicate the temperature of the demagnetization step in °C. a) and b) are reliable directions and polarities from group Q1. c) and d) are reliable polarities but of less reliable directions from group Q2. c) is a typical demagnetization path on which great-circle analysis was performed on a stereographic projection (McFadden and McElhinny, 1988). e) and f) are unreliable directions and polarities from group Q3. Figures were generated using Paleomagnetism.org (Koymans et al., 2016).*

5.3.2. ChRM direction analyses

We calculated the ChRM directions using at least four consecutive heating steps, usually decreasing towards the origin. Line fits were generally not anchored to the origin. However, some demagnetization paths showing a steady direction but no significant intensity decrease were forced to the origin. We rejected the line fits with a Maximum Angular Deviation (MAD) above 30°. When the contribution of a secondary normal polarity direction overlapped a reversed polarity direction carried by only a few points, we carried out a great-circle analysis (McFadden and McElhinny, 1988) (Fig. 42).

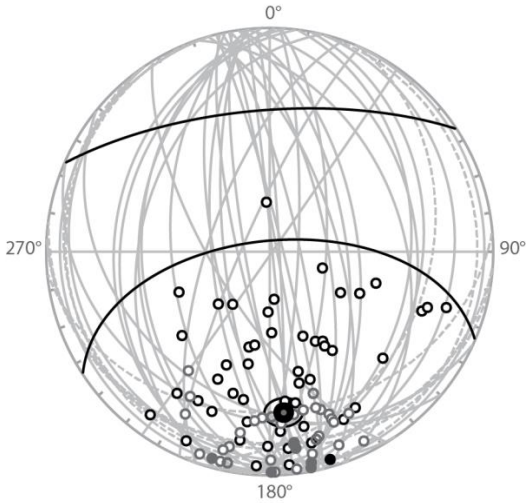

Fig. 42: *Great-circle analysis. Stereographic projections of reverse selected Q1 and Q2 ChRM directions on the lower (filled symbols) and upper (open symbols) hemispheres. The set point represented with thick black open circle is defined by the mean of selected Q1-Q2 directions. Q1 and Q2 directions are represented by black dots. Obtained reverse directions represented with grey dots are defined by the point on each great circle that is nearest to the set point. The dashed and straight lines are the fitted great circles projected in the lower and upper hemisphere, respectively.*

ChRM directions were carefully classified in four quality groups (Figs. 41 and 42), since secondary overprints of normal polarities were common and sometimes persisting at relatively high demagnetization temperatures. Quality 1 (Q1) are well-defined directions determined from a stable linear demagnetization path of MAD <15° (Figs. 41a and 41b). Quality 2 (Q2) have clearly defined polarities but less robust directions because of secondary overprint and/or directional scatter (Figs. 41c and 41d). Quality 3 (Q3) have ambiguous polarities, usually due to a strong overprint and/or a weak scattered signal (Figs. 41e and 41f). Also included in Q3 are poorly indurated samples that crumbled before sufficient measurements were acquired to extract reliable ChRM directions. Quality 4 (Q4) are Q1 or Q2 directions with Virtual Geomagnetic Poles (VGPs) lying more than 45° from the mean VGP (see Figure A in Appendix III). This 45° cut-off procedure was performed separately for

normal and reversed polarity datasets to avoid introducing a bias. In total 25 Q1 and 54 Q2 directions were defined and used for further analyses, while Q3 and Q4 directions were systematically rejected.

These remaining Q1 and Q2 ChRM directions cluster in antipodal fashion after tilt correction indicating the section has not been fully remagnetized, although a fold test was not applicable as the Remi section is homoclinally tilted. The reversal test is negative, suggesting the presence of partial overprints. The normal directions do not share a common true mean direction with the antipodal of the reversed directions (Koymans et al., 2016). This is expected with data that include partial normal overprints affecting both normal and reversed directions. In this case, reverse polarity determinations are clearly reliable but for normal polarities there remains the possibility of a total overprint of an original reverse direction, despite the care taken in isolating ChRM directions. For this reason, we have been especially cautious in defining normal polarities. This is particularly critical in the upper part of the section, where commonly unstable demagnetization yielded non-consecutive normal polarity directions. These included originally reversed directions with normal secondary overprints extending to high temperature ranges, suggesting some other samples may be fully remagnetized into normal polarities. In the lower part of the section, however, normal polarities were usually well defined by higher-temperature linear demagnetization paths and observed in consecutive intervals, validating normal polarity zones. Nevertheless, we present the normal polarity intervals as not fully reliable throughout the section to convey the possibility of normal overprints into the record.

The remaining 79 ChRM directions from Q1 and Q2 groups thus provide paleomagnetic polarity determinations at intervals averaging 13.6 m throughout the Remi section. Several larger gaps could not be avoided due to lack of outcrop or inadequate rock type (generally weathered coarse-grained sandstones) yielding non-interpretable demagnetization paths (Fig. 43). To define polarity zones, isolated polarities were systematically rejected. We thus identified two normal polarity (N1 and N2) and three reverse (R1, R2 and R3) zones in the section. The upper part of the magnetostratigraphic section shows a significant number of isolated normal polarity directions. Because these are isolated and they occur in the coarser-grained part of the sedimentary section where normal overprinting is common, they are considered unreliable. However, it is possible that these isolated normal polarity sites reflect original normal polarity zones that are not confidently deciphered by our results. Also, the isolated reverse polarity samples and the 20-m gap observed within the normal polarity zone N2 could potentially be the poor expression of initial reverse polarity zones.

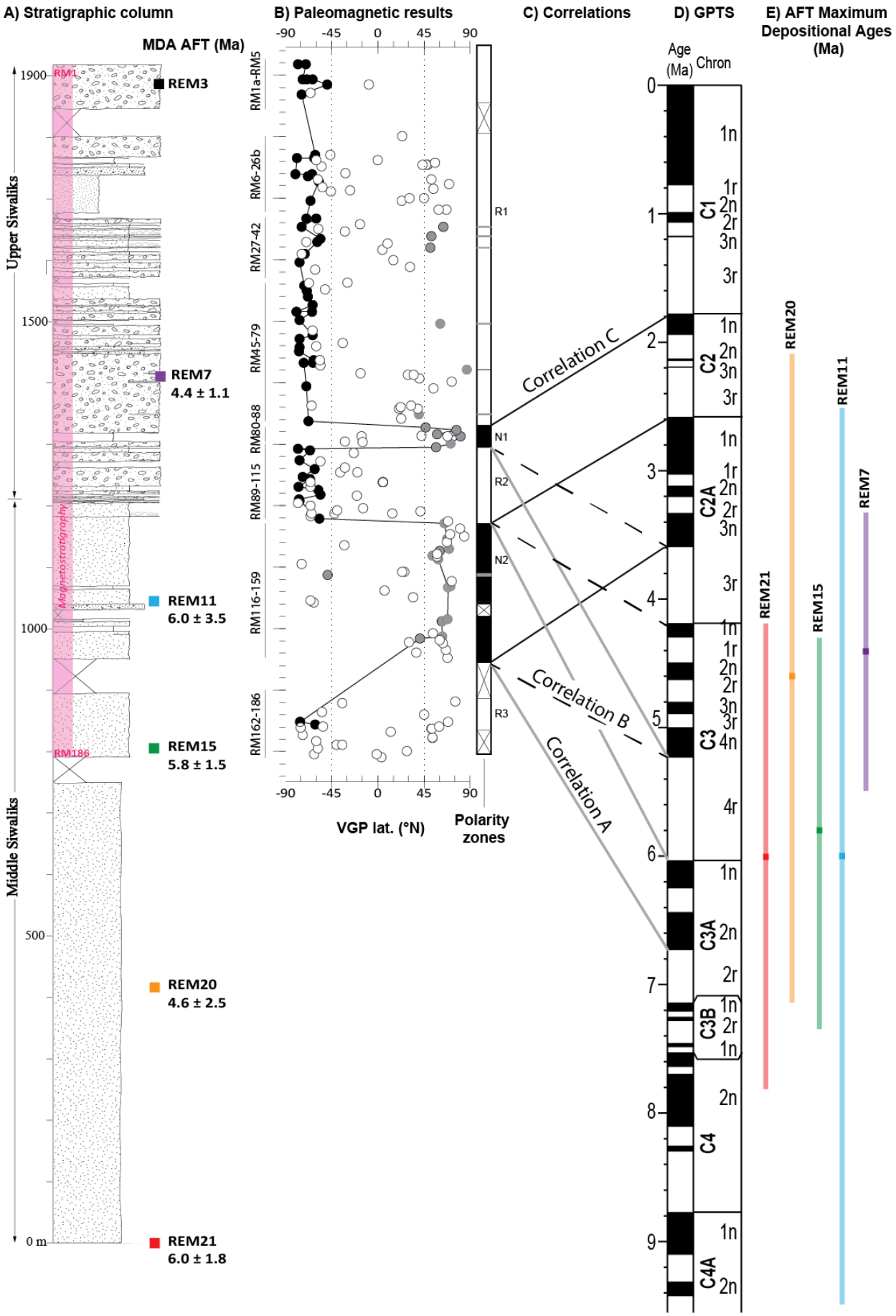
A) Stratigraphic column
MDA AFT (Ma)
1900
1500
1000
500
0 m
Upper Siwaliks
Middle Siwaliks
RM1
RM186
Magnetostratigraphy
REM3
REM7
4.4 ± 1.1
REM11
6.0 ± 3.5
REM15
5.8 ± 1.5
REM20
4.6 ± 2.5
REM21
6.0 ± 1.8
B) Paleomagnetic results
-90
-45
0
45
90
RM1a-RM5
RM6-26b
RM27-42
RM45-79
RM80-88
RM89-115
RM116-159
RM162-186
R1
N1
R2
N2
R3
VGP lat. (°N)
Polarity zones
C) Correlations
Correlation C
Correlation B
Correlation A
D) GPTS
Age (Ma)
Chron
0
1
2
3
4
5
6
7
8
9
1n
1r
2n
2r
3n
3r
4n
4r
C1
C2
C2A
C3
C3A
C3B
C4
C4A
E) AFT Maximum Depositional Ages (Ma)
REM21
REM20
REM15
REM11
REM7

Fig. 43: *Sample location and magnetostratigraphy results of the Remi section. (a) Stratigraphic column and AFT samples with Maximum Depositional Ages in Ma. (b) Magnetostratigraphy samples plotted against their Virtual Geomagnetic Pole Latitudes (VGP Lat.); results are indicated using black dots for reliable Q1 and Q2 ChRM of reverse polarity direction. Grey dots with black outline indicate Q1 normal polarity directions and isolated Q2 reverse polarity directions; plain grey dots indicate Q2 normal polarity directions. Open circles depict unreliable Q3 and Q4 directions. The polarity column is defined from our magnetostratigraphic measurements; black and white intervals indicate normal (N) and reverse (R) polarity zones, respectively. Grey intervals represent poorly constrained polarities defined by only one sample. Intervals with a cross indicate gaps in the sampling or in polarity determination. (c) Proposed correlations of the polarity column to the geomagnetic polarity time scale (GPTS) of Gradstein et al. (2012). Correlation A and B are presented in grey and dashed lines, respectively. The preferred correlation C is presented in solid black lines. (d) GPTS created using TSCreator v. 6.4 software from https://engineering.purdue.edu/Stratigraphy/tscreator/index/index.php, based on time scale of Gradstein et al. (2012). (e) Maximum Depositional Ages determined with AFT indicated by solid squares and the associated errors by light bars, for the samples shown in (a); each color indicates an individual sample.*

5.4. U-Pb zircon and apatite geochronology

In this section we refer to age abundances in order to describe the data; however, we acknowledge that these distributions only approximately represent the natural proportions within a sample, especially when the number of dated grains of a sample is low.

5.4.1. U-Pb zircon cores

Between 32 and 116 zircons from each analysed sample have core U-Pb ages of good quality (Fig. 44). Throughout the combined section, ages range between 21 and 3054 Ma. All samples contain a significant proportion of zircons with ages <300 Ma (between 12% and 54%); within this age range, grains are mainly of Cretaceous-Early Paleogene age (40-140 Ma), with a few zircons younger than 40 Ma, and most samples contain a few zircons of Early Cretaceous age (100-140 Ma). The main population of >300 Ma zircons is Paleozoic in age, defining a peak at around 500 Ma. This 500 Ma population increases from being fairly limited (until REM20), to substantial (from REM15), at around 4 Ma. Two other peaks with Proterozoic ages, around 900 and 1600 Ma, show increasing importance and definition up-section. In Fig. 44, pie charts show the fractions of ages comprised between 0 and 40 Ma, 40 and 300 Ma, and >300 Ma. The proportion of grains aged 40 to 300 Ma shows an

apparent decrease up-section, with a major change occurring between samples SG11 and REM15. This is particularly visible when plotting the zircon ages as a cumulative age distribution (Fig. 45). The cumulative age distribution curve illustrates this change and refines its interval between samples REM21 and REM15; samples SG15, SG11 and REM21 have a significantly larger proportion of 40-300 Ma ages compared to samples from REM15 to SIBO. Sample REM20 appears transitional between the two modes observed.

The results of Lang and Huntington (2014) from the Siang section show the same trend of decreasing proportion of zircons aged between 40 and 300 Ma up-section (Fig. 44). However, the exact percentages of such young grains are not comparable between the two studies due to the different data-processing criteria.

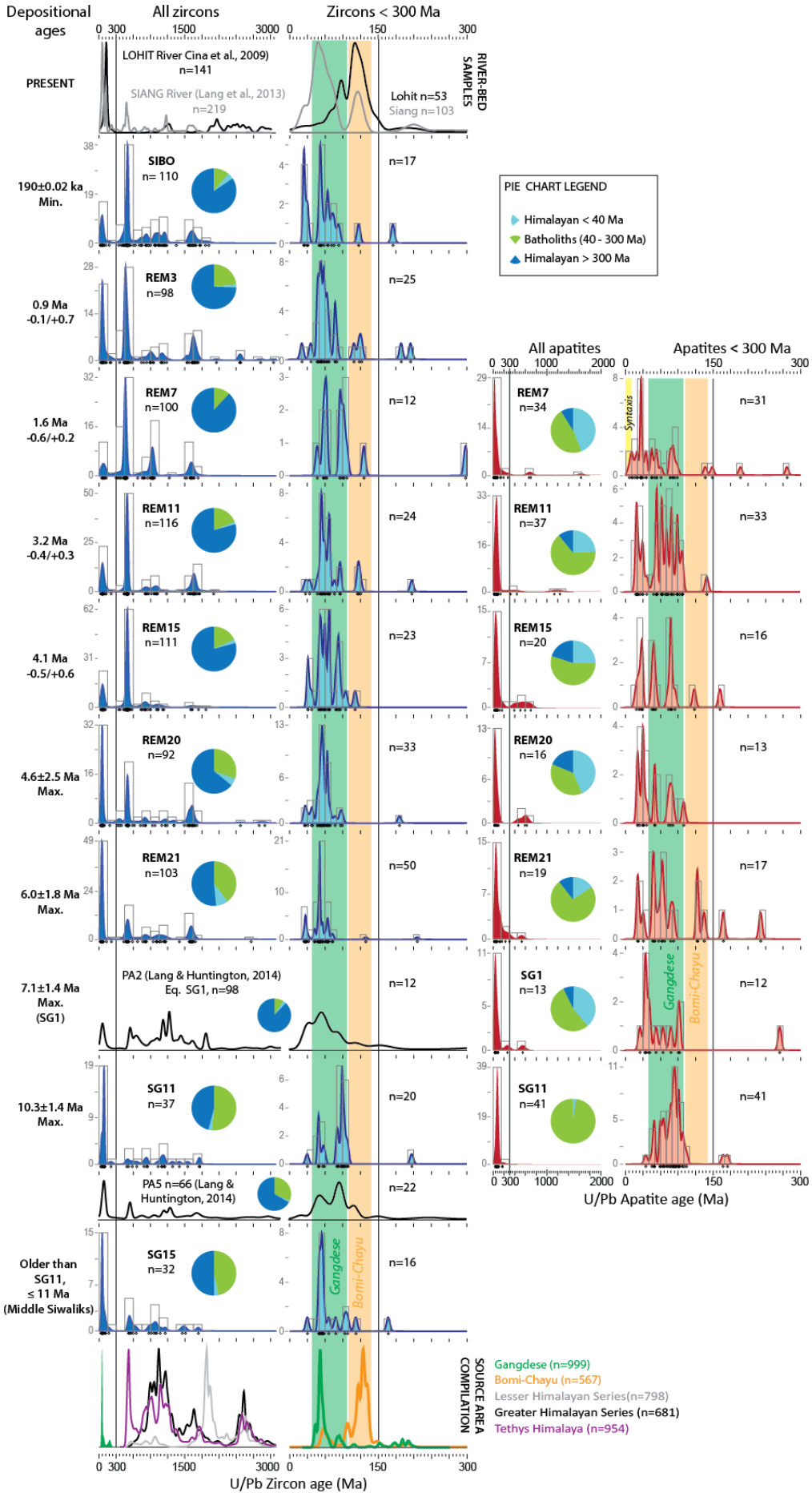
Depositional ages
All zircons
Zircons < 300 Ma
PRESENT
LOHIT River Cina et al., 2009) n=141
SIANG River (Lang et al., 2013) n=219
Lohit n=53
Siang n=103
RIVER-BED SAMPLES
190±0.02 ka Min.
SIBO n= 110
n=17
0.9 Ma -0.1/+0.7
REM3 n=98
n=25
1.6 Ma -0.6/+0.2
REM7 n=100
n=12
3.2 Ma -0.4/+0.3
REM11 n=116
n=24
4.1 Ma -0.5/+0.6
REM15 n=111
n=23
4.6±2.5 Ma Max.
REM20 n=92
n=33
6.0±1.8 Ma Max.
REM21 n=103
n=50
7.1±1.4 Ma Max. (SG1)
PA2 (Lang & Huntington, 2014) Eq. SG1, n=98
n=12
10.3±1.4 Ma Max.
SG11 n=37
n=20
PA5 n=66 (Lang & Huntington, 2014)
n=22
Older than SG11, ≤ 11 Ma (Middle Siwaliks)
SG15 n=32
n=16
Gangdese
Bomi-Chayu
SOURCE AREA COMPILATION
U/Pb Zircon age (Ma)
PIE CHART LEGEND
Himalayan < 40 Ma
Batholiths (40 - 300 Ma)
Himalayan > 300 Ma
All apatites
Apatites < 300 Ma
REM7 n=34
n=31
REM11 n=37
n=33
REM15 n=20
n=16
REM20 n=16
n=13
REM21 n=19
n=17
SG1 n=13
n=12
SG11 n=41
n=41
Syntaxis
U/Pb Apatite age (Ma)
Gangdese (n=999)
Bomi-Chayu (n=567)
Lesser Himalayan Series(n=798)
Greater Himalayan Series (n=681)
Tethys Himalaya (n=954)

Fig. 44: *U-Pb zircon and apatite data for samples from the Sibo-Remi-Siang section and from modern riverbeds compared to potential source regions. Data are plotted as kernel density plots (Vermeesch, 2012) with overlying histograms in grey. Data from this study is plotted in blue for zircon and red for apatite; data from Lang and Huntington (2014) in black. Sample PA2 from Lang and Huntington (2014) is from the same location as sample SG1 from this study (see Fig. 35). Pie charts show the fraction of zircon/apatite U-Pb ages >300 Ma interpreted as Himalayan origin in dark blue, ages comprised between 40 and 150 Ma interpreted as sourced from Gangdese and Bomi-Chayu batholiths in green, and ages <40 Ma interpreted as young Himalayan material in light blue. n=x indicates the number of grains for each column, presenting the total ages and the ages <300 Ma. Zircon U-Pb source-area compilation: ages of zircons characteristic of different Himalayan source units. Greater Himalayan Series ages are plotted in grey, Lesser Himalayan Series in black, Tethyan Himalaya in purple, Gangdese ages in green from Gehrels et al. (2008) and references therein and Bomi-Chayu ages in orange from references in Lang and Huntington (2014). Characteristic ages of Gangdese sources are highlighted in both apatite and zircon columns by light-green shade and characteristic ages of Bomi-Chayu sources by light-orange shade. The yellow shade in the apatite column highlights the range of ages characteristic of the syntaxis for this sample, deposited recently. The top graph presents data from modern riverbeds, the Lohit River ages (Cina et al., 2009) are presented in black and the Siang River ages (Lang et al., 2013) in grey. Depositional ages of samples determined in this study are shown to the left of the plots with their respective errors; depending on the dating method the abbreviations Min. and Max. indicate minimum and maximum depositional age, respectively.*

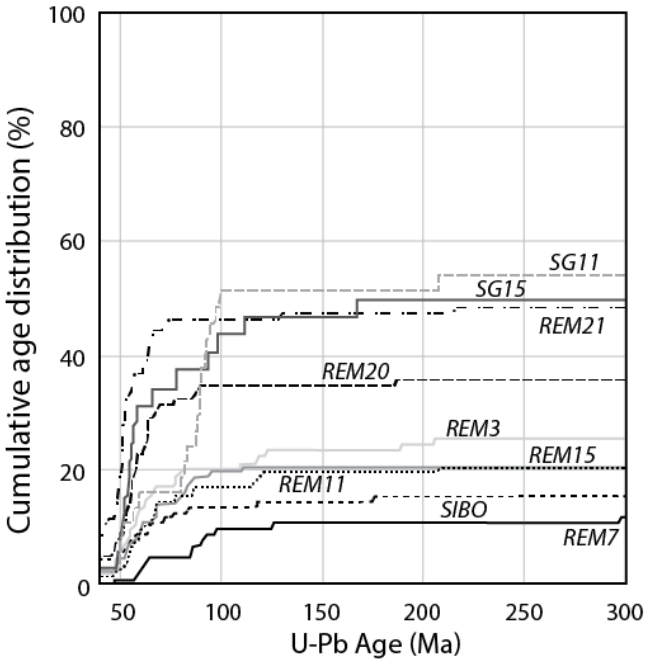

Fig. 45: *Cumulative age distribution of zircon U-Pb data plotted using DZ Stats software (Saylor and Sundell, 2016). The time interval considered (40-300 Ma) is interpreted as the characteristic ages of the Transhimalayan batholiths, including both Bomi-Chayu and Gangdese batholiths.*

5.4.2. U-Pb zircon rims

U-Pb zircon-rim ages with <5% discordance range from 16 to 3704 Ma. If grains with a higher discordance percentage are included, the results present a few ages as young as 15.2±0.4 Ma (6.5% discordant, in sample REM3) for age discordance limited to 10%, and as young as 5.1±0.2 Ma (55.5% discordant, in sample REM7) with no discordance limit on the data (Fig. 46 and Appendix III). The oldest sample to contain rim ages of 10 Ma or less, without discordance distinction, is REM21 (maximum depositional age ~6 Ma). Concordia diagrams of the rim analyses showing ages ≤20 Ma are plotted in Fig. 46. The youngest lower intercept of the discordia line with the concordia curve calculated from several analyses of the same rim is 8.5±1.9 Ma (MSDW=3.00) in sample REM11.

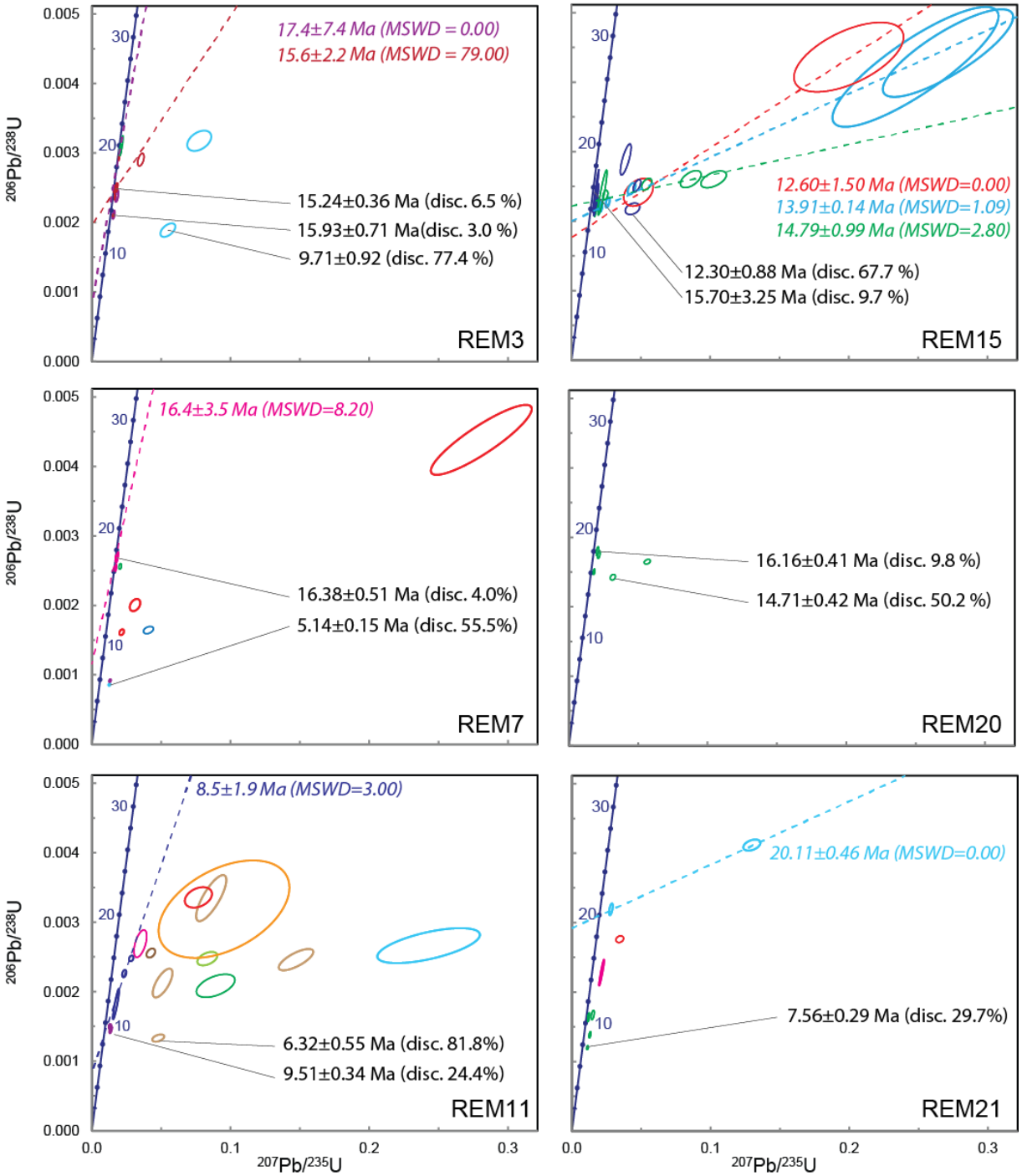

Fig. 46: *Zircon-rim U-Pb concordia diagrams of samples from the Remi section. Data showing ages ≤20 Ma after data screening are plotted as Wetherill concordia diagrams, using the Isoplot v. 4.14 add-in for Microsoft Excel (Ludwig, 2003). The dotted dark blue line is the concordia curve with corresponding ages indicated in Ma. Data-point ellipses are at the 2σ level and coloured as a function of the rim analysed. The youngest data points with discordance <5%, <10% and with no discordance limit, are indicated in black, with the discordance bracketed. Dotted lines are regression lines calculated for several analyses of the same zircon rim; the lower intercept age is indicated in the color corresponding to the rim analysed.*

5.4.3. Apatite U-Pb geochronology

We obtained between 13 to 37 robust U-Pb ages per sample, ranging between 5 and 1635 Ma. The age populations identified using apatite U-Pb dating are similar to those observed using zircon U-Pb dating. The main age peaks and the age distributions follow a similar trend in both datasets. Although the temperature sensitivity (assuming thermally-activated volume diffusion) of these two geochronological systems differ by several hundred °C (U-Pb apatite temperature sensitivity of ~375-550 °C; zircon >900 °C; Cherniak and others, 1991; Cochrane and others, 2014; Schmitz and Bowring, 2003 and references therein), the respective age populations match well, suggesting age spectra are dominated by ages recording igneous crystallization. However, the proportion of grains <300 Ma is higher in the apatite compared to the zircon data, varying from 80 % to 100 %. This contribution decreases up-section, similarly to the zircon ages, but the decrease is less well defined. There is a sharp change between SG11 and SG1, mirroring the zircon data. SG1 and subsequently-deposited samples all yield numerous apatite U-Pb ages <40 Ma, but these are represented by just a single grain in sample SG11 at the base of the sequence. Whilst the signature below the shift is only defined by one sample, we consider the trend meaningful in view of the fact that it mirrors the trend found in the zircon U-Pb data.

Few apatite grains are of Early Cretaceous age, and these are exclusively from samples that also contain zircons of this age, strongly indicating an igneous source as opposed to metamorphic resetting of the more thermally sensitive apatite U-Pb system. Grains older than 300 Ma, low in number compared to the zircon data, tend to be concentrated in age peaks similar to the Paleozoic and Proterozoic age peaks observed for zircons (especially 500 Ma and 1600 Ma). We note the extremely young apatite U-Pb ages in sample REM7 of 5.7±0.5 and 9.5±0.8 Ma, and a well-defined age population between 10 and 40 Ma present in every sample except SG11.

6. DISCUSSION

Here, we first discuss the age model for deposition of the Sibo-Remi-Siang section, followed by the tectonic and geomorphic implications of our U-Pb provenance data.

6.1. Depositional age of the Sibo-Remi-Siang succession

The IRSL results, AFT ages and the magnetostratigraphic analysis, along with the field observations, allowed us to constrain the depositional ages of parts of the sedimentary sections and to propose an age model for the Sibo-Remi-Siang succession.

The Sibo outcrop is interpreted as containing the youngest Upper Siwalik deposit in the studied area, deposited at or before ~190 ka. These sedimentary rocks have subsequently been gently tilted by the active Main Frontal Thrust, associated with the southward propagation of the Himalayan front (e.g. Srivastava et al., 2009).

For the Remi section, AFT ages can provide initial constraints on depositional age if they are not reset by burial heating. Apatites anneal at different temperatures, depending on their chemistry (e.g. Carlson et al., 1999), and it is possible that partially reset ages are present in our data. To investigate this possibility we first review burial estimates from other Siwalik sections. Vitrinite reflectance data and illite crystallinity analyses from Siwalik sections in Nepal have indicated maximum temperature-depth couples that indicate a geothermal gradient of 18-24 °C/km, consistent with well data in western India, and leading to partial resetting of the AFT system at burial depths greater than ~2500 m (e.g. Huyghe et al., 2005; van der Beek et al., 2006). Similar results were obtained in the Kameng section of western Arunachal Pradesh (Chirouze et al., 2013). In the 2200 m thick Dungsam Chu section (Bhutan), the maximum burial temperature determined with vitrinite reflectance is 80 °C and AFT ages are unreset throughout the section (Coutand et al., 2016). The Remi section is only ~1900 m thick; therefore, total resetting of the AFT system is unlikely for any of the Remi samples. This is substantiated by the younging upward trend of minimum ages in the section. Estimating the initial maximum thickness of the Siang section is not straightforward because the upper part of the sedimentary pile does not outcrop at present. Additionally, thrusts both within and bounding the Siang and Remi sections (e.g. Sompa Fault, Mingo Thrust; Fig. 35) could have buried parts of the sections significantly deeper than the stratigraphic depth, rendering the maximum depth and temperature difficult to estimate. However, since apatite fission-track central and minimum ages are also younging up in the Siang section, we interpret our ages as unreset, or at most slightly partially reset due to potential post-depositional burial heating. Thus, we consider the youngest AFT ages as the maximum depositional age for each sample in the Remi and the Siang sections.

In general, the Siwalik sections yield short minimum AFT lag times of <2 Ma in Nepal and in the nearby Kameng section (Chirouze et al., 2013; van der Beek et al., 2006). Furthermore, compiled zircon fission-track and mica $^{40}Ar/^{39}Ar$ lag-time data from the Siwaliks along the Himalayan range indicate shorter lag times in areas proximal to the syntaxes compared to the central part of the range; these short lag times near the eastern syntaxis shorten even more up-section (Lang et al.,

2016). Therefore, the depositional ages in the Remi and the Siang section are likely to be statistically indistinguishable from the minimum AFT age peaks, which have confidence intervals >1.4 Ma.

We conclude that the Siwaliks in the Remi section were deposited from 6.0±1.8 Ma (REM21). In the Siang section, SG11 was deposited at or after 10.3±1.4 Ma and SG1 at or after 7.1±1.4 Ma (Fig. 40). The relatively short time difference between the lowermost sample in the Remi section (REM21) and the uppermost sample in the Siang section (SG1) allows us to assume the Remi-Siang sections to be roughly continuous. As the same relationship is also observed between the Sibo outcrop and the uppermost Remi section sample (REM3), we make the approximation that the entire Sibo-Remi-Siang succession is nearly continuous.

For the Remi section, further age control is provided by correlating our magnetostratigraphic results to the Geomagnetic Polarity Time Scale (GPTS; Gradstein et al., 2012). As a starting point of our correlation we use the reverse zone R2 that is unequivocally defined and is located within the more reliable lower part of the section. Five stratigraphic levels are assigned a maximum depositional age determined using the independent constraints provided by the detrital apatite fission-track dating (Fig. 43). In particular, the stratigraphic age at the base of the Remi paleomagnetic section is <5.8±1.5 Ma (Fig. 43). This age constraint yields three possibilities for correlating R2 to the GPTS: A) to *C3.4r* (starting at 6.0 and ending at 5.2 Ma), B) to *C2A.3r* (4.2 to 3.6 Ma) and C) to the combination of *C2.3r* to *C2.1r* (2.6 to 1.9 Ma) (Fig. 43).

Correlation A links R2 to the oldest reverse chron allowed by the AFT-derived maximum depositional age and the lengths of the N1, R2 and N2 zones relative to each other. This correlation suggests that N2 is correlated to the chrons *C3.1n* to *C3.2n*, implying a missing reverse polarity zone within N2, which would be possible considering the gap and reverse isolated site within N2. Lower in the section, R3 is correlated to *C3A.2r* and the overlying N1 matches chron *C3.4n*. Above N1 however, the correlation is not straightforward. We can speculatively correlate the normal isolated polarities within R2 to the interval from *C3.3r* to sometime in *C2A.3r*, which includes relatively short normal chrons (*C3.1n, C3.2n and C3.3n*).

In correlation B, R2 is correlated to *C2A.3r*. This implies N2 to correspond with the chrons from *C3.1n* to *C3.4n* and the subsequent R3 zone to *C3.4r*. This would imply missing polarity zones *C3.1r*, *C3.2r* and *C3.3r*, which would represent a significant amount of missed reverse polarity directions, possibly due to secondary overprinting. Above R2, N1 is logically correlated to *C2A.3n*, but R1 is too long to

be realistically correlated to *C2A.2r*. This correlation would imply a very significant number of missing polarity zones, reverse in the lower part of the section and normal in the upper part.

In correlation C, correlating R2 with the *C2.1r* to *C2.3r* interval implies that the two very short normal zones of the GPTS within this time interval are missing in our data. Below R2, the correspondence of N2 to the chrons from *C2A.1n* to *C2A.3n* is straightforward, although it implies that the isolated reverse direction site and the sampling gap within N2 respectively reflect and hide the missing chrons *C2A.1r* and *C2A.2r*. Below N2, R3 is easily linked to *C2A.3r*. Above R2, the long reverse zone R1 fits well with the *C1* reverse chrons. From this point, the correlation becomes challenging to interpret with numerous options. These are based on assumptions made on the isolated normal sites, which could independently reflect original normal polarities or result from secondary overprinting. Since the potential solutions are multiple, they are not detailed here. However, as the top of the section clearly indicates a reverse polarity zone, it must be older than *C1.1n,* i.e. ~0.8 Ma.

The correlations A and B are not as straightforward as correlation C, in particular because they do not fit well the upper part of the determined polarity zones with the GPTS. Additionally, correlation A places the Middle to Upper Siwalik transition at ~5.5 Ma, whereas it has been dated between 2 and 3.8 Ma throughout the Himalayan sections from Pakistan to eastern India (e.g. Chirouze et al., 2012; Coutand et al., 2016; Ojha et al., 2009; Sanyal et al., 2004) (Fig. 47). Correlation B requires many assumptions on gaps and isolated polarities; moreover, N1and R2 do not match the GPTS. For these reasons we reject correlations A and B and prefer correlation C, which provides the best fit while omitting the fewest number of chrons.

We therefore infer the base of the magnetostratigraphically dated part of the Remi section to be younger than 4.2 Ma. The Middle to Upper Siwalik boundary in the Remi section is constrained at ~2.5 Ma, which is consistent with the nearby dated Kameng and Siji sections (Chirouze et al., 2012; Lang et al., 2016). The Lower to Middle Siwalik boundary is generally around 10±2 Ma along the Himalayan foreland basin (Chirouze et al., 2012; Gautam and Fujiwara, 2000; Harrison et al., 1993; Johnson et al., 1985; Meigs et al., 1995; Ojha et al., 2000; 2009), which also is in agreement with our interpretation, as the Sibo-Remi-Siang succession does not contain Lower Siwaliks (Fig. 47). Additionally, the oldest dated Lower to Middle Siwalik transition has been constrained at ~11 Ma (Johnson et al., 1985; Ojha et al., 2000; 2009) in the Chinji, Khutia Khola and Tinau Khola sections of Pakistan and Nepal (Fig. 47). Therefore, we assume that the oldest Middle Siwalik sedimentary rocks of the Sibo-Remi-Siang succession are ≤11 Ma.

6.2. Sediment accumulation patterns

The magnetostratigraphy indicates accumulation rates averaging 0.21 mm/yr for the upper part of the Middle Siwaliks and the lowermost part of the Upper Siwaliks in the Remi section. The length of the reverse zone R1 in the top of the section suggests a significant increase in accumulation rates in the Upper Siwaliks, to a minimum of 0.55 mm/yr assuming the age of the top of the Remi section to be close to the base of the Brunhes chron at 0.8 Ma. Such an increase in accumulation rates up-section is recorded in most of the Siwalik sections in the Himalayan foreland basin (Fig. 47), with the notable exception of the Dungsam Chu section in Bhutan. There, accumulation rates decrease up-section, which is interpreted as due to the influence of the adjacent Shillong Plateau (Coutand et al., 2016; Govin et al., in prep). Our results from an area east of Bhutan but unaffected by the Shillong Plateau further support this interpretation for the unusual accumulation rates in the Dungsam Chu section.

The Upper Siwaliks in sedimentary sections of the Himalayan foreland basin from NW to NE India present accumulation rates that vary from 0.1 mm/yr in the Dungsam Chu section and 0.34 mm/yr in the Haripur section to 0.59 mm/yr in the Surai Khola section (Chirouze et al., 2012; Coutand et al., 2016; Meigs et al., 1995; Ojha et al., 2009; Sanyal et al., 2004). The Upper Siwalik alluvial fan deposits are strongly influenced by their proximity to the southward-propagating Himalayan thrust front. Therefore, local faults associated with the Main Frontal Thrust could explain this variability in accumulation rates along strike. For instance, activity on the Mingo Thrust has likely allowed rapid erosion of its hanging wall. Overall, the rates obtained here for NE India are consistent with Upper Siwalik accumulation rates along the range (Fig. 47). This consistency contrasts with the Middle Siwaliks, which show significantly lower rates in both the eastern and western extremities of the Siwalik apron compared to the central region (Fig. 47). This pattern holds true also for the Lower Siwaliks in the western extremity vs the central part of the basin. No data from Lower Siwaliks are currently available to constrain accumulation rates in the eastern Himalaya.

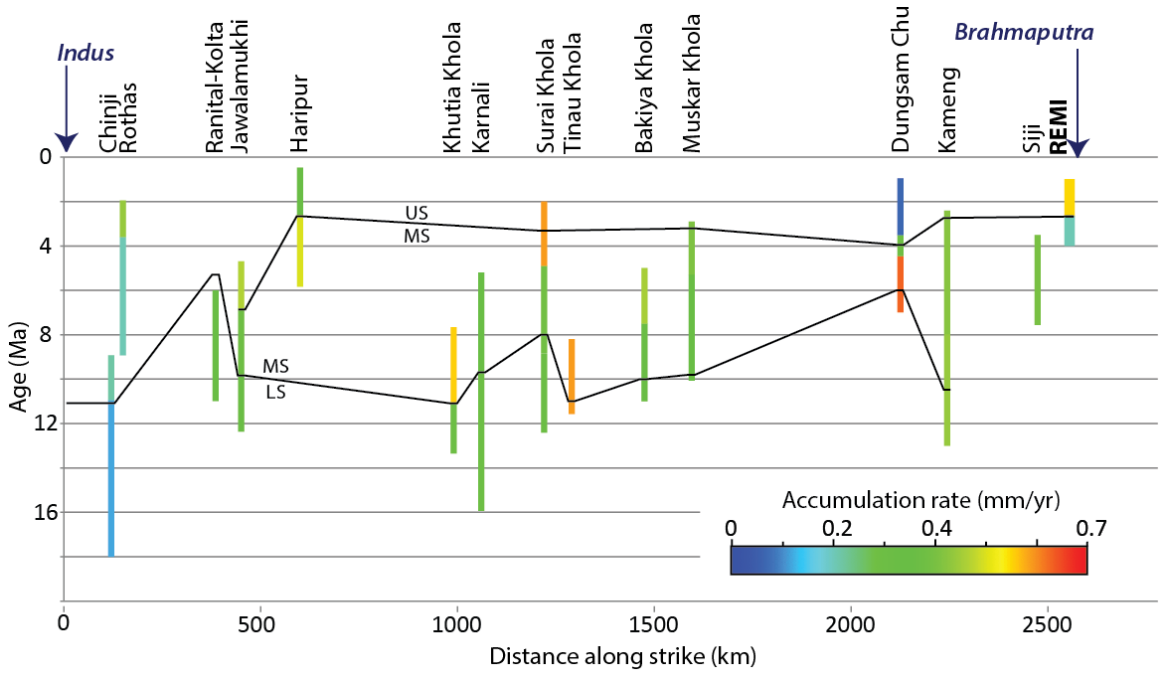

Fig. 47: *Compilation of ages and accumulation rates of Siwalik sections dated with magnetostratigraphy between the Indus and Brahmaputra Rivers. Transitions between Lower Siwaliks (LS) and Middle Siwaliks (MS) and between Middle and Upper Siwaliks (US) are indicated with black lines. The sections presented in this diagram are: Chinji (Johnson et al., 1985); Rothas (Behrensmeyer et al., 2007); Ranital Kolta, Haripur (Sanyal et al., 2004); Jawalamukhi (Meigs et al., 1995); Khutia Khola (Ojha et al., 2000); Karnali (Gautam and Fujiwara, 2000); Surai Khola, Tinau Khola, Muksar Khola (Ojha et al., 2009); Bakiya Khola (Harrison et al., 1993); Dungsam Chu (Coutand et al., 2016); Kameng (Chirouze et al., 2012); Siji (Lang et al., 2016).*

Along-strike variations in flexural subsidence are not likely the cause of the differences in Siwalik accumulation rates along strike of the range. Whereas the wavelength of lithospheric flexure is shorter in the eastern Himalayan foreland basin compared to the west (Hammer et al., 2013), the change in flexural wavelength occurs to the west of Bhutan and cannot explain the differences in accumulation rates between the Remi and Siji sections, which are only ~60 km apart in the easternmost Himalaya. Differences in sediment supply are also unlikely to constitute a suitable explanation for the low accumulation rates in these syntaxial areas in comparison with the central Himalayan foreland basin, since the two major orogen-traversing rivers, the Indus and the Yarlung-Siang-Brahmaputra, provide high sediment influx to both the eastern and western extremities of the foreland basin. Analysis of further records along strike are required to validate whether there is indeed a systematic difference in accumulation rate between the syntaxial regions and the main arc of the orogen, or whether these variations are simply related to differences in activation of local structures through time.

6.3. Provenance and drainage evolution

6.3.1. Syntaxial influence

A significant decrease in the proportion of Jurassic-Early Paleogene ages (40 to 300 Ma) upward in the Sibo-Remi-Siang section has been detected in the zircon and apatite U-Pb data. Although this decrease is observed in the relative abundances of age components, which does not necessarily reflect strictly the natural proportions, we argue it likely approximates the natural trend within the Sibo-Remi-Siang section as the zircon U-Pb cumulative age distributions show a clear transition between REM21 and REM15 (depositional ages of ~6 Ma and 4.1 Ma, respectively) (Fig. 45). This decrease indicates a dilution of Transhimalayan detritus, and thus a relatively increased contribution of detritus sourced from Indian plate Himalayan units. The decrease in the proportion of Transhimalayan ages appears to occur gradually from sample SG11 (depositional age of ~10 Ma; Fig. 40), as illustrated by the zircon core U-Pb data pie charts (Fig. 44). The increase in the 500 Ma population from the Indian plate Tethyan Himalaya occurs sharply, between sample REM20 (4.6 Ma) and REM15 (4.1 Ma). We interpret this dilution of the Transhimalayan detritus as due to the exhumation of the syntaxis in the upstream Siang, in view of the synchronicity with syntaxial exhumation determined from detrital thermochronological data as described below:

Bracciali et al. (2015) have documented zircon-rim ages <10 Ma in deposits of the Surma Basin (Bangladesh) and have interpreted these as indicating syntaxial provenance. We find similarly aged zircon rims in our samples from 6 Ma; the lag times calculated for the youngest zircon-rim U-Pb ages in the Remi samples are ≤10 Ma. If interpreted similarly to Bracciali et al. (2015), this suggests syntaxial input at least as early as the depositional age of sample REM21 (maximum depositional age 6.0±1.8 Ma; Fig. 40). However, these young rim ages are highly discordant (up to >90%) with high common Pb contents, and may also have suffered Pb loss. The lag times calculated with a discordance restriction of <10% are >10 Ma for all samples, and further investigations are necessary to confirm our interpretation. The technical challenge involved in thin zircon-rim U-Pb dating is significant. In this study, the narrowness of the metamorphic zircon overgrowths required the use of small laser spots during analysis, which could lead to significant U-Pb fractionation and therefore a dating bias. For this reason, the analytical methodology of dating young and thin rims needs to be further developed before this technique can be used as a robust self-sufficient syntaxial provenance tool. In our case, the zircon-rim analysis includes ages as young as 8.5±1.9 Ma (MSWD = 3.00) for REM11 (depositional age of ~3.2 Ma), calculated by regression of multiple single-rim analyses (Fig. 46), which provides support for a syntaxial origin of the young-rim zircons, rendering the interpretation less speculative.

The apatite fission-track data show very young ages (as young as 2 Ma), and we suspect lag times shorter than 2 Ma for grains in the REM7, REM11 and REM15 samples (depositional ages of ~1.5, 3.2 and 4.0 Ma, respectively) when comparing the AFT minimum ages to the age of deposition determined by magnetostratigraphy. These short lag times remain speculative, however, since errors on both the depositional and cooling ages are large and both ages overlap. Furthermore, we cannot uniquely interpret these young grains of very short lag time as being derived from the syntaxis, since grains of similarly young AFT age have been recorded in the Himalayan bedrock (e.g. Coutand et al., 2014) and such short lag times are observed in Himalayan foreland basin deposits outside the syntaxial regions (Chirouze et al., 2013; van der Beek et al., 2006).

Apatite double dating provides additional information to AFT-dated grains, with U-Pb ages helping to identify an eastern syntaxis source in the Sibo-Remi-Siang sedimentary rocks. Our results from both apatite and zircon U-Pb systems show similar trends in age population abundances. Zircon and rutile U-Pb ages <10 Ma are unique to the eastern syntaxis and represent its unusually young metamorphism in comparison to the main Himalayan arc (Bracciali et al., 2016). Since the U-Pb geochronological system in rutile has a temperature sensitivity which overlaps with that of apatite U-Pb (~640-490 °C; Kooijman et al., 2010), we interpret apatite grains yielding U-Pb ages of <10 Ma as syntaxial detritus. However, source characterization confirming that young apatite U-Pb ages are unique to the syntaxis remains required to validate this interpretation. In sample REM7, two young double-dated grains have been detected (depositional age of ~1.5 Ma; U-Pb age <10 Ma and AFT age <3 Ma). Such young apatite grains are not found further down-section. The lack of young, potentially syntaxially derived grains further down-section would be at variance with our interpretation of syntaxially derived detritus from ~6 Ma discussed above. This discrepancy may be explained by the overall rarity of these young apatite grains, likely related to large uncertainties on their U-Pb ages, leading to rejection of young ages in the data screening process. The lack of such grains down-section could also be a consequence of the apatite double-dating (U-Pb and fission-track combined) approach. A population of very young grains may go undetected due to their low track density, low U content and/or high common-Pb content in some grains. Therefore, if an independent U-Pb apatite analysis was carried out, without restriction of analyses to grains previously selected for fission-track dating, the results may show younger U-Pb age populations lower down the section, which would mirror the interpretation of the zircon-rim data.

In conclusion, the combination of AFT, U-Pb apatite, U-Pb zircon core and rim dating suggests that the presence of detritus sourced from the rapidly exhuming eastern syntaxis is likely at least from ~6

Ma in the Remi section (sample REM21), as indicated by the U-Pb zircon-rim data, and consistent with the timing suggested from thermochronological studies of the Sibo-Remi-Siang section and the adjacent Siji section (Govin et al., 2016; Lang et al., 2016). Additionally, sample REM7 (depositional age of ~1.5 Ma) exhibits robust young apatite of syntaxial origin.

In the above scenario, the increasing percentage of the 500 Ma grains indicative of Himalayan (Tethyan) input, between ~4.1 Ma and 4.6 Ma, and the dilution of the contribution of Transhimalayan zircon inferred between samples SG11 and REM15, i.e. between ~10.3 Ma and 4.1 Ma, are thus interpreted to result from the progressive exhumation of the syntaxis in the upstream Siang, which would increase the proportion of Himalayan Indian plate input through time. However, these changes could also potentially be explained by two other possible mechanisms; either 1) the progressive southward propagation of the Himalayan thrust belt, or 2) river capture events, specifically a change from Yarlung-Lohit-Brahmaputra routing to Yarlung-Siang-Brahmaputra routing.

Southward propagation of the Himalayan thrust belt would lead to an increase in Himalayan-derived detritus as the thrust belt became more proximal to the foreland basin. However, we prefer to explain the change as due to syntaxial exhumation due to the synchronicity with this event as determined independently from thermochronological data.

A change from Yarlung-Lohit-Brahmaputra routing to Yarlung–Siang–Brahmaputra routing could also explain the decrease in Transhimalayan detritus up-section, and the significant increase in 500 Ma Tethyan Himalayan zircon grains at ~4 Ma. The Tethyan Himalaya does not extend eastward of the Himalayan syntaxis (e.g. see the geological map of Cina and others, 2009). Therefore, a Yarlung-Lohit-Brahmaputra routing would only have contained a small amount of Tethyan aged (500 Ma) zircons, picked up as the Yarlung Tsangpo drained along the suture zone at low gradient. This low percentage of 500 Ma zircons is similar to the present day Yarlung Tsangpo signature, and contrasts with modern day Himalayan transverse rivers which drain the Tethyan Himalaya at high gradient (e.g. Cina et al., 2009). Subsequent cut back and river capture by the Siang would have resulted in a higher proportion of Tethyan input to the sedimentary deposits, because the Tethyan rocks extend to this region. However, the major change in proportion of 500 Ma zircon grains in the Remi section occurs at ~4 Ma, 2 million years after we, and others (e.g. Lang et al., 2016) document a syntaxial signal, diagnostic of Siang drainage. For this reason, we prefer to explain these up-section changes in terms of syntaxial exhumation.

6.3.2. Drainage development

6.3.2.1. Cretaceous-Early Paleogene ages: Yarlung-Brahmaputra connection by Late Miocene

The presence of Cretaceous-Early Paleogene zircons and apatites in the Sibo-Remi-Siang succession since ~11 Ma indicates that the Yarlung-Brahmaputra connection was established since this time. This detritus is interpreted as derived from the Gangdese batholiths and transported by the palaeo-Brahmaputra through the Yarlung Tsangpo and a transverse river such as the Siang (Fig. 48). This conclusion is compatible with previous provenance studies in the eastern Himalayan Siwaliks (Chirouze et al., 2013; Cina et al., 2009; Govin et al., in prep; Lang and Huntington, 2014), which provided evidence for a Yarlung-Brahmaputra connection established at least since deposition of the Middle (and in the case of Lang and Huntington (2014), the Lower) Siwaliks, i.e. since Late-Miocene times. Our data are also consistent with the presence of Transhimalayan detritus in the Bengal Fan since at least 12 Ma (Galy et al., 2010). More distal records in Bangladesh and Myanmar (Bracciali et al., 2015; Robinson et al., 2014) suggest the connection to be even older, i.e. Early Miocene, but cannot distinguish between a possible Yarlung-Lohit-Brahmaputra and a Yarlung-Siang-Brahmaputra connection at this time. Since the Sibo-Remi-Siang succession contains syntaxial deposits from ~6 Ma, the Yarlung-Brahmaputra connection via the Siang has likely existed since at least the Late Miocene (Fig. 48).

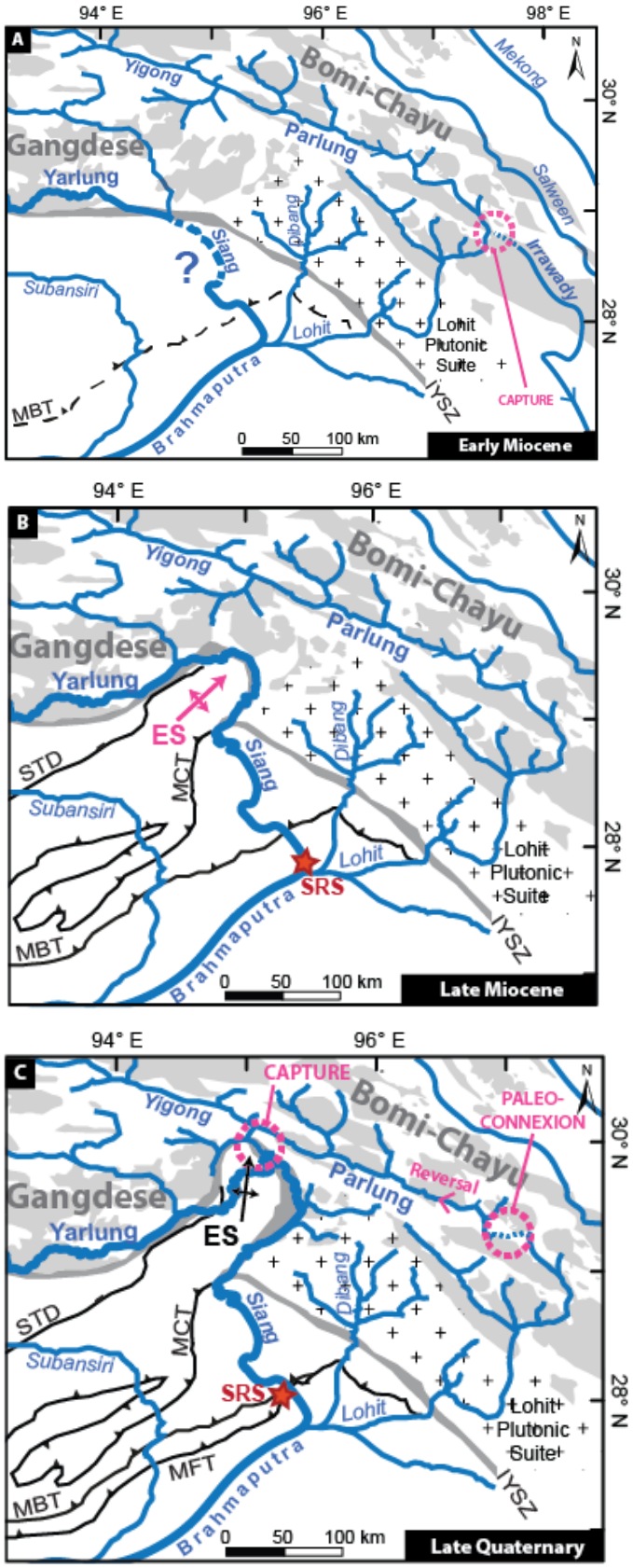

Fig. 48: *Early-Miocene to Late-Quaternary evolutionary model of the drainage system in the eastern syntaxis area (modified from Lang and Huntington, 2014) constructed using provenance analysis*

from this study, Lang and Huntington (2014), Clark et al. (2004), Robinson et al. (2014), and references therein. The question mark and the dotted drainage line indicates a potential paleo-drainage scenario in which the Yarlung-Brahmaputra connection existed through the Siang River since the Early Miocene, but other scenarios are possible such as a Yarlung-Brahmaputra connection through the Lohit River. Red star labelled SRS represents the Sibo-Remi-Siang composite section. The arrows symbolize the northward growth of the antiformal Namche Barwa syntaxis. Abbreviations are: ES – Eastern Syntaxis, MFT - Main Frontal Thrust, MCT - Main Central Thrust, MBT - Main Boundary Thrust, STD - South Tibetan Detachment and IYSZ - Indus-Yarlung Suture Zone.

6.2.3.2. Early-Cretaceous ages: major river reorganization since ~190 ka

Our U-Pb data also show minor input of Early Cretaceous (and Late Jurassic; 100-150 Ma) zircon and apatite throughout the Sibo-Remi-Siang succession. By contrast, the modern Siang River sedimentary rocks show a major contribution of such zircon grains (Lang et al., 2013) (Fig. 44). Early Cretaceous U-Pb ages have been reported as a major age population of the Bomi-Chayu batholiths, in only minor amounts from the Gangdese batholiths, and may also be present in the Lohit Plutonic Suite (Cina et al., 2009; Haproff et al., 2013) (Fig. 44). Due to uncertainty of the paleo-location of our studied Siang-Remi-Sibo sedimentary succession with respect to the trunk Brahmaputra River and its various tributaries draining these potential source regions, we can only speculate as to which region sourced the minor amount of Early Cretaceous grains found in our samples. By contrast, the significant proportion of such grains in the modern Siang River implies a Bomi-Chayu source, in which such grains are prevalent. Therefore, the difference between the modern and paleo-samples suggests major river reorganization since deposition of the Sibo sedimentary rocks, i.e. more recent than ~190 ka.

The Bomi-Chayu granites are eroded by the Parlung River, which currently connects to the Siang via the narrow Parlung gorge north of Namche Barwa (Figs. 34 and 48). Previous workers have proposed that the Parlung River originally flowed southeastward through a Yigong-Parlung-Lohit connection draining the Bomi-Chayu rocks (e.g. Lang and Huntington, 2014) (Fig. 48a). Initiation of the Parlung-Siang connection, implying reversal of the Parlung River, is inferred to have occurred during the Quaternary (Lang and Huntington, 2014) and probably during the past 1 Myr (King et al., 2016) (Fig. 48c). We propose that the arrival of major amounts of Early Cretaceous aged zircons in the foreland basin within the last 190 kyr is a direct consequence of Parlung-Yigong capture by the Siang River. This scenario is consistent with previous studies (King et al., 2016; Lang and Huntington, 2014) and our results more precisely constrain the timing estimates inferred in these studies. This Late

Quaternary age implies that the Parlung capture could have been strongly influenced by glacial activity such as drainage-divide retreat or temporary ice damming (e.g. Korup et al., 2010; Oskin and Burbank, 2005; Riedel et al., 2007). The extremely high recent exhumation rates in the Parlung river area reported by King et al. (2016) may originate from this capture and do not necessarily require northward growth of the syntaxial antiform.

6.4. Sediment recycling

The dilution of Transhimalayan detritus shows an increasing trend toward the top of the Sibo-Remi-Siang section. This general trend can be observed in the U-Pb zircon data throughout the entire section. However, some samples do not follow this trend. In the Siang section, the results of Lang and Huntington (2014) are in accordance with the general trend, but our data show a slight decrease in the dilution of Transhimalayan zircons up-section. This difference is almost certainly due to the relatively small number of grains dated from our Siang samples, compared to the number analysed grains by Lang and Huntington (2014).

In the Remi section, the up-section trend of increasing dilution is well depicted up to sample REM7 (depositional age of ~1.5 Ma). In contrast, from REM7 to REM3 (depositional age of ~1 Ma), the Transhimalayan age proportion doubles, from 12% for REM7 to 26% for REM3. Accumulation rates also drastically increase in the same interval, from ~0.21 mm/yr to ~0.55 mm/yr (Fig. 43). From REM3 to the top of the section (Sibo), the trend is respected again. The high proportion of Transhimalayan ages in sample REM3, distinct from the rest of the section, could reflect either natural variation or sedimentary recycling of older Siwalik material into REM3. In the latter case, a reasonable explanation for such a recycled Siwalik component could be the onset of deformation in the Siwaliks between deposition of REM7 and REM3, possibly through activation of the Mingo thrust (Fig. 35). The onset of activity on the Main Frontal Thrust was estimated at <1 Ma in the Kameng section, with activation of an internal Siwalik thrust (the Tippi Thrust) at ~1 Ma (Chirouze et al., 2013). This scenario appears very similar to the proposed evolution in the Remi section, in which recycling was caused by initiation of the Mingo Thrust between ~1.5 and 1 Ma. This is also consistent with the observed transition to more proximal facies of the Upper Siwaliks and the increase in accumulation rate recorded in the Remi section between 2 and 1 Ma, both of which are diagnostic of thrust propagation and loading.

The zircon U-Pb data do not suggest recycling in the younger Sibo outcrop, as the up-section increase in dilution of Transhimalayan zircon is respected in the SIBO sample. This difference

between the REM3 and the SIBO samples, which are stratigraphically close, may be explained by the geographic distance between the two locations. In effect, the SIBO outcrop is located much closer to the main Siang trunk stream, and deposition at this location may be dominated by material carried by the Siang, overwhelming any locally recycled source.

6.5. Apatite U-Pb data: a promising tool for provenance analysis

Comparison of apatite U-Pb data with the more commonly used zircon U-Pb ages allows assessment of the efficiency of apatite U-Pb dating as a provenance method in the eastern Himalaya. As discussed previously, the zircon U-Pb data contain a major population of ages with Transhimalayan characteristics. Zircon U-Pb age peaks older than 300 Ma are interpreted as mainly derived from Indian-plate Himalayan units (Fig. 44) (Gehrels et al., 2011). The Paleozoic age peak is associated with Tethyan Himalayan units, whereas the two main Proterozoic age peaks could be associated with Lesser, Higher or Tethyan Himalayan units (Fig. 44) (Gehrels et al., 2011). The youngest population of ages <40 Ma is also interpreted as predominantly sourced from metamorphic rocks of the Greater Himalayan Series and the Miocene leucogranites (e.g. Lang and Huntington, 2014). The conformity in age population between zircon and apatite U-Pb data indicates high-temperature sources, such as primary igneous and granulite-facies metamorphic rocks.

Although the apatite U-Pb ages are generally younger than the zircon ages, they are also characteristic of the Transhimalayan Bomi-Chayu and Gangdese batholiths. Proterozoic to Late-Paleozoic and Mid- to Late-Cenozoic age populations likely representative of the Greater Himalayan Series, Lesser Himalayan Series and Miocene leucogranites, respectively, are also present. The important decrease up-section of Transhimalayan age populations observed in zircon U-Pb ages is also noticeable with apatite U-Pb dating. However, we note that the relative abundances of Transhimalayan versus Himalayan ages differ between the two systems. These differences are also recognized for the Proterozoic ages, commonly associated with Lesser Himalayan Series rocks, which are less abundant in the apatite than in the zircon U-Pb data. This could be explained by the fact that datable apatites are notoriously sparse in the Lesser Himalayan Series rocks (e.g. Coutand et al., 2014).

While we can therefore explain some of the age differences between zircon and apatite U-Pb data, apatite U-Pb source characterizations are necessary for more detailed investigations. In this study, apatite U-Pb dating has proven to be particularly relevant, as it allowed the detection of very young grains that we interpret as being sourced from the Namche Barwa syntaxis. The coherence between

apatite and zircon U-Pb data demonstrates the quality of such a dataset. Therefore, the apatite U-Pb system represents a powerful provenance tool, especially convenient when combined with AFT analysis using ICP-MS AFT dating. However, double dating may not be the optimal choice to record very young age populations due to the trade-off between the large spots (~30 µm) desirable for U-Pb analysis, and the smaller spots (~15 µm) typically preferred for AFT analysis in order to target precise grain zones. Apatite U-Pb dating independent of AFT dating, preferably in combination with rutile U-Pb analysis to effectively target the high-grade metamorphic rocks, would be a more promising approach for this purpose.

7. CONCLUSIONS

We have constrained the depositional ages of, and applied geochronological provenance techniques to, a previously unstudied Himalayan foreland-basin sedimentary succession located in the extreme east of the orogen, as summarized in Fig. 49. The composite section covers Middle to Upper Siwalik rocks deposited from Late-Miocene to Pleistocene times, with accumulation rates increasing from ~0.21 mm/yr (Upper Middle Siwaliks) to at least ~0.55 mm/yr (Upper Siwaliks). The depositional dating combined with our detrital zircon U-Pb, and double-dated apatite U-Pb and AFT data, permit the following conclusions on the regional evolution to be drawn:

(1) The previously developed hypothesis that the Yarlung-Brahmaputra fluvial connection has existed since at least the Late Miocene (e.g. Lang and Huntington, 2014) is confirmed. We have demonstrated the systematic presence of Transhimalayan detritus throughout the Sibo-Remi-Siang succession since Middle Siwaliks deposition (from at least ~10 Ma) using zircon-U-Pb dating.

(2) The onset of rapid exhumation in the Namche Barwa syntaxis during the Late Miocene, likely at least from ~6 Ma, is recorded in the Sibo-Remi-Siang section. We infer erosion of syntaxial sources directly by combining apatite U-Pb and zircon-rim U-Pb data, and indirectly from a strong up-section dilution in Transhimalayan aged zircons in the succession. This new constraint on the onset of rapid exhumation is consistent with previous estimates (Lang et al., 2016); however, more precise estimates remain necessary to discriminate between proposed mechanisms for the initiation of very rapid exhumation in the Namche Barwa syntaxis.

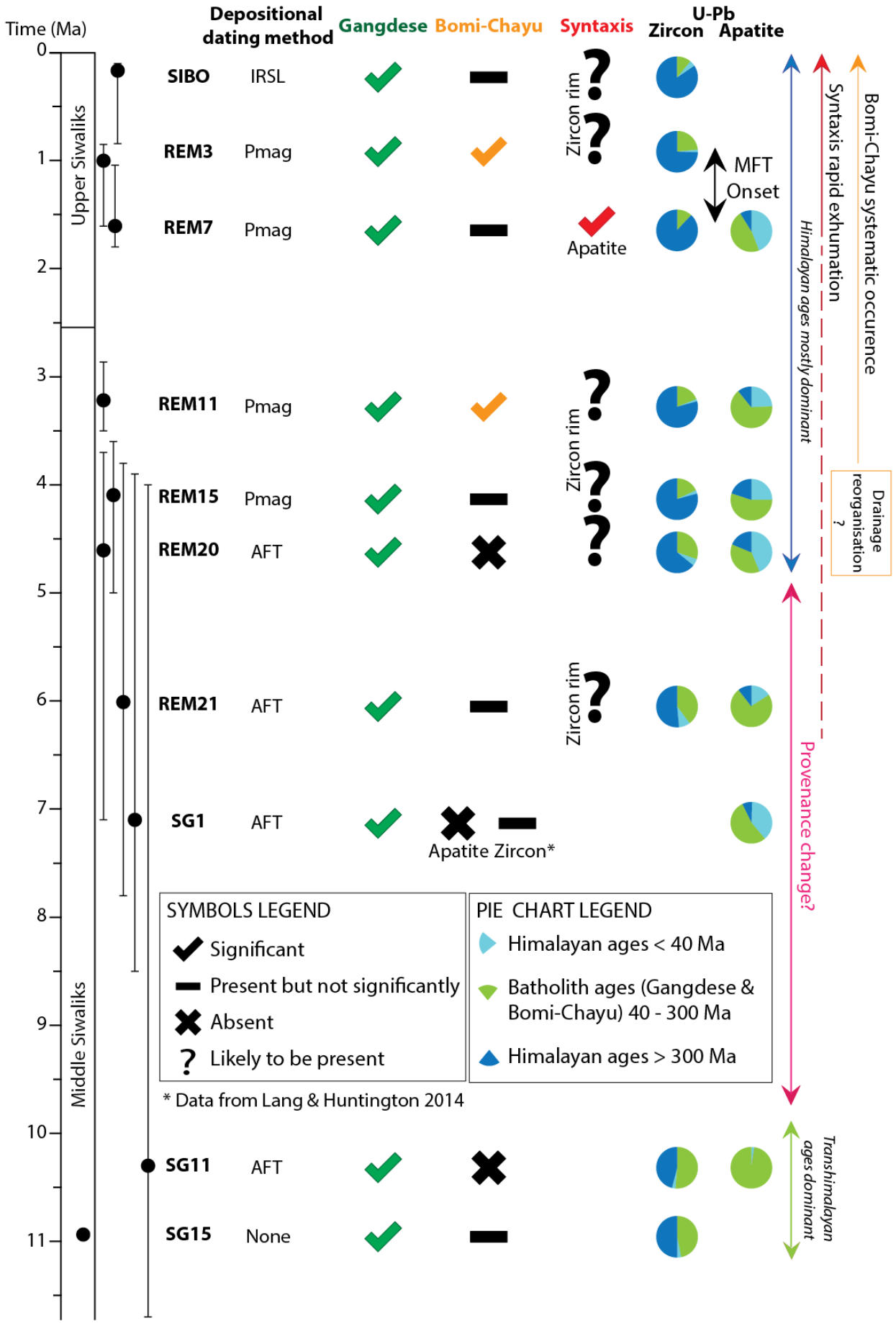
Time (Ma)
Depositional dating method
Gangdese
Bomi-Chayu
Syntaxis
U-Pb Zircon
Apatite
Upper Siwaliks
Middle Siwaliks
SIBO
IRSL
REM3
Pmag
REM7
Pmag
REM11
Pmag
REM15
Pmag
REM20
AFT
REM21
AFT
SG1
AFT
SG11
AFT
SG15
None
Zircon rim
Apatite
MFT Onset
Apatite Zircon*
Bomi-Chayu systematic occurence
Syntaxis rapid exhumation
Himalayan ages mostly dominant
Drainage reorganisation ?
Provenance change?
Transhimalayan ages dominant
SYMBOLS LEGEND
Significant
Present but not significantly
Absent
Likely to be present
PIE CHART LEGEND
Himalayan ages < 40 Ma
Batholith ages (Gangdese & Bomi-Chayu) 40 - 300 Ma
Himalayan ages > 300 Ma
* Data from Lang & Huntington 2014

Fig. 49: *Summary of depositional dating and provenance analysis in Sibo-Remi-Siang succession with main interpreted events. Dating methods are indicated for each sample; IRSL: infra-red stimulated luminescence, Pmag: magnetostratigraphy, AFT: apatite fission-track. Depositional ages for analysed samples are plotted with error bars, determined according to the different dating techniques. As maximum depositional ages below sample REM15 are constrained by AFT dating only, the upper error bars are prolonged up to REM15, the oldest sample dated by magnetostratigraphy. Paleo-Brahmaputra and Bomi-Chayu provenances determined with apatite and zircon U-Pb dating are indicated in green and orange, respectively. Detection of the rapidly exhuming syntaxis with apatite U-Pb dating is shown in red, the possible occurrence of syntaxis signal refers to the U-Pb zircon-rim data. Pie charts of apatite and zircon U-Pb ages are copied from Fig. 44.*

(3) Deformation of Siwalik sedimentary rocks in the Remi section initiated at ~1.5 Ma, resulting from southward propagation of Himalayan deformation and onset of activity on the intra-Siwalik Mingo Thrust. This deformation is recorded by sedimentary zircon U-Pb ages suggesting recycling at ~1 Ma, and is supported by the increase in accumulation rates at the same time.

(4) Parlung-Yigong capture by the Siang River is constrained to have occurred after ~190 ka, as shown by the arrival of significant amounts of Early-Cretaceous zircons characteristic of the Bomi-Chayu batholiths within this time interval. We suggest that this capture has enhanced erosion and exhumation rates in the region NE of the Namche Barwa syntaxis.

ACKNOWLEDGEMENTS

We acknowledge financial support from Marie Curie Initial Training Network iTECC funded by the EU REA under the FP7 implementation of the Marie Curie Action, under grant agreement 316966. We thank L. Gemignani for assistance in sample collection, M. Bernet, M. Balvay, F. Coeur and F. Senebier for helping in AFT mount preparation, R. Abrahami for sharing her experience in IRSL dating and Sally Lowick for the IRSL dating. Isotope analysis at NIGL was funded by an award from NERC Services and Facilities Steering Committee. G. D-N acknowledges funding from the Marie Curie Career Integration Grant FP7 CIG grant 294282 'HIRESDAT' and Horizon 2020 ERC grant 649081 'MAGIC'. ISTerre is part of Labex OSUG@2020 (ANR10 LABX56).

SUPPLEMENTARY MATERIAL

The supplementary material of this chapter is presented in Appendix III as listed here.

Analytical methods:

- Luminescence dating
- Detrital apatite fission-track and U-Pb double dating
- Magnetostratigraphy
- Detrital zircon U-Pb dating

Data tables:

- Table S1: Sample location
- Table S2: Magnetostratigraphy data
- Table S3: Zircon U-Pb source area compilation
- Table S4: Apatite fission-track - U-Pb data
- Table S5A: Zircon core and rim U-Pb data
- Table S5B: Zircon standard U-Pb data

CHAPTER 4

Onset of rapid exhumation in the Namche Barwa syntaxis

To be formatted and submitted for publication, post Ph.D. thesis submission, with additional input and co-authorship of:

Gwladys Govin [1], Yani Najman [1], Peter van der Beek [2], Ian Millar [3], Matthias Bernet [2], Lorenzo Gemignani [4], Pascale Huyghe [2], Jan Wijbrans [4] and Guillaume Dupont-Nivet [5,6]

1- Lancaster Environment Centre, Lancaster University, UK

2- ISTerre, Université Grenoble Alpes, Grenoble, France

3- Geochronology and Tracers Facility, NIGL, British Geological Survey, Keyworth, UK

4 - VU University Amsterdam, Faculty of Earth and Life Sciences, Netherlands

5-Department of Earth and Environmental Sciences, Potsdam University, Germany

6- Key Laboratory of Orogenic Belts and Crustal Evolution, Ministry of Education, Beijing, China

ABSTRACT

The evolution of the eastern and western Himalayan syntaxes is debated: they have been subjected to anomalously young (~10 Ma) high-grade metamorphism, melting and unusually high rates of exhumation (up to 10 mm yr^{-1}), compared to the main arc of the range where peak metamorphism occurred in the Early Miocene and exhumation rates of ≤2 mm/yr are more common. The timing of metamorphism and the onset of rapid exhumation of the eastern Namche Barwa syntaxis is poorly constrained. Bedrock studies suggest rapid exhumation since either 3-4 Ma or 8-10 Ma and detrital studies infer the onset of rapid exhumation in the last 7 Myr, up to Plio-Pleistocene times. Several models have been proposed to explain the syntaxial evolution, invoking different controlling factors, such as compressive crustal-scale folding orthogonal to the strike of the mountain belt, subduction geometry in the indentor region, or tectonic-surface process interactions and crustal channel flow. To understand the Namche Barwa syntaxis evolution, we report new detrital zircon fission-track, white-mica ^{40}Ar-^{39}Ar and rutile U-Pb data from the most proximal detrital record of material eroded from the syntaxis by the paleo-Siang River: the dated Sibo-Remi-Siang Siwalik located directly downstream of the syntaxis. Our results, along with published detrital data from the syntaxis region are incorporated in a 1D version of the thermokinematic model *Pecube*. We highlight the high relevancy of using the rutile U-Pb thermochronological system for studying the syntaxis and we

suggest an older onset of exhumation of the Namche Barwa, as old as ~13 Ma, at slower rate (~4 mm yr^{-}1) than widely expected.

1. SIGNIFICANCE

The Himalaya is the result of ongoing collision between Asian and Eurasian plates which begun at ~60-50 Ma. Evolution of rock exhumation in the main Himalayan arc is relatively well understood over the last ~20 Ma. However, the history of the eastern and western terminations, the Himalayan syntaxes, remains poorly known and vigorously debated. Active research suggests they have been subjected to extremely high exhumation rates in the last 10 Ma. Using thermochronological dating of sediments eroded from the eastern syntaxis, we show that the onset of rapid exhumation is possibly 1-3 Ma older and up to twice as slow as predicted. Our results bring new insights regarding the early development of the eastern Himalayan termination, this is critical information to take into account when attempting to explain the evolution of the eastern Himalayan syntaxis.

2. INTRODUCTION

The development of the Himalayan syntaxes remains highly debated; they have been subjected to anomalously young (<10 Ma) high grade metamorphism, melting and high rates of exhumation (>5 to 10 km/Myr) (Booth et al., 2009; Booth et al., 2004; King et al., 2016; Lang et al., 2016; Seward and Burg, 2008; Zeitler et al., 2014), compared to the central Himalaya where Early Miocene metamorphism and modern exhumation rates of ~2mm/yr are common (e.g. Thiede and Ehlers, 2013). The eastern Namche Barwa syntaxis exhibits extreme erosion rates (>5 mm/yr (Finnegan et al., 2008)) and topography (up to 5.6 km of local relief (Korup et al., 2010)); exceptionally young geo- and thermo-chronologic ages (rutile U-Pb <3 Ma) implying very high exhumation rates (>4 km/Myr) (Bracciali et al., 2016 and references therein); a poorly known complex structural setting (Burg et al., 1998) and a peculiar drainage pattern (Zeitler et al., 2014). These outstanding geologic and geomorphologic features of the Namche Barwa syntaxis provoke a wide interest in the geoscience community.

The processes involved in the evolution of the eastern syntaxis rapid exhumation are poorly understood. Several models have been proposed to explain the syntaxial rapid exhumation: 1) Structural buckling due to contraction in the orogenic indentor corner (Burg et al., 1997); 2) Subduction geometry implying collision and deformation of geometrically-stiffened syntaxial indentor in subducting slab (Bendick and Ehlers, 2014); 3) Ductile extrusion of weak lower crust from beneath Tibet by “channel flow” decompression (Beaumont et al., 2001), initiating modestly in

Miocene times followed by a Pleistocene acceleration of the syntaxis exhumation (Bracciali et al., 2016); 4) Thermomechanical feedback between focused and intense erosion and growth of the Namche Barwa crustal antiform (Zeitler et al., 2014; Zeitler et al., 2001). The latter model has been successively challenged by the work of Wang et al. (2014b) suggesting that fluvial incision in the Namche Barwa region is the result of uplift; and by provenance studies inferring that the major capture leading to the Yarlung-Brahmaputra system predates substantially the onset of the Namche Barwa exhumation and in such oppose the tectonic aneurysm model (e.g. Bracciali et al., 2015; Lang and Huntington, 2014). Although these models are difficult to test, knowledge of the timing of initiation and rates of the exhumation of the eastern syntaxis is a prerequisite necessary to understand how the eastern syntaxis developed.

The decompression related to exhumation has been controversially suggested to have occurred after 4 Ma (Burg et al., 1998; Seward and Burg, 2008) and around 10 Ma (Booth et al., 2009; Zeitler et al., 2014; Zeitler et al., 2001) from bedrock studies. However, the earlier history of the sampled region removed by erosion is archived in the sedimentary record and detrital studies are necessary to fully comprehend the syntaxis exhumation history. Published Neogene detrital thermochronological data from the eastern Himalayan foreland basin have inferred the syntaxial exhumation to have increase by a 5 to 10-fold increase between 5 and 6 Ma (Lang et al., 2016). The modern riverbed detritus present very young thermochronologic ages, in particular zircon fission-track (ZFT) ≤2 Ma, white-mica ^{40}Ar-^{39}Ar (Mar) ≤2 Ma and rutile U-Pb (RU-Pb) ≤9 Ma, which have been interpreted as characteristic syntaxial signals of the syntaxis (Bracciali et al., 2016 and references therein; Gemignani et al., submitted). Here we track these signals in Neogene sediments the most proximal to- and directly downstream from- the syntaxis (Govin et al., in review) and we model these new results along with published detrital data to answer the debated questions: When has the rapid exhumation begun and how substantial was the change in exhumation rate?

3. GEOLOGICAL SETTING

The Himalayan orogen is the result of the Cenozoic collision and ongoing convergence between India and Asia (e.g. Najman et al., 2010), the Indus-Yarlung suture zone (IYSZ) is the boundary between the two plates (Le Fort, 1999) (Fig. 50). The Yarlung-Tsangpo flows eastward along the suture zone before crossing the range as the Siang River, at the eastern termination; where the structural trend direction changes sharply from EW to NS. The Namche Barwa syntaxis corresponds to the NE Indian plate indentor, where the Indian rocks have deformed into a sharp NE terminating complex antiformal uplift that has folded the IYSZ (Burg et al., 1997; Palin et al., 2015). The latter antiform has

been suggested to expand both vertically and laterally and migrate northward since its initiation (Seward and Burg, 2008). The northern tip of the syntaxis is bounded by the YTSZ with the dextral Jiali–Parlung Fault to the NE and the north dipping Nam-La thrust to the south (e.g. Zeitler et al., 2014) which has been proposed to act as the southern boundary of a pop-up structure with the Namche Barwa massif at its core (Ding et al., 2001). The Namche Barwa and the Gyala Peri massifs culminate at >7 km in the core of the syntaxis composed of medium to high grade metamorphic crystalline rocks of the Greater Himalayan Series (GHS) intruded by Miocene leucogranites.

A youngest phase of metamorphism restricted to the northern tip of the syntaxis is recorded by bedrock zircon U-Pb ages of 3–10 Ma (Booth et al., 2004; Zeitler et al., 2014). By contrast, the SW part of the syntaxis shows older ages (e.g. Palin et al., 2015) with, for instance, RU-Pb >9 Ma (Bracciali et al., 2016). Additionally, the entire syntaxial anticline shows evidences of Miocene (c.a. 24 to 16 Ma) metamorphic events within GHS rocks similar to the main part of the Himalaya (Burg et al., 1998; Palin et al., 2015).

South of the syntaxial GHS, the Siang River drains the low grade meta-sediments of the Lesser Himalayan Series (LHS), separated from the GHS by the Main Central Thrust (MCT). Downstream lie the sub-Himalayan series which contain the Neogene-Quaternary sediments of the Siwalik Group and the undeformed deposits of the Himalayan foreland basin. The Siwalik group is bounded by the Main Boundary Thrust (MBT) to the north and the Main Frontal Thrust (MFT) to the south (Gansser, 1983; Hodges, 2000). The easternmost Siwalik sediments of the Sibo-Remi-Siang (SRS) section were deposited between ~11 and 0.2 Ma and constitute the archive the most proximal to the Siang River and thus to the syntaxis (Govin et al., in review) (Fig. 50).

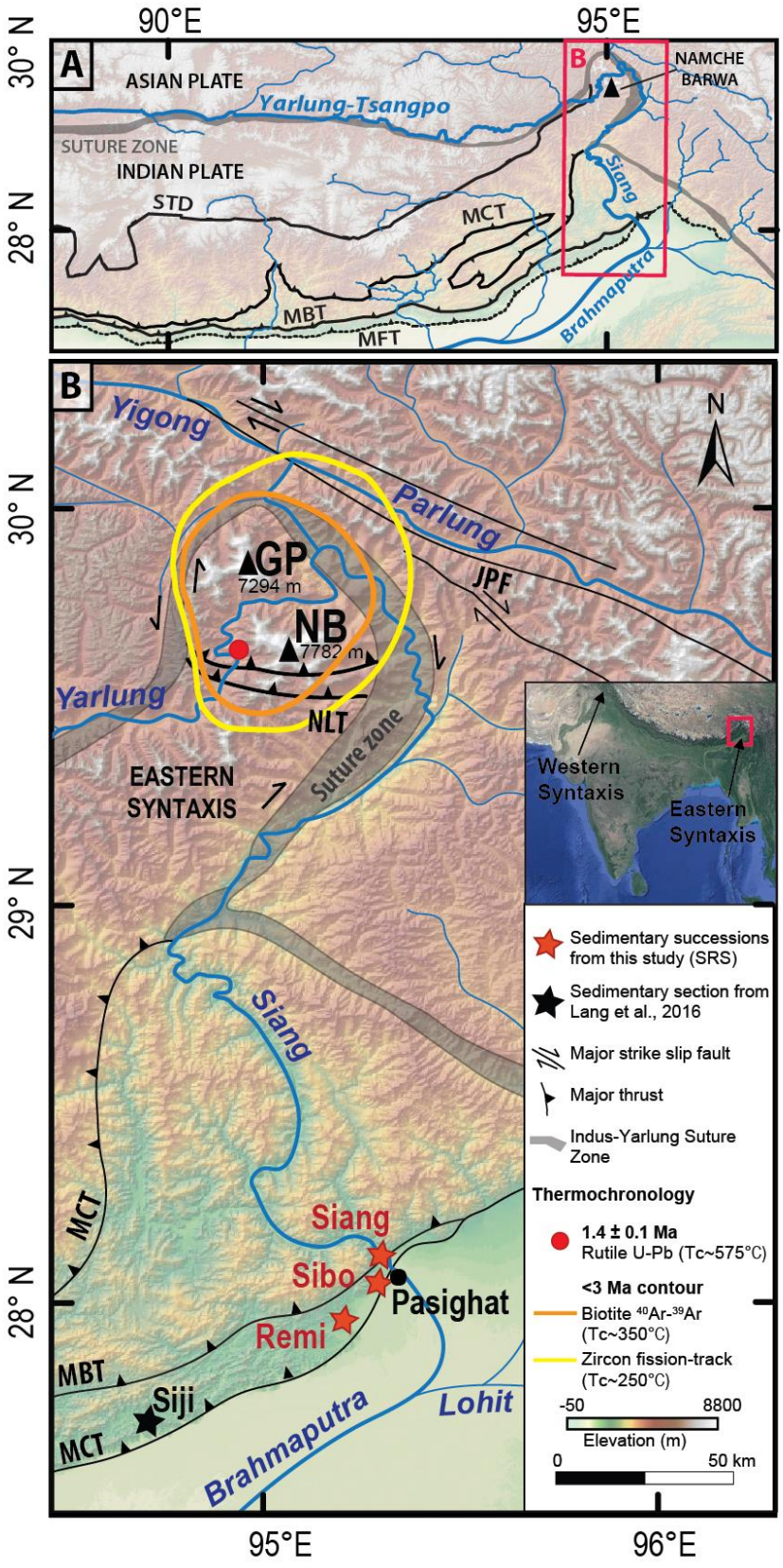

Fig. 50: *(a) Topography and main geologic features of the eastern Himalaya (modified from Govin et al., in review). Abbreviations are: MFT – Main Frontal Thrust; MBT – Main Boundary Thrust; MCT – Main Central Thrust; STD – South Tibetan Detachment. (b) Topography and main geologic features of*

the Namche Barwa syntaxis area (modified from Lang et al., 2016; Bracciali et al., 2016; Govin et al., in review; and references therein). The red stars labelled represent the Sibo-Remi-Siang section (Govin et al., in review); the black star shows the Siji section (Lang et al., 2016). Pasighat is the location of the Siang modern riverbed composite sample from Bracciali et al. (2016); Enkelmann et al. (2011); Gemignani et al. (submitted); Lang et al. (2016); Stewart et al. (2008). Abbreviations are: NB - Namche Barwa, GP – Gyala Peri, NLT – Nam La Thrust, JPF – Jiali-Parlung Fault. Yellow and Orange lines are contours of cooling ages <3 Ma from zircon fission-track and biotite ^{40}Ar-^{39}Ar dating, respectively; red dot indicates rutile U-Pb age of 1.4±0.1 Ma (Bracciali et al., 2016; and references therein).

4. MATERIAL AND METHODS

4.1. Thermochronology

Minerals from ten sandstones, sampled at regular stratigraphic interval throughout the SRS section were isolated by standard mineral separation techniques at the NERC Isotope Geosciences Laboratory (NIGL), Keyworth (UK). The ZFT dating was carried out at ISTerre laboratory, Grenoble (France), the MAr dating at VU University, Amsterdam (The Netherlands) and the RU-Pb dating at NIGL, Keyworth (UK). The extracted youngest age populations for each sample and each system are presented in Fig. 51, against their depositional age from Govin et al. (in review). The minimum age peaks have been determined using the minimum age mixture model from Density Plotter program (Vermeesch, 2012) for ZFT and MAr data; and regressing together the youngest ages through a fixed common Pb for RU-Pb data. Results, sample locations, sample preparation and analytical methods are provided in the Supplementary Material.

4.2. Thermokinematic modelling

We use a modified version of *Pecube*, a finite-element numerical code used for interpreting thermochronological data (Braun, 2003; Braun et al., 2012) to predict a time series of cooling ages resulting from a step change in the late Cenozoic exhumation rate. We use a 1-D version of the code (e.g. Thiede and Ehlers, 2013) and aim to fit the minimum age peaks observed in the detrital data. We therefore model the most rapidly exhuming part of the syntaxis (i.e. the core of the Namche Barwa massif), implicitly assuming the locus of most rapid exhumation has remained fixed through time. Pecube accounts for heat advection during exhumation and predicts thermochronological ages using a mathematical model for fission-track annealing and diffusion models for noble-gas based thermochronometers (Braun et al., 2006). The 1D model neglects lateral heat transfer out of the system as well as potential temporal variations in topographic relief. The former is probably

insignificant compared to the extreme vertical component of heat transfer. Varying topographic relief is extremely hard to resolve from detrital data (e.g. Whipp et al., 2009). Thermal parameters used in the model are detailed in the Supplementary Material. We use the annealing parameters for zero-damage zircon (Rahn et al., 2004) for predicting ZFT ages using the annealing equations of Galbraith and Laslett (1997); the diffusion parameters of Hames and Bowring (1994) and an average grain size of 250 µm for predicting MAr ages; and the diffusion parameters of (Cherniak, 2000) and a grain size of 100 µm for RU-Pb ages.

We use the code in inverse mode, employing the Neighbourhood Algorithm inversion (Sambridge, 1999) to explore the parameter space. We explore simple two-stage exhumation scenarios reflecting changes in three parameters: the time of change in exhumation rate (between 0 and 15 Ma), and the initial, and the final exhumation rate, which were respectively fixed between 0 and 2 km Myr^{-1}, and between 2 and 10 km Myr^{-1}, values characteristic of rates interpreted from bedrock samples. For each model run, we used the chi-square deviation to compare cooling age predictions to our observations for each thermochronometer system. The composite reduced chi-square error from all three sets of models is shown in Fig. 52.

5. RESULTS

ZFT, MAr and RU-Pb minimum age peaks from the SRS section are presented in Fig. 51, and show a general trend of younging up-section although exceptions are common. The minimum age peaks are comprised between 3.3±0.3 and 16.0±1.5 Ma for ZFT; 4.2±0.4 and 18.2±0.4 Ma for MAr; and 2.5±0.1 and 35.8±8.5 Ma for RU-Pb. Comparison of these detrital mineral cooling youngest age components with their host sediment depositional age provides lag times (Garver et al., 1999). The depositional ages of the upper part of the section has been constrained through luminescence dating (SIBO) and magnetostratigraphy (REM3 to REM15); the lower part (REM20 to SG15) is constrained by a maximum depositional age from apatite fission track dating (Govin et al., in review). Although maximum depositional ages approximate the depositional ages, it leads to large uncertainties that we have taken into account when considering lag times. Data points from the upper part of the section (samples SG1 to SIBO, depositional ages of ~0.2 and 7.1 Ma, respectively) generally show young minimum age peaks, especially for RU-Pb ages, and lag times <6 Ma with a majority <2.5 Ma. In contrast, the lower part of the section (samples SG11 and SG15, depositional ages of ~10.3 and 11.0 Ma, respectively) presents older ages and lag times >4 Ma and up to >20 Ma. The lowest temperature thermochronological system of this study is ZFT (Tc up to 380°C; Rahn et al., 2004), followed by MAr (Tc up to 450°C; Hames and Bowring, 1994; Reiners and Brandon, 2006) and the

highest Tc is reached by the RU-Pb system (Tc up to 750°C; Cherniak, 2000). The youngest age peaks show expected older ages for higher Tc thermochronological system, whereas this order is not respected in the upper part of the section.

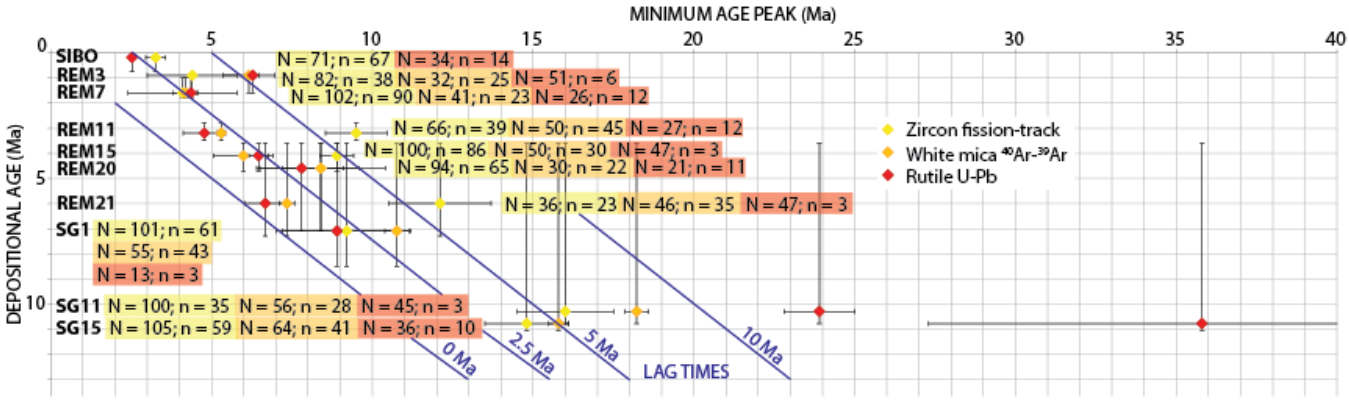

Fig. 51: *Minimum age peak data and lag times from the SRS section. Sample names (from Govin et al., in review) are indicated at their depositional age level. ZFT, MAr and RU-Pb minimum age peaks are represented in yellow, orange and red, respectively; with their horizontal error bars. N indicates the total number of grains dated following data screening and n the number of grains from which the minimum age peak has been determined (see Supplementary Material) for each thermochronological system in its corresponding colour frame. Vertical error bars correspond to the depositional age errors from Govin et al. (in review). Lag times of 0; 2.5; 5 and 10 Ma are indicated with dark blue lines.*

6. DISCUSSION

6.1. Syntaxial signal

Short lag times from ZFT (<3 Ma) and MAr (<4 Ma) dating in Siwalik sediments deposited by the paleo-Brahmaputra River have been interpreted as reflecting the rapid exhumation of the eastern syntaxis (Chirouze et al., 2013; Lang et al., 2016). These lag times are similar to ZFT and MAr lag times from the upper part of the SRS section, approaching cooling ages from modern riverbed sediments. By comparing bedrock and detrital thermochronologic ages in the syntaxis area, Bracciali et al. (2016) have characterised ZFT ages <2Ma and MAr ages <2Ma as typical signals of syntaxial detritus in riverbed; additionally, the authors identify RU-Pb ages <9Ma as unique to the syntaxis and not found in the typical GHS sequence. The RU-Pb <9 Ma ages are systematically observed in the upper part of the SRS section. Therefore, we argue that detritus from this upper part (SG1 to SIBO) are sourced from the rapidly exhuming syntaxis confirming the young zircon-rim U-Pb data interpretation of Govin et al. (in review). By contrast, the lower part of the SRS section (SG15 to SG11) is dominated by longer lag times and older minimum age peaks (RU-Pb>22 Ma). The latter

ages are also observed in the modern Yarlung-Tsangpo deposits upstream of the syntaxis and in Brahmaputra rivers draining the southern Himalayan slopes farther west from the syntaxis (Bracciali et al., 2016). This suggests that the lower part of the SRS section records Himalayan erosion prior to the rapid exhumation of the Namche Barwa syntaxis.

Overall, our data indicate a sharp lag time decrease up-section between ~10 and 7 Ma that we interpret as reflecting the onset of the rapid exhumation of the Namche Barwa syntaxis. This trend is particularly well defined with the RU-Pb system with few exceptions such as sample REM3 which stands out from the neighbouring samples' minimum ages. This sample has previously been inferred to result from sedimentary recycling (Govin et al., in review) and for this reason will not be considered further.

The disrupted order of the minimum age peaks for the different systems in the upper part of the section is also observed, to a minor extent, in samples from modern rivers draining the syntaxis (Bracciali et al., 2016). These disruptions can partly be interpreted as a consequence of isotherm perturbation in the context of rapid exhumation. For instance, under rapid cooling conditions, zircons are likely damage-free leading to an elevation of the ZFT system Tc approaching MAr Tc (Reiners and Brandon, 2006 and references therein). However, in the SRS section, the disruptions seem too substantial to be solely explained by isotherm perturbation, as the youngest ZFT and MAr ages are respectively up to >5 Ma and ~2 Ma older than RU-Pb ages in some samples (e.g. REM21) and the Tc prediction of RU-Pb remain higher of >200°C than ZFT and MAr Tc (Cherniak, 2000). Here we investigate the potential factors explaining these discrepancies.

The minimum age peaks have been defined in the same manner for MAr and ZFT, but differently for RU-Pb ages (see Supplementary Material). However, the youngest RU-Pb age populations determined using the same procedure as for MAr and ZFT are very similar to those defined with the more robust method we have adopted for RU-Pb (see Supplementary Material). Thus, the differences in the minimum age peak determination procedure of this study do not explain the thermochronological disruptions. However, the typical age error for each thermochronological system (e.g. ZFT error >MAr error) influences the minimum age peaks. The number of dated grains together with the data screening strategy also plays an important role in the youngest age peak determination, although for instance in sample SG1, the minimum RU-Pb age peak extracted from a low number of dated rutiles is younger than the minimum MAr age peak determined with a higher number of dated white micas. Gemignani et al. (submitted) have observed dissimilarities in young

age abundances in different samples from the same location (Pasighat), despite the use of similar analytical procedures for both detrital ZFT and MAr systems for each sample (Enkelmann et al., 2011; Lang et al., 2016; Stewart et al., 2008). Generally, age distributions from detrital studies are undoubtedly indicative of major age populations but only approximately represent the natural proportions within a sample, minor age population could unlikely be missed out (e.g. Vermeesch, 2004).

Another possible explanation for the thermochronological disruption is the limitations relative to each thermochronological system, which can occasionally prevent the dating of young ages leading to biases of the minimum age peak toward older ages, and therefore limit the tracking of the rapidly exhuming eastern syntaxis, as discussed by Bracciali et al. (2016). These are 1) the limited robustness of ZFT data in defining the true age components of a sample (e.g. zircon etching, zircon U content, and associated ZFT biases (Malusà et al., 2013)); 2) the potential biases from source fertility (e.g. Malusà et al., 2016) (today, white micas are reputedly scarce in the Namche Barwa area); and 3) the analytical limitation (e.g. grain size, low Ar content for young micas, fission-track density). Since the SRS section is the most proximal location to the syntaxis in the foreland basin, the dilution effects for each dated mineral are minimized. Although RU-Pb ages are commonly discordant due to high Pb content (e.g. Bracciali et al., 2013), Bracciali et al. (2016) demonstrate the efficiency of rutile U-Pb in capturing differences in provenance related to the thermochronologic evolution of the rock sources at upper crustal level, especially those of the rapidly exhuming Namche Barwa. Whilst RU-Pb ages <9 Ma are unique to the syntaxis, such ages for the ZFT and MAr systems are encountered in Himalaya outside of the syntaxial region (e.g. Bracciali et al., 2016). For these reasons and because of the limitations of ZFT and MAr systems that we have discussed, we particularly rely on the RU-Pb data.

6.2. Model of the syntaxial evolution

To quantitatively constrain the evolution of the exhumation of the Namche Barwa syntaxis, we use a 1-D thermokinematic model that predicts cooling ages resulting from a step change in exhumation rate. We model three selections of data, all together incorporating our new data, along with modern riverbed ZFT, MAr and RU-Pb data from Pasighat (Fig. 50) (Bracciali et al., 2016; Enkelmann et al., 2011; Gemignani et al., submitted; Lang et al., 2016; Stewart et al., 2008); and Siwalik ZFT and MAr data from the Siji section (Lang et al., 2016) ~60 km west of the SRS section (Govin et al., in review).

Model A includes all available data (ZFT, MAr and RU-Pb). The inversion results show similar values between best fit and expected model despites a wide low misfit (i.e. high probability) region in the

scatter plot (Fig. 52a). This model predicts an initial exhumation rate similar to the estimations of Gemignani et al. (submitted) from modern riverbed ZFT and MAr ages in the southern Himalayan flank west of the syntaxis region (0.5-1.5 km Myr^{-1}). The model calculations of the final exhumation rate (5.3±1.7 km.Myr^{-1}) are higher than the estimates of Gemignani et al. (submitted) (2-4 km Myr^{-1}), but consistent with those of Bracciali et al. (2016) (>4 km Myr^{-1}). The model predicts an acceleration of exhumation significantly earlier than the suggested Plio-Pleistocene rapid exhumation of the latter authors, but consistent with predictions from a Siwalik study based on detrital ZFT and MAr ages (~6 Ma; Lang et al., 2016). Overall, this model reproduces well the input data although it fits better the RU-Pb data than the ZFT and MAr data.

Despite the fact that it only incorporates the RU-Pb data, model B fits particularly well the entire dataset, including ZFT and MAr data (Fig. 52b). In contrast to model A, it predicts a simple exhumation history for each thermochronologic system. Additionally, the region of low misfit is better defined. Initial and final exhumation rates in this model are lower than in the previous model, and particularly consistent with estimations of Gemignani et al. (submitted). The resulting onset time of 12.8±1.6 Ma is older than inferred from all published estimations (up to 10 Ma, Zeitler et al., 2014).

Lastly, model C (Fig. 52c) compiles the ZFT and MAr solely and its outcome not only does not fit the RU-Pb data, but neither particularly well the ZFT nor MAr data compared with models A and B. The calculated initial exhumation rate is inconsistent with the estimations of Gemignani et al. (submitted). Furthermore, misfit values of the poorly defined low misfit area are higher than those of the previous models.

Ultimately, model B fits better the ages from the three thermochronological systems with more accurate inversion results in comparison with model A and C. For this reason, and considering the RU-Pb efficiency in tracking the syntaxial detritus discussed earlier, we argue that model B is the more conclusive scenario. Consequently, we suggest that the change in exhumation rates of the Namche Barwa could be as old as ~13 Ma, with high but not extreme exhumation rates in the order of ~4 km Myr^{-1}, consistent with the estimates of Gemignani et al. (submitted).

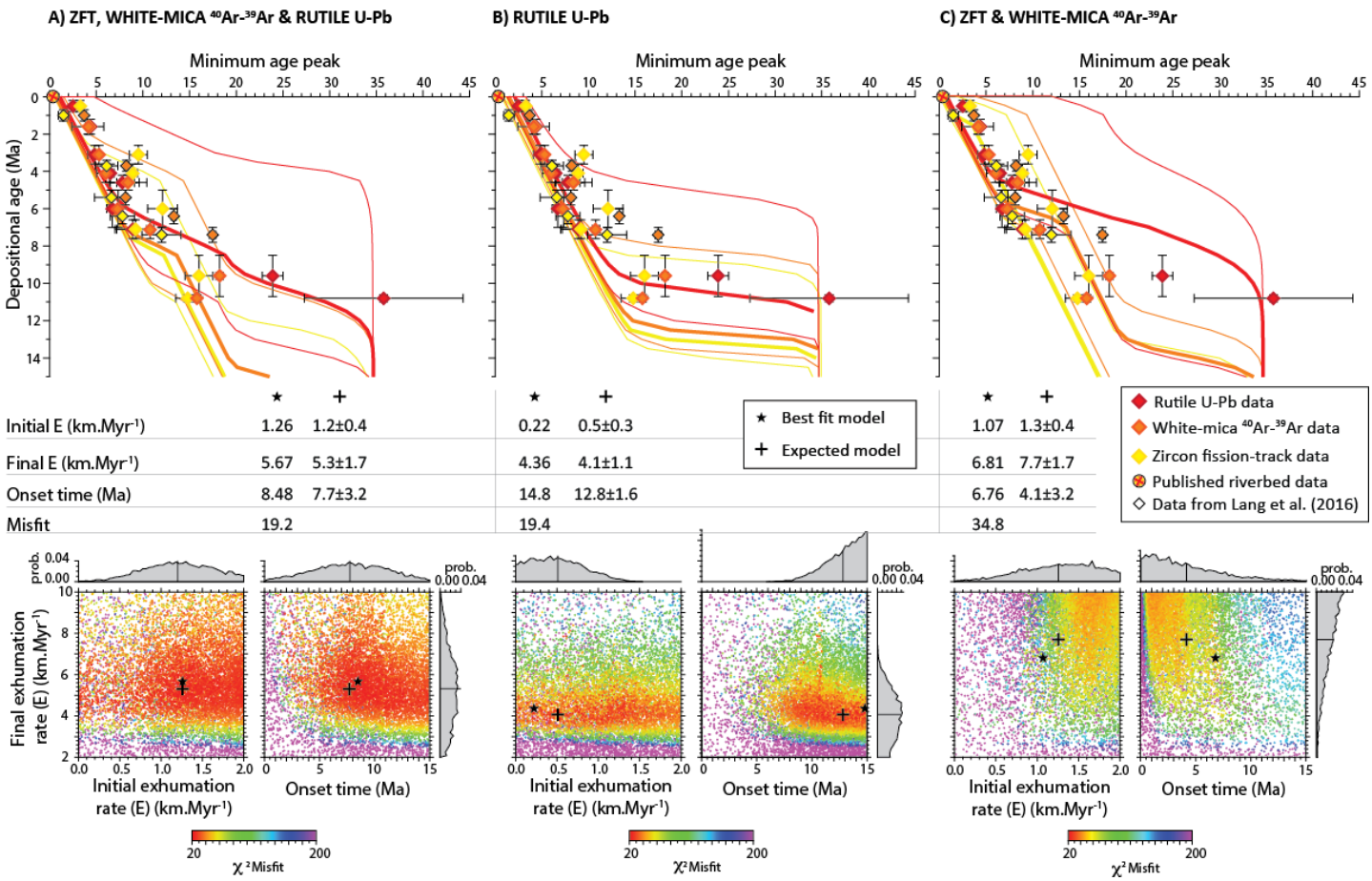

Fig. 52: *Results of thermal modelling of detrital data from Siwalik sediments from this study (ZFT, MAr and RU-Pb), Lang et al. (2016) (ZFT and MAr) and modern riverbed data from Bracciali et al. (2016); Enkelmann et al. (2011); Gemignani et al. (submitted); Lang et al. (2016); Stewart et al. (2008) (ZFT, MAr and RU-Pb). Models incorporating a) all data; b) RU-Pb data only and c) ZFT and MAr data only). The forward lag time results for the three thermochronometers are presented in the top diagrams, in which the bold and thin coloured lines indicate the best fit model results and the end-members of the expected model, respectively. The table indicates the initial and final exhumation (E) rates and the onset time of the best fit and the expected model resulting from the inversion of which the misfit scatter plots along with corresponding probability density plots are illustrated in the bottom.*

6.3. Implications for the syntaxis development

Our new estimates for the initiation of the rapid exhumation of the Namche Barwa syntaxis allows a revision of our knowledge regarding the early development of this peculiar syntaxial evolution and its timing.

As mentioned previously, Bracciali et al. (2016) invoke a ductile extrusion of weak lower crust from beneath Tibet initiating modestly in Miocene times followed by a Pleistocene acceleration of the syntaxis exhumation; such that the domal pop-up of the northern part of the syntaxis has exposed a deep-seated metamorphic zone of GHS rocks "before its time" (relative to the main Himalayan arc), providing a window into processes within the deep crust of the Himalayan hinterland. This interpretation is compatible with the study of Palin et al. (2015) inferring two stage cooling in the syntaxis area, with an initial slow cooling occurring from ~23 Ma and a final rapid cooling from ~8 Ma, the latter corresponding to the rapid exhumation of the syntaxial dome. Since our results indicate that the initiation of the rapid exhumation of the Namche Barwa syntaxis could possibly be as old as ~15 Ma, they are compatible with the hypothesis that both the early Miocene Himalayan exhumation and the later syntaxial exhumation episodes are related. However, our data do not provide indications of extreme syntaxial exhumation rates initiating in Plio-Pleistocene time, as suggested by Bracciali et al. (2016). Our conclusions are thus dissimilar, but if regarded in detail both datasets are not incompatible. Estimates of the onset of rapid exhumation of Bracciali et al. (2016), anytime from 7 to 3 Ma, are mainly based on thermochronological data including ZFT, MAr and RU-Pb ages, are comparable to the results of our model A, also including ZFT, MAr and RU-Pb ages. Additionally, bedrock studies and previous detrital studies (e.g. Bracciali et al., 2016; Burg et al., 1998; Burg et al., 1997; Lang et al., 2016; Seward and Burg, 2008) do not contain as long a history of syntaxial exhumation due to either overprinting by later metamorphism or removal by tectonism or erosion in the source region, or lack of older sedimentary archives. This disadvantage may explain the very young ages (<10 Ma) systematically proposed for the onset of rapid exhumation in previous studies.

The tectonic aneurysm model (Zeitler et al., 2001) implying an early onset of syntaxial exhumation at ~10 Ma, caused by river capture, is better supported by our estimations. The early version of this model (Zeitler et al., 2001) invokes major drainage reorganisation, which would have initiated and sustained rapid exhumation of the syntaxis. A major capture event such as the Yarlung-Irrawaddy by the Siang-Brahmaputra River, has been inferred in Early Miocene times by later studies (e.g. Bracciali et al., 2015; Robinson et al., 2014), implying the non-synchronicity of the two events and therefore calling into question the original tectonic aneurysm model. Our new data showing earlier onset of rapid syntaxial exhumation brings the event closer to synchronicity with the timing of proposed river capture of the Yarlung Tsangpo by the Brahmaputra, although not identically close. Uncertainty in depositional age dating may explain the discrepancy. Furthermore, recent studies (Govin et al., in review; King et al., 2016; Lang and Huntington, 2014) provide evidence of the complexity of the

drainage evolution in the Namche Barwa area and propose multiple capture events in the Late Miocene in the Namche Barwa area. The timing of river capture which first brought arc material to the Bengal Basin need not be the same river capture as caused the river to flow over the syntaxis. Therefore, although we cannot prove the focused and intense erosion of the Yarlung-Siang River at the origin of the rapid growth of the Namche Barwa, we do not challenge this model.

7. CONCLUSION

We have 1) collected detrital thermochronological data using three different systems, ZFT, MAr and RU-Pb in the Siwalik sediments the most proximal to the eastern Himalayan syntaxis deposited from 11 Ma; 2) extracted the minimum age peaks for each system and 3) modelled our results, along with published detrital ages from modern river bed and Siwalik sediments proximal to the syntaxis. Our results highlight the efficiency of detrital analysis to reconstruct the early history of the source area and confirm the efficiency of rutile in tracking the youngest age populations in material eroded from the Namche Barwa syntaxis. We provide evidence of the possibility of an onset of syntaxial exhumation >10 Ma, which is earlier than previously published determinations, and at rates in the order of ~4 mm/yr.

ACKNOWLEDGEMENTS

We acknowledge financial support from a Marie Curie Initial Training Network iTECC funded by the EU REA under the FP7 implementation of the Marie Curie Action, under grant agreement 316966.

SUPPLEMENTARY MATERIAL

The supplementary material of this chapter is presented in Appendix IV as listed here.

Analytical methods:

- Sample preparation
- Zircon fission-track dating
- White mica ^{40}Ar-^{39}Ar dating
- U-Pb rutile dating

Data tables:

- Table S1: Sample location and minimum age peaks
- Table S2: Zircon fission-track data
- Table S3: White-mica ^{40}Ar-^{39}Ar data
- Table S4: Rutile U-Pb data
- Table S5: Model parameters

DISCUSSION

This section is a summary of the major outcomes of the thesis, and their implications in our understanding of the interplays between tectonics, erosion and climate. The discussion is articulated in four parts, the first focuses on the Siwalik sedimentary rocks deposition in the eastern Himalayan foreland basin in comparison with the entire Siwalik apron along the range; the second part summarizes the knowledge acquired on the drainage evolution in the eastern Himalayan region; the third presents the major conclusions on the two main research questions of this work i.e. the evolution of the Shillong Plateau and the Namche Barwa syntaxis; the last section indicates directions for further work in the area.

1. DEPOSITION OF THE SIWALIK SEDIMENTS IN THE EASTERN HIMALAYA FORELAND BASIN

The depositional age of two sedimentary sections in the eastern Himalayan foreland has been constrained in chapter 1 and 3 of this work. These Siwalik sections are the Dungsam Chu section, located in the northern lee of the Shillong Plateau in south-eastern Bhutan, and the easternmost Sibo-Remi-Siang section located in Arunachal Pradesh. The depositional ages have been determined using magnetostratigraphy and apatite fission-track thermochronology, with the additional luminescence dating for the Sibo-Remi-Siang section. Additionally, the sedimentology of these sections has been described and palynology analysis has been performed in the Dungsam Chu section. The results allow the reconstruction of the paleo-environment and the accumulation rates evolution of both sections.

1.1. The Dungsam Chu section

Lower, Middle and Upper Siwalik sedimentary rocks deposited between ~7 Ma and ~1 Ma have been identified in the Dungsam Chu section. The Lower to Middle Siwalik transition has been determined at ~6 Ma and the Middle to Upper Siwalik transition at ~3.8. Note that the authors of chapter 1 have chosen the magnetostratigraphic correlation generated with the Qupydon software (Lallier et al., 2013). However, the author of the thesis prefers the best manual correlation (correlation C), as explained in the Introduction chapter and the Appendix V. Therefore, the best manual correlation is used in chapter 2. The latter correlation places the Lower to Middle Siwalik transition at a similar date to the Qupydon correlation, but the Middle to Upper Siwalik transition at ~2.5 Ma. This age discrepancy highlights the challenges involved in depositional dating by magnetostratigraphy and the uncertainty related to the choice of the preferred correlation introduced in the Introduction chapter. Both correlations indicate a decrease in accumulation rate up-section from ~0.6 mm/yr at

the bottom of the section to ~0.07 mm/yr or ~0.2 mm/yr at the top, using Qupydon or the best manual correlation, respectively. The depositional environments in the Dungsam Chu section include river-dominated and wave-influenced deltaic systems with a marine setting prior to ~5 Ma, likely reflecting marine incursions from the Bay of Bengal at the base of the section. At this time (~4.4 Ma using the preferred manual correlation), a transition to a sandy and then gravelly alluvial environment occurs. The vegetation in the Dungsam Chu area has been inferred as presenting diverse tropical lowlands and rain forests without substantial changes throughout the deposition of the Siwalik sediments in the section.

1.2. The Sibo-Remi-Siang section

The Sibo-Remi-Siang section is a combination of the Sibo outcrop, the Remi section and the Siang section located within a 20 km-long segment along the eastern Himalayan front. The Middle and Upper Siwalik sub-Groups outcrop in the Remi section, whereas Upper and Middle Siwaliks only are found in the Sibo and Siang section, respectively. The Siwalik sedimentary rocks of the Sibo-Remi-Siang section were deposited between ~11.0 Ma and ~0.2 Ma, with the Middle to Upper Siwalik transition constrained at ~2.5 Ma. The accumulation rates over the entire section increase from ~0.21 mm/yr in the upper part of the Middle Siwaliks to at least ~0.55 mm/yr in the Upper Siwaliks. The Middle Siwaliks of the Sibo-Remi-Siang section have been interpreted as braided fluvial facies whereas the Upper Siwaliks are pebbly braided-river deposits. Similar to the Dungsam Chu section, up-section coarsening is interpreted as the progressive transition from deposition by low-gradient sinuous channels in a fluvio-deltaic setting to deposition by steep braided rivers in alluvial fans along the Himalayan front, as the Main Frontal Thrust propagated southward (Chirouze et al., 2012; Coutand et al., 2016). Zircon U-Pb dating in the Remi section indicates the recycling of older Siwalik material in younger Upper Siwalik deposits which have been interpreted as reflecting the onset of activity on the Main Frontal Thrust in the section, at ~1.5 Ma.

1.3. Siwalik deposits along the Himalayan front

The Siwalik record presents multiple variations in terms of depositional age, accumulation rate and depositional environment along strike at the Himalayan scale but also within the eastern foreland basin as documented by this thesis. This section investigates these regional and Himalayan variations though comparison of the Dungsam Chu and the Sibo-Remi-Siang section, to the central and western Himalayan Siwaliks.

The age of the Siwalik sub-Group boundaries differs substantially in the two dated sections of this thesis. Previous magnetostratigraphic correlations in the Neogene-Quaternary Himalayan foreland basin from Pakistan to Arunachal Pradesh document ages ranging from 8 to 12 Ma for the Lower to Middle Siwalik transition (e.g. Chirouze et al., 2012; Gautam and Fujiwara, 2000; Ojha et al., 2009; Ojha et al., 2000; Tokuoka et al., 1986) and from 2 to 3.5 Ma for the Middle to Upper Siwalik transition (e.g. Behrensmeyer et al., 2007; Ojha et al., 2009; Sanyal et al., 2004) (Fig. 53). Therefore, whilst in both Dungsam Chu and Sibo-Remi-Siang sections the Middle to Upper Siwalik transitions are relatively synchronous in comparison with Siwalik deposits along the entire range, the boundary between the Lower and Middle Siwalik subgroups in Dungsam Chu section is 2 to 6 Ma younger than documented elsewhere along the Himalayan arc. Furthermore, the duration of deposition of the Middle Siwalik subgroup varies from 3 to 8 Ma in the Siwalik apron (Chirouze et al., 2012; Meigs et al., 1995; Ojha et al., 2009). The longest Middle Siwalik deposition is observed the Kameng section (~8 Ma; Chirouze et al., 2012), whereas the Middle Siwaliks of the adjacent Dungsam Chu section have been deposited during about 2–3 Ma. These variations in depositional age along strike are not straightforward to explain. Indeed, it has been demonstrated that vertical transitions between lithostratigraphic formations and their lateral diachroneity cannot be interpreted simply in terms of tectonic and climatic forcing, especially in foreland basins (e.g. Barberà et al., 2001; Burbank et al., 1986; Charreau et al., 2009; Heermance et al., 2007). These changes reflect the 4-D space-time evolution of depositional profiles documented by one-dimensional vertical sections located at different positions, more proximal or more distal, with respect to the mountain range and its foreland. Consequently, extensive and careful spatiotemporal constraints, both parallel and perpendicular to the orogenic system, are necessary to properly discuss what controls the vertical and lateral transitions between the lithostratigraphic formations in a foreland basin. Additionally, a sedimentological and stratigraphical reading of such variations in terms of paleoenvironmental, paleogeographical, and sequential evolution is often more pertinent than a strictly lithostratigraphic approach.

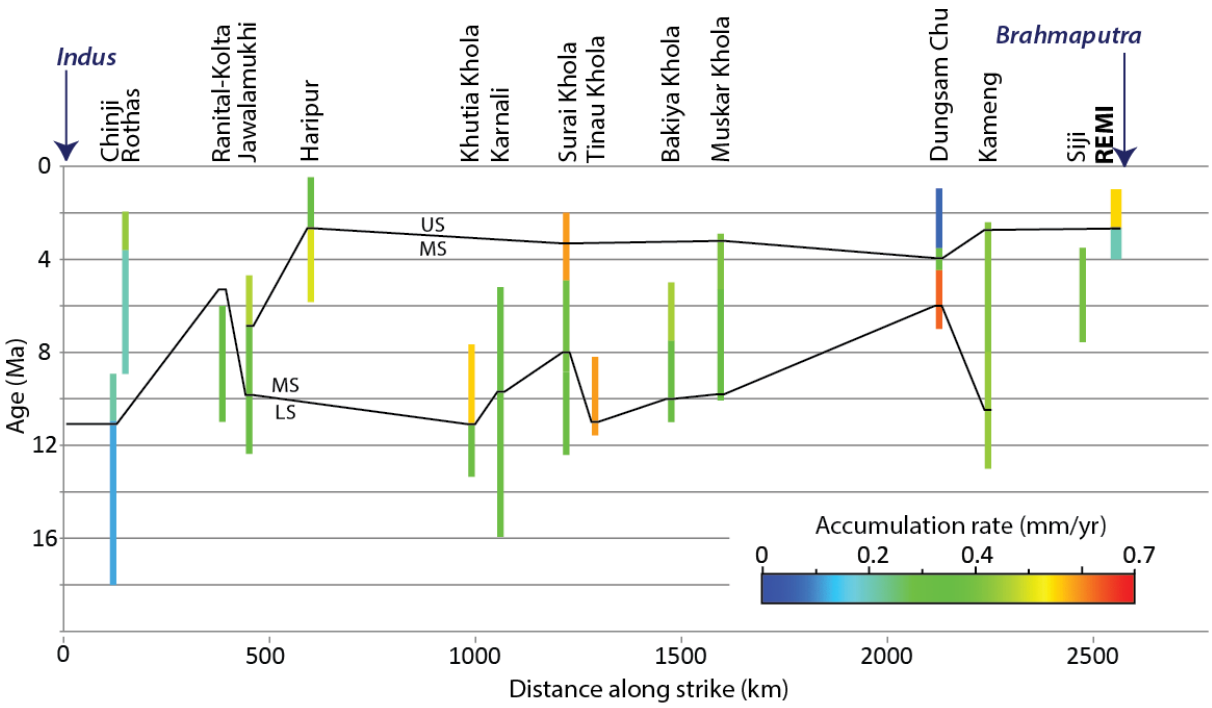

Fig. 53: *Compilation of ages and accumulation rates of Siwalik sections dated with magnetostratigraphy between the Indus and Brahmaputra Rivers, figure extracted from chapter 3. Transitions between Lower Siwaliks (LS) and Middle Siwaliks (MS) and between Middle and Upper Siwaliks (US) are indicated with black lines. The sections presented in this diagram are: Chinji (Johnson et al., 1985); Rothas (Behrensmeyer et al., 2007); Ranital Kolta, Haripur (Sanyal et al., 2004); Jawalamukhi (Meigs et al., 1995); Khutia Khola (Ojha et al., 2000); Karnali (Gautam and Fujiwara, 2000); Surai Khola, Tinau Khola, Muksar Khola (Ojha et al., 2009); Bakiya Khola (Harrison et al., 1993); Dungsam Chu (Coutand et al., 2016); Kameng (Chirouze et al., 2012); Siji (Lang et al., 2016).*

The Dungsam Chu and the Sibo-Remi-Siang sections present distinct accumulation patterns. Whilst the accumulation rates increase up-section in the Sibo-Remi-Siang section similar to most of the Siwalik sections in the Himalayan foreland basin (Fig. 53), the accumulation rates decrease in the Dungsam Chu section. In foreland basins, the rates of sediment deposition are conditioned by the spatiotemporal evolution of subsidence, which primarily generates accommodation space for deposits, and by sediment supply derived from the erosion of the adjacent mountain range (DeCelles and Giles, 1996). Consistent with the forelandward migration of the basin flexure associated with the lateral and vertical growth of the orogenic system, the foredeep depozones of foreland basins are generally characterized by an overall acceleration of subsidence through time recorded by increasing accumulation rates and convex up subsidence curves (e.g. Charreau et al., 2009; Ojha et al., 2009; Xie and Heller, 2009). For the Himalayan foreland basin, such increasing or constant accumulation

rates calculated from the non-decompacted sedimentary thicknesses of the Siwalik deposits have been mostly interpreted in terms of flexure associated with the slip history of the Main Boundary Thrust (MBT) (e.g. Burbank et al., 1996; Meigs et al., 1995; Ojha et al., 2009). Different mechanisms including climatically or tectonically driven decrease in subsidence and/or in sediment supply to the foreland basin may potentially account for the deceleration of accumulation rate in the Dungsam Chu section. These mechanisms have been discussed in chapter 1, and the peculiar accumulation rate pattern of the Dungsam Chu section has been attributed to a tectonically driven change in subsidence and/or detrital influx in the basin, in response to an increasing partitioning of the India-Eurasia total convergence into the Shillong Plateau. However, results from chapter 2 indicate that the sediments of the Dungsam Chu section were deposited by the paleo-Brahmaputra River, from ~5 Ma. At this time, chapter 3 and 4 document that the Yarlung-Brahmaputra River flowed through the rapidly exhuming and eroding eastern syntaxis. Consequently, a low detrital influx in the Dungsam Chu section during the deposition of the upper part of the Middle Siwalik and the Upper Siwalik is unlikely. Instead, the interpretations from chapter 2 are consistent with a tectonically driven change in subsidence related to the surface uplift of the Shillong Plateau during the Middle Siwalik deposition in the Dungsam Chu section, constituting a better explanation for the decrease in accumulation rates. This explanation could also apply to the unusually short duration time of the Middle Siwalik deposition in the Dungsam Chu section, as well as to the young Lower to Middle Siwalik transition. By contrast to the Dungsam Chu section, the accumulation rates in the Upper Siwaliks of the Sibo-Remi-Siang section are very high in comparison with other Upper Siwalik deposits along the Himalayan orogenic-arc (Fig. 53). This can be explained by the fact that the Upper Siwalik alluvial fan deposits are strongly influenced by their proximity to the southward-propagating Himalayan thrust front. Therefore, local faults associated with the Main Frontal Thrust could explain this variability in accumulation rates along strike. The comparison of accumulation rates in the Middle and Lower Siwaliks along the Himalayan front seems to indicate lower rates in both the eastern and western extremities of the Siwalik apron compared to the central region. Potential explanations to this trend have been investigated in chapter 2, however the authors encourage the analysis of further records along strike to validate whether there is indeed a systematic difference in accumulation rate between the syntaxial regions and the main arc of the orogen, or whether these variations are simply related to differences in activation of local structures through time.

The Siwalik Group in the sections investigated in this study show an overall distal to proximal trend as observed everywhere else in the Himalayan foreland basin (e.g. Chirouze et al., 2012; DeCelles et al., 1998b; Kumar et al., 2003; Nakayama and Ulak, 1999). This long-term progradational trend,

which is typical of the filling sequence of foreland basins at their active margin (e.g. Jordan, 1995; Puigdefàbregas et al., 1986; Schlunegger et al., 1997; Sinclair and Allen, 1992; Stockmal et al., 1992) is controlled by the propagation of the deformation front, generally together with an increasing erosion and sediment flux, related to the horizontal and vertical growth of the adjacent mountain range.

Although the observations from the Sibo-Remi-Siang section do not allow straightforward conclusions on the depositional environment in terms of marine vs continental deposition, lacustrine to marine deltaic environment in the lower Siwalik subgroup, before ~10.5 Ma, has been described in the nearby Kameng section (Chirouze et al., 2012). Moreover, the overlying braided river sediments of the Middle Siwaliks and alluvial fan deposits of the Upper Siwaliks in the Kameng section have been reported as bearing paleo-botanical evidences of brackish water or near coastal environments (e.g. Chirouze et al., 2012; Mehrotra et al., 1999; Singh and Tripathi, 1989). To the west of the Himalayan Siwalik apron, meandering and braided fluvial depositional systems (Lower and Middle Siwaliks) grading into alluvial fan systems (Upper Siwaliks) are uniformly observed from Pakistan to Nepal (Abbasi and Friend, 2000; Brozovic and Burbank, 2000; DeCelles et al., 1998b; Huyghe et al., 2005; Johnson et al., 1983; Kumar et al., 2003; 2004; Nakayama and Ulak, 1999; Ojha et al., 2009; Suresh et al., 2004; Willis, 1993; Zaleha, 1997). Floodplains with intermittent lacustrine conditions attributed to seasonal flooding are also recorded (DeCelles et al., 1998b; Hoorn et al., 2000) but always in a continental environment. A paleo-environmental change occurs east of Nepal where thick deltaic deposits appear in the Lower and Middle Siwaliks (Fig. 54). Further east, along the Churanthi River in west Bengal (Fig. 54), brackish water to shallow marine conditions have been documented by palynological data and trace fossils in the undated middle Siwalik subgroup (More et al., 2016).

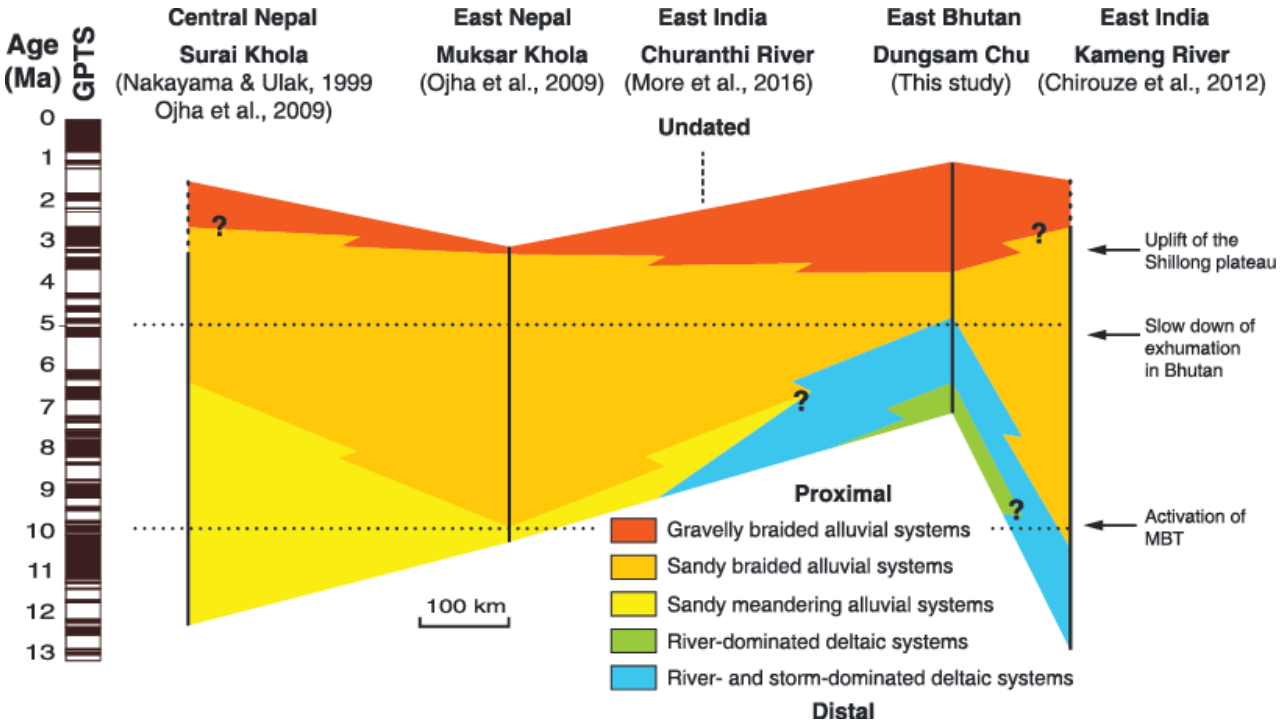

Fig. 54: *Lateral variations of depositional environments, figure extracted from chapter 1. Stratigraphic sections are from Nakayama and Ulak (1999) and Ojha et al. (2009) (Surai and Muksar Khola), this study (Dungsam Chu), and Chirouze et al. (2012) (Kameng River).*

The shallow marine paleo-environment interpreted in the Dungsam Chu section prior to ~5 Ma, as well as similar marine settings to the northeast of the Shillong Plateau in the foreland of the Naga Hills of Assam and to the south in the Surma Basin of northern Bangladesh (e.g. Alam et al., 2003; Bhandari et al., 1973; Najman et al., 2012; Reimann and Hiller, 1993; Worm et al., 1998) are consistent with a post-Miocene complete continentalisation of the eastern Himalayan foreland basin at least 15 Ma later than in the western Himalayan foreland basin. Furthermore, the striking synchronicity of the continentalisation of the Dungsam Chu paleo-location and the surface uplift of the Shillong Plateau, the timing of which has been documented in chapter 2, suggests a cause-effect link between the two events. Indeed, the deformation and surface uplift of the Shillong block must have decreased the subsidence of the eastern Himalayan foreland before creating a topographic barrier into the basin at ~5 Ma.

Since palynological studies are lacking in the Sibo-Remi-Siang section, comparison of paleo-vegetation with the Dungsam Chu section is not possible. However, the author of this thesis has contributed to a study which compares the paleo-vegetation in two Siwalik sections located in the east and in the west of the Himalayan foreland basin using $\delta^{13}C$ and $\delta^{18}O$ values of soil carbonate and associated $\delta^{13}C$ values of bulk organic carbon (Vögeli et al., in press). The latter study uses the

paleo-vegetation archive as a marker of monsoon intensity and seasonality and focuses on the Kameng section for the eastern record, allowing comparison with the nearby Dungsam Chu section and is presented in Appendix VI. The results from the stable isotope analyses in the Kameng section (Vögeli et al., in press) and the palynological analyses from the Dungsam Chu section (chapter 1, Coutand et al., 2016) are consistent. Within the respective depositional duration of both sections (1-13 Ma for the Kameng section, Chirouze et al., 2012; and 1-7 Ma for the Dungsam Chu, chapter 1) the vegetation has remained relatively constant in the two location. Both studies provide evidence of depositional environments and paleoclimate more humid in the east than the coeval central and western Himalayan foreland basin. Since the eastern Kameng section is a lot more proximal to the main moisture source of precipitation (the Bay of Bengal) in comparison with the western Himalaya, Vögeli et al. (in press) suggest that even though climate may have varied, it remained more humid, inhibiting the evolution of plants preferring intense light, warm and water-stressed conditions (C4 plants; Ehleringer, 1989) which likely also reflect less seasonality in the east. Vögeli et al. (in press) also noticed the presence of soil carbonate in the west and its absence in the east, in the Kameng section. Carbonate soil have not been found in the Dungsam Chu and Sibo-Remi-Siang sections neither. Vögeli et al. (in press) interpret this difference in the occurrence of pedogenic carbonates as an indication of lateral climatic variation that ranges from arid in the west to highly humid in the east. This paleo-climate trend is similar to the modern precipitation patterns along the strike of the Himalaya, which are characterized by an east-to-west decrease in the Indian Summer Monsoon (ISM) precipitation intensity. By contrast, a shift from C3 to C4 vegetation has been interpreted at ~7 Ma in central and western Himalaya, through $\delta^{13}C$ and palynological analyses (e.g. Hoorn et al., 2000; Quade and Cerling, 1995; Quade et al., 1989; 1995; Sanyal et al., 2010; Singh et al., 2013). As C3 plants are favoured in a cool and humid climate (Ehleringer, 1989), this vegetation shift also indicates a climate change at that time. This shift has been interpreted as resulting from a regional change towards a more seasonal climate in the west possibly linked to a decrease of the influence of the Westerlies, delivering less winter precipitation and the east being very humid due to its proximity of the moisture source (Vögeli et al., in press). Overall, these observations suggest that the environment and probably the paleoclimate of the eastern Himalayan lowland and floodplains were consistently more humid than the coeval environments and paleoclimate in Nepal, as is the case today (Bookhagen and Burbank, 2006; 2010). In the Bhutanese Dungsam Chu section, the absence of indications of major change in moisture or temperature between 7 and 1 Ma, suggests that the orographic blockage of the ISM precipitations exerted by the surface uplift of the Shillong Plateau as proposed by Grujic et al. (2006) did not measurably modify the wet local climate documented in the Bhutanese foothills. However, a study involving the collaboration of the author of the thesis (Grujic

et al., in prep.) analyses the oxygen isotopic composition of the clay minerals in the Dungsam Chu section. The results show an increase in $\delta^{18}O$ values since ~5-4 Ma. This time corresponds to the initiation of the Shillong Plateau uplift inferred from the chapter 2 of this thesis. The increase of $\delta^{18}O$ values is related to a decrease in mean precipitation rates since this time, which is interpreted as a direct consequence of the Shillong Plateau uplift.

Depositional dating, sedimentology and paleo-environment analyses preformed on Siwalik sedimentary rocks in this thesis, and together with the comparison to Siwalik sediments throughout the entire Himalayan arc leads to critical information on the evolution of the tectonics, the erosion and the climate in the Himalayan range and its foreland basin during the duration their deposition. The major conclusions of the Siwalik deposits analyses described above have been investigated further with- and have permitted- provenance analyses and tectonic reconstructions in the Shillong Plateau and the Namche Barwa syntaxis regions.

2. DRAINAGE EVOLUTION IN THE EASTERN HIMALAYA

Provenance analysis in the Dungsam Chu and the Sibo-Remi-Siang sections, using zircon and apatite U-Pb described in chapters 2 and 3 led to an improved knowledge of the drainage evolution in the eastern Himalaya since the Late Miocene. This section describes the main provenance interpretations from both chapters, firstly in the foreland basin with a reconstruction of the paleo-drainage of the Brahmaputra River and secondly in the eastern syntaxis area, within the orogen.

2.1. Brahmaputra paleo-drainage

Transhimalayan deposits in the eastern Himalayan foreland basin have been interpreted as derived from the Gangdese batholiths and transported by the palaeo-Brahmaputra through the Yarlung Tsangpo crossing the range via a transverse river such as the modern Siang River. Such deposits have been documented as first occurring sometime between 5.2 and 4.4 Ma in the Dungsam Chu section and from ~11 Ma in the Sibo-Remi-Siang section. These new results indicate that the Yarlung-Brahmaputra connection was established since at least 11 Ma, consistently with estimates from previous provenance studies in the foreland basin with the earliest estimation in Early Miocene times (~18 Ma, Bracciali et al., 2015; Chirouze et al., 2013; Cina et al., 2009; Galy et al., 2010; Lang and Huntington, 2014). The combination of these provenance studies with the new results from this thesis allowed the development of an evolutionary model of Brahmaputra drainage presented in chapter 2 (Fig. 55). Since Transhimalayan deposits are present in the Sibo-Remi-Siang section from ~11 Ma, as shown in chapter 3, the Yarlung-Brahmaputra connection must have existed upstream

the paleo-location of the Sibo-Remi-Siang section since at least this time. Therefore, hypotheses of transverse Yarlung-Brahmaputra connection west of the Siang are unlikely (e.g. Cina et al., 2009; Lang and Huntington, 2014; Fig. 55). Prior to 7 Ma, the Brahmaputra flowed directly SSW to the Bengal Fan (Fig. 55a; Uddin and Lundberg, 1999). By 7 Ma, the paleo-Brahmaputra reached the paleo-location of the Kameng section (Chirouze et al., 2013; Fig. 55) interpreted in chapter 2 as possibly due to the rise of the Mikir Hills, deflecting the river northward. The arrival of Transhimalayan detritus at Dungsam Chu between 5.2-4.4 Ma indicates the north- and west-ward diversion of the paleo-Brahmaputra River due to uplift of the Shillong Plateau at this time. The occurrence of unrecycled paleo-Brahmaputra deposits found in the Surma Basin until ~2.5 Ma (Bracciali et al., 2015) is explained in this thesis by an unequal distribution in time and space of displacements on the Oldham and Dauki faults bounding the Shillong Plateau (Biswas et al., 2007), resulting in an irregular uplift pattern and frequent switching of the Brahmaputra to courses east and west of the rising plateau. Eventually, after 2.5-2.0 Ma, the paleo-Brahmaputra course east of the plateau closed due to the combination of westward propagation of the Indo-Burman Ranges and the plateau rise (Najman et al., 2016). Since then, the river has flowed exclusively to the north and west of the plateau.

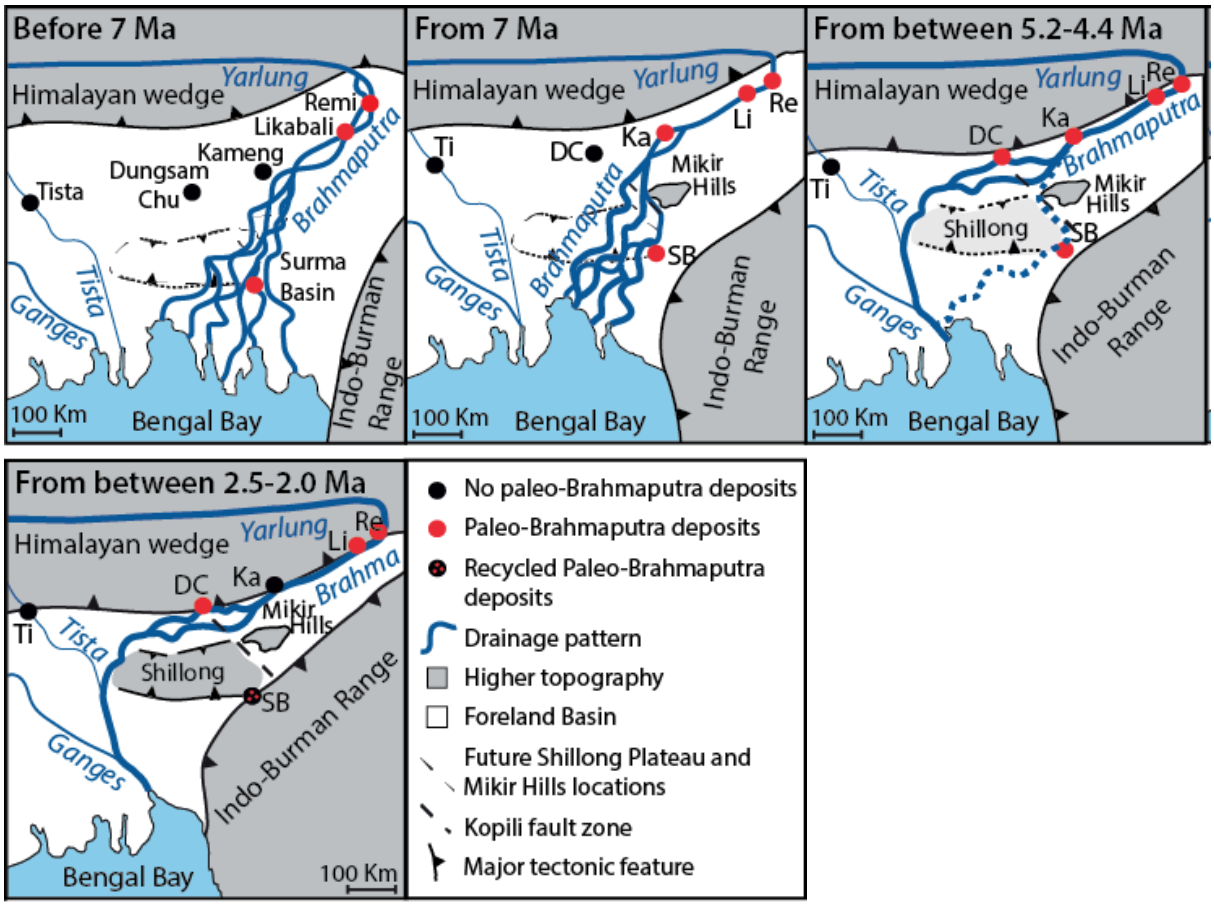

Fig. 55: *Figure extracted from chapter 2. Late-Miocene to present evolutionary model of the Brahmaputra drainage system (modified from Chirouze et al., 2013), constructed using provenance studies from various sedimentary sections: Dungsam Chu (this study); Likabali (Lang and Huntington, 2014); Remi (Govin et al., in review); Tista (Cina et al., 2009); Kameng (Chirouze et al., 2013) and Surma Basin (Bracciali et al., 2015).*

2.2. Paleo-drainage in the eastern syntaxis area

Chapters 3 and 4 of this manuscript provide new constraints on the paleo-drainage in the syntaxis area. The occurrence of syntaxial deposits in the Sibo-Remi-Siang section from sometime between ~10 and 7 Ma indicates that the Yarlung-Brahmaputra connection via the Siang River, flowing through the Namche Barwa syntaxis, has existed since at least this time (Fig. 56). Before then, although the evidence of a Yarlung-Brahmaputra connection through a transverse river upstream of the Sibo-Remi-Siang paleo-location is clear, the river through which the Brahmaputra and the Yarlung rivers were connected remains unclear. A potential connection through the Lohit River has been considered in chapter 3, implying a change from Yarlung-Lohit-Brahmaputra routing to Yarlung–Siang–Brahmaputra routing on the basis of the decrease of Transhimalayan detritus up-section and a substantial increase in Tethyan Himalayan zircon grains from ~4 Ma. However, the occurrence of syntaxial deposits demonstrated in both chapter 3 and 4 is inconsistent with this hypothesis from ~7 Ma. Yet, prior to ~7 Ma this scenario might be possible. In this case, the differences in weathering and in abundance of Cretaceous-Paleogene apatite U-Pb ages between the east bank and the west bank outcrops of the Siang section would be consistent. Indeed, the differences in weathering between the east and the west bank outcrops of the Siang section could reflect a difference in lithology, rendering the sedimentary rocks more or less sensitive to weathering. Furthermore, the apatite U-Pb ages interpreted as sourced from Transhimalayan Batholiths constitute 38 % of the sample from the east bank of the Siang section (SG1), whereas the sample from the west bank of the section (SG11) contains only 2 % of such aged apatite grains (Fig. 49, chapter 3). However, these observations need to be further investigated to test this hypothesis, as developed in the further investigation section (see below).

Overall, the drainage evolution in the Namche Barwa area is complex and necessitates additional research. Indeed, as described in the chapter 3 of this thesis, the Sibo-Remi-Siang section shows various changes in the abundance of different apatite and zircon U-Pb age populations. These changes are of relative clarity, and their interpretation is challenging (see Fig. 49, chapter 3). It is likely that a succession of multiple capture events have modified the paleo-drainage in the eastern

syntaxis area since the Early Miocene. For instance, chapter 3 constrains a Parlung-Yigong capture by the Siang River after ~190 ka, as shown by the arrival of substantial amounts of Early Cretaceous zircons characteristic of the Bomi-Chayu batholiths at this time. The dating of this capture refines the estimates from previous studies (King et al., 2016; Lang and Huntington, 2014). The Parlung-Siang connection implies the reversal of the Parlung River originally flowing south-eastward through a Yigong-Parlung-Lohit connection as suggested by e.g. Lang and Huntington (2014), see Fig. 56.

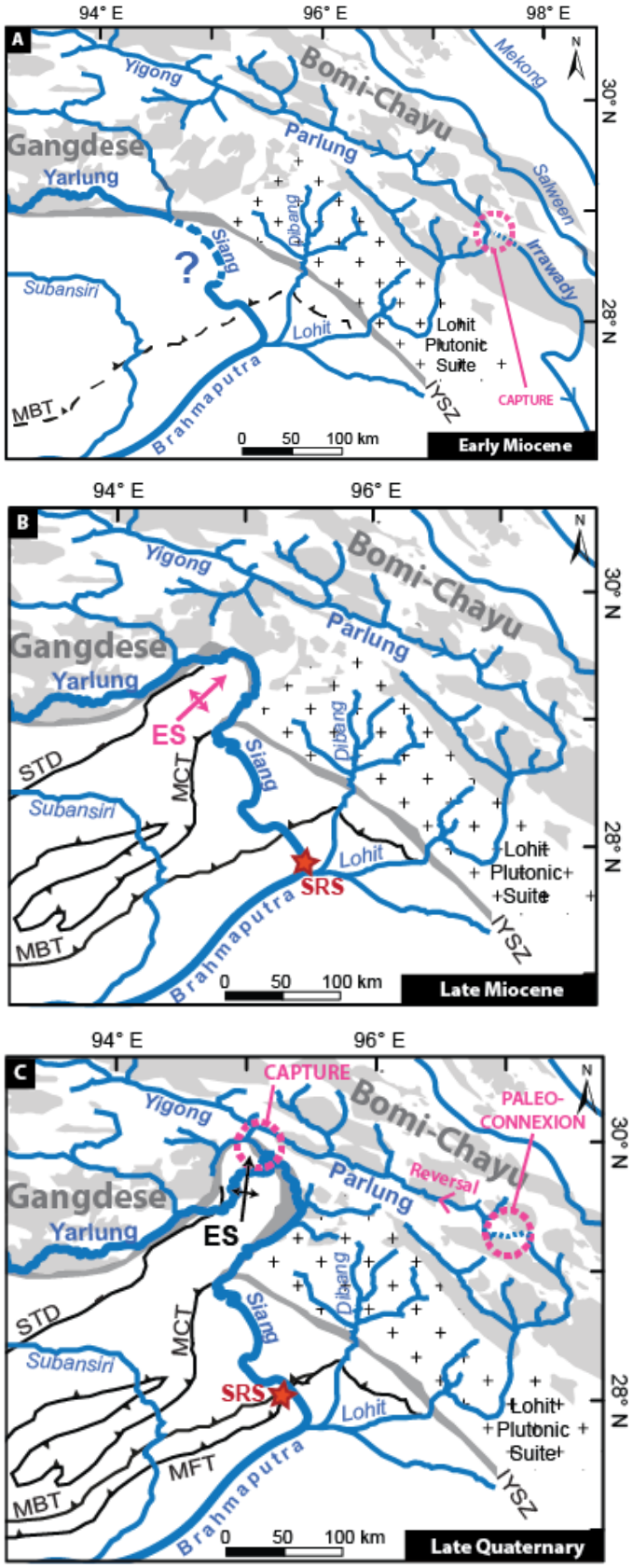

Fig. 56: *Figure extracted from chapter 3. Early-Miocene to Late-Quaternary evolutionary model of the drainage system in the eastern syntaxis area (modified from Lang and Huntington, 2014)*

constructed using provenance analysis from this study, Lang and Huntington (2014), Clark et al. (2004), Robinson et al. (2014), and references therein. The question mark and the dotted drainage line indicates a potential paleo-drainage scenario in which the Yarlung-Brahmaputra connection existed through the Siang River since the Early Miocene, but other scenarios are possible such as a Yarlung-Brahmaputra connection through the Lohit River. Red star labelled SRS represents the Sibo-Remi-Siang composite section. The arrows symbolize the northward growth of the antiformal Namche Barwa syntaxis. Abbreviations are: ES – Eastern Syntaxis, MFT - Main Frontal Thrust, MCT - Main Central Thrust, MBT - Main Boundary Thrust, STD - South Tibetan Detachment and IYSZ - Indus-Yarlung Suture Zone.

3. RECONSTRUCTION OF THE TECTONIC EVOLUTION OF THE STUDY AREAS

This section summarizes the major findings regarding the Shillong Plateau and the eastern syntaxis Late Miocene evolution acquired through this thesis, essentially from chapters 3 and 4.

3.1. Shillong Plateau

Provenance analysis in the Dungsam Chu section using zircon U-Pb dating allows the detection of paleo-Brahmaputra deposits from sometime between 5.2-4.4 Ma at this location. The deposition of these detritus in the Dungsam Chu section are interpreted as reflecting the topographic growth of the Shillong Plateau which has deflected the course of the Brahmaputra in its northern lee. In this way, the study presented in chapter 2 dates the initiation of the surface uplift of the Shillong Plateau between 5.2 and 4.4 Ma, previously estimated between ~4 and 2 Ma (Biswas et al., 2007; Najman et al., 2016). Prior to this time, the rock uplift in the Plateau was balanced by surface erosion from 9-15 Ma, as inferred by previous studies (Biswas et al., 2007; Clark and Bilham, 2008), such that no topography was created. The transition from rock exhumation to surface uplift of the Shillong plateau has previously been tentatively explained by differences in erodibilities between the high erodibility of the Cenozoic sedimentary cover and the hard Precambrian basement of the plateau (Biswas et al., 2007). However, this explanation is called into question in chapter 2, as a 3-4 Myr lag time between the surface uplift initiation and the time of transition from predominantly cover to basement erosion is noted, after comparison of published provenance studies south of the Shillong Plateau, to be in the Quaternary (Bracciali et al., 2015; Najman et al., 2012). Consequently, chapter 2 assesses the role of tectonics in the transition from rock exhumation to surface uplift through lithospheric stress field modelling. The model suggest that the onset of the rise of the Shillong Plateau is instead a result of the convergence of the Shillong and the Tibetan plateaus, leading to increased fault-slip rates in response to stresses caused by the Indian lithosphere bending beneath

the Himalaya. This scenario implies that surface denudation could no longer keep pace with rock uplift, causing topography growth sometime between 5.2-4.4 Ma with an apparent ~3-fold increase in slip rate on the faults bounding the Shillong Plateau inferred from comparing GPS and geological estimates since the Miocene (Biswas et al., 2007; Clark and Bilham, 2008; Vernant et al., 2014). Chapter 2 suggests that the convergence lead to the transport of the Shillong area into the region affected by stresses related to the bending of the Indian lithosphere beneath southern Tibet from ~15 Ma. From this time, rock exhumation of the Shillong plateau occurred and as the convergence continued, the Shillong region has been increasingly affected by the bending stresses. This has eventually led to surface uplift of the Shillong Plateau between 5.2-4.4 Ma. The authors suggest that the uplift history is affected by proximity to the Himalaya and that therefore, the Mikir Hills located north-east of the Shillong Plateau might have been uplifted in a similar way prior to the Shillong Plateau, at ~7 Ma.

3.2. Namche Barwa syntaxis

The Namche Barwa is aptly named, as it translates as “flaming thunderbolt” describing well the rapidly exhuming massif. However, thermochronology results from chapter 4 indicate that the exhumation rates are high but not extreme, and that the initiation of these high exhumation rates is young, but older than previously estimated. Indeed, typical syntaxial rutile U-Pb ages (<9 Ma) and young zircon fission-track and muscovite ^{40}Ar-^{39}Ar ages are documented in the Sibo-Remi-Siang section, from sometime between ~7 and 11 Ma. These are interpreted as derived from the syntaxis, in contrast to typically older thermochronological ages of minerals deposited prior to 7-11 Ma, interpreted as derived from the equivalent of the Himalayan GHS sequence unaffected by the rapidly exhuming syntaxis. Additionally, results from the three thermochronological systems show short lag times in the upper part of the section, reflecting the rapidly exhuming syntaxis. This evidence of syntaxial input confirm the speculations concerning their occurrence raised in chapter 3, using U-Pb dating. The study of the minimum age peaks extracted from the three thermochronometer datasets suggests a better efficiency of the rutile U-Pb system in tracking the erosion products of the Namche Barwa syntaxis. Indeed, the rutile U-Pb system tracks the youngest minimum age peaks in comparison with the two other lower closure temperature systems generally showing older minimum age peaks. The predictions of cooling ages resulting from a step change in exhumation rate using a 1-D thermokinematic model incorporating detrital thermochronological data from published studies and new data from this thesis provides new constraints to the evolution of the eastern syntaxis. This model includes detrital rutile U-Pb documenting an earlier onset of syntaxial exhumation than previously estimated, possibly as old as 13 Ma, with final exhumation

rates as low as ~4 mm/yr. Although these results do not allow discrimination between the models which have been proposed to explain the evolution of the syntaxis, they provide new age constraints, necessary for the understanding of the mechanisms involved in the development of the Namche Barwa syntaxis.

4. CONCLUSION ON THE INTERPLAYS BETWEEN TECTONICS, EROSION AND CLIMATE

This section reviews the outcomes of this Ph.D. work, focusing on how they inform the interactions between tectonics and climate through erosion.

The Shillong Plateau has been suggested to act as an orographic barrier to the ISM coming from the south-eastern Bay of Bengal; the resulting rain shadow might have influenced the erosion rates over the Bhutanese Himalayan foothills, which have been inferred to be higher to the west of the rain shadow and lower north of the plateau (Grujic et al., 2006). The climatic influence of the Shillong Plateau topographic growth in its northern lee has not been recorded in the paleo-vegetation archive of the Dungsam Chu section (Coutand et al., 2016). However, the study of Grujic et al. (in prep.) that analyses the oxygen isotopic composition of clay minerals in the Dungsam Chu section, shows an increase in $\delta^{18}O$ values synchronous with the initiation of the Shillong Plateau uplift, at ~5 Ma. This increase is interpreted as related to a decrease in mean precipitation rates since this time. Based on this evidence, the Shillong Plateau tectonic uplift must have impacted on the regional climate. Although this thesis favours a tectonic explanation for the differential erosion rates in Bhutan observed by Grujic et al. (2006) (see below), the study of Grujic et al. (in prep.) demonstrates that the rain shadow formation by the Shillong Plateau could indeed constitute another possible explanation. Additionally, this thesis has shown the impact of the Shillong Plateau uplift on erosion, with a transition from rock exhumation to surface uplift of the Shillong Plateau. Prior to the transition, the erosion of the sedimentary rocks covering the Shillong basement matched rock exhumation such that no topography, and thus no rain shadow, were created. When surface uplift occurred, erosion could not keep pace with rock exhumation. This constitutes a second order evidence of the erosion effect on climate in the way that erosion initially prevented the rise of the Plateau and therefore, modified the local climate. Nevertheless, results from chapter 3 have shown that the causes of the Shillong Plateau uplift is of tectonic origin rather than of erosional origin as suggested by Biswas et al. (2007). Shillong Plateau uplift has also modified the paleo-drainage of the Brahmaputra River which might have had an influence on the erosion pattern within the Himalayan foreland basin. Although this study does not document such effects, it highlights the influences of the tectonics related to the uplift of the Shillong Plateau on the accumulation rates in the northern

lee of the Shillong Plateau. The results from chapter 2 and 4 suggest that the sediment influx in the Dungsam Chu section transported and deposited by the paleo-Brahmaputra River was derived from the rapidly exhuming and eroding eastern syntaxis. Therefore, the very low accumulation rates in the upper part of the section cannot be explained by a low sediment input. Instead, this work suggests that a reduction in accommodation space resulting in low accumulation rates of the Siwalik sediments north of the plateau is a consequence of the strain partitioning related to the uplift of the Shillong Plateau. Such strain partitioning as proposed by Coutand et al. (2014) and consistent with the conclusions of chapter 3, might explain the differential erosion rates observed in Bhutan (Grujic et al., 2006). Furthermore, the uplift of the Shillong Plateau has likely contributed to the transition in depositional environments of the Siwalik sediments in the Dungsam Chu section, from marine-influenced to entirely continental. The change in depositional environment itself has had a substantial impact on the sedimentation processes.

The eastern syntaxis is the locus of extreme erosion rates of >5 mm/yr (e.g. Larsen and Montgomery, 2012) and rapid exhumation rates of ~4 mm/yr as inferred by this study. These two coeval dynamic processes are related, as erosion contributes to exhumation. If it is difficult to decipher which of these mechanisms drives the other, it is clear that surface uplift tends to increase erosion rates through glacial erosion (e.g. Egholm et al., 2009) or through slope and river gradient steepening causing landslides (e.g. Lang et al., 2013). In the case of the high topography of the Namche Barwa syntaxis, the direct influence of glacial processes (itself highly dependent on tectonics and on climate) on the fluvial and hillslope erosion has been demonstrated (Korup and Montgomery, 2008; Korup et al., 2010). The eastern syntaxis data and conclusions in this thesis do not provide suitable material to explicitly discuss the impact of tectonics on erosion; however, it illustrates the links between these two processes. For instance, the short lag times observed in the Sibo-Remi-Siang section reflect the combination of rapid exhumation and erosion. Indeed, although we cannot quantitatively differentiate the time of rock exhumation from the time of erosion and deposition of the detrital mineral considered from the lag times, we qualitatively evaluate the efficiency of both processes in the Namche Barwa syntaxis area.

Thermomechanical feedback between focused and intense erosion and growth of the Namche Barwa crustal antiform has been proposed to explain the evolution of the syntaxis (Zeitler et al., 2014; Zeitler et al., 2001). This model, the tectonic aneurysm model, suggests that the removal of upper crust has facilitated a local flow of a weaker lower crust with ductile behaviour in the region of intense erosion, the syntaxis (Bracciali et al., 2016; Zeitler et al., 2014; Zeitler et al., 2001). The early

version of this model (Zeitler et al., 2001) invokes a major drainage reorganisation, which would have initiated and sustained the Late Miocene rapid exhumation of the syntaxis (e.g. Booth et al., 2009; Burg et al., 1998; Ding et al., 2001; Finnegan et al., 2008; Seward and Burg, 2008; Stewart et al., 2008). A major capture event such as the Yarlung-Irrawaddy by the Siang-Brahmaputra River, has been inferred in Early Miocene times by later studies (e.g. Bracciali et al., 2015; Robinson et al., 2014), suggesting the non-synchronicity of the two events and therefore calling into question the original tectonic aneurysm model. However, the paleo-drainage reconstruction from chapter 3 and discussed in section II of this discussion chapter, demonstrates the complexity of the drainage evolution and the multiplicity of the capture events in the Namche Barwa region, consistent with previous studies (King et al., 2016; Lang and Huntington, 2014). The tectonic aneurysm model has also been opposed by Wang et al. (2014b) who propose that the rapid erosion of the Tsangpo gorge was a passive response to rapid uplift at ~2.5 Ma, on the basis of the observation of a buried canyon upstream of the gorges from this time. However, taking into account the arguments of Zeitler et al. (2015) and of Korup and Montgomery (2008; 2010), one can argue that temporary glacial and landslide damming could significantly decrease the erosional efficiency and explain the buried canyon, not requiring a rapid uplift strictly from 2.5 Ma. The early onset of syntaxial exhumation (~10 Ma) implied by the revised version of the tectonic aneurysm model (Zeitler et al., 2014) compared to younger estimates largely inferred from thermo- and geo- chronological ages from detrital and in situ studies (e.g. Bracciali et al., 2016; Burg et al., 1998; Burg et al., 1997; Lang et al., 2016; Seward and Burg, 2008), is better supported by the estimations of chapter 4. Although this Ph.D. work cannot test the tectonic aneurysm model it does not challenge it.

To conclude, this work has helped to document the tectonic, erosion and climate processes in the eastern Himalayan region. However, the author 1) acknowledges the circular reasoning of this digressive section; 2) suggests that this circularity is representative of the interplays between tectonics, erosion and climate; 3) has overall provided a study consistent with the chicken and egg polemic (Molnar, 2009; Molnar and England, 1990).

5. FURTHER WORK

In this section, the author encourages further studies in the continuity of this thesis to better document the newly formulated and remaining research questions.

5.1. Method development

On a methodological aspect, the author suggests further development of the thin zircon rims U-Pb dating in the Namche Barwa area. Bracciali et al. (2015) have interpreted detrital zircon-rim ages <10 Ma in the eastern Himalayan foreland basin as indicating a syntaxial provenance. This thesis tentatively reproduced this method in order to track syntaxial signature, but, as described in chapter 3, the ages obtained were highly discordant and their interpretation challenging. The authors explained this dating bias as principally due to the narrowness of the metamorphic zircon overgrowths requiring the use of small laser spots during analysis resulting in substantial U-Pb fractionation. Therefore, before considering reproducing this type of analysis on thin zircon rims, the author strongly recommends further development of the method such as trying with an ion micoprobe spectrometer.

By contrast, successful results were obtained using apatite U-Pb dating, in the same chapter. The authors have stressed the utility of this method as a provenance tool in the eastern Himalaya. However, this thesis provides the first apatite U-Pb data in the Himalayas and yet, no source characterization has been performed in this region. Therefore, it would be of great relevance to collect further apatite U-Pb data, especially in light of the complex drainage evolution in the eastern Himalaya which might be better constrained using this dating technique, as developed below.

Furthermore, this study has confirmed the efficiency of the rutile U-Pb high temperature thermochronometer in tracking the youngest detrital age populations within a detrital sample and in providing information on the early development of the source rocks. For these reasons, the author strongly encourages expanding the use of detrital and in situ rutile U-Pb dating to reconstruct tectonic histories.

5.2. Paleo-drainage reconstruction in the Namche Barwa area

The main question raised from this thesis is where did the Yarlung-Brahmaputra connection occur prior to 7-10 Ma, and how did it evolve in the late Miocene? This is of primary importance to investigate further the paleo-drainage of the Yarlung-Brahmaputra in this area, because the implications are significant. If it has remained through the Siang throughout the deposition of the

sediments of the Sibo-Remi-Siang section, then the study of chapter 4 would not be challenged. In this scenario, if the paleo-drainage in the syntaxis area had not suffered substantial change since ~15 Ma then the tectonic aneurysm model would be called into question. On the contrary, if such a change occurred around ~13 Ma, the tectonic aneurysm model would have to be considered further. Another possible scenario is a major capture occurring at ~7-10 Ma, for instance the potential Yarlung-Brahmaputra connection through the Lohit River capture by the Siang River. In this case, the interpretations of chapter 4 would need to be reassessed, as the change from old thermochronologic ages and long lag times to young ages and short lag times observed in the Sibo-Remi-Siang section would be explained by a capture event, and not necessarily by the rapidly exhuming syntaxis.

In order to decipher which of these hypothesizes is valid, the author suggests 1) to collect more data from the Siang section and 2) to characterize better the rock sources drained by the modern Lohit River. The first recommendation implies more analysis on samples from the Siang section, at shorter stratigraphic intervals, including more zircon U-Pb dating, apatite U-Pb dating and detailed sandstone petrology analysis which would help to track a potential change in provenance. Additional zircon U-Pb dating would help to better observe the Tethyan zircon grains abundance throughout the section. The apatite U-Pb data from the Siang section seem to indicate a sharp change in provenance (between sample SG11 and SG1) but the data are too scarce to allow robust conclusions. Therefore, supplemental apatite U-Pb dating might be particularly interesting for this purpose. Complementary Hf/Nd geochemistry on zircons might also deliver relevant information. The second suggestion involves further source characterization from the poorly constrained Lohit plutonic suite and the Bomi-Chayu rocks, using both zircon and apatite U-Pb dating to allow a better provenance analysis in the Sibo-Remi-Siang section.

5.3. Evolution of the eastern syntaxis

Supplemental paleo-drainage analysis as prescribed above would document the tectonic aneurysm model but additional bedrock studies would also inform the syntaxial development. Indeed, further thermochronological studies, especially with the rutile U-Pb system, would certainly provide key information. In situ rutile U-Pb dating along a NE-SW transect following the syntaxial antiform axis would constrain better the NE progression of the syntaxis.

5.4. Detrital syntaxial signal evolution downstream

In the eastern foreland basin, the young rutile grains characteristics of the syntaxis appear surprisingly scarce. The eastern syntaxis (only 2 % of the Yarlung-Tsangpo drainage area) has been suggested to contribute up to 50-70% of the Brahmaputra sediments (Enkelmann et al., 2011; Garzanti et al., 2004; Lang et al., 2013; Singh and France-Lanord, 2002; Stewart et al., 2008), therefore one would expect a substantial occurrence of young thermochronological ages from syntaxial detritus as far downstream as the Bengal Fan. However, the paleo-Brahmaputra sediments from the Surma basin do not record such young ages until Pliocene times (Bracciali et al., 2015). Additionally, preliminary rutile U-Pb results from recent investigations in the Bay of Bengal with the IODP expedition, acquired by Y. Najman seem to confirm this trend of scarce young rutile grains downstream. However, clear rutile U-Pb age populations <9 Ma have been found in the paleo-Brahmaputra deposits from the Dungsam Chu section by G. Govin and I. Millar (see Appendix VII). These discrepancies in abundance of young rutile grains within the eastern Himalayan foreland basin should be investigated further, with additional dating in the Miocene-Quaternary sedimentary record. A dilution study similar to the one preformed on zircon fission-track and white mica ^{40}Ar-^{39}Ar Gemignani et al. (submitted) focusing on rutile U-Pb, and as well as on zircon U-Pb, would allow quantifying the dilution effect on both U-Pb systems and document the signal evolution downstream the syntaxis and the Transhimalayan sources.

5.5. Review paper

Lastly, it is certain that this work and other Siwalik studies would have been and would be hugely facilitated by a review publication on the Siwalik sedimentary record. Indeed, the extensive amount of studies of various kinds such as dating, provenance, tectonic and climatic reconstructions, weathering, vegetation, paleo-environment, seismology and others should be compiled and summarized in one document, to render these studies more accessible for Siwalik investigators.

Great things happen when man and mountain meet.

William Blake

ACKNOWLEDGEMENTS

First of all, the author thanks the readers of this thesis, for their interest and their patience; especially the examiners who, I am afraid, will appreciate the rather long writing style. On this point I thank Yani for the extensive pruning of this work which would have been probably twice as long as this (or even longer!) without her sharp look.

But this is not the only reason why I am grateful to Yani, and I will enjoy the word-count freedom to argument. I am extremely lucky to have had such a good Ph.D. supervisor, she has offered me more guidance than one could expect. By guidance I mean the scientific guidance indubitably, without which this work would not have been completed, but I also mean the trust and the support she had given me throughout the Ph.D. She has always been in my side, encouraging me to follow my ideas (or to forget about them when necessary!). In short, this work would not have been 1) possible 2) such a good overall experience and 3) something that I am as proud of as I am now, without such a good supervision.

This supervision is the ideal combination of Yani and my co-supervisors, Peter and Pascale offering to this work a multi-perspective criticism, refinement and encouragements. I thank Peter, who believed in me and gave me his full support for this accomplishment (not finished yet I have to admit, but certainly in good progression) even before the story seven started. This thesis and its author have benefitted from the strong and high-standard scientific and positive commitment of Peter. I thank Pascale, my third supervisor, who was also supportive and very generous in good advices, until the very end!

This work is the fruit of a joined collaboration in which a large group of scientist have participated. I thank all the coauthors for their respective contributions which have allowed this thesis and its chapters to shape. I thank them all for their help in the field, in the lab, in the writing process and in the submission step. Thank you, Ian for your advices, the good laughs, the time in Keyworth in between the Mass Spec bedroom and the world's finest kitchen! I thank you Djordje for introducing me to the Bhutanese country, culture and geology in the best conditions. Thank you Isa for your support and the good scientific production of this first chapter. Thank you Guillaume for your

guidance in the field and during the (brain destructive!) Pmag data acquisition and for your cheerful enthusiasm. Thank you Matthias for your help, positivity and kindness that I am glad to have benefited of, once again during my Ph.D. after the good experience with you during my Masters (I still like ZFT, even the counting, and I definitely owe you this!). I thank particularly Alex for the modelling, Paul and Jan for the data and Chris for his input. I also thank the labs in which I have worked (ISTerre, the VU, Rennes, NIGL, CRPG), their teams, their technicians of precious help, especially Melanie. And I thank the technical support and beyond, in the field given by Kattu, Tending and Djordje (the Bhutanese Djordje) in India and Bhutan.

I acknowledge the project which has permitted this research happen, with its collaborations, secondments, protagonists and travels. I thank my fellows from the iTECC project, and my friends, who contributed to this thesis in terms of co-authorship, of course, but not only. Thank you Jesse for hosting me in Nancy and for your help on the Ion Probe. Thank you Lolo for welcoming me in Amsterdam and your massive help in the Ar-Ar data collection, and your strength in the field.

Et en haut du panier il y a Nana! Et oui, the best field assistant ever (of whom I also am the best (? => Surely yes!) field assistant). Merci Nana pour ton soutien, ton aide, ta cuisine, ton rire et tout le reste. Tu es incroyable, et je te dois beaucoup. La première chose ce sont les Dolomites, maintenant que les vacances commencent pour moi et que c'est fini pour nous deux il faut y aller !

I thank the entire iTECC team especially GZ, Mo, Svetlana, Ruben, Eric, Zak and Madelaine for their friendship and the great time we had all around the world! Thank you Ruben for hosting me like a queen in Bremen, and initiated me to the box and the real, lactose free cappuccinos! Thank you Mo for sharing track counting hours and delicious Iranian food, thank you Svetlana for the Russian lessons (Поехали!), thank you GZ for your support in Lancaster!

I thank Tamsin who introduced me to Lancaster University and Lancaster Environment Center like a professional student guide, and for her encouragements and friendship. I also thank Laura for her presence and friendship.

Aha and I thank the Lancaster canal crew, who is the best floating couple, canal sailors, boating partiers and hosts that I know on the planet!! I had such amazing times with you guys that I am ready to colonize and for even more sailing in the Lakes!

Dear Amblesiders, dear friends, Meg, Chris, Benedetta, Maria, Laura.. you made the entire Ph.D. experience so good. Thank you for sharing your experiences, your support, kindness and overall for having tolerated my crises throughout the years! I had great examples with you for academic success! And great Lancastrian family, including Jim!

Rachel, Sophie, Mariana, Natalie, Lisi, Victor, Gina, Victoria.. Climbing, dancing, running, yogaing, partying, great time with great friends, thank you for making this period as nice as it was to be amongst you in between and despites so many travels! Sophie, thank you for the great and often crazy adventures, and for the reinsuring you have provided me in this last tough part of the writing.

Thank you to the horse, the pie eater, the gardener, the neighbor, the Ceilidh dancer, the jam maker, the crazy gymnast, the companion of all adventures but climbing: the smile (but also the pearl) of Lancaster.

I also thank Filbert Bakery for three and half English years of delicious bread who allowed my *brioche* to survive☺. Thanks to Morecambe bay sea school, I enjoyed very much the northwest of England from the sea which helped my Ph.D. rat brain to get some fresh marine air!

Rein de tout cela n'aurait vu le jour sans mon *pater*, oui Papa je te le dis, je l'écris même noir sur blanc, devant témoins: Je ne te dois surement pas la réussite de mon bac. En revanche, et c'est peut-être encore mieux, je te dois la poursuite de cette thèse. Je dirais même plus, je te la dédie. Merci Papa, je suis contente de te connaitre ! Je n'omets pas non plus tes largages de papillons messagers aux couleurs et à la douceur de l'arc-en-ciel. Merci aussi a Tonton Baudruche pour son aide, ses conseils avertis et efficaces que je continue de suivre, et cela probablement ad vitam aeternam ! Merci Maman pour tes attentions, tes petits colis qui réchauffent le Cœur et le palais! Merci Charles pour tes encouragements et quelques bonnes sessions! Antoine, merci de m'avoir fait découvrir un pays merveilleux lorsqu'il était temps pour moi de prendre quelques vacances. Merci Stan pour ta bienveillance d'en haut.

GP et BM, incroyable jeunesse, merci pour vos attentions démesurées, vos caramels et autres gourmandises. Je suis bien trop gâtée depuis bien trop longtemps et bientôt docteur en cailloux, grâce à vous ! Babishka, jeunesse incroyable, merci pour ta fraicheur, tes mots doux et ta résistance! Maryse, merci de m'avoir rendu visite à Lancaster.

Jérôme, Denis, Nanouche, Cécile, tous mes chers oncles et tantes, parrains, marraine, merci pour votre soutien et Cécile tes tablettes qui ont été vitales ces derniers temps et qui m'ont permis de mener à bien ce projet de rédaction ! Mes cousins, cousines, merci pour votre aide, mentale et physique ! Particulièrement Sophie pour ses qualités de data enterring, et Delphine pour son soutien moral ! Et mon filleul préféré, Thibault Vitalik : le plus doué pour ça ; rien qu'avec tes yeux on comprend que tout est possible !

Je remercie le ciel et les étoiles pour m'avoir emmené aux quatre coins du monde pendant cette thèse d'aventurière. Notamment sur cette ile du soleil non couchant qui m'a tant touche, et toutes les belles rencontres qui ont rythmé et enchanté toutes ces explorations. Je remercie particulièrement tous les propriétaires de lits que j'ai eu la chance de délecter (je vous l'assure, le repos du thésard est crucial). Je réalise que ceci peut porter à confusion mais mes hôtes se reconnaitront et sauront à quelle plume je fais référence (e.g. Sommeiller et al., 2000). Et parmi eux la championne, j'ai nommé Nini (le E s'est envolé pour l'occasion !). Oui Nini sur la bonne literie je te dois au moins la moitié de ma thèse, et pour le reste c'est inestimable.

Merci à vous mes compères du soir, du jour et de la nuit (lorsque Morphée se refusait a moi), Jules Renard, Sylvain Tesson, Antoine de Saint Exupéry et ton Petit Prince, Papa, Nicolas Bouvier, Romain et Ugo pour avoir bercé ce chemin de poésie, de rêves et d'imaginaire voyageur.

Merci à vous, mes acolytes, mes clefs de voute indestructibles, mes amis de toujours qui avez assure pour votre présence, vos pensées, vos apéros, vos messages, vos visites, vos aventures partagées, vos regards, vos sourires, vos nouveau-nées, ton rôle de grand-frère parfaitement exécuté (même en sortie de boite), vos bras, vos attentions et la liste est non exhaustive, mais en voilà une suivante, dans le désordre (je regrette mais je fais fi de la structure car elle n'a plus mérite d'être): Ben, Domidom, Loulou, Matoutou, Ma, Clem, Pierro, Leslette, Ninie (oh oui, il est revenu), Palomine, Yordie, Camcam, Rominets, ClemD, Dich, Ju, Gat', toutes les crakies et tous les autres qui se reconnaitront. Ahh et merci à Rachel, Cécile, Marion pour leur aide experte, et John et Marion pour les péripéties privilégiées. Je remercie aussi Audrey et Guillaume, pour tout ce qu'ils m'ont apporté pendant cette thèse, pour leur soutien, leur aide et pour le meilleur.

And last, but not least les deux compères, mon petit couple favori. Des boules de neige, de la poudre d'artifice, de la crème chantilly maison sur un lit de fraises, fidèles compagnons qui prennent tant de place. Je nomme Sutra et Boubou de sausau, allias petit chou et attachiante, Tof et Dide, Sylvain et

Sylvette, la lune et le soleil… Je pourrai ajouter une dizaine de milliers de mots je doute que ça plaise à Yani, alors je m'arrête ici. Hehe j'ai pris un malin plaisirs à imaginer vos yeux baladeurs arrivé jusqu'ici sans se reconnaitre!! Merci mes globes terrestres, pour l'inestimable valeur que vous avez ajouté à cette période de thèse (à commencer par du stove-pasta-cooking teaching). Vous êtes présents en continu, vous ne connaissez pas la pause, et ce dès le début (si toute fois on peut mettre des bords à l'infini) avec une installation épique. D'ailleurs je compte sur cette fiabilité continue pour la désinstallation!! Kiss love & Merci

APPENDICES

APPENDIX I: Supplementary Material of Chapter 1 - Late Miocene-Pleistocene evolution of India-Eurasia convergence partitioning between the Bhutan Himalaya and the Shillong plateau: New evidences from foreland basin deposits along the Dungsam Chu section, Eastern Bhutan

Vitrinite reflectance: sampling strategy and analytical procedure

Eight coal-bearing mudstones were collected along the section (for sample location, see Fig. 18). Kerogen was isolated by Global Geolab Ltd. (Medicine Hat, Alberta, Canada), mounted using epoxy resin (EPO-TEK 301) in predrilled plastic stubs, polished and measured by Mike Avery at the Geological Survey of Canada - Atlantic (Dartmouth, Nova Scotia, Canada). The mounts were examined under oil immersion, incident light at 1000-x magnification using a Zeiss Photometer III system. The methodology and procedure used for vitrinite reflectance measurements are standard and available in (ASTM, 2010).

The reflectance was recorded as random reflectance (R_0, %). For each sample 34 to 50 measurements were made (Figure A), from which the mean random vitrinite reflectance (R_m) was calculated. All samples yielded a histogram with a single mode in the distribution curve tightly clustered about a mean value, which was determined using the Probability Density Plot software by Vermeesch (2012). We then used the empirical calibration of the R_m by Barker and Pawlewicz (1994) to determine the peak temperature due to sedimentary burial (*T*peak).

R_0 %
0.42
0.43
0.42
0.39
0.38
0.42
0.39
0.43
0.43
0.44
0.44
0.41
0.42
0.39
0.40
0.42
0.40
0.41
0.42
0.45
0.40
0.37
0.41
0.43
0.43
0.46
0.43
0.46
0.48
0.45
0.41
0.41
0.40
0.38
0.36
0.38
0.41
0.40
38 points

Mean	0.42
Standard devi	0.026
minimum	0.36
maximum	0.48

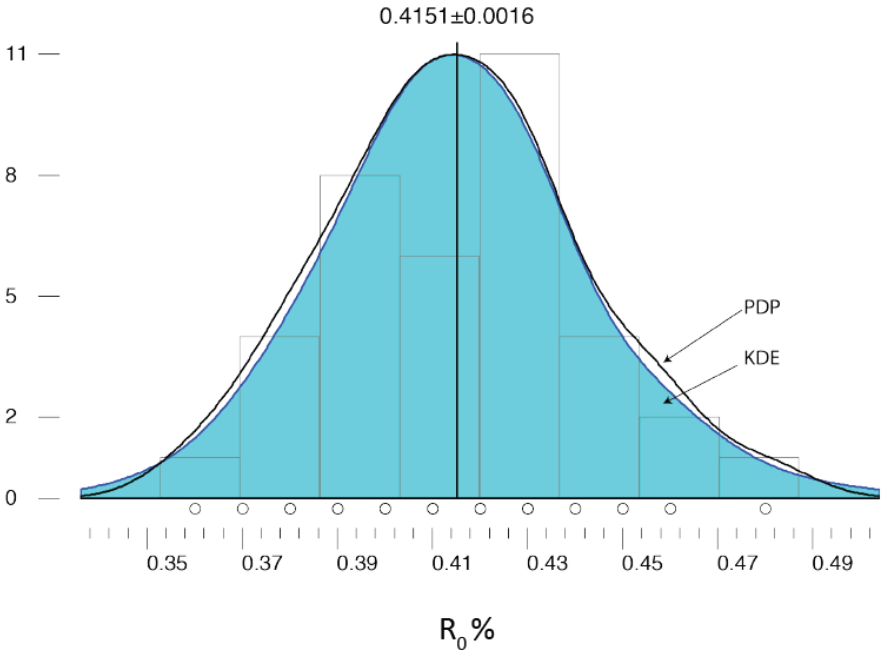

R_0 %
0.40
0.40
0.39
0.37
0.35
0.37
0.37
0.33
0.42
0.42
0.35
0.37
0.38
0.41
0.41
0.37
0.38
0.40
0.42
0.40
0.41
0.40
0.40
0.37
0.37
0.40
0.42
0.40
0.37
0.43
0.37
0.37
0.39
0.39
0.38
0.37
0.40
0.38
0.43
0.41
0.41
0.38
0.37
43 points

Mean	0.39
Standard devi	0.023
minimum	0.33
maximum	0.43

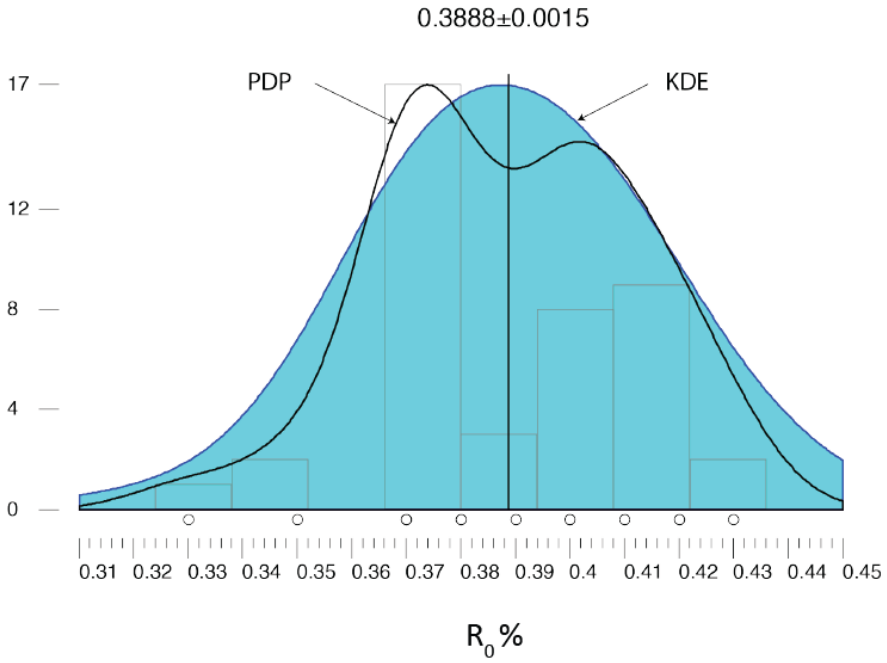

R_0 %
0.46
0.46
0.41
0.43
0.44
0.44
0.41
0.42
0.45
0.45
0.44
0.46
0.39
0.44
0.46
0.44
0.42
0.43
0.44
0.43
0.47
0.44
0.43
0.45
0.44
0.46
0.44
0.42
0.48
0.44
0.46
0.43
0.45
0.42
0.44
0.43
0.43
0.46
0.44
0.42
0.44
0.42
0.44
0.44
0.46
0.46
0.46
0.46
48 points

Mean	0.44
Standard devi	0.018
minimum	0.39
maximum	0.48

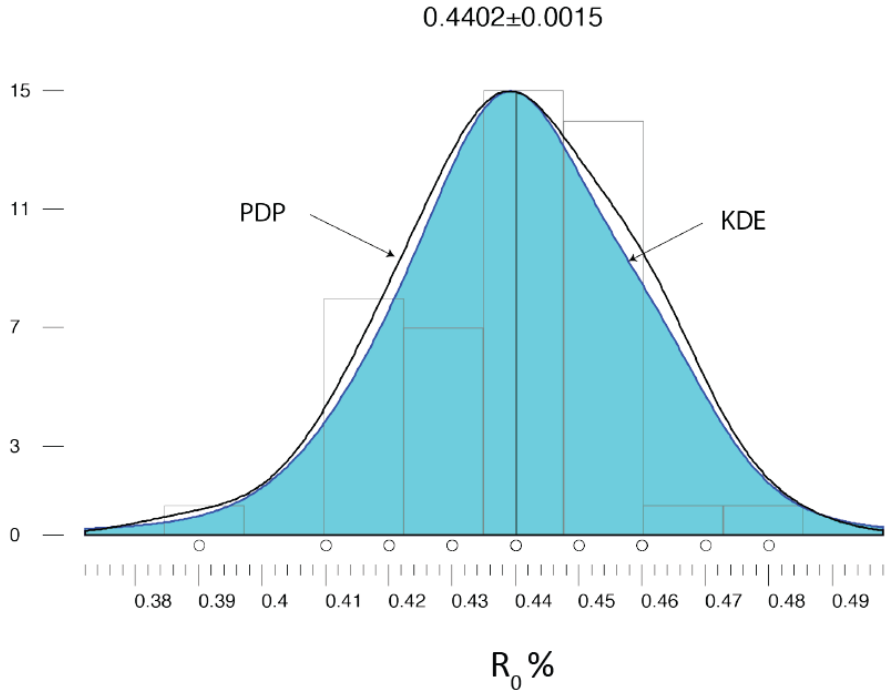

R_0 %
0.37
0.39
0.40
0.42
0.38
0.37
0.44
0.40
0.41
0.37
0.39
0.42
0.38
0.39
0.37
0.40
0.42
0.43
0.38
0.37
0.41
0.44
0.41
0.41
0.40
0.39
0.39
0.39
0.40
0.38
0.41
0.39
0.36
0.44
0.41
0.38
0.39
0.38
0.42
0.42
0.43
0.37
0.42
0.38
0.39
45 points

Mean	0.4
Standard devi	0.021
minimum	0.36
maximum	0.44

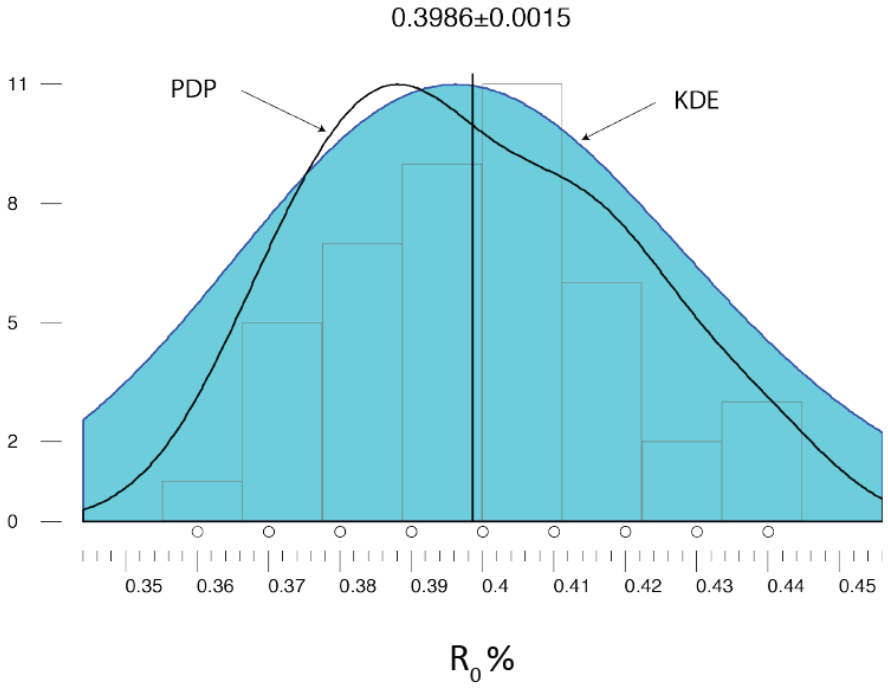

R_0 %
0.49
0.45
0.49
0.42
0.42
0.45
0.44
0.39
0.45
0.48
0.47
0.46
0.44
0.44
0.49
0.48
0.40
0.50
0.47
0.42
0.46
0.45
0.44
0.48
0.49
0.50
0.43
0.44
0.47
0.42
0.44
0.45
0.43
0.47
0.47
0.49
0.45
0.49
0.49
0.52
0.44
0.50
0.52
0.39
0.43
0.44
46 points

Mean	0.46
Standard devi	0.032
minimum	0.39
maximum	0.52

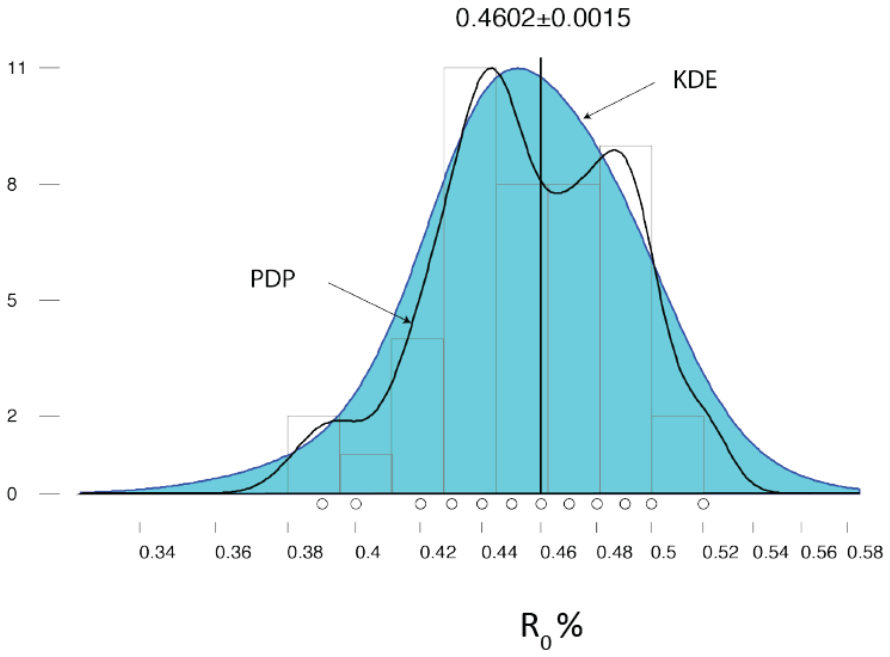

R_0 %
0.48
0.49
0.49
0.40
0.46
0.46
0.48
0.43
0.50
0.49
0.44
0.46
0.44
0.46
0.49
0.54
0.45
0.50
0.50
0.40
0.42
0.41
0.46
0.45
0.47
0.47
0.46
0.42
0.47
0.46
0.54
0.49
0.58
0.39
0.45
0.49
0.51
0.49
0.49
0.47
0.48
0.51
0.49
0.49
0.49
0.47
0.54
47 points

Mean	0.44
Standard devi	0.018
minimum	0.39
maximum	0.48

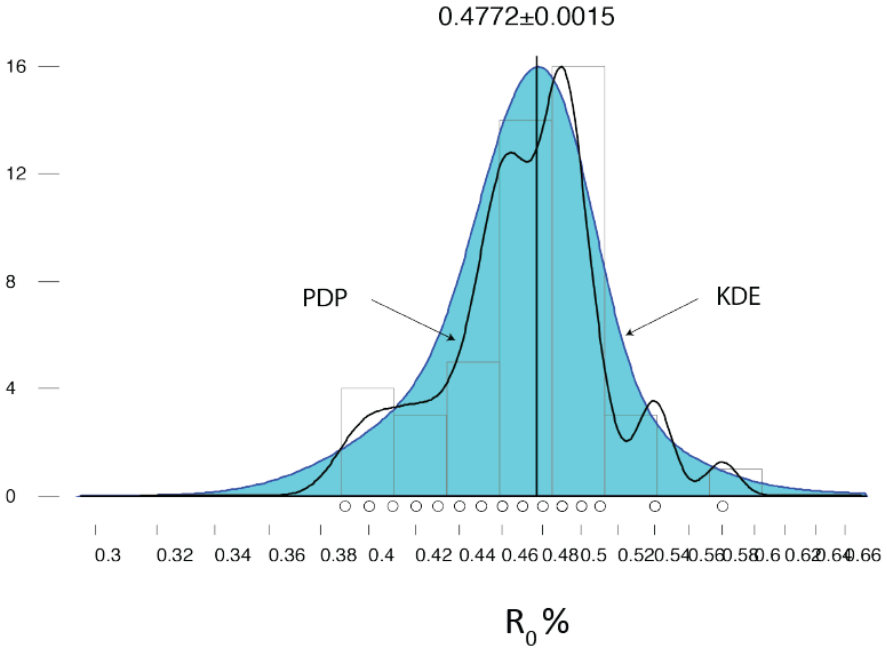

R_0 %
0.42
0.42
0.40
0.39
0.44
0.42
0.44
0.41
0.40
0.47
0.41
0.42
0.50
0.41
0.40
0.48
0.41
0.41
0.41
0.39
0.38
0.40
0.44
0.46
0.39
0.37
0.40
0.41
0.46
0.43
0.40
0.44
0.38
0.39
0.44
0.41
0.44
0.41
0.42
0.36
0.44
0.42
0.46
0.40
0.37
0.42
0.40
0.45
0.39
0.39
50 points

Mean	0.42
Standard devi	0.029
minimum	0.36
maximum	0.50

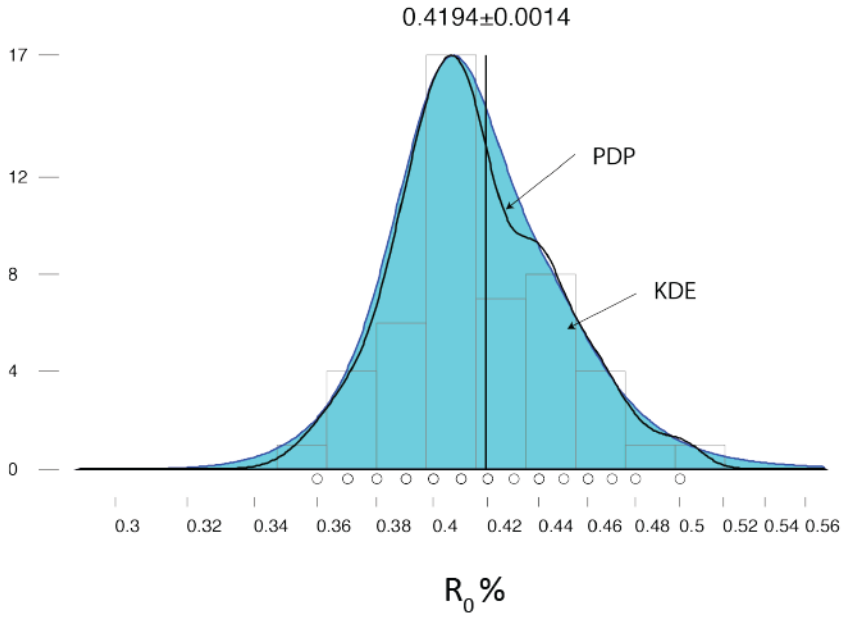

R_0 %
0.34
0.36
0.32
0.32
0.35
0.30
0.36
0.33
0.33
0.35
0.34
0.34
0.30
0.34
0.36
0.32
0.30
0.35
0.34
0.35
0.39
0.31
0.36
0.28
0.33
0.34
0.34
0.37
0.31
0.35
0.33
0.32
0.33
0.36
0.34
0.34
0.31
0.37
0.35
0.36
0.36
0.35
0.29
0.30
0.31
0.33
0.35
0.34
48 points

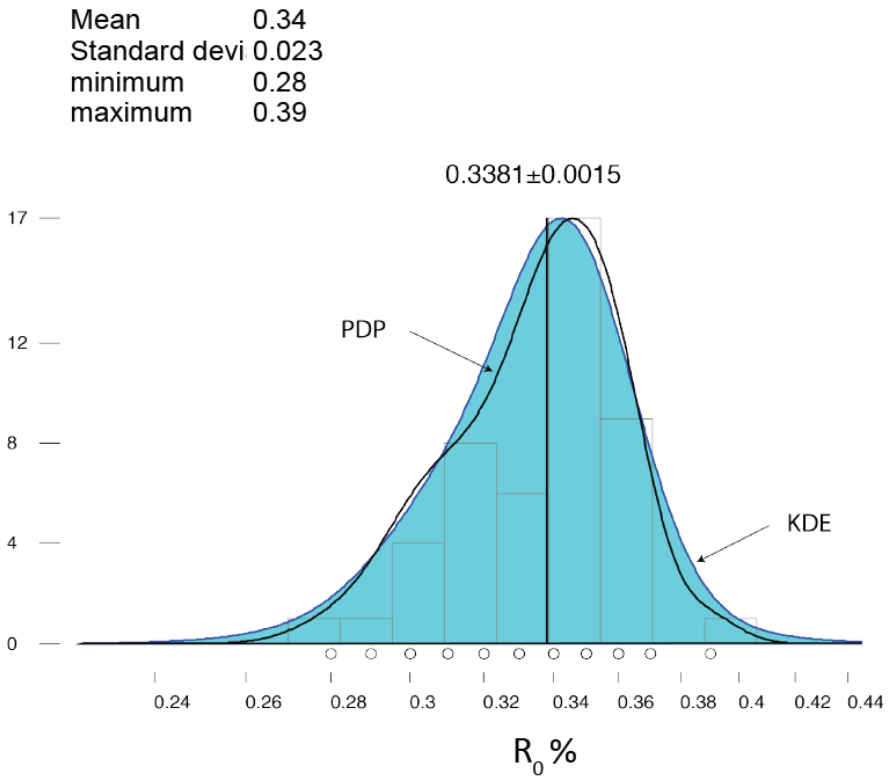

Figure A: *Vitrinite Reflectance data*

Detrital apatite fission-track (DAFT) thermochronometry method and sampling

Apatite fission-track is a thermochronometric method based on the formation and retention of linear damage zones (or fission tracks) in the crystal lattice of uranium-bearing minerals, caused by the spontaneous radioactive decay of ^{238}U. The tracks are retained at temperature below ~120±20 °C (e.g., Donelick et al., 2005) and may be partially annealed through diffusion processes until temperatures down to 60 °C (for an apatite of average composition and a holding time of about 10 Ma; see (Reiners and Brandon, 2006)). This temperature interval is called the Partial Annealing Zone (PAZ). Detrital apatite crystals contained into clastic sediments yield cooling ages that are representative of the bedrock cooling age in the source area when post-depositional burial and heating has been limited such as the age remains unreset. Alternatively, the source signal may be partially or fully altered by thermally-induced diffusion and resulting track annealing.

Six medium- to coarse-grained sandstones, about 5-8 kg in weight, were collected through the stratigraphic section at an average stratigraphic spacing of 300 m (for sample location, see Fig. 18 and Table 1). The samples were processed and analysed at the Dalhousie University Thermochronology Laboratory using the procedure described in Coutand et al. (2014). Most of the fractions were of moderate quality with only few apatites available, cracks and zircon inclusions within the crystal were common and sometimes heterogeneous distribution of uranium was recorded. To overcome these limitations, we prepared and processed two mounts for each sample; yet, it was possible to date only 14 to 26 crystals per sample. For each sample, fission-track grain-age distributions were decomposed using the binomial peak-fit method (Galbraith and Green, 1990) incorporated into the *Binomfit* program (Brandon, 1992; Brandon, 1996; Brandon, 2002) to identify discrete grain-age populations.

Table S1: *Apatite fission-track counting data. Ns, number of spontaneous tracks counted; Ni, number of induced tracks counted; ρd, induced track density in external detector adjacent to dosimetry glass; Na, number of microscope grid squares counted.*

Zeta factor: 370.6 ± 5.0
Counting area per N_a square: 9E-07 cm^2

Sample SB07
ρ_d: 1458500 cm^{-2}

N_s	N_i	N_a
8	274	50
1	92	80
2	89	100
3	168	49
7	250	100
8	258	60
8	427	70
53	1100	100
2	64	50
10	285	100
2	50	50
2	57	100
5	175	50
3	151	50
14	405	50
4	177	40
8	190	30
4	140	49
1	126	100
19	920	100
20	776	64
5	183	60
5	156	60

Sample SB54
ρ_d: 1488950 cm^{-2}

Ns	Ni	Na
9	296	100
2	44	70
14	276	81
1	66	36
6	305	50
13	400	70
5	218	100
6	500	100
4	184	36
10	505	100
13	470	100
6	164	30
10	896	80
2	56	100
4	385	100
10	375	100
6	365	50
8	417	90
15	770	100
8	310	100
6	650	100
15	760	80
4	156	80
3	160	100
3	35	50
0	87	80

Sample SB75
ρ_d: 1486500 cm^{-2}

Ns	Ni	Na
4	82	30
5	139	40
6	356	100
4	179	100
7	468	100
15	675	100
2	95	100
5	301	100
5	390	100
7	575	100
1	16	100
7	215	100
3	375	70
13	655	100
3	120	60

7	326	100
4	148	60
11	294	50
6	370	50
4	60	70
7	265	60

Sample SB76

ρ_d: 1488200 cm^{-2}

Ns	Ni	Na
4	502	80
10	410	30
4	220	100
6	418	90
7	266	70
5	139	64
13	668	40
3	342	60
1	48	60
0	56	80
1	78	100
2	128	100
1	158	100
2	148	60

Sample SB79

ρ_d: 1489900 cm^{-2}

Ns	Ni	Na
5	284	100
2	214	100
1	64	100
4	235	60
4	173	100
1	48	100
6	321	49
8	275	100
11	1120	100
2	134	49
1	39	70
14	673	100
9	199	60
2	530	100
8	539	70
5	425	100
7	384	40
12	520	70
13	810	100
59	1240	100
1	269	80
7	624	80
5	226	80
8	672	70

Sample SB83

ρ_d: 1491600 cm^{-2}

Ns	Ni	Na
1	64	100
13	314	98
8	412	100
9	108	80
5	395	20
11	399	70
6	136	100
3	221	40
6	380	50
21	1540	100
2	261	50
8	94	35
2	179	100
7	826	70
21	340	60
7	784	70
7	575	100

Paleomagnetic analysis: sampling and analytical procedure

We sampled the Dungsam Chu section maintaining, when possible, a stratigraphic spacing of the paleomagnetic sites to about five meters, although some larger gaps could not be avoided due to the lack of outcrop or unfavourable lithologies (for sample location, see Fig. 19). Using an electric drill powered by rechargeable batteries and mounted with a diamond-coated drill-bit cooled with water, one to three cores, 2.5 cm in diameter, were collected from each paleomagnetic site, targeting the finest possible lithologies. Cores were oriented with a custom device integrating a clinometer and a compass. Minor local declination (<0.5°) was neglected. Because fine-grained sediments were rare, coarser lithologies (medium- to coarse-grained sandstones) were also collected. Out of a total of 364 sampled paleomagnetic sites, 303 have yielded results (Fig. 19). Bedding attitudes were measured at each site and averaged for portions of the sections with similar attitudes for tilt corrections. Remanent magnetizations of samples were measured on a 2G Enterprises DC SQUID cryogenic magnetometer within an amagnetic chamber, at the Geosciences Rennes paleomagnetic laboratory, France. Pilot samples distributed at 50 meters intervals throughout the stratigraphic section were stepwise thermally demagnetized in a shielded oven. Tight heating steps from 20 to 670 °C were applied to determine (1) the characteristic demagnetization behaviour, (2) the most efficient demagnetization temperature steps, (3) which lithology provides the best signal, and (4) identify stratigraphic intervals with potential paleomagnetic reversals. These preliminary results guided further processing of the remaining samples at higher stratigraphic resolution. Thermal demagnetization was then applied to the remaining samples with a carefully defined set of small thermal demagnetization steps including 50 to 100 °C steps up to 550 °C and 10 to 15 °C steps between 550 and 670 °C. When multiple samples were available from one sampling site, if the result from a first sample at a site was ambiguous, a second or a third sample was processed to unambiguously identify the polarity at that site.

Table S2: *ChRM directions. Abbreviations are: Sample ID. sample identification; level. location in the stratigraphic column (0 meters is the bottom); Dec IS and Inc IS. ChRM declination and inclination in geographic coordinates. in situ (before tilt-correction); Dec and Inc. ChRM declination and Inclination in stratigraphic coordinates in situ (IS) and after tilt-correction (TC); Int. Intensity of magnetization; MAD. maximum angular deviation of ChRM direction; Q. reliability criteria Q1. Q2 and Q3 (see text); Line fit. calculation of ChRM direction: O – line forced to the origin; * –line unforced. GC– great circle (see text); Tinf and Tsup. temperature minimum and maximum in between ChRM; VGP lat. Virtual Geomagnetic Pole latitude derived from ChRM direction at sampling location; Dip az. and Dip. azimuth of bedding dip and dip averaged over portions of the section.*

Sample ID	Level (m)	Dec IS (°)	Inc IS (°)	Dec TC (°)	Inc TC (°)	Int 10-5 A/m	MAD (°)	Q	Line fit	Tinf (°C)	Tsup (°C)	VGP lat (°)	Dip az. (°N)	Dip (°)
SJ001A	1.0	163.2	21.5	178.0	45.5	30237.8	1.0	1	*	10	230	-36	308	32
SJ002A	5.0	195.8	-32.7	182.5	-16.8	gc	6.9	2	GC	20	260	-71.4	308	32
SJ003A	17.0	195.7	-58	166.3	-37.8	544.7	3.5	1	O	130	260	-76.2	308	32
SJ004A	17.0	350.7	-31.7	14.5	-51.0	188.1	5.7	3	O	10	130	29.7	308	32
SJ005B	39.4	225.7	51.1	201.3	-2.1	49.6	11.6	2	*	130	240	-57	170	68
SJ005A	39.4	215.5	-23.5	271.1	-48.2	84.4	8.5	3	O	130	240	-11.9	170	68
SJ007A	64.6	341.8	-59.8	134.2	-59.8	1175.2	3.9	4	O	150	260	-50.1	328	59
SJ008A	69.5	139.3	-73.8	145.5	-15.0	463.3	4.5	1	O	120	280	-52	328	59
SJ009A	79.1	78.8	-65.0	99.3	-22.6	426.1	1.5	4	O	130	260	-13.5	295	46
SJ010A	99.0	3.1	45.9	337.8	18.2	1157.2	14.4	1	*	150	300	62.6	295	46
SJ011A	102.1	335.1	37.8	325.6	-0.5	4410.6	10.6	3	O	150	260	47.2	295	46
SJ012A	112.7	214.3	-26.7	190.8	-24.6	182.8	4.6	1	O	180	260	-72.6	295	46
SJ014A	122.5	208.1	-42.7	172.9	-30.0	1622.0	2.3	1	O	130	260	-77.3	295	46
SJ013A	122.5	0.6	-35.7	39.1	-40.3	80.5	5.6	3	O	150	240	27.4	295	46
SJ015A	146.8	331.2	30.4	327.5	-5.4	1218.0	3.8	3	O	200	300	46.8	305	39
SJ016A	155.9	186.4	-43	167.5	-18.0	1203.8	1.1	1	O	130	260	-68.6	305	39
SJ018A	171.9	180.6	-56	143.6	-43.7	166.7	3.6	2	O	200	260	-57.5	273	32
SJ019A	190.1	48.3	-3.7	45.2	18.7	339.2	4.3	4	O	10	180	44.1	273	32
SJ019B	190.1	67.2	23.3	53.9	50.7	100.6	6.3	4	O	130	300	43.2	273	32
SJ020A	199.2	181.8	-17.8	172.4	-14.4	gc	11.9	3	GC	20	300	-69	273	32
SJ021A	223.8	159.6	-22.6	151.7	-7.6	gc	5.6	3	GC	20	260	-54.4	273	32
SJ022A	237.0	350.5	33.2	341.7	-0.8	119.1	20.0	2	*	10	460	57.4	305	44
SJ022B	237.0	8.7	28.9	356.9	4.5	67.8	5.3	3	O	130	240	65.1	305	44
SJ024A	256.2	19.4	55.9	343.3	29.4	95135.5	3.8	2	O	20	260	70.9	305	44
SJ023A	256.2	74.2	26.2	43.3	45.3	313.8	4.7	4	O	20	210	51.5	305	44
SJ025A	260.6	249.1	17.3	251.8	-9.1	3470.2	1.7	4	O	180	260	-18.3	305	44
SJ026A	269.9	43.5	57.6	350.0	41.5	164.7	4.0	2	O	150	280	80.5	305	44
SJ027A	272.8	204	-41.8	177.3	-22.4	60.5	3.8	2	O	100	240	-74.4	305	44
SJ028A	275.6	0.3	39.2	345.1	8.5	156.0	4.2	2	O	20	140	63.2	305	44
SJ029A	290.0	21.3	37.8	358.9	18.1	113.9	8.3	2	O	180	300	72.2	305	44
SJ031A	302.1	293.1	74.5	312.8	45.1	235.5	3.7	2	O	150	269	48.1	324	31
SJ032A	303.8	25.7	43.9	8.3	24.7	117.4	6.8	2	O	150	260	73.9	324	31

SJ033A	307.6	345.2	46.8	339.0	17.2	224.2	4.2	2	O	150	260	63.1	324	31
SJ034A	309.8	16.6	32.2	6.3	15.6	337.1	5.2	2	O	150	300	70	317	28
SJ035A	310.4	10.7	27.6	3.4	9.4	90.2	7.0	2	O	200	340	67.5	317	28
SJ036A	312.0	345.2	48.5	343.8	24.6	50.8	13.4	2	O	150	210	69.3	340	24
SJ039A	326.0	287.9	46.8	301.6	29.7	143.4	6.1	2	O	20	140	35	340	24
SJ040A	358.3	14.8	55.9	2.9	34.7	127.3	18.9	3	O	30	280	81.6	340	24
SJ041A	363.1	324.6	-15.5	334.2	-46.0	102.0	6.8	2	O	200	280	30.3	302	34
SJ042A	364.3	356.3	48.8	337.9	24.1	375.3	7.9	3	*	20	270	64.8	302	34
SJ043A	368.9	278.0	29.4	280.2	-2.4	159.8	4.1	4	O	130	260	8.5	295	33
SJ044A	381.0	24.7	31.7	2.7	26.6	276.0	3.5	1	O	150	400	76.8	291	38
SJ045A	385.7	13	30.8	358.9	23.3	107.3	9.4	1	*	150	260	75.1	291	28
SJ046A	389.4	6.5	51	348.9	12.5	127.9	12.0	1	*	130	260	66.8	322	46
SJ047A	391.7	15.2	41.5	359.3	7.9	94.4	17.5	1	*	130	260	66.9	322	46
SJ048A	393.5	6.9	43.3	353.1	6.1	116.0	12.8	1	*	180	260	65.2	322	46
SJ049A	396.3	8.0	-4.2	21.2	-33.3	102.3	21.5	3	*	130	380	40.4	322	46
SJ050A	398.1	353.7	30.8	349.3	-9.8	58.9	12.4	3	*	150	240	56.4	322	46
SJ051A	404.0	200.4	-33.8	190.3	-33.9	72.2	1.4	2	O	200	260	-77.3	285	15
SJ052A	407.4	177.3	-21.9	172.3	-16.7	gc	21.9	2	GC	20	320	-70.1	285	15
SJ053A	408.4	172.7	0.2	173.4	5.8	129.2	10.4	2	O	150	260	-59.4	285	15
SJ054A	409.4	33.8	38.9	21.2	42.2	97.3	11.9	3	O	150	300	70.7	285	15
SJ055A	409.9	189.1	-44.8	175.3	-41.4	18252.4	5.0	1	*	130	260	-84.7	285	15
SJ056A	410.8	174.9	-36.7	163.4	-17.4	1045.6	3.3	1	O	230	360	-66	300	29
SJ057A	415.7	192.1	-45.8	171.7	-30.8	gc	3.9	3	GC	130	240	-77.1	302	29
SJ058A	418.7	185.6	-20.5	179.5	-6.0	35.4	9.1	2	O	150	240	-66	302	29
SJ059A	418.7	183.4	-29.3	173.8	-13.0	gc	22.0	3	GC	130	380	-68.8	302	29
SJ060A	423.5	40.6	64.9	354.3	50.1	57.3	27.0	2	*	150	240	83.7	313	31
SJ061A	423.5	181.2	-39.5	169.8	-16.3	gc	8.7	3	GC	20	340	-69	313	31
SJ063A	427.0	239.9	-61	187.6	-55.3	169.3	3.9	2	O	180	260	-79	313	31
SJ064A	429.0	181.5	-40.5	169.6	-17.3	gc	18.9	3	GC	180	340	-69.4	313	31
SJ065A	432.0	3.0	16.9	0.3	-3.9	407.7	6.2	3	O	150	360	61	313	31
SJ067A	438.1	173.3	-19.1	173.1	10.7	150.5	8.4	2	O	150	260	-56.9	347	30
SJ068A	442.2	121.8	-32.3	123.2	15.0	35.3	11.4	4	O	180	300	-25.1	313	48
SJ069A	450.3	215	-19.2	203.9	-14.3	153.9	4.8	2	O	180	260	-59.9	307	36
SJ070A	458.0	16.7	61.3	341.7	37.7	88.1	8.3	2	O	150	300	72.4	307	36
SJ071A	464.8	192	-37.5	175.8	-17.2	gc	7.3	2	GC	20	260	-71.4	307	36
SJ072A	475.7	315.7	-10.5	319.4	-45.9	75.5	6.3	3	O	160	380	23.1	307	36

SJ073A	480.2	68.3	31.2	46.8	47.9	44.4	7.3	3	O	180	260	48.9	295	30
SJ074A	484.7	7.9	28.8	356.0	16.7	38.3	12.8	3	O	200	260	71.1	295	30
SJ075A	488.4	340	45.6	327.2	21.8	123.9	7.5	2	*	100	150	55.4	295	30
SJ076A	518.5	24.2	11.2	18.7	9.3	186.8	2.8	2	O	150	320	61.4	295	30
SJ078A	518.5	354.9	31.6	344.4	13.9	399.8	7.0	1	*	130	260	65.2	295	30
SJ077A	518.5	21.1	32.4	4.4	25.8	212.0	5.3	1	O	130	260	76	295	30
SJ079A	538.8	356.3	-7.1	3.0	-20.2	71.0	10.1	2	O	150	260	52.5	295	30
SJ080A	541.6	347.2	44.1	332.9	22.5	86.6	25.9	1	*	180	380	60.3	295	30
SJ081A	551.0	331.4	36	324.2	10.6	130.5	9.2	1	*	150	280	49.6	295	30
SJ082A	557.6	7.2	40.7	348.9	26.7	755.5	5.5	1	*	130	260	73.5	295	30
SJ083A	563.6	334.2	37.7	325.9	12.9	75.0	21.7	1	*	130	260	51.7	295	30
SJ084A	573.7	19.3	65.5	335.1	50.1	66.6	21.9	1	*	180	320	67.9	295	30
SJ085A	578.3	337.1	29.1	331.0	5.6	58.2	25.6	1	*	130	240	53.2	295	30
SJ086A	582.3	359.5	29.3	345.3	19.3	30.8	14.6	1	*	150	260	68	280	32
SJ087A	585.0	350.1	26.8	339.4	12.8	666.7	22.9	1	*	210	420	61.6	280	32
SJ088A	588.3	324.1	41.4	312.9	16.0	122.7	9.9	2	O	180	320	41.7	280	32
SJ089A	593.0	359.2	27.9	336.7	-2.8	70.5	13.0	1	*	150	260	53.8	275	85
SJ090A	596.1	100.0	34.2	266.6	60.4	76.0	7.9	3	O	180	300	15.1	275	85
SJ091A	636.8	198.0	-12.8	173.0	-13.8	gc	15.1	3	GC	150	280	-68.9	275	85
SJ092A	642.3	185.1	-44.0	166.9	-24.6	gc	11.0	3	GC	20	280	-71.3	302	32
SJ093A	647.1	2.4	15.9	358.8	-1.1	88.9	25.0	3	*	130	260	62.4	302	32
SJ094A	652.6	186.5	33.8	211.3	41.4	177.3	2.8	4	O	150	260	-30.9	302	32
SJ095A	656.7	2.7	49.8	346.1	33.9	72.7	13.0	1	*	150	260	74.7	305	24
SJ096A	659.5	4.9	34.2	354.7	20.2	109.0	19.1	1	*	160	300	72.7	305	24
SJ097A	661.5	252.4	75.3	286.9	49.5	74.5	5.8	4	O	180	260	27	305	30
SJ098A	662.5	310.2	27.6	311.5	-7.8	87.5	8.5	2	O	150	240	33.9	322	36
SJ099A	665.3	353.1	50.8	342.1	18.0	232.7	10.4	1	*	130	250	65.5	322	36
SJ100A	667.7	9.4	36.5	358.8	9.3	62.2	17.1	1	*	150	280	67.7	322	36
SJ101A	669.0	28.2	47.5	5.4	25.9	100.6	17.5	1	*	130	340	75.7	322	36
SJ102A	670.1	2.7	28.5	357.0	-0.3	67.5	11.4	1	*	130	280	62.7	322	36
SJ103A	671.1	185.4	-43.7	172.9	-14.5	gc	10.2	3	GC	20	240	-69.2	322	36
SJ104A	672.5	5.2	32.2	357.5	3.9	95.5	13.3	1	*	160	340	64.8	322	36
SJ106A	676.2	15.4	27.1	7.7	3.2	62.4	20.8	2	*	150	340	63.6	322	36
SJ107A	677.6	185	-42.7	173.0	-13.5	gc	14.0	2	GC	20	280	-68.8	322	36
SJ108A	679.3	190	-38.8	176.2	-10.3	gc	29.8	2	GC	180	320	-67.9	317	40
SJ109A	688.7	191.6	-25.5	184.4	0.4	69.1	4.0	2	O	150	260	-62.5	317	40

SJ111A	693.0	185	-29.7	177.0	-6.4	gc	10.0	2	GC	20	260	-66	315	33
SJ112A	698.0	198.3	-3.9	200.1	10.8	gc	12.3	2	GC	130	400	-52.2	315	33
SJ113A	703.7	181.8	-53.8	163.9	-27.2	301.3	2.5	1	O	150	260	-70.4	315	33
SJ114A	710.7	159.9	-38.7	154.4	-8.0	117.9	7.1	1	O	130	260	-56.4	315	33
SJ115A	714.7	18.2	51.8	354.8	30.5	70.7	6.4	2	O	150	260	78.3	315	33
SJ116A	721.0	177.8	-34.5	169.5	-8.4	gc	11.8	2	GC	20	280	-65.1	315	33
SJ117A	723.2	161.8	-59.1	150.2	-28.0	55.1	7.3	2	O	150	240	-59.7	315	33
SJ119A	736.2	174.6	-36.7	163.3	-20.4	671.8	1.7	1	O	130	260	-67.2	297	26
SJ120A	738.3	207.8	-50.7	179.4	-44.4	705.9	3.3	1	O	230	400	-89	297	26
SJ121A	742.1	135.1	6.8	138.2	31.3	252.6	9.4	3	*	20	220	-30.2	297	26
SJ122A	745.1	329.4	-38.0	349.2	-57.7	43.0	22.8	3	*	150	260	23.9	297	26
SJ123A	746.4	205.7	-59.2	169.9	-50.1	185.2	6.4	1	O	150	300	-80.4	297	26
SJ124A	747.6	245.1	-41.8	218.7	-53.2	468.8	4.8	4	O	30	270	-56.1	297	26
SJ126A	759.4	172	-53.6	166.8	-11.2	gc	6.9	2	GC	20	220	-65.2	339	43
SJ127A	762.8	183.9	-47.7	175.6	-7.2	gc	4.9	2	GC	20	280	-66.2	339	43
SJ128A	766.4	254.9	-73.3	183.4	-46.1	79.6	8.6	1	O	220	360	-86.9	339	43
SJ129A	768.2	116.8	-50.1	132.7	-13.7	61.0	5.3	1	O	130	240	-42.2	339	43
SJ130A	770.8	180.9	-44.1	174.6	-3.1	gc	4.0	2	GC	20	260	-64	339	43
SJ131A	771.7	180.6	-57.1	171.0	-15.6	gc	7.6	2	GC	20	260	-69.1	339	43
SJ132A	818.4	262.3	-36.8	231.2	-35.9	103.8	4.0	4	O	230	260	-42.8	338	40
SJ133A	823.5	180.7	-53	171.9	-14.8	gc	3.1	2	GC	20	260	-69.1	338	40
SJ134A	835.0	173.7	-42.5	169.5	-3.5	gc	18.0	2	GC	20	260	-62.8	338	40
SJ135A	838.9	213.8	-76.2	173.2	-41.1	92.7	4.5	1	O	150	260	-83	338	40
SJ136A	841.4	189.2	-41.8	180.8	-5.8	gc	21.3	2	GC	20	360	-65.9	338	40
SJ137A	845.2	198.7	-41.9	187.4	-8.6	110.0	2.4	1	O	130	240	-66.2	338	40
SJ138A	854.2	212.8	-43.3	196.0	-14.8	141.8	2.2	1	O	130	260	-65.3	338	40
SJ139A	876.3	178.9	-45.6	174.7	3.5	gc	9.2	2	GC	20	260	-60.8	345	50
SJ140A	881.5	187.9	-41.9	181.9	5.5	531.6	2.7	1	O	220	340	-60.2	345	50
SJ141A	884.7	191.8	-59	178.7	-11.5	30.5	3.8	1	O	130	260	-68.8	345	50
SJ142A	888.9	185.6	-62.9	174.5	-14.2	gc	8.8	2	GC	20	260	-69.5	345	50
SJ143A	891.0	219.4	-35.1	206.7	-6.7	100.4	1.7	1	O	180	260	-55.2	344	42
SJ144A	894.7	221.1	11.1	236.0	30.0	71.9	3.2	4	O	230	320	-20.6	344	42
SJ145A	897.7	168.1	-36.1	167.3	5.8	gc	9.6	2	GC	20	260	-57.7	344	42
SJ146A	899.7	180	-38.9	176.4	1.9	gc	9.8	2	GC	20	220	-61.8	344	42
SJ147A	900.9	215.9	-59.7	190.1	-25.7	82.7	8.6	1	O	20	240	-73.6	344	42
SJ148A	938.5	194.5	74.8	301.7	55.7	111.8	5.5	4	O	150	260	40.3	323	42

SJ149A	942.0	192.7	-42.9	177.7	-10.9	gc	22.2	2	GC	20	260	-68.4	323	42
SJ150A	947.2	190.2	-32.7	181.1	-1.1	gc	14.4	2	GC	130	300	-63.5	323	42
SJ152A	953.6	224.3	-66.9	173.4	-40.1	27.0	9.5	2	O	230	320	-82.7	323	42
SJ153A	969.9	183.5	-43.2	175.2	-6.7	156.8	4.1	1	O	20	210	-65.9	334	40
SJ154A	974.2	177	-61.8	165.6	-23.3	242.1	3.5	1	O	30	400	-69.9	334	40
SJ155A	976.4	169.6	-49	164.3	-9.9	gc	12.0	2	GC	20	260	-63.4	334	40
SJ156A	987.1	233.0	-17.9	224.2	-6.8	96.7	32.3	4	*	120	340	-41.7	334	40
SJ157A	990.9	182.6	-52.5	171.6	-15.3	gc	4.3	2	GC	20	220	-69.2	334	40
SJ158A	994.7	182.8	-50.7	172.3	-13.7	gc	6.9	2	GC	20	260	-68.7	334	40
SJ159A	1009.3	202.7	-54	182.4	-21.7	gc	13.9	2	GC	20	340	-74.1	334	40
SJ160A	1009.3	177.8	-35.8	173.1	1.7	gc	12.1	3	GC	0	400	-61.4	334	40
SJ162A	1068.8	193.4	-69.6	150.8	-28.9	50.9	2.7	1	O	150	240	-60.6	310	50
SJ163A	1073.4	261.2	-71.5	151.9	-50.3	148.7	2.7	1	O	180	240	-65.2	310	50
SJ164A	1073.4	223.5	-1.1	221.4	-3.4	29.5	6.2	4	O	220	300	-43	310	50
SJ165A	1081.4	351	43.8	338.3	1.6	49.3	16.5	2	*	130	220	56.6	310	50
SJ166A	1090.4	152.1	-14.3	155.4	31.9	146.4	3.1	1	O	150	240	-39.7	310	50
SJ167A	1098.6	33.5	71.2	346.7	43.1	197.8	9.5	3	*	20	220	77.9	322	38
SJ168A	1102.4	170.4	-50.4	160.3	-15.2	140.8	3.8	1	O	180	280	-63.2	322	38
SJ169A	1112.3	276.7	-56.2	204.7	-63.6	229.0	2.3	4	O	130	320	-63.2	322	38
SJ170A	1117.0	186	-42.9	173.4	-12.2	gc	11.9	2	GC	20	260	-68.2	322	38
SJ171A	1119.3	188.8	-42	175.7	-12.4	gc	2.9	2	GC	20	240	-68.9	322	38
SJ172A	1121.7	225.1	-85.8	148.7	-51.3	29251.0	4.9	1	*	210	380	-62.4	322	38
SJ173A	1124.0	206.3	-51.1	181.2	-26.5	6831.5	6.7	1	*	90	270	-77	322	38
SJ174A	1126.3	266.7	-80.8	155.8	-56.5	187.4	1.4	1	O	130	240	-67.2	322	38
SJ175A	1128.7	223.4	-40.3	199.1	-26.1	270.6	2.4	1	O	130	240	-67.8	322	38
SJ176A	1131.0	225.3	-28	209.1	-17.8	127.5	5.9	1	O	210	340	-57.2	322	38
SJ177A	1133.4	192.4	-41.2	178.5	-12.9	gc	5.8	2	GC	20	280	-69.5	322	38
SJ178A	1135.7	193.7	-17.4	191.0	7.4	gc	19.1	2	GC	130	380	-57.5	322	38
SJ179A	1138.0	167.4	-21.2	166.3	13.5	gc	11.2	2	GC	20	320	-53.6	322	38
SJ180A	1140.4	225.5	-62.1	180.4	-41.6	337.4	10.7	1	*	220	400	-86.9	322	38
SJ181A	1142.7	193.1	-34.9	182.1	-7.7	gc	6.6	2	GC	20	380	-66.8	322	38
SJ182A	1145.0	172.7	-31.9	167.7	1.9	gc	7.6	2	GC	20	180	-59.6	322	38
SJ183A	1147.4	193.2	-39.1	180.1	-11.4	gc	23.3	3	GC	130	280	-68.8	322	38
SJ184A	1149.7	194.8	-21.8	189.8	3.0	gc	25.4	3	GC	20	300	-60	322	38
SJ185A	1159.0	187.9	-50.4	168.7	-17.3	gc	8.0	2	GC	20	240	-68.9	318	42
SJ186A	1162.6	187.8	-39.4	174.6	-7.9	gc	13.8	2	GC	20	380	-66.4	318	42

SJ187A	1167.0	145.5	-11.4	146.5	30.2	93.4	4.3	1	O	130	240	-35.9	318	42
SJ188A	1170.0	205.9	-62.1	169.0	-32.6	159.9	4.0	1	O	230	400	-76.3	318	42
SJ189A	1172.9	189.1	-49.3	170.0	-16.8	gc	9.1	2	GC	20	240	-69.3	318	42
SJ190A	1175.9	177.0	-49.8	162.7	-13.4	gc	7.7	3	GC	20	380	-64	318	42
SJ191A	1178.9	204.7	-44.4	182.1	-19.3	58.1	2.5	1	O	150	240	-72.8	318	42
SJ192A	1181.9	180.7	-58.8	160.3	-22.4	gc	21.9	2	GC	20	340	-66	318	42
SJ193A	1184.8	202.6	-60.7	168.9	-30.5	79.9	2.5	1	O	180	240	-75.3	318	42
SJ194A	1187.8	206.5	-37.2	188.0	-14.7	131.8	3.2	1	O	150	240	-69.1	318	42
SJ195A	1190.8	183.5	-21.1	180.5	9.8	127.5	2.0	1	O	130	240	-58.1	318	42
SJ196A	1194.3	333.6	56.4	333.8	11.4	33.6	23.2	2	*	180	360	57.2	334	45
SJ198A	1210.2	16.7	29.9	10.2	-5.6	47.0	24.9	2	*	130	280	58.6	334	45
SJ199A	1216.4	313.1	34.6	316.7	-8.2	102.9	12.7	2	*	180	320	37.9	334	45
SJ200A	1219.1	322.7	76.9	331.0	32.1	47.1	21.2	2	*	210	320	61.6	334	45
SJ201A	1221.9	336.5	54.2	335.5	9.2	77.3	22.7	1	*	130	320	57.6	334	45
SJ202A	1234.3	7.2	44.1	347.7	21.9	109.1	20.3	1	*	130	320	70.5	304	36
SJ203A	1291.9	11.1	47.1	348.2	25.9	274.7	3.0	1	O	130	280	72.7	304	36
SJ204A	1295.4	9.6	58.6	339.1	34.3	47.3	18.7	1	*	130	340	69.1	304	36
SJ205A	1297.8	350.9	54.6	331.9	25.3	452.0	2.0	1	O	130	320	60.4	304	36
SJ206A	1299.0	3.1	49.6	341.8	24.9	90.7	11.5	1	*	130	240	68	304	36
SJ207A	1304.3	338.3	32.2	332.5	1.2	97.7	11.2	1	*	130	240	52.7	304	36
SJ208A	1306.6	177.9	-16.5	175.2	5.9	184.5	5.6	1	O	220	300	-59.7	304	36
SJ209A	1309.0	243.8	-54	188.8	-55.7	78.1	3.7	1	O	150	240	-78.1	304	36
SJ210A	1315.5	167.4	-24.9	162.6	2.7	gc	19.7	2	GC	20	320	-57.1	304	36
SJ211A	1320.7	133.0	-76.8	126.7	-40.9	117.3	4.3	4	O	150	240	-42	304	36
SJ212A	1325.4	198.1	-54.1	167.0	-34.1	222.8	4.1	1	O	180	360	-75.5	304	36
SJ213A	1329.0	195.7	-81.1	163.0	-49.0	1381.2	3.6	1	O	280	380	-74.8	334	34
SJ215A	1339.6	178.9	-40.6	172.9	-8.9	gc	8.7	2	GC	20	280	-66.5	334	34
SJ216A	1354.4	202.5	-66.1	176.5	-37.4	112.3	20.2	1	*	240	380	-83.1	334	34
SJ217A	1369.2	14.4	38.0	5.2	10.1	80.0	7.7	3	O	130	280	67.5	334	34
SJ218A	1371.7	255.9	-83.5	165.7	-56.8	72.1	4.1	1	O	220	340	-74	334	34
SJ219A	1374.8	189.1	-39.2	182.4	-8.4	gc	14.0	2	GC	20	280	-67.1	340	34
SJ220A	1378.0	177.4	-50.2	171.5	-16.2	gc	11.7	2	GC	20	280	-69.6	340	35
SJ221A	1382.0	167.8	-48.5	165.3	-13.7	gc	3.6	2	GC	20	150	-65.6	340	35
SJ222A	1383.9	240.2	-67.8	192.5	-46.2	gc	13.6	3	GC	130	280	-78.9	340	35
SJ223A	1388.0	175.2	-50.3	170.0	-16.1	gc	6.8	3	GC	20	190	-69	340	35
SJ224A	1390.2	247.4	-34.5	223.7	-23.3	33.6	4.0	4	O	220	300	-46.5	340	42

SA1B	1392.9	193.2	-49.5	174.0	-17.0	gc	8.8	2	GC	0	450	-70.8	322	42
SA1C	1392.9	175.6	-21.7	174.0	14.1	gc	6.5	2	GC	0	575	-55.4	322	42
SA2B	1404.1	174.6	-82.8	147.2	-41.8	328.3	14.1	1	*	565	670	-60.4	322	42
SA4A	1410.8	357.7	52.5	343.6	15.0	1097.2	13.0	2	*	0	585	65.2	322	42
SA5A	1418.9	348.3	36.8	342.8	-2.0	572.6	12.7	2	*	0	575	57.5	322	42
SA6A	1425.6	310.6	8.3	308.6	-32.8	248.2	14.8	2	O	300	620	22.6	322	42
SA7A	1433.1	179.8	-38.7	170.6	-3.0	gc	16.2	2	GC	0	600	-63	322	42
SA8A	1439.8	176.3	-19.5	175.5	15.9	gc	26.3	3	GC	0	575	-54.6	322	42
SA9A	1448.7	178.9	-34.6	171.6	1.1	gc	9.5	3	GC	0	550	-61.3	322	42
SA10A	1456.9	193.1	-40.2	179.0	-9.1	gc	8.8	3	GC	0	500	-67.6	322	42
SA10B	1456.9	191.0	-46.4	174.4	-13.6	gc	12.8	3	GC	0	565	-69.2	322	42
SA12A	1471.8	9.3	46.9	353.1	13.4	567.0	7.3	3	*	0	600	68.7	322	42
SA13A	1476.3	357.9	59.6	340.6	21.5	424.8	13.9	3	O	0	600	65.9	322	42
SA17A	1490.4	188	-47.3	172.1	-13.4	gc	6.0	2	GC	0	585	-68.4	322	42
SA18A	1500.0	187.3	-67.3	160.5	-30.3	920.5	16.8	1	*	450	640	-69	322	42
SA19A	1511.2	145.5	-42.6	144.6	-0.7	331.3	18.4	1	*	500	620	-46.8	322	42
SA20B	1519.4	192.9	-22.1	188.3	6.4	408.1	24.0	2	*	550	600	-58.8	322	42
SA20A	1519.4	328.3	48.2	326.2	6.4	532.1	11.2	3	*	0	575	49.9	322	42
SA21A	1526.9	206.6	-46.9	183.1	-20.3	gc	28.1	3	GC	150	585	-73.2	322	42
SA22A	1537.3	176.2	-35.3	169.3	1.3	gc	11.5	3	GC	0	585	-60.5	322	42
SA23A	1545.5	190.3	-48	173.1	-14.7	gc	10.6	2	GC	0	585	-69.4	322	42
SA24A	1551.4	342.4	61.0	332.4	20.2	1106.8	7.0	3	*	0	585	59.2	322	42
SA25A	1559.6	202.6	-50.9	178.2	-21.7	gc	11.3	3	GC	0	585	-74.2	322	42
SA26A	1565.4	12.2	28.3	4.6	-1.4	1975.6	13.4	2	*	0	585	62	322	42
SA27A	1571.2	191.9	-46.2	175.0	-13.8	gc	7.0	2	GC	0	450	-69.4	322	42
SA28A	1577.0	197.7	-52.4	174.7	-21.0	gc	17.2	2	GC	0	565	-73.1	322	42
SA3B	1581.3	3.4	39.6	352.8	5.0	337.9	11.7	3	*	0	500	64.6	322	42
SA29A	1581.3	176.6	-50.2	163.9	-12.6	gc	15.7	3	GC	0	450	-64.3	322	42
SA3A	1581.3	166.8	-36.3	161.8	2.8	gc	21.6	3	GC	0	450	-56.6	322	42
SA30A	1587.8	138.4	-57.4	140.0	-15.4	gc	7.2	3	GC	0	500	-47.6	322	42
SA30B	1587.8	57.1	44.0	21.8	34.0	275.8	10.3	3	O	300	565	68.3	322	42
SA31A	1587.8	188.6	-7.9	192.3	20.7	143.3	28.1	3	*	300	575	-50.4	322	42
SA33A	1605.9	181.1	-41.7	170.3	-6.1	gc	26.7	2	GC	0	585	-64.3	322	42
SA34A	1611.0	200.4	-54.9	174.4	-24.0	gc	16.3	2	GC	0	585	-74.6	322	42
SA35A	1618.2	197.7	-31.9	186.7	-4.2	gc	23.7	3	GC	0	585	-64.3	322	42
SA36A	1622.5	27.6	22.3	19.5	1.5	359.5	24.6	3	*	0	565	57.8	322	42

SA37A	1627.5	46.0	17.8	35.6	9.2	1647.3	9.8	3	O	0	600	49.3	322	42
SA40A	1641.3	182.5	-57.9	163.7	-21.1	gc	10.8	2	GC	0	500	-67.8	322	42
SA41A	1644.9	187	-15.3	187.0	15.1	1160.3	14.5	1	*	400	660	-54.7	322	42
SA42A	1648.5	200.9	19.2	222.0	34.8	876.0	15.6	4	*	500	660	-28.4	322	42
SA43A	1653.6	32.7	16.1	27.1	-0.4	468.0	17.3	2	*	150	620	52.4	322	42
SA44A	1658.9	183.4	-24.5	179.5	8.5	gc	11.9	3	GC	0	565	-58.7	322	42
SA45A	1663.5	182.4	-44.1	170.1	-8.7	gc	24.1	3	GC	0	575	-65.5	322	42
SA46A	1668.1	187.6	-41.8	174.6	-8.4	gc	20.3	3	GC	0	565	-66.6	322	42
SA47B	1671.2	340	19.5	340.1	-20.6	1349.0	13.9	2	*	0	670	47.7	322	42
SA48A	1675.0	343.1	16.9	343.9	-22.4	973.1	20.3	2	*	0	640	48.3	322	42
SA49A	1681.2	334.5	26.3	333.6	-14.9	8002.8	12.5	2	*	0	565	47	322	42
SA50B	1689.6	21.1	43.9	1.9	15.5	1603.5	6.2	2	O	0	565	70.8	322	42
SA50A	1689.6	13.8	31.7	4.0	2.2	1780.0	7.1	3	O	0	565	63.8	322	42
SA51A	1694.2	174.5	-44	164.9	-6.3	gc	8.5	2	GC	0	550	-62.1	322	42
SA52A	1700.4	183.9	-61.5	162.5	-24.6	gc	8.5	3	GC	0	620	-68.4	322	42
SA53A	1709.6	41.8	32.0	22.8	17.1	718.0	10.9	3	O	350	585	61.8	322	42
SA54A	1718.0	202.8	-39.7	185.6	-12.9	gc	6.6	3	GC	0	640	-68.9	322	42
SA55A	1723.4	164.1	-42.9	158.0	-3.0	gc	6.6	3	GC	0	450	-56.9	322	42
SA56A	1731.8	142.4	-60.6	142.2	-18.6	339.5	14.5	1	*	400	585	-50.3	322	42
SA57A	1740.3	130.1	14.8	121.4	55.4	1760.1	5.3	3	O	350	550	-6.3	322	42
SA58A	1744.9	22.3	27.6	12.4	2.9	899.7	10.3	1	*	300	620	61.8	322	42
SA59A	1751.0	186.4	-60.5	164.2	-24.3	gc	8.9	2	GC	0	450	-69.4	322	42
SA61A	1753.3	353.6	6.1	358.7	-29.2	2019.9	1.7	2	O	300	565	47.4	322	42
SA60A	1753.3	183.1	-34.3	174.9	-0.1	gc	7.1	3	GC	0	400	-62.6	322	42
SA63A	1775.5	26.2	32.3	12.3	8.7	2945.1	13.1	1	*	300	640	64.5	322	42
SA64A	1781.8	19.0	11.6	19.1	-12.0	398.2	11.5	3	O	550	640	52.1	322	42
SA65A	1787.4	119.2	-56.8	129.2	-16.5	gc	12.4	3	GC	450	640	-38.6	322	42
SA66A	1796.1	175.2	-15.9	176.0	19.6	gc	24.7	2	GC	0	585	-52.7	322	42
SA75A	1812.7	296.4	37.1	301.8	-1.9	1909.4	7.3	3	O	150	600	27.5	322	42
SA70B	1830.9	190.3	-54.4	169.6	-20.2	gc	7.8	2	GC	0	500	-70.7	322	42
SA77A	1835.0	354.9	42.9	345.6	5.4	490.9	12.0	2	O	0	620	62.1	322	42
SA78A	1840.4	283.9	-5.8	271.9	-36.8	849.0	6.4	3	O	300	620	-7.5	322	42
SA74A	1847.5	198.6	-56.6	172.4	-24.7	gc	6.2	2	GC	300	550	-74.3	322	42
SA79A	1850.7	31.3	39.3	11.1	16.7	382.7	7.3	2	O	300	575	68.7	322	42
SA80A	1861.0	76.6	-21.5	84.2	-0.8	769.6	11.2	3	*	565	670	5	322	42
SA82A	1879.2	137.1	-39.1	138.2	2.8	1628.6	12.7	1	O	300	640	-40.8	322	42

SA83A	1889.5	184.9	-39.1	174.0	-5.1	gc	13.0	2	GC	0	600	-64.9	322	42
SA84A	1899.8	212.1	-48.2	185.2	-23.7	3908.9	8.0	1	*	300	670	-74.6	322	42
SA85A	1907.7	118.9	-25.7	120.7	13.4	322.8	9.0	4	O	150	575	-23.5	322	42
SA86A	1918.8	131.1	-18.5	130.8	22.8	796.1	10.4	4	O	300	585	-28.4	322	42
SA87A	1928.9	268.2	-42.9	219.2	-52.7	1646.5	5.5	4	O	150	575	-55.7	322	42
SA88A	1939.0	174.7	-30.4	170.0	6.3	gc	22.8	2	GC	0	600	-58.3	322	42
SA89A	1946.6	177.8	-26.2	174.1	9.1	gc	14.8	2	GC	0	450	-57.9	322	42
SA90A	1955.0	50.4	80.1	336.5	46.8	1954.1	20.1	3	*	200	670	69.2	322	42
SA90B	1955.0	102.0	-48.7	116.2	-12.7	2020.7	5.9	4	*	400	620	-26.2	322	42
SA91A	1964.2	137.3	-62.4	139.7	-20.5	1366.5	21.0	1	*	550	660	-48.7	322	42
SA92A	1973.5	167.9	-38.5	162.0	0.5	gc	8.3	2	GC	0	550	-57.7	322	42
SA93A	1981.0	191.8	-44.4	175.9	-12.2	gc	6.0	2	GC	0	500	-68.8	322	42
SA94A	1988.6	262.4	-68.8	174.6	-54.6	gc	7.3	3	GC	0	400	-80.7	322	42
SA95A	1996.2	346.1	54.1	336.3	14.1	442.2	15.0	2	*	150	600	60	322	42
SA98A	2000.0	43.1	33.6	22.5	19.0	516.4	12.3	2	O	300	620	62.6	322	42
SA99A	2007.1	174.9	12.3	190.7	45.0	455.1	16.3	2	O	300	565	-35.4	322	42
SA97A	2007.1	265.9	-30.0	233.9	-44.0	772.9	19.1	4	*	350	575	-42.1	322	42
SA100B	2013.8	232.9	-40	203.2	-29.1	gc	20.1	2	GC	0	620	-65.6	322	42
SA100A	2013.8	39.1	27.2	24.4	11.9	605.6	12.2	3	O	300	600	58.7	322	42
SA106A	2018.0	279.1	22.7	282.5	-9.5	520.4	20.1	4	*	550	600	8.9	322	42
SA101A	2021.4	317.9	15.4	317.6	-26.5	662.1	10.2	2	O	400	585	31.9	322	42
SA103A	2025.0	188.3	-49.3	171.2	-15.2	gc	17.1	3	GC	0	450	-69	322	42
SA102A	2029.8	324.3	69.7	322.9	27.7	257.3	7.3	1	O	300	550	53.4	322	42
SA111A	2042.0	197.9	-19	194.0	6.5	gc	34.6	2	GC	0	660	-56.9	322	42
SA104A	2046.5	191	-36.7	179.4	-5.3	gc	5.1	2	GC	0	550	-65.6	322	42
SA105A	2047.0	175.2	-47.4	164.1	-9.7	gc	25.0	2	GC	0	600	-63.2	322	42
SA110A	2048.1	336.4	-69.7	129.1	-67.2	488.4	20.6	3	*	450	620	-45.2	322	42
SA112A	2061.1	204.7	-27.7	194.1	-4.2	289.8	22.9	1	*	550	640	-61.7	322	42
SA114A	2071.6	182.8	-38.7	172.7	-4.0	gc	2.7	3	GC	0	500	-64	322	42
SA115A	2078.1	196.1	-21.2	191.4	5.6	gc	23.1	2	O	0	565	-58.2	322	42
SA117A	2085.0	160	-58.7	151.7	-17.7	570.8	15.9	1	*	300	600	-57.8	322	42
SA123A	2089.6	0.4	46.6	347.7	10.3	481.6	10.5	2	*	300	575	65.3	322	42
SA124A	2101.5	36.7	35.3	17.2	16.6	779.0	3.3	2	O	300	500	65.3	322	42
SA119A	2101.5	199.4	-7.4	202.0	15.2	835.2	26.2	3	*	0	565	-49.3	322	42
SA120A	2108.0	239.8	-39.3	207.7	-32.8	gc	16.8	3	GC	200	600	-62.9	322	42
SA125A	2112.8	55.1	-0.3	54.5	1.8	551.4	4.1	4	O	300	500	31.6	322	42

SA121A	2112.8	228.5	16.8	240.9	14.7	1169.0	4.6	4	O	300	565	-21.7	322	42
SA127A	2138.7	179.8	-0.7	187.8	31.3	257.5	30.9	1	*	300	585	-45.4	322	42
SA127AB	2138.7	304.0	26.2	305.4	-14.1	511.2	10.6	3	*	350	575	27.1	322	42
SA128AB	2147.6	173	-28.3	169.3	8.8	gc	16.2	2	GC	300	600	-56.9	322	42
SA128A	2147.6	13.3	37.7	0.5	7.1	482.8	15.2	3	*	0	450	66.6	322	42
SA133A	2171.4	65.2	23.5	44.9	25.9	610.6	5.8	4	O	350	565	46.1	322	42
SA135A	2186.3	22.1	49.1	359.2	20.1	1657.2	12.6	3	*	0	550	73.4	322	42
SA136A	2192.3	14.4	81.3	331.3	42.3	744.6	18.8	2	*	300	565	64.1	322	42
SA137A	2199.0	20.8	50.9	357.3	21.0	377.2	19.7	2	*	300	575	73.7	322	42
SA138A	2203.4	14.4	34.6	2.9	4.9	97.8	20.3	3	O	300	500	65.3	322	42
SA139A	2206.4	57.1	66.9	355.5	45.0	1505.4	3.1	1	*	150	680	86	322	42
SA140A	2212.4	345.6	20.5	345.3	-18.3	2246.1	6.7	1	*	100	630	50.9	322	42

Sedimentological analysis: method

We carried out our sedimentological analysis using a standard faciological method. Twelve facies were identified on the basis of their lithology, sedimentary structures and trace fossils before being interpreted in terms of depositional processes (Table 3). Along the Dungsam Chu section, these facies co-occur in four associations, which were interpreted in terms of depositional environments (Table 4). Indeed, facies associations are more representative of depositional environments than individual facies alone, the latter rather depending on the sediment nature or on elementary hydrodynamic processes. The facies associations were recognized in specific locations throughout the sedimentary section and used to divide it into four units bearing different environmental characteristics. The distribution of these units was documented by a stratigraphic column constructed from outcrop observations along the Dungsam Chu transect (Figs. 19 and 26). Along this transect, horizontal distances were measured using both a GPS and a measuring tape before being converted into sediment thicknesses using strike and dip measurements.

Palynological analysis: sampling and analytical procedure

Twenty three samples from brown, grey and black silty/sandy claystones along the Dungsam Chu section were selected for palynological analyses. The samples were processed at the Institute for Biodiversity and Ecosystem Dynamics (University of Amsterdam, The Netherlands) following a standard analytical procedure applied on pre- Quaternary siltstones and claystones and described in Hoorn et al. (2000). In general, the palynological slides were rich in organic debris but low in pollen and spores (hereafter collectively referred to as sporomorphs). Sixteen samples contained sufficient sporomorphs for further analysis, with sums ranging between 87 and 608 specimens (for sample location, see Fig. 19b). Modern generic names were used following (Traverse, 1988), while unknown species were labelled by their key morphological characteristics. In addition, some suspected extinct forms were indicated by their form-generic names. All taxa are listed with individual scores in Table S3. The taxa were grouped overall following ecological affinity (Table 5 and Fig. 26d) to display the results in compact format and to compare the results with those obtained at the Surai Khola section in central Nepal by Hoorn et al. (2000) (Figure. B).

Table S3: *Palynological data sheet with counts of sporomorphs found in the Dungsam Chu section.*

Sample along the Dungsam Chu section	**PN13**	**PN14**	**PN20**	**PN21**	**PN28**	**PN31**	**PN37**	**PN51**	**PN55**	**PN58**	**PN60**	**PN65**	**PN74**	**PN82**	**PN85**	**PN86**
Stratigraphic thickness	252	297	398	416	568	630	666	854	1032	1067	1081	1158	1366	2180	2205	2209
POLLEN																
Acer				1				2								
Alangium (Type 42)	1						1								3	
Alnus	7	1		8		7			3	1		1	1	3		
Anacardiaceae? (Type 32)							1									
Apocynaceae? (Type 65)															1	1
Asteraceae (diverse)			21	24		1					1			1	1	
Betula			1													
Bombacoideae? Malvaceae (Type 35)					1		3							2		
Bombacoideae? Malvaceae (Type 57)															1	
Brownlowia, Malvaceae (Type 18)					1											
Caesalpineacea? (Type 73)				2				7						1		
Carpinus? (Type 63, 99 or 35)				6		1		6	2		5		1	4	2	
Chenopodiaceae/Amaranthaceae						1									1	
Clavate, monocolpate (Type 40)							1									
Corylus (Type 48 & 55)	4	1		1		1	1	1		2			1		2	4
Croton? (Euphorbiaceae)									1							
Echinate, tricolporate	1		1	3												
Engelhardtia										1				1		
Ephedra (Type 41)			1				1									
Ericaceae	1															1
Euphorbiaceae spp.													2			
Fagaceae spp. (Type 83 and others)		4	1	2				3	2		2	12	4	2		3
Foveolate, tricolpate															4	
Gemmate/verrucate, tricolpate (Type 88)		1									1					
Ilex? (Type 21 & 47)		5		1	1	1		1	1			3			1	2
Juglandaceae/Pandaceae? *Momipites*? (Type 19)					1				1				2			1
Larix/Magnolia? (Type 22)			1	5	6			2			1	2			2	
Leguminosae, prcp													1			
Lilium?													1			
Liquidambar						1										
Malvaceae? (Type 52)		2														
Meliaceae (Type 29)				1			1	1				1	1	1	1	
Microechinate, tricolpate							2									
Microechinate, tricolporate															2	
Microechinate, triporate							2									
Microreticulate, tricolporate (Type 96)									1							
Monocolpate, echinate (Type 5)		2	1			1		1				1				
Myrica (Type 9 & 43)			1				1				1					

Myrtaceae (Type 14 & 20)	1			1	1	1		3	1		3		6	1		
Naucleae type, Rubiaceae (Type 89)		1							2		47	3	1		1	3
Neocouperipollis R.K. Kar & M. Kumar, 1987 (Type 36)		1					1			1		2			1	
Nypa (Type 38)							1							4		1
Nypa (Type 50)		1													1	
Pelliciera, Tetrameristaceae (Type 10)			1		1			1								
Pinaceae (corroded)	1	2		1	1	4	4	2				2				2
Platanus?/Cinctiporipollis mulleri M. Salard-Cheboldaeff, 1975 (Type 39)				1		1	1								4	
Poaceae	**6**	**23**	185	182	13	10	29	27	32	8	37	21	11	32	15	20
Polygonum persicaria type			6	1				1			1			1		1
Potamogeton? (Type 84)				1	1						1		2	1	1	
Proteaceae (Type 24)					1									1		
Psilate, brevitricolpate												1				
Psilate, monocolpate					1											
Psilate, stephanocolporate (Type 9)								1								
Psilate, tricolpate						1		2								
Psilate, tricolpate								2								
Psilate, tricolpate (Type 82)											2			1		
Psilate, tricolpate (Type 93)									6							
Psilate, tricolporate (Type 26)							1									
Psilate, tricolporate (Type 46)		1				1				1	1			1	2	
Psilatricolporate, costate (Type 69)				1												
Tiliaceae								1								
Quercus	1	1	2	1	1	3	1	2				4	2	1	2	3
Quercus microhenrici			1													
Reticulate, tricolporate costate	1											1	3			2
Reticulate, brevitricolpate (Type 79)														2		
Reticulate, tricolpate			8	1	2			4							1	
Reticulate, tricolpate (Type 12)								1								
Reticulate, tricolpate (Type 2)			14		3		1	2								
Reticulate, tricolpate (Type 23)					1											
Reticulate, tricolpate (Type 44)		1		1		1	2	2	1					4		
Reticulate, tricolpate (Type 94)									6							
Reticulate, tricolpate (Type 97)									1							
Reticulate, tricolporate (Type 16)								1								
Reticulate, tricolporate (Type 4)			1													
Reticulate, tricolporate (Type 66)	1			3		1		3	2		1	3	3	5	8	
Reticulate, tricolporate (Type 67)				3												
Reticulate, tricolporate (Type 90)											1					
Reticulate, triporate (Type 64)															1	
Reticulate/striate, tricolporate (Type 95)									1							
Rubiaceae (Type 7 & 25)			2		2			1					1			2
Rubiaceae, reticulate, tricolpate (Type 80)									2		4			7		

Rubiaceae, reticulate, triporate (Type 74 & 86)				1				3	3		1		2	1		1
Rubiaceae? (Type 6)			1		1		1	1				3	4			
Rutaceae															1	1
Saxifraga? (Type 100)		1		3				1	2			1		1	1	
Scabrate, tricolpate (Type 59)															3	
Stephanocolporate (Type 85)													1	1		1
Strobilanthus? Acanthaceae, Justicia type (Type 75)				1												
Tiliaceae?													1			4
Typha (Type 56)											2			1	1	1
Ulmus?															1	
Verrucate, tricolporate (Type 61)								1						1	1	
Verrucate, tricolporate (Type 71)				1												
Verrucate, triporate (Type 53)															2	
diverse unclassified		1	1			3				3		6	2			4
Sub-sum pollen (Angiosperms/Gymnosperms)	25	48	249	256	39	37	56	85	70	14	110	61	51	79	63	53
SPORES																
Athyriaceae spp. (Type 27 & 81)							1						1	1	2	
Baculate, monolete (Type 51)		1				1			1	1		2		5		
Baculate, trilete				1												
Baculate, trilete (Type 54)															1	
Ceratopteris, Pteridaceae			2			10				2		2				
Clavate, monolete		1								1						
Cyatheaceae, psilate, trilete	1	1	3		3	8	3	2		6	2	16	1	10	4	6
Echinate, monolete						1			1	1		1		1		
Echinate, trilete (Type 72)				1				2								
Granulate, monolete													1			
Lophosoria (Type 68 & 92)	1	1		1						1		1	1		1	1
Lycopodium foveolate (Type 31)	1	1				1	2	1			2			6		11
Lycopodium spp.	1	1	1	2											1	
Lygodium (Type 3)		4	1									2				
Polypodiaceae spp., psilate, monolete	56	86	64	37	211	30	65	8	37	23	50	44	27	66	48	25
Polypodiaceae, psilate, monolete (Type 1)	1	2	6	14		6		2	7	1	14	10	2	16	20	
Polypodiaceae, verrucate, monolete					5											
Polypodiaceae, verrucate, monolete (flat verrucae)	14			4		9	2	4	6		4		2		13	
Polypodiaceae, verrucate, monolete (large verrucae)	1		1	6		1		1							2	
Polypodiaceae, verrucate/rugulate, monolete	1															
Psilate, trilete (thick spore wall) (Type 78)				1						1				8		
Psilate, trilete (Type 78)						1										
Pteridaceae (Type 49)		1														
Pteris type, Pteridaceae (Type 11)			1													
Pteris type, Pteridaceae (Type 30)							2	2								
Pteris type, Pteridaceae (Type 33)							1		1			1		2	1	
Pteris type, Pteridaceae (Type 60)															1	

Punctate/striate, trilete (Type 76)				1	1	1										
Reticulate, monolete									3							
Reticulate, trilete							1									
Reticulate, trilete (Type 28)					1		1									
Rugulate, trilete (Type 34)		1				1	2							38		1
Selaginella? (Type 62a & b, 77)				1		1						3	2	2	2	
Selaginellaceae spp.		3				1				1	2	1				
Striate, trilete		4					3	1								
Thelipteraceae? (Type 45)		3									1		1	2		
Verrucate, trilete	1	6	1		1		1	1	1	5		1		2	4	1
Verrucate/baculate, trilete (Type 37)							1								1	
Verrucatosporites spp.		26	1	10	18	3	6		1	12		27	1	10		5
Verrucatosporites usmensis type	8	2		16		12		4	58	1	14				6	8
Sub-sum ferns	86	144	81	95	240	87	91	28	116	56	89	111	39	169	107	58
TOTAL SUM	136	241	580	608	318	164	203	199	256	87	311	239	143	329	238	169
pteridophytes indeterminate	**2**	**26**	10	18	7	7	3	9	8	2	6	6	4	37	24	5
all corroded/indeterminate	**20**	**43**	34	37	23	18	28	100	47	18	34	35	15	81	53	10
Others palynomorphs																
Type 17-Spirogyra?				1				1							1	
Type 51-Briophyte?		1														
Type 58-Cingulate, briophyte?														2	2	
Type 98-Briophyte?									1							

Broad-leaved forest
Mangroves
Grasses
Ferns
Asteraceae

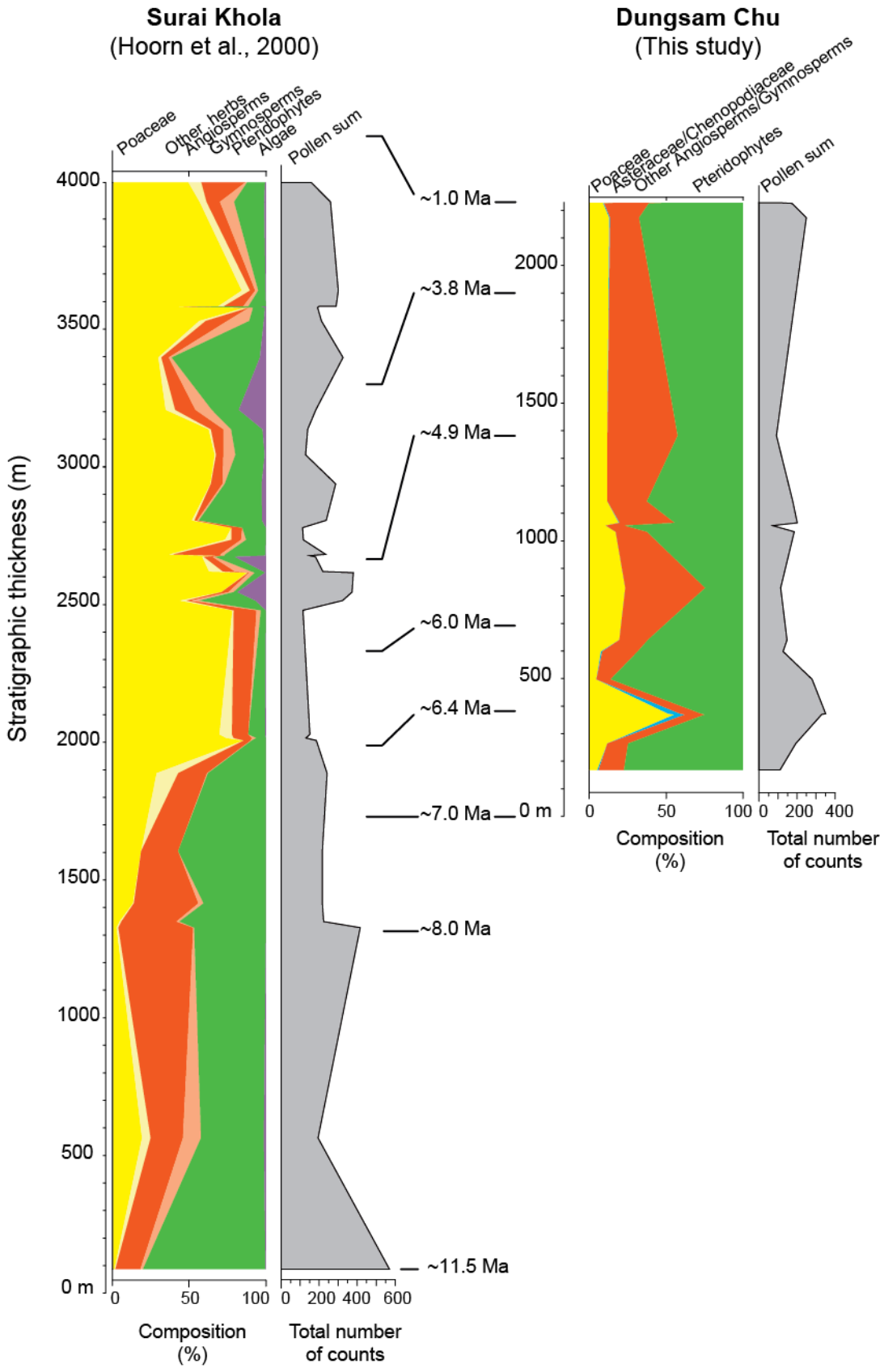

Figure B. *Palynological results along a) the Surai Khola section (central Nepal) (Hoorn et al., 2000) and b) the Dungsam Chu section (eastern Bhutan).*

APPENDIX II: Supplementary Material of Chapter 2 - Timing and mechanism of the rise of the Shillong Plateau in the Himalayan foreland

ANALYTICAL AND NUMERICAL METHODS

Zircon U-Pb dating

Six medium-grained sandstones were selected at regular intervals throughout the Dungsam Chu section of Siwalik sedimentary rocks (SJ1b, SJ2, SJ4, SJ6b, SJ9 and SJ12) and analysed at GRPG, Nancy (France). Two further samples of similar grain size were selected once the change in provenance had been detected, within the relevant gap (i.e. between samples SJ6b and SJ9, where the change in provenance is observed). These samples were analysed at NIGL, Keyworth (UK).

Prior to analysis, samples were dried and sieved to extract the <500-µm fraction at Lancaster University. Heavy minerals were extracted at NIGL, BGS Keyworth (UK) by wet separation on a Haultain superpanner, and di-iodomethane heavy liquid (with a density of 3.3). Magnetic separation was kept to a minimum to avoid biasing mineral populations. Zircon grains were handpicked, taking special care to select all grain types with respect to morphology, color and grain size, within a particular fraction of the separate. The zircons were mounted in epoxy, polished and photographed to help identify the analysed grains. They were also imaged by cathodo-luminescence using an FEI Scanning Electron Microscope to ensure suitable core areas were targeted during analysis. Each analysis corresponds to a different zircon grain. Since the objective was to date a maximum number of zircon grains, and not their potential metamorphic overgrowth, no multiple analyses were carried out on the same grain.

The zircons mounts of samples SJ1b, SJ2, SJ4, SJ6b, SJ9 and SJ12, were subsequently gold-plated at CRPG, Nancy (France). U-Pb zircon dating for these samples was performed using the CAMECA IMS 1270 E7 ion microprobe facility at CRPG. The analysed masses were: 203.5 (background noise, measured for 4 sec), Zr_2O (4 sec), ^{204}Pb (8 sec), ^{206}Pb (4 sec), ^{207}Pb (16 sec), ^{208}Pb (4 sec), ^{238}U (4 sec), $^{238}U^{16}O$ (3 sec) and $^{238}U^{16}O_2$ (3 sec). Counting was performed in mono-collection using an electron multiplier. Each analysis consists of 12 or 16 iterative cycles over each mass. The mass resolution was about 6000, which is sufficient to separate the molecular interferences. The primary current was ~5 nA using the duoplasmatron (oxygen source). The O^{2-} primary beam is a projected beam of about 20 µm in diameter (corresponding to the projection of a diaphragm of 200 µm). Before each measurement, there is a 120-second pre-sputtering with a 10 µm x 10 µm raster, a centering of the secondary beam within the field aperture, the contrast aperture and the energy slit and a centering of the mass on Zr_2O.

The zircon reference material 91500, with an age of 1064 Ma (Wiedenbeck et al., 1995), was analysed at regular intervals and was used for determination of the correlation line between $^{206}Pb/^{238}U$ and UO/U in order to correct data for instrumental fractionation. The age calculations were based on the isotope ratios corrected for background noise and common lead (using ^{204}Pb). The U and Pb abundances are calculated on the basis of the Zr_2O and UO correlation for the standard, and the isotope ratio $^{238}U/^{206}Pb$. The $^{207}Pb/^{206}Pb$ ratio is directly derived from each spot analysis.

U-Pb dating of zircons from samples SJ7 and SJ8 was performed using a Nu Instruments AttoM single-collector inductively coupled plasma mass spectrometer (SC-ICP-MS). The instrument was tuned such that oxides of U and Th represented less than 0.4% of the signal obtained from the metal ion peaks. The Nu AttoM SC-ICP-MS was used in peak-jumping mode with measurement on a MassCom secondary electron multiplier. The analysed masses in each sweep were: ^{202}Hg, $^{204}Pb+Hg$, ^{206}Pb, ^{207}Pb, and ^{235}U. Each data integration records 100 sweeps of the measured masses, which roughly equates to 0.22 seconds. Dwell times on each mass are 400 µs on ^{207}Pb and ^{235}U, and 200 µs on all other masses; the switching between masses takes 40µs. ^{238}U is calculated using $^{238}U/^{235}U$ = 137.818. Laser ablation was performed with a NewWave UP193SS solid-state laser ablation system. Ablation parameters were optimized to suit the Pb and U contents of the material and parameters adopted were a frequency of 10 Hz, with a fluence of 1.8 to 2.5 J/cm^2, a 30 second ablation time, and a 25-µm spot size. Three zircon reference materials (91500, GJ-1 and Plesovice; Jackson et al., 2004; Sláma et al., 2008; Wiedenbeck et al., 1995) were analysed at regular intervals in order to correct data for instrumental fractionation. The average bias of the $^{207}Pb/^{206}Pb$ and $^{206}Pb/^{238}U$ ratios from preferred values derived by TIMS analysis are used for normalization. $^{206}Pb/^{238}U$ and $^{207}Pb/^{206}Pb$ uncertainties were propagated in the manner advocated by Horstwood (2008), utilizing the measurement uncertainty and the reproducibility of the ablation reference material used.

For the two sets of samples, respective in-house Excel spreadsheets were used for data reduction and error propagation, and Density Plotter (Vermeesch, 2012) was used for data presentation. Data reduction was undertaken with the age filters summarized in the following screening procedure table. Concordant ages within the limits defined in this table were accepted. It is important to consider that young zircon grains contain low levels of radiogenic Pb, which means that even low levels of common Pb may lead to discordance. Many of the young analysed grains in this study have been discarded in order for robustness of the ages to prevail. Concordia diagrams for each sample are presented in Figure A. Zircon U-Pb data are presented in data tables S3 and S4 of Appendix II in the electronic document attached to the thesis.

Table: *Data screening procedure*

1	Failed	Discarded
2	$^{206}Pb/^{238}U$ age >100 Ma, uncertainty >10%	Discarded
3	>10% discordant	Discarded
4	$^{206}Pb/^{238}U$ age 100 – 1200 Ma, >5% discordant	Discarded
5	Young grain - $^{206}Pb/^{238}U$ age <100 Ma, <10% discordant	$^{206}Pb/^{238}U$ age used
6	$^{206}Pb/^{238}U$ age 100 – 1200 Ma, <5% discordant	$^{206}Pb/^{238}U$ age used
7	$^{206}Pb/^{238}U$ age >1200 Ma, <10% discordant	$^{207}Pb/^{206}Pb$ age used

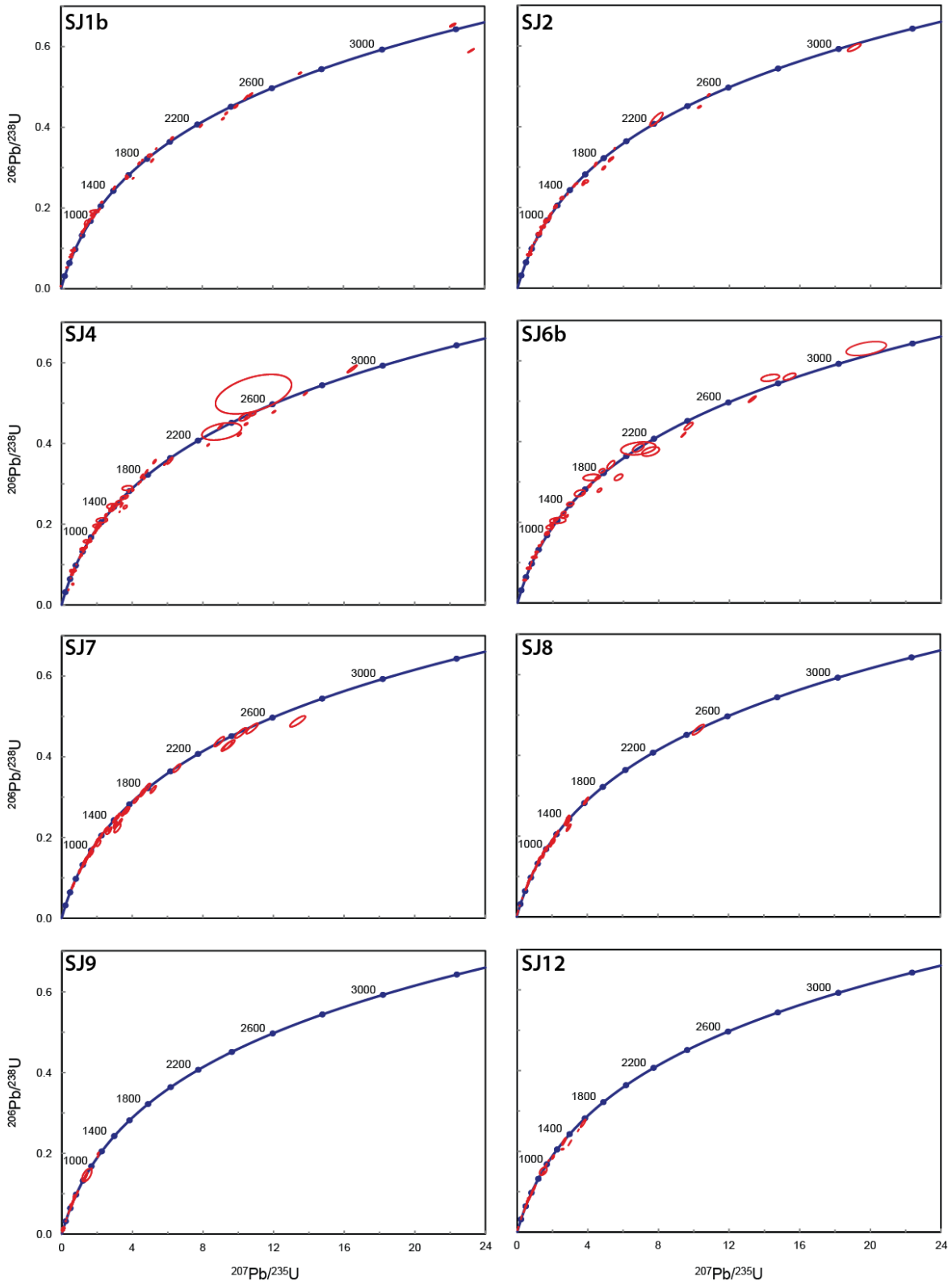

Figure A: *Zircon U-Pb concordia diagrams of samples from the Dungsam Chu section. Data are plotted as Wetherill concordia diagrams, using the Isoplot v. 4.14 add-in for Microsoft Excel (Ludwig, 2003), after data screening. The dotted dark blue line is the concordia curve where ages are indicated in Ma. Data point ellipses are at the 2σ level.*

Stress calculation

Here we summarize the steps Copley et al. (2011) used to calculate the distribution of stress in the Indian lithosphere. Earthquakes and active faults have been observed where the Indian lithosphere bends beneath the Himalaya, and also further south within the Indian shield. Copley et al. (2011) therefore assumed that the stress within the lithosphere is limited to what can be supported by the faults before they break in earthquakes. Two independent estimates of the force balance were then used to estimate the stress distribution within the Indian plate: the locations, mechanisms, and stress drops of earthquakes within the Indian lithosphere (which give an increase in differential stress with depth of ~5 MPa km^{-1}), and the net force transmitted through the Indian plate (estimated from the motion of the plate and the forces exerted between India and Tibet; 5.5±1.5 TN m^{-1} along-strike).

If the stress drops in the earthquakes are summed over the seismogenic layer, the total force supported by the faults can be estimated to be approximately the same as the independent estimate of the total force transmitted through the Indian plate. This result has two implications: (1) the majority of the force transmitted through the Indian plate is supported by stresses on faults, and (2) the stress drops in the earthquakes represent close to the total pre-earthquake shear stresses on the faults. Point (2) means that the variation of stress drop with depth gives an estimate of the total stress distribution within the Indian plate, south of the region of bending beneath the Ganges foreland basin.

Beneath the Ganges foreland basin, the far-field tectonic compression is still present, but there are additional stresses related to the bending of the Indian plate beneath the Himalaya. This results in shallow normal faulting, and deeper thrust faulting. The depth of the transition from normal- to thrust-faulting is at 25±5 km. Copley et al. (2011) used this transition depth, along with the constraint that the net force transmitted through the lithosphere should match the far-field tectonic driving stresses, to calculate the variation of stress with depth within the Indian lithosphere underlying the foreland basin. They found that, in order to match the depth of transition from normal faulting to thrust faulting, and to also obtain the correct net force transmitted through the lithosphere, the faults underlying the foreland basin must have similar coefficients of friction to those further south within the Indian shield. In this foreland region, faults that cut through the entire seismogenic layer (e.g. the Oldham Fault on the northern margin of the Shillong Plateau that ruptured in a M8 earthquake in 1897) have resolved stresses that result in thrust motion. Faults that only cut the upper part of the seismogenic layer slip in a normal sense, and those that cut only the lower part slip as thrusts (see focal mechanisms in Figure B).

The variation of stress with depth suggests that differential stresses at the brittle-ductile transition are ~1.5 times higher in the foreland basin than further south within the Indian shield. These estimates therefore provide a picture of the changes in stress distribution as an area of the Indian Plate moves northwards towards the Tibetan Plateau, and becomes affected by the stresses related to bending beneath the Himalaya.

In models of dislocation creep, the relationship between stress and strain-rate is of the form $\dot{\varepsilon} \propto \sigma^3$ where $\dot{\varepsilon}$ is strain rate, and σ is stress. For rate-dependent fault creep, a change in shear stress would result in a change in sliding velocity by a factor of $exp(\Delta\sigma/aN)$, where $\Delta\sigma$ is the change in stress, a is the rate-dependent frictional parameter, and N is the effective normal stress. In either of these rheological laws, a change in the driving stress by a factor of 1.5 would result in a change in the fault-loading rate by a factor of 2 or more.

In these calculations we neglect local effects relating to erosion, deposition, isostatic balance, and strain accumulation in the hangingwalls and footwalls of the faults. As displacement accumulates on a thrust fault, the difference in gravitational potential energy across the fault increases, which acts to inhibit motion. This effect can be decreased is material is eroded from the hangingwall and deposited in the footwall, and if vertical motions occur to maintain isostatic equilibrium. Our inference that the slip rates on the faults on the margins of the Shillong Plateau has through time, rather than decreased, implies that these local effects on faulting are small compared to the imposed far-field compressive and bending stresses.

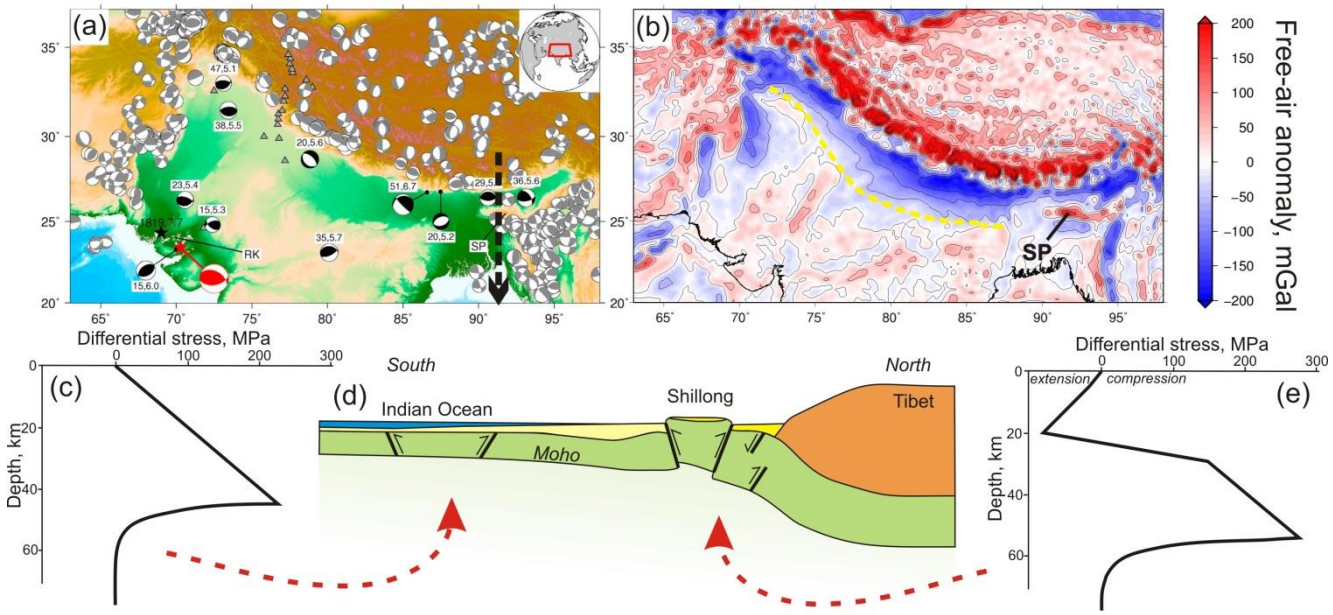

Figure B: *(a) Topography and focal mechanisms for the India-Tibet region. Black focal mechanisms are thrust and normal earthquakes within the Indian lithosphere, labelled with their centroid depth in*

km and moment magnitude (see Copley et al. (2011) for details). Thrust faulting occurs throughout the seismogenic layer in central India. Beneath the foreland basin, shallow normal faulting is underlain by deeper thrust faulting. The red focal mechanism corresponds to the Bhuj earthquake (case study of Copley et al., 2011). SP, Shillong Plateau; RK, Rann of Kachchh. (b) Free-air gravity anomaly in the same region as shown in (a), from the EIGEN-6C gravity model (Förste et al., 2012). The contour interval is 50 mGal. The yellow dashed line shows the southern edge of the negative anomaly representing the foreland basin in the central and western part of the Himalayan arc. The Shillong Plateau is the positive anomaly marked 'SP'. (c) and (e) show profiles of differential stress against depth form locations in central India, and in the foreland basin, as shown schematically in (d) (calculations from Copley et al., 2011).

DATA TABLES

Data tables are listed here and are presented in the electronic document attached to the thesis, in the file of Appendix II.

Table S1: Sample location

Table S2: Zircon U-Pb data from source-areas compilation

Table S3A: Zircon U-Pb Ion Probe data

Table S3B: Zircon standard U-Pb Ion Probe

Table S4A: Zircon U-Pb laser ablation data

Table S4B: Zircon standard U-Pb laser ablation

APPENDIX III: Supplementary Material of Chapter 3 - Paleo-drainage evolution and rapid exhumation of the Namche Barwa Syntaxis recorded in the Siwaliks of the easternmost Himalaya (Arunachal Pradesh, India)

ANALYTICAL METHODS

Luminescence dating

Sample for optically stimulated luminescence (OSL) dating was prepared and analysed in the OSL Laboratory of the University of Bern, simultaneously with- and following the exact same protocol as for samples from (Abrahami et al., in review) described here. The core sample was collected and transported with extreme care to avoid exposition to light. The entire analysis was performed under subdued orange light. The outer part of the core, i.e. the part susceptible to have been exposed to day light during sampling, storage and transport, was removed in the laboratory. The remaining part was etched to isolate feldspar and quartz grains. First, the sample was treated with 32% hydrochloric acid and 30% hydrogen peroxide to remove carbonates and organic component, respectively. Then it was sieved to isolate the dominant size fraction of the sample, 150-200 µm. Quartz and potassium-rich feldspar fractions were gravimetrically separated with Lithium Polytungstate (LST) at δ = 2.70 and 2.58 g cm^{-3} respectively. In order to remove the part of the grains affected by alpha irradiation and any contamination from the potentially remaining feldspars, the coarse-grained quartz was etched in 40 % HF for 60 minutes. Then, grains were immersed in hydrochloric acid to eradicate the fluorides.

Coarse grains were fixed to stainless steel discs using silicon oil. The large grain size of the sample allowed the application of 3–20 grains on individual aliquots. Measurements were conducted using automated Risø TL/OSL DA-20 readers, fitted with an EMI 9235QA photomultiplier tube.

Stimulation was performed at 90 % power, using blue (IR) LEDs for quartz (feldspar and polyminerals) with the signal detected through 7.5 mm of Hoya U-340 transmission filter (410 nm interference filter and one Schott BG-39). A Lifelite full spectrum daylight lamp was used for bleaching grains prior to dose recovery tests and measurement of residual doses. For De determination, an instrument error of 1.5 % was included for single aliquot measurement.

About 450 g of material was taken from the surrounding sediment for dose rate calculations. U, Th, and K specific activities were measured using high-resolution gamma spectrometry (Preusser and Kasper, 2001).

The sample was analysed for radioactive disequilibrium in the Uranium decay chain using the approach described by Zander et al. (2007); some evidence for disequilibrium was found with a loss of 238U. Therefore age determination should be considered as a minimum age only. The present day

water content of samples was not considered to satisfactorily represent average water content over burial time. The deposit will have lain below the water table, and in saturation, for half of the year and therefore a water content of 10±5 % was considered to encompass fluctuating water content with time and was applied to the sample for dose rate determination. For information, it should be noted that a 10 % underestimation of water content over time would result in a 10 % underestimation in age.

Estimated doses values absorbed during burial (D_e) were measured using modified versions of the SAR protocol (Blair et al., 2005; Murray and Wintle, 2000; Murray and Wintle, 2003; Wallinga et al., 2000). Preliminary analysis of the OSL signal of quartz was conducted and a combination of very dim signals, and feldspar contamination rendered further measurements impractical. For feldspar measurement, IRSL50 analysis was carried out using a preheat at 250 °C for 60 s, and the signal was stimulated using IR LEDs at 50 °C for 300 s. De values for single aliquot measurements were determined using the first 10 s of the IRSL decay curve, with background subtraction calculated using the last 200 s. IRSL dose response curve was well represented by a saturating exponential plus linear function and this was used to determine De value. Measurements with a recycling ratio of >10 % were rejected. The measurement of a zero dose was used to monitor recuperation of the signal, and expressed as a percentage of the natural signal.

The Central Age Model (CAM) (Galbraith et al., 1999) was applied to determine the mean age, and to determine the over-dispersion of De distribution. The Minimum Age Model (MAM) (Galbraith et al., 1999) also used to determine the age, as this is recommended to overcome partial bleaching in sediments, and used to identify that population of De values that represent grains that were well bleached prior to burial.

Dose recovery tests were performed using single aliquot measurements to determine the ability of the measurement protocol to recover a known laboratory dose (Wintle and Murray, 2006). For the sample, 28 aliquots were given laboratory doses of 430±21 Gy in average; this performed well returning dose recovery ratios of 1.03±0.06.

Fading tests were conducted in order to correct the burial age and avoid underestimation. To determine fading of the IRSL50 signal, six aliquots were measured; these were already sensitized having previously been measured for De values. A dose of ~160 Gy was given, and this dose was then measured (Auclair et al., 2003). A test dose of ~16 Gy was applied. Fading rates for all aliquots were very uniform with an average g-value of 4.73±0.83 % per decade. This resulting g-value was used to correct the mean burial dose of 430±21 Gy, resulting to a corrected burial dose of 700±35 Gy, and an age of 190.2±18.2 kyr.

Gamma spectrometry measurements detected radioactive disequilibrium in the sample, with a loss of 238U over time, and subsequently any age determinations are rendered minimum age only. Dose recovery tests confirmed that the IRSL50 protocol could successfully recover doses to within 10 % unity. OD value of 25 % lay within a similar range to those recorded for the feldspar fraction of waterlain sediments from Peru that were understood to be well bleached (Trauerstein et al., 2014), and would suggest that this sample does not suffer partial bleaching. OD values for all measurements from this study and from Abrahami et al. (in review) remain within the same range despite the large variation in grain size, and therefore numbers of grains on aliquots, the sample is assumed to be well bleached.

Detrital apatite fission-track and U-Pb double dating

Prior to analysis, samples were crushed, dried, sieved (fraction <500 μm) and washed with tap water at Lancaster University. Apatite separation for all samples was performed using standard gravimetric and magnetic mineral separation techniques at ISTerre, Université Grenoble Alpes (France) and by GeoSep Services (USA). Apatite grains were handpicked taking special care in sampling the greatest range of observable characteristics such as roundness, size and colour.

Apatite grain mounts were prepared and fission-track and U-Pb analysis was performed by Paul O'Sullivan at GeoSep Services (USA), using the LA–ICP–MS method (Donelick et al., 2005). Spontaneous fission tracks were counted using unpolarised transmitted light under a Zeiss Axiotron microscope. LA-ICP-MS data were collected for the isotopic masses 43, 147, 204, 206, 207, 232, and 238 using a NewWave laser ablation system in line with a Finnigan Element2 magnetic sector, inductively coupled plasma mass spectrometer at the Washington State University Geoanalytical Laboratory in Pullman (USA). Apatite reference materials (see below) of known U-Pb age were analysed at regular intervals for U-Pb data correction. Similarly, an apatite fission-track standard was analysed for $^{238}U/^{43}Ca$ calibration.

For each sample subjected to apatite fission-track (AFT) analysis, at least one 1 cm^2 grain mount, consisting of apatite grains immersed in epoxy resin, was prepared, cured at 90 °C for 1 hour, and polished to expose the internal surfaces of the apatite grains. After polishing, mounts were immersed in 5.5 N HNO_3 for 20.0±0.5 s at 21±1 °C to reveal all natural fission tracks that intersected the polished grain surfaces.

A representative kinetic parameter, D_{par} (the maximum diameter of fission track etch pits at their intersection with the polished and etched c-axis-parallel apatite surface), which is used as a proxy for the solubility of fission tracks in their host apatite grains (e.g. Donelick et al., 1999), was measured

and spontaneous fission-track densities were counted for each grain considered suitable for dating. Between one and four etch pit diameters were measured and an arithmetic mean D_{par} value was calculated for each datable grain.

Grains were then revisited using the LA-ICP-MS to make spot analyses within the area used for counting spontaneous tracks, to determine U, Th, and Sm concentrations of each grain for which natural fission-track densities had been previously determined. A single stationary spot of 16-µm diameter was used for each grain, centred in the approximate centre of the area where tracks had been counted. Note that if optical examination suggested that natural track densities were even moderately variable within a grain, which is evidence of U zoning, that grain was not dated.

For apatite, the fundamental assumption is made that Ca occurs in stoichiometric amounts in all grains analysed. The isotope ^{43}Ca is used as the indicator of the volume of apatite ablated. Samples were ablated in a helium atmosphere to reduce condensation and elemental fractionation. A total of 50 scans over 47 seconds for ^{238}U, ^{232}Th, ^{147}Sm, and ^{43}Ca were performed for each spot analysed. Of these scans, approximately 10 were performed while the laser was warming up and blocked from contacting the grain surface, during which time background counts were collected. Once the laser was permitted to hit the grain surface, a cylindrical pit was excavated to a depth beyond which uranium did not contribute fission tracks to the etched grain surface. Between 25 and 35 scans performed during pit excavation were required to reach this depth. The depths of a representative number of laser pits were measured and the $^{238}U/^{43}Ca$ value for each pit as a whole was determined based on the weighted mean of the $^{238}U/^{43}Ca$ value for individual scans relative to the depths from which the ablated material was derived (See Donelick et al., 2005; Hasebe et al., 2004).

Fission-track ages and errors were calculated using: (a) the ratio of the density of natural fission tracks present in the grain to the amount of ^{238}U present and (b) a modified version of the radioactive decay equation that includes a LA-ICP-MS zeta-calibration factor (See equations 1b for age equation and 2b for error calculation in Donelick et al., 2005). The zeta-calibration factor is determined for each sample analysed during each LA-ICP-MS session by analysing the U:Ca ratio of apatite calibration standards with known ages at the beginning and at the end of each LA-ICP-MS session. The standard used was Durango apatite with an age of 30.6±0.3 Ma (Boyce and Hodges, 2005; McDowell et al., 2005).

The youngest age was identified using the minimum-age peak method as implemented in Density Plotter software (Vermeesch, 2012). Youngest age peaks have been generated using the data set of ages comprised between 0 and 20 Ma in order to reduce the error on the minimum-age peak. The resulting youngest ages obtained with this method were used to constrain the maximum depositional age for each sample.

Use of the LA-ICP-MS technique for AFT analyses has the advantage that it permits U-Pb ages to be determined on the same grains in the same analytical session. Apatite standards (Durango, Duluth Complex, Fish Canyon Tuff, Mount Dromedary, McClure Mountain, Otter Lake, Tioga Bed B) for which independently accepted ages are published (Barfod et al., 2005; Boyce and Hodges, 2005; Kuiper et al., 2008; Lanphere and Baadsgaard, 2001; McDowell et al., 2005; Paces and Miller, 1993; Renne et al., 1998; Roden et al., 1990; Schoene and Bowring, 2006) were designated as primary, secondary, and tertiary standards for purposes of age calibration. Two primary and two secondary standard spots were analysed prior to and following each group of ~25-30 tertiary standards and/or unknown sample spots. Five spots of each tertiary standard were analysed near the beginning and again near the end of the session. Standard analyses were used to correct for down-hole fractionation, mass bias, and intra-session instrument drift. Fractionation factors were determined for each data scan of each primary standard spot and were calculated based on: a) ^{235}U values calculated from measured values, b) no fractionation was assumed between ^{206}Pb and ^{207}Pb, and c) the independently measured common-Pb $^{207}Pb/^{206}Pb$ ratio for McClure Mountain apatite (Schoene and Bowring, 2006). No alpha-damage correction was applied to fractionation factors.

Uranium decay constants and the $^{238}U/^{235}U$ isotopic ratio reported in Steiger and Jäger (1977) were used in this study. $^{207}Pb/^{235}Uc$ ($^{235}Uc = 137.88^{238}U$), $^{206}Pb/^{238}U$, and $^{207}Pb/^{206}Pb$ ages were calculated and background-corrected isotopic sums of each isotope were calculated for all concordant scans. The fractionation factor for each data scan was weighted according to the ^{238}U or ^{232}Th signal value for that data scan; an overall weighted-mean fractionation factor for all concordant data scans was used for final age calculation. If the number of concordant scans for a zircon was greater than zero, then either the $^{206}Pb/^{238}U$ or $^{207}Pb/^{206}Pb$ age was chosen as the preferred age, whichever exhibited the lower relative error.

Due to the usually high common-Pb content incorporated during crystallization, apatite is typically discordant in the U-Pb isotope system. Despite the corrections described previously, all grains remained discordant, often strongly so. Following the approach of Chew et al. (2011), a ^{207}Pb-based correction was employed, using an iterative approach to obtain a $^{207}Pb/^{206}Pb$ intercept value based on a starting estimate generated from the terrestrial Pb evolution model of Stacey and Kramers (1975). As the ^{207}Pb-based correction assumes U-Pb* (radiogenic Pb) concordance, which may not be the case for detrital grains, knowledge of likely source-area ages is required to discriminate partially reset ages in the same manner as for detrital AFT analysis. Since none of the apatite U-Pb ages were concordant, the data cannot be evaluated for quality using discordance criteria such as used for zircon U-Pb. However, low-U or very high common-Pb (Pb_C) content exhibited by some grains leads to large analytical uncertainty. Therefore, we follow the approach of Zattin et al. (2012) and Mark et

al. (2016) in excluding apatite grains yielding 2σ errors >25%. As radiogenic Pb content is proportional to age, younger grains commonly have correspondingly greater age uncertainty. Therefore, 2σ errors up to 100% were accepted for apatite grains yielding U-Pb ages <100 Ma. Data reduction of apatite U-Pb age measurements was undertaken with the ^{207}Pb age uncertainty filters summarized in the screening procedure table (table A). Density Plotter (Vermeesch, 2012) was used for data presentation. Ages within the limits defined in table A were accepted. Apatite fission-track and U-Pb data are presented in data table S4 of Appendix III in the electronic document attached to the thesis.

Table A: *Apatite U-Pb data screening procedure*

1	Failed	Discarded
2	^{207}Pb age >100 Ma, uncertainty > 25%	Discarded
3	^{207}Pb age 10-100 Ma, uncertainty >50%	Discarded
4	^{207}Pb age <10 Ma, uncertainty >100%	Discarded
5	All other ages	Accepted

Magnetostratigraphy

One to three core samples of 2.5-cm diameter were collected at each site with an electric drill powered by portable batteries and mounted with a diamond-coated drill-bit cooled with water. The finest possible lithologies were targeted for each of the 186 sites but coarser lithologies (medium- to coarse-grained sandstones) were locally collected to avoid long gaps. Cores were oriented with a custom device integrating a clinometer and a compass; bedding orientation was measured regularly and averaged throughout the section as similar attitudes were observed. Minor local declination (<0.5°) was neglected.

Remanent magnetizations of samples were analysed on a 2G Enterprises DC SQUID cryogenic magnetometer inside a magnetically shielded room, at the Geosciences Rennes paleomagnetic laboratory (France). A first selection of pilot samples distributed at ~50 m intervals throughout the stratigraphic section was stepwise thermally demagnetized in a shielded oven. Heating steps from 20 °C to 670 °C were applied to these samples in order to (1) determine the characteristic demagnetization behaviour, (2) establish the most efficient demagnetization temperature steps, (3) determine which lithology provided the best signal, and (4) identify stratigraphic intervals with potential paleomagnetic reversals. Guided by these preliminary results, thermal demagnetization was applied to the remaining samples with thermal demagnetization steps of 50 °C to 100 °C up to

550 °C and 10 °C to 15 °C from 550 °C to 670 °C. When the result from a first sample at a site was ambiguous, a second or a third sample was processed to determine the polarity.

Once the polarities have been determined for each sample, as detailed in the manuscript, a 45° cut-off procedure was performed separately for normal and reversed polarity datasets as illustrated in Figure A.

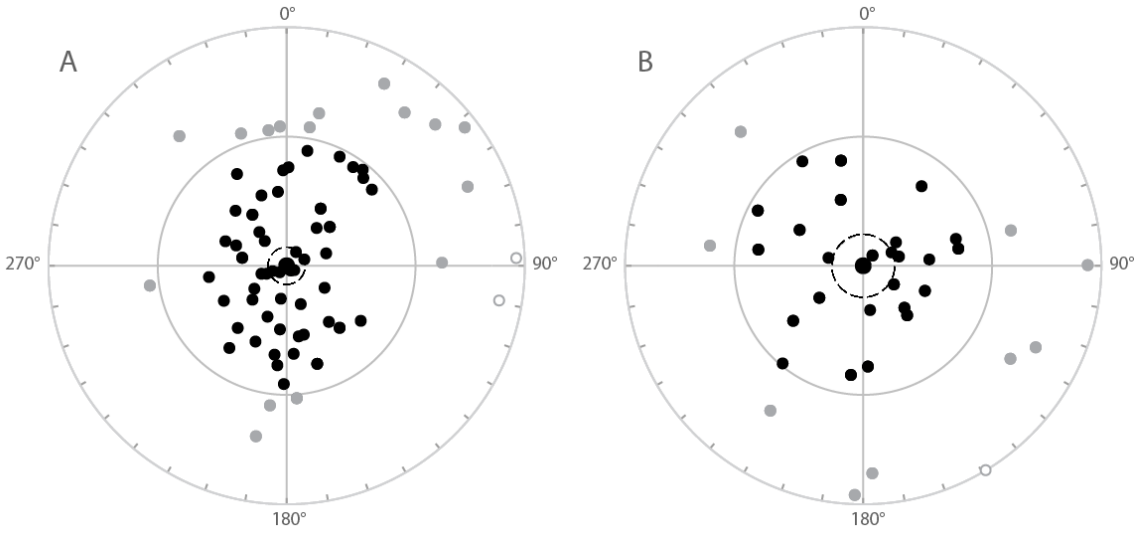

Figure A: *Projections of Q1 and Q2 A) Reverse and B) Normal VGP directions. Directions reported in grey and black have VGP over and under 45° from the mean VGP, respectively. The mean VGP is represented by the black dot in the centre of the projections. Directions represented in grey are rejected after cut-off procedure.*

Magnetostratigraphy data are presented in data table S2 of Appendix III in the electronic document attached to the thesis.

Detrital zircon U-Pb dating

Prior to analysis, samples were dried and sieved to extract the <500-µm fraction at Lancaster University. Heavy minerals were extracted at NIGL, BGS Keyworth (UK) by wet separation on a Haultain superpanner, and di-iodomethane heavy liquid (with a density of 3.3). Magnetic separation was kept to a minimum to avoid biasing mineral populations. Zircon grains were hand-picked, taking special care to select all grain types with respect to morphology, colour and grain size, within a particular fraction of the separate. The zircons were mounted in epoxy, polished and photographed to help identify the analysed grains. They were also imaged by cathodo-luminescence using an FEI Scanning Electron Microscope to ensure suitable growth zones were targeted during analysis, i.e. zircon cores and metamorphic overgrowths.

U-Pb dating of zircons was performed using a Nu Instruments Attom single-collector inductively coupled plasma mass spectrometer (SC-ICP-MS). The instrument was tuned such that oxides of U and Th represented less than 0.4% of the signal obtained from the metal ion peaks. The Nu Attom SC-ICP-MS was used in peak-jumping mode with measurement on a MassCom secondary electron multiplier. The analysed masses in each sweep were: ^{202}Hg, ^{204}Pb+Hg, ^{206}Pb, ^{207}Pb, and ^{235}U. Each data integration records 100 sweeps of the measured masses, which roughly equates to 0.22 seconds. Dwell times on each mass are 400 µs on ^{207}Pb and ^{235}U, and 200 µs on all other masses; the switching between masses takes 40µs. ^{238}U is calculated using ^{238}U/^{235}U = 137.818. Laser ablation was performed with either a NewWave Research UP193SS or UP193FX laser ablation system. Ablation parameters were optimized to suit the Pb and U contents of the material and adapted for the cores and the rims analysis. For the cores measurements, a frequency of 10 Hz, with a fluence of 1.5 to 3.0 J/cm^2, a 30 second ablation time, and a 25- to 35-µm spot size were used.

Several rim measurement methods were tried to increase the chances of measuring the <20-µm thin rims in the most robust way. A first method was to measure unpolished zircon mounts for some samples, in order to increase the targeted surface and to have as much material as possible from potential zircon rims. For this trial, we used a 100-µm raster line, a 20-µm laser spot and 6 passes for each measurement. The laser speed was set at 20 µm/s. Conclusive evidence was not obtained using this “blind” strategy, so the polished and CL-imaged mounts were used again for more rim measurements.

In the second method, zircon tips were targeted with a 15-µm laser spot. Despite the significant fractionation of U and Pb as a consequence of the use of a small laser spot, the second trial was more satisfying. In order to increase the dating precision of the youngest rims dated with the second strategy, the relevant zircons were extracted from the mount, flipped over and measured several times more using the first rim measurement described previously.

Three zircon reference materials (91500, GJ-1 and Plesovice; Jackson et al. (2004); Sláma et al. (2008); Wiedenbeck et al. (1995) were analysed at regular intervals in order to correct data for instrumental fractionation. The average bias of the ^{207}Pb/^{206}Pb and ^{206}Pb/^{238}U ratios from preferred values derived by TIMS analysis are used for normalization. ^{206}Pb/^{238}U and ^{207}Pb/^{206}Pb uncertainties were propagated in the manner advocated by Horstwood (2008), utilizing the measurement uncertainty and the reproducibility of the ablation reference material used.

In-house Excel spreadsheets were used for data reduction and error propagation, and Density Plotter (Vermeesch, 2012) was used for data presentation. Data reduction of zircon-core measurements was undertaken with the age filters summarized in the screening procedure table (table B). Concordant ages within the limits defined in this table were accepted.

Table B: *Zircon-core data screening procedure*

1	Failed	Discarded
2	$^{206}Pb/^{238}U$ age >100 Ma, uncertainty >10%	Discarded
3	>10% discordant	Discarded
4	$^{206}Pb/^{238}U$ age 100 – 1200 Ma, >5% discordant	Discarded
5	Young grain - $^{206}Pb/^{238}U$ age <100 Ma, <5% discordant	$^{206}Pb/^{238}U$ age used
6	$^{206}Pb/^{238}U$ age <100 Ma, 5 - 10% discordant	$^{206}Pb/^{238}U$ age used
7	$^{206}Pb/^{238}U$ age 100 – 1200 Ma, <5% discordant	$^{206}Pb/^{238}U$ age used
8	$^{206}Pb/^{238}U$ age >1200 Ma, <10% discordant	$^{207}Pb/^{206}Pb$ age used

It is important to consider that young zircon grains contain low levels of radiogenic Pb, which means that even low levels of common Pb may lead to discordance. Moreover, a small laser-spot diameter, used for analysing narrow zircon rims, leads to increased fractionation bias. Because of these analytical difficulties when dating young metamorphic rims we used a different screening and regression procedure for zircon-rim dating, presented in table C. Zircon U-Pb data are presented in data tables S5A and S5B of Appendix III in the electronic document attached to the thesis, and in Figure B.

Table C: *Zircon-rim data screening procedure*

1	Failed	Discarded
2	$^{206}Pb/^{238}U$ age >100 Ma, uncertainty >10%	Discarded
3	$^{206}Pb/^{238}U$ age >100 Ma, >10% discordant	Discarded
4	$^{206}Pb/^{238}U$ age >1200 Ma, >5% discordant	Discarded
5	$^{206}Pb/^{238}U$ age <100 Ma, <5% discordant	$^{206}Pb/^{238}U$ age used
6	$^{206}Pb/^{238}U$ age <100 Ma, 5 - 10% discordant	$^{206}Pb/^{238}U$ age used
7	$^{206}Pb/^{238}U$ age <30 Ma, >10% discordant	Age from fixed common Pb regression used
8	$^{206}Pb/^{238}U$ age 30 – 100 Ma >10% discordant	$^{206}Pb/^{238}U$ age used
9	$^{206}Pb/^{238}U$ age 100 – 1200 Ma, <5% discordant	$^{206}Pb/^{238}U$ age used
10	$^{206}Pb/^{238}U$ age >1200 Ma, <10% discordant	$^{207}Pb/^{206}Pb$ age used

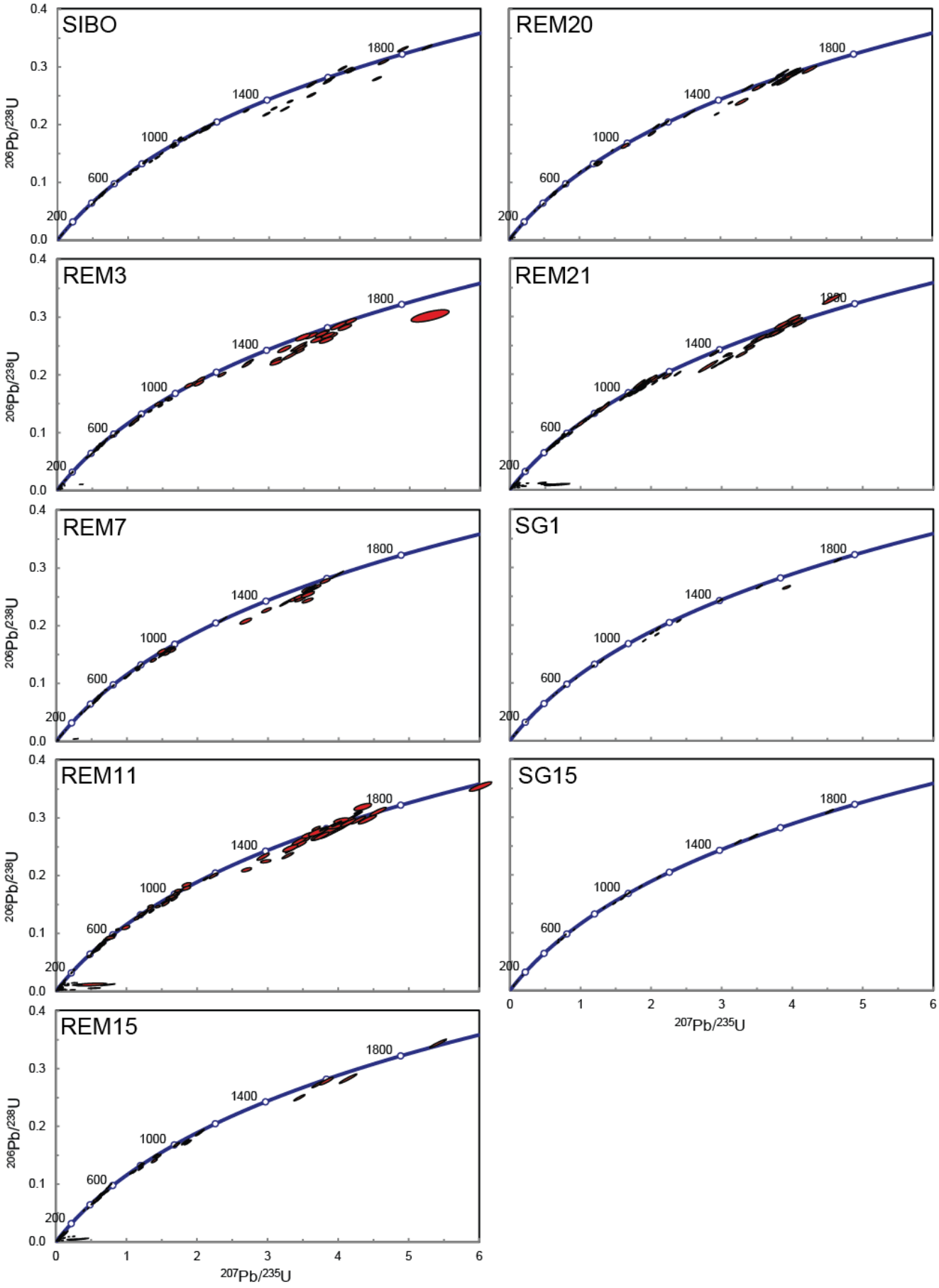
SIBO
REM20
REM3
REM21
REM7
SG1
REM11
SG15
REM15
206Pb/238U
207Pb/235U
0.0
0.1
0.2
0.3
0.4
0
1
2
3
4
5
6
200
600
1000
1400
1800

Figure B: *Zircon U-Pb concordia diagrams of samples from the Sibo-Remi-Siang section. Data are plotted as Wetherill concordia diagrams, using the Isoplot v. 4.14 add-in for Microsoft Excel (Ludwig, 2003), after data screening. The dotted dark blue line is the concordia curve where ages are indicated in Ma. Data point ellipses are at the 2σ level.*

DATA TABLES

Data tables are listed here and are presented in the electronic document attached to the thesis, in the file of Appendix III.

Table S1: Sample location

Table S2: Magnetostratigraphy data

Table S3: Zircon U-Pb data from source-areas compilation

Table S4: Apatite fission-track - U-Pb data

Table S5A: Zircon core and rim U-Pb data

Table S5B: Zircon standard U-Pb data

APPENDIX IV: Supplementary Material of Chapter 4 - Onset of rapid exhumation in the Namche Barwa syntaxis

ANALYTICAL METHODS

Sample preparation

Prior to analysis, the samples were dried, sieved (fraction <500 µm) and washed with tap water at Lancaster University. Heavy minerals were extracted by wet separation on a Haultain superpanner, standard di-iodomethane heavy liquid (density of 3.3), and magnetic separation, which was kept to a minimum to avoid biasing mineral populations, at the NERC Isotope Geosciences Laboratory, Keyworth, UK (NIGL). Zircon and rutile grains were hand-picked, taking special care to select all grain types with respect to morphology, colour and grain size, within a particular fraction of the separate. White micas where handpicked from the light fraction, separated with the Haultain superpanner.

Zircon fission-track dating

Zircon grains were mounted in two to four Teflon® sheets per sample, polished and etched in a NaOH-KOH solution at 228 °C for 36 to 70 hours, at thermochronology laboratory at ISTerre, Université Grenoble Alpes, Grenoble (France). The multi-mount technique with different etch times allowed to obtain countable grains from the whole grain age spectrum of a sample (Bernet et al., 2004b; Naeser et al., 1987). Zircon grain mounts were then covered with muscovite external detectors and irradiated together with IRMM541 (50 ppm) dosimeter glasses and Fish Canyon Tuff age standards in the FRMII reactor at the Technical University of Munich (Germany). Following the thermal neutron irradiation, muscovite sheets, were etched at 21 °C for 18 min in 48% HF. Spontaneous (Ns) and induced (Ni) tracks were counted dry, using an optical Olympus BH2 microscope with 1250× magnification. Between 36 and 105 grains per sample were dated, depending on available sample material and zircon quality with respect to zonation, fracture, inclusions, defect and metamictisation, using a zeta factor of 105.79±3.68 (Hurford and Green, 1983). Fission-track data are presented in data table S2 of Appendix IV in the electronic document attached to the thesis, and in Figure A. The youngest age populations have been determined for each sample, from the data fraction of ages <30 Ma, in linear density plots, using the minimum mixture model of the Density Plotter program (Vermeesch, 2012), as illustrated in Figure A. Density Plotter (Vermeesch, 2012) was also used for data presentation (radial and Kernel density estimations plots).

ZIRCONS < 30 Ma

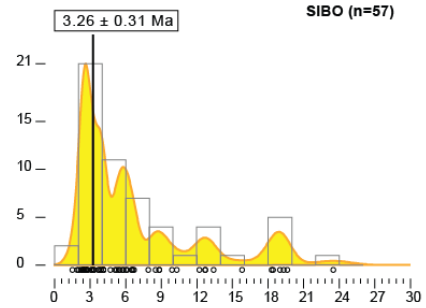

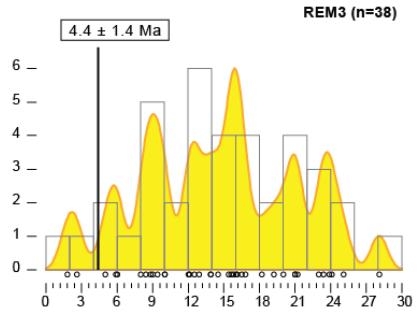

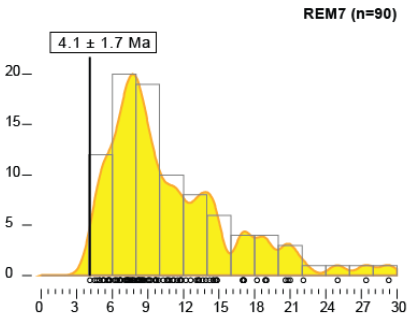

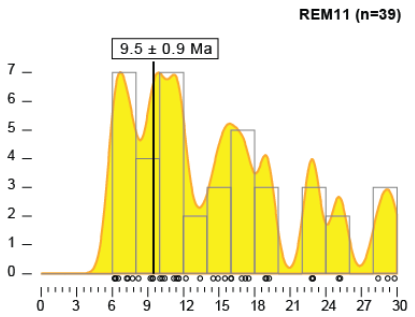

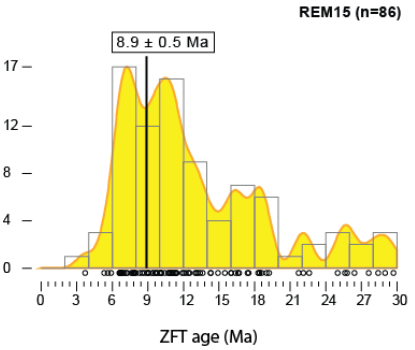

ALL ZIRCONS

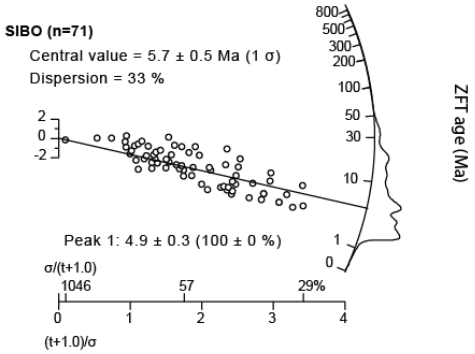

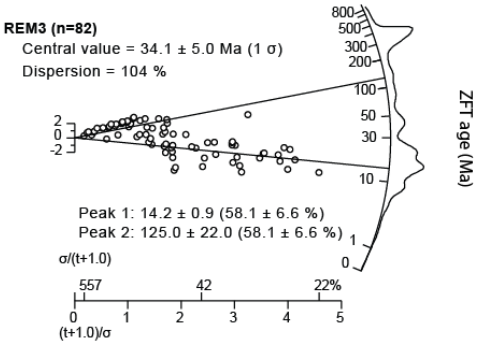

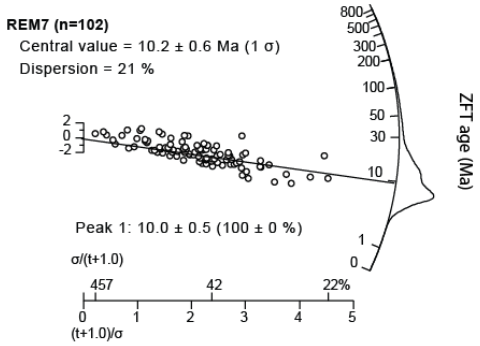

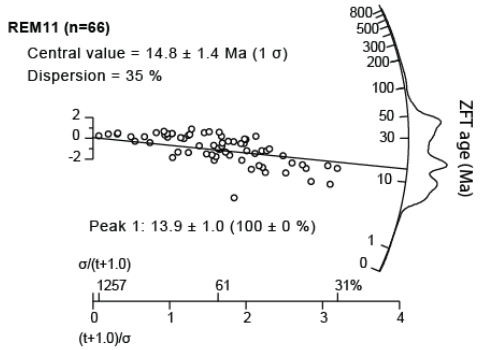

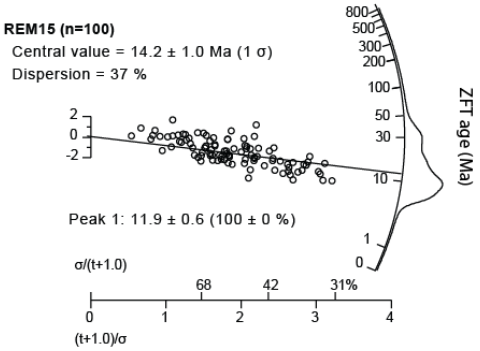

ZIRCONS < 30 Ma

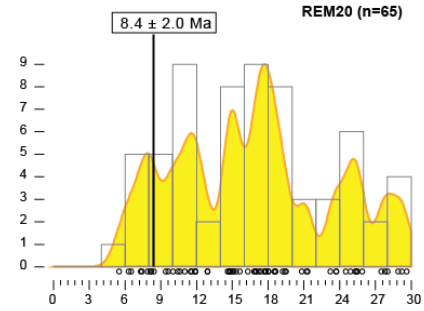

ALL ZIRCONS

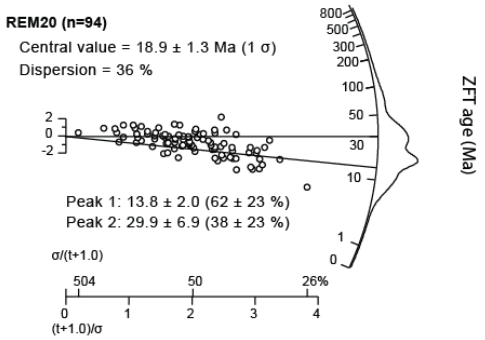

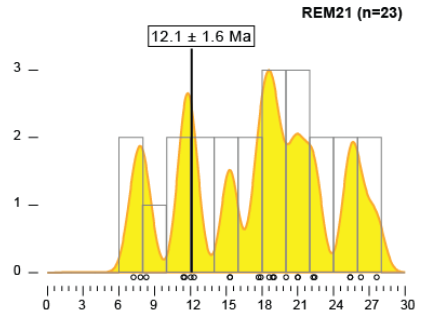

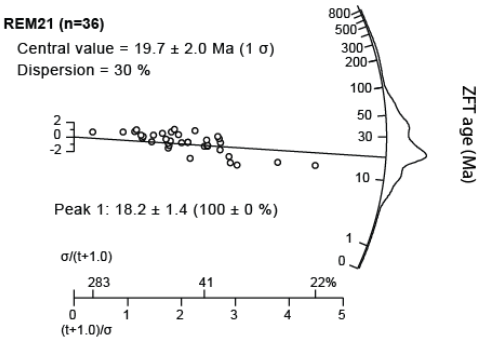

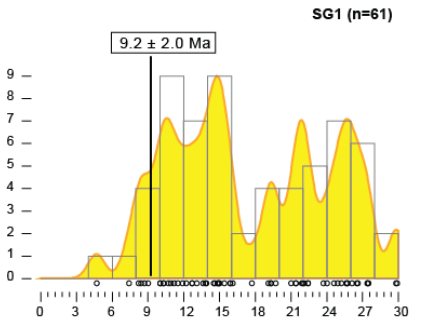

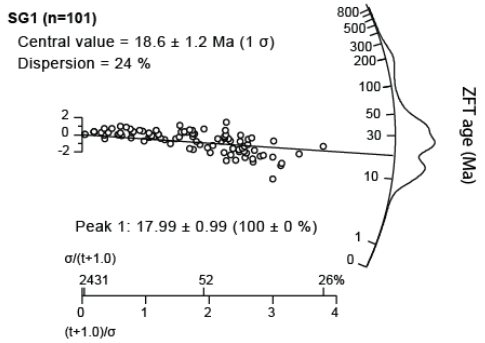

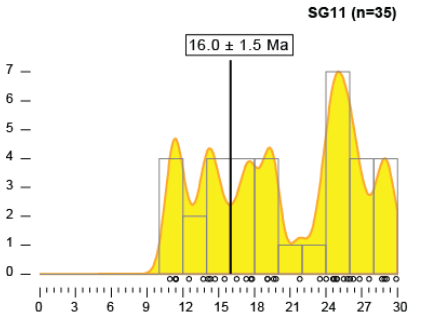

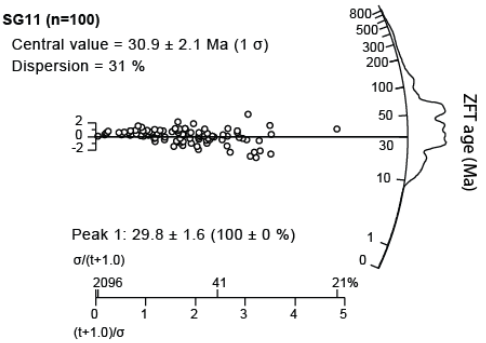

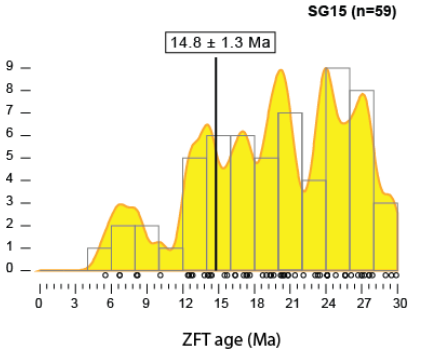

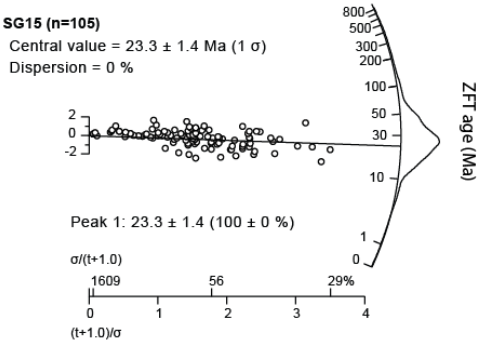

Figure A: *Zircon fission-track data for samples from the Sibo-Remi-Siang sections. The left column shows ages <30 Ma for each sample, plotted as adaptive Kernel density plots (Vermeesch, 2012) with overlying histograms; n=number of grains <30 Ma. Framed number shows the minimum age peak generated with Density Plotter program (Vermeesch, 2012). The right column shows ZFT data reported in radial plots and considering the total number of dated grains in each sample, indicated next to sample name (n=X). The central age, dispersion and main peak ages (± 1σ, with percentages referring to the relative importance of each peak) are indicated.*

White mica ^{40}Ar-^{39}Ar dating

White mica ^{40}Ar-^{39}Ar dating by single grain single fusion was performed at the VU University, Amsterdam (The Netherlands). More than 100 white mica minerals have been grouped in a 9 mm diameter aluminium foil package for each sample. These packages, along with packages of ~5 mg aliquot of reference material, DRA-2 sanidine (Kuiper et al., 2008; Wijbrans et al., 1995) were stacked in a 10 mm diameter quartz glass tube. The tube was irradiated in a standard Al-irradiation capsule for 12 hrs in the in-core CLICIT facility of the Oregon State University TRIGA reactor. After irradiation, minerals were unpacked and loaded in Cu sample trays. Each tray of 66 mm diameter contains 185 holes of 2 mm diameter and 3 mm depth. One mica crystal is loaded per hole. The trays are then placed in a low volume vacuum UHV gas sample purification line. Single grains were fused with a CO_2 laser (Synrad 48-5, 25 W + 25 W dual plasma tube instrument, 10.5 µm wave length continuous laser). The laser power can be adjusted through a 0–5 V analogue signal to the laser control/power supply units. Positioning of the laser beam was achieved using an analogue Raylase scan head fitted with a dual mirror system (X-axis and Y-axis adjustment) and a ZnS 300mm focusing lens. The beam delivery system achieved a beam diameter of ~300 µm at the focal point. At these settings a 5% laser power setting was sufficient to fuse the samples. The scanhead was used to track three concentric circles for 0.5 – 1.5 mm diameter to ensure that the grain in the hole was exposed to the laser beam.

In sequence measurements of about 50 grains per sample were performed and before, during and after each fourth run system blanks were measured. The system blanks have been stable and predictable during the runs. Between every 20 runs, air reference gas measurements were carried out to monitor mass discrimination and system performance. The baseline corrected beam intensities of the five isotopes of Argon (m/e 40–36) were measured simultaneously on a ThermoFisher Helix MC+ multi-collector noble gas mass spectrometer. The beam intensities of the ^{40}Ar and ^{39}Ar beams were measured on the faraday collectors each fitted with the new 10^{13} Ohm resistor faraday amplifier. The beam intensities of ^{38}Ar and ^{37}Ar were measured on standard compact

discrete dynode secondary electron multipliers in pulse counting mode. The beam intensity of ^{36}Ar was measured on a compact discrete dynode SEM fitted with a high resolution (>1700) collector slit. In this configuration full resolution between argon and hydrocarbon beams is assured. For off-line data reduction, we used ArArCalc2.5 (Koppers, 2002). The ages are reported with uncertainties at 2σ uncertainty level and since small and young grains lead to low sample beam intensity and are therefore difficult to measure we applied the filters presented in the following table to accept or reject results from individual runs:

Table A: White mica ^{40}Ar-^{39}Ar *data screening procedure*

	Failed	Discarded
	Age >20 Ma, uncertainty >20 %	Discarded
	Age <20 Ma and >5 Ma, uncertainty >50 %	Discarded
	Age <5 Ma, ^{39}Ar V <0.5	Discarded
	Age <5 Ma, uncertainty >100 %	Discarded
	All other data	Accepted

After the screening, the youngest age populations have been determined for each sample, from the data fraction of ages <30 Ma, in linear density plots, using the minimum mixture model from Density Plotter program (Vermeesch, 2012) as illustrated in Figure. B. White-mica ^{40}Ar-^{39}Ar data are presented in data table S3 of Appendix IV in the electronic document attached to the thesis, and in Figure B.

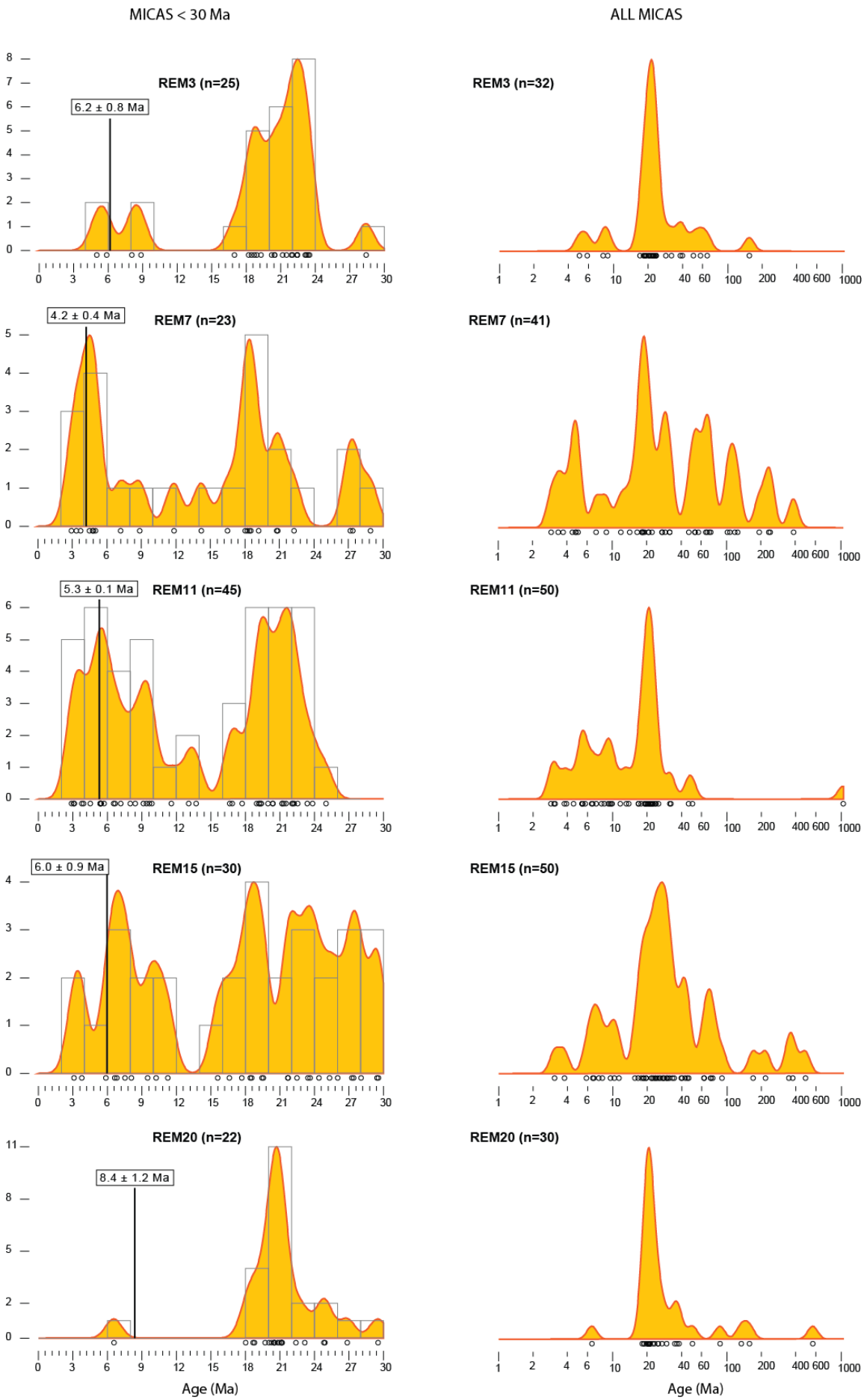
MICAS < 30 Ma
ALL MICAS
REM3 (n=25)
6.2 ± 0.8 Ma
REM3 (n=32)
REM7 (n=23)
4.2 ± 0.4 Ma
REM7 (n=41)
REM11 (n=45)
5.3 ± 0.1 Ma
REM11 (n=50)
REM15 (n=30)
6.0 ± 0.9 Ma
REM15 (n=50)
REM20 (n=22)
8.4 ± 1.2 Ma
REM20 (n=30)
Age (Ma)
Age (Ma)

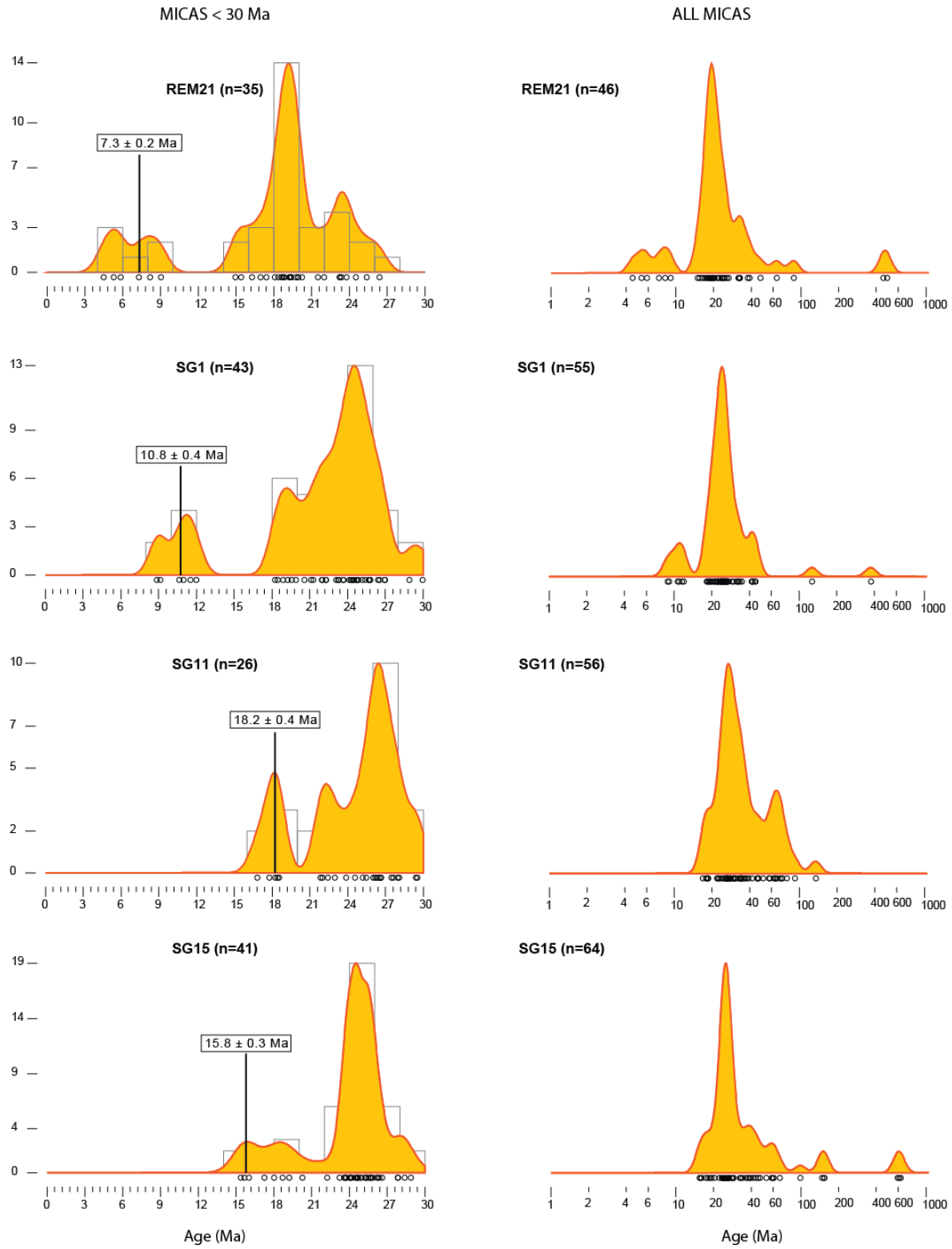

Figure B: *White-mica ^{40}Ar-^{39}Ar data for samples from the Sibo-Remi-Siang sections, plotted as adaptive Kernel density plots (Vermeesch, 2012). The left column shows ages <30 Ma for each sample, with overlying histograms; n=number of grains <30 Ma. Framed number shows the minimum age peak generated with Density Plotter program (Vermeesch, 2012). The right column shows ^{40}Ar-^{39}Ar ages for the total number of dated grains in each sample, indicated next to sample name (n=X).*

U-Pb rutile dating

The rutiles were mounted in epoxy, polished, and photographed to help identify the analysed grains. U-Pb rutile dating was performed using a Nu Instruments AttoM single-collector inductively coupled plasma mass spectrometer (SC-ICP-MS) at NIGL. The instrument was tuned to ensure that ThO and UO were less than 0.4%. The Nu Attom SC-ICP-MS was used in peak-jumping mode with measurement on a MassCom secondary electron multiplier. The analysed masses in each sweep were: ^{202}Hg, ^{204}Pb+Hg, ^{206}Pb, ^{207}Pb, and ^{235}U. Each data integration records 100 sweeps of the measured masses, which roughly equates to 0.22 seconds. Dwell times on each mass are 400 µs on ^{207}Pb and ^{235}U, and 200 µs on all other masses; the switching between masses takes 40 µs. ^{238}U is calculated using ^{238}U/^{235}U = 137.818.

Laser ablation was performed using a New Wave Research UP193SS laser ablation system, with a low-volume cell (Horstwood et al., 2003). This cell has a washout to less than 1% of the peak signal in less than one second. Ablation parameters were optimized to suit the Pb and U contents with a frequency of 5Hz, a fluence of 1.5 to 3.0 J/cm^2, a 30 second ablation time, and a 30 to 35 µm spot size.

Four rutile reference materials Sugluk-4, PCA-S207 (Bracciali et al., 2013) and R10, R19 (Luvizotto et al., 2009) were analysed at regular intervals in order to correct data for instrumental fractionation. The average bias of the ^{207}Pb/^{206}Pb and ^{206}Pb/^{238}U ratios from preferred values derived by TIMS analysis are used for normalization. ^{206}Pb/^{238}U and ^{207}Pb/^{206}Pb uncertainties were propagated in the manner advocated by Horstwood (2008), utilising the measurement uncertainty and the reproducibility of the ablation reference material used.

An in-house Excel spreadsheet was used for data reduction and error propagation; Density Plotter (Vermeesch, 2012) and Isoplot (Ludwig, 2003) were used for data presentation.

Data reduction of rutile measurements was undertaken with the age filters summarised in the following screening procedure table. Since rutile material is commonly discordant due to relatively high common Pb, model ages were derived by regressing data points through a fixed common Pb (0.844±0.008) composition on Tera-Wasserburg plots as described in (Bracciali et al., 2013).

Table B: *U-Pb rutile data screening procedure*

1	Failed	Discarded
2	^{207}Pb/^{206}Pb >0.5	Discarded
3	^{206}Pb <100 counts	Discarded
4	^{207}Pb/^{206}Pb <0.5 and ^{206}Pb >100 counts	Common Pb-corrected ages

The youngest age population has been determined using Isoplot (Ludwig, 2003), a minimum of three of the youngest single grain ages have been commonly regressed through the fixed common Pb (0.844±0.008), together showing an MSWD value <2. The resulting age defines the youngest population for each sample, as shown in Figure C. Rutile U-Pb data are presented in data table S4 of Appendix IV in the electronic document attached to the thesis, and in Figure C.

YOUNGEST POPULATION

TOTAL ANALYSES

SIBO
190.00
±0.02 ka
Min.

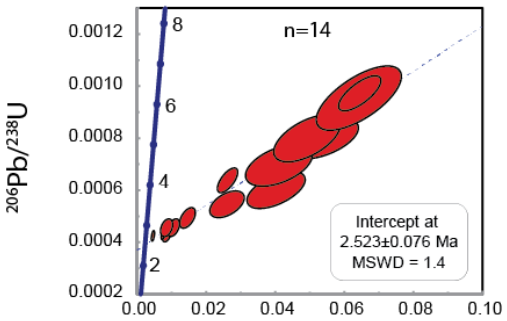

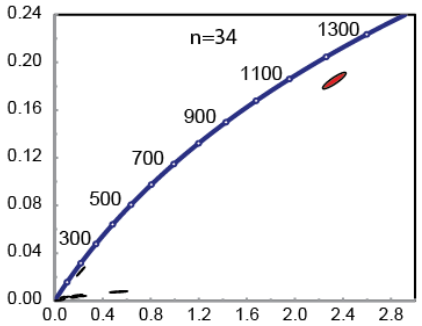

REM3
0.9 Ma
-0.1/+0.7

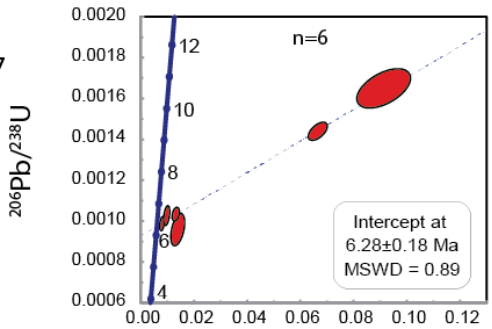

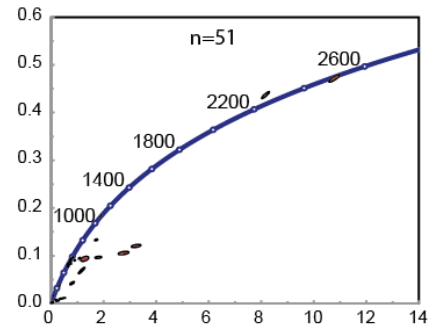

REM7
1.6 Ma
-0.6/+0.2

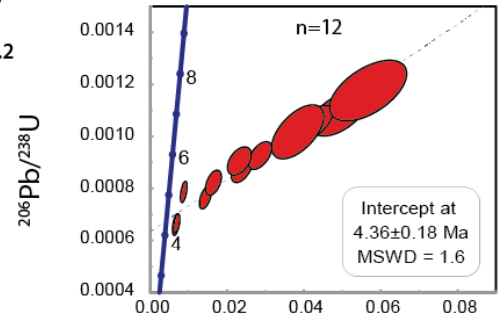

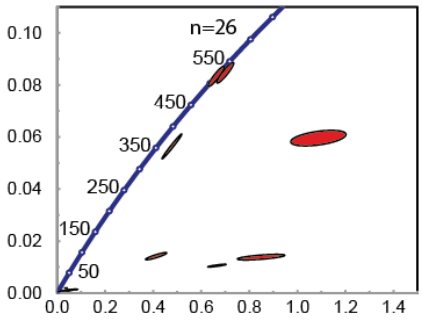

REM11
3.2 Ma
-0.4/+0.3

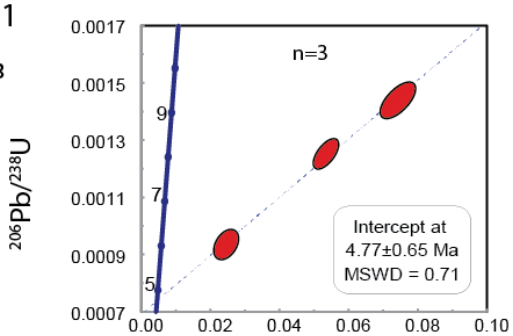

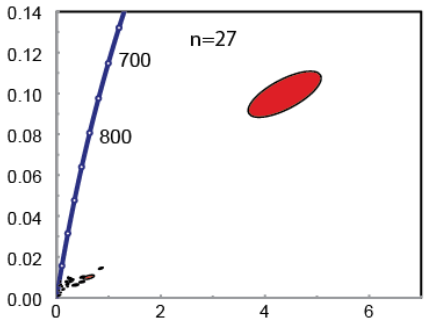

REM15
4.1 Ma
-0.5/+0.6

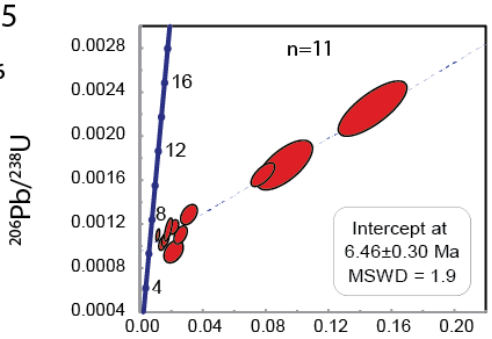

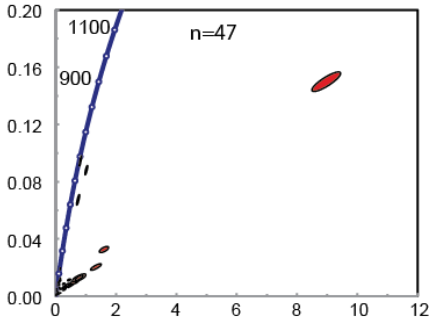

YOUNGEST POPULATION

TOTAL ANALYSES

REM20
4.6±2.5 Ma
Max.

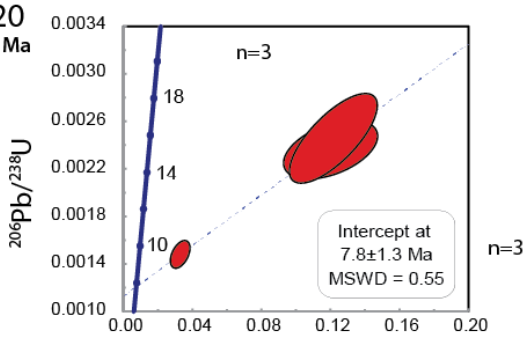

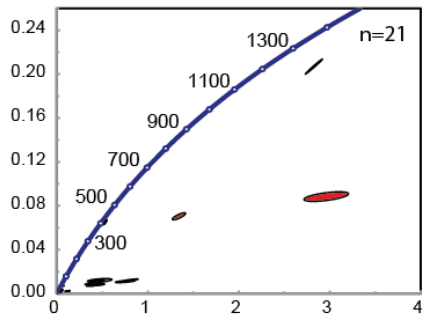

REM21
6.0±1.8 Ma
Max.

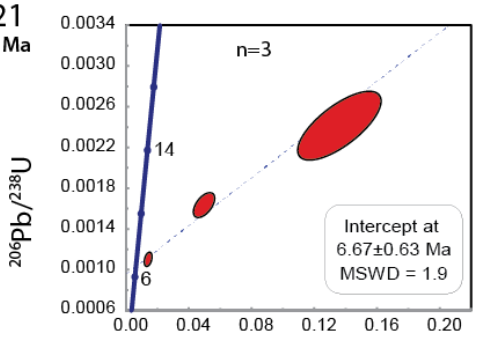

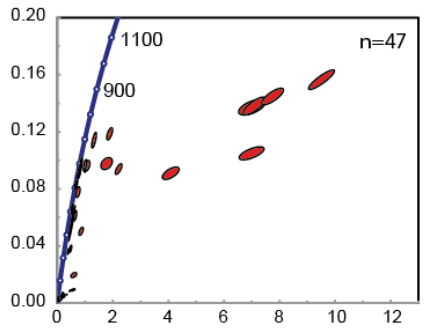

SG1
7.1±1.4 Ma
Max.

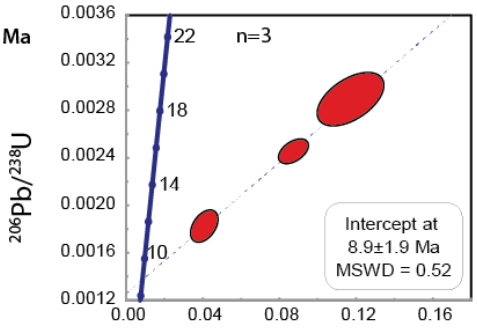

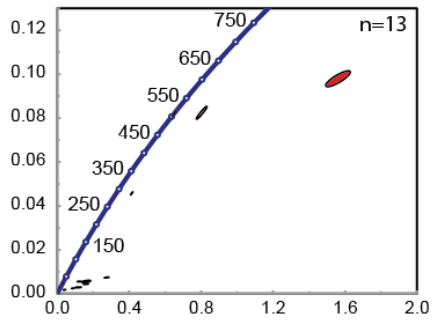

SG11
10.3±1.4 Ma
Max.

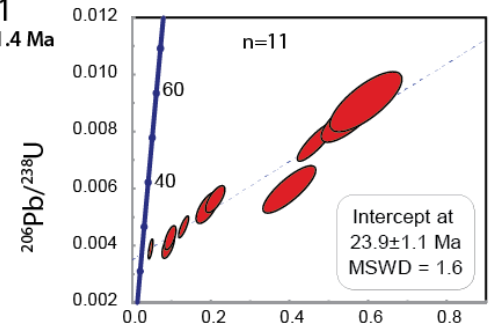

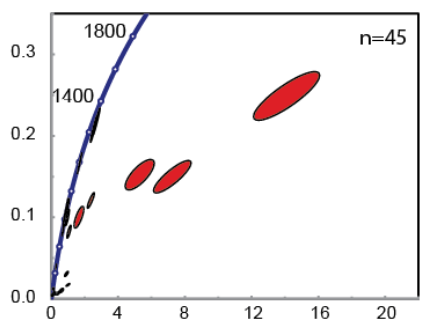

SG15
≤ 11 Ma

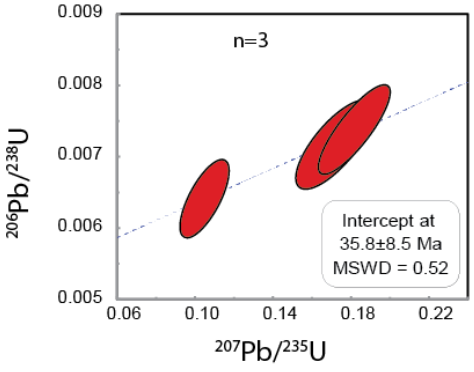

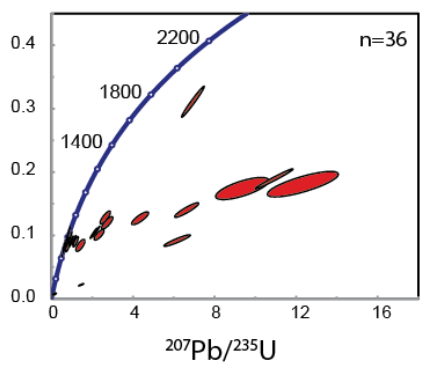

***Figure C**: Rutile U-Pb concordia diagrams of samples from the Sibo-Remi-Siang section. Data are plotted as Wetherill concordia diagrams before correction for common Pb content, using the Isoplot v. 4.14 add-in for Microsoft Excel (Ludwig, 2003), after data screening. The dotted dark blue line is the concordia curve where ages are indicated in Ma. Data point ellipses are at the 2σ level. Sample names and depositional ages from Govin et al. (in review) are indicated to the left. The left column presents the minimum age population regression, n is the number of rutile grains defining the population and the dotted line is the regression line calculated for these analyses. The right column presents the total n number of dated grains.*

DATA TABLES

Data tables are listed here and are presented in the electronic document attached to the thesis, in the file of Appendix IV.

Table S1: Sample location and minimum age peaks

Table S2: Zircon fission-track data

Table S3: White-mica ^{40}Ar-^{39}Ar data

Table S4: Rutile U-Pb data

Table S5: Model parameters

APPENDIX V: Magnetostratigraphic correlation of the Dungsam Chu section

G. Govin interpreted the magnetostratigraphic results in the study of Coutand et al. (2016), in collaboration with co-authors. However, the author of this thesis does not agree with the final preferred correlation of the publication of Coutand et al. (2016). Coutand et al. (2016) prefers the best numerical correlation determined with the Qupydon software (Lallier et al., 2013) whereas the third author of Coutand et al. (2016) prefers the best manual correlation, correlation C which is the closest manual correlation to the best numerical correlation. The explanations for this preference are provided in this appendix, below.

Magnetostratigraphic dating is based on the correlation of the geomagnetic polarity column of the sampled sedimentary sequence with the GPTS. This approach is based the hypothesis that the sedimentation rates are relatively constant on short time scales, as the thicknesses of the detected inversions are correlated with the length of the GPTS inversions. Generally, several correlations are possible and the choice of the preferred correlation represents a substantial factor of bias in magnetostratigraphic dating. The quality of a correlation depends on the quality of the column (sampling density, magnetic properties, lithology and continuous exposure of outcrop), independent constraints and where applicable, supplemental statistical analysis.

In the case of the Dungsam Chu section, the outcrop exposure is sufficiently continuous; the sampling density is satisfactory; and the apatite fission-track and vitrinite reflectance data provide robust independent constraints. However, the quality of the polarity column is limited in the upper part of the section. Indeed, the coarser-grained lithology in the upper part of the section leads to less reliable normal polarity zones, since normal overprinting commonly occurs in coarse-grained lithologies. Consequently, three possible correlations have been proposed for the upper part of the Dungsam Chu section. In order to discriminate between these three correlations, Coutand et al. (2016) have performed stochastic modelling of the polarity column using the software Qupydon (Lallier et al., 2013). The most conclusive correlation obtained with the Qupydon software is closer to the manual correlation C. The best numerical and manual correlations are both presented in Figure A. The depositional ages in the lower part of the Dungsam Chu section is identical for both C and Q correlations. However, in the upper part of the section, the correlation Q places the Middle to Upper Siwalik transition at ~3.8 whereas the correlation C places this boundary at ~2.5. The maximum age discrepancy between the two correlations is ~1.6 Ma, in the Upper Siwalik sediments (at the ~1800 m stratigraphic level, see Figure B).

Coutand et al. (2016) have concluded that the numerical correlation (correlation Q) is the best option for the Dungsam Chu section. However, G. Govin does not share the same opinion and considers here the reasons why the manual correlation C is the more realistic correlation.

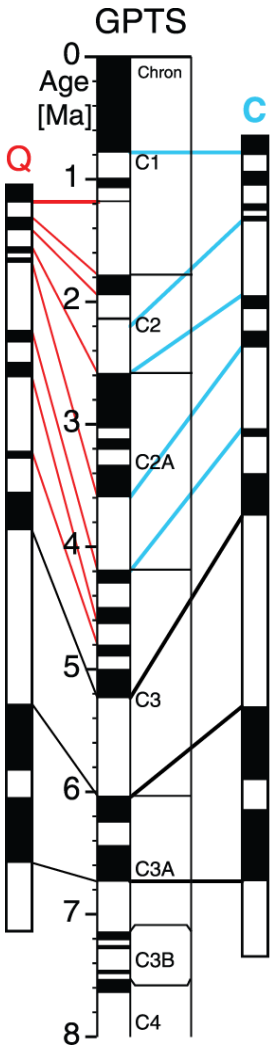

Figure A: *modified version of Fig. 25c. Comparison of the best numerical correlation obtained with the Qupydon software (left), with the best manual correlation C (right). The middle column is the GTPS of Gradstein et al. (2012) and the right and left columns are the magnetostratigraphic results from the Dungsam Chu section. Correlations in black represent similar results for the manual and numerical correlations, correlations in red represent the best numerical correlation (Q), and correlations in blue represent the best manual correlation.*

Lallier et al. (2013) point out that the main flaw of the Qupydon correlation technique is that it assumes that all polarity changes recorded in the studied sedimentary section are known in the GPTS. Indeed, Lallier et al. (2013) acknowledge that when local sediment re-magnetisation occurs,

this limitation may represent an obstacle to a good correlation. As demonstrated in chapter 2, this is the case in the coarser-grained lithology of the upper part of the Dungsam Chu section. Therefore, the ambiguities in the correlation of the upper part of the section can only be documented by Qupydon, and not necessarily solved. The solutions can be explored by ignoring debatable polarity zones in the correlation computation and automatically managed by adding a gap if they are actually identified in the GPTS, since the Qupydon correlation method manages gaps well (Lallier et al., 2013). Although few debatable polarity zones from the Dungsam Chu section have been ignored before running the software in Coutand et al. (2016), the polarity zones of the upper part of the section (from the ~1400 m stratigraphic level) remain generally not completely reliable (Coutand et al., 2016). Therefore extreme care must be taken in the magnetostratigraphic interpretation of this part of the section, and a careful handle on such delicate correlation is certainly better attained manually. The use of Qupydon software should be regarded as a guide in this particular case, instead of a judge.

The software is forced to find correlations that minimize local variations of the sedimentations rates (Coutand et al., 2016; Lallier et al., 2013), and this advantage is pertinent in the choice of the best manual correlation. However, the resulting correlation strongly depends on the credit accorded to the polarities. Therefore, G. Govin acknowledges the efficiency of the Qupydon software in guiding the choice of the best manual correlation for the upper part of the Dungsam Chu section, as it provides a general overview of the best option. Nevertheless, in detail, the ambiguities related to the local variations in the accumulation rates are better addressed with a manual correlation. As illustrated in Figure B, correlation Q is forced to the lower local variations in accumulation rates; by contrast, correlation C takes into account the less reliable definition of the normal polarity zones.

Furthermore, the one-stage decrease in accumulation rates in the Dungsam Chu section determined with the manual correlation C (Figure B) is synchronous with the arrival of paleo-Brahmaputra deposits in the section, interpreted as the initiation of the uplift of the Shillong Plateau (see chapter 2 and discussion). By contrast, the accumulation rates observed using the numerical correlation Q show a two-stage decrease and although the first decrease is also synchronous to the uplift of the Shillong Plateau, the second stage is more difficult to explain.

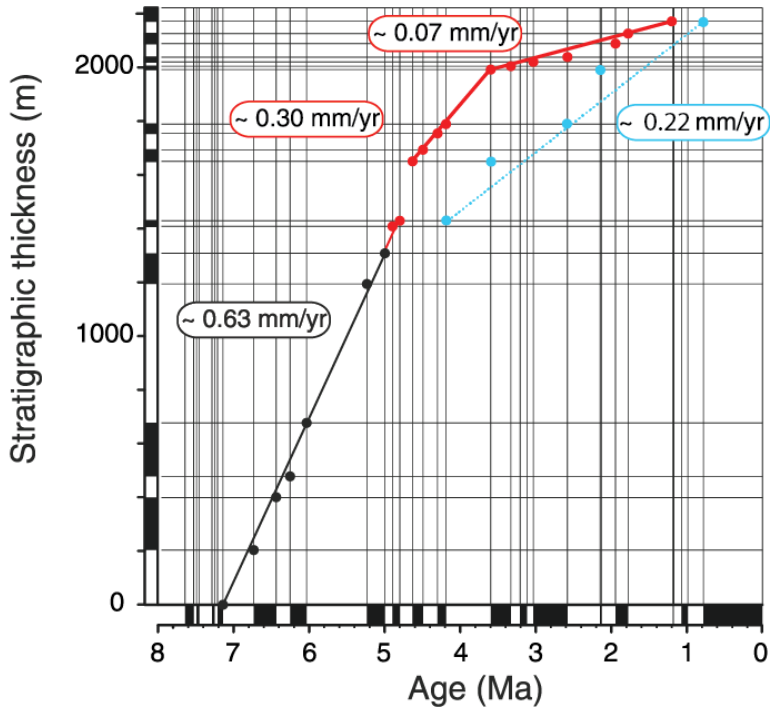

Figure B: *modified version of Fig. 28 Age versus depth plot of the Dungsam Chu section using the best numerical correlation in red, and the best manual correlation in blue. In black are the results similar for both correlations. Accumulation rates are presented in their corresponding color.*

Note that the rutile U-Pb data from the Dungsam Chu section presented in Appendix VII are consistent with correlation C. Indeed, the youngest rutile grain from sample SJ8 (see chapter 2) is dated at 4.8±0.3 Ma. This age constitutes a maximum depositional age for the stratigraphic level of sample SJ8 (~1400 m). If correlation C is used to determine the depositional age of the rocks, the stratigraphic level of sample SJ8 has a younger depositional age of ~4.4 Ma; by contrast if correlation Q is used, the depositional age is ~4.9 Ma which is older than or within error to the maximum depositional age determined with rutile U-Pb dating. Therefore, the rutile U-Pb dating in the Dungsam Chu section constitutes supplementary evidence that the manual correlation C is closer to the true depositional age of the Dungsam Chu section than the numerical correlation Q. However, this depends on the degree of error on the depositional ages determined with both correlations. Indeed, the rutile U-Pb ages <9 Ma are sourced from the rapidly exhuming syntaxis, as characterised by Bracciali et al. (2016) and this implies that the rutile U-Pb lag times are expected to be very short (see chapter 4).

APPENDIX VI: Lateral variations in vegetation in the Himalaya since the Miocene and implications for climate evolution

Natalie Vögeli[1], Yani Najman[2], Peter van der Beek[1], Pascale Huyghe[1], Peter M. Wynn[2], **Gwladys Govin[2]**, Iris van der Veen[3,4], Dirk Sachse[3,4].

[1] *Université Grenoble Alpes, Institut des Sciences de la Terre (ISTerre), CS 40700, 38058 Grenoble Cedex 9, France*

[2] ***Lancaster Environment Centre, Lancaster University, LA1 4YQ, UK***

[3] *GFZ German Research Centre for Geosciences, Earth Surface Geochemistry, Telegrafenberg, 14473 Potsdam, Germany.*

[4] *Department of Earth and Environmental Sciences, University of Potsdam, 14476 Potsdam, Germany.*

Manuscript accepted for publication in Earth and Planetary Science Letters. 471, p. 1-9.

DOI: 10.1016/j.epsl.2017.04.037

ABSTRACT

The Himalaya has a major influence on global and regional climate, in particular on the Asian monsoon system. The foreland basin of the Himalaya contains a record of tectonics and paleoclimate since the Miocene. Previous work on the evolution of vegetation and climate has focused on the central and western Himalaya, where a shift in vegetation has been observed at ~7 Ma and linked to increased seasonality, but the climatic evolution of the eastern part of the orogen is less well understood. In order to track vegetation as a marker of monsoon intensity and seasonality, we analysed $\delta^{13}C$ and $\delta^{18}O$ values of soil carbonate and associated $\delta^{13}C$ values of bulk organic carbon from previously dated sedimentary sections exposing the syn-orogenic detrital Dharamsala and Siwalik Groups in the west, and, for the first time, the Siwalik Group in the east of the Himalayan foreland basin. Sedimentary records span from 20 to 1 Myr in the west (Joginder Nagar, Jawalamukhi, and Haripur Kolar sections) and from 13 to 1 Myr in the east (Kameng section), respectively. The presence of soil carbonate in the west and its absence in the east is a first indication of long-term lateral climatic variation, as soil carbonate requires seasonally arid conditions to develop. $\delta^{13}C$ values in soil carbonate show a shift from around -10 ‰ to -2 ‰ at ~7 Ma in the west, which is confirmed by $\delta^{13}C$ analyses on bulk organic carbon that show a shift from around -23 ‰ to -19 ‰ at the same time. Such a shift in isotopic values is likely to be associated with a change

from C3 to C4 vegetation. In contrast, $\delta^{13}C$ values of bulk organic carbon remain at ~-23 ‰ in the east. Thus, our data show that the current east-west variation in climate was established at 7 Ma. We propose that the regional change towards a more seasonal climate in the west is linked to a decrease of the influence of the Westerlies, delivering less winter precipitation to the western Himalaya, while the east remained annually humid due to its proximity to the monsoonal moisture source.

1. INTRODUCTION

The Himalayan belt has a major influence on global and regional climate, by acting as an orographic barrier for air masses and humidity (Boos and Kuang, 2010; Molnar et al., 2010). Modern climate shows significant east-west variation in the Himalaya: both mean-annual and winter precipitation on the plains and foothills are higher in the east, while the west is characterized by more pronounced winter aridity (Fig. 1; Bookhagen and Burbank, 2006; 2010). This variation is due to the two major atmospheric circulation systems influencing the climate of the Himalayan region: the Indian Summer Monsoon (ISM) and the Westerlies (Kotlia et al., 2015). The ISM takes up moisture in the Bay of Bengal and transports it towards the Himalaya during the northern-hemisphere summer months (e.g. Molnar et al., 2010), whereas the Westerlies bring moisture from the Mediterranean, Black and Caspian Seas and are most efficient in winter (Benn and Owen, 1998; Cannon et al., 2015). Generally, the influence of the Westerlies is greater in the western part of the Himalayan region (Cannon et al., 2015; Caves et al., 2015; Kotlia et al., 2015). The proximity to the moisture source in the Bay of Bengal, makes the eastern Himalaya very humid (Bookhagen and Burbank, 2010).

These lateral variations in modern climate are linked to vegetation patterns, in particular the relative importance of C3 versus C4 plants. C3 plants are favoured in a cool and humid climate, whereas C4 plants prefer intense light, warm and water-stressed conditions (Ehleringer, 1989). An additional factor that possibly influences the evolution of C4 plants is growing season temperature and precipitation, favouring C4 plants in drier periods (Cotton et al., 2016). The distinct stable carbon-isotopic signature of C3 versus C4 vegetation allows paleo-vegetation to be tracked from the sedimentary record: pure C3 vegetation has $\delta^{13}C_{org}$ values between -22 ‰ and -30 ‰, whereas $\delta^{13}C_{org}$ values of C4 plants range from -10 ‰ to -14 ‰ (Cerling et al., 1997). The lateral variations in modern climate and vegetation are expressed by the signature of modern organic carbon transported in the foreland (Galy et al., 2008b; Fig. 1): sediments sampled from Himalayan tributaries at the mountain front have $\delta^{13}C_{org}$ values around -25 ‰, indicating dominance of C3 plants at higher elevations within the mountain belt. These values remain stable within the eastern

Brahmaputra catchment, whereas they increase to values around -22 ‰ in the Western Ganga catchment (Fig. 1), implying laterally varying vegetation (from C4 in the west to C3 in the east) in the floodplain.

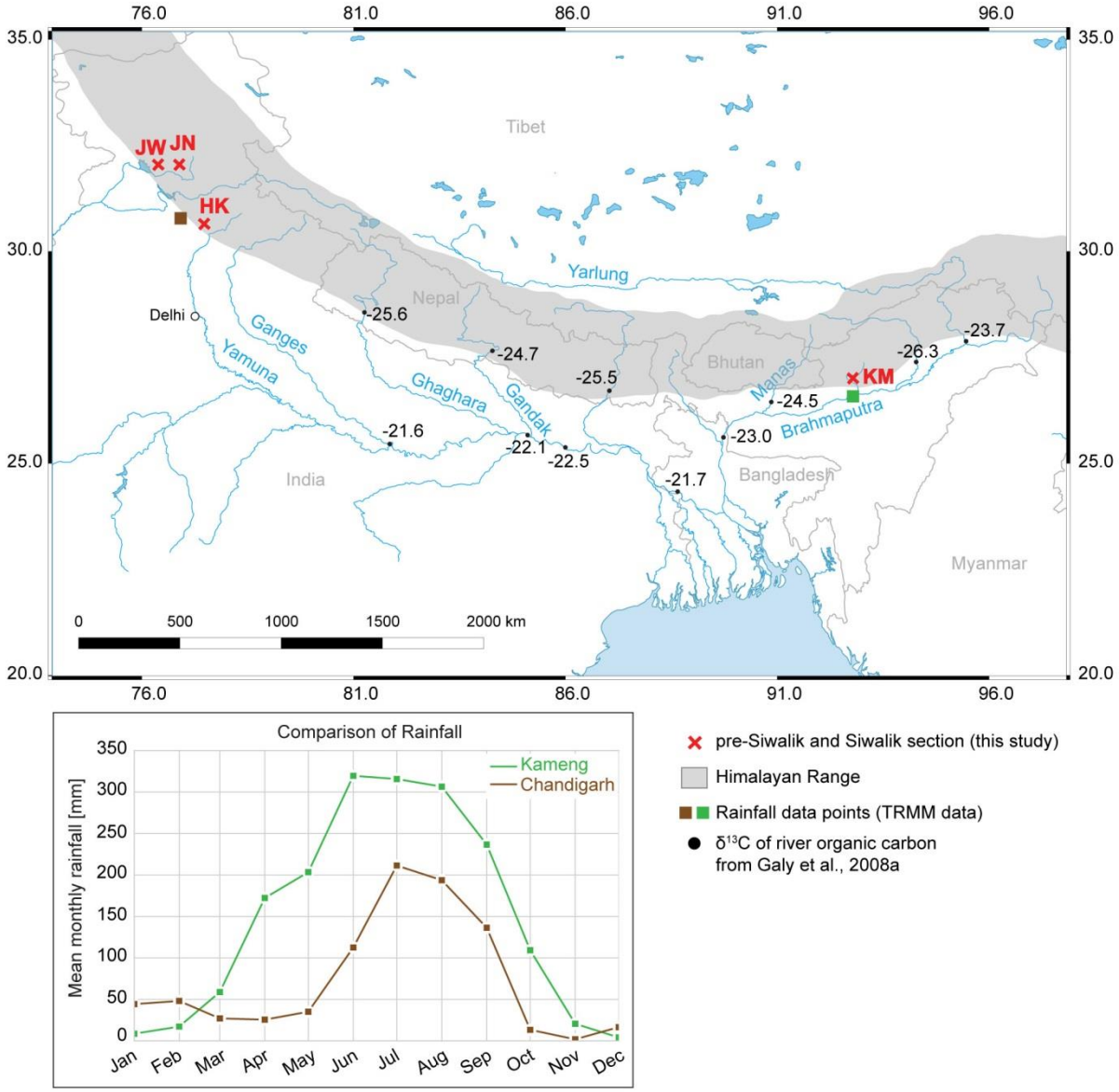

Fig. 1*: Map of the Himalayan region, with $\delta^{13}C$ of modern river organic carbon from Galy et al., 2008b. The Himalayan range is indicated schematically in grey. Sections are indicated in red: JW: Jawalamukhi; JN: Joginder Nagar; HK: Haripur Kolar; KM: Kameng. Lower plot shows comparison of modern annual precipitation data (TRMM) in proximity to the sampled sedimentary sections in the west and east.*

An important question is when and why the modern spatial patterns in climate and vegetation were established in the Himalayan foreland. The onset of the ISM is dated back to at least the middle

Miocene (Dettman et al., 2001) and possibly the Late Eocene (Licht et al., 2014). Likewise, the Westerlies have been argued to influence Asian climate since the Eocene (Caves et al., 2015). However, the evolution of regional climate and vegetation patterns will depend on the relative strength of these two systems through time, which remains largely unknown.

The foreland basin of the Himalaya contains a sedimentary record of vegetation and paleoclimate since Miocene times, within the continental detrital pre-Siwalik and Siwalik Groups. The record of spatial and temporal variations in vegetation holds information on climate evolution, in particular patterns of atmospheric circulation, seasonality and the origin and transport of humidity (e.g. Hoorn et al., 2000; Sanyal et al., 2004). Carbon and oxygen isotopic compositions of soil carbonates and soil organic matter from pre-Siwalik and Siwalik sediments in Nepal, Northwest India and Pakistan have been used to reconstruct changes in vegetation and climate during the Neogene (Quade and Cerling, 1995; Quade et al., 1989; 1995a; Sanyal et al., 2010; Singh et al., 2013). These records consistently show a shift in $\delta^{13}C$ values at ~7 Ma, which has been interpreted as a change from C3 to C4 vegetation, which was initially interpreted to be related to an intensification of the ISM (Quade et al., 1989). Steinke et al. (2010) suggest that this change was rather linked to an increase in aridity, and therefore a weakening of the ISM. A similar shift has also been recorded in the distal Himalayan-derived sediments of the Bay of Bengal (France-Lanord and Derry, 1994). It has been argued that the late-Miocene expansion of C4 plants is a global phenomenon due to a decrease in atmospheric pCO_2 (Cerling et al., 1997), global cooling and/or increased aridity (Herbert et al., 2016). Others, however, argue that pCO_2 was already at a level favourable for C4 plants during Oligocene times (Beerling and Royer, 2011; Pagani et al., 2005) and that the spread of C4 plants during the late Miocene should therefore have other, more regional triggers.

The focus of previous studies on Himalayan climate and vegetation records has been entirely on the western and central Himalayan foreland; no climate and vegetation data are available east of Nepal. In order to obtain better spatial insight into the evolution of the monsoon climate, precipitation patterns and the expansion of C4 plants along strike in the Himalaya, we present and compare new $\delta^{13}C$ and $\delta^{18}O$ data of pedogenic carbonate and organic matter from the north-western and the poorly studied eastern Himalayan foreland basin. Lateral variations in the evolution of the vegetation yield further insight into how and under what climatic conditions C4 plants developed or not, suggesting that regional influences play a major role.

2. SETTING

Neogene Himalayan foreland-basin sediments are composed of the fluvial Dharamsala Group of Late Oligocene and early Miocene age (Burbank et al., 1996), and the Siwalik Group deposited since the early Miocene. The Dharamsala rocks consist of continental fluvial, lacustrine or deltaic sediments, and contain fine-to medium grained sandstones, siltstones and overbank mudstones with soil carbonate nodules. The sediments of the Siwalik Group are exposed nearly continuously along the front of the Himalayan range, with only minor age variation along strike (Burbank et al., 1996). They were deposited in the foreland before being incorporated in the foothills due to southward propagation of deformation and onset of motion on the Main Frontal Thrust (MFT).

The Siwalik Group shows an overall coarsening- and thickening-upward trend, interpreted as recording increasingly proximal deposition (DeCelles et al., 1998a), and is divided into the Lower, Middle and Upper Siwaliks (LS, MS, US). The LS were deposited by high-sinuosity streams (Nakayama and Ulak, 1999). The Middle Siwaliks (MS) are characterized by thickly bedded sandstones, which are medium- to coarse-grained and often rich in mi~The MS represent a depositional environment of large braided rivers. The Upper Siwaliks (US) consist of beds of conglomerates alternating with sandstone beds, deposited by gravelly braided rivers. Paleosols are developed throughout most of the Siwalik sections, with lateral and temporal variations in abundance: they are more abundant in the LS and in the west. Paleosols are characterized in western and central Himalayan sections by the presence of soil-carbonate nodules.

We sampled three sections exposing Dharamsala and Siwalik deposits in the western Himalaya; the Joginder Nagar (JN), Jawalamukhi (JW) and Haripur Kolar (HK) sections in Himachal Pradesh, and one Siwalik section in the eastern Himalaya; the Kameng River (KM) section in Arunachal Pradesh (Figs. 1, 2). All sections have previously been dated by magnetostratigraphy (Chirouze et al., 2012; Meigs et al., 1995; Sangode et al., 1996; White et al., 2001). They span a time range of 20-1 Ma in the west and 13-1 Ma in the east. In the western sections, we collected paleosols and associated carbonate nodules, as well as fine-grained mudstone in zones without well-developed paleosols. Carbonate nodules are lacking in the Kameng section (Fig. 2); therefore only mudstones, where possible from paleosols, were sampled. Additionally, modern river mud was sampled from riverbanks in proximity to the sections in both the west and the east. Modern river samples in the west (Beas River and Jner Khad River) were collected at an elevation of ~640 m within the sections, whereas the modern Kameng River sample was collected at an elevation of ~100 m downstream of the Siwalik.

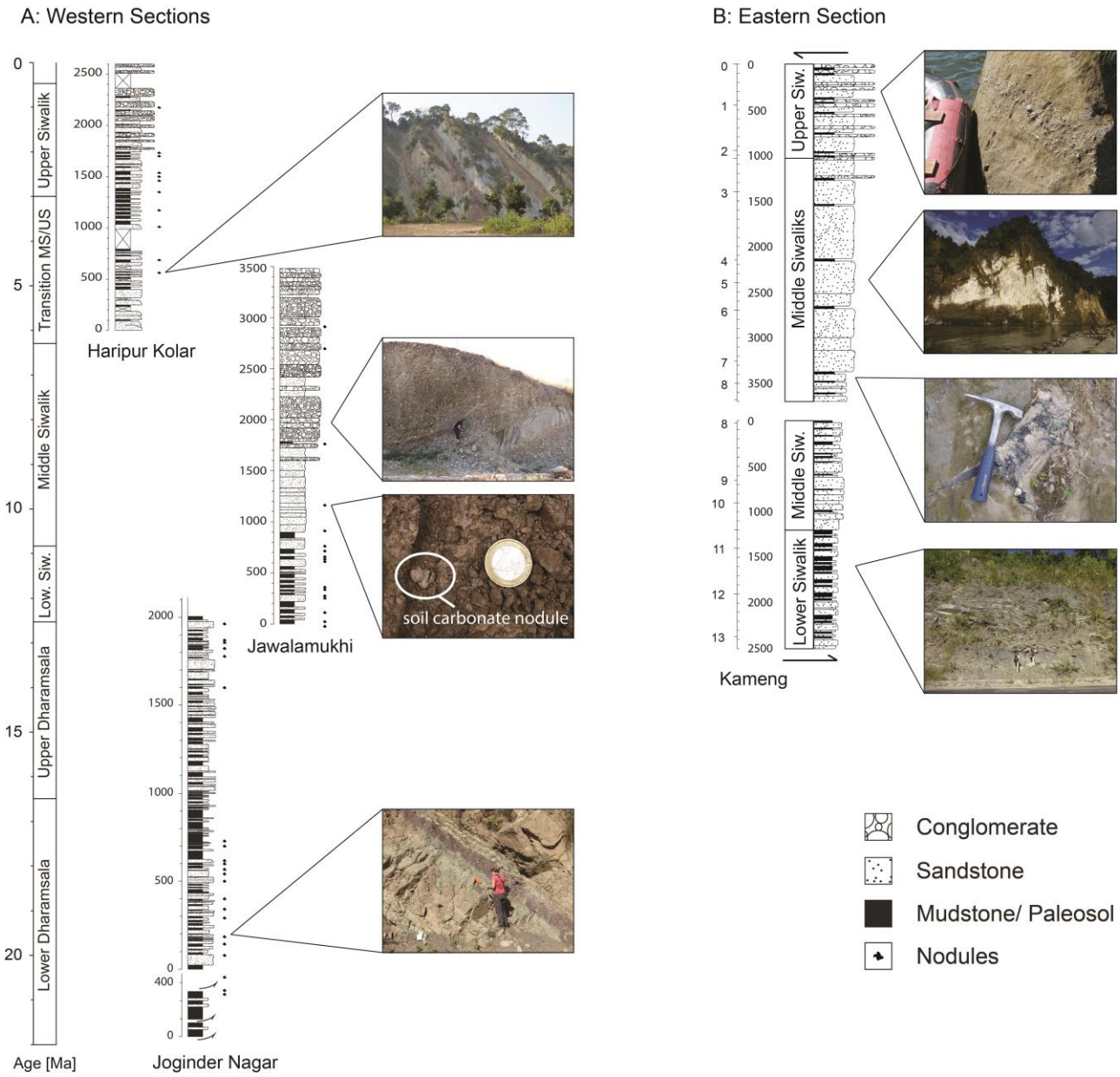

***Fig. 2**: Stratigraphy of sections of the Dharamsala and Siwalik Groups in the west (A) and in the east (B), with field photos showing sedimentological characteristics of different sub-groups.*

3. METHODS

$^{13}C/^{12}C$ and $^{18}O/^{16}O$ ratios (expressed as $\delta^{13}C$ and $\delta^{18}O$ values respectively) of soil carbonate nodules were determined using a multiflow analyser linked to an Isoprime 100 continuous flow mass spectrometer at the Lancaster University, UK. Approximately 600-700 µg of sample powder was drilled from each carbonate nodule and digested online at 90°C with dehydrated phosphoric acid in a He-flushed exetainer. Product CO_2 was analysed for $\delta^{13}C_{CO2}$ and $\delta^{18}O_{CO2}$ and corrected against VPDB and VSMOW, respectively, using within-run analyses of international standards NBS18, LSVEC and CO-1. Within-run standard replication (1 σ) was <0.1 ‰ for both C and O isotope ratios. Sample

replication based on separate drill aliquots of powder from the same carbonate nodule was <0.1‰ for $\delta^{13}C$ and <0.2 ‰ for $\delta^{18}O$ (1 σ).

$^{13}C/^{12}C$ ratios (expressed as $\delta^{13}C$ values) of bulk organic matter were determined using an Elementar Vario Micro elemental analyser linked to a VisION continuous flow mass spectrometer at the University of Lancaster. The carbonate content of each sample was removed by acid digestion using 1M ultrapure HCl and the resultant sample washed repeatedly using de-ionised water and centrifugation. Approximately 10 mg of each prepared sample was combusted within tin capsules at 960 °C to yield CO_2 for determination of $\delta^{13}C_{org}$. $\delta^{13}C$ values were corrected against VPDB using internal reference materials calibrated to international standards. Within-run $\delta^{13}C$ replication (1 σ) was <0.2 ‰ for standards and <0.25 ‰ for samples.

4. RESULTS

The three sections in Himachal Pradesh (Western Himalaya) provide a continuous age record over the past 20 Ma (Fig. 3). Prior to ~7 Ma, $\delta^{13}C$ values of soil carbonate ($\delta^{13}C_{soil\ carb.}$) range between -8 ‰ and -13 ‰, whereas at ~7 Ma a shift towards more positive $\delta^{13}C$ values, ranging from +2 ‰ to -8 ‰, is observed (Fig. 3; Supplementary Material 1). $\delta^{18}O$ values range mostly from -11 ‰ to -4 ‰, except in the older part of the sections, where some values are as low as -14 ‰. A weak trend towards more positive $\delta^{18}O$ values over time is observed. As noted above, soil carbonate was not present in the eastern Himalayan section.

We additionally measured a continuous record of $\delta^{13}C$ in organic carbon ($\delta^{13}C_{org}$) in both the western and eastern sections (Fig. 4; Supplementary Material 1). In the west, a clear shift towards more positive $\delta^{13}C_{org}$ values is observed at ~7 Ma, synchronous with the $\delta^{13}C_{soil\ carb}$. Before 7 Ma, $\delta^{13}C_{org}$ values range between -23 ‰ and -27 ‰, while values are less negative, from -18 ‰ to -23 ‰, after 7 Ma. In the east, in contrast, $\delta^{13}C_{org}$ values remain constant between -29 ‰ and -23 ‰ since the middle Miocene and no shift towards more positive values is observed. Organic matter from modern river sediments show $\delta^{13}C$ values of approximately -26 ‰ and -23.5 ‰ in the west and in the east, respectively (Fig. 4). Total Organic Carbon content (TOC) in the western samples is mostly <0.5 % although samples from the JN can have up to 15% TOC (Fig. 5). TOC of most Kameng samples is also <0.5 %, with some samples showing values up to 3%. There is no correlation between $\delta^{13}C_{org}$ values and TOC (Supplementary Material 2).

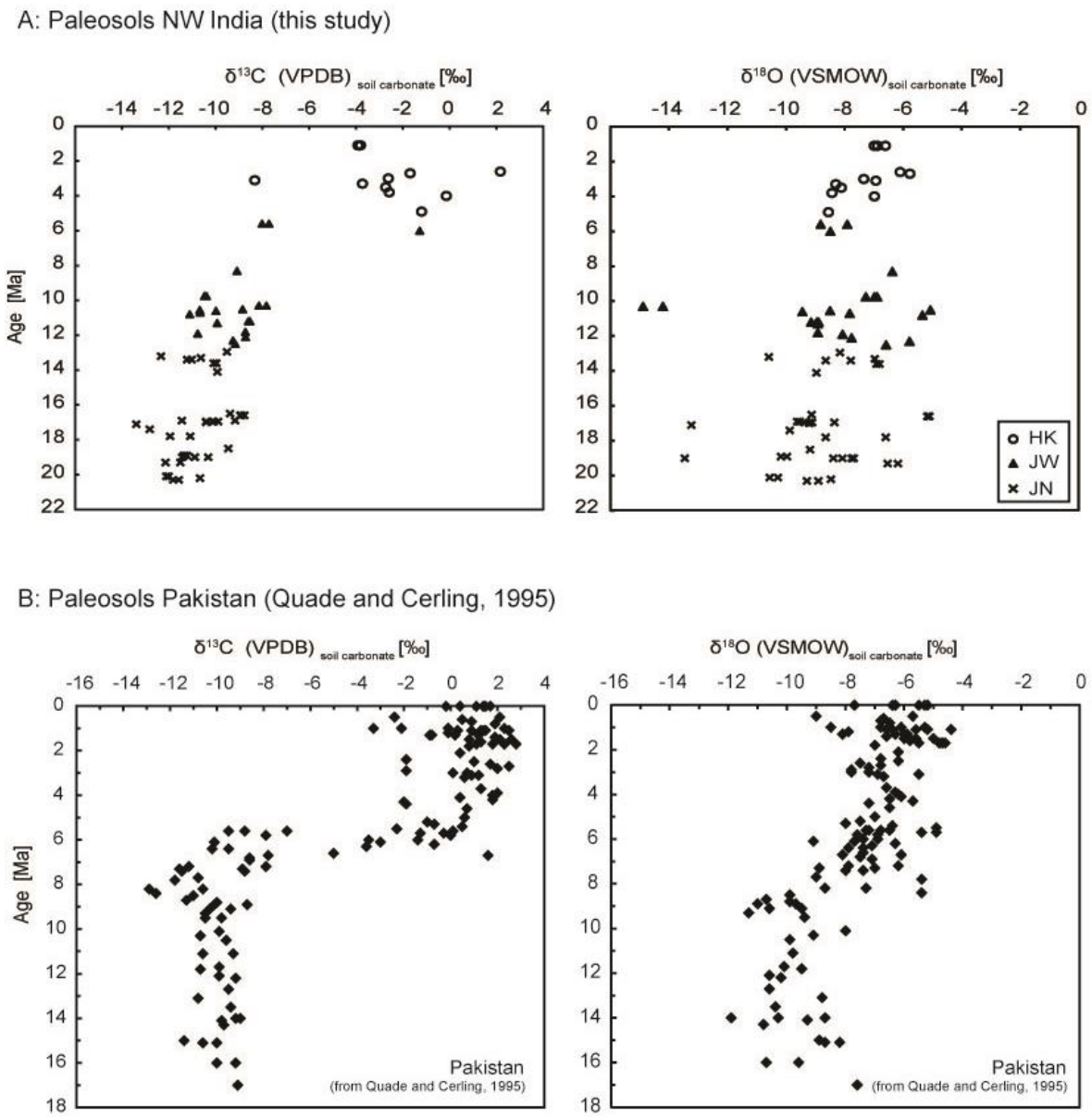

***Fig. 3**: A: $\delta^{13}C_{soil\ carb.}$ and $\delta^{18}O$ values of soil carbonate in the western Himalaya. Different symbols indicate the different sections (HK: Haripur Kolar; JW: Jawalamukhi; JN: Joginder Nagar). B: $\delta^{13}C_{soil\ carb.}$ and $\delta^{18}O$ values of soil carbonate in Pakistan from Quade and Cerling (1995).*

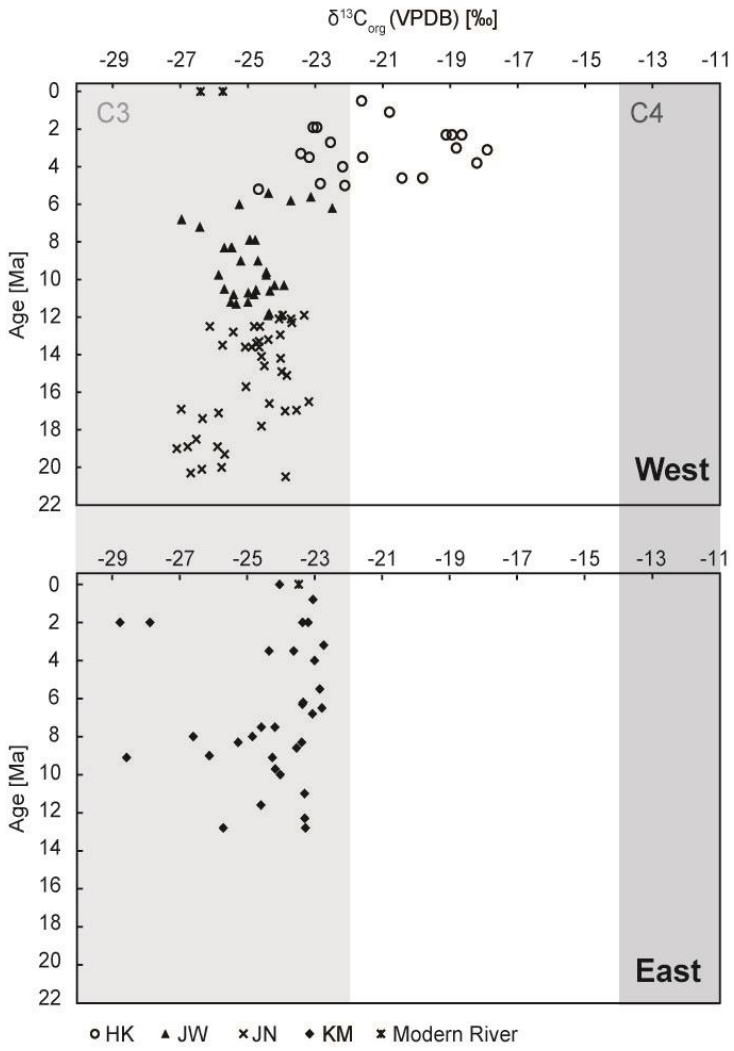

***Fig. 4**: $\delta^{13}C_{org}$ of bulk organic carbon in the western (HK: Haripur Kolar; JW: Jawalamukhi; JN Joginder Nagar) and the eastern (KM: Kameng) Himalayan sections. Light and dark grey shaded bars indicate $\delta^{13}C_{org}$ values characteristic of C3 and C4 plants, respectively (Cerling et al., 1997).*

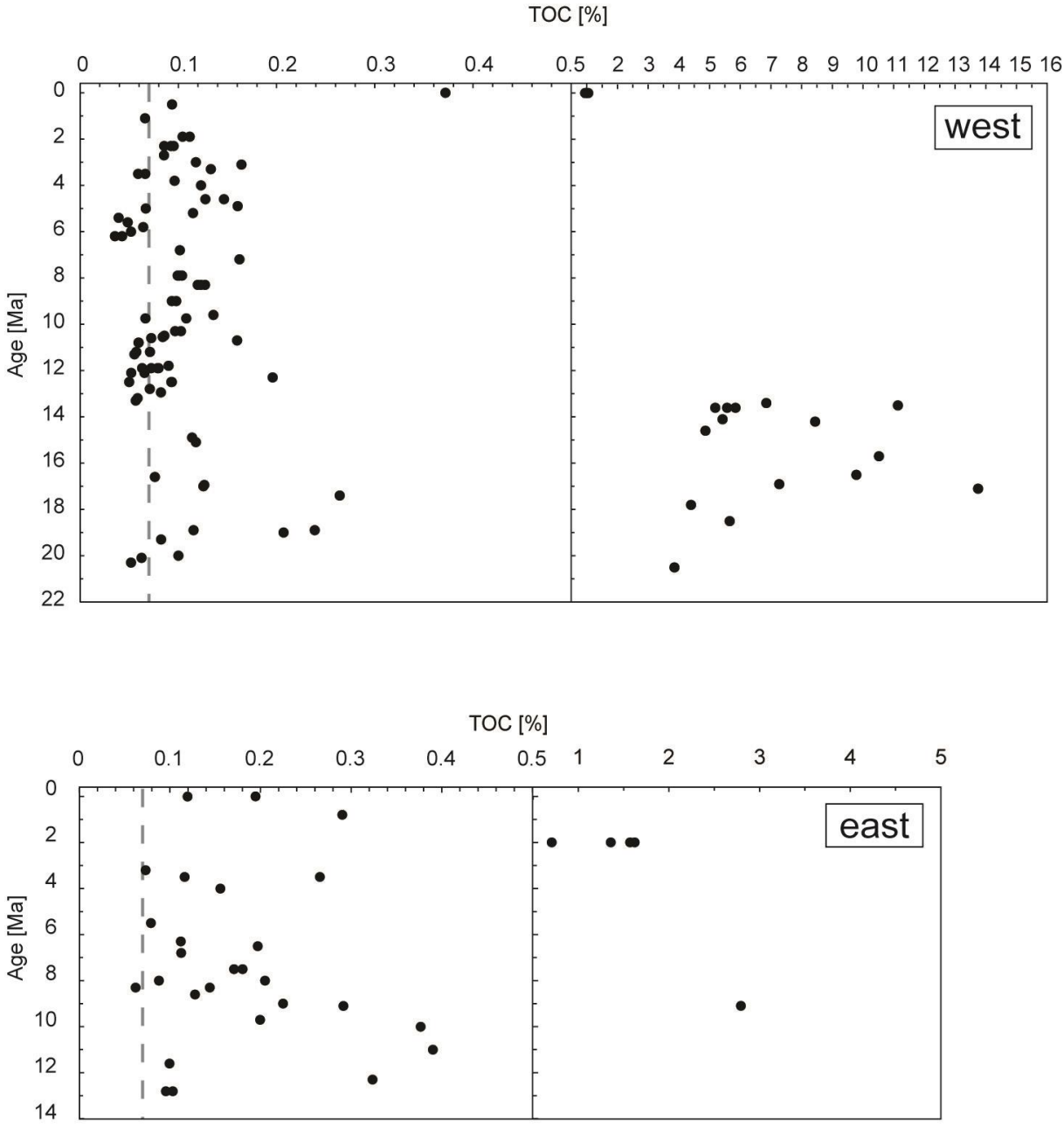

***Fig. 5**: Total organic carbon content (TOC) vs age [Ma], zoomed in to values below 0.5 % on the left and values above 0.5 % on the right. TOC values above 0.07% indicate dominant biogenic C_{org}, from soil organic matter and floodplain vegetation, rather than detrital and fossil C_{org} (Galy et al., 2008a).*

5. DISCUSSION

5.1. Modern river sediments and vegetation

The modern Ganga/Brahmaputra floodplain is widely used for agriculture and is therefore predominantly covered in C3 plants such as rice crops, and in the east by tea plantations (Blasco et al., 1996). This is not reflected by the organic carbon transported in the Ganga and Brahmaputra Rivers: $\delta^{13}C_{org}$ values of ~-21.9 ‰ in the modern Ganga floodplain are representative of a mixture of C4 and C3 plants, suggesting the presence of C4 plants in the west, whereas the modern Brahmaputra River carries organic carbon with $\delta^{13}C_{org}$ values of -23.0 ‰ in the range of C3 plants (Galy et al., 2008b).

Measured $\delta^{13}C_{org}$ values of modern river muds in both the west (Beas and Jner Khad River) and the east (Kameng River) are in the range of C3 plants. However, these modern river sediments were not collected in the floodplain but at the mountain front, where they will contain detrital organic carbon of C3 plants transported from higher elevations (Dobremez, 1978) and/or fossil organic carbon from Himalayan formations (Galy et al., 2008b), which both have a more negative isotopic signal. Dharamsala and Siwalik sediments were deposited further into the floodplain, and hence should carry a signal of floodplain vegetation.

5.2. Possible factors influencing the isotopic signal

Earlier studies (Quade et al., 1995a; Quade and Cerling, 1995; Sanyal et al., 2010; Singh et al., 2007) measured $\delta^{13}C$ on soil carbonate nodules, which can only be found in the western and central Himalayan Siwalik sections, and have consistently shown a change towards more positive values at ~7 Ma from Pakistan to Nepal (Quade et al., 1995a; Quade and Cerling, 1995). This change was interpreted in terms of a shift in vegetation, from initially dominated by C3 plants to containing C4 species. In order to compare the western and the eastern Himalaya in this study, we rely on $\delta^{13}C_{org}$ of bulk organic matter, as soil carbonate nodules are absent in the east. In both the western and the eastern sections, $\delta^{13}C_{org}$ values range between -23 ‰ and -29 ‰ before 7 Ma, indicating vegetation dominated by C3 plants. After 7 Ma, $\delta^{13}C_{org}$ in the western sections demonstrates an isotopic shift to values enriched in ^{13}C (~-19 ‰), suggesting that a component of the organic matter comprises C4 species. Carbonate nodules from western Himalayan sections analysed in this study show a trend similar to $\delta^{13}C_{org}$, demonstrating a shift from C3-dominated vegetation composition, to an increasing proportion of C4 species in the younger sections. In the east, in contrast, $\delta^{13}C_{org}$ values stay in the range of C3 plants throughout the sedimentary succession (Fig. 4).

In modern soils, carbonate precipitates in equilibrium with soil CO_2 (Cerling et al., 1989) following an isotopic enrichment in ^{13}C of 10.36 ‰, (Cerling et al., 1989). Diffusional effects cause soil-respired CO_2 to be further enriched in ^{13}C by 4.4 ‰. The total fractionation between soil organic matter and soil carbonate is ~14 ‰, at 25°C to ~17 ‰ at 0°C (Cerling et al., 1989). $\delta^{13}C_{soil\ carb.}$ values show a greater (~+10‰) shift towards more positive values after 7 Ma than the $\delta^{13}C_{org}$ values (~+ 6 ‰; Fig. 6). This discrepancy in the absolute value of the isotopic shift to signatures more enriched in ^{13}C likely reflects the nature of carbonate nodule production and organic matter source. Whereas soil carbonates reflect only the soil CO_2 characteristics and temperature during formation, the $\delta^{13}C_{org}$ values are more susceptible to bias by inherited and transported material.

Although $\delta^{13}C_{org}$ is usually interpreted to represent isotopic values of vegetation in the floodplain at the time of sediment deposition, it can potentially be biased by several factors, such as input of (likely C3 plant dominated) organic carbon from high elevations (Dobremez, 1978) and/or input of fossil organic carbon. The amount of fossil organic carbon present in Himalayan river sediments was estimated using the radiocarbon content of total organic carbon (TOC) of modern suspended and bedload sediments (Galy et al., 2008a; 2008b). Galy et al. (2008a) estimated the total amount of fossil organic carbon transported in the Ganga and Brahmaputra Rivers between 0.02 and 0.03 %. Sediments of the sampled sections mostly have TOC values >0.1 % (Fig. 5) suggesting that the proportion of fossil carbon should be low, <30 % at most, if the modern amounts of transported fossil organic carbon can be extrapolated to the past. $\delta^{13}C_{org}$ of fossil organic carbon from Himalayan source rocks varies from -28 to -14.6‰ (Galy et al., 2008b); it is therefore unclear what the effect of varying proportions of fossil organic carbon on the observed $\delta^{13}C_{org}$ signal would be. However, we have no reason to assume the influence of fossil carbon to be very different from east to west and our data suggest this influence to be rather constant over time (see below). It is therefore unlikely that the spatial and temporal variations in $\delta^{13}C_{org}$ values could be explained by variable fossil organic carbon content.

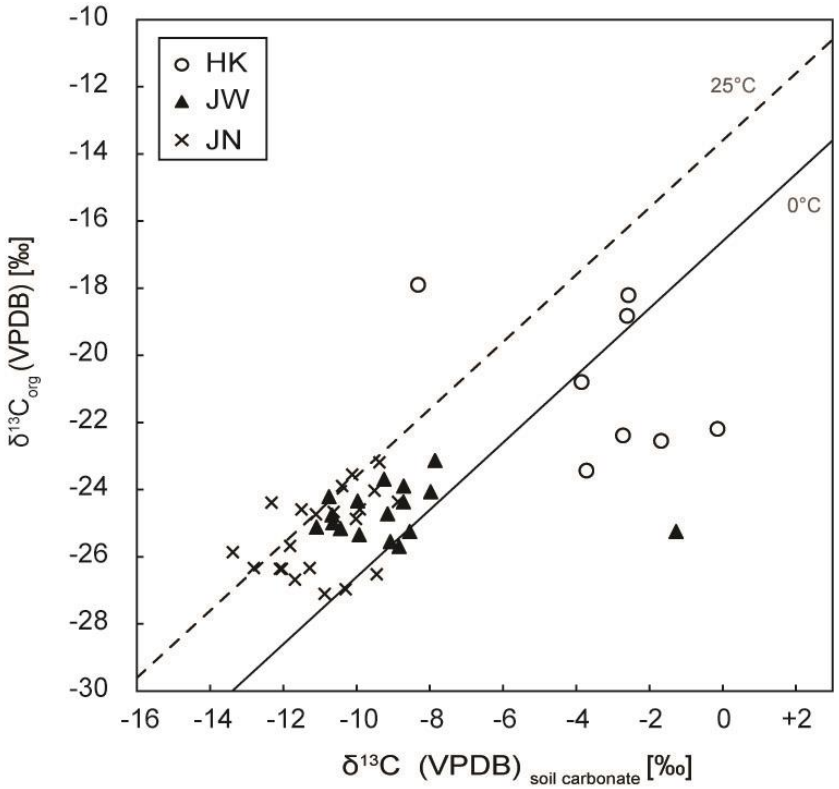

***Fig. 6**: $\delta^{13}C_{soil\ carb.}$ of soil carbonate nodules vs. $\delta^{13}C_{org}$ of co-existing organic matter of the western Dharamsala and Siwalik Group sections. Solid and dashed lines represent isotopic values of pedogenic carbonate in isotopic equilibrium with the soil CO_2 derived from irreversible oxidation of organic matter in a diffusion controlled soil system at different temperatures (Cerling et al., 1989).*

Additionally, the efficiency of oxidation of organic carbon and hence the replacement of inherited carbon by floodplain carbon can influence the $\delta^{13}C_{org}$ signal in modern river sediments (Galy et al., 2008b; 2011). Organic-carbon oxidation varies between the Ganges and Brahmaputra foreland basin, being more efficient in the Ganges floodplain due to different hydrological settings: the Ganges is a meandering river, whereas the Brahmaputra is a braided river with a narrower floodplain (Galy et al., 2008b). Oxidation of inherited organic carbon from vegetation at higher altitudes, hence with a C3 signal, is efficient in the Ganges floodplain (Galy et al., 2008b), as shown by the proportion of C4 organic matter increasing downstream in the Ganges floodplain (Fig. 1). This pattern is not present in the Brahmaputra floodplain, suggesting that the influence of inherited carbon could therefore be greater in the Brahmaputra. Even though paleosols are less developed in the east, high TOC values indicate the presence of organic matter acquired from surface organic litter during pedogenesis (Fig. 5). Degradation of organic matter in soils could have an influence on the $\delta^{13}C_{org}$: detrital organic matter has a ~1-2 ‰ more negative $\delta^{13}C$ signal than soil organic matter (von Fischer and Tieszen, 1995 and references therein). The more negative $\delta^{13}C$ values in the Kameng section

could therefore be explained by the presence of more detrital organic matter. Differences in floodplain dynamics during transport and a greater influence of inherited organic carbon could possibly bias the signal but are unlikely to cancel out the entire C4 signal in the eastern Himalaya.

Further information on different organic carbon sources could potentially be derived from lipid biomarker analysis (i.e. compound-specific C- and H-isotope analysis; Freeman and Colarusso, 2001; Sachse et al., 2012). We extracted n-alkanes from samples of both the western and the eastern sections (see Supplementary Material 3), but unfortunately n-alkane preservation was generally low in the sediments. Moreover, evidence of diagenetic overprinting was found in sediments with a sufficient concentration, evidenced by an absence of the predominance of odd carbon numbered n-alkane chain lengths (expressed as the carbon preference index, CPI), which is prevalent in modern plant and sediment samples. In modern plant material and immature sediments, CPI values are generally significantly >3 and up to 20, whereas we found values around 1 in the Kameng samples, indicating diagenetic overprinting or addition of fossil carbon at the time of sedimentation. As a result of this, compound-specific hydrogen and carbon stable isotopic values would likely have been altered towards less negative values (Radke et al., 2005). While diagenetic overprinting could also have affected bulk $\delta^{13}C_{org}$ values by homogenizing the isotopic signal (Bera et al., 2010; Cerling, 1984), our CPI data remained uniform at values around 1 from the base of the section until ~2 Ma, indicating a similar degree of overprinting in these samples. Since we did not find any change in bulk $\delta^{13}C_{org}$ values corresponding to changes in CPI values, we argue that any potential overprinting affected all samples equally and as such relative changes can still be interpreted from bulk $\delta^{13}C_{org}$ values. In addition, the samples presented in Fig. 3 are in the same isotopic range as modern soil carbonate nodules, indicating that diagenesis is unlikely to have influenced the isotopic values of the sedimentary samples.

The isotopic values of pedogenic carbonate are in equilibrium with soil CO_2 derived from irreversible oxidation of organic matter in a diffusion-controlled soil system at different temperatures. The isotopic equilibrium factor is dependent on temperature, hence if pedogenic carbonate precipitates in equilibrium with soil CO_2, $\delta^{13}C_{soil\ carb}$ should be enriched by ~14 ‰ at 25 °C and by 17 ‰ at 0 °C, respectively (Cerling, 1984; Cerling et al., 1989). Carbonate nodules and their corresponding organic matter of the Dharamsala and Siwalik paleosols plot mostly at temperatures between 0 and 25°C and are therefore not isotopically altered by diagenesis (Fig. 6), but rather formed within this soil temperature range. Samples below the 0°C line could reflect an inconsistency in the enrichment of ^{13}C in soil carbonate nodules compared to the co-existing organic matter. Most of the samples

plotting under the 0°C line show a strong C4 signal, and the offset between $\delta^{13}C_{org}$ and $\delta^{13}C_{soil\ carb.}$ in these samples is greater than expected from isotopic equilibrium considerations. A possible explanation for this enhanced offset could be that the carbonate nodule formed in a sediment body (e.g. another paleosol horizon) that was separate from the parent organic matter. Alternatively, organic matter may be more influenced by inherited organic matter from C3 vegetation, whereas the $\delta^{13}C_{soil\ carb}$ would more directly represent the local vegetation cover. However, this inconsistency does not reflect a diagenetic overprint, as it is found in the youngest samples, where diagenesis is least likely to occur.

$\delta^{18}O_{soil\ carb}$. values of the three western sections show a slight change towards more positive values (Fig. 3), comparable to $\delta^{18}O$ values of the Surai Khola section in Nepal (Quade et al., 1995a). Only $\delta^{18}O_{soil\ carb.}$ values from Pakistan show a clear shift from values <-8 towards more positive values at ~8-6 Ma (Quade and Cerling, 1995). In contrast, samples from this study already show $\delta^{18}O_{soil\ carb.}$ values >-8 before 7 Ma (Fig. 3). A change in $\delta^{18}O_{soil\ carb.}$, which forms in-situ from soil water, can be associated with a change in either soil temperature ($\delta^{18}O_{soil\ carb.}$ being positively correlated with mean annual temperature; Cerling, 1984) and/or precipitation source: $\delta^{18}O$ values of precipitation of moisture transported from the Bay of Bengal are generally lighter (more negative) than $\delta^{18}O$ values of moisture transported by the Westerlies (Caves et al., 2015 and references therein). The isotopic change over time was measured on samples of three separate sections (Fig. 2) at different longitudinal locations; therefore the isotopic signature from precipitation may be location specific rather than representing change over time. However, there is no clear shift in $\delta^{18}O_{soil\ carb.}$ values going from one section to another (Fig. 3), suggesting this effect to be minimal. As all sediments were deposited in the foreland, the influences of any altitudinal effects (Dansgaard, 1961) can also be excluded.

The coarsening-upward trend of sedimentary rocks throughout the sections reflects a change in depositional environment and location in the foreland basin, which varies from a distal floodplain for the Dharamsala and Lower Siwaliks to deposition closer to the mountain front in the Upper Siwaliks. At different locations in the foreland basin, the source of precipitation may vary from moisture influenced by the Westerlies, to moisture sourced from the ISM. More positive $\delta^{18}O_{soil\ carb.}$ values over time could therefore indicate an increasing influence of Westerlies with respect to ISM moisture sources, and/or a trend towards a warmer, drier climate, conducive to the growth of C4 vegetation.

5.3. What caused the change of vegetation at ~7 Ma?

C3 and C4 plants grow in different environments and the $\delta^{13}C$ signal can therefore be used as an indirect climate indicator. Our data show that a change in vegetation occurred at ~7 Ma in the western Himalaya, but not in the east, where C3 plants have been dominant since the middle Miocene. As we have argued above, differences in floodplain setting (Galy et al., 2008b; 2011), while influencing the signal, cannot explain the observed lateral difference and neither can input of fossil organic carbon (Galy et al., 2008a). For this reason, there must be a remarkable lateral variation in the evolution of climate in the Himalayan region. The change at 7 Ma in the west and central Himalaya has been interpreted as resulting from a "stronger monsoon", characterized by greater seasonality (Quade and Cerling, 1995; Quade et al., 1989; 1995a). However, increased seasonality does not necessarily reflect higher amounts of monsoon precipitation; it could also indicate relatively less winter precipitation and thus a more arid (annual-average) climate (Molnar, 2005). C3 plants in the east indicate lower seasonality and higher annually averaged precipitation, consistent with modern precipitation patterns (Bookhagen and Burbank, 2010). The expansion of C4 plants in the west could therefore be a consequence of decreased winter precipitation, hence more seasonality associated with less (annually averaged) humidity, leading to a more arid climate. Overall, this difference in the $\delta^{13}C$ composition post-7 Ma is proposed to reflect water availability, with lower water availability in the west initiating a decline in C3 plants and a rise in C4 species (see Freeman and Colarusso, 2001). Dettman et al. (2001) likewise suggest a change in Indian summer monsoon characteristics and drying of the climate at 7.5 Ma. This scenario is supported by a change in $\delta^{18}O_{soil\ carb.}$ towards more positive values.

Higher humidity in the east could be explained by the proximity to the Bay of Bengal, which is the major moisture source of precipitation in this area (Bookhagen et al., 2005a). The western Himalaya is influenced by the Westerlies (Kotlia et al., 2015), which bring in winter precipitation. A decrease in the intensity of the Westerlies at 7 Ma would lead to more seasonality in the western floodplain, with drier periods in winter. An alternative explanation for a generally more arid climate in the western Himalaya could be a decrease of moisture transport from the Bay of Bengal and the Arabian Sea, possibly linked to a decrease in the intensity of the ISM. However, this would result in less seasonality, hence a less favourable climate for C4 plants. The spatially variable record of $\delta^{13}C_{org}$ values strongly suggests that the change in vegetation at 7 Ma did not occur simultaneously along the Himalayan foreland, indicating that the change is at least partly driven by regional factors rather than being linked only to a global change in atmospheric pCO_2. This supports the findings of Pagani et al. (2005) and Beerling and Royer (2011), who noted that atmospheric pCO_2 levels favouring C4

plants were already reached during the Oligocene. Other dry regions such as the Mediterranean have been dominated by C3 plants since the Miocene (Quade et al., 1995b; Quade et al., 1994), also indicating that the late-Miocene expansion of C4 plants was not a global phenomenon. Regionally dependent factors, such as differences in seasonality or humidity, have clearly played a role in determining Himalayan vegetation patterns through time. Lateral variations in vegetation suggest that there is a threshold somewhere along the Himalayan front, where the amount of (either annual or winter) precipitation becomes too large for C4 plants to spread.

6. CONCLUSIONS

Stable carbon and oxygen isotopes were analysed in carbonate nodules of the Joginder Nagar, Jawalamukhi and Haripur Kolar sections in the western Himalaya. $\delta^{13}C_{soilcarb.}$ values show a clear shift towards more positive values at 7 Ma, similar to the results of earlier studies in the western and central Himalaya. The lack of carbonate nodules in Siwalik sediments of the Kameng section, eastern Himalaya, is a first indicator that the lateral environmental and climatic differences in the modern Himalaya are representative of long-term climatic patterns. In order to directly compare the western and eastern sections, stable carbon isotopes on organic matter were analysed and show a clear spatial difference. In the west, $\delta^{13}C_{org}$ values shift towards more positive values at 7 Ma, consistent with the results on carbonate nodules, whereas they remain constant over the last 13 Ma in the east. The $\delta^{13}C$ of organic matter reflects the evolution of vegetation, with the development of C4 plants in the west and an environment that remains favourable for C3 plants in the east. Such variations in vegetation imply differences in climate, which became more seasonal and overall drier in the west at 7 Ma. The eastern Himalaya is more proximal to the main moisture source for precipitation (the Bay of Bengal); therefore, even though climate may have varied, it remained less seasonal and more humid, inhibiting the evolution of C4 plants. Therefore, the change in climate in the west and the onset of lateral variation is most likely caused by a change in strength of atmospheric circulation, such as a weakening of the influence of the Westerlies. These findings suggest that the late-Miocene expansion of C4 vegetation does not depend solely on atmospheric pCO_2 but also on regional changes in aridity and seasonality. Newly developed methods, such as clumped isotopes or stable isotopes on compound-specific organic carbon, even though unsuccessful in this study, could provide further insight into the climatic evolution and the development of C4 vegetation, both globally and regionally in the Himalayan region. This study has provided the first paleo-climate and -vegetation data from the eastern Himalaya; however, more such studies are needed to refine our understanding of the evolution of climate and vegetation in this area.

ACKNOWLEDGEMENTS

Montserrat Auladell-Mestre and David Hughes are thanked for the help preparing and measuring the samples. We acknowledge financial support from Initial Training Network (ITN) iTECC funded by the EU REA under the FP7 implementation of the Marie Curie Action, under grant agreement # 316966. ISTerre is part of the Labex OSUG@2020 (ANR10 LABX56). Reviews of earlier versions of this manuscript by Greg Retallack, Seema Sing and 3 anonymous reviewers have helped to significantly improve its clarity and focus.

SUPPLEMENTARY MATERIAL

Supplementary Material 1:

Sample overview and results of $\delta^{13}C_{org}$, $\delta^{13}C_{soil\ carb.}$ and $\delta^{18}O_{soil\ carb.}$ are presented in the data table of Appendix VI in the electronic document attached to the thesis.

Supplementary Material 2:

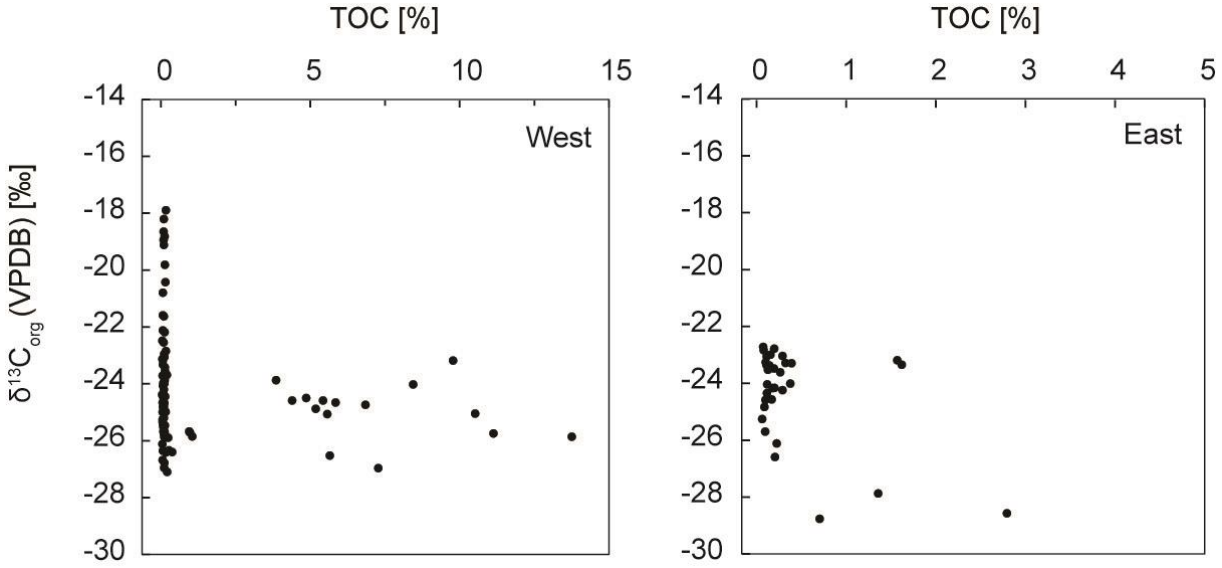

Figure: *Total organic carbon (TOC) vs. $\delta^{13}C_{org}$ in the western (a) and eastern (b) sections, respectively.*

Supplementary Material 3: n-alkane analysis on the Kameng river section

Supplementary Material 3: n-alkane analysis on the Kameng river section

Method

Sediments were freeze-dried, after which a Total Lipid Extract (TLE) was extracted using a Dionex ASE 350 Accelerated Solvent Extractor, with a solvent mixture of 9:1 Dichloromethane (DCM): Methanol (MeOH). Samples were separated using silica columns, rinsing them with 12 mL hexane to obtain the *n*-alkane fraction, and 12 mL of 9:1 DCM:MeOH to obtain the polar fraction containing fatty acids.

The n-alkane fraction of 27 samples were quantified using an Agilent GC MSD (Agilent 5975C MSD, Agilent 7890A GC with Agilent J&W HP-5ms column, 30 m x 0.25 mm x 0.25 µm film) connected to a Flame Ionization Detector (FID). All analyses were conducted at the organic geochemistry laboratory of the Institut für Erd- und Umweltwissenschaften at the University of Potsdam.

The Carbon Preference Index (CPI) and Average Chain Length (ACL) were calculated as follows.

$$\text{CPI}=\frac{\sum odd(C21-33)+\sum odd(c23-25)]}{2\sum even(c22-34)} \qquad \text{ACL}=\frac{\sum(Cn\times n)}{\sum(Cn)}$$

In sediments CPI is used as an indicator of thermal maturity of the rocks and as a source indicator, and ACL indicates different biological source of n-alkanes (Eglinton and Hamilton, 1967).

Results

Overall, very few *n*-alkanes were found in the sediments, and in particular long chain *n*-alkanes (>C_{25}) were scarce. CPI values varied between 0.6 and 5.8, and only 8 samples were found to have a CPI >1 (Figure 1). The total concentration of alkanes in the samples varied between 1 µg/g sediment – 2.7 µg/g sediment. Ultimately, as little as 3 samples would have been suitable for carbon and isotope analysis on long chain *n*-alkanes, which is too few for any substantiated data analysis.

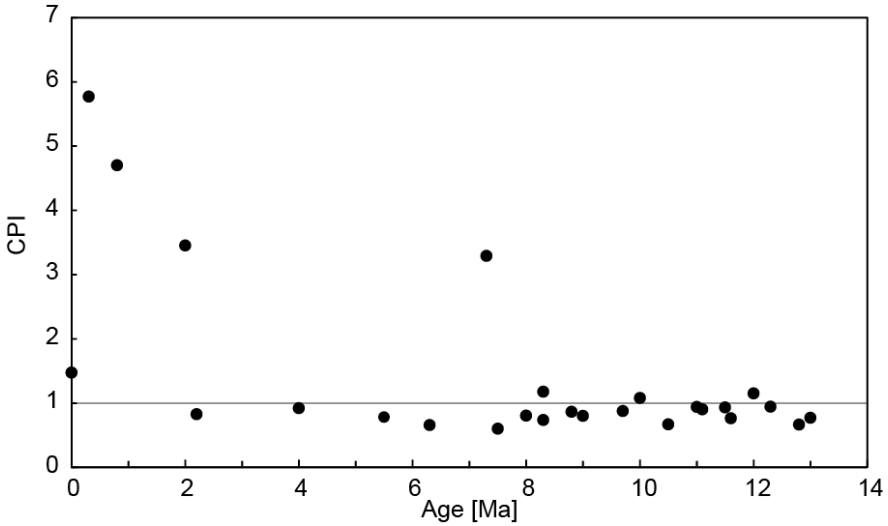

Figure 1: Carbon Preference Index (CPI). CPI >1 shows an odd over even numbered chain length preference; indicating original leaf waxes.

APPENDIX VII: Detrital rutile U-Pb dating from the Dungsam Chu section

G. Govin acquired rutile U-Pb data from the sample SJ8 of the Dungsam Chu section (see chapter 2 for location), under the instruction of I. Millar. This appendix describes the method used and the results; the latter are presented in detail in the table corresponding to this appendix.

Sample preparation

Prior to analysis, the sample was dried, sieved (fraction <500 µm) and washed with tap water at Lancaster University. Heavy minerals were extracted by wet separation on a Haultain superpanner, standard di-iodomethane heavy liquid (density of 3.3), and magnetic separation, which was kept to a minimum to avoid biasing mineral populations, at the NERC Isotope Geosciences Laboratory, Keyworth, UK (NIGL). Rutile grains were hand-picked, taking special care to select all grain types with respect to morphology, colour and grain size, within a particular fraction of the separate.

Rutile U-Pb dating

The rutiles were mounted in epoxy, polished, and photographed to help identify the analysed grains. U-Pb rutile dating was performed using a Nu Instruments AttoM single-collector inductively coupled plasma mass spectrometer (SC-ICP-MS) at NIGL. The instrument was tuned to ensure that ThO and UO were less than 0.4%. The Nu Attom SC-ICP-MS was used in peak-jumping mode with measurement on a MassCom secondary electron multiplier. The analysed masses in each sweep were: ^{202}Hg, ^{204}Pb+Hg, ^{206}Pb, ^{207}Pb, and ^{235}U. Each data integration records 100 sweeps of the measured masses, which roughly equates to 0.22 seconds. Dwell times on each mass are 400 µs on ^{207}Pb and ^{235}U, and 200 µs on all other masses; the switching between masses takes 40 µs. ^{238}U is calculated using ^{238}U/^{235}U = 137.818.

Laser ablation was performed using a New Wave Research UP193SS laser ablation system, with a low-volume cell (Horstwood et al., 2003). This cell has a washout to less than 1% of the peak signal in less than one second. Ablation parameters were optimized to suit the Pb and U contents with a frequency of 5Hz, a fluence of 1.5 to 3.0 J/cm^2, a 30 second ablation time, and a 30 to 35 µm spot size.

Four rutile reference materials, Sugluk-4, PCA-S207 (Bracciali et al., 2013) and R10 (Luvizotto et al., 2009) were analysed at regular intervals in order to correct data for instrumental fractionation. The average bias of the ^{207}Pb/^{206}Pb and ^{206}Pb/^{238}U ratios from preferred values derived by TIMS analysis are used for normalization. ^{206}Pb/^{238}U and ^{207}Pb/^{206}Pb uncertainties were propagated in the manner advocated by Horstwood (2008), utilising the measurement uncertainty and the reproducibility of the ablation reference material used.

Rutile commonly incorporates a significant amount of common Pb during crystallisation, and as a result is typically discordant in the U-Pb isotope system. Following the approach of Chew et al. (2011), a ^{207}Pb-based correction was employed, using an iterative approach to obtain a ^{207}Pb/^{206}Pb intercept value based on a starting estimate generated from the terrestrial Pb evolution model of Stacey and Kramers (1975). This was used to calculate rutile ^{207}Pb-corrected ^{206}Pb/ ^{238}Uages.

Data reduction of rutile measurements was undertaken with the age filters summarised in the following screening procedure table.

Table: U-Pb rutile data screening procedure

1	Failed	Discarded
2	^{207}Pb-corr. age >100 Ma, uncertainty >10 %	Discarded
3	^{207}Pb-corr. age 10-100 Ma, uncertainty >20 %	Discarded
4	^{207}Pb-corr. age <10 Ma, uncertainty >25 %	Discarded
5	All other ages	Accepted

The analytical results are presented in the data table of Appendix VII in the electronic document attached to the thesis, and the accepted ages are plotted in the figure below.

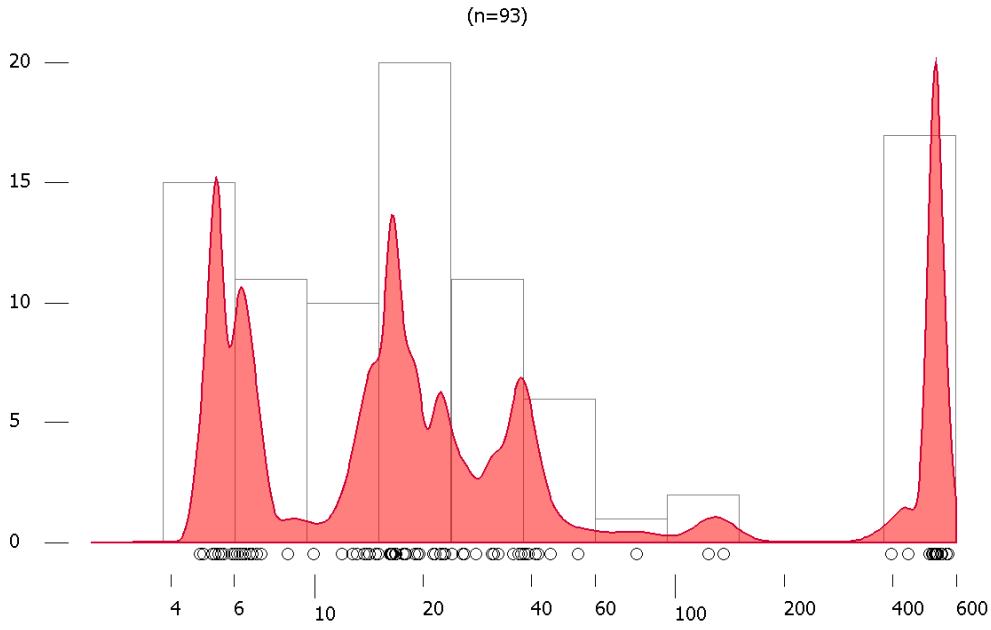

Figure: *Detrital rutile U-Pb ages for the sample SJ8 from the Dungsam Chu section, plotted as adaptive Kernel density plots (Vermeesch, 2012) with overlying histograms; n=number of dated grains.*

REFERENCES

Abbasi, I., and Friend, P., 2000, Exotic conglomerates of the Neogene Siwalik succession and their implications for the tectonic and topographic evolution of the Western Himalaya: Geological Society, London, Special Publications, v. 170, no. 1, p. 455-466.

Abrahami, R., 2015, Erosion et flux sédimentaires associés dans un bassin versant soumis à un régime de mousson : l'exemple de la Tista (Inde), du Sikkim au Mégafan: Université de Grenoble.

Abrahami, R., Huyghe, P., van der Beek, P., Lowick, S., Carcaillet, J., and Chakraborty, T., in review, Formation and abandonment of the Tista megafan (West Bengal, India): 10Be cosmogenic and IRSL age constraints: Quaternary Science Reviews.

Achache, J., Courtillot, V., and Xiu, Z. Y., 1984, Paleogeographic and tectonic evolution of southern Tibet since middle Cretaceous time: New paleomagnetic data and synthesis: Journal of Geophysical Research: Solid Earth, v. 89, no. B12, p. 10311-10339.

Adams, B., Hodges, K., Whipple, K., Ehlers, T., Soest, M., and Wartho, J., 2015, Constraints on the tectonic and landscape evolution of the Bhutan Himalaya from thermochronometry: Tectonics, v. 34, no. 6, p. 1329-1347.

Adlakha, V., Lang, K. A., Patel, R., Lal, N., and Huntington, K. W., 2013, Rapid long-term erosion in the rain shadow of the Shillong Plateau, Eastern Himalaya: Tectonophysics, v. 582, p. 76-83.

Alam, M., Alam, M. M., Curray, J. R., Chowdhury, M. L. R., and Gani, M. R., 2003, An overview of the sedimentary geology of the Bengal Basin in relation to the regional tectonic framework and basin-fill history: Sedimentary Geology, v. 155, no. 3, p. 179-208.

Allegre, C. J., Courtillot, V., Tapponnier, P., Hirn, A., Mattauer, M., Coulon, C., Jaeger, J. J., Achache, J., Scharer, U., Marcoux, J., Burg, J. P., Girardeau, J., Armijo, R., Gariepy, C., Gopel, C., Li, T. D., Xiao, X. C., Chang, C. F., Li, G. Q., Lin, B. Y., Teng, J. W., Wang, N. W., Chen, G. M., Han, T. L., Wang, X. B., Den, W. M., Sheng, H. B., Cao, Y. G., Zhou, J., Qiu, H. R., Bao, P. S., Wang, S. C., Wang, B. X., Zhou, Y. X., and Ronghua, X., 1984, Structure and Evolution of the Himalaya-Tibet Orogenic Belt: Nature, v. 307, no. 5946, p. 17-22.

Armstrong, P. A., 2005, Thermochronometers in sedimentary basins: Reviews in Mineralogy and Geochemistry, v. 58, no. 1, p. 499-525.

ASTM, 2010, D2798-09a: Standard test method for microscopical determination of the vitrinite reflectance of coal, Annual Book of American Society for Testing and Materials-ASTM Standards: Petroleum Products, Lubricants, and Fossil Fuels; Gaseous Fuels; Coal and Coke, edited: West Conshohocken, Pa, ASTM Int., p. 406–410.

Auclair, M., Lamothe, M., and Huot, S., 2003, Measurement of anomalous fading for feldspar IRSL using SAR: Radiation measurements, v. 37, no. 4, p. 487-492.

Auden, J., 1935, Traverses in the Himalaya: Rec. Geol. Surv. India, v. 69, no. 2, p. 123-167.

Avouac, J.-P., 2003, Mountain building, erosion, and the seismic cycle in the Nepal Himalaya: Advances in geophysics, v. 46, p. 1-80.

Avouac, J.-P., and Burov, E., 1996, Erosion as a driving mechanism of intracontinental mountain growth: Journal of Geophysical Research: Solid Earth, v. 101, no. B8, p. 17747-17769.

Barberà, X., Cabrera, L., Marzo, M., Parés, J., and Agustı, J., 2001, A complete terrestrial Oligocene magnetobiostratigraphy from the Ebro Basin, Spain: Earth and Planetary Science Letters, v. 187, no. 1, p. 1-16.

Barfod, G. H., Krogstad, E. J., Frei, R., and Albarède, F., 2005, Lu-Hf and PbSL geochronology of apatites from Proterozoic terranes: A first look at Lu-Hf isotopic closure in metamorphic apatite: Geochimica et Cosmochimica Acta, v. 69, no. 7, p. 1847-1859.

Barker, C. E., and Pawlewicz, M. J., 1994, Calculation of vitrinite reflectance from thermal histories and peak temperatures-A comparison of methods: Vitrinite reflectance as a maturity parameter, v. 570, p. 216-229.

Beaumont, C., Fullsack, P., and Hamilton, J., 1992, Erosional control of active compressional orogens, *in* McClay, K. R., ed., Thrust tectonics: London, Chapman & Hal, p. 1-18.

Beaumont, C., Jamieson, R. A., Nguyen, M., and Lee, B., 2001, Himalayan tectonics explained by extrusion of a low-viscosity crustal channel coupled to focused surface denudation: Nature, v. 414, no. 6865, p. 738-742.

Beaumont, C., Kooi, H., and Willett, S., 2000, Coupled tectonic-surface process models with applications to rifted margins and collisional orogens: Geomorphology and global tectonics, p. 29-55.

Beerling, D. J., and Royer, D. L., 2011, Convergent cenozoic CO2 history: Nature Geoscience, v. 4, no. 7, p. 418-420.

Behrensmeyer, A. K., Quade, J., Cerling, T. E., Kappelman, J., Khan, I. A., Copeland, P., Roe, L., Hicks, J., Stubblefield, P., and Willis, B. J., 2007, The structure and rate of late Miocene expansion of C4 plants: Evidence from lateral variation in stable isotopes in paleosols of the Siwalik Group, northern Pakistan: Geological Society of America Bulletin, v. 119, no. 11-12, p. 1486-1505.

Bendick, R., and Bilham, R., 2001, How perfect is the Himalayan arc?: Geology, v. 29, no. 9, p. 791-794.

Bendick, R., and Ehlers, T. A., 2014, Extreme localized exhumation at syntaxes initiated by subduction geometry: Geophysical Research Letters, v. 41, no. 16, p. 5861-5867.

Benn, D., and Owen, L., 1998, The role of the Indian summer monsoon and the mid-latitude westerlies in Himalayan glaciation: review and speculative discussion: Journal of the Geological Society, v. 155, no. 2, p. 353-363.

Bera, M., Sarkar, A., Tandon, S., Samanta, A., and Sanyal, P., 2010, Does burial diagenesis reset pristine isotopic compositions in paleosol carbonates?: Earth and Planetary Science Letters, v. 300, no. 1, p. 85-100.

Berger, A., Jouanne, F., Hassani, R., and Mugnier, J. L., 2004, Modelling the spatial distribution of present-day deformation in Nepal: how cylindrical is the Main Himalayan Thrust in Nepal?: Geophysical Journal International, v. 156, no. 1, p. 94-114.

Bernet, M., 2009, A field-based estimate of the zircon fission-track closure temperature: Chemical Geology, v. 259, no. 3, p. 181-189.

Bernet, M., Brandon, M. T., Garver, J. I., and Molitor, B., 2004a, Downstream changes of Alpine zircon fission-track ages in the Rhône and Rhine Rivers: Journal of Sedimentary Research, v. 74, no. 1, p. 82-94.

Bernet, M., Brandon, M. T., Garver, J. I., and Molitor, B. R., 2004b, Fundamentals of detrital zircon fission-track analysis for provenance and exhumation studies with examples from the European Alps: Geological Society of America Special Papers, v. 378, p. 25-36.

Bernet, M., and Garver, J. I., 2005, Fission-track analysis of detrital zircon: Reviews in Mineralogy and Geochemistry, v. 58, no. 1, p. 205-237.

Bernet, M., van der Beek, P., Pik, R., Huyghe, P., Mugnier, J. L., Labrin, E., and Szulc, A., 2006, Miocene to Recent exhumation of the central Himalaya determined from combined detrital zircon fission-track and U/Pb analysis of Siwalik sediments, western Nepal: Basin Research, v. 18, no. 4, p. 393-412.

Besse, J., and Courtillot, V., 1988, Paleogeographic maps of the continents bordering the Indian Ocean since the Early Jurassic: Journal of Geophysical Research: Solid Earth, v. 93, no. B10, p. 11791-11808.

Besse, J., and Courtillot, V., 1991, Revised and synthetic apparent polar wander paths of the African, Eurasian, North American and Indian plates, and true polar wander since 200 Ma: Journal of Geophysical Research: Solid Earth, v. 96, no. B3, p. 4029-4050.

Bhandari, L., Fuloria, R., and Sastri, V., 1973, Stratigraphy of Assam Valley, India: AAPG Bulletin, v. 57, no. 4, p. 642-654.

Bhargava, O., 1995, The Bhutan Himalaya, a geological account, Geological Survey of India, v. 39.

Bhatia, S., and Bhargava, O., 2006, Biochronological continuity of the Paleogene sediments of the Himalayan Foreland Basin: paleontological and other evidences: Journal of Asian Earth Sciences, v. 26, no. 5, p. 477-487.

Bhattarai, K. R., Vetaas, O. R., and Grytnes, J. A., 2004, Fern species richness along a central Himalayan elevational gradient, Nepal: Journal of Biogeography, v. 31, no. 3, p. 389-400.

Bilham, R., and England, P., 2001, Plateau 'pop-up' in the great 1897 Assam earthquake: Nature, v. 410, no. 6830, p. 806-809.

Biswas, S., Coutand, I., Grujic, D., Hager, C., Stöckli, D., and Grasemann, B., 2007, Exhumation and uplift of the Shillong plateau and its influence on the eastern Himalayas: New constraints from apatite and zircon (U-Th-[Sm])/He and apatite fission track analyses: Tectonics, v. 26, no. 6.

Biswas, S., and Grasemann, B., 2005, Quantitative morphotectonics of the southern Shillong plateau (Bangladesh/India): Austrian Journal of Earth Sciences, v. 97, no. 82, p. e93.

Blair, M., Yukihara, E., and McKeever, S., 2005, Experiences with single-aliquot OSL procedures using coarse-grain feldspars: Radiation Measurements, v. 39, no. 4, p. 361-374.

Blasco, F., Bellan, M., and Aizpuru, M., 1996, A vegetation map of tropical continental Asia at scale 1: 5 million: Journal of Vegetation Science, v. 7, no. 5, p. 623-634.

Bonnet, S., and Crave, A., 2003, Landscape response to climate change: Insights from experimental modeling and implications for tectonic versus climatic uplift of topography: Geology, v. 31, no. 2, p. 123-126.

Bookhagen, B., and Burbank, D., 2010, Toward a complete Himalayan hydrological budget: Spatiotemporal distribution of snowmelt and rainfall and their impact on river discharge: J. Geophys. Res, v. 115, p. F03019.

Bookhagen, B., and Burbank, D. W., 2006, Topography, relief, and TRMM-derived rainfall variations along the Himalaya: Geophysical Research Letters, v. 33, no. 8.

Bookhagen, B., Thiede, R. C., and Strecker, M. R., 2005a, Abnormal monsoon years and their control on erosion and sediment flux in the high, arid northwest Himalaya: Earth and Planetary Science Letters, v. 231, no. 1, p. 131-146.

Bookhagen, B., Thiede, R. C., and Strecker, M. R., 2005b, Late Quaternary intensified monsoon phases control landscape evolution in the northwest Himalaya: Geology, v. 33, no. 2, p. 149-152.

Boos, W. R., and Kuang, Z., 2010, Dominant control of the South Asian monsoon by orographic insulation versus plateau heating: Nature, v. 463, no. 7278, p. 218-222.

Booth, A. L., Chamberlain, C. P., Kidd, W. S., and Zeitler, P. K., 2009, Constraints on the metamorphic evolution of the eastern Himalayan syntaxis from geochronologic and petrologic studies of Namche Barwa: Geological Society of America Bulletin, v. 121, no. 3-4, p. 385-407.

Booth, A. L., Zeitler, P. K., Kidd, W. S., Wooden, J., Liu, Y., Idleman, B., Hren, M., and Chamberlain, C. P., 2004, U-Pb zircon constraints on the tectonic evolution of southeastern Tibet, Namche Barwa Area: American Journal of Science, v. 304, no. 10, p. 889-929.

Boyce, J., and Hodges, K., 2005, U and Th zoning in Cerro de Mercado (Durango, Mexico) fluorapatite: insights regarding the impact of recoil redistribution of radiogenic 4 He on (U–Th)/He thermochronology: Chemical Geology, v. 219, no. 1, p. 261-274.

Bracciali, L., Najman, Y., Parrish, R. R., Akhter, S. H., and Millar, I., 2015, The Brahmaputra tale of tectonics and erosion: Early Miocene river capture in the Eastern Himalaya: Earth and Planetary Science Letters, v. 415, p. 25-37.

Bracciali, L., Parrish, R. R., Horstwood, M. S., Condon, D. J., and Najman, Y., 2013, U Pb LA-(MC)-ICP-MS dating of rutile: New reference materials and applications to sedimentary provenance: Chemical Geology, v. 347, p. 82-101.

Bracciali, L., Parrish, R. R., Najman, Y., Smye, A., Carter, A., and Wijbrans, J., 2016, Pleistocene exhumation of the eastern Himalayan syntaxis and its domal pop-up: Earth Science Reviews, v. 160, p. 350-385.

Brandon, M. T., 1992, Decomposition of fission-track grain-age distributions: American Journal of Science, v. 292, no. 8, p. 535-564.

Brandon, M. T., 1996, Probability density plot for fission-track grain-age samples: Radiation Measurements, v. 26, no. 5, p. 663-676.

Brandon, M. T., 2002, Decomposition of mixed grain age distributions using Binomfit: On track, v. 24, no. 8, p. 13-18.

Braun, J., 2003, Pecube: A new finite-element code to solve the 3D heat transport equation including the effects of a time-varying, finite amplitude surface topography: Computers & Geosciences, v. 29, no. 6, p. 787-794.

Braun, J., van der Beek, P., and Batt, G., 2006, Quantitative thermochronology: numerical methods for the interpretation of thermochronological data, Cambridge University Press.

Braun, J., van der Beek, P., Valla, P., Robert, X., Herman, F., Glotzbach, C., Pedersen, V., Perry, C., Simon-Labric, T., and Prigent, C., 2012, Quantifying rates of landscape evolution and tectonic processes by thermochronology and numerical modeling of crustal heat transport using PECUBE: Tectonophysics, v. 524, p. 1-28.

Brookfield, M., 1998, The evolution of the great river systems of southern Asia during the Cenozoic India-Asia collision: rivers draining southwards: Geomorphology, v. 22, no. 3, p. 285-312.

Brozovic, N., and Burbank, D. W., 2000, Dynamic fluvial systems and gravel progradation in the Himalayan foreland: Geological Society of America Bulletin, v. 112, no. 3, p. 394-412.

Buatois, L. A., Santiago, N., Herrera, M., Plink-Björklund, P., Steel, R., Espin, M., and Parra, K., 2012, Sedimentological and ichnological signatures of changes in wave, river and tidal influence along a Neogene tropical deltaic shoreline: Sedimentology, v. 59, no. 5, p. 1568-1612.

Burbank, D., Raynolds, R., and Johnson, G., 1986, Late Cenozoic tectonics and sedimentation in the north-western Himalayan foredeep. II: Eastern limb of the Northwest Syntaxis and regional synthesis: Special publication of the International Association of Sedimentologists, no. 8, p. 293-306.

Burbank, D. W., Beck, R. A., and Mulder, T., 1996, The Himalayan foreland basin, *in* Yin, A., and Harrison, T. M., eds., ed., The tectonics of Asia, London, Cambridge University Press.

Burchfiel, B. C., Zhiliang, C., Hodges, K. V., Yuping, L., Royden, L. H., Changrong, D., and Jiene, X., 1992, The South Tibetan detachment system, Himalayan orogen: Extension contemporaneous with and parallel to shortening in a collisional mountain belt: Geological Society of America Special Papers, v. 269, p. 1-41.

Burg, J.-P., Nievergelt, P., Oberli, F., Seward, D., Davy, P., Maurin, J.-C., Diao, Z., and Meier, M., 1998, The Namche Barwa syntaxis: evidence for exhumation related to compressional crustal folding: Journal of Asian Earth Sciences, v. 16, no. 2, p. 239-252.

Burg, J. P., Davy, P., Nievergelt, P., Oberli, F., Seward, D., Diao, Z., and Meier, M., 1997, Exhumation during crustal folding in the Namche-Barwa syntaxis: Terra Nova, v. 9, no. 2, p. 53-56.

Burgess, W. P., Yin, A., Dubey, C. S., Shen, Z.-K., and Kelty, T. K., 2012, Holocene shortening across the Main Frontal Thrust zone in the eastern Himalaya: Earth and Planetary Science Letters, v. 357, p. 152-167.

Butler, R., 1992, Paleomagnetism: magnetic domains to geologic terrains. Backwell Sci. Publ, Oxford.

Cannon, F., Carvalho, L. M., Jones, C., and Bookhagen, B., 2015, Multi-annual variations in winter westerly disturbance activity affecting the Himalaya: Climate Dynamics, v. 44, no. 1-2, p. 441-455.

Carlson, W. D., Donelick, R. A., and Ketcham, R. A., 1999, Variability of apatite fission-track annealing kinetics: I. Experimental results: American mineralogist, v. 84, no. 9, p. 1213-1223.

Carter, A., and Moss, S. J., 1999, Combined detrital-zircon fission-track and U-Pb dating: A new approach to understanding hinterland evolution: Geology, v. 27, no. 3, p. 235-238.

Caves, J. K., Winnick, M. J., Graham, S. A., Sjostrom, D. J., Mulch, A., and Chamberlain, C. P., 2015, Role of the westerlies in Central Asia climate over the Cenozoic: Earth and Planetary Science Letters, v. 428, p. 33-43.

Cerling, T. E., 1984, The stable isotopic composition of modern soil carbonate and its relationship to climate: Earth and Planetary science letters, v. 71, no. 2, p. 229-240.

Cerling, T. E., Harris, J. M., MacFadden, B. J., Leakey, M. G., Quade, J., Eisenmann, V., and Ehleringer, J. R., 1997, Global vegetation change through the Miocene/Pliocene boundary: Nature, v. 389, no. 6647, p. 153-158.

Cerling, T. E., Quade, J., Wang, Y., and Bowman, J., 1989, Carbon isotopes in soils and palaeosols as ecology and palaeoecology indicators: Nature, v. 341, no. 6238, p. 138-139.

Chakraborty, A., 1972, On the rock-stratigraphy, sedimentation and tectonics of the sedimentary belt in the southwest of the Shillong plateau, Meghalaya: Bull. ONGC, v. 9, no. 2, p. 133-141.

Chan, M., and Dott Jr, R., 1986, Depositional facies and progradational sequences in Eocene wave-dominated deltaic complexes, southwestern Oregon: AAPG Bulletin, v. 70, no. 4, p. 415-429.

Charreau, J., Chen, Y., Gilder, S., Barrier, L., Dominguez, S., Augier, R., Sen, S., Avouac, J. P., Gallaud, A., and Graveleau, F., 2009, Neogene uplift of the Tian Shan Mountains observed in the magnetic record of the Jingou River section (northwest China): Tectonics, v. 28, no. 2.

Chatterjee, N., Mazumdar, A., Bhattacharya, A., and Saikia, R., 2007, Mesoproterozoic granulites of the Shillong–Meghalaya Plateau: evidence of westward continuation of the Prydz Bay Pan-African suture into Northeastern India: Precambrian Research, v. 152, no. 1, p. 1-26.

Cherniak, D., 2000, Pb diffusion in rutile: Contributions to Mineralogy and Petrology, v. 139, no. 2, p. 198-207.

Cherniak, D., Lanford, W., and Ryerson, F., 1991, Lead diffusion in apatite and zircon using ion implantation and Rutherford backscattering techniques: Geochimica et Cosmochimica Acta, v. 55, no. 6, p. 1663-1673.

Cherniak, D. J., 2010, Diffusion in accessory minerals: zircon, titanite, apatite, monazite and xenotime: Reviews in Mineralogy and Geochemistry, v. 72, no. 1, p. 827-869.

Cherniak, D. J., and Watson, E. B., 2001, Pb diffusion in zircon: Chemical Geology, v. 172, no. 1-2, p. 5-24.

Chew, D. M., Sylvester, P. J., and Tubrett, M. N., 2011, U–Pb and Th–Pb dating of apatite by LA-ICPMS: Chemical Geology, v. 280, no. 1, p. 200-216.

Chirouze, F., 2011, Exhumation et évolution du drainage himalayen depuis 15 Ma - Apport des archives sédimentaires [Ph.D.: Université de Grenoble.

Chirouze, F., Dupont-Nivet, G., Huyghe, P., van der Beek, P., Chakraborti, T., Bernet, M., and Erens, V., 2012, Magnetostratigraphy of the Neogene Siwalik Group in the far eastern Himalaya: Kameng section, Arunachal Pradesh, India: Journal of Asian Earth Sciences, v. 44, p. 117-135.

Chirouze, F., Huyghe, P., van der Beek, P., Chauvel, C., Chakraborty, T., Dupont-Nivet, G., and Bernet, M., 2013, Tectonics, exhumation, and drainage evolution of the eastern Himalaya since 13 Ma from detrital geochemistry and thermochronology, Kameng River Section, Arunachal Pradesh: Geological Society of America Bulletin, v. 125, no. 3-4, p. 523-538.

Chiu, H.-Y., Chung, S.-L., Wu, F.-Y., Liu, D., Liang, Y.-H., Lin, I.-J., Iizuka, Y., Xie, L.-W., Wang, Y., and Chu, M.-F., 2009, Zircon U–Pb and Hf isotopic constraints from eastern Transhimalayan batholiths on the precollisional magmatic and tectonic evolution in southern Tibet: Tectonophysics, v. 477, no. 1, p. 3-19.

Chu, M.-F., Chung, S.-L., Song, B., Liu, D., O'Reilly, S. Y., Pearson, N. J., Ji, J., and Wen, D.-J., 2006, Zircon U-Pb and Hf isotope constraints on the Mesozoic tectonics and crustal evolution of southern Tibet: Geology, v. 34, no. 9, p. 745-748.

Cina, S. E., Yin, A., Grove, M., Dubey, C. S., Shukla, D. P., Lovera, O. M., Kelty, T. K., Gehrels, G. E., and Foster, D. A., 2009, Gangdese arc detritus within the eastern Himalayan Neogene foreland basin: implications for the Neogene evolution of the Yalu–Brahmaputra River system: Earth and Planetary Science Letters, v. 285, no. 1, p. 150-162.

Clark, M., Schoenbohm, L., Royden, L., Whipple, K., Burchfiel, B., Zhang, X., Tang, W., Wang, E., and Chen, L., 2004, Surface uplift, tectonics, and erosion of eastern Tibet from large-scale drainage patterns: Tectonics, v. 23, no. 1.

Clark, M. K., and Bilham, R., 2008, Miocene rise of the Shillong Plateau and the beginning of the end for the Eastern Himalaya: Earth and Planetary Science Letters, v. 269, no. 3, p. 337-351.

Clift, P. D., Blusztajn, J., and Nguyen, A. D., 2006, Large-scale drainage capture and surface uplift in eastern Tibet–SW China before 24 Ma inferred from sediments of the Hanoi Basin, Vietnam: Geophysical Research Letters, v. 33, no. 19.

Clift, P. D., Degnan, P. J., Hannigan, R., and Blusztajn, J., 2000, Sedimentary and geochemical evolution of the Dras forearc basin, Indus suture, Ladakh Himalaya, India: Geological Society of America Bulletin, v. 112, no. 3, p. 450-466.

Clift, P. D., Giosan, L., Blusztajn, J., Campbell, I. H., Allen, C., Pringle, M., Tabrez, A. R., Danish, M., Rabbani, M., and Alizai, A., 2008a, Holocene erosion of the Lesser Himalaya triggered by intensified summer monsoon: Geology, v. 36, no. 1, p. 79-82.

Clift, P. D., Hodges, K. V., Heslop, D., Hannigan, R., Van Long, H., and Calves, G., 2008b, Correlation of Himalayan exhumation rates and Asian monsoon intensity: Nature Geoscience, v. 1, no. 12, p. 875-880.

Clift, P. D., Shimizu, N., Layne, G., Blusztajn, J., Gaedicke, C., Schlüter, H.-U., Clark, M., and Amjad, S., 2001, Development of the Indus Fan and its significance for the erosional history of the Western Himalaya and Karakoram: Geological Society of America Bulletin, v. 113, no. 8, p. 1039-1051.

Cochrane, R., Spikings, R. A., Chew, D., Wotzlaw, J.-F., Chiaradia, M., Tyrrell, S., Schaltegger, U., and Van der Lelij, R., 2014, High temperature (>350 C) thermochronology and mechanisms of Pb loss in apatite: Geochimica et Cosmochimica Acta, v. 127, p. 39-56.

Collinson, J. D., 1969, The sedimentology of the Grindslow Shales and the Kinderscout Grit: a deltaic complex in the Namurian of northern England: Journal of Sedimentary Research, v. 39, no. 1.

Copley, A., Avouac, J. P., Hollingsworth, J., and Leprince, S., 2011, The 2001 Mw 7.6 Bhuj earthquake, low fault friction, and the crustal support of plate driving forces in India: Journal of Geophysical Research: Solid Earth, v. 116, no. B8.

Corfield, R. I., Searle, M. P., and Green, O. R., 1999, Photang thrust sheet: an accretionary complex structurally below the Spontang ophiolite constraining timing and tectonic environment of ophiolite obduction, Ladakh Himalaya, NW India: Journal of the Geological Society, v. 156, no. 5, p. 1031-1044.

Cotton, J. M., Cerling, T. E., Hoppe, K. A., Mosier, T. M., and Still, C. J., 2016, Climate, CO2, and the history of North American grasses since the Last Glacial Maximum: Science advances, v. 2, no. 3, p. e1501346.

Coutand, I., Barrier, L., Govin, G., Grujic, D., Hoorn, C., Dupont-Nivet, G., and Najman, Y., 2016, Late Miocene-Pleistocene evolution of India-Eurasia convergence partitioning between the Bhutan Himalaya and the Shillong plateau: New evidences from foreland basin deposits along the Dungsam Chu section, Eastern Bhutan: Tectonics.

Coutand, I., Carrapa, B., Deeken, A., Schmitt, A. K., Sobel, E. R., and Strecker, M. R., 2006, Propagation of orographic barriers along an active range front: Insights from sandstone petrography and detrital apatite fission-track thermochronology in the intramontane Angastaco basin, NW Argentina: Basin Research, v. 18, no. 1, p. 1-26.

Coutand, I., Whipp, D. M., Grujic, D., Bernet, M., Fellin, M. G., Bookhagen, B., Landry, K. R., Ghalley, S., and Duncan, C., 2014, Geometry and kinematics of the Main Himalayan Thrust and Neogene crustal exhumation in the Bhutanese Himalaya derived from inversion of

multithermochronologic data: Journal of Geophysical Research: Solid Earth, v. 119, no. 2, p. 1446-1481.

Craig, T. J., and Copley, A., 2014, An explanation for the age independence of oceanic elastic thickness estimates from flexural profiles at subduction zones, and implications for continental rheology: Earth and Planetary Science Letters, v. 392, p. 207-216.

Craig, T. J., Copley, A., and Jackson, J., 2012, Thermal and tectonic consequences of India underthrusting Tibet: Earth and Planetary Science Letters, v. 353, p. 231-239.

Dadson, S. J., Hovius, N., Chen, H., Dade, W. B., Hsieh, M.-L., Willett, S. D., Hu, J.-C., Horng, M.-J., Chen, M.-C., and Stark, C. P., 2003, Links between erosion, runoff variability and seismicity in the Taiwan orogen: Nature, v. 426, no. 6967, p. 648-651.

Dansgaard, W., 1961, The isotopic composition of natural waters: Medd. om Gronland, v. 165, no. 2, p. 1-120.

Dasgupta, S., 2000, Seismotectonic atlas of India and its environs, Geological Survey of India, Kolkota.

Dasgupta, S., Mukhopadhyay, M., and Nandy, D., 1987, Active transverse features in the central portion of the Himalaya: Tectonophysics, v. 136, no. 3-4, p. 255-264.

Davis, D. W., and Krogh, T. E., 2001, Preferential dissolution of 234U and radiogenic Pb from [alpha]-recoil-damaged lattice sites in zircon: implications for thermal histories and Pb isotopic fractionation in the near surface environment: Chemical Geology, v. 172, no. 1-2, p. 41-58.

Dazé, A., Lee, J. K., and Villeneuve, M., 2003, An intercalibration study of the Fish Canyon sanidine and biotite 40 Ar/39 Ar standards and some comments on the age of the Fish Canyon Tuff: Chemical Geology, v. 199, no. 1, p. 111-127.

De Franceschi, D., Hoorn, C., Antoine, P.-O., Cheema, I. U., Flynn, L. J., Lindsay, E. H., Marivaux, L., Métais, G., Rajpar, A. R., and Welcomme, J.-L., 2008, Floral data from the mid-Cenozoic of central Pakistan: Review of Palaeobotany and Palynology, v. 150, no. 1, p. 115-129.

Debon, F., Le Fort, P., Sheppard, S., MF, and Sonet, J., 1986, The four plutonic belts of the Transhimalaya-Himalaya: A chemical, mineralogical, isotopic, and chronological synthesis along a Tibet-Nepal section: Journal of Petrology, v. 27, no. 1, p. 219-250.

DeCelles, P. G., Gehrels, G. E., Najman, Y., Martin, A., Carter, A., and Garzanti, E., 2004, Detrital geochronology and geochemistry of Cretaceous–Early Miocene strata of Nepal: implications for timing and diachroneity of initial Himalayan orogenesis: Earth and Planetary Science Letters, v. 227, no. 3, p. 313-330.

DeCelles, P. G., Gehrels, G. E., Quade, J., LaReau, B., and Spurlin, M., 2000, Tectonic implications of U-Pb zircon ages of the Himalayan orogenic belt in Nepal: Science, v. 288, no. 5465, p. 497-499.

DeCelles, P. G., Gehrels, G. E., Quade, J., and Ojha, T., 1998a, Eocene-early Miocene foreland basin development and the history of Himalayan thrusting, western and central Nepal: Tectonics, v. 17, no. 5, p. 741-765.

DeCelles, P. G., Gehrels, G. E., Quade, J., Ojha, T., Kapp, P. A., and Upreti, B., 1998b, Neogene foreland basin deposits, erosional unroofing, and the kinematic history of the Himalayan fold-thrust belt, western Nepal: Geological Society of America Bulletin, v. 110, no. 1, p. 2-21.

DeCelles, P. G., and Giles, K. A., 1996, Foreland basin systems: Basin research, v. 8, no. 2, p. 105-123.

Delcaillau, B., 1997, Les fronts de chaînes actives, genèse des reliefs et relations tectoniqueérosion-sédimentation: Habilitation à diriger des recherches, Université de Caen.

Dercourt, J., Ricou, L. E., and Vrielynck, B., 1993, Atlas Tethys Palaeoenvironmental Maps: Explanatory Notes. Liste Des Articles, Communications, Cartes Et Thèses. Programme GS-Téthys, 1986-1993, Gauthier-Villars.

Dettman, D. L., Kohn, M. J., Quade, J., Ryerson, F., Ojha, T. P., and Hamidullah, S., 2001, Seasonal stable isotope evidence for a strong Asian monsoon throughout the past 10.7 my: Geology, v. 29, no. 1, p. 31-34.

Diehl, T., Singer, J., Hetényi, G., Grujic, D., Clinton, J., and Kissling, E., 2016, The seismic gap of Bhutan: Evidence for segmentation of the Himalayas and its link to foreland deformation: paper presented at Himalayan-Karakorum-Tibet Workshop, Aussois, France, 9-12 May.

Dietrich, V. J., Frank, W., and Honegger, K., 1983, A Jurassic-Cretaceous island arc in the Ladakh-Himalayas: Journal of Volcanology and Geothermal Research, v. 18, no. 1-4, p. 405-433.

Ding, L., Zhong, D., Yin, A., Kapp, P., and Harrison, T. M., 2001, Cenozoic structural and metamorphic evolution of the eastern Himalayan syntaxis (Namche Barwa): Earth and Planetary Science Letters, v. 192, no. 3, p. 423-438.

Dobremez, J., 1978, Carte écologique du Népal 1/250 000: University of Grenoble, Grenoble.

Dodson, M. H., 1973, Closure temperature in cooling geochronological and petrological systems: Contributions to Mineralogy and Petrology, v. 40, no. 3, p. 259-274.

Donelick, R. A., Ketcham, R. A., and Carlson, W. D., 1999, Variability of apatite fission-track annealing kinetics: II. Crystallographic orientation effects: American Mineralogist, v. 84, no. 9, p. 1224-1234.

Donelick, R. A., O'Sullivan, P. B., and Ketcham, R. A., 2005, Apatite fission-track analysis: Reviews in Mineralogy and Geochemistry, v. 58, no. 1, p. 49-94.

Dumitru, T. A., 1993, A new computer-automated microscope stage system for fission-track analysis: Nuclear Tracks and Radiation Measurements, v. 21, no. 4, p. 575-580.

Duncan, C., Masek, J., and Fielding, E., 2003, How steep are the Himalaya? Characteristics and implications of along-strike topographic variations: Geology, v. 31, no. 1, p. 75-78.

Dupont-Nivet, G., Lippert, P. C., Van Hinsbergen, D. J., Meijers, M. J., and Kapp, P., 2010, Palaeolatitude and age of the Indo–Asia collision: palaeomagnetic constraints: Geophysical Journal International, v. 182, no. 3, p. 1189-1198.

Egholm, D., Nielsen, S., Pedersen, V. K., and Lesemann, J.-E., 2009, Glacial effects limiting mountain height: Nature, v. 460, no. 7257, p. 884-887.

Eglinton, G., and Hamilton, R. J., 1967, Leaf epicuticular waxes: Science, v. 156, no. 3780, p. 1322-1335.

Ehleringer, J. R., 1989, Carbon isotope ratios and physiological processes in aridland plants, Stable isotopes in ecological research, Springer, p. 41-54.

Enkelmann, E., Ehlers, T., Zeitler, P., and Hallet, B., 2011, Denudation of the Namche Barwa antiform, eastern Himalaya: Earth and Planetary Science Letters, v. 307, no. 3, p. 323-333.

Evans, P., 1932, Tertiary succession in Assam: Trans. Min. Geol. Inst. India, v. 27, no. 3, p. 155-260.

Finnegan, N. J., Hallet, B., Montgomery, D. R., Zeitler, P. K., Stone, J. O., Anders, A. M., and Yuping, L., 2008, Coupling of rock uplift and river incision in the Namche Barwa–Gyala Peri massif, Tibet: Geological Society of America Bulletin, v. 120, no. 1-2, p. 142-155.

Fitzgerald, P. G., Sorkhabi, R. B., Redfield, T. F., and Stump, E., 1995, Uplift and denudation of the central Alaska Range: A case study in the use of apatite fission track thermochronology to determine absolute uplift parameters: Journal of Geophysical Research: Solid Earth, v. 100, no. B10, p. 20175-20191.

Förste, C., Bruinsma, S., Flechtner, F., Marty, J., Lemoine, J., Dahle, C., Abrikosov, O., Neumayer, H., Biancale, R., and Barthelmes, F., A preliminary update of the Direct approach GOCE Processing and a new release of EIGEN-6C, *in* Proceedings AGU Fall Meeting Abstracts2012, Volume 1, p. 0923.

France-Lanord, C., and Derry, L. A., 1994, δ13C of organic carbon in the Bengal Fan: Source evolution and transport of C3 and C4 plant carbon to marine sediments: Geochimica et Cosmochimica Acta, v. 58, no. 21, p. 4809-4814.

Frank, W., Grasemann, B., Guntli, P., and Miller, C., 1995a, Geological map of the Kishtwar-Chamba-Kulu region (NW Himalayas, India): Jahrbuch der Geologischen Bundesanstalt, v. 138, no. 2, p. 299-308.

Frank, W., Miller, C., and Grasemann, B., Ar/Ar-ages of detrital micas and palaeogeographic provenance of Proterozoic clastic sediments in the Himalayas., *in* Proceedings 10th Himalayan-Karakoram-Tibet Workshop, Ascona, Switzerland, 1995b.

Freeman, K., and Colarusso, L., 2001, Molecular and isotopic records of C 4 grassland expansion in the late Miocene: Geochimica et Cosmochimica Acta, v. 65, no. 9, p. 1439-1454.

Friend, P., Jones, N., and Vincent, S., 1999, Drainage Evolution in Active Mountain Belts: Extrapolation Backwards from Present-Day Himalayan River Patterns: Special Publication of the International Association of Sedimentologists, v. 28, p. 305-313.

Gaetani, M., 1997, The Karakorum block in central Asia, from Ordovician to Cretaceous: Sedimentary Geology, v. 109, no. 3-4, p. 339-359.

Gaetani, M., and Garzanti, E., 1991, Multicyclic History of the Northern India Continental-Margin (Northwestern Himalaya): American Association of Petroleum Geologists Bulletin, v. 75, no. 9, p. 1427-1446.

Gaetani, M., Gosso, G., and Pognante, U., 1990, A geological transect from Kun Lun to Karakorum (Sinkiang, China): the western termination of the Tibetan Plateau. Preliminary note: Terra nova, v. 2, no. 1, p. 23-30.

Galbraith, R., and Green, P., 1990, Estimating the component ages in a finite mixture: International Journal of Radiation Applications and Instrumentation. Part D. Nuclear Tracks and Radiation Measurements, v. 17, no. 3, p. 197-206.

Galbraith, R., and Laslett, G., 1997, Statistical modelling of thermal annealing of fission tracks in zircon: Chemical Geology, v. 140, no. 1, p. 123-135.

Galbraith, R. F., 2005, Statistics for fission track analysis, CRC Press.

Galbraith, R. F., Roberts, R. G., Laslett, G., Yoshida, H., and Olley, J. M., 1999, Optical dating of single and multiple grains of quartz from Jinmium rock shelter, northern Australia: Part I, experimental design and statistical models: Archaeometry, v. 41, no. 2, p. 339-364.

Gallagher, K., Brown, R., and Johnson, C., 1998, Fission track analysis and its applications to geological problems: Annual Review of Earth and Planetary Sciences, v. 26, no. 1, p. 519-572.

Galy, A., and France-Lanord, C., 1999, Weathering processes in the Ganges–Brahmaputra basin and the riverine alkalinity budget: Chemical Geology, v. 159, no. 1, p. 31-60.

Galy, V., Beyssac, O., France-Lanord, C., and Eglinton, T., 2008a, Recycling of graphite during Himalayan erosion: a geological stabilization of carbon in the crust: Science, v. 322, no. 5903, p. 943-945.

Galy, V., Eglinton, T., France-Lanord, C., and Sylva, S., 2011, The provenance of vegetation and environmental signatures encoded in vascular plant biomarkers carried by the Ganges–Brahmaputra rivers: Earth and Planetary Science Letters, v. 304, no. 1, p. 1-12.

Galy, V., France-Lanord, C., and Lartiges, B., 2008b, Loading and fate of particulate organic carbon from the Himalaya to the Ganga–Brahmaputra delta: Geochimica et Cosmochimica Acta, v. 72, no. 7, p. 1767-1787.

Galy, V., France-Lanord, C., Peucker-Ehrenbrink, B., and Huyghe, P., 2010, Sr–Nd–Os evidence for a stable erosion regime in the Himalaya during the past 12Myr: Earth and Planetary Science Letters, v. 290, no. 3, p. 474-480.

Gani, M. R., and Alam, M. M., 2004, Fluvial facies architecture in small-scale river systems in the Upper Dupi Tila Formation, northeast Bengal Basin, Bangladesh: Journal of Asian Earth Sciences, v. 24, no. 2, p. 225-236.

Gani, M. R., and Bhattacharya, J. P., 2007, Basic building blocks and process variability of a Cretaceous delta: Internal facies architecture reveals a more dynamic interaction of river, wave, and tidal processes than is indicated by external shape: Journal of Sedimentary Research, v. 77, no. 4, p. 284-302.

Gansser, A., 1964, Geology of the Himalayas, London, Interscience Publishers, 273 p.:

Gansser, A., 1977, The great suture zone between Himalaya and Tibet, a preliminary account: Himalaya, Sciences de la Terre, Colloques internationaux du CNRS, v. 268, p. 181-191.

Gansser, A., 1983, Geology of the Bhutan Himalaya: Mem. Soc. Helv. Sci. Nat, v. 96, p. 181.

Garcia-Castellanos, D., and Jiménez-Munt, I., 2015, Topographic evolution and climate aridification during continental collision: insights from computer simulations: PloS one, v. 10, no. 8, p. e0132252.

Garver, J. I., and Brandon, M. T., 1994, Erosional denudation of the British Columbia Coast Ranges as determined from fission-track ages of detrital zircon from the Tofino basin, Olympic Peninsula, Washington: Geological Society of America Bulletin, v. 106, no. 11, p. 1398-1412.

Garver, J. I., Brandon, M. T., Roden-Tice, M., and Kamp, P. J., 1999, Exhumation history of orogenic highlands determined by detrital fission-track thermochronology: Geological Society, London, Special Publications, v. 154, no. 1, p. 283-304.

Garzanti, E., Baud, A., and Mascle, G., 1987, Sedimentary Record of the Northward Flight of India and Its Collision with Eurasia (Ladakh Himalaya, India): Geodinamica Acta, v. 1, no. 4-5, p. 297-312.

Garzanti, E., Casnedi, R., and Jadoul, F., 1986, Sedimentary evidence of a Cambro-Ordovician orogenic event in the northwestern Himalaya: Sedimentary Geology, v. 48, no. 3-4, p. 237-265.

Garzanti, E., and van Haver, T., 1988, The Indus Clastics - Fore-Arc Basin Sedimentation in the Ladakh Himalaya (India): Sedimentary Geology, v. 59, no. 3-4, p. 237-249.

Garzanti, E., Vezzoli, G., Andò, S., France-Lanord, C., Singh, S. K., and Foster, G., 2004, Sand petrology and focused erosion in collision orogens: the Brahmaputra case: Earth and Planetary Science Letters, v. 220, no. 1, p. 157-174.

Gautam, P., and Appel, E., 1994, Magnetic-polarity stratigraphy of Siwalik Group sediments of Tinau Khola section in west central Nepal, revisited: Geophysical Journal International, v. 117, no. 1, p. 223-234.

Gautam, P., and Fujiwara, Y., 2000, Magnetic polarity stratigraphy of Siwalik Group sediments of Karnali River section in western Nepal: Geophysical Journal International, v. 142, no. 3, p. 812-824.

Gautam, P., and Rösler, W., 1999, Depositional chronology and fabric of Siwalik Group sediments in central Nepal from magnetostratigraphy and magnetic anisotropy: Journal of Asian Earth Sciences, v. 17, no. 5, p. 659-682.

Gehrels, G., Kapp, P., DeCelles, P., Pullen, A., Blakey, R., Weislogel, A., Ding, L., Guynn, J., Martin, A., and McQuarrie, N., 2011, Detrital zircon geochronology of pre-Tertiary strata in the Tibetan-Himalayan orogen: Tectonics, v. 30, no. 5.

Gehrels, G. E., DeCelles, P. G., Martin, A., Ojha, T. P., Pinhassi, G., and Upreti, B. N., 2003, Initiation of the Himalayan Orogen as an Early Paleozoic Thin-skinned Thrust Belt: GSA Today, v. 13, no. 9, p. 4-9.

Gehrels, G. E., Valencia, V., and Pullen, A., 2006, Detrital zircon geochronology by laser-ablation multicollector ICPMS at the Arizona Laser-Chron Center, *in* Olszewski, T. H., W., ed., Geochronology: Emerging Opportunities: Philadelphia, Pennsylvania, Paleontological Society Short Course, p. 1-10.

Gehrels, G. E., Valencia, V. A., and Ruiz, J., 2008, Enhanced precision, accuracy, efficiency, and spatial resolution of U-Pb ages by laser ablation–multicollector–inductively coupled plasma–mass spectrometry: Geochemistry, Geophysics, Geosystems, v. 9, no. 3.

Gemignani, L., van der Beek, P., Braun, J., Najman, Y., Bernet, M., Garzanti, E., and Wijbrans, J. R., submitted, Present-day and long-term erosion of the eastern Himalaya as detected by detrital thermochronology: Earth and Planetary Science Letters.

Ghosh, S., Paul, D., Bhalla, J., Bishui, P., Gupta, S., and Chakraborty, S., 1994, New Rb-Sr isotopic ages and geochemistry of granitoids from Meghalaya and their significance in middle-to late Proterozoic crustal evolution: Indian Minerals, v. 48, no. 1-2, p. 33-44.

Giesen, W., Wulffraat, S., Zieren, M., and Scholten, L., 2007, Mangrove guidebook for Southeast Asia: Mangrove guidebook for Southeast Asia.

Govin, G., Najman, Y., Copley, A., Millar, I., van der Beek, P., Huyghe, P., Grujic, D., and Davenport, J., in prep, Timing and mechanism of the rise of the Shillong Plateau in the Himalayan foreland: Geology.

Govin, G., Najman, Y., Millar, I., Dupont-Nivet, G., van der Beek, P., Huyghe, P., O'Sullivan, P., Mark, C., and Vögeli, N., in review, Paleo-drainage evolution and rapid exhumation of the Namche Barwa Syntaxis recorded in the Siwaliks of the easternmost Himalaya (Arunachal Pradesh, India): American Journal of Science

Govin, G., Najman, Y., van der Beek, P., Huyghe, P., Millar, I., Bernet, M., Dupont-Nivet, G., Wijbrans, J., Gemignani, L., and Vögeli, N., 2016, Constraining the timing of exhumation of the Eastern Himalayan syntaxis from a study of the palaeo-Brahmaputra deposits, Siwalik Group, Eastern Arunachal Pradesh, India: Abstract HKT Workshop.

Gradstein, F. M., Ogg, J. G., Schmitz, M., and Ogg, G., 2012, The geologic time scale 2012 2-volume set, elsevier.

Grujic, D., Coutand, I., Bookhagen, B., Bonnet, S., Blythe, A., and Duncan, C., 2006, Climatic forcing of erosion, landscape, and tectonics in the Bhutan Himalayas: Geology, v. 34, no. 10, p. 801-804.

Grujic, D., Cowan, B., Hren, M., Coutand, I., Barrier, L., and Govin, G., in prep., Formation of a rain shadow: O and H stable isotope records in authigenic clays from Siwalik Group in eastern Bhutan.

Guillot, S., Garzanti, E., Baratoux, D., Marquer, D., Mahéo, G., and De Sigoyer, J., 2003, Reconstructing the total shortening history of the NW Himalaya: Geochemistry, Geophysics, Geosystems, v. 4, no. 7.

Guillot, S., Pêcher, A., Rochette, P., and Le Fort, P., 1993, The emplacement of the Manaslu granite of central Nepal: field and magnetic susceptibility constraints: Geological Society, London, Special Publications, v. 74, no. 1, p. 413-428.

Hames, W., and Bowring, S., 1994, An empirical evaluation of the argon diffusion geometry in muscovite: Earth and Planetary Science Letters, v. 124, no. 1-4, p. 161-169.

Hammer, P., Berthet, T., Hetényi, G., Cattin, R., Drukpa, D., Chophel, J., Lechmann, S., Moigne, N. L., Champollion, C., and Doerflinger, E., 2013, Flexure of the India plate underneath the Bhutan Himalaya: Geophysical Research Letters, v. 40, no. 16, p. 4225-4230.

Hansen, J., Sato, M., Russell, G., and Kharecha, P., 2013, Climate sensitivity, sea level and atmospheric carbon dioxide: Phil. Trans. R. Soc. A, v. 371, no. 2001, p. 20120294.

Haproff, P., Yin, A., and Dubey, C., Tectonic framework of the easternmost Himalayan orogen based on U-Pb zircon geochronology and detailed geologic mapping, NE India, *in* Proceedings AGU Fall Meeting Abstracts2013, Volume 1, p. 2422.

Harrison, T. M., Copeland, P., Hall, S. A., Quade, J., Burner, S., Ojha, T. P., and Kidd, W., 1993, Isotopic preservation of Himalayan/Tibetan uplift, denudation, and climatic histories of two molasse deposits: The Journal of Geology, p. 157-175.

Harrison, T. M., Copeland, P., Kidd, W. S., and Yin, A., 1992, Raising tibet: Science, v. 255, no. 5052, p. 1663-1670.

Hasebe, N., Barbarand, J., Jarvis, K., Carter, A., and Hurford, A. J., 2004, Apatite fission-track chronometry using laser ablation ICP-MS: Chemical Geology, v. 207, no. 3, p. 135-145.

Hébert, R., Bezard, R., Guilmette, C., Dostal, J., Wang, C., and Liu, Z., 2012, The Indus–Yarlung Zangbo ophiolites from Nanga Parbat to Namche Barwa syntaxes, southern Tibet: first synthesis of petrology, geochemistry, and geochronology with incidences on geodynamic reconstructions of Neo-Tethys: Gondwana Research, v. 22, no. 2, p. 377-397.

Heermance, R. V., Chen, J., Burbank, D. W., and Wang, C., 2007, Chronology and tectonic controls of Late Tertiary deposition in the southwestern Tian Shan foreland, NW China: Basin Research, v. 19, no. 4, p. 599-632.

Helland-Hansen, W., 2010, Facies and stacking patterns of shelf-deltas within the Palaeogene Battfjellet Formation, Nordenskiöld Land, Svalbard: implications for subsurface reservoir prediction: Sedimentology, v. 57, no. 1, p. 190-208.

Henderson, A., 2010, The geology of the Indus Basin Sedimentary Rocks, Ladakh Himalaya, NW India.

Henderson, A. L., Najman, Y., Parrish, R. R., BouDagher-Fadel, M., Barford, D., Garzanti, E., and Andò, S., 2010, Geology of the Cenozoic Indus Basin sedimentary rocks: Paleoenvironmental interpretation of sedimentation from the western Himalaya during the early phases of India-Eurasia collision: Tectonics, v. 29, no. 6.

Henderson, A. L., Najman, Y., Parrish, R. R., Mark, D. F., and Foster, G. L., 2011, Constraints to the timing of India–Eurasia collision; a re-evaluation of evidence from the Indus Basin sedimentary rocks of the Indus–Tsangpo Suture Zone, Ladakh, India: Earth-Science Reviews, v. 106, no. 3, p. 265-292.

Herbert, T. D., Lawrence, K. T., Tzanova, A., Peterson, L. C., Caballero-Gill, R., and Kelly, C. S., 2016, Late Miocene global cooling and the rise of modern ecosystems: Nature Geoscience.

Hiess, J., Condon, D. J., McLean, N., and Noble, S. R., 2012, 238U/235U systematics in terrestrial uranium-bearing minerals: Science, v. 335, no. 6076, p. 1610-1614.

Hilley, G., Blisniuk, P., and Strecker, M., 2005, Mechanics and erosion of basement-cored uplift provinces: Journal of Geophysical Research: Solid Earth, v. 110, no. B12.

Hirschmiller, J., Grujic, D., Bookhagen, B., Coutand, I., Huyghe, P., Mugnier, J.-L., and Ojha, T., 2014, What controls the growth of the Himalayan foreland fold-and-thrust belt?: Geology, v. 42, no. 3, p. 247-250.

Hodges, K. V., 2000, Tectonics of the Himalaya and southern Tibet from two perspectives: Geological Society of America Bulletin, v. 112, no. 3, p. 324-350.

Hodges, K. V., Parrish, R. R., and Searle, M. P., 1996, Tectonic evolution of the Central Annapurna Range, Nepalese Himalayas.: Tectonics, v. 15, p. 1264-1291.

Honegger, K., Dietrich, V., Frank, W., Gansser, A., Thoni, M., and Trommsdorff, V., 1982, Magmatism and Metamorphism in the Ladakh Himalayas (the Indus- Tsangpo Suture Zone): Earth and Planetary Science Letters, v. 60, no. 2, p. 253-292.

Hoorn, C., Ohja, T., and Quade, J., 2000, Palynological evidence for vegetation development and climatic change in the Sub-Himalayan Zone (Neogene, Central Nepal): Palaeogeography, Palaeoclimatology, Palaeoecology, v. 163, no. 3, p. 133-161.

Horstwood, M., 2008, Data reduction strategies, uncertainty assessment and resolution of LA-(MC-) ICP-MS isotope data, Mineralogical Association of Canada.

Horstwood, M. S., Foster, G. L., Parrish, R. R., Noble, S. R., and Nowell, G. M., 2003, Common-Pb corrected in situ U–Pb accessory mineral geochronology by LA-MC-ICP-MS: Journal of Analytical Atomic Spectrometry, v. 18, no. 8, p. 837-846.

Hu, X., Sinclair, H. D., Wang, J., Jiang, H., and Wu, F., 2012, Late Cretaceous-Palaeogene stratigraphic and basin evolution in the Zhepure Mountain of southern Tibet: implications for the timing of India-Asia initial collision: Basin Research, v. 24, no. 5, p. 520-543.

Hubbard, M. S., 1989, Thermobarometric constraints on the thermal history of the Main Central Thrust Zone and Tibetan Slab, eastern Nepal Himalaya: Journal of Metamorphic Geology, v. 7, no. 1, p. 19-30.

Hurford, A. J., 1990, Standardization of fission track dating calibration: recommendation by the Fission Track Working Group of the IUGS Subcommission on Geochronology: Chemical Geology: Isotope Geoscience Section, v. 80, no. 2, p. 171-178.

Hurford, A. J., and Carter, A., 1991, The role of fission track dating in discrimination of provenance: Geological Society, London, Special Publications, v. 57, no. 1, p. 67-78.

Hurford, A. J., and Green, P. F., 1983, The zeta age calibration of fission-track dating: Chemical Geology, v. 41, p. 285-317.

Huyghe, P., Mugnier, J. L., Gajurel, A. P., and Delcaillau, B., 2005, Tectonic and climatic control of the changes in the sedimentary record of the Karnali River section (Siwaliks of western Nepal): Island Arc, v. 14, no. 4, p. 311-327.

Hyne, N. J., Cooper, W. A., and Dickey, P. A., 1979, Stratigraphy of intermontane, lacustrine delta, Catatumbo river, Lake Maracaibo, Venezuela: AAPG Bulletin, v. 63, no. 11, p. 2042-2057.

ICCP, 2001, The new vitrinite classification (International Committee For Coal and Organic Petrology-ICCP System 1994): Fuel, v. 80, p. 459-471.

Islam, M. S., Shinjo, R., and Kayal, J., 2011, Pop-up tectonics of the Shillong Plateau in northeastern India: Insight from numerical simulations: Gondwana Research, v. 20, no. 2, p. 395-404.

Jackson, S. E., Pearson, N. J., Griffin, W. L., and Belousova, E. A., 2004, The application of laser ablation-inductively coupled plasma-mass spectrometry to in situ U–Pb zircon geochronology: Chemical Geology, v. 211, no. 1, p. 47-69.

Jaffey, A. H., Flynn, K. F., Glendenin, L. E., Bentley, W. C., and Essling, A. M., 1971, Precision Measurement of Half-Lives and Specific Activities of U235 and U238: Physical Review C, v. 4, no. 5, p. 1889.

Jäger, E., 1967, Die Bedeutung der Biotit-alterswerte, *in* Jäger, E. N., E. Wenk, E., ed., Rb-Sr Altersbestimmungen an glimmern der Zentralalpen. Beitrage zur Geologischen Karte der Schweiz, Volume 134, p. 28-31.

Jain, V., and Sinha, R., 2003, River systems in the Gangetic plains and their comparison with the Siwaliks: a review: Current Science, v. 84, no. 8, p. 1025-1033.

Jessup, M. J., Newell, D. L., Cottle, J. M., Berger, A. L., and Spotila, J. A., 2008, Orogen-parallel extension and exhumation enhanced by denudation in the trans-Himalayan Arun River gorge, Ama Drime Massif, Tibet-Nepal: Geology, v. 36, no. 7, p. 587-590.

Ji, W.-Q., Wu, F.-Y., Chung, S.-L., Li, J.-X., and Liu, C.-Z., 2009a, Zircon U–Pb geochronology and Hf isotopic constraints on petrogenesis of the Gangdese batholith, southern Tibet: Chemical Geology, v. 262, no. 3, p. 229-245.

Ji, W., Wu, F., Liu, C., and Chung, S., 2009b, Geochronology and petrogenesis of granitic rocks in Gangdese batholith, southern Tibet: Science in China Series D: Earth Sciences, v. 52, no. 9, p. 1240-1261.

Jo, H., Rhee, C., and Chough, S., 1997, Distinctive characteristics of a streamflow-dominated alluvial fan deposit: Sanghori area, Kyongsang Basin (Early Cretaceous), southeastern Korea: Sedimentary Geology, v. 110, no. 1, p. 51-79.

Johnson, G. D., Opdyke, N. D., Tandon, S., and Nanda, A., 1983, The magnetic polarity stratigraphy of the Siwalik Group at Haritalyangar (India) and a new last appearance datum for Ramapithecus and Sivapithecus in Asia: Palaeogeography, palaeoclimatology, palaeoecology, v. 44, no. 3-4, p. 223-233, 237-241, 245-249.

Johnson, N. M., Stix, J., Tauxe, L., Cerveny, P. F., and Tahirkheli, R. A., 1985, Paleomagnetic chronology, fluvial processes, and tectonic implications of the Siwalik deposits near Chinji Village, Pakistan: The Journal of Geology, p. 27-40.

Johnson, S. Y., and Alam, A. M. N., 1991, Sedimentation and tectonics of the Sylhet trough, Bangladesh: Geological Society of America Bulletin, v. 103, no. 11, p. 1513-1527.

Jordan, T. E., 1995, Retroarc Foreland and Relaterd Basins, *in* Busby, C., and Ingersoll, R., eds., Tectonics of sedimentary Basins, Blackwell Sci., Cambridge, Mass, p. 331-362.

Jouanne, F., Mugnier, J.-L., Gamond, J., Le Fort, P., Pandey, M., Bollinger, L., Flouzat, M., and Avouac, J., 2004, Current shortening across the Himalayas of Nepal: Geophysical Journal International, v. 157, no. 1, p. 1-14.

Kayal, J., Arefiev, S. S., Baruah, S., Tatevossian, R., Gogoi, N., Sanoujam, M., Gautam, J., Hazarika, D., and Borah, D., 2010, The 2009 Bhutan and Assam felt earthquakes (Mw 6.3 and 5.1) at the Kopili fault in the northeast Himalaya region: Geomatics, Natural Hazards and Risk, v. 1, no. 3, p. 273-281.

Kellett, D. A., Grujic, D., Coutand, I., Cottle, J., and Mukul, M., 2013, The South Tibetan detachment system facilitates ultra rapid cooling of granulite-facies rocks in Sikkim Himalaya: Tectonics, v. 32, no. 2, p. 252-270.

Kelley, S., 2002, K-Ar and Ar-Ar dating: Reviews in Mineralogy and Geochemistry, v. 47, no. 1, p. 785-818.

King, G. E., Herman, F., and Guralnik, B., 2016, Northward migration of the eastern Himalayan syntaxis revealed by OSL thermochronometry: Science, v. 353, no. 6301, p. 800-804.

Kooijman, E., Mezger, K., and Berndt, J., 2010, Constraints on the U–Pb systematics of metamorphic rutile from in situ LA-ICP-MS analysis: Earth and Planetary Science Letters, v. 293, no. 3, p. 321-330.

Koons, P. O., Zeitler, P. K., and Hallet, B., 2013, Tectonic Aneurysms and Mountain Building, *in* Shroder, J., and Owen, L.A., ed., Treatise on Geomorphology, Volume 5: Tectonic Geomorphology. Academic Press, San Diego, CA,, p. 318–349.

Koppers, A. A., 2002, ArArCALC—software for 40 Ar/39 Ar age calculations: Computers & Geosciences, v. 28, no. 5, p. 605-619.

Korup, O., and Montgomery, D. R., 2008, Tibetan plateau river incision inhibited by glacial stabilization of the Tsangpo gorge: Nature, v. 455, no. 7214, p. 786-789.

Korup, O., Montgomery, D. R., and Hewitt, K., 2010, Glacier and landslide feedbacks to topographic relief in the Himalayan syntaxes: Proceedings of the National Academy of Sciences, v. 107, no. 12, p. 5317-5322.

Kotlia, B. S., Singh, A. K., Joshi, L. M., and Dhaila, B. S., 2015, Precipitation variability in the Indian Central Himalaya during last ~4,000 years inferred from a speleothem record: Impact of Indian Summer Monsoon (ISM) and Westerlies: Quaternary International, v. 371, p. 244-253.

Koymans, M. R., Langereis, C. G., Pastor-Galán, D., and van Hinsbergen, D. J., 2016, Paleomagnetism. org: an online multi-platform open source environment for paleomagnetic data analysis: Computers & Geosciences, v. 93, p. 127-137.

Kudrass, H., Hofmann, A., Doose, H., Emeis, K., and Erlenkeuser, H., 2001, Modulation and amplification of climatic changes in the Northern Hemisphere by the Indian summer monsoon during the past 80 ky: Geology, v. 29, no. 1, p. 63-66.

Kuiper, K., Deino, A., Hilgen, F., Krijgsman, W., Renne, P., and Wijbrans, J., 2008, Synchronizing rock clocks of Earth history: science, v. 320, no. 5875, p. 500-504.

Kumar, R., Ghosh, S. K., Mazari, R., and Sangode, S., 2003, Tectonic impact on the fluvial deposits of Plio-Pleistocene Himalayan foreland basin, India: Sedimentary Geology, v. 158, no. 3, p. 209-234.

Kumar, R., Sangode, S. J., and Ghosh, S. K., 2004, A multistorey sandstone complex in the Himalayan Foreland Basin, NW Himalaya, India: Journal of Asian Earth Sciences, v. 23, no. 3, p. 407-426.

Kumar, S., Wesnousky, S. G., Rockwell, T. K., Briggs, R. W., Thakur, V. C., and Jayangondaperumal, R., 2006, Paleoseismic evidence of great surface rupture earthquakes along the Indian Himalaya: Journal of Geophysical Research: Solid Earth, v. 111, no. B3.

Lallier, F., Antoine, C., Charreau, J., Caumon, G., and Ruiu, J., 2013, Management of ambiguities in magnetostratigraphic correlation: Earth and Planetary Science Letters, v. 371, p. 26-36.

Lang, K. A., and Huntington, K. W., 2014, Antecedence of the Yarlung–Siang–Brahmaputra River, eastern Himalaya: Earth and Planetary Science Letters, v. 397, p. 145-158.

Lang, K. A., Huntington, K. W., Burmester, R., and Housen, B., 2016, Rapid exhumation of the eastern Himalayan syntaxis since the late Miocene: Geological Society of America Bulletin, no. B31419. 1.

Lang, K. A., Huntington, K. W., and Montgomery, D. R., 2013, Erosion of the Tsangpo Gorge by megafloods, eastern Himalaya: Geology, v. 41, no. 9, p. 1003-1006.

Lanphere, M. A., and Baadsgaard, H., 2001, Precise K–Ar, 40 Ar/39 Ar, Rb–Sr and U/Pb mineral ages from the 27.5 Ma Fish Canyon Tuff reference standard: Chemical Geology, v. 175, no. 3, p. 653-671.

Larsen, I. J., and Montgomery, D. R., 2012, Landslide erosion coupled to tectonics and river incision: Nature Geoscience, v. 5, no. 7, p. 468-473.

Lavé, J., Yule, D., Sapkota, S., Basant, K., Madden, C., Attal, M., and Pandey, R., 2005, Evidence for a great Medieval earthquake (~1100 AD) in the central Himalayas, Nepal: Science, v. 307, no. 5713, p. 1302-1305.

Le Fort, P., 1975, Himalayas: the collided range. Present knowledge of the continental arc: American Journal of Science, v. 275, no. 1, p. 44.

Le Fort, P., 1996, Evolution of the Himalaya., *in* Yin, A. a. H., T.M., ed., The tectonic Evolution of Asia, Cambridge University Press, p. 95-109.

Le Fort, P., 1999, Lesser Himalayan crystalline nappes of Nepal: Problems of their origin: Himalaya and Tibet: mountain roots to mountain tops, v. 328, p. 225.

Le Fort, P., Cuney, M., Deniel, C., France-Lanord, C., Sheppard, S. M. F., Upreti, B. N., and Vidal, P., 1987, Crustal Generation of the Himalayan Leucogranites: Tectonophysics, v. 134, no. 1-3, p. 39-57.

Le Fort, P., Tongiorgi, M., and Gaetani, M., 1994, Discovery of a crystalline basement and Early Ordovician marine transgression in the Karakorum mountain range, Pakistan: Geology, v. 22, no. 10, p. 941-944.

Le Pichon, X., Fournier, M., and Jolivet, L., 1992, Kinematics, topography, shortening, and extrusion in the India-Eurasia collision: Tectonics, v. 11, no. 6, p. 1085-1098.

Lee, H.-Y., Chung, S.-L., Wang, J.-R., Wen, D.-J., Lo, C.-H., Yang, T. F., Zhang, Y., Xie, Y., Lee, T.-Y., and Wu, G., 2003, Miocene Jiali faulting and its implications for Tibetan tectonic evolution: Earth and Planetary Science Letters, v. 205, no. 3, p. 185-194.

Lee, H., Chung, S., Wang, Y., Zhu, D., Yan, J., Song, B., and Liu, D., 2007, Age, Petrogenesis and Geological Significance of the Linzizong Volcanic Successions in the Linzhou Basin, Southern Tibet: Evidence from Zircon U–Pb Dates and Hf Isotopes, Volume 23, Acta Petrologica Sinica, p. 493-500.

Liang, Y.-H., Chung, S.-L., Liu, D., Xu, Y., Wu, F.-Y., Yang, J.-H., Wang, Y., and Lo, C.-H., 2008, Detrital zircon evidence from Burma for reorganization of the eastern Himalayan river system: American Journal of Science, v. 308, no. 4, p. 618-638.

Licht, A., France-Lanord, C., Reisberg, L., Fontaine, C., Soe, A. N., and Jaeger, J.-J., 2013, A palaeo Tibet–Myanmar connection? Reconstructing the Late Eocene drainage system of central Myanmar using a multi-proxy approach: Journal of the Geological Society, v. 170, no. 6, p. 929-939.

Licht, A., Van Cappelle, M., Abels, H., Ladant, J.-B., Trabucho-Alexandre, J., France-Lanord, C., Donnadieu, Y., Vandenberghe, J., Rigaudier, T., and Lécuyer, C., 2014, Asian monsoons in a late Eocene greenhouse world: Nature, v. 513, no. 7519, p. 501-506.

Lin, T. H., Chung, S. L., Kumar, A., Wu, F. Y., Chiu, H. Y., and Lin, I., 2013, Linking a prolonged Neo-Tethyan magmatic arc in South Asia: Zircon U-Pb and Hf isotopic constraints from the Lohit Batholith, NE India: Terra Nova, v. 25, no. 6, p. 453-458.

Long, S., McQuarrie, N., Tobgay, T., Grujic, D., and Hollister, L., 2011, Geologic map of Bhutan: Journal of Maps, v. 7, no. 1, p. 184-192.

Lowick, S. E., Trauerstein, M., and Preusser, F., 2012, Testing the application of post IR-IRSL dating to fine grain waterlain sediments: Quaternary Geochronology, v. 8, p. 33-40.

Ludwig, K. R., 2003, User's manual for Isoplot 3.00: a geochronological toolkit for Microsoft Excel, Kenneth R. Ludwig, v. 4.

Luirei, K., and Bhakuni, S., 2008, Ground tilting in Likhabali area along the frontal part of Arunachal Himalaya: Evidence of neotectonics: Journal of the Geological Society of India, v. 71, no. 6, p. 780-786.

Luvizotto, G., Zack, T., Meyer, H., Ludwig, T., Triebold, S., Kronz, A., Münker, C., Stockli, D., Prowatke, S., and Klemme, S., 2009, Rutile crystals as potential trace element and isotope mineral standards for microanalysis: Chemical Geology, v. 261, no. 3, p. 346-369.

Mahéo, G., Bertrand, H., Guillot, S., Mascle, G., Pêcher, A., Picard, C., and De Sigoyer, J., 2000, Evidence of a Tethyan immature arc within the South Ladakh ophiolites (NW Himalaya, India): Comptes Rendus de l'Academie des Sciences Series IIA Earth and Planetary Science, v. 330, no. 4, p. 289-295.

Maheo, G., Fayoux, X., Guillot, S., Garzanti, E., Capiez, P., and Mascle, G., 2006, Relicts of an intra-oceanic arc in the Sapi-Shergol melange zone (Ladakh, NW Himalaya, India): implications for the closure of the Neo-Tethys Ocean: Journal of Asian Earth Sciences, v. 26, no. 6, p. 695-707.

Mallet, F., 1876, On the Coal-fields of the Naga Hills Bordering the Lakhimpur and Sibsagar Districts, Assam, Geological Survey of India.

Malusà, M. G., Carter, A., Limoncelli, M., Villa, I. M., and Garzanti, E., 2013, Bias in detrital zircon geochronology and thermochronometry: Chemical Geology, v. 359, p. 90-107.

Malusà, M. G., Resentini, A., and Garzanti, E., 2016, Hydraulic sorting and mineral fertility bias in detrital geochronology: Gondwana Research, v. 31, p. 1-19.

Mark, C., Cogné, N., and Chew, D., 2016, Tracking exhumation and drainage divide migration of the Western Alps: A test of the apatite U-Pb thermochronometer as a detrital provenance tool: Geological Society of America Bulletin, v. 128, p. 1439–1460.

Marone, C., 1998, Laboratory-derived friction laws and their application to seismic faulting: Annual Review of Earth and Planetary Sciences, v. 26, no. 1, p. 643-696.

Marshall, J. D., 2000, Sedimentology of a Devonian fault-bounded braidplain and lacustrine fill in the lower part of the Skrinkle Sandstones, Dyfed, Wales: Sedimentology, v. 47, no. 2, p. 325-342.

Mascle, G., Pêcher, A., and Guillot, S., 2010, Himalaya-Tibet: la collision continental Inde-Eurasie, Vuibert.

Maurin, T., and Rangin, C., 2009, Structure and kinematics of the Indo-Burmese Wedge: Recent and fast growth of the outer wedge: Tectonics, v. 28, no. 2.

Mazurek, M., Hurford, A. J., and Leu, W., 2006, Unravelling the multi-stage burial history of the Swiss Molasse Basin: integration of apatite fission track, vitrinite reflectance and biomarker isomerisation analysis: Basin Research, v. 18, no. 1, p. 27-50.

McCormick, D. S., and Grotzinger, J. P., 1993, Distinction of marine from alluvial Facies in the Paleoproterozoic (1.9 Ga) burnside formation, Kilohigok basin, NWT, Canada: Journal of Sedimentary Research, v. 63, no. 3.

McDougall, I., and Harrison, T. M., 1999, Geochronology and Thermochronology by the 40Ar/39Ar Method, Oxford University Press, 288 p.:

McDowell, F. W., McIntosh, W. C., and Farley, K. A., 2005, A precise 40 Ar–39 Ar reference age for the Durango apatite (U–Th)/He and fission-track dating standard: Chemical Geology, v. 214, no. 3, p. 249-263.

McFadden, P., and McElhinny, M., 1988, The combined analysis of remagnetization circles and direct observations in palaeomagnetism: Earth and Planetary Science Letters, v. 87, no. 1, p. 161-172.

McQuarrie, N., and Ehlers, T. A., 2015, Influence of thrust belt geometry and shortening rate on thermochronometer cooling ages: Insights from thermokinematic and erosion modeling of the Bhutan Himalaya: Tectonics, v. 34, no. 6, p. 1055-1079.

Mehrotra, R., Awasthi, N., and Dutta, S., 1999, Study of fossil wood from the Upper Tertiary sediments (Siwalik) of Arunachal Pradesh, India and its implication in palaeoecological and phytogeographical interpretations: Review of Palaeobotany and Palynology, v. 107, no. 3, p. 223-247.

Meigs, A. J., Burbank, D. W., and Beck, R. A., 1995, Middle-late Miocene (>10 Ma) formation of the Main Boundary thrust in the western Himalaya: Geology, v. 23, no. 5, p. 423-426.

Metcalfe, I., 1996, Gondwanaland dispersion, Asian accretion and evolution of eastern Tethys∗: Australian Journal of Earth Sciences, v. 43, no. 6, p. 605-623.

Mezger, K., Hanson, G., and Bohlen, S., 1989, High-precision UPb ages of metamorphic rutile: application to the cooling history of high-grade terranes: Earth and Planetary Science Letters, v. 96, no. 1-2, p. 106-118.

Miall, A. D., 1977, A review of the braided-river depositional environment: Earth-Science Reviews, v. 13, no. 1, p. 1-62.

Miall, A. D., 1985, Architectural-element analysis: a new method of facies analysis applied to fluvial deposits: Earth-Science Reviews, v. 22, no. 4, p. 261-308.

Miller, D. S., Duddy, I. R., Green, P. F., Hurford, A. J., and Naeser, C. W., 1985, Results of interlaboratory comparison of fission-track age standards: fission-track workshop—1984: Nuclear Tracks and Radiation Measurements (1982), v. 10, no. 3, p. 383-391.

Miller, K. G., Kominz, M. A., Browning, J. V., Wright, J. D., Mountain, G. S., Katz, M. E., Sugarman, P. J., Cramer, B. S., Christie-Blick, N., and Pekar, S. F., 2005, The Phanerozoic record of global sea-level change: science, v. 310, no. 5752, p. 1293-1298.

Mitra, S., and Mitra, S., 2001, Tectonic setting of the Precambrian of the north-eastern India (Meghalaya Plateau) and age of the Shillong Group of rocks: Geological Survey of India Special Publication 64, p. 653-658.

Mitra, S., Priestley, K., Bhattacharyya, A. K., and Gaur, V., 2005, Crustal structure and earthquake focal depths beneath northeastern India and southern Tibet: Geophysical Journal International, v. 160, no. 1, p. 227-248.

Mo, X., Hou, Z., Niu, Y., Dong, G., Qu, X., Zhao, Z., and Yang, Z., 2007, Mantle contributions to crustal thickening during continental collision: evidence from Cenozoic igneous rocks in southern Tibet: Lithos, v. 96, no. 1, p. 225-242.

Molnar, P., 1984, Structure and Tectonics of the Himalaya: Constraints and Implications of Geophysical Data: Annual Review of Earth and Planetary Sciences, v. 12.

Molnar, P., 2005, Mio-Pliocene growth of the Tibetan Plateau and evolution of East Asian climate: Palaeontologia Electronica, v. 8, no. 1, p. 1-23.

Molnar, P., 2009, The state of interactions among tectonics, erosion, and climate: A polemic: GSA Today, v. 19, no. 7, p. 44-45.

Molnar, P., Boos, W. R., and Battisti, D. S., 2010, Orographic controls on climate and paleoclimate of Asia: thermal and mechanical roles for the Tibetan Plateau: Annual Review of Earth and Planetary Sciences, v. 38, p. 77-102.

Molnar, P., and England, P., 1990, Late Cenozoic uplift of mountain ranges and global climate change: chicken or egg?: Nature, v. 346, no. 6279, p. 29-34.

Molnar, P., and Stock, J. M., 2009, Slowing of India's convergence with Eurasia since 20 Ma and its implications for Tibetan mantle dynamics: Tectonics, v. 28, no. 3.

Molnar, P., and Tapponnier, P., 1975, Cenozoic tectonics of Asia: effects of a continental collision: science, v. 189, no. 4201, p. 419-426.

Monga, P., Kumar, M., Prasad, V., and Joshi, Y., 2015, Palynostratigraphy, palynofacies and depositional environment of a lignite-bearing succession at Surkha Mine, Cambay Basin, north-western India: Acta Palaeobotanica, v. 55, no. 2, p. 183-207.

More, S., Paruya, D. K., Taral, S., Chakraborty, T., and Bera, S., 2016, Depositional Environment of Mio-Pliocene Siwalik Sedimentary Strata from the Darjeeling Himalayan Foothills, India: A Palynological Approach: PloS one, v. 11, no. 3, p. e0150168.

Morley, R., 1991, Tertiary stratigraphic palynology in Southeast Asia: current status and new directions: Bull. Geol. Soc. Malaysia, v. 28, p. 1-36.

Morton, A. C., and Hallsworth, C. R., 1999, Processes controlling the composition of heavy mineral assemblages in sandstones: Sedimentary Geology, v. 124, no. 1, p. 3-29.

Mugnier, J.-L., Chalaron, E., Mascle, G., Pradier, B., and Herail, G., 1995, Structural and thermal evolution of the Siwaliks of western Nepal: Journal of Nepal Geological Society, v. 11, p. 171-178.

Mugnier, J.-L., Gajurel, A., Huyghe, P., Jayangondaperumal, R., Jouanne, F., and Upreti, B., 2013, Structural interpretation of the great earthquakes of the last millennium in the central Himalaya: Earth-Science Reviews, v. 127, p. 30-47.

Mugnier, J.-L., Huyghe, P., Leturmy, P., and Jouanne, F., 2004, Episodicity and rates of thrust-sheet motion in the Himalayas (western Nepal): Thrust Tectonics and Petroleum Systems (Ed. by K.C. McClay), Am. Assoc. Petr. Geol. Memoir., v. 82, p. 1-24.

Murray, A. S., and Wintle, A. G., 2000, Luminescence dating of quartz using an improved single-aliquot regenerative-dose protocol: Radiation measurements, v. 32, no. 1, p. 57-73.

Murray, A. S., and Wintle, A. G., 2003, The single aliquot regenerative dose protocol: potential for improvements in reliability: Radiation measurements, v. 37, no. 4, p. 377-381.

Myrow, P., Lukens, C., Lamb, M., Houck, K., and Strauss, J., 2008, Dynamics of a transgressive prodeltaic system: Implications for geography and climate within a Pennsylvanian intracratonic basin, Colorado, USA: Journal of Sedimentary Research, v. 78, no. 8, p. 512-528.

Myrow, P. M., Hughes, N. C., Paulsen, T. S., Willlams, I. S., Parcha, S. K., Thompson, K. R., Bowring, S. A., Peng, S. C., and Ahluwalia, A. D., 2003, Integrated tectonostratigraphic analysis of the Himalaya and implications tor its tectonic reconstruction: Earth and Planetary Science Letters, v. 212, no. 3-4, p. 433-441.

Nábělek, J., Hetényi, G., Vergne, J., Sapkota, S., Kafle, B., Jiang, M., Su, H., Chen, J., and Huang, B.-S., 2009, Underplating in the Himalaya-Tibet collision zone revealed by the Hi-CLIMB experiment: Science, v. 325, no. 5946, p. 1371-1374.

Naeser, N. D., Zeitler, P. K., Naeser, C. W., and Cerveny, P. F., 1987, Provenance studies by fission-track dating of zircon-etching and counting procedures: International Journal of Radiation Applications and Instrumentation. Part D. Nuclear Tracks and Radiation Measurements, v. 13, no. 2, p. 121-126.

Najman, Y., 2006, The detrital record of orogenesis: A review of approaches and techniques used in the Himalayan sedimentary basins: Earth-Science Reviews, v. 74, no. 1, p. 1-72.

Najman, Y., 2007, Comment on “Biochronological continuity of the paleogene sediments of the Himalayan foreland basin: Paleontological and other evidences”–Bhatia, SB & Bhargava ON, 2006, JAES 26, 477–487: Journal of Asian Earth Sciences, v. 30, no. 2, p. 417-421.

Najman, Y., Allen, R., Willett, E., Carter, A., Barfod, D., Garzanti, E., Wijbrans, J., Bickle, M., Vezzoli, G., and Ando, S., 2012, The record of Himalayan erosion preserved in the sedimentary rocks of the Hatia Trough of the Bengal Basin and the Chittagong Hill Tracts, Bangladesh: Basin Research, v. 24, no. 5, p. 499-519.

Najman, Y., Appel, E., Boudagher-Fadel, M., Bown, P., Carter, A., Garzanti, E., Godin, L., Han, J., Liebke, U., and Oliver, G., 2010, Timing of India-Asia collision: Geological, biostratigraphic, and palaeomagnetic constraints: Journal of Geophysical Research: Solid Earth, v. 115, no. B12.

Najman, Y., Bracciali, L., Parrish, R. R., Chisty, E., and Copley, A., 2016, Evolving strain partitioning in the Eastern Himalaya: The growth of the Shillong Plateau: Earth and Planetary Science Letters, v. 433, p. 1-9.

Najman, Y., Jenks, D., Godin, L., Boudagher-Fadel, M., Millar, I., Garzanti, E., Horstwood, M., and Bracciali, L., 2017, The Tethyan Himalayan detrital record shows that India–Asia terminal collision occurred by 54 Ma in the Western Himalaya: Earth and Planetary Science Letters, v. 459, p. 301-310.

Najman, Y., Pringle, M., Godin, L., and Oliver, G., 2001, Dating of the oldest continental sediments from the Himalayan foreland basin: Nature, v. 410, no. 6825, p. 194-197.

Najman, Y., Pringle, M. S., Johnson, M. R. W., Robertson, A. H. F., and Wijbrans, J. R., 1997, Laser Ar-40/Ar-39 dating of single detrital muscovite grains from early foreland-basin sedimentary deposits in India: Implications for early Himalayan evolution: Geology, v. 25, no. 6, p. 535-538.

Nakayama, K., and Ulak, P. D., 1999, Evolution of fluvial style in the Siwalik Group in the foothills of the Nepal Himalaya: Sedimentary Geology, v. 125, no. 3, p. 205-224.

Neymark, L. A., and Amelin, Y. V., 2008, Natural radionuclide mobility and its influence on U-Th-Pb dating of secondary minerals from the unsaturated zone at Yucca Mountain, Nevada: Geochimica et Cosmochimica Acta, v. 72, no. 8, p. 2067-2089.

Oberlander, T., 1985, Origin of drainage transverse to structures in orogens, *in* Morisawa, M., and Hack, J. T., eds., Tectonic Geomorphology, the Binghampton Symposia in Geomorphology, Volume 15, p. 155-182.

Ojha, T., Butler, R., DeCelles, P. G., and Quade, J., 2009, Magnetic polarity stratigraphy of the Neogene foreland basin deposits of Nepal: Basin Research, v. 21, no. 1, p. 61-90.

Ojha, T., Butler, R., Quade, J., DeCelles, P. G., Richards, D., and Upreti, B., 2000, Magnetic polarity stratigraphy of the Neogene Siwalik Group at Khutia Khola, far western Nepal: Geological Society of America Bulletin, v. 112, no. 3, p. 424-434.

Olariu, C., and Bhattacharya, J. P., 2006, Terminal distributary channels and delta front architecture of river-dominated delta systems: Journal of sedimentary research, v. 76, no. 2, p. 212-233.

Oldham, R. D., 1899, Report of the great earthquake of 12th June, 1897, Office of the Geological survey.

Oliver, G. J. H., Johnson, M. R. W., and Fallick, A. E., 1995, Age of Metamorphism in the Lesser Himalaya and the Main Central Thrust Zone, Garhwal India - Results of Illite Crystallinity, Ar-40-Ar-39 Fusion and K-Ar Studies: Geological Magazine, v. 132, no. 2, p. 139-149.

Oskin, M., and Burbank, D. W., 2005, Alpine landscape evolution dominated by cirque retreat: Geology, v. 33, no. 12, p. 933-936.

Paces, J. B., and Miller, J. D., 1993, Precise U-Pb ages of Duluth complex and related mafic intrusions, northeastern Minnesota: Geochronological insights to physical, petrogenetic, paleomagnetic, and tectonomagmatic processes associated with the 1.1 Ga midcontinent rift system: Journal of Geophysical Research: Solid Earth, v. 98, no. B8, p. 13997-14013.

Pagani, M., Zachos, J. C., Freeman, K. H., Tipple, B., and Bohaty, S., 2005, Marked decline in atmospheric carbon dioxide concentrations during the Paleogene: Science, v. 309, no. 5734, p. 600-603.

Palin, R., Searle, M., St-Onge, M., Waters, D., Roberts, N., Horstwood, M., Parrish, R., and Weller, O., 2015, Two-stage cooling history of pelitic and semi-pelitic mylonite (sensu lato) from the Dongjiu–Milin shear zone, northwest flank of the eastern Himalayan syntaxis: Gondwana Research, v. 28, no. 2, p. 509-530.

Palin, R., Searle, M., St-Onge, M., Waters, D., Roberts, N., Horstwood, M., Parrish, R., Weller, O., Chen, S., and Yang, J., 2014, Monazite geochronology and petrology of kyanite-and sillimanite-grade migmatites from the northwestern flank of the eastern Himalayan syntaxis: Gondwana Research, v. 26, no. 1, p. 323-347.

Parrish, R. R., and Hodges, K. V., 1996, Isotopic constraints on the age and provenance of the Lesser and Greater Himalayan sequences, Nepalese Himalaya: Geological Society of America Bulletin, v. 108, no. 7, p. 904-911.

Patriat, P., and Achache, J., 1984, India–Eurasia collision chronology has implications for crustal shortening and driving mechanism of plates: Nature, v. 311, p. 615-621.

Plink-Björklund, P., and Steel, R., 2006, Deltas on falling-stage and lowstand shelf margins, the Eocene Central Basin of Spitsbergen: importance of sediment supply, *in* Giosan, L., and Bhattacharya, J., eds., River Delta - Concepts, Models, and Examples, SEPM Spec. Publ., p. 179-206.

Powell, C. M., and Conaghan, P., 1973, Plate tectonics and the Himalayas: Earth and Planetary Science Letters, v. 20, no. 1, p. 1-12.

Preusser, F., and Kasper, H. U., 2001, Comparison of dose rate determination using high-resolution gamma spectrometry and inductively coupled plasma-mass spectrometry: Ancient tL, v. 19, no. 1, p. 19-23.

Prince, C. I., Foster, G., Vance, D., Harris, N., and Baker, J., 1999, The thermochronology of the High Himalayan Crystallines in the Garhwal Himalaya; prograde history of a polymetamorphic slab.: Terra Nostra, v. 99/2, p. 119-120.

Puigdefàbregas, C., Muñoz, J., and Marzo, M., 1986, Thrust belt development in the eastern Pyrenees and related depositional sequences in the southern foreland basin, *in* Allen, P., and Homewood, P., eds., Foreland basins, Spec. Publ.: Oxford, Int. Assoc. of Sedimentology, p. 229-246.

Quade, J., Cater, J. M., Ojha, T. P., Adam, J., and Harrison, T. M., 1995a, Late Miocene environmental change in Nepal and the northern Indian subcontinent: Stable isotopic evidence from paleosols: Geological Society of America Bulletin, v. 107, no. 12, p. 1381-1397.

Quade, J., and Cerling, T. E., 1995, Expansion of C 4 grasses in the Late Miocene of Northern Pakistan: evidence from stable isotopes in paleosols: Palaeogeography, Palaeoclimatology, Palaeoecology, v. 115, no. 1, p. 91-116.

Quade, J., Cerling, T. E., Andrews, P., and Alpagut, B., 1995b, Paleodietary reconstruction of Miocene faunas from Paşalar, Turkey using stable carbon and oxygen isotopes of fossil tooth enamel: Journal of Human Evolution, v. 28, no. 4, p. 373-384.

Quade, J., Cerling, T. E., and Bowman, J. R., 1989, Development of Asian monsoon revealed by marked ecological shift during the latest Miocene in northern Pakistan: Nature, v. 342, no. 6246, p. 163-166.

Quade, J., Solounias, N., and Cerling, T. E., 1994, Stable isotopic evidence from paleosol carbonates and fossil teeth in Greece for forest or woodlands over the past 11 Ma: Palaeogeography, Palaeoclimatology, Palaeoecology, v. 108, no. 1-2, p. 41-53.

Radke, J., Bechtel, A., Gaupp, R., Püttmann, W., Schwark, L., Sachse, D., and Gleixner, G., 2005, Correlation between hydrogen isotope ratios of lipid biomarkers and sediment maturity: Geochimica et Cosmochimica Acta, v. 69, no. 23, p. 5517-5530.

Rahn, M. K., Brandon, M. T., Batt, G. E., and Garver, J. I., 2004, A zero-damage model for fission-track annealing in zircon: American Mineralogist, v. 89, no. 4, p. 473-484.

Rajendran, C., Rajendran, K., Duarah, B., Baruah, S., and Earnest, A., 2004, Interpreting the style of faulting and paleoseismicity associated with the 1897 Shillong, northeast India, earthquake: Implications for regional tectonism: Tectonics, v. 23, no. 4.

Ramos, A., and Sopeña, A., 1983, Gravel Bars in Low-Sinuosity Streams (Permian and Triassic, Central Spain): Modern and ancient fluvial systems, p. 301-312.

Rao, M. R., 1973, The subsurface geology of the Indo-Gangetic plains: Geological Society of India, v. 14, no. 3, p. 217-242.

Rath, S., Singh, S., and SARMA, S., 1997, Hydrocarbon prospects of the poorly explored north bank of Brahmaputra, north east India: Journal of Association of Exploration Geophysicists, v. 18, no. 3, p. 159-164.

Raymo, M., and Ruddiman, W. F., 1992, Tectonic forcing of late Cenozoic climate: Nature, v. 359, no. 6391, p. 117-122.

Reimann, K.-U., and Hiller, K., 1993, Geology of Bangladesh, Berlin, Borntraeger, 160 p.:

Reiners, P. W., and Brandon, M. T., 2006, Using thermochronology to understand orogenic erosion: Annu. Rev. Earth Planet. Sci., v. 34, p. 419-466.

Reiners, P. W., Ehlers, T. A., Mitchell, S. G., and Montgomery, D. R., 2003, Coupled spatial variations in precipitation and long-term erosion rates across the Washington Cascades: Nature, v. 426, no. 6967, p. 645-647.

Renne, P. R., Swisher, C. C., Deino, A. L., Karner, D. B., Owens, T. L., and DePaolo, D. J., 1998, Intercalibration of standards, absolute ages and uncertainties in 40 Ar/39 Ar dating: Chemical Geology, v. 145, no. 1, p. 117-152.

Replumaz, A., and Tapponnier, P., 2003, Reconstruction of the deformed collision zone between India and Asia by backward motion of lithospheric blocks: Journal of Geophysical Research: Solid Earth, v. 108, no. B6.

Retallack, G. J., 1988, Field recognition of paleosols: Geological Society of America Special Papers, v. 216, p. 1-20.

Reuber, I., 1989, The Dras Arc - 2 Successive Volcanic Events on Eroded Oceanic- Crust: Tectonophysics, v. 161, no. 1-2, p. 93-106.

Reuber, I., Colchen, M., and Mevel, C., 1987, The geodynamic evolution of the South-Tethyan, margin in Zanskar, NW-Himalaya, as revealed by the Spongtang ophiolitic melanges: Geodinamica Acta, v. 1, no. 4-5, p. 283-296.

Richards, A., Argles, T. W. A., Harris, N. B. W., Parrish, R. R., Ahmad, T., Darbeyshire, F., and Draganits, E., 2005, Himalayan architecture constrained by isotopic tracers from clastic sediments: Earth and Planetary Science Letters, v. 236, p. 773-796.

Riedel, J., Haugerud, R., and Clague, J., 2007, Geomorphology of a Cordilleran Ice Sheet drainage network through breached divides in the North Cascades Mountains of Washington and British Columbia: Geomorphology, v. 91, no. 1, p. 1-18.

Robert, X., 2008, Séquence d'activité des failles et dynamique du prisme himalayen: apports de la thermochronologie et de la modélisation numérique: Université Joseph-Fourier-Grenoble I.

Robert, X., van der Beek, P., Braun, J., Perry, C., and Mugnier, J. L., 2011, Control of detachment geometry on lateral variations in exhumation rates in the Himalaya: Insights from low-temperature thermochronology and numerical modeling: Journal of Geophysical Research: Solid Earth, v. 116, no. B5.

Roberts, M. P., and Finger, F., 1997, Do U-Pb zircon ages from granulites reflect peak metamorphic conditions?: Geology, v. 25, no. 4, p. 319-322.

Robertson, A., 2000, Formation of melanges in the Indus suture zone, Ladakh Himalaya by successive subduction-related, collisional and post-collisional processes during late Mesozoic-late Tertiary time: Geological Society, London, Special Publications, v. 170, no. 1, p. 333-374.

Robertson, A., and Degnan, P., 1994, The Dras Arc Complex - Lithofacies and Reconstruction of a Late Cretaceous Oceanic Volcanic Arc in the Indus Suture Zone, Ladakh-Himalaya: Sedimentary Geology, v. 92, no. 1-2, p. 117-145.

Robertson, A. H. F., and Collins, A. S., 2002, Shyok Suture Zone, N Pakistan: late Mesozoic-Tertiary evolution of a critical suture separating the oceanic Ladakh Arc from the Asian continental margin: Journal of Asian Earth Sciences, v. 20, no. 3, p. 309-351.

Robinson, R. A., Brezina, C. A., Parrish, R. R., Horstwood, M. S., Oo, N. W., Bird, M. I., Thein, M., Walters, A. S., Oliver, G. J., and Zaw, K., 2014, Large rivers and orogens: The evolution of the Yarlung Tsangpo–Irrawaddy system and the eastern Himalayan syntaxis: Gondwana Research, v. 26, no. 1, p. 112-121.

Roden, M. K., Parrish, R. R., and Miller, D. S., 1990, The absolute age of the Eifelian Tioga ash bed, Pennsylvania: The Journal of Geology, p. 282-285.

Roe, G. H., 2005, Orographic precipitation: Annu. Rev. Earth Planet. Sci., v. 33, p. 645-671.

Rolland, Y., Pêcher, A., and Picard, C., 2000, Middle Cretaceous back-arc formation and arc evolution along the Asian margin: the Shyok Suture Zone in northern Ladakh (NW Himalaya): Tectonophysics, v. 325, no. 1-2, p. 145-173.

Rolland, Y., Picard, C., Pêcher, A., Carrio, E., Sheppard, S. M., Oddone, M., and Villa, I. M., 2002a, Presence and geodynamic significance of Cambro-Ordovician series of SE Karakoram (N Pakistan): Geodinamica Acta, v. 15, no. 1, p. 1-21.

Rolland, Y., Picard, C., Pecher, A., Lapierre, H., Bosch, D., and Keller, F., 2002b, The cretaceous Ladakh arc of NW himalaya-slab melting and melt-mantle interaction during fast northward drift of Indian Plate: Chemical Geology, v. 182, no. 2-4, p. 139-178.

Rowley, D. B., 1996, Age of initiation of collision between India and Asia: A review of stratigraphic data: Earth and Planetary Science Letters, v. 145, no. 1, p. 1-13.

Royden, L., Clark, M., Whipple, K., and Burchfiel, B., 2000, River incision and capture related to tectonics of the eastern Himalayan Syntaxis: Eos, Transactions of the American Geophysical Union, v. 81, p. S413.

Sachse, D., Billault, I., Bowen, G. J., Chikaraishi, Y., Dawson, T. E., Feakins, S. J., Freeman, K. H., Magill, C. R., McInerney, F. A., and Van der Meer, M. T., 2012, Molecular paleohydrology: interpreting the hydrogen-isotopic composition of lipid biomarkers from photosynthesizing organisms: Annual Review of Earth and Planetary Sciences, v. 40, p. 221-249.

Sambridge, M., 1999, Geophysical inversion with a neighbourhood algorithm—II. Appraising the ensemble: Geophysical Journal International, v. 138, no. 3, p. 727-746.

Sangode, S., Kumar, R., and Ghosh, S. K., 1996, Magnetic polarity stratigraphy of the Siwalik sequence of Haripur area (HP), NW Himalaya: Geological Society of India, v. 47, no. 6, p. 683-704.

Sanyal, P., Bhattacharya, S., Kumar, R., Ghosh, S., and Sangode, S., 2004, Mio–Pliocene monsoonal record from Himalayan foreland basin (Indian Siwalik) and its relation to vegetational change: Palaeogeography, Palaeoclimatology, Palaeoecology, v. 205, no. 1, p. 23-41.

Sanyal, P., Sarkar, A., Bhattacharya, S., Kumar, R., Ghosh, S., and Agrawal, S., 2010, Intensification of monsoon, microclimate and asynchronous C 4 appearance: isotopic evidence from the Indian Siwalik sediments: Palaeogeography, Palaeoclimatology, Palaeoecology, v. 296, no. 1, p. 165-173.

Saylor, J. E., and Sundell, K. E., 2016, Quantifying comparison of large detrital geochronology data sets: Geosphere, p. GES01237. 01231.

Schärer, U., Xu, R.-H., and Allègre, C. J., 1984, UPb geochronology of Gangdese (Transhimalaya) plutonism in the Lhasa-Xigaze region, Tibet: Earth and Planetary Science Letters, v. 69, no. 2, p. 311-320.

Schlunegger, F., Jordan, T. E., and Klaper, E. M., 1997, Controls of erosional denudation in the orogen on foreland basin evolution: the Oligocene central Swiss Molasse Basin as an example: Tectonics, v. 16, no. 5, p. 823-840.

Schmitz, M. D., and Bowring, S. A., 2003, Constraints on the thermal evolution of continental lithosphere from U-Pb accessory mineral thermochronometry of lower crustal xenoliths, southern Africa: Contributions to Mineralogy and Petrology, v. 144, no. 5, p. 592-618.

Schoene, B., and Bowring, S. A., 2006, U–Pb systematics of the McClure Mountain syenite: thermochronological constraints on the age of the 40Ar/39Ar standard MMhb: Contributions to Mineralogy and Petrology, v. 151, no. 5, p. 615-630.

Schulte-Pelkum, V., Monsalve, G., Sheehan, A., Pandey, M., Sapkota, S., Bilham, R., and Wu, F., 2005, Imaging the Indian subcontinent beneath the Himalaya: Nature, v. 435, no. 7046, p. 1222-1225.

Searle, M. P., Cooper, D. J. W., and Rex, A. J., 1988, Collision tectonics of the Ladakh-Zanskar Himalaya., *in* Shackleton, R. M., Dewey, J.F., Windley, B.F., ed., Tectonic Evolution of the Himalayas and Tibet., Volume A 326, Philosophical Transactions of the Royal Society of London, p. 117-150.

Searle, M. P., Parrish, R. R., Hodges, K. V., Hurford, A., Ayres, M. W., and Whitehouse, M. J., 1997, Shisha Pangma leucogranite, south Tibetan Himalaya: Field relations, geochemistry, age, origin, and emplacement: Journal of Geology, v. 105, no. 3, p. 295-317.

Searle, M. P., Pickering, K. T., and Cooper, D. J. W., 1990, Restoration and Evolution of the Intermontane Indus Molasse Basin, Ladakh Himalaya, India: Tectonophysics, v. 174, no. 3-4, p. 301-314.

Searle, M. P., Waters, D. J., Rex, D. C., and Wilson, R. N., 1992, Pressure, Temperature and Time Constraints on Himalayan Metamorphism from Eastern Kashmir and Western Zanskar: Journal of the Geological Society, v. 149, p. 753-773.

Seeber, L., and Armbruster, J. G., 1981, Great detachment earthquakes along the Himalayan Arc and long-term forecasting: Earthquake prediction, p. 259-277.

Seeber, L., and Gornitz, V., 1983, River profiles along the Himalayan arc as indicators of active tectonics: Tectonophysics, v. 92, no. 4, p. 335341-337367.

Selvam, A. P., Prasad, R., Raju, R. D., and Sinha, R., 1995, Rb-Sr Age of the Metaluminous Granitoids of South Khasi Batholith, Meghalaya: Implications on its Genesis and Pan-African Activity in Northeastern India: Geological Society of India, v. 46, no. 6, p. 619-624.

Seward, D., and Burg, J.-P., 2008, Growth of the Namche Barwa Syntaxis and associated evolution of the Tsangpo Gorge: Constraints from structural and thermochronological data: Tectonophysics, v. 451, no. 1, p. 282-289.

Shukla, U., Singh, I., Sharma, M., and Sharma, S., 2001, A model of alluvial megafan sedimentation: Ganga Megafan: Sedimentary Geology, v. 144, no. 3, p. 243-262.

Simpson, R. L., Parrish, R. R., Searle, M. P., and Waters, D. J., 2000, Two episodes of monazite crystallization during metamorphism and crustal melting in the Everest region of the Nepalese Himalaya: Geology, v. 28, no. 5, p. 403-406.

Sinclair, H., and Allen, P., 1992, Vertical versus horizontal motions in the Alpine orogenic wedge: stratigraphic response in the foreland basin: Basin Research, v. 4, no. 3-4, p. 215-232.

Singh, B., Lee, Y. I., Pawar, J., and Charak, R., 2007, Biogenic features in calcretes developed on mudstone: examples from Paleogene sequences of the Himalaya, India: Sedimentary Geology, v. 201, no. 1, p. 149-156.

Singh, C., Khanna, A., and Singh, S., 1998, Seismic velocities for effective planning of exploratory well in virgin area: a case from north bank areas of Upper Assam: Journal of geophysics, v. 19, no. 2, p. 101-107.

Singh, S., Awasthi, A., Parkash, B., and Kumar, S., 2013, Tectonics or climate: What drove the Miocene global expansion of C4 grasslands?: International Journal of Earth Sciences, v. 102, no. 7, p. 2019-2031.

Singh, S. K., and France-Lanord, C., 2002, Tracing the distribution of erosion in the Brahmaputra watershed from isotopic compositions of stream sediments: Earth and Planetary Science Letters, v. 202, no. 3, p. 645-662.

Singh, T., and Tripathi, S., 1989, Siwalik sediments of Arunachal Himalaya: Palynology, palaeoecology and palaeogeography.

Sláma, J., Košler, J., Condon, D. J., Crowley, J. L., Gerdes, A., Hanchar, J. M., Horstwood, M. S., Morris, G. A., Nasdala, L., and Norberg, N., 2008, Plešovice zircon—a new natural reference material for U–Pb and Hf isotopic microanalysis: Chemical Geology, v. 249, no. 1, p. 1-35.

Smye, A. J., and Stockli, D. F., 2014, Rutile U–Pb age depth profiling: a continuous record of lithospheric thermal evolution: Earth and Planetary Science Letters, v. 408, p. 171-182.

Srivastava, P., Bhakuni, S. S., Luirei, K., and Misra, D. K., 2009, Morpho-sedimentary records at the Brahmaputra River exit, NE Himalaya: climate–tectonic interplay during the Late Pleistocene–Holocene: Journal of Quaternary Science, v. 24, no. 2, p. 175-188.

Stacey, J. t., and Kramers, J., 1975, Approximation of terrestrial lead isotope evolution by a two-stage model: Earth and planetary science letters, v. 26, no. 2, p. 207-221.

Steiger, R. H., and Jäger, E., 1977, Subcommission on geochronology: convention on the use of decay constants in geo-and cosmochronology: Earth and planetary science letters, v. 36, no. 3, p. 359-362.

Steinke, S., Groeneveld, J., Johnstone, H., and Rendle-Bühring, R., 2010, East Asian summer monsoon weakening after 7.5 Ma: Evidence from combined planktonic foraminifera Mg/Ca and δ 18 O (ODP Site 1146; northern South China Sea): Palaeogeography, Palaeoclimatology, Palaeoecology, v. 289, no. 1, p. 33-43.

Stewart, R., Hallet, B., Zeitler, P., Malloy, M., Allen, C. M., and Trippett, D., 2008, Brahmaputra sediment flux dominated by highly localized rapid erosion from the easternmost Himalaya: Geology, v. 36, no. 9, p. 711-714.

Stockmal, G. S., Cant, D. J., and Bell, J. S., 1992, Relationship of the Stratigraphy of the Western Canada Foreland Basin to Cordilleran Tectonics: Insights from Geodynamic Models: Am. Assoc. Pet. Geol. Mem., v. 55, p. 107-124.

Stokes, M., Mather, A. E., Belfoul, A., and Farik, F., 2008, Active and passive tectonic controls for transverse drainage and river gorge development in a collisional mountain belt (Dades Gorges, High Atlas Mountains, Morocco): Geomorphology, v. 102, no. 1, p. 2-20.

Strecker, M. R., Hilley, G. E., Bookhagen, B., and Sobel, E. R., 2011, Structural, geomorphic, and depositional characteristics of contiguous and broken foreland basins: examples from the eastern flanks of the central Andes in Bolivia and NW Argentina, *in* Busby, J. C., and Azor, A., eds., Tectonics of Sedimentary Basins: Recent Advances: Oxford, U. K., Blackwell, p. 508-521.

Suresh, N., Ghosh, S. K., Kumar, R., and Sangode, S., 2004, Clay-mineral distribution patterns in late Neogene fluvial sediments of the Subathu sub-basin, central sector of Himalayan foreland basin: implications for provenance and climate: Sedimentary Geology, v. 163, no. 3, p. 265-278.

Sutre, E., 1990, Les formations de la marge nord-Neotethsieene et les melanges ophiolitic de la zone de suture de l'Indus en Himalaya du Ladakh.: Universite de Poiters.

Szulc, A. G., Najman, Y., Sinclair, H., Pringle, M., Bickle, M., Chapman, H., Garzanti, E., Ando, S., Huyghe, P., and Mugnier, J. L., 2006, Tectonic evolution of the Himalaya constrained by detrital 40Ar–39Ar, Sm–Nd and petrographic data from the Siwalik foreland basin succession, SW Nepal: Basin Research, v. 18, no. 4, p. 375-391.

Tagami, T., 2005, Zircon fission-track thermochronology and applications to fault studies: Reviews in Mineralogy and Geochemistry, v. 58, no. 1, p. 95-122.

Tagami, T., Galbraith, R. F., Yamada, G. M., and Laslett, G. M., 1998, Revised annealing kinetics of fission-tracks in zircon and geological implications., *in* Van den Haute, P., ed., Advances in Fission Track Geochronology, Volume 99-112: Amsterdam, Kluwer Academic Press.

Tapponnier, P., Peltzer, G., Le Dain, A., Armijo, R., and Cobbold, P., 1982, Propagating extrusion tectonics in Asia: New insights from simple experiments with plasticine: Geology, v. 10, no. 12, p. 611-616.

Tapponnier, P., Zhiqin, X., Roger, F., Meyer, B., Arnaud, N., Wittlinger, G., and Jingsui, Y., 2001, Oblique stepwise rise and growth of the Tibet Plateau: science, v. 294, no. 5547, p. 1671-1677.

Tauxe, L., 1998, Paleomagnetic principles and practice, Dordrecht, Netherlands, Kluwer Acad.

Tewari, V. C., 1993, Precambrian and Lower Cambrian stromatolites of the Lesser Himalaya.: Geophytology, v. 23, p. 19-39.

Thiede, R. C., Arrowsmith, J. R., Bookhagen, B., McWilliams, M., Sobel, E. R., and Strecker, M. R., 2006, Dome formation and extension in the Tethyan Himalaya, Leo Pargil, northwest India: Geological Society of America Bulletin, v. 118, no. 5-6, p. 635-650.

Thiede, R. C., Arrowsmith, J. R., Bookhagen, B., McWilliams, M. O., Sobel, E. R., and Strecker, M. R., 2005, From tectonically to erosionally controlled development of the Himalayan orogen: Geology, v. 33, no. 8, p. 689-692.

Thiede, R. C., Bookhagen, B., Arrowsmith, J. R., Sobel, E. R., and Strecker, M. R., 2004, Climatic control on rapid exhumation along the Southern Himalayan Front: Earth and Planetary Science Letters, v. 222, no. 3, p. 791-806.

Thiede, R. C., and Ehlers, T. A., 2013, Large spatial and temporal variations in Himalayan denudation: Earth and Planetary Science Letters, v. 371, p. 278-293.

Tokuoka, T., Takayasu, K., Yoshida, M., and Hisatomi, K., 1986, The Churia (Siwalik) group of the Arung Khola area, west central Nepal: Memoirs of the Faculty of Science, Shimane University, v. 20, p. 135-210.

Tomlinson, P. B., and Tomlinson, P. B., 1994, The botany of mangroves, Cambridge University Press.

Trauerstein, M., Lowick, S. E., Preusser, F., and Schlunegger, F., 2014, Small aliquot and single grain IRSL and post-IR IRSL dating of fluvial and alluvial sediments from the Pativilca valley, Peru: Quaternary Geochronology, v. 22, p. 163-174.

Traverse, A., 1988, Paleopalynology, Dordrecht, Netherlands, Springer.

Treloar, P. J., Petterson, M. G., Jan, M. Q., and Sullivan, M. A., 1996, A re-evaluation of the stratigraphy and evolution of the Kohistan arc sequence, Pakistan Himalaya: implications for magmatic and tectonic arc-building processes: Journal of the Geological Society, v. 153, no. 5, p. 681-693.

Treloar, P. J., Rex, D. C., Guise, P. G., Coward, M. P., Searle, M. P., Windley, B. F., Petterson, M. G., Jan, M. Q., and Luff, I. W., 1989, K-Ar and Ar-Ar Geochronology of the Himalayan Collision in Nw Pakistan - Constraints on the Timing of Suturing, Deformation, Metamorphism and Uplift: Tectonics, v. 8, no. 4, p. 881-909.

Tye, R. S., and Coleman, J. M., 1989, Depositional processes and stratigraphy of fluvially dominated lacustrine deltas: Mississippi delta plain: Journal of Sedimentary Research, v. 59, no. 6.

Uddin, A., and Lundberg, N., 1999, A paleo-Brahmaputra? Subsurface lithofacies analysis of Miocene deltaic sediments in the Himalayan–Bengal system, Bangladesh: Sedimentary Geology, v. 123, no. 3, p. 239-254.

Uddin, A., and Lundberg, N., 2004, Miocene sedimentation and subsidence during continent–continent collision, Bengal basin, Bangladesh: Sedimentary Geology, v. 164, no. 1, p. 131-146.

Upreti, B., 1999, An overview of the stratigraphy and tectonics of the Nepal Himalaya: Journal of Asian Earth Sciences, v. 17, no. 5, p. 577-606.

Valdiya, K. S., 1980, Geology of Kumaun Lesser Himalaya., Dehra Dun, India, Wadia Institute of Himalayan Geology, 291 p.:

Valdiya, K. S., and Bhatia, S. B., 1980, Stratigraphy and Correlations of Lesser Himalayan Formations: India, Hindustan Publishing Corporation, p. 330.

van der Beek, P., Robert, X., Mugnier, J. L., Bernet, M., Huyghe, P., and Labrin, E., 2006, Late Miocene–recent exhumation of the central Himalaya and recycling in the foreland basin assessed by apatite fission-track thermochronology of Siwalik sediments, Nepal: Basin Research, v. 18, no. 4, p. 413-434.

van Haver, T., 1984, Etude stratigraphique, sedimentologique et structurale d'un bassin d'avant arc: Exemple du bassin de l'Indus, Ladakh, Himalaya: Univ. de Grenoble, France.

Vance, D., Bickle, M., Ivy-Ochs, S., and Kubik, P. W., 2003, Erosion and exhumation in the Himalaya from cosmogenic isotope inventories of river sediments: Earth and Planetary Science Letters, v. 206, no. 3, p. 273-288.

Vance, D., and Harris, N., 1999, Timing of prograde metamorphism in the Zanskar Himalaya: Geology, v. 27, no. 5, p. 395-398.

Vannay, J. C., and Hodges, K. V., 1996, Tectonometamorphic evolution of the Himalayan metamorphic core between Annapurna and Dhaulagiri, central Nepal: Journal of Metamorphic Geology, v. 14, no. 5, p. 635-656.

Verma, R., and Mukhopadhyay, M., 1977, An analysis of the gravity field in northeastern India: Tectonophysics, v. 42, no. 2, p. 283-317.

Vermeesch, P., 2004, How many grains are needed for a provenance study?: Earth and Planetary Science Letters, v. 224, no. 3, p. 441-451.

Vermeesch, P., 2012, On the visualisation of detrital age distributions: Chemical Geology, v. 312, p. 190-194.

Vernant, P., Bilham, R., Szeliga, W., Drupka, D., Kalita, S., Bhattacharyya, A., Gaur, V., Pelgay, P., Cattin, R., and Berthet, T., 2014, Clockwise rotation of the Brahmaputra Valley relative to India: Tectonic convergence in the eastern Himalaya, Naga Hills, and Shillong Plateau: Journal of Geophysical Research: Solid Earth, v. 119, no. 8, p. 6558-6571.

Vögeli, N., Najman, Y., van der Beek, P., Huyghe, P., Wynn, P., Govin, G., Veen, I. v. d., and Sachse, D., in press, Lateral variations in vegetation in the Himalaya since the Miocene and implications for climate evolution: Earth and Planetary Science Letters, v. 471, p. 1-9.

von Fischer, J. C., and Tieszen, L. L., 1995, Carbon isotope characterization of vegetation and soil organic matter in subtropical forests in Luquillo, Puerto Rico: Biotropica, p. 138-148.

Wagner, G. A., and Van den haute, P., 1992, Fission-track dating: Enke, Stuttgart.

Walker, J. D., Martin, M. W., Bowring, S. A., Searle, M. P., Waters, D. J., and Hodges, K. V., 1999, Metamorphism, melting, and extension: Age constraints from the High Himalayan Slab of southeast Zanskar and northwest Lahaul: Journal of Geology, v. 107, no. 4, p. 473-495.

Wallinga, J., Murray, A., and Wintle, A., 2000, The single-aliquot regenerative-dose (SAR) protocol applied to coarse-grain feldspar: Radiation Measurements, v. 32, no. 5, p. 529-533.

Wang, J. G., Wu, F.-Y., Tan, X.-C., and Liu, C.-Z., 2014a, Magmatic evolution of the Western Myanmar Arc documented by U–Pb and Hf isotopes in detrital zircon: Tectonophysics, v. 612, p. 97-105.

Wang, P., Scherler, D., Liu-Zeng, J., Mey, J., Avouac, J.-P., Zhang, Y., and Shi, D., 2014b, Tectonic control of Yarlung Tsangpo Gorge revealed by a buried canyon in Southern Tibet: Science, v. 346, no. 6212, p. 978-981.

Wen, D.-R., Liu, D., Chung, S.-L., Chu, M.-F., Ji, J., Zhang, Q., Song, B., Lee, T.-Y., Yeh, M.-W., and Lo, C.-H., 2008, Zircon SHRIMP U–Pb ages of the Gangdese Batholith and implications for Neotethyan subduction in southern Tibet: Chemical Geology, v. 252, no. 3, p. 191-201.

Whipp, D., Ehlers, T., Braun, J., and Spath, C., 2009, Effects of exhumation kinematics and topographic evolution on detrital thermochronometer data: Journal of Geophysical Research: Earth Surface, v. 114, no. F4.

Whipple, K. X., 2009, The influence of climate on the tectonic evolution of mountain belts: Nature Geoscience, v. 2, no. 2, p. 97-104.

Whipple, K. X., 2014, Can erosion drive tectonics?: Science, v. 346, no. 6212, p. 918-919.

White, N. M., Parrish, R. R., Bickle, M. J., Najman, Y., Burbank, D., and Maithani, A., 2001, Metamorphism and exhumation of the NW Himalaya constrained by U–Th–Pb analyses of detrital monazite grains from early foreland basin sediments: Journal of the Geological Society, v. 158, no. 4, p. 625-635.

White, N. M., Pringle, M., Garzanti, E., Bickle, M., Najman, Y., Chapman, H., and Friend, P., 2002, Constraints on the exhumation and erosion of the High Himalayan Slab, NW India, from foreland basin deposits: Earth and Planetary Science Letters, v. 195, no. 1, p. 29-44.

Wiedenbeck, M., Alle, P., Corfu, F., Griffin, W., Meier, M., Oberli, F., Quadt, A. v., Roddick, J., and Spiegel, W., 1995, Three natural zircon standards for U-Th-Pb, Lu-Hf, trace element and REE analyses: Geostandards newsletter, v. 19, no. 1, p. 1-23.

Wiedenbeck, M., Hanchar, J. M., Peck, W. H., Sylvester, P., Valley, J., Whitehouse, M., Kronz, A., Morishita, Y., Nasdala, L., and Fiebig, J., 2004, Further characterisation of the 91500 zircon crystal: Geostandards and Geoanalytical Research, v. 28, no. 1, p. 9-39.

Wijbrans, J., Pringle, M., Koppers, A., and Scheveers, R., Argon geochronology of small samples using the Vulkaan argon laserprobe, *in* Proceedings Proceedings of the Royal Netherlands Academy of Arts and Sciences1995, Volume 2, p. 185-218.

Willett, S. D., 1999, Orogeny and orography: The effects of erosion on the structure of mountain belts: Journal of Geophysical Research: Solid Earth, v. 104, no. B12, p. 28957-28981.

Willis, B., 1993, Evolution of Miocene fluvial systems in the Himalayan foredeep through a two kilometer-thick succession in northern Pakistan: Sedimentary Geology, v. 88, no. 1, p. 77-121.

Wintle, A. G., and Murray, A. S., 2006, A review of quartz optically stimulated luminescence characteristics and their relevance in single-aliquot regeneration dating protocols: Radiation Measurements, v. 41, no. 4, p. 369-391.

Wizevich, M. C., 1992, Sedimentology of Pennsylvanian quartzose sandstones of the Lee Formation, central Appalachian Basin: fluvial interpretation based on lateral profile analysis: Sedimentary Geology, v. 78, no. 1, p. 1-47.

Wobus, C. W., Hodges, K. V., and Whipple, K. X., 2003, Has focused denudation sustained active thrusting at the Himalayan topographic front?: Geology, v. 31, no. 10, p. 861-864.

Worm, H.-U., Ahmed, A., Ahmed, N., Islam, H., Huq, M., Hambach, U., and Lietz, J., 1998, Large sedimentation rate in the Bengal Delta: magnetostratigraphic dating of Cenozoic sediments from northeastern Bangladesh: Geology, v. 26, no. 6, p. 487-490.

Wu, F.-Y., Ji, W.-Q., Liu, C.-Z., and Chung, S.-L., 2010, Detrital zircon U–Pb and Hf isotopic data from the Xigaze fore-arc basin: constraints on Transhimalayan magmatic evolution in southern Tibet: Chemical Geology, v. 271, no. 1, p. 13-25.

Wu, F. Y., Clift, P. D., and Yang, J. H., 2007, Zircon Hf isotopic constraints on the sources of the Indus Molasse, Ladakh Himalaya, India: Tectonics, v. 26, no. 2.

Xie, X., and Heller, P. L., 2009, Plate tectonics and basin subsidence history: Geological Society of America Bulletin, v. 121, no. 1-2, p. 55-64.

Xu, Y.-G., Yang, Q.-J., Lan, J.-B., Luo, Z.-Y., Huang, X.-L., Shi, Y.-R., and Xie, L.-W., 2012, Temporal–spatial distribution and tectonic implications of the batholiths in the Gaoligong–Tengliang–Yingjiang area, western Yunnan: constraints from zircon U–Pb ages and Hf isotopes: Journal of Asian Earth Sciences, v. 53, p. 151-175.

Yin, A., 2006, Cenozoic tectonic evolution of the Himalayan orogen as constrained by along-strike variation of structural geometry, exhumation history, and foreland sedimentation: Earth-Science Reviews, v. 76, no. 1, p. 1-131.

Yin, A., Dubey, C., Kelty, T., Gehrels, G. E., Chou, C., Grove, M., and Lovera, O., 2006, Structural evolution of the Arunachal Himalaya and implications for asymmetric development of the Himalayan orogen: Current Science, v. 90, no. 2, p. 195-200.

Yin, A., Dubey, C., Webb, A., Kelty, T., Grove, M., Gehrels, G. E., and Burgess, W., 2010, Geologic correlation of the Himalayan orogen and Indian craton: Part 1. Structural geology, U-Pb zircon geochronology, and tectonic evolution of the Shillong Plateau and its neighboring regions in NE India: Geological Society of America Bulletin, v. 122, no. 3-4, p. 336-359.

Yin, A., and Harrison, T. M., 2000, Geologic evolution of the Himalayan-Tibetan orogen: Annual Review of Earth and Planetary Sciences, v. 28, no. 1, p. 211-280.

Zaleha, M. J., 1997, Intra-and extrabasinal controls on fluvial deposition in the Miocene Indo-Gangetic foreland basin, northern Pakistan: Sedimentology, v. 44, no. 2, p. 369-390.

Zander, A., Degering, D., Preusser, F., Kasper, H. U., and Brückner, H., 2007, Optically stimulated luminescence dating of sublittoral and intertidal sediments from Dubai, UAE: Radioactive disequilibria in the uranium decay series: Quaternary Geochronology, v. 2, no. 1, p. 123-128.

Zattin, M., Andreucci, B., Thomson, S. N., Reiners, P. W., and Talarico, F. M., 2012, New constraints on the provenance of the ANDRILL AND-2A succession (western Ross Sea, Antarctica) from apatite triple dating: Geochemistry, Geophysics, Geosystems, v. 13, no. 10.

Zeitler, P. K., Koons, P. O., Hallet, B., and Meltzer, A. S., 2015, Comment on “Tectonic control of Yarlung Tsangpo Gorge revealed by a buried canyon in southern Tibet”: Science, v. 349, no. 6250, p. 799-799.

Zeitler, P. K., Meltzer, A. S., Brown, L., Kidd, W. S., Lim, C., and Enkelmann, E., 2014, Tectonics and topographic evolution of Namche Barwa and the easternmost Lhasa block, Tibet, *in* Nie, J., Hoke, G.D., Horton, B., ed., Towards an Improved Understanding of Uplift Mechanisms and the Elevation History of the Tibetan Plateau., Geological Society of America Special Papers, p. 23-58.

Zeitler, P. K., Meltzer, A. S., Koons, P. O., Craw, D., Hallet, B., Chamberlain, C. P., Kidd, W. S., Park, S. K., Seeber, L., and Bishop, M., 2001, Erosion, Himalayan geodynamics, and the geomorphology of metamorphism: GSA Today, v. 11, no. 1, p. 4-9.

Zhang, J., Yin, A., Liu, W., Wu, F., Lin, D., and Grove, M., 2012, Coupled U-Pb dating and Hf isotopic analysis of detrital zircon of modern river sand from the Yalu River (Yarlung Tsangpo) drainage system in southern Tibet: Constraints on the transport processes and evolution of Himalayan rivers: Geological Society of America Bulletin, v. 124, no. 9-10, p. 1449-1473.

Zhang, R., Xu, W., Guo, J., Zong, K., Cai, H., and Yuan, H., 2007, Zircon U-Pb and Hf isotopic composition of deformed granite in the southern margin of the Gangdese belt, Tibet:

Evidence for Early Jurassic subduction of Neo-Tethyan oceanic slab: Acta Petrologica Sinica, v. 23, no. 6, p. 1347-1353.

Zhao, W., Nelson, K., Che, J., Quo, J., Lu, D., Wu, C., and Liu, X., 1993, Deep seismic reflection evidence for continental underthrusting beneath southern Tibet: Nature, v. 366, no. 6455, p. 557-559.

Zhu, D.-C., Mo, X.-X., Niu, Y., Zhao, Z.-D., Wang, L.-Q., Liu, Y.-S., and Wu, F.-Y., 2009, Geochemical investigation of Early Cretaceous igneous rocks along an east–west traverse throughout the central Lhasa Terrane, Tibet: Chemical Geology, v. 268, no. 3, p. 298-312.

Zhu, D.-C., Zhao, Z.-D., Niu, Y., Mo, X.-X., Chung, S.-L., Hou, Z.-Q., Wang, L.-Q., and Wu, F.-Y., 2011, The Lhasa Terrane: record of a microcontinent and its histories of drift and growth: Earth and Planetary Science Letters, v. 301, no. 1, p. 241-255.

Zhuang, G., Najman, Y., Guillot, S., Roddaz, M., Antoine, P.-O., Métais, G., Carter, A., Marivaux, L., and Solangi, S. H., 2015, Constraints on the collision and the pre-collision tectonic configuration between India and Asia from detrital geochronology, thermochronology, and geochemistry studies in the lower Indus basin, Pakistan: Earth and Planetary Science Letters, v. 432, p. 363-373.

Zoback, M. D., and Townend, J., 2001, Implications of hydrostatic pore pressures and high crustal strength for the deformation of intraplate lithosphere: Tectonophysics, v. 336, no. 1, p. 19-30.